

AWARD NUMBER: W81XWH-18-1-0431

TITLE: Receptors in Endosomes Mediate Chronic Pain Associated with Trauma and Stress: Nonopioid Targets for Pain

PRINCIPAL INVESTIGATOR: Nigel Bunnett, PhD

CONTRACTING ORGANIZATION: Columbia University Medical Center
New York, NY 10032

REPORT DATE: September 2019

TYPE OF REPORT: Annual

PREPARED FOR: U.S. Army Medical Research and Materiel Command
Fort Detrick, Maryland 21702-5012

DISTRIBUTION STATEMENT: Approved for Public Release;
Distribution Unlimited

The views, opinions and/or findings contained in this report are those of the author(s) and should not be construed as an official Department of the Army position, policy or decision unless so designated by other documentation.

REPORT DOCUMENTATION PAGE

Form Approved
OMB No. 0704-0188

Public reporting burden for this collection of information is estimated to average 1 hour per response, including the time for reviewing instructions, searching existing data sources, gathering and maintaining the data needed, and completing and reviewing this collection of information. Send comments regarding this burden estimate or any other aspect of this collection of information, including suggestions for reducing this burden to Department of Defense, Washington Headquarters Services, Directorate for Information Operations and Reports (0704-0188), 1215 Jefferson Davis Highway, Suite 1204, Arlington, VA 22202-4302. Respondents should be aware that notwithstanding any other provision of law, no person shall be subject to any penalty for failing to comply with a collection of information if it does not display a currently valid OMB control number. **PLEASE DO NOT RETURN YOUR FORM TO THE ABOVE ADDRESS.**

| | | | | | |
|--|--------------------|---|-----------------------------------|--|--|
| 1. REPORT DATE September 2019 | | 2. REPORT TYPE Annual Technical/Progress Report | | 3. DATES COVERED 1Sep2018 - 31Aug2019 | |
| 4. TITLE AND SUBTITLE Receptors in Endosomes Mediate Chronic Pain Associated with Trauma and Stress: Nonopioid Targets for Pain | | | | 5a. CONTRACT NUMBER W81XWH-18-1-0431 | |
| | | | | 5b. GRANT NUMBER PR170507 | |
| | | | | 5c. PROGRAM ELEMENT NUMBER | |
| 6. AUTHOR(S) Nigel Bunnett, PhD E-Mail: nb2733@cumc.columbia.edu | | | | 5d. PROJECT NUMBER 0011176521-0001 | |
| | | | | 5e. TASK NUMBER | |
| | | | | 5f. WORK UNIT NUMBER | |
| 7. PERFORMING ORGANIZATION NAME(S) AND ADDRESS(ES) Trustees of Columbia University in the City of New York 630 W 168 th St Fl 4 New York, NY 10032-3725 | | | | 8. PERFORMING ORGANIZATION REPORT NUMBER 268 | |
| 9. SPONSORING / MONITORING AGENCY NAME(S) AND ADDRESS(ES) U.S. Army Medical Research and Materiel Command Fort Detrick, Maryland 21702-5012 | | | | 10. SPONSOR/MONITOR'S ACRONYM(S) | |
| | | | | 11. SPONSOR/MONITOR'S REPORT NUMBER(S) | |
| 12. DISTRIBUTION / AVAILABILITY STATEMENT Approved for Public Release; Distribution Unlimited | | | | | |
| 13. SUPPLEMENTARY NOTES | | | | | |
| 14. ABSTRACT The grant seeks to determine whether G protein-coupled receptors (GPCRs) in endosomes, rather than at the plasma membrane, are mediators and therapeutic targets for chronic pain. Aim 1 examines whether GPCRs in endosomes control activity of ion channels and expression of genes that induce sustained neuronal excitation. Aim 2 determines whether endosomally-targeted antagonists inhibit channel activity, gene expression and hyperexcitability of neurons. Aim 3 evaluates the therapeutic potential of endosomally-targeted GPCR antagonists in trauma- and stress-induced pain relevant to military personnel. Progress has been made in all aims. Neuropeptides (substance P, calcitonin gene-related peptide) and proteases (trypsin) stimulated GPCR endocytosis and evoked sustained signals and hyperexcitability in pain-sensing neurons. Dynamin and clathrin inhibitors suppressed endocytosis, signaling and hyperexcitability. Therapies have been developed to block endosomal signaling and evaluated in preclinical models of trauma- and stress-induced pain. Therapies include: dynamin and clathrin inhibitors; lipid-conjugated antagonists that accumulate in endosomes; antagonists encapsulated into nanoparticles that disassemble in acidic endosomes. These antagonists effectively reversed nociception in preclinical models of visceral pain, migraine pain, and nerve injury pain. They were more effective than conventional antagonists of plasma membrane GPCRs. Thus, endosomal GPCRs have been identified as major mediators and therapeutic targets for chronic pain. | | | | | |
| 15. SUBJECT TERMS Chronic pain; neuropathic pain; head injury pain; migraine pain; irritable bowel syndrome pain; G protein-coupled receptors; endosomes; analgesics. | | | | | |
| 16. SECURITY CLASSIFICATION OF: | | | 17. LIMITATION OF ABSTRACT | 18. NUMBER OF PAGES | 19a. NAME OF RESPONSIBLE PERSON |
| a. REPORT | b. ABSTRACT | c. THIS PAGE | | | 19b. TELEPHONE NUMBER (include area code) |
| Unclassified | Unclassified | Unclassified | Unclassified | 268 | USAMRMC |

Table of Contents

| | <u>Page</u> |
|---|-------------|
| 1. Introduction..... | 4 |
| 2. Keywords..... | 4 |
| 3. Accomplishments..... | 4 |
| 4. Impact..... | 12 |
| 5. Changes/Problems..... | 12 |
| 6. Products..... | 12 |
| 7. Participants and Other Collaborating Organizations..... | 14 |
| 8. Special Reporting Requirements..... | 19 |
| 11. Appendices..... | 20 |

1. INTRODUCTION

G protein-coupled receptors (GPCRs) are the largest class of transmembrane signaling proteins. They control most physiological and pathological processes, including pain, and the target of over one third of FDA-approved drugs. GPCRs are traditionally considered to function at the plasma membrane, allowing cells to detect extracellular ligands. However, plasma membrane signaling is transient, and activated GPCRs usually undergo clathrin- and dynamin-mediated endocytosis. Endosomes were once considered merely conduits for GPCR trafficking to recycling or degradatory pathways. This grant investigates the novel concept that endosomes are a vital site for continued GPCR signaling in pain-sensing neurons that mediates sustained neuronal activity and pain. Thus, selective antagonists of endosomal GPCRs might provide superior relief from chronic pain than conventional drugs that are designed to target GPCRs at the plasma membrane. The inability of such drugs to effectively engage GPCRs in acidic endosomes might explain their lack of efficacy in clinical trials of chronic pain. The application focuses on receptors for neuropeptides (substance P [SP] neurokinin 1 receptor [NK₁R]; calcitonin gene-related peptide [CGRP] calcitonin like receptor [CLR]) and proteases (protease-activated receptor-2 [PAR₂]). These receptors have been implicated in nerve injury pain, migraine pain, and colonic pain of irritable bowel syndrome (IBS).

2. KEY WORDS

Chronic pain; neuropathic pain; head injury pain; migraine pain; irritable bowel syndrome pain; G protein-coupled receptors; endosomes; analgesics

3. ACCOMPLISHMENTS

Goals of Project. The table indicates approved Statement of Work tasks, date of completed tasks, and percentage of tasks accomplished by those dates.

Abbreviations: GPCR, G Protein-Coupled Receptor; DRG, Dorsal Root Ganglia; PAR₂, Protease-Activated Receptor-2; NK₁R, Neurokinin 1 Receptor; CLR, Calcitonin Receptor-like Receptor; TRP, Transient Receptor Potential (ion channel); muGFP, monomeric ultrastable Green Fluorescent Protein; IBS-D, Irritable Bowel Syndrome, Diarrhea-Predominant; HC, Healthy Control; ABP, Activity-Based Probe; PTH, Post Traumatic Headache; FRET, Förster Resonance Energy Transfer; BRET, Bioluminescence Resonance Energy Transfer; RNA-Seq, RNA Sequencing

| Aim 1: To determine whether GPCRs in endosomes of pain-sensing neurons control the activity of ion channels and the transcription of genes that induce sustained neuronal excitation. | Date | % |
|--|-------------|----------|
| Major Task 1: Determine whether endosomal PAR ₂ in DRG neurons generates compartmentalized signals that regulate channel activity and sensitization | | |
| <u>Subtask 1:</u> Establish breeding colonies of PAR ₂ -muGFP mice. | 1/1/19 | 100 |
| <u>Subtask 2:</u> Analyze endocytosis-dependent compartmentalized signaling in DRG neurons | 1/1/19 | 100 |
| <u>Subtask 3:</u> Assess PAR ₂ -mediated sensitization and TRP channel activation in DRG neurons | 1/1/19 | 50 |
| Major Task 2: Determine whether proteases in human colon biopsy specimens activate endosomal PAR ₂ in DRG neurons to generate signals that regulate channel activity and sensitization | | |

| | | |
|---|--------|-----|
| <u>Subtask 1:</u> Collect and process human colon biopsies from IBS-D (N=50) and HC (N=50) patients | 8/1/19 | 25 |
| <u>Subtask 2:</u> Determine whether proteases in human IBS-D biopsies sensitize DRG neurons and activate TRP channel through endosomal PAR ₂ . | 8/1/19 | 50 |
| <u>Subtask 3:</u> Profile activated serine and cysteine proteases in supernatants of IBS-D and HC biopsies using ABPs | 8/1/19 | 10 |
| Major Task 3: Determine whether endosomal PAR ₂ , NK ₁ R and CLR signals regulate transcription in pain-sensing neurons | | |
| <u>Subtask 1:</u> Determine whether endosomal PAR ₂ , NK ₁ R and CLR signaling regulates transcription in DRG and spinal neurons | 8/1/19 | 10 |
| Aim 2: To determine whether endosomally-targeted antagonists inhibit endosomal GPCR signaling, channel activation, gene transcription and sustained hyperexcitability of pain-sensing neurons. | | |
| <u>Subtask 1:</u> Generate small molecule tripartite PAR ₂ , NK ₁ R and CLR antagonists; generate small molecule quadripartite NK ₁ R and CLR antagonists; generate fluorescent probes | 8/1/19 | 100 |
| Major Task 1: Determine whether tripartite and quadripartite antagonists disrupt endosomal PAR ₂ , NK ₁ R and CLR signaling in HEK293 cells | | |
| <u>Subtask 1:</u> Determine whether lipidated antagonists disrupt ligand/receptor interactions in endosomes | 8/1/19 | 75 |
| <u>Subtask 2:</u> Determine whether lipidated antagonists inhibit endosomal signaling of PAR ₂ , NK ₁ R and CLR in HEK293 cells | 8/1/19 | 100 |
| Major Task 2: Determine whether tripartite and quadripartite antagonists target PAR ₂ in endosomes of DRG neurons and NK ₁ R and CLR in endosomes of spinal neurons, and inhibit endosomal signaling | | |
| <u>Subtask 1:</u> Determine whether tripartite and quadripartite antagonists colocalize with PAR ₂ , NK ₁ R and CLR on endosomes of pain-sensing neurons | 8/1/19 | 75 |
| <u>Subtask 2:</u> Determine whether tripartite and quadripartite antagonists inhibit endosomal signaling of PAR ₂ , NK ₁ R and CLR in pain-sensing neurons | 8/1/19 | 75 |
| Major Task 3: Determine whether tripartite and quadripartite antagonists disrupt PAR ₂ -induced sensitization and transcription in DRG neurons and NK ₁ R- and CLR-induced sensitization and transcription in spinal neurons | | |
| <u>Subtask 1:</u> Determine whether tripartite and quadripartite antagonists inhibit sensitization and TRP activation in neurons | 8/1/19 | 50 |
| <u>Subtask 2:</u> Examine whether antagonists suppress gene expression | 8/1/19 | 0 |
| Aim 3: To investigate the therapeutic potential of endosomally-targeted GPCR antagonists in trauma- and stress-induced pain that is relevant to disorders of military personnel and veterans. | | |
| Major Task 1: Conduct studies in preclinical model of migraine headache to determine feasibility of using tripartite CLR antagonists for migraine pain. | | |

| | | |
|--|--------|-----|
| <u>Subtask 1:</u> Generate tripartite antagonists of PAR ₂ , NK ₁ R and CLR; generate quadripartite probes for NK ₁ R and CLR antagonists, similar to Aim 2 above | 8/1/19 | 100 |
| <u>Subtask 2:</u> Develop a GTN-evoked model of migraine headache pain in C57BL/6 mice | 8/1/19 | 50 |
| <u>Subtask 3:</u> Determine efficacy of tripartite or non-lipidated CLR antagonists | 8/1/19 | 50 |
| Major Task 2: Conduct studies in preclinical model of nerve injury pain to determine feasibility of using quadripartite NK ₁ R/CLR antagonists for nerve injury pain. | | |
| <u>Subtask 1:</u> Develop a spared nerve injury model of neuropathic pain in C57BL/6 mice | 8/1/19 | 50 |
| <u>Subtask 2:</u> Determine efficacy of quadripartite NK ₁ R/CLR antagonists and non-lipidated antagonists | 8/1/19 | 50 |
| Major Task 3: Conduct studies in preclinical model of IBS pain to determine feasibility of using tripartite PAR ₂ antagonists for post-inflammatory IBS pain. | | |
| <u>Subtask 1:</u> Generate an IBS mouse model in C57BL/6 mice | 8/1/19 | 50 |
| <u>Subtask 2:</u> Training of electrophysiologist in Dr. Schmidt's laboratory by Dr. Bunnett's team on visceromotor responses following graded colorectal distention | 8/1/19 | 10 |
| <u>Subtask 3:</u> Determine efficacy of tripartite PAR ₂ antagonists and non-lipidated antagonists | 8/1/19 | 10 |

Accomplishments

a. Knockin mice to study GPCR trafficking. Many antibodies to GPCRs lack selectivity. Antibodies cannot be readily used to study trafficking of GPCRs in real time. To surmount these challenges, we have generated knockin mice expressing GPCRs of interest (PAR₂, NK₁R) tagged with either GFP or a Flag epitope. The characterization of these mice is complete and manuscripts are in preparation.

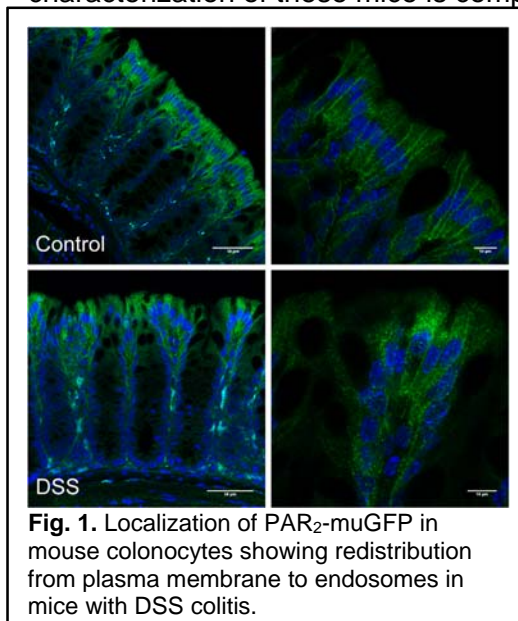


Fig. 1. Localization of PAR₂-muGFP in mouse colonocytes showing redistribution from plasma membrane to endosomes in mice with DSS colitis.

Par₂-muGFP mice. We generated knockin mice in which muGFP was fused to the C-terminus of mouse PAR₂ (*Par₂-muGFP* mice), as described in the original grant. In brief, a 7.9 Kb segment of genomic DNA containing exon 2 of the murine *Par₂* gene was sub-cloned from the C57 mouse genomic BAC clone RP23-143N17 into a high copy plasmid. A targeting construct was generated comprising *Par₂-muGFP*, a downstream phosphoglycerine kinase neomycin cassette flanked by loxP sites (floxed PGK neomycin cassette), and a downstream KpnI site for Southern screening of the ES cells. The targeting vector electroporated into Bruce4 (C57BL/6) ES cells. Selection in G418 generated clonal cells expressing the construct. Clones were injected into BalbC mouse blastocysts. Chimeras were generated and bred with wild-type C57/BL6 mice to generate black F1 progeny, which were bred. We have used these mice to localize PAR₂ and examine trafficking in tissue explants and *in vivo*. PAR₂-muGFP was abundantly expressed in epithelial cells (e.g., colonocytes, keratinocytes) and expressed in lower levels in neurons. In the unstimulated state, PAR₂-muGFP was mostly confined to the plasma membrane (**Fig. 1**). However, in mice with colitis (induced with dextran sodium sulfate, DSS), PAR₂-muGFP was redistributed to endosomes, which is attributable to protease-

evoked activation. When explants of colon or DRG neurons were incubated with PAR₂ agonists, PAR₂-muGFP was also redistributed to endosomes. Thus, we have generated and characterized *Par₂-muGFP* mice, which can be used to study endocytosis and endosomal signaling of PAR₂.

Flag-hNK₁R mice. Knockin mice were generated in which the full length human NK₁R (407 aa) was fused to an extracellular N-terminal Flag epitope (DYKDDDDA) (Flag-hNK₁R) and expressed under control of the mouse promoter, as described in the original grant. The targeting vector was generated by homologous recombination using a 10 Kb segment of mouse genomic DNA from a C57 BAC clone (RP23-143N17). Synthetic cDNA encoding human NK₁R407 was codon optimized for mouse. The targeting construct comprised a tdTomato reporter followed by a 2A self-cleaving peptide incorporated upstream from the Flag-hNK₁R cDNA; tdTomato reporter cleaved from Flag-hNK₁R at the 2A site would identify NK₁R expressing cells. A phosphoglycerine kinase neomycin cassette flanked by loxP sites (floxed PGK neomycin cassette) was incorporated downstream from the Flag-hNK₁R cDNA. The cassette was inserted at the ATG site of mouse NK₁R and deleted the first coding exon of NK₁R. The targeting vector was electroporated into Bruce4 (C57BL/6) ES cells. Selection in G418 generated clones that were injected into BalbC mouse blastocysts. Male chimeras were generated from all clones, and were bred with female wild-type C57/BL6 mice. F1 progeny were generated and bred.

b. Lipidated antagonists of endosomal GPCRs. To generate antagonists of endosomal GPCRs, we conjugated peptidic and small molecule antagonists to PEG12 and the transmembrane lipid cholesterol (tripartite antagonists). We have reported that tripartite antagonists of NK₁R, CLR and PAR₂ effectively inhibit endosomal signaling of GPCRs and suppress sustained neuronal excitation. They provide more effective relief from pain than conventional antagonists of plasma membrane GPCRs. We have further characterized the mechanism of action of these tripartite antagonists, and also characterized quadripartite probes in which antagonists of two GPCRs are conjugated to PEG12 and cholesterol. These studies are largely completed and manuscripts are in preparation.

Tripartite NK₁R antagonists. To target endosomal receptors, we conjugated the NK₁R peptide antagonist Spantide I to cholesterol, a sterol-based lipid anchor that promotes membrane association and internalization. The potential for lipidated antagonists to regulate receptor trafficking and spatiotemporal NK₁R signaling was assessed using live cell imaging, biophysical approaches and nociceptive behavioral assays. While the soluble antagonist Spantide provided short-term inhibition of cell surface processes, lipid conjugation provided sustained inhibition of β -arrestin coupling, plasma membrane-delimited signaling, and selective inhibition NK₁R endosomal-derived nuclear ERK activity and cytosolic cAMP production. Nociceptive assays demonstrated that Span-Chol, but not a Cholesterol-PEG conjugate, provided sustained analgesia. These studies demonstrate that membrane-anchoring enhances the intracellular drug distribution of GPCR antagonists for sustained inhibition of endosomal receptor signaling and pain transmission.

To further understand how lipid-anchored drugs may target the NK₁R in endosomes, we synthesized and characterized a lipid-drug conjugate comprising the NK₁R antagonist Spantide I, conjugated to cholestanol and Cyanine-5 (Cy5-PEG-Chol-Span). Live cell fluorescence microscopy revealed the intracellular distribution of Cy5-PEG-Chol-Span relative to SP-stimulated NK₁R, and quantitative FRET analyses confirmed that lipidated

ligand-receptor interactions can occur at the plasma membrane and in endosomes. This study confirms that lipid anchors alter the subcellular distribution of antagonists, and demonstrates the utility of a fluorescent lipidated antagonist as a drug discovery tool for quantitative assessment of endosomal GPCR-ligand binding.

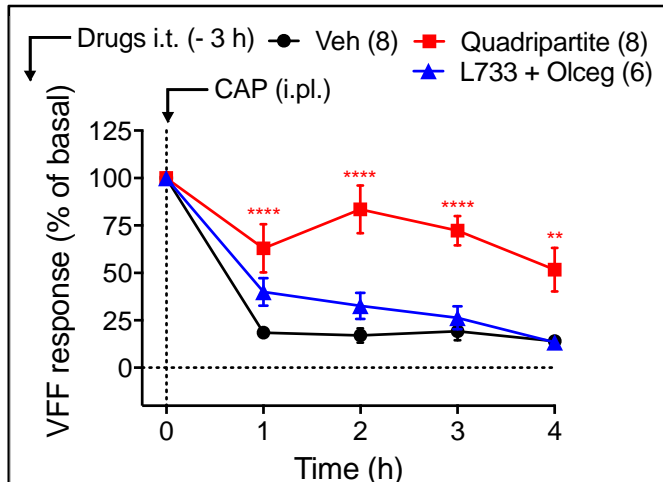


Fig. 2. Intrathecal (i.t.) injection of a quadripartite probe (L7330660 NK₁R antagonist plus Olcegepant CLR antagonist conjugated to PEG and cholestanol) provided more complete anti-nociception than the combination of non-conjugated drugs in mice treated with capsaicin (CAP, intraplantar). (N).

Quadripartite NK₁R and CLR antagonists. Painful stimuli evoke the corelease of SP and CGRP from primary sensory neurons within the dorsal horn of the spinal cord, where these peptides might coactivate NK₁R and CLR on second order spinal neurons. Thus, the simultaneous antagonists of both receptors might be required for optimal control of pain. To accomplish such antagonism, we have generated and characterized quadripartite probes in which antagonists of the NK₁R (L7330660) and CLR (Olcegepant) are coupled to PEG12 and cholestanol. Although NK₁R and CLR antagonists had anti-nociceptive actions when administered separately to mice, the administration of a cholestanol-conjugated dual antagonist provided superior anti-nociception (**Fig. 2**).

c. Endosomal signaling of GPCRs and IBS colonic pain. A study has been completed and published that describes the role of endosomal PAR₂ signaling for sustained hyperexcitability of nociceptors and colonic pain. PAR₂ has been proposed to mediate pain in patients with irritable bowel syndrome (IBS). PAR₂ is robustly internalized upon activation and can continue to signal from endosomes. However, whether PAR₂ in endosomes generate signals that contribute to human disease is unknown. Trypsin, cathepsin-S (CS) and neutrophil elastase (NE), which are activated in the colonic mucosa of patients with IBS and in experimental animals with colitis, caused persistent PAR₂-dependent hyperexcitability of nociceptors, sensitization of colonic afferent neurons to mechanical stimuli, and somatic mechanical allodynia. Inhibitors of clathrin- and dynamin-dependent endocytosis and of mitogen-activated protein kinase kinase-1 prevented trypsin-induced hyperexcitability, sensitization and allodynia. However, they did not affect NE- or CS-induced hyperexcitability, sensitization or allodynia. Trypsin stimulated endocytosis of PAR₂, which signaled from endosomes to activate extracellular signal regulated kinase. NE and CS did not stimulate endocytosis of PAR₂, which signaled from the plasma membrane to activate adenylyl cyclase. Biopsies of colonic mucosa from IBS patients released proteases that induced persistent PAR₂-dependent hyperexcitability of nociceptors, and PAR₂ association with β-arrestins, which mediate endocytosis. Conjugation to cholestanol promoted delivery and retention of antagonists in endosomes containing PAR₂. A cholestanol-conjugated PAR₂ antagonist prevented persistent trypsin- and IBS protease-induced hyperexcitability of nociceptors. The results reveal that PAR₂ signaling from endosomes underlies the persistent hyperexcitability of nociceptors that mediates chronic pain of IBS. Endosomally-targeted PAR₂ antagonists are potential therapies for IBS pain. GPCRs in endosomes transmit signals that contribute to human diseases.

d. Nanoparticle-encapsulated antagonists of endosomal GPCRs. We have used an alternative approach to target GPCRs in endosomes that entails incorporation into pH-responsive nanoparticles. This work has been resubmitted and is under review. Stimulus-responsive nanoparticles (NPs) are widely used to release drug payloads in specific tissues, such as tumors to induce cytotoxicity, but are seldom used to precisely control disease-relevant intracellular signaling events. During chronic pain, the SP NK₁R redistributes from the plasma membrane to acidified endosomes, where it signals to maintain pain. Hence, the NK₁R in endosomes is a key pain target. We investigated the potential for soft polymeric pH-responsive NPs to alter the distribution and efficacy of an FDA-approved NK₁R antagonist (Aprepitant, AP), which is used for treatment of emesis.

To obtain pH-responsive NPs, we synthesized diblock copolymers a hydrophilic shell of P(PEGMA-co-DMAEMA) and a hydrophobic core of P(DIPMA-co-DEGMA). To examine pH-dependent disassembly, NPs were loaded with Nile Red (NR), which fluoresces only in the hydrophobic NP core. DIPMA-NR fluorescence declined with increasing buffer acidity, with a 50% decrease in fluorescence at pH 6.08 ± 0.06, consistent with the protonation of the tertiary amine (pK_a 6.1) of DIPMA and resultant disassembly. The uptake and intracellular trafficking of DIPMA NPs labeled with Cyanine 5 (DIPMA-Cy5) was examined by confocal microscopy. DIPMA-Cy5 NPs were extensively localized to NK₁R-positive early endosomes. We examined the kinetics and mechanism of cellular uptake and disassembly of DIPMA NPs loaded with Coumarin153 (DIPMA-CO), which fluoresces in an aqueous environment but not in the hydrophobic core, by confocal microscopy. When DIPMA-CO NPs were incubated with HEK-293 cells, there was a marked increase in intracellular fluorescence. Inhibitors of clathrin, dynamin, and endosomal acidification all attenuated fluorescence. These results are consistent with clathrin- and dynamin-dependent endocytosis of NPs, and pH-dependent disassembly of NPs in endosomes.

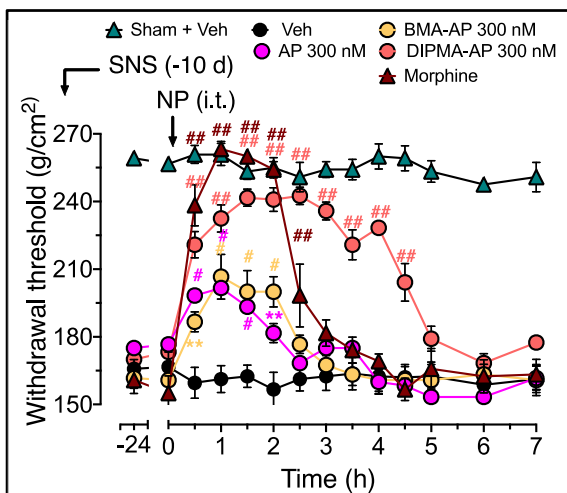


Fig. 3. Intrathecal (i.t.) injection of Aprepitant (AP) in a pH-tunable DIPMA NP provided more complete and sustained anti-nociception in rats with the sural nerve spared (SNS) model of 10 d neuropathic pain compared to free AP, AP in a stable BMA NP, morphine or vehicle (Veh). N=6 per group.

To examine the hypothesis that incorporation into NPs enhances the anti-nociceptive actions of AP due to delivery to NK₁R-positive endosomes in spinal neurons, AP formulations were administered to mice or rats. Acute nociceptive pain and chronic inflammatory and neuropathic pain were examined. NPs or free AP was administered by intrathecal injection. Nociception was examined in mice after intraplantar injection of capsaicin (evokes acute nociceptive pain) or complete Freund's adjuvant (chronic inflammatory pain), and in rats after spared sural nerve injury (evokes chronic neuropathic pain). Paw withdrawal responses to mechanical stimuli (von Frey filaments, Randal-Selitto test) were assessed. In all models, DIPMA-AP produced larger and more sustained anti-nociception than free AP (**Fig. 3**). The therapeutic efficacy of DIPMA-AP was superior to morphine. Thus, encapsulation into pH-responsive DIPMA NPs enhances the anti-nociceptive actions of AP in models of acute, inflammatory and neuropathic nociception in two species, increasing the magnitude and duration of the response.

These results demonstrate that NP approaches have potential beyond bulk drug delivery for cancer therapy and in fields where,

to date, their applicability has been unrecognized. The use of NPs to direct drugs to subcellular compartments from which GPCRs can generate persistent signals that underlie disease has broad applicability. The discovery that encapsulation within NPs allows delivery of antagonists to GPCRs within endosomes to enhance and prolong their analgesic properties provides opportunities for the development of much-needed non-opioid

therapies for pain.

e. Activity-based probes for protease profiling in diseased tissues. An important objective of the grant is to profile proteases that are activated in diseased tissues collected from veterans with IBS and healthy control subjects. The collection of these specimens is underway (~10 specimens have been collected from IBS and control patients). Since proteases are regulated by post-translational control of activity, rather than by gene or protein expression, profiling requires assessment of protease activity. Activity-based probes, which covalently bind to activated proteases, are the state-of-the-art tools for protease profiling. We have developed two new probes. Manuscripts are under review.

Cathepsin Probes. Cathepsin X/Z/P is cysteine cathepsin with unique carboxypeptidase activity. Its expression has been associated with several diseases, although its roles during normal physiology are still poorly understood. Advances in our understanding of its function have been hindered by a lack of available tools that can specifically measure the proteolytic activity of cathepsin X. We identified a series of new activity-based probes that incorporate a novel sulfoxonium ylide warhead. These probes exhibited improved specificity and potency for cathepsin X compared to previously reported probes. We demonstrated the ability of these probes to detect the activity of cathepsin X in cell and tissue lysates, in live cells and *in vivo* and to localize active cathepsin X in mouse tissues by confocal microscopy. We demonstrated that the most optimal probe, sCy5-Nle-SY, is efficacious in clinical cancer samples and that cathepsin X activity is strongly upregulated in human oral squamous carcinoma tissue compared to patient-matched normal oral mucosa. Finally, we developed an improved method to generate chloromethylketones, necessary intermediates for synthesis of acyloxymethylketones probes, by way of sulfoxonium ylide intermediates. Sulfoxonium ylide probes are more potent and specific than the acylmethylketone analogues, further validating the utility of this new warhead. These new probes will be valuable for investigating cathepsin X pathophysiology and for validating its proteolytic activity as a clinical biomarker for multiple diseases.

Elastase Probes. NE, a serine protease, is implicated in the pathogenesis of inflammatory bowel disease. Due to post-translational control of its activation and the high expression of its inhibitors in the gut, measurements of total expression (mRNA or protein) poorly reflect the activation status of NE. Fluorogenic substrate probes have previously been used to measure neutrophil elastase activity, though these tools lack specificity and traceability. PK105 is a recently described fluorescent activity-based probe, which binds to NE in an activity-dependent manner. The covalent, irreversible nature of this probe allows for accurate identification of its targets in complex protein mixtures. We characterized the reactivity of profile of PK105b, a close analogue of PK105, against recombinant serine proteases and in tissue extracts from healthy mice and from models of inflammation induced by oral cancer and *Legionella* infection. We ultimately applied PK105b to measure NE activation in an acute model of experimental colitis. NE activity was detected in inflamed, but not healthy colons, and the active species corresponded to a unique maturation form of NE that was not present in healthy tissue. We corroborated this finding in mucosal biopsies from patients with inflammatory bowel disease. Thus, PK105b is a new tool that facilitates detection of NE activity in complex protein lysates, and we have applied it to demonstrate, explicitly for the first time, its activation during colitis. This method will be critical for further functional studies of NE activation and for validating this important protease as a therapeutic target during inflammation of the gut.

Training and Professional Development

Opportunities for training and professional development include mentoring of post-doctoral fellows, graduate students and visiting scientists. Trainees learn laboratory skills from experience investigators, and receive mentorship from the PI on literature reviews, experimental design, data analysis, scientific writing and presentation. They attend weekly laboratory meetings and journal clubs, and attend symposia and seminars at

Columbia University.

Rocco Latorre PhD and Alan Hegron PhD are postdoctoral fellows mentored by the PI. They attend weekly laboratory meetings and journal clubs, and attend symposia and seminars at Columbia University.

Shavonne Teng is a graduate student from the Department of Physiology at Columbia University who completed a rotation in the PI's laboratory, where she participated in the characterization of *par₂-muGFP* mice. She was trained in experimental skills and was mentored by the PI. Ms. Shavonne attended symposia and seminars at Columbia University on receptor signaling, pain and itch.

Zachary Snow is a medical student at Columbia University who completed a summer project in the PI's laboratory to examine endosomal signaling of GPCRs. He was trained to study endosomal signaling in model cell lines. Mr. Snow attended symposia and seminars at Columbia University on receptor signaling and pain.

Dissemination of Results

The Bunnett and Schmidt laboratories meet as a group each month to evaluate progress, provide feedback on technical issues and results, arrange transfer of mice and chemical resources, and trouble-shoot problems. Technical methods specific to the project are discussed. Member of the laboratory including students, postdoctoral fellows, scientists and principal investigators attend this joint laboratory meeting.

Dr. Bunnett has presented findings at the following meetings and seminar series:

2018

International Neuroscience Winter Conference, Solden, Austria
Gordon Conference on Proteolytic Enzymes and Their Inhibitors, Tuscany, Italy
Department of Pharmacology, Icahn School of Medicine, Mt. Sinai

2019

National Center for Advancing Translational Science, Washington DC
The Opioid Crisis and the Future of Addiction and Pain Therapeutics: Opportunities, Tools, and Technologies Symposium, NIH Washington DC
US Army Medical Research and Materiel Command Congressionally Directed Medical Research Programs: Chronic Pain Management Research Program Stakeholders Meeting, Baltimore, MD
9th Congress of Federation of Asian and Oceanian Physiological Societies, Kobe, Japan
American Gastroenterological Association, San Diego, CA
Biogen, Boston, MA.

Plans for Next Reporting Period

Priorities for the next reporting period include:

Analysis of the contribution of endosomal GPCR signaling to neuropeptide- and protease-evoked gene expression and TRP channel activity in pain-sensing neurons.

Collection of biopsies of colonic mucosa from veterans suffering from IBS and from healthy control subjects, and profiling of activated proteases using activity-based probes, including newly developed and existing probes for serine and cysteine proteases. Investigation of whether activate proteases cause hyperexcitability of nociceptors

via endosomal PAR₂.

Analysis of the contribution of endosomal CLR signaling to migraine pain using endocytosis inhibitors and lipidated and nanoparticle-encapsulated CLR antagonists.

Generation of nanoparticles designed to target pain-sensing neurons and containing antagonists of multiple endosomal GPCRs. Characterization of such nanoparticles in model cells, primary neurons and preclinical models of nerve injury, migraine and IBS pain.

4. IMPACT

Impact on principal discipline. This work has identified new targets for the treatment of chronic pain. We have discovered that painful stimuli cause the translocation of receptors from the cell surface to endosomes of neurons that sense and transmit pain. Receptors in endosomes are primarily responsible for signaling persistent pain. Drugs that target these receptors provide more effective relief from chronic pain than conventional drugs that target receptors at the surface of cells. The failure of conventional drugs in clinical trials of chronic pain may be due to their inability to inhibit receptors in endosomes.

Impact on other disciplines. GPCRs mediate many diseases beyond pain, including cardiovascular disease, inflammatory diseases and cancer. Antagonists and agonists of GPCRs represent the single largest class of drugs; more than one third of FDA-approved drugs target GPCRs. The concept that GPCRs in endosomes generate sustained signals that may underlie disease processes raises the prospect that GPCRs in endosomes might be the optimal target for the treatment of many chronic diseases.

Impact on technology transfer. The PI is a scientific founder of Endosome Therapeutics, a start-up company that seeks to develop and commercialize drugs that target endosomal GPCRs. The National Center for Advancing Translational Science (NCATS) has initiated a collaboration to develop nanoparticle-encapsulated antagonists of GPCRs for the treatment of chronic pain.

Impact on society. Nothing to report.

5. CHANGES/PROBLEMS

PI Dr. N.W. Bunnett has accepted the Chair of Basic Science and Craniofacial Biology at New York University, effective 10/1/2019. This relocation will facilitate collaborations with Dr. B.L. Schmidt, the partnering PI.

There are no other changes or problems to report.

6. PRODUCTS

* Papers included in appendix

Journal publications

1. *Jimenez-Vargas, N.N., Pattison, L.A., Zhao, P., Lieu, T., Latorre, R., Jensen, D.D., Castro, J., Aurelio, L., Le, G.T., Flynn, B., Herenbrink, C.K., Yeatman, H.R., Edgington-Mitchell, L., Porter, C.J.H., Halls, M.L., Canals, M., Veldhuis, N.A., Poole, D.P., McLean, P., Hicks, G.A., Scheff, N., Chen, E.,

- Bhattacharya, A., Schmidt, B.L., Brierley, S.M., Vanner, S.J. & Bunnett, N.W. Protease-activated receptor-2 in endosomes signals persistent pain of irritable bowel syndrome. *Proc Natl Acad Sci U S A* 115, E7438-E7447 (2018). PMC6077730. Federal support: Yes
2. *Logu FD, Puma SL, Landini L, Portelli F, Innocenti A, Monteiro de Araujo DS, Janal MN, Patacchini R, Bunnett NW, Geppetti P, Nassini R. Schwann Cells and TRPA1 orchestrate ethanol-evoked neuropathic pain in mice. *J Clin Invest* In press (2019). Federal support: Yes
 3. *Thomsen, A.R.B., Jensen, D.D., Hicks, G.A. & Bunnett, N.W. Therapeutic Targeting of Endosomal G-Protein-Coupled Receptors. *Trends Pharmacol Sci.* 2018 Oct;39(10):879-891. doi: 10.1016/j.tips.2018.08.003. Epub 2018 Sep 1. Review. PMID: 30180973. Federal support: Yes
 4. *Canals M, Poole DP, Veldhuis NA, Schmidt BL, Bunnett NW. G Protein-Coupled Receptors are Dynamic Regulators of Digestion and Targets for Digestive Diseases. *Gastroenterology.* 2019 May;156(6):1600-1616. doi: 10.1053/j.gastro.2019.01.266. Epub 2019 Feb 13. Review. PMID: 30771352. Federal support: Yes
 5. *Roitman M, Edgington-Mitchell LE, Mangum J, Ziogas J, Adamides AA, Myles P, Choo-Bunnett H, Bunnett NW, Gunnarsen JM. Sez6 levels are elevated in cerebrospinal fluid of patients with inflammatory pain-associated conditions. *Pain Rep.* 2019 Mar 25;4(2):e719. doi: 10.1097/PR9.0000000000000719. eCollection 2019 Mar-Apr. PMID: 31041421. Federal support: Yes
 6. *Ramírez-García PD, Retamal JS, Shenoy P, Imlach W, Sykes M, Truong N, Constandil L, Pelissier T, Nowell CJ, Khor SY, Layani LM, Lumb C, Poole DP, Lieu T, Stewart GD, Mai QN, Jensen DD, Latorre R, Scheff NN, Schmidt BL, Quinn JF, Whittaker MR, Veldhuis NA, Davis TP, Bunnett NW. Nanomedicines that Target the Neurokinin 1 Receptor in Endosomes Provide Superior Pain Relief. *Nature Nano* (2019) In press (2019). Federal support: Yes
 7. *Mountford SJ, Anderson BM, Xu B, Szabo M, Hoang M-L, Diao J, Aurelio L, Campden RI, Lindström E, Sloan EK, Yates RM, Schmidt BL, Bunnett NW, Thompson PE, Edgington-Mitchell LE. Application of a sulfoxonium ylide electrophile to generate cathepsin X-selective activity-based probes. *J Med Chem.* Submitted (2019). Federal support: Yes
 8. *Anderson BM, Poole DP, Aurelio L, Ng GZ, Fleischmann M, Kasperkiewicz P, Morissette C, Drag M, van Driel IR, Schmidt BL, Vanner SJ, Bunnett NW, Edgington-Mitchell LE. A new method to detect neutrophil elastase activation during inflammatory bowel disease. *Scientific Reports.* In press (2019). Federal support: Yes
 9. Mai QN, Shenoy P, Quach T, Retamal-Santibanez J, Yeatman HR, Aurelio L, Conner JW, Canals M, Graham B, Bridson SJ, Hill SJ, Porter CJ, Bunnett NW, Halls ML, Veldhuis NA. Endosomally-targeted antagonists of the neurokinin-1 receptor provide sustained inhibition intracellular signaling and nociception. *J Biol Chem.* Submitted (2019). Federal support: Yes
 10. Conner JW, Mai QN, Nowell CJ, Davis TP, Bunnett NW, Scammells PJ, Graham B, Veldhuis NA. Lipid conjugation for delivery of a soluble antagonist to the neurokinin 1 receptor in endosomes. *Br J Pharmacol.* Submitted (2019). Federal support: Yes

Books. Nothing to report.

Other. Nothing to report.

Websites. Nothing to report.

Technologies and techniques. Nothing to report.

Inventions and patents. Nothing to report.

Other products. Nothing to report.

7. PARTICIPANTS AND OTHER COLLABORATING ORGANIZATIONS

Individuals who have worked on project

COLUMBIA UNIVERSITY

| | |
|--|---|
| Name: | Nigel Bunnett, PhD |
| Project Role: | PI |
| Researcher Identifier (e.g. ORCID ID): | 0000-0003-3367-0644 |
| Nearest person month worked: | 3 calendar |
| Contribution to Project: | Project conception; experimental design; interpreting results; writing manuscripts. |
| Funding Support: | 5R01NS102722; 5R01DE026806; 5R01DK118971 |

| | |
|--|--|
| Name: | Aristidis Floratos, PhD |
| Project Role: | Co-Investigator |
| Researcher Identifier (e.g. ORCID ID): | N/A |
| Nearest person month worked: | 0.36 calendar |
| Contribution to Project: | Design of experiments to examine endosomal signaling and gene transcription. |
| Funding Support: | 5P50AR070588; 5UL1 TR001873-03; 5U54 CA209997-03; U19AI128949; U01CA217858 |

| | |
|--|--|
| Name: | Alex Thomsen, PhD |
| Project Role: | Co-Investigator |
| Researcher Identifier (e.g. ORCID ID): | N/A |
| Nearest person month worked: | 3.0 calendar |
| Contribution to Project: | Design of experiments to examine endosomal signaling pathways. |
| Funding Support: | Leo Foundation; 5R01NS102722;5R01DK118971; |

| | |
|--|---------------------------------|
| Name: | Rocco Latorre, PhD |
| Project Role: | Postdoctoral Research Scientist |
| Researcher Identifier (e.g. ORCID ID): | 0000-0003-2737-8233 |
| Nearest person month worked: | 4.1 calendar |

| | |
|--------------------------|--|
| Contribution to Project: | Analysis of the role of endosomal signaling in preclinical models of pain. |
| Funding Support: | 5R01NS102722; 5R01DK118971 |

| | |
|--|---|
| Name: | Alan Hegron, PhD |
| Project Role: | Postdoctoral Research Scientist |
| Researcher Identifier (e.g. ORCID ID): | 0000-0002-7588-9209 |
| Nearest person month worked: | 4.0 calendar |
| Contribution to Project: | Analysis of the pathways of endosomal signaling and gene transcription. |
| Funding Support: | 5R01NS102722; 5R01DK118971; |

| | |
|--|--|
| Name: | Jeong Lee |
| Project Role: | Technician |
| Researcher Identifier (e.g. ORCID ID): | N/A |
| Nearest person month worked: | 3.0 calendar |
| Contribution to Project: | Management of cell lines and mouse colonies. |
| Funding Support: | 5R01NS102722; 5R01DE026806; 5R01DK118971 |

SALISBURY FOUNDATION

| | |
|--|---|
| Name: | Michael Gaspari, MD |
| Project Role: | Subcontract PI |
| Researcher Identifier (e.g. ORCID ID): | N/A |
| Nearest person month worked: | 1 calendar |
| Contribution to Project: | Oversees the study, Makes Eligibility /Termination decisions, Direct Medical Care of Subject, Evaluates Adverse Events, Obtains tissue and colonic fluid during the Colonoscopy |
| Funding Support: | none |

| | |
|--|---|
| Name: | John Sanders, MD |
| Project Role: | Co-Investigator |
| Researcher Identifier (e.g. ORCID ID): | N/A |
| Nearest person month worked: | 1 calendar |
| Contribution to Project: | Serves as back up to the PI, Makes Eligibility /Termination decisions, Direct Medical Care of Subject, Evaluates Adverse Events |
| Funding Support: | VA funding, U19AI067773 |

| | |
|--|---|
| Name: | Neil Kassman, MD |
| Project Role: | Co-Investigator |
| Researcher Identifier (e.g. ORCID ID): | N/A |
| Nearest person month worked: | 1 calendar |
| Contribution to Project: | Makes Eligibility /Termination decisions, Direct Medical Care of Subject, Evaluates Adverse Events, Obtains tissue and colonic fluid during the Colonoscopy |
| Funding Support: | none |

| | |
|--|---|
| Name: | Dorothea Johnson |
| Project Role: | Research Coordinator |
| Researcher Identifier (e.g. ORCID ID): | N/A |
| Nearest person month worked: | 6 calendar |
| Contribution to Project: | Makes Eligibility/ Termination decisions, Obtains Informed Consent, Makes data entries and corrections, Maintains product Accountability, Processes specimens for transport, Regulatory |
| Funding Support: | none |

| | |
|--|---|
| Name: | Tracey Jones |
| Project Role: | Back Up Coordinator |
| Researcher Identifier (e.g. ORCID ID): | N/A |
| Nearest person month worked: | 1 calendar |
| Contribution to Project: | Makes Eligibility/ Termination decisions, Obtains Informed Consent, Makes data entries and corrections, Maintains product Accountability, Processes specimens for transport |
| Funding Support: | none |

Change in support since last reporting period

Nigel Bunnett, PhD (PI)

NEW SUPPORT

None

COMPLETED SUPPORT

Research Award (Bunnett) 10/4/2017 – 10/3/2018 0.60 calendar
Chiesi Farmaceutici
Elastase Signaling in the Airways
The major goal of this project is to define the mechanism by which neutrophil elastase regulates airway functions.

Aristitidis Floratos, PhD

NEW SUPPORT

None

COMPLETED SUPPORT

5P30CA013696-44 Abate-Shen (PI) 7/01/97 – 6/30/19 1.18 CM
NCI
Cancer Center Support Grant
To support cancer research within the various Core facilities of Columbia's Herbert Irving Comprehensive Cancer Center.
Role: Core Director

SAICCU10-1925 Floratos (PI) 07/01/2010 – 12/31/18
International Serious Adverse Events Consortium
Data Coordinating Center for International Serious Adverse Events Consortium
To analyze whole genome data in order to identify and validate DNA-variants useful in predicting the risk of drug-related serious adverse events (SAEs) and to provide infrastructure for the storage and dissemination of raw data and analysis results.
Role: PI

U19AI118610 Fernandez-Sesma (PI) 06/01/2017 – 05/31/2019 0.36 CM
NIH/NIAID
Dengue Human Immunology Project Consortium (DHIPC)
The long-term goal is to develop molecular signatures that define immune response and categories/fingerprints/profiles that correlate with the outcome of infection and vaccination.
Role: Subaward PI

Alex Thomsen, PhD

NEW SUPPORT

LF18043 (Thomsen) 10/08/18 - 10/07/21 6.00 calendar
LEO FOUNDATION
Endosomal Chemokine Receptor Signaling as Basis for Metastasis in Malignant Melanoma
The major goal is to investigate the role of endosomal chemokine receptor signaling in melanoma cell migration in vitro and to study a detailed molecular mechanism of this cell biological event using a combination of APEX2-based proteomics and cryo-electron tomography.

Michael Gaspari, MD

NEW SUPPORT

None

John Sanders, MD

NEW SUPPORT

None

COMPLETED SUPPORT

W81XWH-15-2-0029 (Sanders) 3/1/2016-7/14/2019 1.2 calendar
Henry M. Jackson Foundation
Non-human Primate Study for Selecting Vaccine Delivery Method
Pre-clinical trial building on data produced in earlier study of delivery mechanisms designed to assess various delivery mechanisms of a DNA dengue vaccine in a non-human primate model utilizing a prime:boost model (DNA vaccine combined with either a live, attenuated vaccine or an inactivated vaccine)

TMG-SUBK-004-12 (Sanders) 4/1/2017-9/28/2018 1.2 calendar
The McConnell Group (subaward)
Dengue Vaccine Development for the Viral and Rickettsial Diseases Department (VRDD) at Naval Medical Research Center (NMRC)
This is a pre-clinical study utilizing both mouse and non-human primate models designed to compare the efficacy of two different methods of viral inactivation in vaccine development and to assess the efficacy of combining an inactivated vaccine with a DNA vaccine in a "Dual Platform" approach for dengue vaccination.

Institutional Pilot fund (no grant #) (David Caudell) 7/1/2017-6/30/18 0.1 calendar
Wake Forest Pathology Grant Center for Medical Countermeasures against Radiation (CMCR)
Systematic Immunophenotyping of the Intestinal Mucosal Immune System in Rhesus Macaques with Delayed Radiation Injury
This study is utilizing intestinal tissue blocks collected from irradiated non-human primates to develop a better description of gut immunity and the potential effects of radiation on immunologic response. It is an internally funded pilot study being conducted in association with externally funded CMCR work to prepare baseline data for use in larger proposals.

Other organizations.

Salisbury Foundation for Research and Education. 1601 *Brenner Ave Salisbury, NC 28144*

Partner's contribution to the project: Collaboration (provided biopsy specimens).

8. SPECIAL REPORTING REQUIREMENTS

This is a collaborative award between Dr. N.W. Bunnett (Columbia University) and B.L. Schmidt (New York University). Dr. Schmidt will submit his report for the 9/30/2019 deadline.

9. APPENDICES. PDF of most relevant published manuscripts and manuscripts under revision and re-review.

Protease-activated receptor-2 in endosomes signals persistent pain of irritable bowel syndrome

Nestor N. Jimenez-Vargas^{a,1}, Luke A. Pattison^{b,1}, Peishen Zhao^{b,1}, TinaMarie Lieu^{b,1}, Rocco Latorre^{c,d}, Dane D. Jensen^{c,d}, Joel Castro^{e,f}, Luigi Aurelio^b, Giang T. Le^b, Bernard Flynn^b, Carmen Klein Herenbrink^b, Holly R. Yeatman^b, Laura Edgington-Mitchell^b, Christopher J. H. Porter^b, Michelle L. Halls^b, Meritxell Canals^b, Nicholas A. Veldhuis^b, Daniel P. Poole^{b,g}, Peter McLean^h, Gareth A. Hicks^h, Nicole Scheffiⁱ, Elyssa Chenⁱ, Aditi Bhattacharyaⁱ, Brian L. Schmidtⁱ, Stuart M. Brierley^{e,f}, Stephen J. Vanner^a, and Nigel W. Bunnett^{b,c,d,j,2}

^aGastrointestinal Diseases Research Unit, Division of Gastroenterology, Queen's University, Kingston, ON K7L 2V7, Canada; ^bMonash Institute of Pharmaceutical Sciences and Australian Research Council Centre of Excellence in Convergent Bio-Nano Science and Technology, Monash University, Parkville, VIC 3052, Australia; ^cDepartment of Surgery, Columbia University College of Physicians and Surgeons, Columbia University, New York, NY 10032; ^dDepartment of Pharmacology, Columbia University College of Physicians and Surgeons, Columbia University, New York, NY 10032; ^eVisceral Pain Research Group, Human Physiology, Centre for Neuroscience, Flinders University, Adelaide, SA 5000, Australia; ^fCentre for Nutrition and Gastrointestinal Diseases, Discipline of Medicine, University of Adelaide, South Australian Health and Medical Research Institute, Adelaide, SA 5000, Australia; ^gDepartment of Anatomy and Neuroscience, University of Melbourne, Parkville, VIC 3010, Australia; ^hGastrointestinal Drug Discovery Unit, Takeda Pharmaceuticals, Inc., Cambridge, MA 02139; ⁱBluestone Center for Clinical Research, New York University College of Dentistry, New York, NY 10010; and ^jDepartment of Pharmacology and Therapeutics, University of Melbourne, Parkville, VIC 3010, Australia

Edited by Robert J. Lefkowitz, Howard Hughes Medical Institute and Duke University Medical Center, Durham, NC, and approved June 22, 2018 (received for review January 8, 2018)

Once activated at the surface of cells, G protein-coupled receptors (GPCRs) redistribute to endosomes, where they can continue to signal. Whether GPCRs in endosomes generate signals that contribute to human disease is unknown. We evaluated endosomal signaling of protease-activated receptor-2 (PAR₂), which has been proposed to mediate pain in patients with irritable bowel syndrome (IBS). Trypsin, elastase, and cathepsin S, which are activated in the colonic mucosa of patients with IBS and in experimental animals with colitis, caused persistent PAR₂-dependent hyperexcitability of nociceptors, sensitization of colonic afferent neurons to mechanical stimuli, and somatic mechanical allodynia. Inhibitors of clathrin- and dynamin-dependent endocytosis and of mitogen-activated protein kinase kinase-1 prevented trypsin-induced hyperexcitability, sensitization, and allodynia. However, they did not affect elastase- or cathepsin S-induced hyperexcitability, sensitization, or allodynia. Trypsin stimulated endocytosis of PAR₂, which signaled from endosomes to activate extracellular signal-regulated kinase. Elastase and cathepsin S did not stimulate endocytosis of PAR₂, which signaled from the plasma membrane to activate adenylyl cyclase. Biopsies of colonic mucosa from IBS patients released proteases that induced persistent PAR₂-dependent hyperexcitability of nociceptors, and PAR₂ association with β -arrestins, which mediate endocytosis. Conjugation to cholestanol promoted delivery and retention of antagonists in endosomes containing PAR₂. A cholestanol-conjugated PAR₂ antagonist prevented persistent trypsin- and IBS protease-induced hyperexcitability of nociceptors. The results reveal that PAR₂ signaling from endosomes underlies the persistent hyperexcitability of nociceptors that mediates chronic pain of IBS. Endosomally targeted PAR₂ antagonists are potential therapies for IBS pain. GPCRs in endosomes transmit signals that contribute to human diseases.

endosomes | receptors | pain | proteases

There is a growing realization that G protein-coupled receptors (GPCRs), which were formerly considered to function principally at the surface of cells, can continue to signal from endosomes by mechanisms that involve β -arrestins (β ARRs) and G proteins (1). Although GPCR signaling begins at the plasma membrane, activated receptors associate with β ARRs, which mediate receptor desensitization and endocytosis (2). These processes efficiently terminate GPCR signaling at the plasma membrane. The detection of GPCR signaling complexes in endosomes, and the finding that disruption of endocytosis can suppress signaling, both suggest that GPCRs signal from endosomes (3–12). GPCRs in endosomes can generate persistent signals in subcellular com-

partments that control gene transcription and neuronal excitation (8, 11, 12). Although endosomal signaling of GPCRs can regulate important physiological processes, including pain transmission (8, 12), the contribution of endosomal signaling to human disease is far from clear.

Protease-activated receptor-2 (PAR₂) mediates the proinflammatory and pronociceptive actions of proteases (13). Given the irreversible mechanism of proteolytic activation, PAR₂ may be capable of persistent signaling at the plasma membrane and in

Significance

Activated G protein-coupled receptors (GPCRs) internalize and can continue to signal from endosomes. The contribution of endosomal signaling to human disease is unknown. Proteases that are generated in the colon of patients with irritable bowel syndrome (IBS) can cleave protease-activated receptor-2 (PAR₂) on nociceptors to cause pain. We evaluated whether PAR₂ generates signals in endosomes of nociceptors that mediate persistent hyperexcitability and pain. Biopsies of colonic mucosa from IBS patients released proteases that induced PAR₂ endocytosis, endosomal signaling, and persistent hyperexcitability of nociceptors. When conjugated to the transmembrane lipid cholestanol, PAR₂ antagonists accumulated in endosomes and suppressed persistent hyperexcitability. The results reveal the therapeutic potential of endosomally targeted PAR₂ antagonists for IBS pain, and expand the contribution of endosomal GPCR signaling to encompass processes that are relevant to disease.

Author contributions: P.Z., T.L., B.F., C.K.H., H.R.Y., L.E.-M., C.J.H.P., M.L.H., M.C., N.A.V., D.P.P., P.M., G.A.H., B.L.S., S.M.B., S.J.V., and N.W.B. designed research; N.N.J.-V., L.A.P., P.Z., T.L., R.L., D.D.J., J.C., L.A., G.T.L., C.K.H., H.R.Y., M.L.H., M.C., N.A.V., N.S., E.C., and A.B. performed research; L.A., G.T.L., B.F., and B.L.S. contributed new reagents/analytic tools; N.N.J.-V., L.A.P., P.Z., T.L., J.C., C.K.H., H.R.Y., M.L.H., M.C., N.A.V., D.P.P., B.L.S., S.M.B., S.J.V., and N.W.B. analyzed data; and M.L.H., M.C., D.P.P., B.L.S., S.M.B., S.J.V., and N.W.B. wrote the paper.

Conflict of interest statement: P.M. and G.A.H. work for Takeda Pharmaceuticals, Inc. Research in N.W.B.'s laboratory is supported in part by Takeda Pharmaceuticals, Inc. N.W.B. and G.A.H. are founding scientists of Endosome Therapeutics, Inc.

This article is a PNAS Direct Submission.

Published under the PNAS license.

¹N.N.J.-V., L.A.P., P.Z., and T.L. contributed equally to this work.

²To whom correspondence should be addressed. Email: nb2733@cumc.columbia.edu.

This article contains supporting information online at www.pnas.org/lookup/suppl/doi:10.1073/pnas.1721891115/-DCSupplemental.

endosomes. Trypsin and mast cell tryptase activate PAR₂ by canonical mechanisms that induce receptor association with βARRs, endocytosis, and endosomal signaling (5, 14). Neutrophil elastase (NE) and macrophage cathepsin S (CS) cleave PAR₂ at different sites and activate PAR₂ by biased mechanisms that do not induce receptor interactions with βARRs or endocytosis (15, 16). The contribution of PAR₂ signaling at the plasma membrane and in endosomes to the disease-relevant actions of proteases is unknown.

Proteases and PAR₂ have been implicated in the hypersensitivity of sensory nerves in the colon that may account for chronic pain in patients with irritable bowel syndrome (IBS) (17). Biopsies of colonic mucosa from IBS patients secrete proteases, including tryptase and trypsin-3, which induce PAR₂-dependent hyperexcitability of nociceptors and colonic nociception in mice (18–21). PAR₂ agonists induce a remarkably long-lasting hyperexcitability of neurons by unknown mechanisms (22, 23). Whether PAR₂ at the plasma membrane or in endosomes is a target for the treatment of IBS pain remains to be determined.

We examined the hypothesis that two components of PAR₂ signaling contribute to the persistent hyperexcitability of nociceptors in IBS: the irreversible mechanism of proteolytic activation and the capacity of PAR₂ to generate sustained signals from endosomes.

Results

PAR₂-Mediated Nociception. Proteases may induce pain by activating PAR₂ on nociceptors or other cell types. To determine the

contribution of PAR₂ on nociceptors, we bred mice expressing *Par₂* flanked by LoxP sites (*Par₂^{lox/lox}*) with mice expressing Cre recombinase targeted to nociceptors using the *Nav1.8* promoter (*Scn10a*). *Par₂-Nav1.8* mice lacked immunoreactive PAR₂ in Nav1.8⁺ neurons of the dorsal root ganglia (DRG) (Fig. 1A). Whereas 31% (20 of 65) of small-diameter (<25 μm) DRG neurons from WT mice responded to trypsin (100 nM) with increased [Ca²⁺]_i, only 6% (3 of 51) of neurons from *Par₂-Nav1.8* mice responded (Fig. 1B and *SI Appendix, Fig. S1 A and B*). We assessed nociception by measuring withdrawal responses to stimulation of the plantar surface of the hindpaw with von Frey filaments (VFF). In WT mice, intraplantar injection (10 μL) of trypsin (80 nM), NE (3.9 μM), or CS (5 μM) induced mechanical allodynia within 30 min, which was maintained for 180 min (Fig. 1C–E). In *Par₂-Nav1.8* mice, the initial responses were maintained, but responses after 120 min were diminished. At 180 min, when mechanical allodynia in WT mice was fully maintained, responses in *Par₂-Nav1.8* mice had returned to baseline (trypsin, NE) or were significantly attenuated (CS). In WT mice, intraplantar trypsin increased paw thickness—measured using calipers—which peaked at 1 h and was maintained for 4 h, and stimulated an influx of neutrophils after 4 h, consistent with inflammation (*SI Appendix, Fig. S1 C and D*). Trypsin-induced inflammation was markedly diminished in *Par₂-Nav1.8* mice.

To assess the contribution of endocytosis to protease-induced nociception, Dyngo4a (Dy4, dynamin inhibitor) (24), PitStop2 (PS2, clathrin inhibitor) (25), inactive (inact) analogs (50 μM), or vehicle (0.2% DMSO, 0.9% NaCl) (10 μL) was administered by

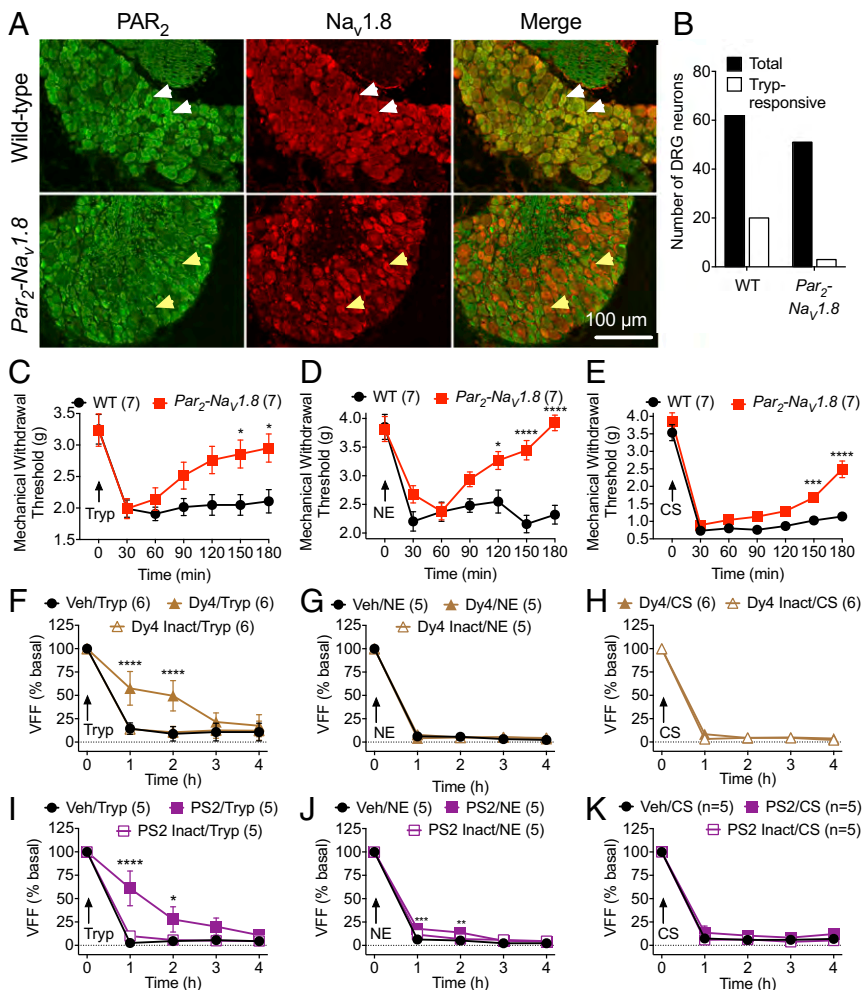


Fig. 1. Protease-induced mechanical nociception. (A) Localization of PAR₂ and Nav1.8 immunoreactivity in DRG from WT or *Par₂-Nav1.8* mice. White arrowheads: neurons coexpressing PAR₂ and Nav1.8 in WT mice. Yellow arrowheads: neurons expressing Nav1.8 but not PAR₂ in *Par₂-Nav1.8* mice. (B) Total number and number of trypsin (100 nM)-responsive DRG neurons (<25 μm) from WT and *Par₂-Nav1.8* mice. (C–E) VFF withdrawal responses in WT and *Par₂-Nav1.8* mice after intraplantar injection of trypsin (C, Tryp), NE (D), or CS (E). (F–K) VFF withdrawal responses in WT mice after intraplantar injection of Dy4 or Dy4 inact (F–H, dynamin inhibitor), PS2 or PS2 inact (I–K, clathrin inhibitor), or vehicle (Veh), followed 30 min later by intraplantar trypsin (F and I), NE (G and J), or CS (H and K). **P* < 0.05, ***P* < 0.01, ****P* < 0.001, *****P* < 0.0001. Numbers in parentheses denote mouse number.

intraplantar injection to mice. After 30 min, trypsin (10 nM), NE (1.2 μ M), or CS (2.5 μ M) (10 μ L) was injected into the same paw. In controls (vehicle or inactive analogs), trypsin, NE, and CS induced mechanical allodynia that was fully maintained for 4 h (Fig. 1 F–K). Dy4 and PS2 inhibited trypsin-induced allodynia at 1 and 2 h (Fig. 1 F and I), whereas NE- (Fig. 1 G and J) and CS- (Fig. 1 H and K) induced allodynia was unchanged. Endocytic inhibitors or proteases did not influence withdrawal responses of the noninjected contralateral paw (SI Appendix, Fig. S2 A and B). Trypsin, NE, and CS increased paw thickness, consistent with edema (SI Appendix, Fig. S2 C–H). Dynamin and clathrin inhibitors did not affect edema.

The results suggest that proteases induce persistent nociception and neurogenic inflammation in large part by activating PAR₂ on Na_v-1.8⁺ neurons. PAR₂ endocytosis is necessary for the nociceptive actions of trypsin, but not NE or CS.

PAR₂-Mediated Hyperexcitability of Nociceptors. To evaluate the contribution of endocytosis to protease-induced hyperexcitability of nociceptors, the rheobase (the minimal input current required to fire one action potential) of small diameter neurons of mouse DRG was measured by patch-clamp recording. Neurons were preincubated with trypsin (50 nM, 10 min), NE (390 nM, 30 min), CS (500 nM, 60 min) (conditions selected to cause robust hyperexcitability), or vehicle, and washed. Rheobase was measured 0 or 30 min after washing. The mean rheobase of protease- or vehicle-treated neurons was calculated. Trypsin, NE, and CS decreased rheobase at 0 and 30 min, indicating an initial hyperexcitability that is maintained for at least 30 min (Fig. 2). Dy4 (30 μ M) or PS2 (15 μ M) did not affect the capacity of trypsin, NE, or CS to cause initial hyperexcitability (0 min). Dy4 and PS2 abolished the persistent effects of trypsin (Fig. 2 A–C), but not of NE (Fig. 2 D and E) or CS (Fig. 2 F and G) (30 min). Dy4, PS2, or vehicle (0.3% DMSO) did not affect the basal excitability of DRG neurons (SI Appendix, Fig. S3).

I-343 is an imidazopyridazine derivative that has been described as a potent PAR₂ antagonist in the patent literature (26) (SI Appendix, Fig. S4A). I-343 belongs to the same family of PAR₂ antagonists as I-191, a full antagonist of PAR₂ that inhibits multiple components of PAR₂ signaling, including those that may mediate protease-induced pain (27). We investigated whether I-343 inhibits PAR₂ signaling in HT-29 and HEK293 cells, which express endogenous PAR₂, and in KNRK cells transfected with human (h) PAR₂. Accumulation of inositol phosphate-1 (IP₁) was measured in response to trypsin or the PAR₂-selective agonist 2-Furoyl-LIGRLO-NH₂ (2F), an analog of the trypsin-exposed tethered ligand. I-343 inhibited 2F (300 nM)-induced IP₁ in HT-29 cells (pIC₅₀ 8.93 \pm 0.11, IC₅₀ 1.1 nM) and 2F (100 nM)-induced IP₁ in KNRK-hPAR₂ cells (pIC₅₀ 6.18 \pm 0.11, IC₅₀ 666 nM) (SI Appendix, Fig. S4 B–D). I-343 inhibited trypsin (30 nM)-induced IP₁ in HEK293 cells (pIC₅₀ 9.36 \pm 0.20, IC₅₀ 0.4 nM) and in KNRK-hPAR₂ cells (pIC₅₀ 5.13 \pm 0.14, IC₅₀ 7507 nM). I-343 did not affect ATP (10 μ M)-stimulated IP₁ in KNRK cells (SI Appendix, Fig. S4E).

I-343 (10 μ M) prevented the decrease in rheobase 30 min after trypsin and CS, but not NE (Fig. 3 A–C). However, I-343 prevented the decrease in rheobase 0 min after NE (Fig. 3D). I-343 (100 nM, 300 nM) also prevented the decrease in rheobase 0 min after trypsin (SI Appendix, Fig. S5A). When neurons were incubated with thrombin (50 nM, 20 min) and washed, there was an immediate decrease in rheobase that was prevented by preincubation with the PAR₁ antagonist SCH79797 (1 μ M, 10 min) (28); SCH79797 alone had no effect (SI Appendix, Fig. S5B) and SCH79797 did not affect the response to trypsin (SI Appendix, Fig. S5C). Thus, PAR₂ mediates the immediate and persistent actions of trypsin, the persistent actions of CS, and the initial effects of NE; NE causes persistent hyperexcitability by a different mechanism. PAR₁ does not mediate the initial actions of trypsin.

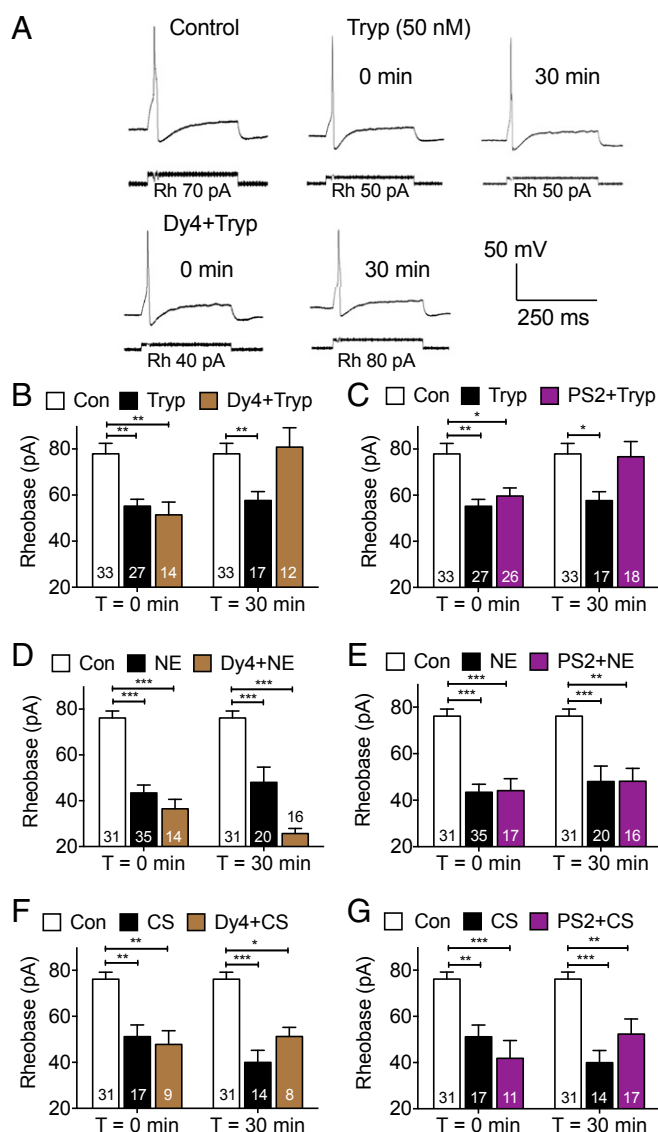


Fig. 2. Protease-induced hyperexcitability of nociceptors. Rheobase of mouse DRG neurons preincubated with Dy4 (A, B, D, and F, dynamin inhibitor), PS2 (C, E, and G, clathrin inhibitor), or vehicle control (Con). Neurons were challenged with trypsin (A–C), NE (D and E), or CS (F and G), washed, and rheobase was measured 0 or 30 min later. (A) Representative traces. Rh, rheobase. (B–G) Mean responses. * P < 0.05, ** P < 0.01, *** P < 0.001. Numbers in bars denote neuron numbers.

Another PAR₂ antagonist, GB88, also prevents trypsin, NE, and CS activation of nociceptors (29). Trypsin-activated PAR₂ signals from endosomes by β ARR- and Raf-1-dependent processes, which activate ERK (5). PD98059 (50 μ M), which inhibits activation of mitogen-activated protein kinase kinase-1 (MEK1) (30), did not affect initial trypsin-induced hyperexcitability, but prevented persistent trypsin-induced hyperexcitability (Fig. 3E). In contrast, GF109203X (Bis-1, 10 μ M), which inhibits PKC α and other kinases (30), prevented the initial but not the persistent effects of trypsin (Fig. 3F).

The results suggest that trypsin induces initial hyperexcitability of nociceptors by PAR₂/PKC signaling from the plasma membrane, and persistent hyperexcitability by PAR₂/ERK signaling from endosomes. Adenylyl cyclase and PKA mediate NE- and CS-induced hyperexcitability of nociceptors (15, 16), which was not further studied.

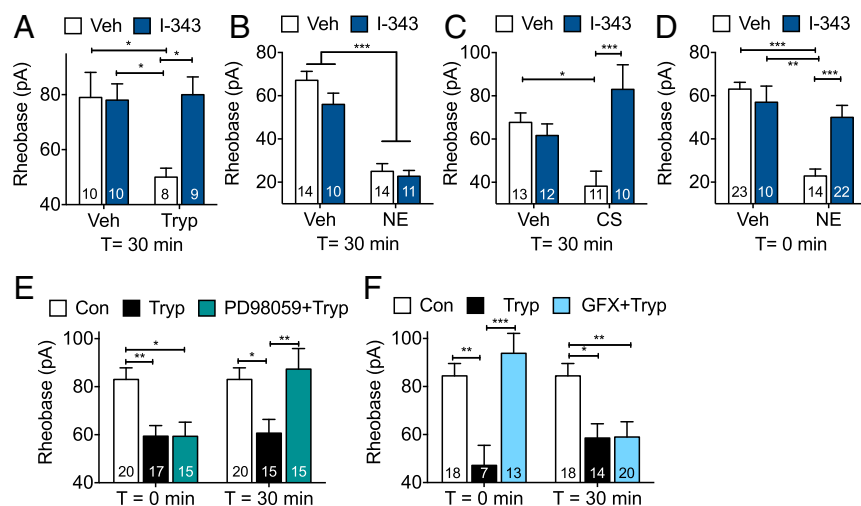


Fig. 3. Mechanisms of protease-induced hyperexcitability of nociceptors. Rheobase of mouse DRG neurons preincubated with I-343 (A–D, PAR₂ antagonist), PD98059 (E, MEK1 inhibitor), or GF109203X (F, GFXT, PKC inhibitor). Neurons were challenged with trypsin (A, E, and F, Tryp), NE (B and D), or CS (C), washed, and rheobase was measured 0 or 30 min later. **P* < 0.05, ***P* < 0.01, ****P* < 0.0001. Numbers in bars denote neuron numbers.

PAR₂ Endocytosis and Compartmentalized Signaling in Nociceptors.

To assess endocytosis of PAR₂ in nociceptors, we transfected mouse (m) PAR₂-GFP into mouse DRG neurons. In vehicle-treated neurons, mPAR₂-GFP was detected at the plasma membrane and in intracellular compartments that may correspond to the prominent stores of PAR₂ in the Golgi apparatus (Fig. 4A) (31). Trypsin, but not NE or CS (100 nM, 30 min), induced removal of mPAR₂-GFP from the plasma membrane and accumulation in endosomes (Fig. 4A and B). Dy4, but not Dy4 inact, inhibited trypsin-induced endocytosis of mPAR₂-GFP (Fig. 4C). To determine whether PAR₂ recruits βARRs, which mediate endocytosis of PAR₂ (14), we expressed bioluminescence resonance energy transfer (BRET) sensors for PAR₂-RLuc8 (donor) and βARR2-YFP (acceptor) in mouse DRG neurons. Trypsin, but not NE or CS, stimulated PAR₂-RLuc8/βARR2-YFP BRET over 25 min (Fig. 4D).

To determine whether trypsin causes PAR₂-dependent activation of PKC and ERK, which respectively mediate the initial and persistent phases of trypsin-induced hyperexcitability of nociceptors, we expressed genetically encoded FRET biosensors in neurons. The biosensors are targeted to subcellular compartments and are reversibly modified by kinases and phosphatases. They are suitable for analysis of signaling in subcellular compartments with high spatial and temporal resolution (8, 12). Biosensors for plasma membrane PKC (pmCKAR), cytosolic PKC (CytoCKAR), cytosolic ERK (CytoEKAR), and nuclear ERK (NucEKAR) were expressed in DRG neurons from rat, because pilot studies revealed more robust and consistent PAR₂ responses than in mouse neurons. Trypsin (100 nM) activated PKC at the plasma membrane but not in the cytosol (Fig. 4E–G), and activated ERK in the cytosol and nucleus (Fig. 4H–J). The PAR₂ antagonist I-343 (10 μM) inhibited trypsin-induced activation of PKC and ERK, whereas the PAR₁ antagonist SCH530348 (100 nM) had no effect (Fig. 4F and I). At the end of experiments, neurons were challenged with the positive controls phorbol 12,13-dibutyrate (PDBu) for EKAR biosensors or PDBu plus phosphatase inhibitor mixture-2 for CKAR biosensors, to ensure that the response of the biosensor was not saturated.

The results suggest that trypsin, but not NE or CS, stimulates βARR2 recruitment and dynamin-dependent endocytosis of PAR₂ in nociceptors. Trypsin causes PAR₂-dependent activation of PKC at the plasma membrane and ERK in the cytosol and nucleus.

Mechanisms of PAR₂ Endocytosis and Endosomal Signaling. We examined the mechanism of PAR₂ endocytosis and endosomal signaling in HEK293 cells. To quantify the removal of PAR₂ from the plasma membrane and its accumulation in early endosomes, we measured bystander BRET between PAR₂ and

proteins that are resident at the plasma membrane (Ras-like protein expressed in many tissues, or RIT) and early endosomes (Ras-related protein Rab5a) (8, 12). This application of BRET takes advantage of nonspecific protein–protein interactions to track movement of membrane proteins through different compartments (32). Trypsin induced a decrease in PAR₂-RLuc8/RIT-Venus BRET (EC₅₀ 2.9 nM), and an increase in PAR₂-RLuc8/Rab5a-Venus BRET (EC₅₀ 2.7 nM) (Fig. 5A and B and *SI Appendix, Fig. S6A–D*). Neither NE nor CS (100 nM) affected PAR₂-RLuc8/RIT-Venus or Rab5a-Venus BRET (Fig. 5A and B). PS2, but not PS2 inact, suppressed the trypsin-induced decrease in PAR₂-RLuc8/RIT-Venus BRET and increase in PAR₂-RLuc8/Rab5a-Venus BRET (Fig. 5C and D and *SI Appendix, Fig. S6E and F*). Dominant-negative dynaminK44E (DynK44E), which is deficient in GTP binding (33), inhibited the increase in PAR₂-RLuc8/Rab5a-Venus BRET, but did not affect PAR₂-RLuc8/RIT-Venus BRET (Fig. 5C and D and *SI Appendix, Fig. S6G and H*). WT dynamin (DynWT) had minimal effects. Because GTP binding is required for scission of budding vesicles from the plasma membrane, DynK44E presumably traps PAR₂ in membrane vesicles, which would impede interaction with Rab5a but not RIT. Thus, trypsin, but not CS or NE, induces clathrin- and dynamin-dependent endocytosis of PAR₂.

We investigated the contribution of endocytosis to trypsin-induced signaling in HEK293 cells expressing Flag-PAR₂-HA11 and FRET biosensors for cytosolic and nuclear ERK (CytoEKAR, NucEKAR), plasma membrane and cytosolic PKC (pmCKAR, CytoCKAR), and plasma membrane and cytosolic cAMP (pmEpac, CytoEpac). Trypsin (10 nM), but not NE or CS (100 nM), stimulated a rapid and persistent activation of ERK in the cytosol and nucleus (EC₅₀, 5 nM) (Fig. 5E and F and *SI Appendix, Fig. S7A–F*). I-343 (10 μM) but not the PAR₁ antagonist SCH530348 (100 nM) inhibited trypsin activation of cytosolic and nuclear ERK (Fig. 5G). PS2 and DynK44E inhibited trypsin-stimulated activation of cytosolic and nuclear ERK compared with PS2 inact and DynWT controls (Fig. 5H and I and *SI Appendix, Fig. S7G–J*). AG1478 (1 μM), an inhibitor of EGF receptor tyrosine kinase (34), UBO-QIC (100 nM), which inhibits Gα_q and certain Gβγ signals (35), and Gö6983 (1 μM), which inhibits all isoforms of PKC (36), suppressed trypsin-stimulated activation of cytosolic ERK (Fig. 5J and *SI Appendix, Fig. S7K*). UBO-QIC and Gö6983 also inhibited activation of nuclear ERK (Fig. 5K and *SI Appendix, Fig. S7L*). The results suggest that PAR₂ signals from endosomes by Gα_q-dependent mechanisms to activate ERK in the cytosol and nucleus.

To determine whether trypsin induces translocation of βARR and Gα_q to endosomes, we measured BRET between βARR1-RLuc8 or Gα_q-RLuc8 and Rab5a-Venus in HEK293 cells. Trypsin (100 nM)

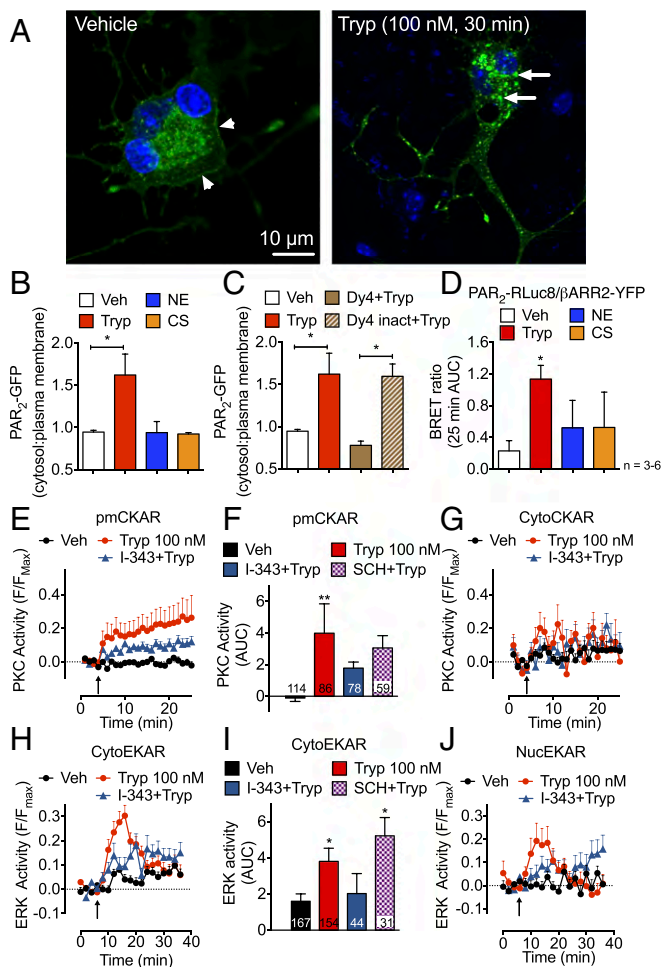


Fig. 4. PAR₂ endocytosis, β ARR2 recruitment, and compartmentalized signaling in nociceptors. (A–C) PAR₂ endocytosis. (A) Representative images (of three experiments) of effects of trypsin (Tryp) on the distribution of mPAR₂-GFP in mouse DRG neurons. Arrowheads (A, Left) show PAR₂-GFP at the plasma membrane. Arrows (A, Right) show PAR₂-GFP in endosomes. (B and C) Cytosol/plasma membrane ratio of mPAR₂-GFP in mouse DRG neurons after 30-min incubation with trypsin, NE, or CS (B), or after preincubated with Dy4 or Dy4 inact and then trypsin (C). (D) PAR₂-RLuc8/ β ARR2-YFP BRET in mouse DRG neurons exposed to trypsin, NE or CS. AUC, area under curve (25 min) **P* < 0.05 to vehicle. *n*, experimental replicates, triplicate observations. (E–J) Compartmentalized signaling. Effects of trypsin on PKC activity at the plasma membrane (E and F) and in the cytosol (G), and on ERK activity in the cytosol (H and I), and nucleus (J) of rat DRG neurons. Numbers in bars denote neuron numbers. **P* < 0.05, ***P* < 0.01 to vehicle.

stimulated an increase in β ARR1-RLuc8/Rab5a-Venus BRET and in $G\alpha_q$ -RLuc8/Rab5a-Venus BRET (SI Appendix, Fig. S8 A and B). We used immunofluorescence and structured illumination microscopy to localize PAR₂-HA, $G\alpha_q$ and early endosomal antigen-1 (EEA1) in HEK-293 cells. In unstimulated cells, PAR₂ was confined to the plasma membrane, although $G\alpha_q$ was detected in early endosomes (SI Appendix, Fig. S8C). Trypsin (10 nM, 30 min) induced translocation of PAR₂ to early endosomes containing $G\alpha_q$. The results support the hypothesis that trypsin causes assembly of a PAR₂/ β ARR/ $G\alpha_q$ signalosome in early endosomes.

Trypsin (10 nM) caused a rapid and sustained activation of PKC and generation of cAMP at the plasma membrane and in the cytosol of HEK293 cells (SI Appendix, Fig. S9 A–H). DynK44E strongly inhibited these signals, but DynWT had no effect. I-343, but not SCH530348, inhibited trypsin stimulation of PKC and cAMP, which thus depend on PAR₂ (SI Appendix, Fig. S9 G and H). These results suggest that endocytosis is necessary

for multiple components of PAR₂ signaling. cAMP signaling at the plasma membrane is usually desensitized by β ARR delivery of phosphodiesterases, which degrade cAMP (37). The sustained plasma membrane cAMP response to trypsin support the existence of mechanisms that allow persistent PAR₂ signaling, which warrant further investigation. Stimulation of cells with the positive controls PDBu (EKAR), PDBu + phosphatase inhibitor mixture-2 (CKAR), or forskolin + 3-isobutyl-1-methylxanthine (Epac) revealed that responses to proteases did not saturate the FRET biosensors (Fig. 5 E and F and SI Appendix, Fig. S9 A–D).

IBS-Induced Hyperexcitability of Nociceptors. We investigated whether proteases from mucosal biopsies of IBS patients cause a persistent hyperexcitability of nociceptors by a mechanism that entails endosomal signaling of PAR₂. Biopsies of colonic mucosa from patients with diarrhea-predominant IBS (IBS-D) or healthy control (HC) subjects were placed in culture medium (24 h, 37 °C). Mouse DRG neurons were then exposed to biopsy supernatants (30 min, 37 °C) and washed. Rheobase was measured 30 min after washing to assess persistent hyperexcitability. Supernatants of biopsies from IBS-D patients caused a persistent decrease in rheobase, consistent with hyperexcitability, compared with supernatants from HC subjects (rheobase at 30 min: HC, 78.33 \pm 4.41 pA, 12 neurons, supernatant from four IBS-D; 54.55 \pm 4.74 pA, 11 neurons, supernatant from four IBS-D; *P* < 0.05; ANOVA, Tukey's multiple comparisons test) (Fig. 6 A and B). I-343 (PAR₂ antagonist, 10 μ M), Dy4 (dynamin inhibitor, 30 μ M), and PD98059 (MEK1 inhibitor, 50 μ M) abolished IBS-D-induced hyperexcitability of nociceptors (Fig. 6 A–D). Dy4 caused a nonsignificant decrease in the rheobase of neurons exposed to HC supernatant, but I-343 and PD98059 had no effect.

To examine whether proteases in IBS-D supernatants can stimulate endocytosis of PAR₂, BRET was used to assess the proximity between PAR₂-RLuc8 and Rab5a-Venus expressed in HEK293 cells. IBS-D supernatant increased PAR₂-RLuc8/Rab5a-Venus BRET after 60 min compared with HC supernatant (Fig. 6E). Trypsin (10 nM, positive control) also increased PAR₂-RLuc8/Rab5a-Venus BRET.

These results suggest that proteases that are released from biopsies of colonic mucosa from patients with IBS-D cause long-lasting hyperexcitability of nociceptors by a mechanism that requires dynamin-dependent endocytosis of PAR₂ and PAR₂ ERK signaling from endosomes.

Antagonist Delivery to PAR₂ in Endosomes. If endosomal signaling of PAR₂ sustains the hyperexcitability of nociceptors exposed to supernatants from IBS-D patients, do PAR₂ antagonists that are targeted to endosomal receptors effectively reverse this process? Conjugation to the transmembrane lipid cholesterol facilitates endosomal delivery of antagonists of the neurokinin 1 receptor (NK₁R) and calcitonin receptor-like receptor (CLR), which provide more efficacious and long-lasting antinociception than conventional antagonists that do not target receptors in endosomes (8, 12). To evaluate whether PAR₂ in endosomes is a therapeutic target, tripartite probes were synthesized comprising: cholesterol to anchor probes to membranes or ethyl ester that does not incorporate into membranes; a polyethylene glycol (PEG) 12 linker to facilitate presentation in an aqueous environment; and a cargo of cyanine 5 (Cy5) for localization or PAR₂ antagonist I-343 (SI Appendix, Fig. S10 A and B). To determine whether tripartite probes accumulate in endosomes containing PAR₂, mouse DRG neurons expressing mPAR₂-GFP were incubated with Cy5-PEG-cholesterol (Cy5-Chol) or Cy5-PEG-Ethyl ester (Cy5-Ethyl ester) (200 nM, 60 min, 37 °C). Neurons were washed and imaged (37 °C). Cy5-Ethyl ester was not taken up by neurons, whereas Cy5-Chol inserted into the plasma membrane and then accumulated in endosomes of the soma and neurites over 3 h (Fig. 7). Trypsin induced endocytosis of PAR₂-GFP into endosomes in close proximity to vesicles containing

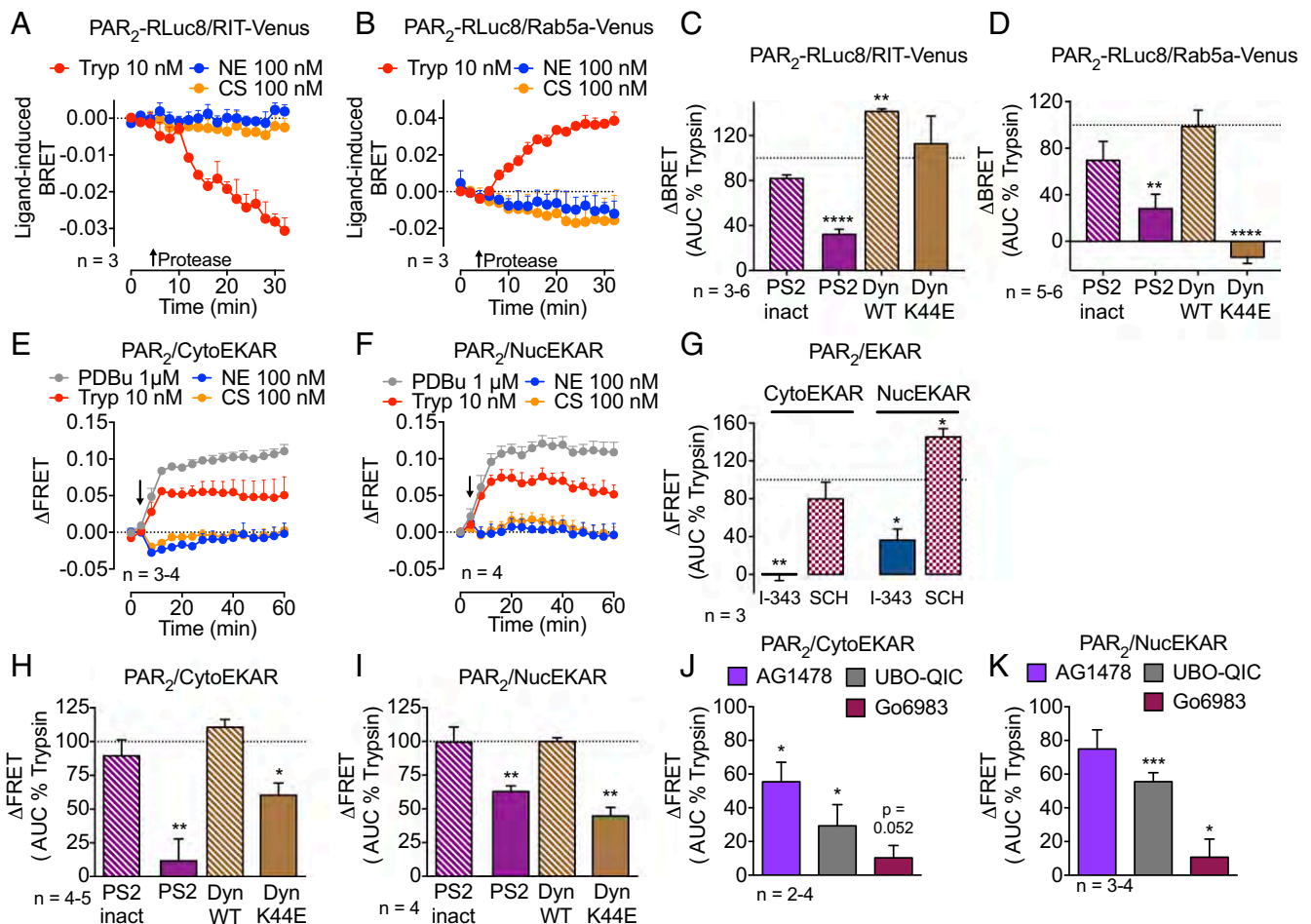


Fig. 5. PAR₂ endocytosis and compartmentalized ERK signaling in HEK293 cells. (A–D) BRET assays of endocytosis. PAR₂-RLuc8/RIT-Venus BRET (A and C) and PAR₂-RLuc8/Rab5a-Venus BRET (B and D). (E–K) FRET assays of cytosolic (E, G, H, and J) and nuclear (F, G, I, and K) ERK activity. AUC, area under curve. **P* < 0.05, ***P* < 0.01, ****P* < 0.001, *****P* < 0.0001 compared with trypsin alone. *n*, experimental replicates in triplicate.

Cy5-Chol. Video-imaging revealed frequent association of endosomes containing PAR₂-GFP and Cy5-Chol (Movie S1). I-343-PEG-cholestanol (MIPS15479) (SI Appendix, Fig. S10A) antagonized 2F-stimulated IP₁ accumulation in HT-29 cells (pIC₅₀ 6.18 ± 0.07; IC₅₀, 670 nM), albeit with reduced potency compared with the parent compound I-343 (pIC₅₀ 8.96 ± 0.10; IC₅₀ 1.1 nM) (SI Appendix, Fig. S10C).

Antagonism of Endosomal PAR₂ and Hyperexcitability of Nociceptors.

To evaluate the capacity of an endosomally targeted PAR₂ antagonist to inhibit protease-induced hyperexcitability of nociceptors, mouse DRG neurons were preincubated with MIPS15479 (30 μM) or vehicle (60 min, 37 °C), washed, and recovered in antagonist-free medium for 180 min to allow accumulation of antagonist in endosomes (Fig. 8A). Transient incubation with trypsin decreased rheobase of vehicle-treated neurons at 0 and 30 min (Fig. 8B). MIPS15479 did not affect the initial excitability at 0 min, but prevented the persistent response at 30 min. MIPS15479 had no effect on baseline rheobase at either time point. Similarly, transient incubation with IBS-D supernatant decreased rheobase at 30 min compared with HC supernatant (Fig. 8C). MIPS15479 completely prevented the persistent actions of IBS-D supernatant on nociceptor excitability (rheobase at 30 min: vehicle IBS-D, 40 ± 3.89 pA, 12 neurons, supernatant from four patients; MIPS15479 IBS-D, 64.7 ± 3.84 pA, 17 neurons, supernatant from four patients; *P* < 0.05) (Fig. 8C). MIPS15479 did not affect excitability of neurons treated with HC supernatant. These

results support the hypothesis that PAR₂ in endosomes generates signals that underlie the persistent hyperexcitability of nociceptors, and is a potential therapeutic target for IBS pain.

PAR₂ Endosomal Signaling Mediates Trypsin-Induced Sensitization of Colonic Afferent Neurons and Colonic Nociception.

The sensitization of colonic afferent neurons to mechanical stimuli is a leading hypothesis for IBS pain (17). To examine whether proteases cleave PAR₂ on the peripheral terminals of colonic nociceptors to induce mechanical hypersensitivity, we made single-unit recordings from afferent neurons innervating the mouse colon. Receptive fields were identified by mechanical stimulation of the mucosal surface with VFF, proteases were applied to the mucosal receptive fields, and mechanical responses were reevaluated to assess sensitization. Under basal conditions, repeated mechanical stimulation (2-g filament) induced reproducible firing (Fig. 9A). Exposure to trypsin (10 nM, 10 min) amplified the frequency of firing to mechanical stimulation by 35.8 ± 5.9%, to NE (100 nM, 10 min) by 41.0 ± 11.8%, and to CS (100 nM, 10 min) by 52.0 ± 13.2% (Fig. 9B–E).

Colitis in mice induces hypersensitivity of colonic afferent neurons that persists even after inflammation is resolved (17). This chronic hypersensitivity resembles postinfectious/inflammatory IBS. To determine whether proteases can further amplify chronic hypersensitivity, mice were treated with trinitrobenzene sulphonic acid (TNBS enema) to induce colitis. At 28 d post-TNBS, when inflammation was resolved, mechanical stimulation

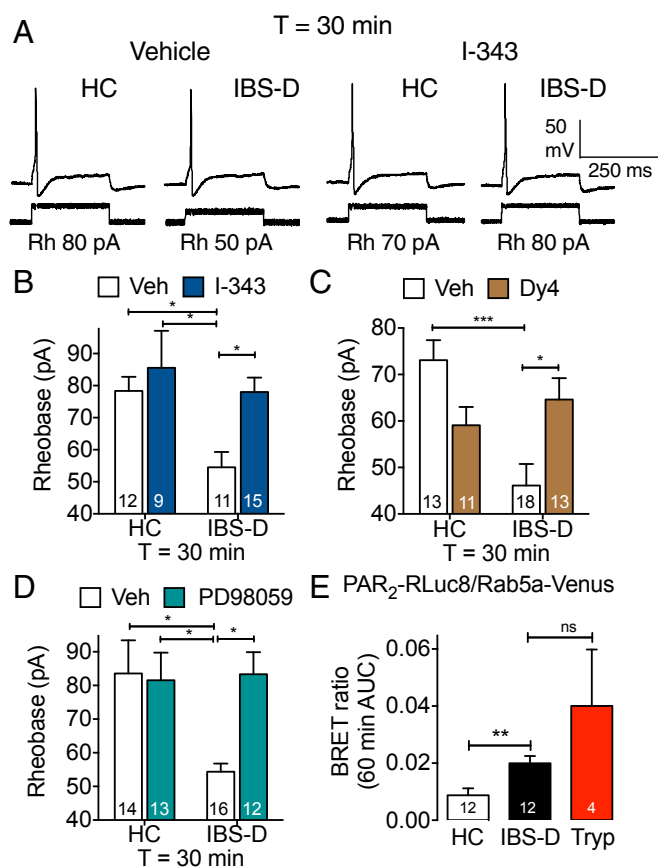


Fig. 6. IBS-D-induced hyperexcitability of nociceptors. (A–D) Rheobase of mouse nociceptors 30 min after exposure to supernatant from biopsies of colonic mucosa from HC and IBS-D subjects. (A) Representative traces of vehicle- or I-343-treated neurons. Rh, rheobase. (B–D) Mean responses of neurons preincubated with I-343 (B, PAR₂ antagonist), Dy4 (C, dynamin inhibitor), or PD98059 (D, MEK1 inhibitor). (E) PAR₂-RLuc8/Rab5a-Venus BRET in HEK293 cells measured after 60-min incubation with HC or IBS-D biopsy supernatant, or trypsin. **P* < 0.05, ***P* < 0.01, ****P* < 0.001; ns, not significant. Numbers in bars denote neuron numbers.

of the colon induced a larger firing rate than in healthy control mice, consistent with chronic hyperexcitability (SI Appendix, Fig. S11 A–D). Compared with basal responses, trypsin further amplified responses by $16.4 \pm 7.9\%$, NE by $30.6 \pm 9.0\%$, and CS by $29.6 \pm 9.2\%$. Thus, proteases can still amplify the excitability of colonic nociceptors even when they are already sensitized as a result of prior inflammation.

To determine the contribution of endosomal PAR₂ signaling to trypsin-induced sensitization of colonic afferent neurons in normal healthy mice, I-343 (10 μM), PS2, or PS2 inact (50 μM) was applied to the receptive fields before exposure to trypsin. I-343 and PS2 did not affect basal mechanical sensitivity, but abolished trypsin-induced sensitization of mechanical responses (Fig. 9 F and G). PS2 inact did not affect basal responses or trypsin-induced sensitization (Fig. 9H).

Noxious colorectal distension (CRD) triggers the visceromotor response (VMR), a nociceptive brainstem reflex consisting of contraction of abdominal muscles, which can be monitored by electromyography. This approach allows assessment of visceral sensitivity in awake mice (38). To examine protease-induced hypersensitivity, a protease mixture (10 nM trypsin + 100 nM NE + 100 nM CS) or vehicle (saline) (100 μL) was instilled into the colon (enema) of healthy mice. After 15 min, the VMR was measured in response to graded CRD (20–80 mm Hg) with a

barostat balloon. In vehicle-treated mice, CRD induced a graded VMR (Fig. 9I). The protease mixture amplified VMR at all pressures from 40 to 80 mm Hg. Administration of I-343 (30 mg/kg) into the colon (100 μL enema) 30 min before the protease mixture, abolished the response (Fig. 9J). Because alterations in the compliance of the colon can alter VMR to CRD, the pressure/volume relationship was measured at all distending pressures. Compliance of the colon was unaffected by the protease mixture or I-343 (SI Appendix, Fig. S11 E and F).

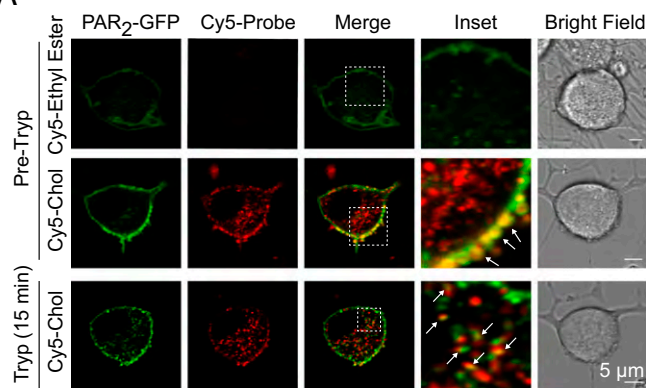
The results support the hypothesis that PAR₂ endocytosis is required for trypsin-induced sensitization of colonic afferent neurons and colonic nociception.

Discussion

We propose that two components of PAR₂ signaling contribute to persistent hyperexcitability on nociceptors: irreversible proteolytic activation and sustained signaling from endosomes or the plasma membrane, depending on the mechanism of activation (Fig. 10 and Movie S2). In the case of trypsin and proteases from the mucosa of patients with IBS-D, PAR₂ endocytosis and endosomal ERK signaling mediate persistent hyperexcitability. In the case of NE and CS, which do not cause PAR₂ endocytosis, plasma membrane signaling underlies persistent hyperexcitability. The observation that an endosomally targeted PAR₂ antagonist blocks the persistent actions of trypsin and IBS proteases identifies PAR₂ in endosomes as a therapeutic target. The combined results reveal that endosomal GPCR signaling can contribute to processes that are relevant to human disease, and support the proposal that GPCRs in endosomes are a target for therapy (8, 12).

Mechanisms of Persistent Hyperexcitability of Nociceptors and Nociception. The contribution of plasma membrane and endosomal signaling of PAR₂ to protease-induced hyperexcitability of nociceptors depends

A DRG Soma



B DRG Neurite

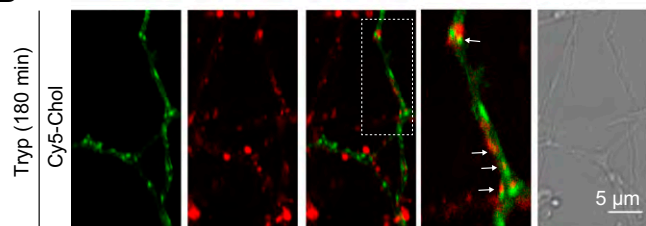


Fig. 7. Targeting PAR₂ in endosomes of nociceptors. Representative images (of three experiments) of trafficking of Cy5 tripartite probes and mPAR₂-GFP to the soma (A) and neurites (B) of mouse DRG neurons. The scale bar (5 μm) in the bright-field image applies to all panels in the same row, except for *Inset*, which is a magnification of the dashed box in the merged panels. Arrows show proximity of vesicles containing mPAR₂-GFP and Cy5-Chol.

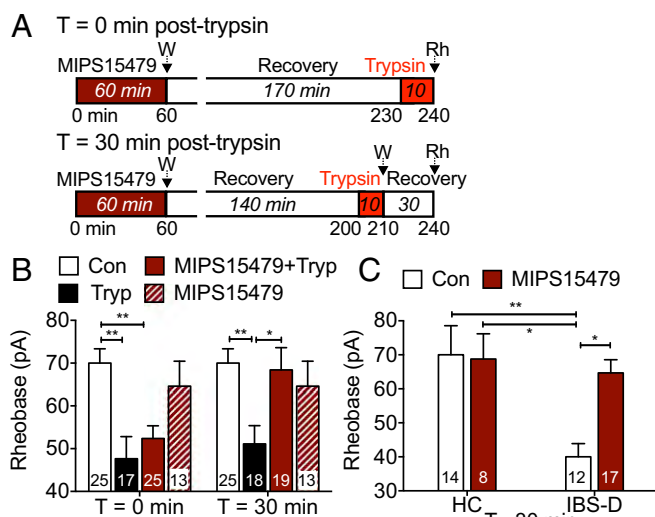


Fig. 8. Antagonism of endosomal PAR₂ and hyperexcitability of nociceptors. (A and B) Trypsin-induced hyperexcitability of mouse DRG neurons. Neurons were preincubated with MIPS15479 or vehicle (control, con) for 60 min, washed, and recovered for 170 or 140 min. Neurons were then exposed to trypsin (10 min). Rheobase was measured 0 or 30 min after trypsin and 180 min post-MIP15479. (C) IBS-induced hyperexcitability of mouse DRG neurons. Neurons were preincubated with MIPS15479 or vehicle (control, con) for 60 min, washed, and recovered for 60 min. Neurons were then exposed to HC or IBS-D supernatant for 30 min, washed, and rheobase was measured 30 min later (T 30 min), 120 min post-MIP15479. **P* < 0.05, ***P* < 0.01. Numbers in bars denote neuron numbers.

on the protease and the timing of the response. Trypsin, but not NE or CS, caused dynamin- and clathrin-dependent endocytosis of PAR₂ in nociceptors. Because inhibitors of endocytosis did not affect the initial effects of trypsin, NE, or CS on excitability, hyperexcitability initially involves PAR₂ signaling at the plasma membrane. Clathrin and dynamin inhibitors prevented persistent trypsin-induced hyperexcitability (at a time when activated PAR₂ was in endosomes), and also suppressed trypsin-induced sensitization of colonic afferent nociceptors and somatic mechanical allodynia. Thus, PAR₂ endocytosis and continued endosomal signaling are necessary for persistent trypsin-induced hyperexcitability of nociceptors and nociception. Inhibitors of endocytosis did not affect NE- or CS-induced neuronal hyperexcitability or mechanical allodynia, which is consistent with the inability of these proteases to induce PAR₂ endocytosis.

PAR₂/PKC signaling at the plasma membrane mediates initial trypsin-induced hyperexcitability of nociceptors, because trypsin induced PAR₂-dependent PKC activation at the plasma membrane, and a PKC inhibitor blocked the initial hyperexcitability. Several observations indicate that PAR₂/ERK signaling from endosomes mediates persistent trypsin-induced hyperexcitability: trypsin stimulated PAR₂-dependent ERK activity in the cytosol and nucleus, clathrin and dynamin inhibitors suppressed ERK activation, and a MEK1 inhibitor prevented the persistent actions of trypsin. The finding that inhibitors of G α_q , PKC, and the EGF receptor block trypsin activation of ERK, suggest that several pathways mediate PAR₂ signaling in endosomes. A PAR₂/ β ARR/Raf-1/MEK signaling complex in endosomes mediates activation of ERK in the cytosol (5), and G α_q and G α_s transduce signals from other GPCRs in endosomes (7, 8, 12). G α_q was detected in early endosomes of HEK293 cells under basal conditions and after exposure to trypsin by immunofluorescence and superresolution microscopy. In agreement with previous studies (5, 14), trypsin induced translocation of PAR₂ and β ARR to early endosomes, detected by BRET and microscopy. Together, these findings support involvement of G α_q and β ARR in endosomal signaling of PAR₂. NE and CS induce PAR₂-dependent stimulation of adenylyl

cyclase and protein kinase A-mediated activation of transient receptor potential vanilloid 4 in nociceptors, which likely underlie hyperexcitability (15, 16). The inability to recruit β ARRs and internalize may contribute to the sustained signaling of NE- and CS-activated PAR₂ at the plasma membrane.

The finding that a cholestanol-conjugated PAR₂ antagonist inhibited the ability of trypsin and IBS-D proteases to cause persistent hyperexcitability of nociceptors reinforces the importance of endosomal PAR₂ signaling. After transient incubation and recovery, cholestanol-conjugated tripartite probes were removed from the plasma membrane of nociceptors and accumulated in endosomes containing PAR₂, which demonstrates effective targeting. The observation that I-343-PEG-cholestanol and inhibitors of clathrin and dynamin inhibited the persistent, but not initial, actions of trypsin and IBS-proteases on nociceptor excitability suggests selective targeting of PAR₂ in endosomes represents a viable therapeutic strategy. Because I-343-PEG-cholestanol abolished persistent hyperexcitability despite reduced potency, endosomal targeting, retention, and local concentration are probably important determinants of efficacy.

There are several limitations of this investigation. Further studies are required to characterize the composition of PAR₂ signaling complexes in different subcellular domains, and to define the mechanisms by which PAR₂/PKC signaling at the plasma membrane and PAR₂/ERK signaling in endosomes amplify the sensitivity of nociceptors. Involvement of PKC and ERK are consistent with reports that painful stimulants activate PKC ϵ and ERK1/2 in primary sensory neurons, and that inhibitors of PKC ϵ and MEK attenuate nociception (39, 40). PKC and ERK can activate channels that control the sensitivity of nociceptors (41). GPCRs in endosomes can also regulate transcription, which may contribute to chronic hyperexcitability of nociceptors (8, 11). Additional studies are required to define the specificity of I-343 and I-343-PEG-cholestanol (MIP15479) for PAR₂ over other GPCRs. Although I-343 shows remarkable potency for PAR₂, high concentrations of I-343 can inhibit thrombin signaling, suggesting antagonism of PAR₁ (26). However, I-343, at concentrations that do not affect thrombin signaling, prevented trypsin-induced hyperexcitability of nociceptors, whereas a PAR₁-selective antagonist had no effect. Thus, PAR₂, not PAR₁, mediates these actions of trypsin.

A limitation to the use of inhibitors of endocytosis is that clathrin and dynamin control the trafficking of many receptors and channels that control neuronal activity and nociception. Although Dy4 may have off-target effects (42), we obtained similar results by overexpressing dominant-negative dynamin or inhibiting clathrin. Dy4 and PS2 did not affect basal excitability of nociceptors or affect hyperexcitability or allodynia to NE or CS, which do not cause PAR₂ endocytosis. These findings argue against nonselective effects of inhibitors on the function of nociceptors. The finding that an endosomally targeted PAR₂ antagonist (I-343-PEG-cholestanol) replicated the inhibitory actions of Dy4 and PS2 on trypsin-induced hyperexcitability, supports the involvement of endosomal PAR₂ signaling.

PAR₂ Endosomal Signaling and IBS Pain. PAR₂ endosomal signaling may underlie persistent hyperexcitability of nociceptors in patients with IBS-D, because an endosomally targeted PAR₂ antagonist and inhibitors of dynamin and MEK1 prevented the persistent effects of IBS-D proteases on the hyperexcitability of nociceptors. Although we did not identify the proteases that are released from colonic biopsies that mediate these effects, trypsin and trypsin-3 are likely candidates; both proteases are activated in the colonic mucosa of IBS patients, and trypsin and trypsin inhibition or PAR₂ deletion prevent IBS-dependent hyperexcitability of nociceptors (18–21). The finding that a dynamin inhibitor and an endosomally targeted PAR₂ antagonist prevented hypersensitivity supports involvement of proteases that activate PAR₂ by canonical mechanisms and induce receptor endocytosis, such as trypsin and trypsin-3 (13).

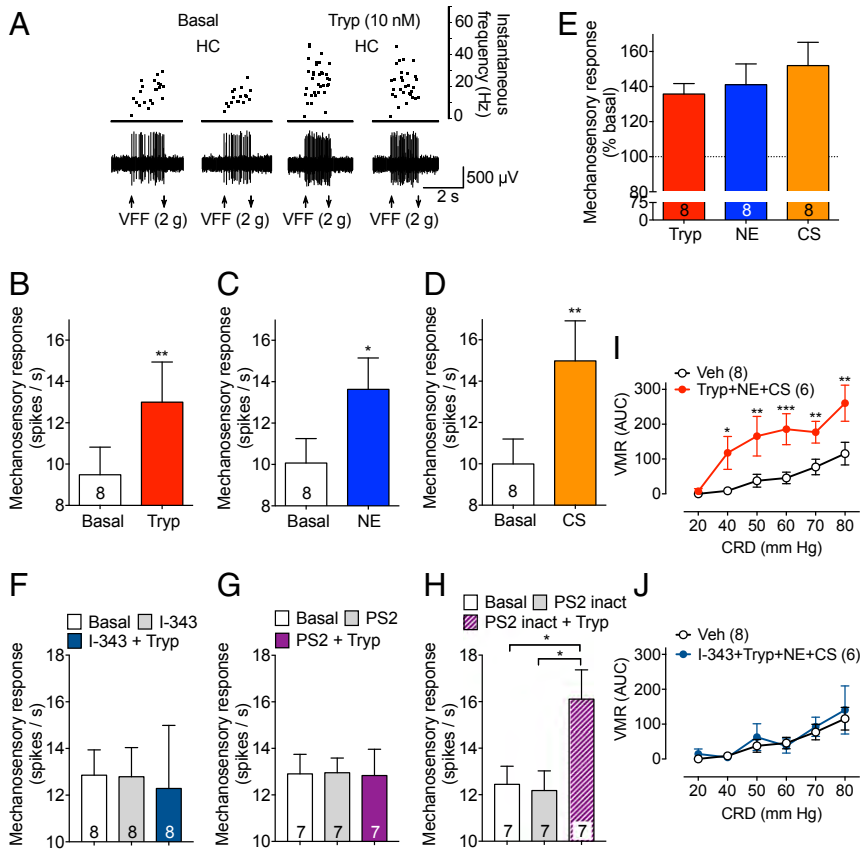


Fig. 9. Sensitization of colonic afferents and colonic nociception. (A–H) Mechanosensory responses in healthy control mice to stimulation of the colonic mucosa with a 2 g VFF under basal conditions and after exposure of receptive fields to trypsin (A, B, and E–H), NE (C and E), or CS (D and E). (A) Representative results. (B–D and F–H) Mean responses. (E) Responses as percent basal. Numbers in bars denote afferent numbers. (I and J) VMR to CRD in awake normal mice. Numbers in parentheses denote mouse number. * $P < 0.05$, ** $P < 0.01$, *** $P < 0.001$.

Hypersensitivity to colorectal distension is a hallmark of IBS (17). Our results show that proteases that activate PAR₂ by canonical (trypsin) and biased (NE, CS) mechanisms sensitize colonic nociceptors to mechanical stimuli in basal and postinflammatory states. Trypsin-evoked sensitization requires PAR₂ endocytosis and endosomal signaling. The administration of a mixture of proteases (trypsin, NE, CS) into the colonic lumen of mice amplified VMR to CRD, which is consistent with mechanical hyperalgesia in the colon. I-343 abolished these effects, which are thus dependent on PAR₂. We did not determine whether inhibitors of endocytosis or endosomally targeted PAR₂ antagonists suppress trypsin-evoked

colonic nociception due to the impracticality of systemic administration of broadly acting and lipophilic drugs. Such studies will require pharmacokinetic studies of endocytic inhibitors and I-343-PEG-cholestanol to determine whether these drugs are capable of targeting pain-sensing neurons in the colonic wall. However, when administered by local injection into the paw, inhibitors of dynamin and clathrin prevented the ability of trypsin to cause mechanical allodynia. These results support a role for endosomal signaling in mechanical nociception.

Our results show that PAR₂ expressed by Na_v1.8⁺ neurons mediates the long-lasting pronociceptive actions of trypsin, NE,

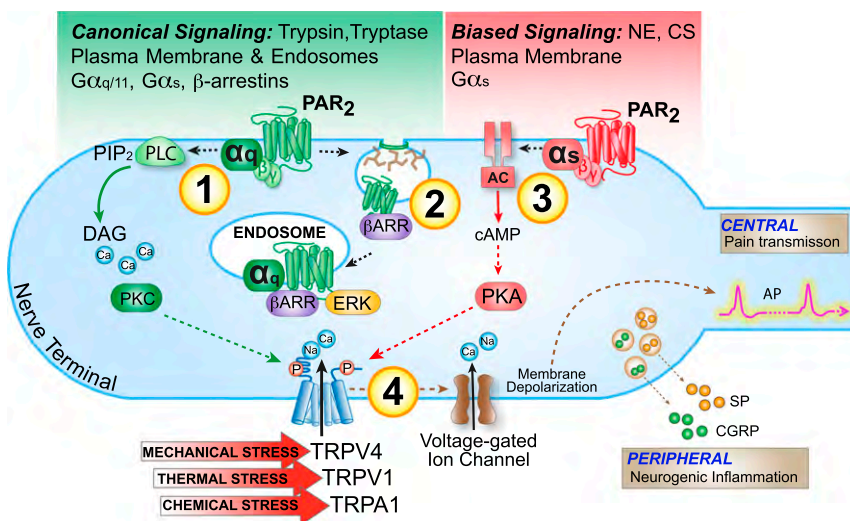


Fig. 10. Mechanisms of protease- and PAR₂-induced hyperexcitability of nociceptors. After activation by canonical mechanisms, PAR₂ signals at the plasma membrane to activate PKC, which mediates initial hyperexcitability (1). PAR₂ then undergoes clathrin-, dynamin-, and β ARR-dependent endocytosis (2). PAR₂ continues to signal from endosomes by β ARR- and G α_q -mediated mechanisms to activate ERK, which mediates persistent hyperexcitability. After activation by biased mechanisms, PAR₂ signals from the plasma membrane to activate adenylyl cyclase (AC) and PKA, which mediate the initial and persistent hyperexcitability (3). Kinases may regulate the activity of TRP channels and voltage-gated ion channels, to control nociceptor hyperexcitability (4).

and CS, because the sustained actions of these proteases were absent or diminished in *Par2-NaV1.8* mice. Because global deletion of PAR₂ attenuates the algic actions of these proteases (15, 16, 43), the initial effects may involve activation of PAR₂ on other cell types involved in nociception, including keratinocytes and colonocytes that highly express PAR₂ (13). The findings that deletion of PAR₂ in NaV1.8⁺ neurons or treatment with a PAR₂ antagonist suppressed trypsin signaling in DRG cultures support the suggestion that proteases can directly activate nociceptors by cleaving PAR₂. However, we cannot exclude the possibility that proteases activate PAR₂ on nonneuronal cells that control nociceptor function, or that proteases may cause pain by activating other receptors, such as PAR₁. PAR₂ in NaV1.8⁺ neurons markedly inhibited trypsin-induced edema and neutrophil infiltration, which supports the proposal that trypsin causes inflammation by a neurogenic mechanism (44).

Our results have implications for the treatment of IBS pain. GPCRs are the target of over one-third of therapeutic drugs, most of which are designed to target cell surface receptors. The realization that GPCRs can continue to signal from endosomes to control important pathophysiological processes, has led to the proposal that receptors in endosomes are a target for therapy (1, 8, 12). The capacity of endosomally targeted PAR₂ antagonists to abolish IBS-dependent persistent hyperexcitability of nociceptors highlights the importance of endosomal signaling of GPCRs for human disease, and reveals endosomal PAR₂ as a therapeutic target for IBS pain.

- Murphy JE, Padilla BE, Hasdemir B, Cottrell GS, Bunnett NW (2009) Endosomes: A legitimate platform for the signaling train. *Proc Natl Acad Sci USA* 106:17615–17622.
- DeWire SM, Ahn S, Lefkowitz RJ, Shenoy SK (2007) Beta-arrestins and cell signaling. *Annu Rev Physiol* 69:483–510.
- Cheloha RW, Gellman SH, Vilardaga J-P, Gardella TJ (2015) PTH receptor-1 signalling-mechanistic insights and therapeutic prospects. *Nat Rev Endocrinol* 11:712–724.
- DeFea KA, et al. (2000) The proliferative and antiapoptotic effects of substance P are facilitated by formation of a beta-arrestin-dependent scaffolding complex. *Proc Natl Acad Sci USA* 97:11086–11091.
- DeFea KA, et al. (2000) Beta-arrestin-dependent endocytosis of proteinase-activated receptor 2 is required for intracellular targeting of activated ERK1/2. *J Cell Biol* 148:1267–1281.
- Eichel K, Jullié D, von Zastrow M (2016) β -Arrestin drives MAP kinase signalling from clathrin-coated structures after GPCR dissociation. *Nat Cell Biol* 18:303–310.
- Irannejad R, et al. (2013) Conformational biosensors reveal GPCR signalling from endosomes. *Nature* 495:534–538.
- Jensen DD, et al. (2017) Neurokinin 1 receptor signaling in endosomes mediates sustained nociception and is a viable therapeutic target for prolonged pain relief. *Sci Transl Med* 9:eal3447.
- May V, Parsons RL (2017) G protein-coupled receptor endosomal signaling and regulation of neuronal excitability and stress responses: Signaling options and lessons from the PAC1 receptor. *J Cell Physiol* 232:698–706.
- Thomsen ARB, et al. (2016) GPCR-G protein- β -arrestin super-complex mediates sustained G protein signaling. *Cell* 166:907–919.
- Tsvetanova NG, von Zastrow M (2014) Spatial encoding of cyclic AMP signaling specificity by GPCR endocytosis. *Nat Chem Biol* 10:1061–1065.
- Yarwood RE, et al. (2017) Endosomal signaling of the receptor for calcitonin gene-related peptide mediates pain transmission. *Proc Natl Acad Sci USA* 114:12309–12314.
- Ossovskaya VS, Bunnett NW (2004) Protease-activated receptors: Contribution to physiology and disease. *Physiol Rev* 84:579–621.
- Déry O, Thoma MS, Wong H, Grady EF, Bunnett NW (1999) Trafficking of proteinase-activated receptor-2 and beta-arrestin-1 tagged with green fluorescent protein. beta-arrestin-dependent endocytosis of a proteinase receptor. *J Biol Chem* 274:18524–18535.
- Zhao P, et al. (2014) Cathepsin S causes inflammatory pain via biased agonism of PAR2 and TRPV4. *J Biol Chem* 289:27215–27234.
- Zhao P, et al. (2015) Neutrophil elastase activates PAR2 and TRPV4 to cause inflammation and pain. *J Biol Chem* 290:13875–13887.
- Azpiroz F, et al. (2007) Mechanisms of hypersensitivity in IBS and functional disorders. *Neurogastroenterol Motil* 19(Suppl 1):62–88.
- Barbara G, et al. (2007) Mast cell-dependent excitation of visceral-nociceptive sensory neurons in irritable bowel syndrome. *Gastroenterology* 132:26–37.
- Cenac N, et al. (2007) Role for protease activity in visceral pain in irritable bowel syndrome. *J Clin Invest* 117:636–647.
- Rolland-Fourcade C, et al. (2017) Epithelial expression and function of trypsin-3 in irritable bowel syndrome. *Gut* 66:1767–1778.
- Valdez-Morales EE, et al. (2013) Sensitization of peripheral sensory nerves by mediators from colonic biopsies of diarrhea-predominant irritable bowel syndrome patients: A role for PAR2. *Am J Gastroenterol* 108:1634–1643.
- Kayssi A, Amadesi S, Bautista F, Bunnett NW, Vanner S (2007) Mechanisms of protease-activated receptor 2-evoked hyperexcitability of nociceptive neurons innervating the mouse colon. *J Physiol* 580:977–991.
- Reed DE, et al. (2003) Mast cell tryptase and proteinase-activated receptor 2 induce hyperexcitability of guinea-pig submucosal neurons. *J Physiol* 547:531–542.
- Robertson MJ, Deane FM, Robinson PJ, McCluskey A (2014) Synthesis of Dynole 34-2, Dynole 2-24 and Dyngo 4a for investigating dynamin GTPase. *Nat Protoc* 9:851–870.
- Robertson MJ, et al. (2014) Synthesis of the Pitstop family of clathrin inhibitors. *Nat Protoc* 9:1592–1606.
- Farmer LJ (2013) Imidazopyridazines useful as inhibitors of the PAR-2 signaling pathway. US Patent Appl WO 2015/048245.
- Jiang Y, et al. (2018) A potent antagonist of protease-activated receptor 2 that inhibits multiple signaling functions in human Cancer cells. *J Pharmacol Exp Ther* 364:246–257.
- Ahn HS, et al. (2000) Inhibition of cellular action of thrombin by N3-cyclopropyl-7-[[4-(1-methylethyl)phenyl]methyl]-7H-pyrrolo[3, 2-f]quinazoline-1,3-diamine (SCH 79797), a nonpeptide thrombin receptor antagonist. *Biochem Pharmacol* 60:1425–1434.
- Lieu T, et al. (2016) Antagonism of the proinflammatory and pronociceptive actions of canonical and biased agonists of protease-activated receptor-2. *Br J Pharmacol* 173:2752–2765.
- Davies SP, Reddy H, Caivano M, Cohen P (2000) Specificity and mechanism of action of some commonly used protein kinase inhibitors. *Biochem J* 351:95–105.
- Jensen DD, et al. (2016) Protein kinase D and G β 1 subunits mediate agonist-evoked translocation of protease-activated receptor-2 from the Golgi apparatus to the plasma membrane. *J Biol Chem* 291:11285–11299.
- Lan TH, Liu Q, Li C, Wu G, Lambert NA (2012) Sensitive and high resolution localization and tracking of membrane proteins in live cells with BRET. *Traffic* 13:1450–1456.
- Herskovits JS, Burgess CC, Obar RA, Vallee RB (1993) Effects of mutant rat dynamin on endocytosis. *J Cell Biol* 122:565–578.
- Levitzki A, Gazit A (1995) Tyrosine kinase inhibition: An approach to drug development. *Science* 267:1782–1788.
- Gao ZG, Jacobson KA (2016) On the selectivity of the G α q inhibitor UBO-QIC: A comparison with the G α i inhibitor pertussis toxin. *Biochem Pharmacol* 107:59–66.
- Gschwend M, et al. (1996) Inhibition of protein kinase C mu by various inhibitors. Differentiation from protein kinase c isoenzymes. *FEBS Lett* 392:77–80.
- Perry SJ, et al. (2002) Targeting of cyclic AMP degradation to beta 2-adrenergic receptors by beta-arrestins. *Science* 298:834–836.
- Castro J, et al. (2017) Cyclic analogues of alpha-conotoxin Vc1.1 inhibit colonic nociceptors and provide analgesia in a mouse model of chronic abdominal pain. *Br J Pharmacol* 175:2384–2398.
- Aley KO, et al. (2001) Nociceptor sensitization by extracellular signal-regulated kinases. *J Neurosci* 21:6933–6939.
- Khasar SG, et al. (1999) A novel nociceptor signaling pathway revealed in protein kinase C epsilon mutant mice. *Neuron* 24:253–260.
- Cheng JK, Ji RR (2008) Intracellular signaling in primary sensory neurons and persistent pain. *Neurochem Res* 33:1970–1978.
- Park RJ, et al. (2013) Dynamin triple knockout cells reveal off target effects of commonly used dynamin inhibitors. *J Cell Sci* 126:5305–5312.
- Vergnolle N, et al. (2001) Proteinase-activated receptor-2 and hyperalgesia: A novel pain pathway. *Nat Med* 7:821–826.
- Steinhoff M, et al. (2000) Agonists of proteinase-activated receptor 2 induce inflammation by a neurogenic mechanism. *Nat Med* 6:151–158.

Materials and Methods

Human Subjects. The Queen's University Human Ethics Committee approved human studies. All subjects gave informed consent.

Animal Subjects. Institutional Animal Care and Use Committees of Queen's University, Monash University, Flinders University, New York University, and the South Australian Health and Medical Research Institute approved studies in mice and rats.

Nociception, Inflammation, Nociceptor Hyperexcitability. The analysis of somatic nociception and inflammation (8, 12), nociceptor hyperexcitability (21), sensitization of colonic afferent neurons, and colonic nociception (38) have been described.

BRET, FRET Assays. Endocytosis was studied by BRET and compartmentalized signaling was analyzed by FRET, as described previously (8, 12).

Statistics. Results are mean \pm SEM. Differences were assessed using Student's *t* test (two comparisons) or one- or two-way ANOVA (multiple comparisons).

ACKNOWLEDGMENTS. This work was supported by NIH Grant NS102722 (to N.W.B.); National Health Medical and Research Council (NHMRC) Grants 63303, 1049682, and 1031886 (to N.W.B.); Australian Research Council Centre of Excellence in Convergent Bio-Nano Science and Technology (N.W.B.); Takeda Pharmaceuticals, Inc. (N.W.B.); NIH Grant DE026806 (to N.W.B. and B.L.S.); NIH Grant DE025393 (to B.L.S.); and the Canadian Institute of Health (S.J.V.). M.L.H. is an NHMRC RD Wright Career Development Fellow (1061687); S.M.B. is an NHMRC RD Wright Biomedical Research Fellow (1126378); and M.C. is a Monash Fellow.

Supplementary Information for

PROTEASE-ACTIVATED RECEPTOR-2 IN ENDOSOMES SIGNALS PERSISTENT PAIN OF IRRITABLE BOWEL SYNDROME

Nestor N. Jimenez-Vargas, Luke A. Pattison, Peishen Zhao, TinaMarie Lieu, Rocco Latorre, Dane D. Jensen, Joel Castro, Luigi Aurelio, Giang T. Le, Bernard Flynn, Carmen Klein Herenbrink, Holly R. Yeatman, Laura Edgington-Mitchell, Christopher J.H. Porter, Michelle L. Halls, Meritxell Canals, Nicholas A. Veldhuis, Daniel P. Poole, Peter McLean, Gareth A. Hicks, Nicole Scheff, Elyssa Chen, Aditi Bhattacharya, Brian L. Schmidt, Stuart M. Brierley, Stephen J. Vanner, Nigel W. Bunnett

Corresponding Author: Nigel W. Bunnett, Ph.D., Columbia University College of Physicians and Surgeons, 21 Audubon Avenue, Rm 209, New York City, New York 10032, USA
Email: nb33@cumc.columbia.edu

This PDF file includes:

Supplementary text
Figs. S1 to S11
Captions for movies S1 to S2
References for SI reference citations

Other supplementary materials for this manuscript include the following:

Movies S1 to S2

Supplementary Information Text

Methods

Human biopsy samples. The Queen's University Human Ethics Committee approved human studies. All subjects gave informed consent. Endoscopic biopsies were obtained from the descending colon of 13 adult IBS-D patients (12 female) diagnosed using ROME III criteria for diarrhea-predominant IBS and of 12 healthy controls. All IBS patients had symptoms greater than 1 year and most were greater than 5 years. Celiac disease was excluded by blood test and patients over 40 years with daily diarrhea were biopsied at the time of colonoscopy to exclude microscopic colitis. None of the patients had a history suggestive of post-infectious IBS. Control biopsies were obtained from patients undergoing colon screening who did not have gastrointestinal symptoms. Biopsies (8 samples per patient) were incubated in 250 μ l of RPMI medium containing 10% fetal calf serum, penicillin/streptomycin and gentamicin/amphotericin B (95%O₂/5%CO₂, 24 h, 37°C) (1). Supernatants were stored at -80°C. Supernatants from 4-6 patients were pooled and studied in individual experiments.

Animals. Institutional Animal Care and Use Committees of Queen's University, Monash University, Flinders University, New York University, and the South Australian Health and Medical Research Institute approved all studies. Mice (C57BL/6, males, 6-15 weeks) and rats (Sprague-Dawley, males, 8-12 weeks) were studied. Animals were maintained in a temperature-controlled environment with a 12 h light/dark cycle and free access to food and water. Animals were killed by CO₂ inhalation or anesthetic overdose and thoracotomy. Animals were randomized for treatments and no animals were excluded from studies.

Par₂-Nav_v1.8 mice. *F2rll* conditional knock-out C57BL/6 mice were generated by genOway (Lyon, France). The last exon of *F2rll*, encoding for the transmembrane, extracellular and cytoplasmic domains of F2RL1, was flanked by *loxP* sites and a neomycin cassette in intron 1. The neomycin cassette was excised by breeding these mice with a C57BL/6 FLP-expressing mouse line. To delete *Par₂* in peripheral neurons, *F2rll* conditional knock-out mice were bred with mice expressing Cre recombinase under the control of the *Scn10a* gene promoter (B6.129-Scn10a^{tm2(cre)Jnw/H}) (2). Deletion of PAR₂ in Nav_v1.8 nociceptors was evaluated by immunofluorescence. DRG from wild-type and *Par₂-Nav_v1.8* mice were fixed in 10% formalin for 3 h, transferred to 70% alcohol, and embedded in paraffin. Sections (5 μ m) were deparaffinized, rehydrated, microwaved in sodium citrate buffer, washed, and then blocked in SuperBlock™ (ThermoFisher Scientific) for one hour at room temperature. Sections were incubated with mouse antibody to PAR₂ conjugated to Alexa-488 (Santa Cruz Biotechnology, SC-13504, 1:200, 4°C, overnight), and with guinea pig antibody to Nav_v1.8 (Alomone Labs, AGP-029, 1:200, 4°C, overnight), followed by goat anti-guinea pig secondary antibody conjugated to Alexa Fluor-594 (Life Technologies, A11076, 1:500, room temperature, 1 hour). Sections were imaged with a Nikon Eclipse Ti microscope using 10x magnification; images were captured with a Photometrics CoolSNAP camera.

Somatic nociception and inflammation. Mice were acclimatized to the experimental apparatus, room and investigator for 1-2 h on 2 successive days before studies. Investigators were blinded to the test agents. Mice were sedated (5% isoflurane) for intraplantar injections. Dy4a, Dy4 inact, PS2, PS2 inact (all 50 μ M) or vehicle (0.2% DMSO in 0.9% NaCl) (10 μ l) was injected into the left hindpaw. After 30 min, trypsin (10 or 80 nM), CS (2.5 or 5 μ M) or NE (1.2 or 3.9 μ M) (all 10

µl) was injected into the same hindpaw. Mechanical nociceptive responses were evaluated by examining paw withdrawal to stimulation of the plantar surface of the hind-paw with calibrated von Frey filaments (VFF) (3). VFF scores were measured in triplicate to establish a baseline for each animal on the day before experiments, and were then measured for up to 4 h after protease administration. To assess edema, paw thickness was measured at the site of injection between the plantar and the dorsal surfaces of the paw using digital calipers. For evaluation of neutrophil infiltration, paws were collected at 4 h after intraplantar injection of trypsin (10 µl, 80 nM) or vehicle, fixed in 10% neutral buffered formalin for 48-72 h, bisected, and fixed in formalin for an additional 12 h. Tissue was decalcified in 10% 0.5 M EDTA for 6 days, washed in water, transferred to 70% ethanol for 24 h, and embedded in paraffin. Sections (5 µm) were incubated with neutrophil antibody Ly6G/6C clone NIMP-R14 (Abcam # ab2557, Lot # GR135037-1, AB_303154, 1:800, room temperature, 12 h). Sections were processed for chromogenic immunohistochemistry on a Ventana Medical Systems Discovery XT platform with online deparaffinization using Ventana's reagents. Ly6G/Ly6c was enzymatically treated with protease-3 (Ventana Medical Systems) for 8 min. Ly6G/Ly6c was detected with goat anti-rat horseradish peroxidase conjugated multimer incubated for 16 min.

Dissociation of DRG neurons for electrophysiological studies. DRG innervating the colon (T9-T13) were collected from C57BL/6 mice. Ganglia were digested by incubation in collagenase IV (1 mg/ml, Worthington) and dispase (4 mg/ml, Roche) (10 min, 37°C). DRG were triturated with a fire-polished Pasteur pipette, and further digested (5 min, 37°C). Neurons were washed, plated onto laminin- (0.017 mg/ml) and poly-D-lysine- (2 mg/ml) coated glass coverslips, and were maintained in F12 medium containing 10% fetal calf serum, penicillin and streptomycin (95% air, 5% CO₂, 16 h, 37°C) until retrieval for electrophysiological studies.

Patch clamp recording. Small-diameter (<30 pF capacitance) neurons were studied because they display characteristics of nociceptors (1). Changes in excitability were quantified by measuring rheobase. Whole-cell perforated patch-clamp recordings were made using Amphotericin B (240 µg/ml, Sigma Aldrich) in current clamp mode at room temperature. The recording chamber was perfused with external solution at 2 ml/min. Recordings were made using Multiclamp 700B or Axopatch 200B amplifiers, digitized by Digidata 1440A or 1322A, and processed using pClamp 10.1 software (Molecular Devices). Solutions had the composition (mM): pipette - K-gluconate 110, KCl 30, HEPES 10, MgCl₂ 1, CaCl₂ 2; pH 7.25 with 1 M KOH; external - NaCl 140, KCl 5 HEPES 10, glucose 10, MgCl₂ 1, CaCl₂ 2; pH to 7.3-7.4 with 3 M NaOH. Neurons were preincubated with supernatants of colonic mucosal biopsies from HC or IBS-D subjects (200 µl supernatant were combined with 500 µl of F12 medium, filtered) for 30 min. Neurons were also preincubated with trypsin (50 nM, 10 min), NE (390 nM, 30 min), CS (500 nM, 60 min), thrombin (50 nM, 20 min), or vehicle (37°C), and washed. Rheobase was measured at T 0 or T 30 min after washing. To investigate mechanisms of protease-evoked effects, neurons were incubated with I-343 (100 nM, 300 nM, 10 µM, 30 min preincubation), SCH79797 (1 µM, 10 min), Dy4 (30 µM, 30 min), PS2 (15 µM, 30 min), PD98059 (50 µM, 30 min), GF109203X (10 µM, 30 min), or vehicle (preincubation and inclusion throughout). In experiments using the tripartite antagonist, neurons were preincubated with MIPS15479 (30 µM, 60 min, 37°C) or vehicle and washed. They were recovered in F12 medium at 37°C for variable times, challenged with HC or IBS-D supernatant or trypsin (50 nM, 10 min), and washed. Rheobase was measured 0 or 30 min after washing. In all experiments, the mean rheobase was calculated for neurons exposed to supernatants, proteases or vehicle.

Colonic afferent recordings. The colon and rectum (5-6 cm) was removed from C57BL/6 mice.

Afferent recordings were made from splanchnic nerves, as described (4, 5). Briefly, the intestine was opened and pinned flat, mucosal side up, in an organ bath. Tissue was superfused with a modified Krebs solution (mM: 117.9 NaCl, 4.7 KCl, 25 NaHCO₃, 1.3 NaH₂PO₄, 1.2 MgSO₄ (H₂O)₇, 2.5 CaCl₂, 11.1 D-glucose; 95% O₂, 5% CO₂, 34°C), containing the L-type calcium channel antagonist nifedipine (1 μM) to suppress smooth muscle activity, and the cyclooxygenase inhibitor indomethacin (3 μM) to suppress inhibitory actions of prostaglandins. The splanchnic nerve was extended into a paraffin-filled recording compartment, in which finely dissected strands were laid onto a platinum electrode for single-unit extracellular recordings of action potentials generated by mechanical stimulation of receptive fields in the colon. Receptive fields were identified by mechanical stimulation of the mucosal surface with a brush of sufficient stiffness to activate all types of mechanosensitive afferents. Once identified, receptive fields were tested with three distinct mechanical stimuli to enable classification: static probing with calibrated VFF (2 g force; 3 times for 3 sec), mucosal stroking with VFF (10 mg force; 10 times), or circular stretch (5 g; 1 min) (4, 5). Colonic nociceptors displayed high-mechanical activation thresholds and responded to noxious distension (40 mmHg), circular stretch (≥7g) or 2 g filament probing, but not to fine mucosal stroking (10 mg filament). These neurons express an array of channels and receptors involved in pain, become mechanically hypersensitive in models of chronic visceral pain, and have a nociceptor phenotype (4, 5). In the current study, they are therefore referred to as “colonic nociceptors”. Once baseline colonic nociceptor responses to mechanical stimuli (2 g filament) had been established, mechanosensitivity was re-tested after 10 min application of trypsin (10 nM), NE (100 nM) or CS (100 nM). Proteases were applied to a metal cylinder placed over the receptive mucosal field of interest. This route of administration has been shown to activate colonic afferents (5). Action potentials were analyzed using the Spike 2 wavemark function and discriminated as single units on the basis of distinguishable waveform, amplitude and duration.

Colonic visceral hypersensitivity. Post-inflammatory hypersensitivity was induced by intracolonic administration of trinitrobenzene sulphonic acid (TNBS), as described (4, 5). Briefly, 12 week old mice were fasted overnight with access to 5% glucose solution. TNBS (100 μl, containing 4 mg TNBS in 30% EtOH) was administered to sedated mice (5% isoflurane) through a polyethylene catheter inserted 3 cm past the anus. Mice were then allowed to recover for 28 days. At this time, mice display colonic mechanical hypersensitivity, allodynia and hyperalgesia (4, 5).

Visceromotor Responses (VMR) to Colorectal Distension (CRD). Electromyography (EMG) of abdominal muscles was used to monitor VMR to CRD (6). Electrodes were implanted into the right abdominal muscle of mice under isoflurane anesthesia. Mice were recovered for at least three days before assessment of VMR. On the day of VMR assessment, mice were sedated with isoflurane, and vehicle (saline) or protease cocktail (10 nM trypsin, 100 nM NE, 100 nM CS) (100 μl) was administered into the colon *via* enema. In one group of mice, I-343 (30 mg/kg, 100 μl) was administered into the colon 30 min before the protease cocktail. A lubricated balloon (2.5 cm) was introduced into the colorectum to 0.25 cm past the anus. The balloon catheter was secured to the base of the tail and connected to a barostat (Isobar 3, G&J Electronics) for graded and pressure-controlled balloon distension. Mice were allowed to recover from anesthesia for 15 min before the CRD sequence. Distensions were applied at 20, 40, 50, 60, 70 and 80 mm Hg (20 s duration) at 4 min-intervals; the final distension was 30 min after administration of protease or vehicle. The EMG signal was recorded (NL100AK headstage), amplified (NL104), filtered (NL 125/126, Neurolog, Digitimer Ltd, bandpass 50–5000 Hz), and digitized (CED 1401, Cambridge Electronic Design) for off-line analysis using Spike2 (Cambridge Electronic Design). The analog EMG signal was rectified and integrated. To quantify the magnitude of the VMR at each distension pressure, the area under the curve (AUC) during the distension (20 s) was corrected for the baseline activity (AUC pre-distension, 20 s). Colonic compliance was assessed by applying

graded volumes (40-200 μ l, 20 s duration) to the balloon in awake mice, while recording the corresponding colorectal pressure, as described (6, 7).

Dissociation and transfection of DRG neurons for signaling and trafficking studies. DRG were collected from C57BL/6 mice and Sprague-Dawley rats (all levels). DRG were incubated with collagenase IV (2 mg/ml) and dispase II (1 mg/ml) for 30 min (mice) and 45 min (rats) at 37°C. DRG were dispersed by trituration with a fire-polished Pasteur pipette. Dissociated neurons were transfected with mPAR₂-GFP (1 μ g), the FRET biosensors CytoEKAR, NucEKAR, pmCKAR or CytoCKAR (all 1 μ g), or with the BRET biosensors PAR₂-RLuc8 (125 ng) and β ARR2-YFP (475 ng) using the Lonza 4D-Nucleofector X unit according to the manufacturer's instructions. Neurons were plated on laminin- (0.004 mg/ml) and poly-L-lysine- (0.1 mg/ml) coated glass coverslips for confocal microscopy and [Ca²⁺]_i assays, on ViewPlate-96 plates (PerkinElmer) for FRET assays, or on CulturPlates (PerkinElmer) for BRET assays. Neurons were maintained in Dulbecco's modified Eagle medium (DMEM) containing 10% fetal bovine serum (FBS), antibiotic-antimitotic, and N1 supplement for 48 h before study.

PAR₂ trafficking in DRG neurons. Mouse DRG neurons expressing mPAR₂-GFP were incubated with trypsin (10 nM), CS (100 nM), NE (100 nM) or vehicle (30 min, 37°C), and then fixed (4% paraformaldehyde, 20 min, 4°C). NeuN was detected by indirect immunofluorescence as described (3). Neurons were observed using a Leica SP8 confocal microscope with a HCX PL APO 63x (NA 1.40) oil objective. PAR₂ internalization in NeuN-positive neurons was quantified using ImageJ software. The border of the cytoplasm in the neuronal soma was defined by NeuN fluorescence. mPAR₂-GFP fluorescence within 0.5 μ m of the border was defined as plasma membrane-associated receptor. The ratio of plasma membrane to cytosolic mPAR₂-GFP was determined (3).

FRET assays in DRG neurons. Rat DRG neurons expressing FRET biosensors were serum-restricted (0.5% FBS overnight), and equilibrated in HBSS-HEPES (10 mM HEPES, pH 7.4, 30 min, 37°C). FRET was analyzed using an Operetta CLS High-Content Imaging System (PerkinElmer) or an INCell Analyzer 2000 (GE Healthcare Life Sciences) (8-10). For CFP/YFP emission ratio analysis, cells were sequentially excited using a CFP filter (410-430 nm) with emission measured using YFP (520-560 nm) and CFP (460-500 nm) filters. Cells were imaged at 1 or 2 min intervals. Baseline was measured, neurons were challenged with trypsin (10 or 100 nM) or vehicle, and responses recorded for a further 30 min. Neurons were then incubated with the positive controls phorbol 12,13-dibutyrate (PDBu, 200 nM) for EKAR biosensors or PDBu (200 nM) plus phosphatase inhibitor cocktail-2 (SigmaAldrich, 1X, 10 min) for CKAR biosensors, and FRET was recorded for an additional 4-6 min. The use of positive controls ensured that the biosensor responses were not saturated. Data were analyzed using Harmony 4.1 or Image J 1.51 software. Images taken were aligned, cells were selected based on diameter, and fluorescence intensity was calculated for both FRET and CFP channels. Background intensity was subtracted and the FRET ratio was determined as the change in the FRET/donor (EKAR) or donor/FRET (CKAR) emission ratio relative to the baseline for each cell (F/F_0). Cells with >5% change in F/F_0 after stimulation with positive controls were selected for analysis. Neurons were incubated with I-343 (10 μ M), SCH530348 (100 nM) or vehicle (0.3% DMSO) (30 min, 37°C preincubation and inclusion throughout).

BRET assays in DRG neurons. Mouse DRG neurons were equilibrated in HBSS-HEPES (30 min, 37°C), and incubated with the Renilla luciferase substrate coelenterazine h (NanoLight Technologies) (5 μ M, 5 min). BRET signals were measured at 475 \pm 30 nm and 535 \pm 30 nm using

a CLARIOstar Monochromometer Microplate Reader (BMG LabTech) before and after challenge with trypsin (10 nM), NE (100 nM) or CS (100 nM) (10). The YFP/RLuc8 ratios were normalized to baseline, and data are plotted as area under the curve for the 25 min assay.

Ca²⁺ assays in DRG neurons. [Ca²⁺]_i was measured in DRG neurons from WT and *Par2-Nay1.8* mice, as described (11). Neurons were loaded with Fura-2AM (1 μM) in Ca²⁺- and Mg²⁺-containing DMEM (45 min, room temperature). Fluorescence of individual neurons was measured at 340 nm and 380 nm excitation and 530 nm using a Nikon Eclipse Ti microscope with 20x magnification and a Photometrics CoolSNAP camera. Data were analyzed using Nikon Ti Element Software. Cultures were first challenged with KCl (65 mM), to identify responsive neurons, and were then exposed to trypsin (100 nM). Cells ≤ 25 μm diameter were selected for analysis. For determination of the activation threshold, the magnitude of the 340/380 ratio after exposure to trypsin was compared to the baseline ratio. Neurons were considered responsive to trypsin if the 340/380 ratio was ≥ 0.1 from baseline.

Uptake of tripartite probes in DRG neurons. Mouse DRG neurons transfected with mPAR₂-GFP were incubated with Cy5-Ethyl ester (control) or Cy5-Chol (200 nM, 60 min, 37°C), and then washed in HBSS-HEPES. Neurons were transferred to a heated chamber (37 °C) in HBSS-HEPES and were observed by confocal microscopy before or after treatment with trypsin (100 nM, 15 min). Images were obtained using a Leica TCS SP8 Laser-scanning confocal microscope with a HCX PL APO 63x (NA 1.40) oil objective. Image acquisition settings were consistent for Cy5-Chol and Cy5-ethyl ester fluorescence detection.

Cell lines, transfection. HEK293 cells were cultured in DMEM supplemented with 10% (v/v) FBS (5% CO₂, 37°C). When necessary serum restriction was achieved by replacing culture medium with DMEM containing 0.5% FBS overnight. Cells were transiently transfected using polyethylenimine (PEI) (1:6 DNA:PEI).

FRET assays in HEK293 cells. HEK293 cells were transiently transfected in 10 cm dishes (~50% confluency) with Flag-PAR₂-HA (2.5 μg) and FRET biosensors CytoEKAR, NucEKAR, pmCKAR, CytoEKAR, pmEpac or CytoEpac (2.5 μg) (8, 10). In experiments examining the role of dynamin, cells were transfected with FLAG-PAR₂-HA (1.25 μg), FRET biosensor (1.25 μg) and either DynWT-HA, DynK44E-HA or pcDNA3.1 (2.5 μg). At 24 h after transfection, cells were seeded on ViewPlate-96 well plates (PerkinElmer). FRET was assessed 72 h post-transfection, following overnight serum restriction. Cells were equilibrated in HBSS-HEPES (30 min, 37°C). FRET was measured using a PHERAstar FSX Microplate Reader (BMG LabTech). For CFP/YFP emission ratio analysis, cells were sequentially excited using a CFP filter (425/10 nm) with emission measured using YFP (550/50 nm) and CFP (490/20 nm) filters. FRET was measured before and after stimulation with trypsin (10 nM), NE (100 nM), CS (100 nM), or vehicle. To ensure that the biosensor responses were not saturated, cells were also stimulated with positive controls: PDBu (1 μM) for EKAR biosensors, PDBu (200 nM) + phosphatase inhibitor cocktail-2 (1X) for CKAR biosensors, or forskolin (10 μM) + 3-isobutyl-1-methylxanthine (100 μM) for Epac biosensors. FRET ratios (donor/acceptor intensity for EKAR, or acceptor/donor intensity for CKAR and Epac) were calculated and corrected to baseline and vehicle treatments to determine ligand-induced FRET (ΔFRET). Treatment effects were determined by comparison of area under the curve values. Signaling inhibitors were dissolved in HBSS-HEPES. PS2 and PS2 inact were dissolved in HBSS-HEPES + 1% DMSO. Cells were incubated with UBO-QIC (100 nM), AG1478 (1 μM), Gö6983 (1 μM), PS2 or PS2 inact (30 μM) or vehicle (30 min preincubation, inclusion throughout).

BRET assays in HEK293 cells. HEK293 cells were transiently transfected in 10 cm dishes (~50% confluency) with: PAR₂-RLuc8 (1 µg) and either RIT-Venus or Rab5a-Venus (both 4 µg); Flag-PAR₂-HA (1 µg) and βARR1-RLuc8 (1 µg) plus Rab5a-Venus (4 µg); or Flag-PAR₂-HA (1 µg) and Gα_q-RLuc8 (0.5 µg), Gβ (1 µg), Gγ (1 µg) and Rab5a-Venus (4 µg). To examine the role of dynamin, cells were transfected with PAR₂-RLuc8 (0.5 µg), RIT-Venus or Rab5a-Venus (2 µg), and DynWT-HA, DynK44E-HA or pcDNA3.1 (2.5 µg). At 24 h after transfection, cells were seeded on CulturPlates (PerkinElmer). The following day, cells were equilibrated in HBSS-HEPES and incubated with coelenterazine h (NanoLight Technologies) (5 µM, 5 min). RLuc8 and YFP intensities were measured at 475±30 nm and 535±30 nm, respectively, using a LUMIstar Omega Microplate Reader (BMG LabTech) before and after challenge with proteases, biopsy supernatants or vehicle. Data are presented as ligand-induced BRET, calculated as the ratio of YFP to RLuc8 signals normalized to the baseline average, followed by vehicle subtraction. Treatment effects were determined by comparison of area under the curve values.

Immunofluorescence and Structured Illumination Microscopy. HEK293 cells transiently expressing Flag-PAR₂-HA were seeded on poly-D-lysine-coated high tolerance cover-glass and incubated overnight. Cells were incubated with trypsin (10 nM) or vehicle in DMEM for 30 min at 37°C. Cells were fixed in 4% paraformaldehyde on ice for 20 min and washed in PBS. Cells were blocked for 1 h at room temperature in PBS + 0.3% saponin + 3% NHS. Cells were incubated with primary antibodies to HA (rat anti-HA, 1:1,000, Roche), EEA-1 (rabbit anti-EEA-1 1:100, Abcam), Gα_q (mouse anti-GNAQ 1:100, Millipore) in PBS + 0.3% saponin + 1% NHS overnight at 4°C. Cells were washed in PBS and incubated with secondary antibodies (goat anti-Rat Alexa568, donkey anti-rabbit Alexa488, goat anti-mouse Dylight405, 1:1,000, Invitrogen) for 1 h at room temperature. Cells were washed with PBS and mounted on glass slides with prolong Diamond mounting medium (ThermoFisher). Cells were observed by super-resolution structured illumination microscopy (SIM) using a Nikon N-SIM Eclipse TiE inverted microscope with an SR Apo-TIRF100x/1.49 objective. Images were acquired in 3D-SIM mode using 405, 488, and 561 nm lasers and filter sets for standard blue, green, and red emission on an Andor iXon 3 EMCCD camera. Z-stacks were collected with a 125 nm z interval. NIS-Elements AR Software was used to reconstruct SIM images.

cDNAs. BRET sensors for PAR₂-RLuc8, KRas-Venus, Rab5a-Venus, βARR2-YFP, βARR2-RLuc8 and Gα_q-RLuc8 have been described (3, 10). FRET sensors CytoEKAR, NucEKAR, CytoCKAR and pmCKAR (8) were from Addgene (plasmids 18680, 18681, 14870, 14862, respectively).

IP₁ accumulation assay. KNRK-hPAR₂, KNRK, HEK293, or HT-29 cells were seeded at a density of 50x10³ cells/well onto clear 96-well plates (PerkinElmer). After 24 h of culture, medium was replaced with IP₁ stimulation buffer (10 mM HEPES, 1 mM CaCl₂, 0.5 mM MgCl₂, 4.2 mM KCl, 146 mM NaCl, 5.5 mM glucose, 50 mM LiCl; 37°C, 5% CO₂). Cells were pre-incubated with the antagonist or vehicle for 30 min prior to the addition of agonist. Cells were then further incubated for 40 min. Stimulation buffer was aspirated and the cells were incubated in lysis buffer for 10 min (IP-One HTRF® assay kit, Cisbio). Lysates were transferred to a 384-well OptiPlate (PerkinElmer), and IP₁ was detected (IP-One HTRF® assay kit, Cisbio). Homogeneous time resolved FRET was measured with an Envision plate reader (PerkinElmer Life Sciences).

Synthesis of I-343, MIPS15479, Cy5-cholestanol, Cy5-ethyl ester. Reagents were from Chem-Impex, Aldrich and Novabiochem. ¹H NMR spectra were obtained using a Bruker Advance DPX

300 spectrometer at 300.13 MHz, or a Varian Unity Inova 600 spectrometer at 599.8 MHz. ¹³C NMR spectra were obtained using a Varian Unity Inova 600 spectrometer at 150.8 MHz, or on a Bruker Avance DPX 300 spectrometer at 75.4 MHz. Unless stated otherwise, samples were dissolved in CDCl₃. Thin-layer chromatography used 0.2 mm plates and Merck silica gel 60 F254. Column chromatography used Merck silica gel 60 (particle size 0.063-0.200 μm, 70- 230 mesh). High resolution mass spectra (HR-ESI) were obtained using a Waters LCT Premier XE (TOF) with electrospray ionization. Compound purity was analyzed via LCMS (Agilent 1200 series LC coupled directly to a photodiode array detector and an Agilent 6120 Quadrupole MS) using a Phenomenex column (Luna 5 μm C8, 50 mm 4.60 mm ID). All compounds were of >95% purity.

I-343. 5-methyl-1*H*-1,2,4-triazole-3-carboxylic acid (1.2 eq) was dissolved in DMSO, and then mixed with HATU (1.2 eq), the corresponding amine (1.0 eq), and DIPEA (2.5 eq) (RT, overnight). Water was added and the solids were filtered and washed to generate the product (88% yield). ¹H NMR (400 MHz, DMSO) δ 8.52 (d, *J* = 7.2 Hz, 1H), 8.18 – 8.10 (m, 2H), 7.48 (d, *J* = 8.8 Hz, 1H), 7.45 – 7.36 (m, 2H), 4.34 – 3.66 (m, 6H), 2.43 – 2.30 (m, 3H), 1.61 (s, 6H), 1.56 (s, 3H), 1.54 (s, 3H), 1.48 (s, 3H). LCMS: *R*_f = 3.37, *m/z* = 519.3 (M+H, ⁺).

MIPSI5479. Sodium azide (5 mmol) and tert-butyl bromoacetate (5 mmol) were mixed with DMF (10 ml) (RT, 72 h). Propiolic acid (5 mmol) and CuI (0.5 mmol) were added and the stirring continued (RT, 48 h). The reaction mixture was adjusted to pH4 with 1N HCl, and the resultant mixture poured into brine. The aqueous phase was extracted with DCM, dried over MgSO₄, and evaporated to dryness. The crude residue was purified on silica gel to generate the product (29.5% yield). ¹H NMR (401 MHz, DMSO) δ 8.76 – 7.63 (m, 2H), 5.42 – 5.19 (m, 2H), 1.43 (s, 9H). LCMS: *R*_f = 2.90, *m/z* = 225.9 (M-H, C₉H₁₂N₃O₄⁻). The triazole acid (1.1 eq), the amine HCl salt (from WO 2015048245 patent; 1.0 equivalent) and DIPEA (2.5 to 3.5 eq) were dissolved in DMF. PyOxim (1.25 eq) was added and the mixture was stirred (RT, overnight). Water and EtOAc were added and the phases separated. The organic phase was washed 2 times with 1N HCl and then saturated bicarbonate solution. The aqueous phase was back extracted with more EtOAc. All EtOAc phases were combined, dried over MgSO₄, filtered, and evaporated under reduced pressure. The product was purified on silica gel to generate the ester, which was deprotected with TFA and DCM (1:1) to provide the product (95% yield). LCMS: *R*_f = 3.56, *m/z* = 562.9 (M+H, C₂₈H₃₂FN₈O₄⁺) (ester intermediate, ¹H NMR (401 MHz, CDCl₃) δ 8.37 (s, 1H), 8.27 (d, *J* = 5.8 Hz, 1H), 7.93 (dd, *J* = 8.8, 5.3 Hz, 2H), 7.24 (d, *J* = 4.1 Hz, 1H), 7.19 (t, *J* = 8.6 Hz, 2H), 5.13 – 5.07 (m, 2H), 4.60 – 4.44 (m, 4H), 3.96 – 3.89 (m, 2H), 1.70 (s, 2H), 1.66 (s, 4H), 1.63 – 1.58 (m, 9H), 1.49 – 1.47 (m, 9H). LCMS: *R*_f = 3.71, *m/z* = 619.0 (M+H, C₃₂H₄₀FN₈O₄⁺). The spacer-lipid conjugate (NH₂-PEG₁₂-Asp(OChol)-resin) was prepared by manual peptide synthesis with standard Fmoc chemistry on NovaSyn®TG^R R resin (loading 0.18 mmol/g). Coupling of the Fmoc-Asp(OChol)-OH (1.5 eq) with (1*H*-Benzotriazol-1-yloxy)(tri-1-pyrrolidinyl)phosphonium hexafluorophosphate (PyBOP, 2 eq) in dichloromethane (DCM) with activation *in situ* was accomplished using diisopropylethylamine (DIPEA, 3 eq) for 3 h. Fmoc deprotection was achieved using 20% piperidine in *N,N*-dimethylformamide (DMF). Fmoc-PEG₁₂-OH (2 eq) was coupled to resin-bound NH₂-Asp(OChol) with PyBOP (2 eq) and DIPEA (3 eq) in DCM. Fmoc deprotection was achieved using 20% piperidine in *N,N*-dimethylformamide (DMF). Following final deprotection, the antagonists were coupled to the spacer-lipid conjugate on resin. The triazole acetic acid (2-3eq) was coupled to resin-bound NH₂-PEG₁₂-Asp(OChol)-resin (250 mg) with PyBOP (2 eq) and DIPEA (3 eq) in DCM overnight. The construct was then cleaved from resin using 95% trifluoroacetic acid and purified by reverse-phase high-performance liquid chromatography (HPLC) (Phenomenex Luna C8 column) with 0.1% TFA/H₂O and 0.1% TFA/ACN as solvents, providing the lipidated antagonists as viscous oils (45% yield). ¹H NMR (401 MHz, CDCl₃) δ 8.43 (d, *J* = 4.2 Hz, 2H), 7.99 – 7.90 (m, 2H), 7.74 – 7.50 (m, 3H), 7.34 – 7.26 (m, 2H), 7.19 (dt, *J* = 19.6, 7.5 Hz, 3H), 5.22 (s, 2H), 4.95 – 4.86 (m, 1H), 4.74 – 4.64 (m,

1H), 4.62 – 4.40 (m, 4H), 4.28 – 4.17 (m, 1H), 3.97 – 3.79 (m, 3H), 3.74 – 3.54 (m, 45H), 3.49 (dd, $J = 10.9, 5.7$ Hz, 2H), 3.03 (dd, $J = 17.2, 5.1$ Hz, 1H), 2.70 (dd, $J = 17.9, 5.9$ Hz, 1H), 2.57 (t, $J = 3.8$ Hz, 2H), 1.96 (dd, $J = 9.3, 3.1$ Hz, 1H), 1.86 – 1.18 (m, 43H), 1.18 – 0.78 (m, 26H), 0.67 – 0.58 (m, 4H). LCMS (high res): $m/z = 824.5132$ (M+2H, $C_{86}H_{138}FN_{11}O_{19}^{2+}$).

Cy5-cholestanol, Cy5-ethyl ester. These tripartite probes were synthesized as described (3).

Statistics. Results are mean \pm SEM. Differences were assessed using Student's t test (two comparisons), or one- or two-way ANOVA (multiple comparisons) followed by Tukey's multiple comparisons test (electrophysiology assays) or Dunnett's multiple comparisons test (somatic nociception, single cell FRET assays). For BRET assays and population FRET assays, area under the curve data were normalized to matched trypsin alone responses, and compared to 100% using a one-sample t-test. For assays of colonic nociception (VMR to CRD), data were statistically analyzed by generalized estimating equations followed by Fisher's Least Significant Difference post-hoc test when appropriate using SPSS 23.0. GraphPad Prism 7 Software (San Diego, CA, USA) was used for statistical analysis and preparation of graphs.

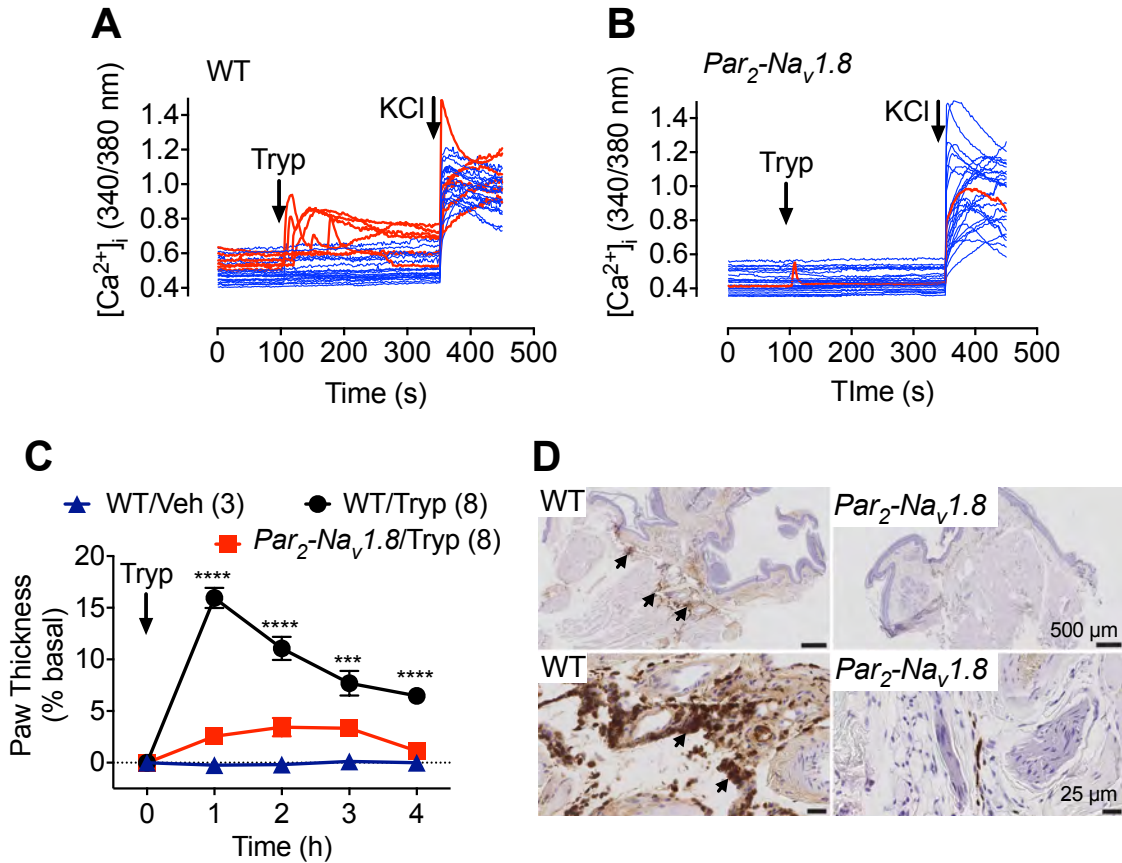


Fig. S1. Expression of functional PAR₂ in DRG neurons, and PAR₂-dependent inflammation. **A, B.** Representative traces of effects of trypsin (100 nM) on [Ca²⁺]_i in DRG neurons from WT (**A**) and *Par₂-Na_v1.8* (**B**) mice. Traces from 25 neurons are shown; traces from trypsin-responsive neurons are shown in red. In WT mice, 20/65 (31%) of neurons responded to trypsin. In *Par₂-Na_v1.8* mice, 3/51 (6%) of neurons responded to trypsin. Neurons were collected from 4 mice per group. **C.** Effect of intraplantar injection of trypsin on paw thickness in WT and *Par₂-Na_v1.8* mice. ****P*<0.001, *****P*<0.0001. Numbers in parentheses denote mouse numbers. **D.** Effect of intraplantar injection of trypsin on neutrophil infiltration into the paw at 4 h in WT and *Par₂-Na_v1.8* mice. Arrows show neutrophil influx in WT mice.

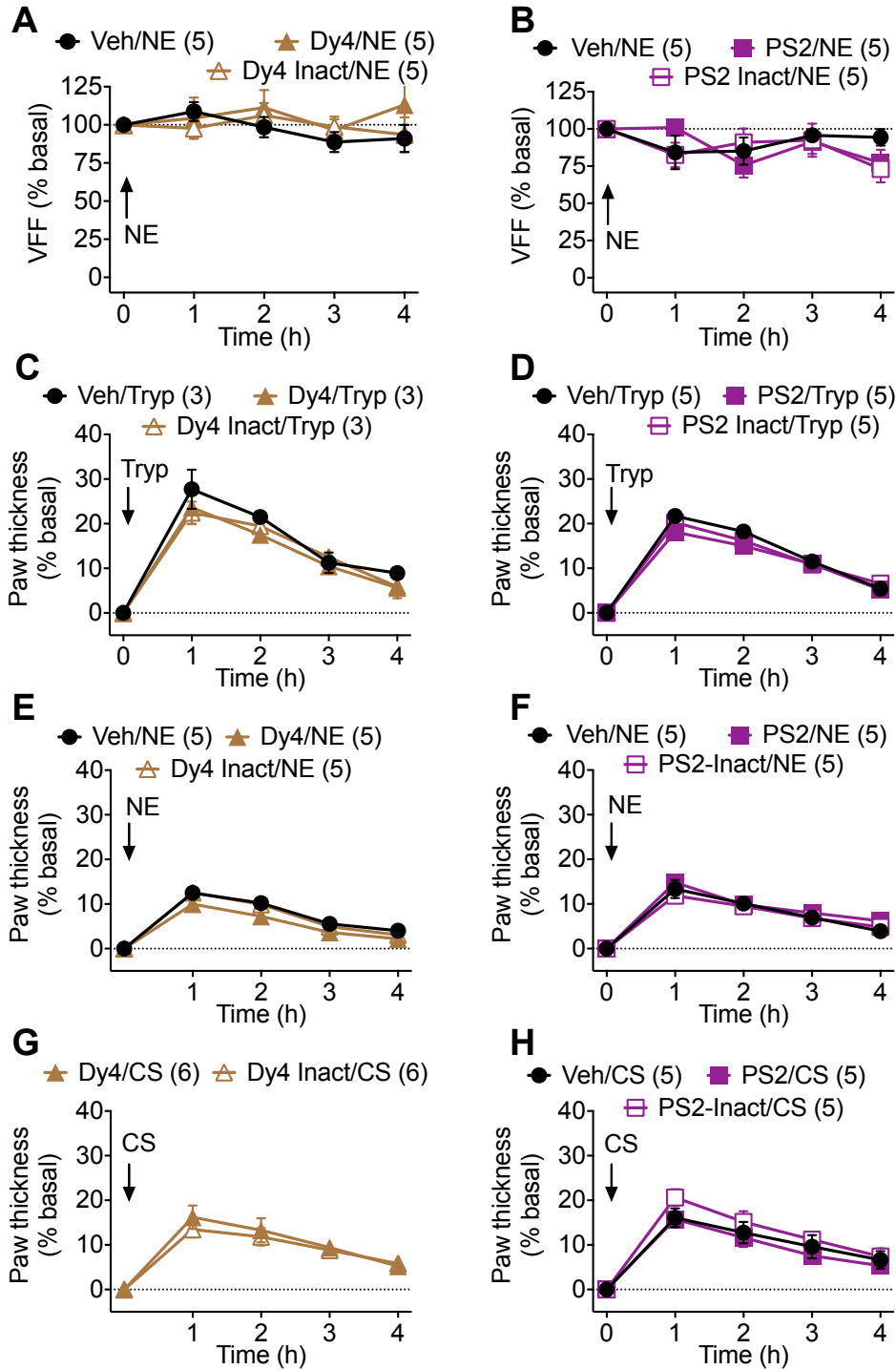


Fig. S2. Protease-induced mechanical nociception and edema. **A, B.** VFF withdrawal responses of the contralateral (right) paw after intraplantar injections into the ipsilateral (left) paw of Dy4 or Dy4 inact (**A**), PS2 or PS2 inact (**B**), or vehicle (Veh), followed by NE. **C-H.** Thickness of the ipsilateral paw. Dy4 or Dy4 inact (**C, E, G**), PS2 or PS2 inact (**D, F, H**), or vehicle (Veh) was administered by intraplantar injection into mouse paw. After 30 min, trypsin (Tryp) (**C, D**), NE (**E, F**) or CS (**G, H**) was injected. Paw thickness (edema) was measured. Numbers in parentheses denote mouse numbers.

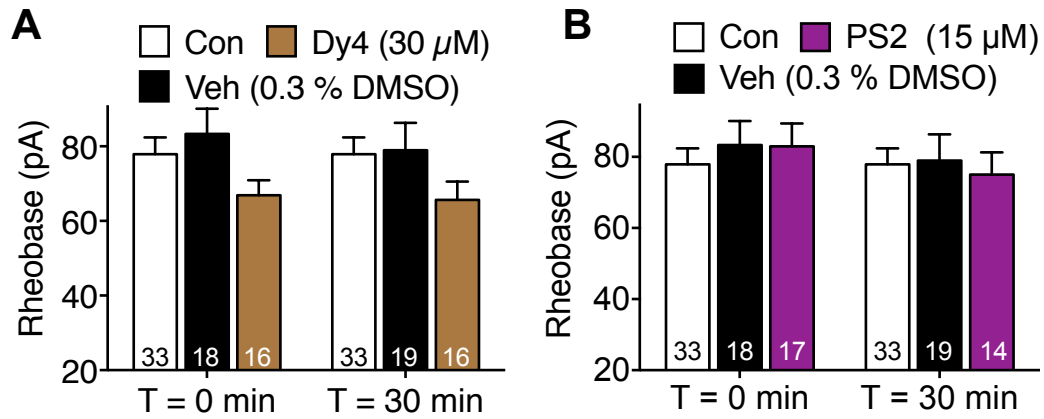


Fig. S3. Endocytic inhibitors and baseline hyperexcitability of nociceptors. Rheobase of mouse DRG neurons preincubated with buffer control (Con), vehicle (Veh, 0.3% DMSO), Dy4 (A) or PS2 (B). Rheobase was measured at T 0 min or T 30 min after washing. Numbers in bars denote neuron numbers.

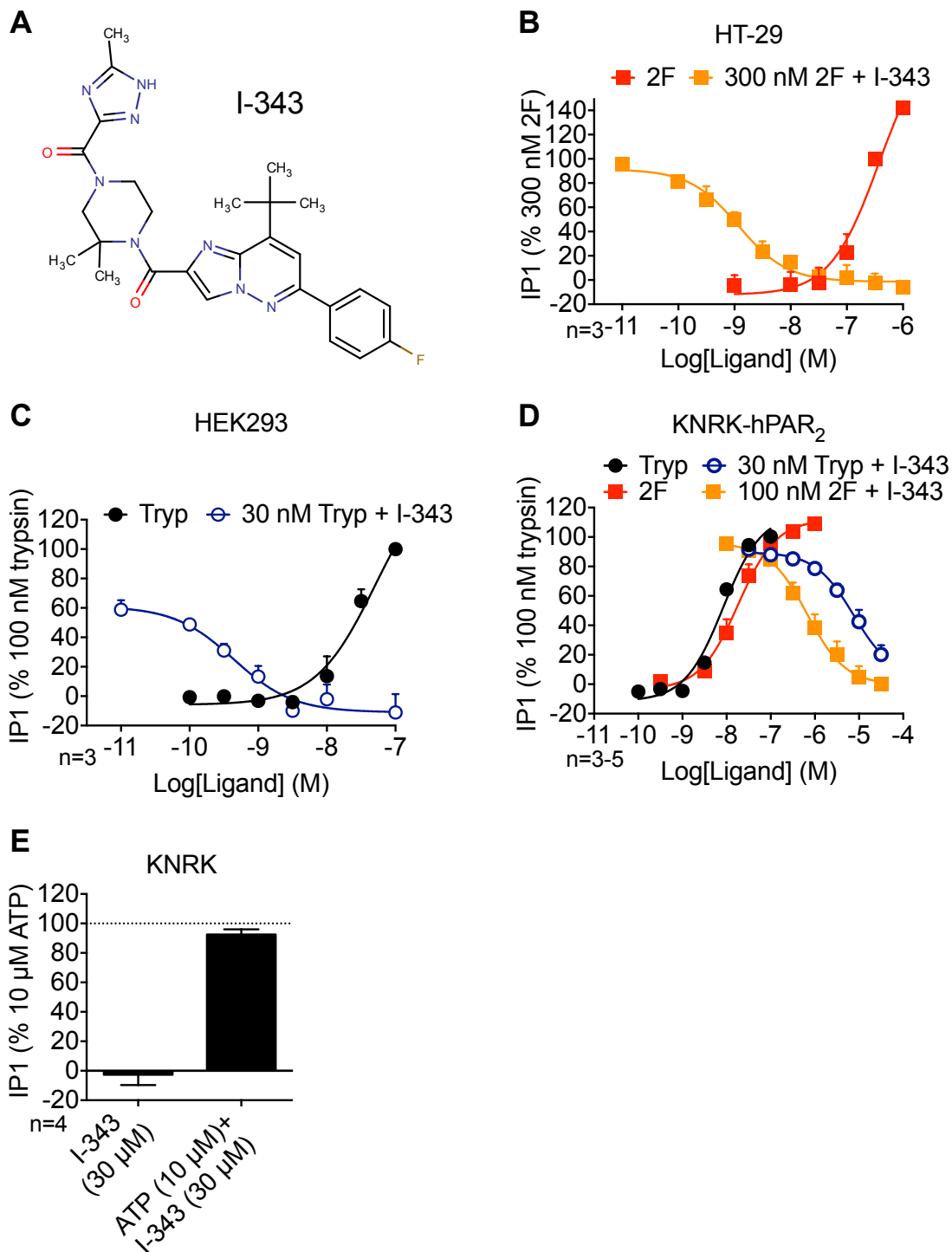


Fig. S4. Characterization of PAR₂ antagonist I-343. **A.** I-343 structure. **B-D.** Concentration-response analysis of the effects of I-343 on 2F- and trypsin-induced IP₁ accumulation in HT-29 (**B**), HEK293 (**C**) and KNRK-hPAR₂ (**D**) cells. **E.** Effects of I-343 on ATP-induced IP₁ accumulation in HEK cells. n, experimental replicates from triplicate observations.

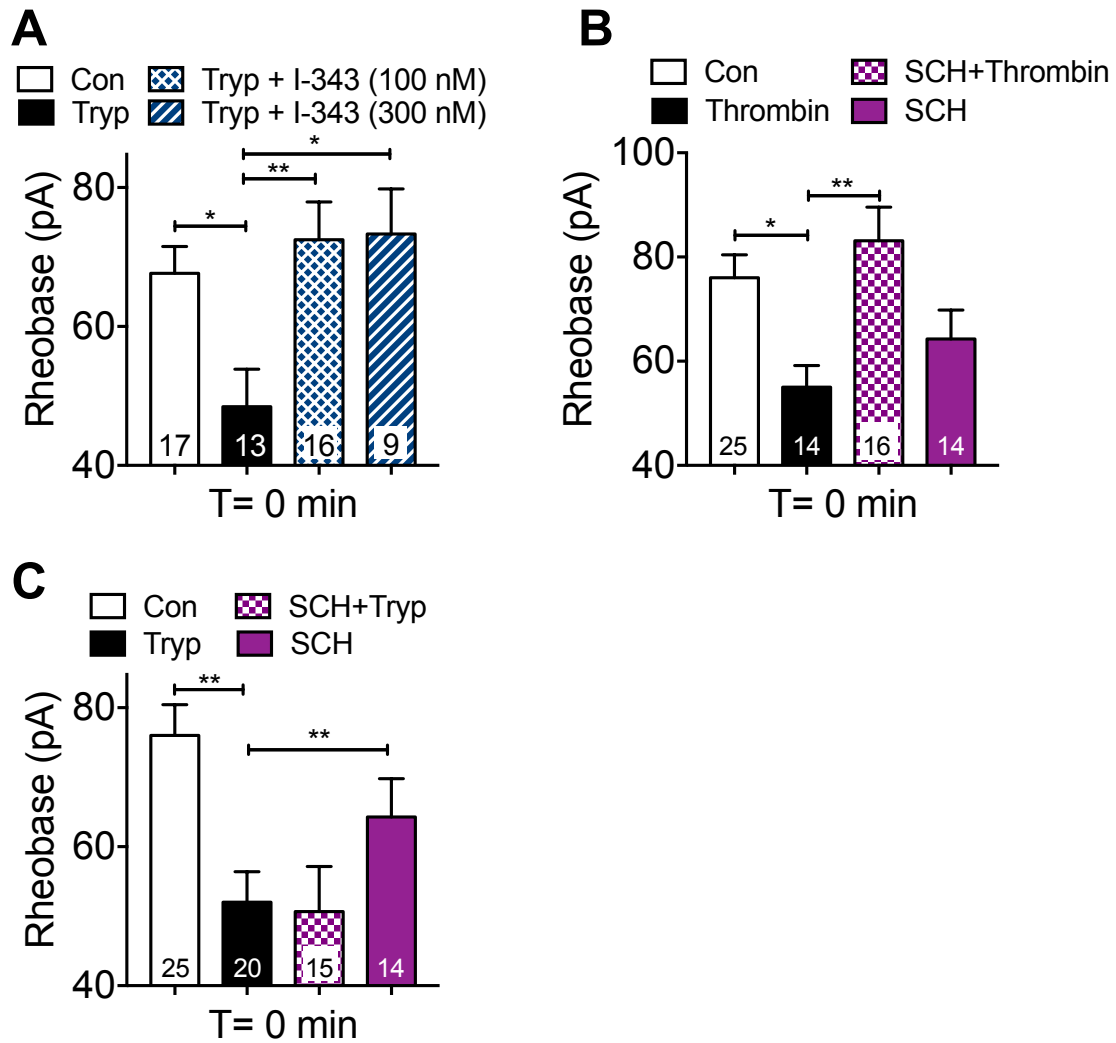


Fig. S5. Trypsin- and thrombin-induced hyperexcitability of nociceptors. Rheobase of mouse DRG neurons preincubated with I-343 (A, PAR₂ antagonist) or SCH79797 (B, C, PAR₁ antagonist). Neurons were challenged with trypsin (A, C) or thrombin (B), washed, and rheobase was measured 0 min later. * $P < 0.05$, ** $P < 0.01$. Numbers in bars denote neuron numbers.

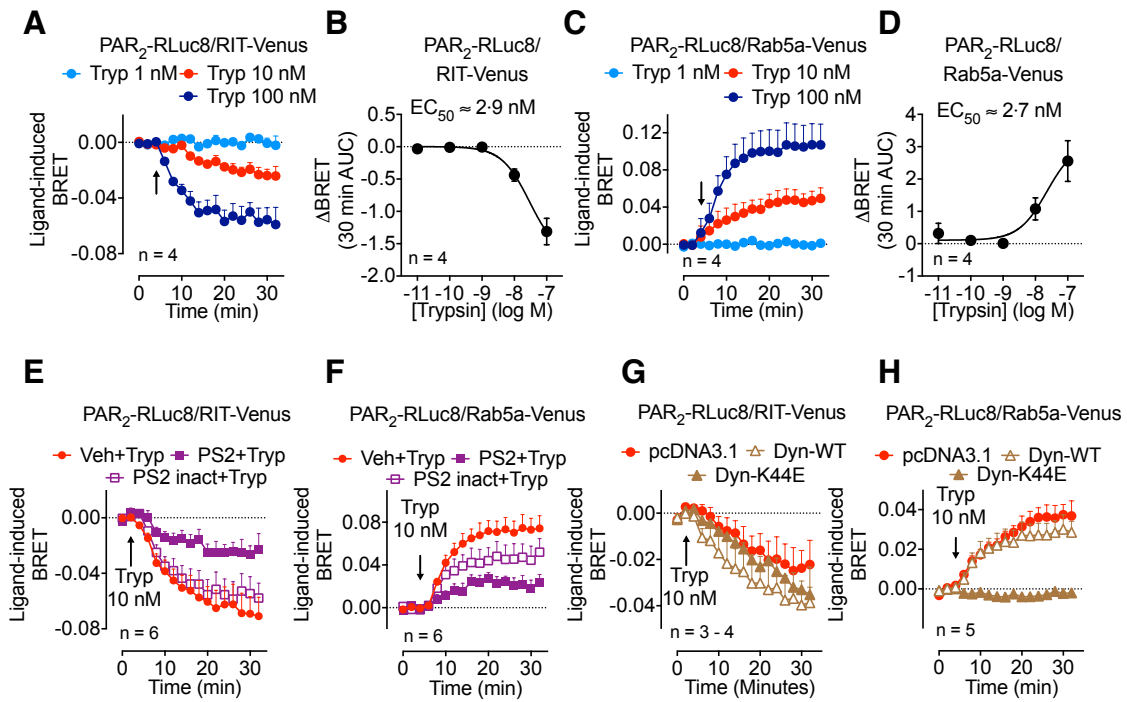


Fig. S6. PAR₂ endocytosis in HEK293 cells. PAR₂-RLuc8/RIT-Venus BRET (**A, B, E, G**) and PAR₂-RLuc8/Rab5a-Venus BRET (**C, D, F, H**) in HEK293 cells. n, experimental replicates from triplicate observations.

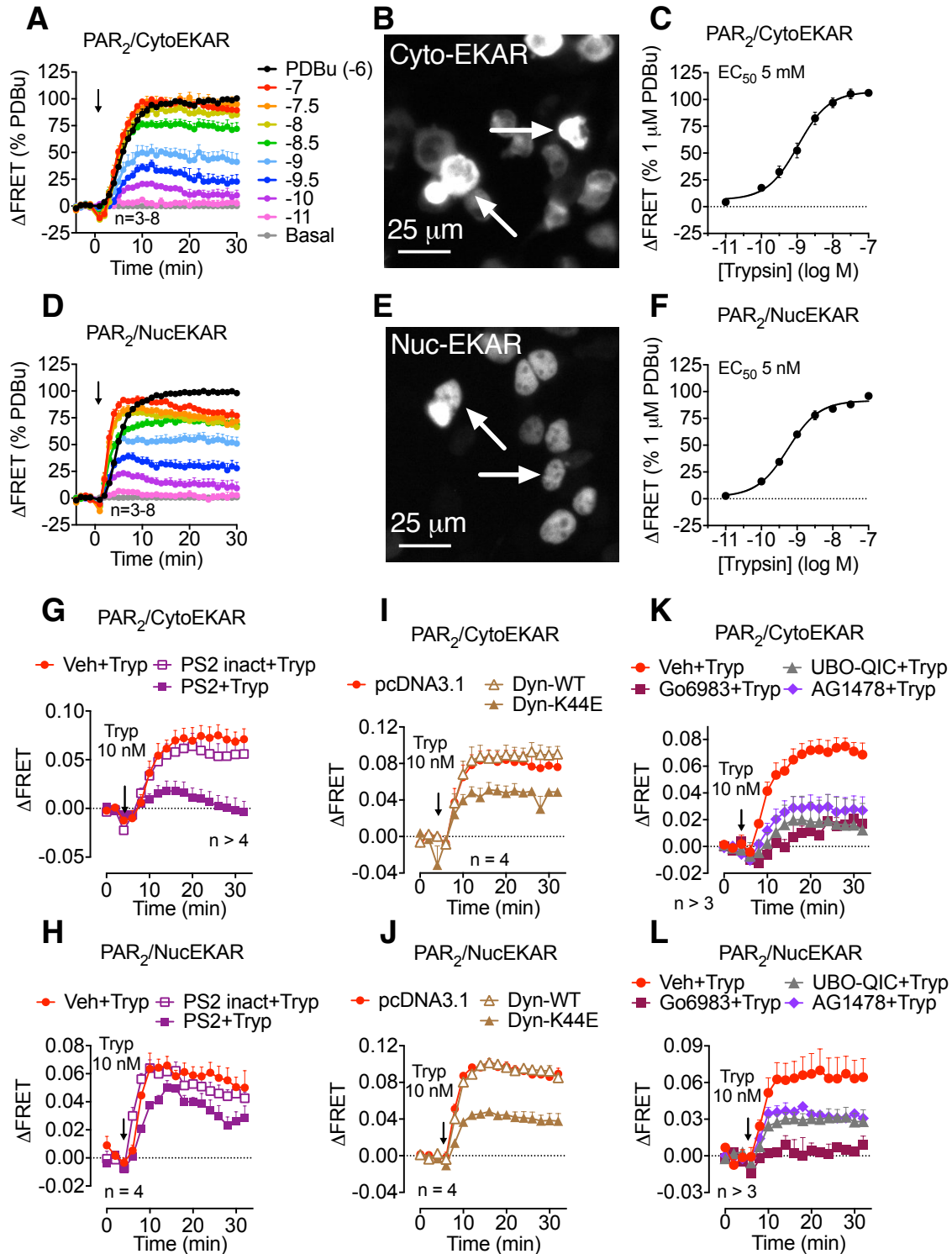


Fig. S7. PAR₂ compartmentalized ERK signaling in HEK293 cells. FRET assays of cytosolic (A-C, G, I, K) and nuclear (D-F, H, J, L) ERK activity in HEK293 cells. B, E. Sensor localization. n, experimental replicates from triplicate observations.

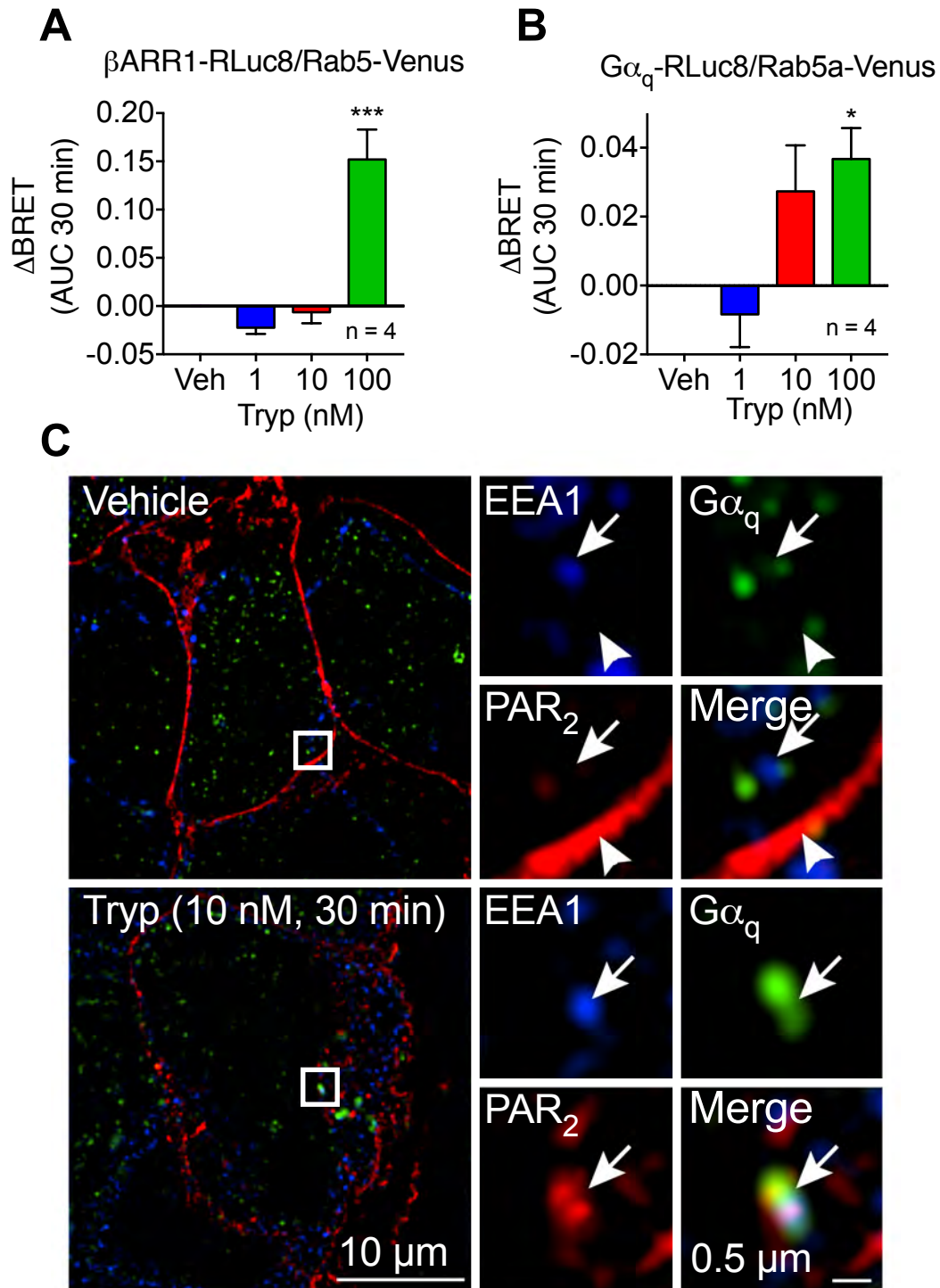


Fig. S8. Trafficking of PAR₂, β ARR1 and $G\alpha_q$ to early endosomes in HEK293 cells. A, B. β ARR1-RLuc8/Rab5a-Venus BRET (A) and $G\alpha_q$ -RLuc8/Rab5a-Venus BRET (B) in HEK293 cells. * P <0.05, *** P <0.001 compared to vehicle. n, experimental replicates from triplicate observations. C. Localization of EEA1, $G\alpha_q$, and PAR₂ in endosomes after treatment with vehicle or trypsin for 30 min. Arrow heads show colocalization of EEA1, $G\alpha_q$, and PAR₂ in endosomes of trypsin-treated cells.

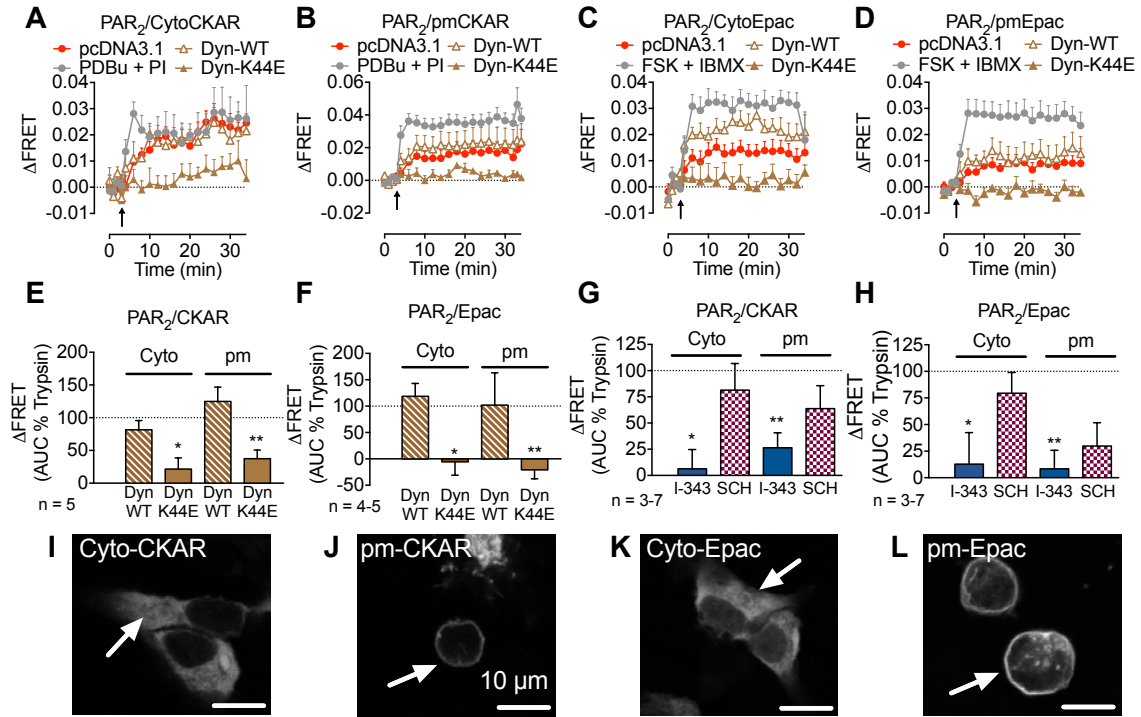


Fig. S9. PAR₂ compartmentalized PKC and cAMP signaling in HEK293 cells. FRET assays of cytosolic PKC (A, E, G), plasma membrane PKC (B, E, G), cytosolic cAMP (C, F, H) and plasma membrane cAMP (D, F, H) in HEK293 cells. I-L. Sensor localization. AUC, area under curve. * $P < 0.05$, ** $P < 0.01$ compared to control. n, experimental replicates, triplicate observations.

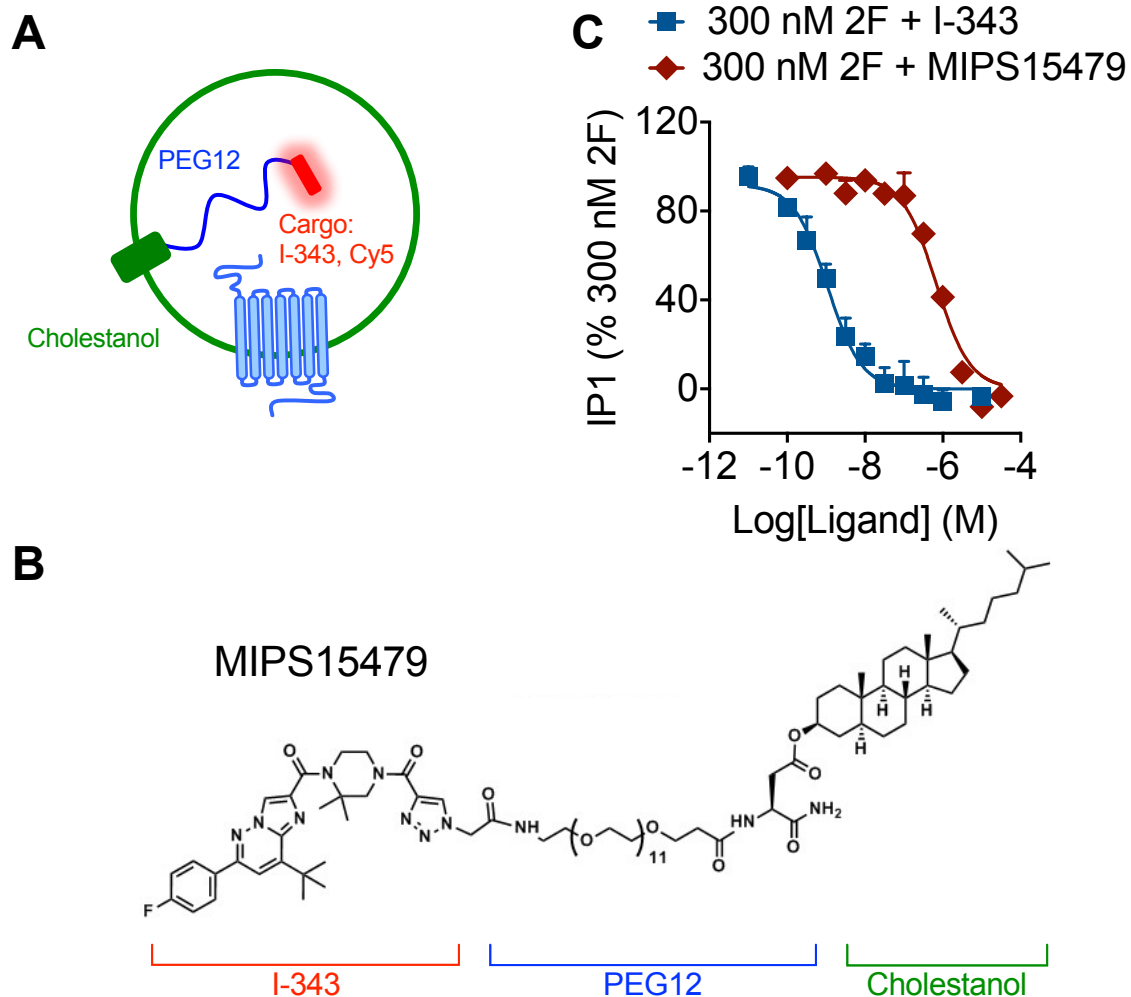


Fig. S10. Tripartite PAR₂ antagonist. **A.** Principal of targeting PAR₂ in endosomes using a tripartite probe. **B.** Structure of MIPS15479 tripartite PAR₂ antagonist. **C.** Concentration-response analysis of the effects of I-343 and MIPS15479 on 2F-induced IP₁ accumulation in HT-29 cells.

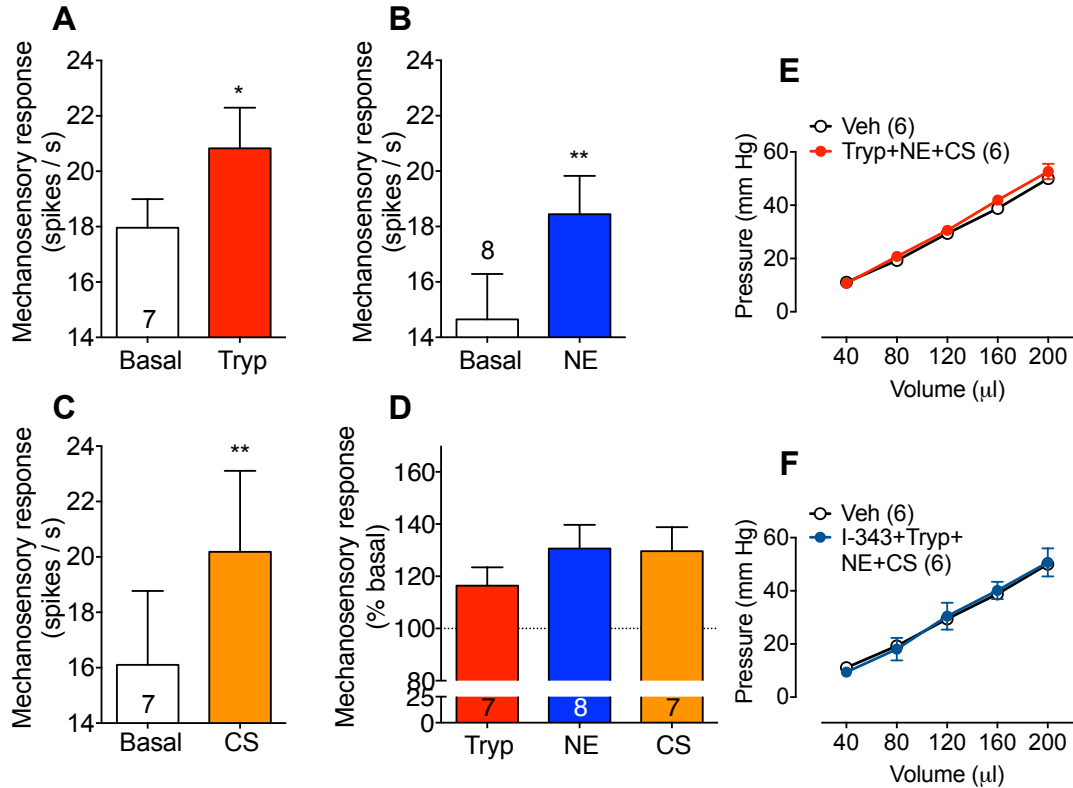


Figure S11. Sensitization of colonic afferents and colonic compliance. A-D. Mechanosensory responses of mice measured 28 d after exposure to TNBS. The colonic mucosa was stimulated with a 2 g VFF under basal conditions and after exposure of receptive fields to trypsin (A, D, Tryp), NE (B, D) or CS (C, D). D. Responses as % basal. Numbers in bars denote afferent numbers. E, F. Colonic compliance in awake healthy control mice. Pressure/volume relationships were unchanged by a protease cocktail (E) or by I-343 (F), which indicates that compliance of the colon is unchanged. Numbers in parentheses denote mouse numbers. * $P < 0.05$, ** $P < 0.01$.

Movie S1. Targeting PAR₂ in endosomes of nociceptors. The movie shows trafficking of endosomes containing mPAR₂-GFP and Cy5-Chol in neurites of mouse DRG neurons. Neurons were incubated with Cy5-Chol, washed and recovered for 3 h. Neurons were then challenged with trypsin for 15 min, and imaged.

Movie S2. Mechanisms of protease- and PAR₂-induced hyperexcitability of nociceptors. The movie illustrates mechanisms by which trypsin, NE and CS induce PAR₂-dependent hyperexcitability of nociceptors.

References

1. Valdez-Morales EE, *et al.* (2013) Sensitization of peripheral sensory nerves by mediators from colonic biopsies of diarrhea-predominant irritable bowel syndrome patients: a role for PAR2. *Am J Gastroenterol* 108(10):1634-1643.
2. Stirling LC, *et al.* (2005) Nociceptor-specific gene deletion using heterozygous Nav1.8-Cre recombinase mice. *Pain* 113(1-2):27-36.
3. Jensen DD, *et al.* (2017) Neurokinin 1 receptor signaling in endosomes mediates sustained nociception and is a viable therapeutic target for prolonged pain relief. *Sci Transl Med* 9(392).
4. Brierley SM, Jones RC, 3rd, Gebhart GF, & Blackshaw LA (2004) Splanchnic and pelvic mechanosensory afferents signal different qualities of colonic stimuli in mice. *Gastroenterology* 127(1):166-178.
5. Hughes PA, *et al.* (2009) Post-inflammatory colonic afferent sensitisation: different subtypes, different pathways and different time courses. *Gut* 58(10):1333-1341.
6. Castro J, *et al.* (2017) Cyclic analogues of alpha-conotoxin Vc1.1 inhibit colonic nociceptors and provide analgesia in a mouse model of chronic abdominal pain. *Br J Pharmacol* 10.1111/bph.14115.
7. Vermeulen W, *et al.* (2013) Role of TRPV1 and TRPA1 in visceral hypersensitivity to colorectal distension during experimental colitis in rats. *Eur J Pharmacol* 698(1-3):404-412.
8. Halls ML, Poole DP, Ellisdon AM, Nowell CJ, & Canals M (2015) Detection and Quantification of Intracellular Signaling Using FRET-Based Biosensors and High Content Imaging. *Methods Mol Biol* 1335:131-161.
9. Jensen DD, *et al.* (2014) Endothelin-converting Enzyme 1 and beta-Arrestins Exert Spatiotemporal Control of Substance P-induced Inflammatory Signals. *J Biol Chem* 289(29):20283-20294.
10. Yarwood RE, *et al.* (2017) Endosomal signaling of the receptor for calcitonin gene-related peptide mediates pain transmission. *Proc Natl Acad Sci USA* 114(46):12309-12314.
11. Ono K, *et al.* (2017) Cutaneous pigmentation modulates skin sensitivity via tyrosinase-dependent dopaminergic signalling. *Sci Rep* 7(1):9181.

Schwann cells expressing nociceptive channel TRPA1 orchestrate ethanol-evoked neuropathic pain in mice

Francesco De Logu¹, Simone Li Puma¹, Lorenzo Landini¹, Francesca Portelli² Alessandro Innocenti³, Daniel Souza Monteiro de Araujo^{1,4}, Malvin N. Janal⁵, Riccardo Patacchini⁶, Nigel W. Bunnett⁷, Pierangelo Geppetti^{1*}, Romina Nassini¹

¹Department of Health Sciences, Section of Clinical Pharmacology and Oncology, University of Florence, Florence, Italy; ²Department of Health Sciences, Histopathology and Molecular Diagnostics; University of Florence, Florence, Italy; ³Plastic and Reconstructive Microsurgery, Careggi University Hospital, Florence, Italy; ⁴Department of Neurobiology and Program of Neurosciences, Institute of Biology, Fluminense Federal University, Niterói, RJ, Brazil; ⁵Department of Epidemiology and Health Promotion, New York University College of Dentistry, New York, USA; ⁶Department of Corporate Drug Development, Chiesi Farmaceutici SpA, Parma, Italy; ⁷Departments of Surgery and Pharmacology, Columbia University in the City of New York, USA.

*** Corresponding Author**

Pierangelo Geppetti, MD

Department of Health Sciences, University of Florence

Viale Pieraccini 6, 50139 Florence, Italy

geppetti@unifi.it

Mobile: +39 349 271 0476

Conflict of interest. RP is fully employed at Chiesi Farmaceutici SpA, Parma, Italy. NWB is a founding scientist of Endosome Therapeutics Inc. The other authors declare no competing financial interests.

Abstract

Excessive alcohol consumption is associated with spontaneous burning pain, hyperalgesia and allodynia. Although acetaldehyde has been implicated in the painful alcoholic neuropathy, the mechanism by which the ethanol metabolite causes pain symptoms is unknown. Acute ethanol ingestion caused delayed mechanical allodynia in mice. Inhibition of alcohol dehydrogenase (ADH) or deletion of transient receptor potential ankyrin 1 (TRPA1), a sensor for oxidative and carbonyl stress, prevented allodynia. Acetaldehyde generated by ADH in both liver and Schwann cells surrounding nociceptors was required for TRPA1-induced mechanical allodynia. *Plp1-Cre;Trpa1^{fl/fl}* mice with a tamoxifen-inducible specific deletion of TRPA1 in Schwann cells revealed that channel activation by acetaldehyde in these cells initiates a NADPH oxidase-1 (NOX-1)-dependent production of hydrogen peroxide (H₂O₂) and 4-hydroxynonenal (4-HNE), which sustains allodynia by paracrine targeting of nociceptor TRPA1. Chronic ethanol ingestion caused prolonged mechanical allodynia and loss of intraepidermal small nerve fibers in WT mice. While *Trpa1^{-/-}* or *Plp1-Cre;Trpa1^{fl/fl}* mice did not develop mechanical allodynia, they did not show any protection from the small fiber neuropathy. Human Schwann cells express ADH/TRPA1/NOX1 and recapitulate the proalgesic functions of mouse Schwann cells. TRPA1 antagonists might attenuate some symptoms of alcohol-related pain.

Keywords

TRPA1, ethanol, Schwann cells, oxidative stress, neuropathic pain

Introduction

Alcohol abuse and dependence are among the major healthcare problems in the world (1). The impact of alcohol abuse continues to grow due to the rising incidence of excessive drinking by women and young people (2). Nevertheless, the male/female ratio of current drinkers and heavy episodic drinkers, which is 1.7 and 2.5, respectively, indicate twice the prevalence in men compared to women (2). About 60% of alcoholics exhibit a peripheral polyneuropathy, associated with pain and dysesthesias of the lower extremities (3). Reduced thiamine levels (4), which cause peripheral neuropathy in patients with post-gastrectomy polyneuropathy or beriberi, have been reported in alcoholics, and have been considered responsible for the peripheral neuropathy (5, 6). However, the observation that painful polyneuropathy is present in alcoholics with normal thiamine status (6), and that the clinical and pathological features of alcoholic neuropathy are distinct from those associated with thiamine deficiency (7) led to the conclusion that alcohol exerts a direct toxic effect on peripheral nerves. However, the mechanism by which ethanol targets peripheral nerves to cause the painful condition remains unknown.

Alcohol dehydrogenase (ADH) converts ethanol into the reactive and toxic product acetaldehyde, which is rapidly metabolized to acetic acid by the mitochondrial aldehyde dehydrogenase-2 (ALDH2) (8). Acetaldehyde is considered as the major contributor of the detrimental effects produced by acute and chronic alcohol consumption, including flushing, headache, cirrhosis and cancer (9-12). Mutations of the ADH and ALDH2 genes, which respectively accelerate ethanol conversion to acetaldehyde and slow down acetaldehyde metabolism, make East Asians susceptible to alcohol-induced symptoms with lower rates of alcohol use (13, 14). Acetaldehyde generates advanced glycation end-products and increases oxidative stress, which can contribute to ethanol-induced painful

neuropathy (15). In particular, preclinical studies and clinical evidence have implicated acetaldehyde in the genesis of the neuronal damage associated with ethanol consumption (3). However, the pathways by which acetaldehyde causes ethanol-evoked neuropathic pain are poorly understood.

Elevated local concentrations (1-3%) of ethanol have been shown to activate the transient receptor potential vanilloid 1 (TRPV1) channel on primary sensory nerves to induce pain and neurogenic inflammation (16). A related channel, TRP ankyrin 1 (TRPA1), is uniquely sensitive to multiple ROS, reactive nitrogen (RNS) and carbonyl (RCS) species (17-19). Saturated and unsaturated aldehydes, including acetaldehyde and 4-hydroxynonenal (4-HNE), also activate TRPA1 to cause pain-like responses (20, 21). TRPV1, TRPA1 and other TRP channels, including the vanilloid 4 (TRPV4), are expressed by a subpopulation of primary sensory neurons that signal pain (19). In the present study, we explored the role of TRP channels in the pain-like responses evoked by acute and chronic ethanol ingestion in mice.

We found that local (intraplantar) injection of ethanol in the mouse hind paw caused an acute nociceptive response due to direct activation of TRPV1, as previously reported (16). In addition, ethanol (either intraplantar or intragastric) caused a delayed and prolonged TRPV1-independent mechanical allodynia of the hind paw that was prevented by ADH and TRPA1 inhibition. Surprisingly, Schwann cells that ensheath plantar nerve fibers expressed ADH, which mediated the local conversion of ethanol to acetaldehyde. Selective deletion of TRPA1 on Schwann cells or nociceptors revealed that acetaldehyde, generated in the liver or locally, activates TRPA1 on Schwann cells (22) to produce oxidative and carbonylic stress, which target neuronal TRPA1 to sustain allodynia. Notably, mice fed daily with an ethanol-containing diet, which mimics chronic alcohol ingestion by alcoholics, developed a prolonged allodynia that was associated with loss of intraepidermal nerve fibers (IENF). Allodynia caused by chronic ethanol ingestion

was prevented by the same genetic and pharmacological disruptions of TRPA1 and oxidative stress that attenuated allodynia evoked by acute ethanol exposure. Thus, TRPA1 antagonism might represent an effective treatment for pain in alcoholics.

Results

TRPV1 mediates acute nociception but not sustained allodynia to local administration of ethanol

To explore the mechanisms of alcohol-induced nociception, ethanol was administered locally to the hind paw of C57BL/6J mice. Injection of intraplantar ethanol (15-80% in 0.9% NaCl) caused dose-dependent immediate nociceptive behavior, which did not last more than 5 min (Figure 1A). Ethanol also produced a delayed and prolonged (1-6 h) mechanical allodynia (Figure 1B). The short-lived nociceptive response was absent in *Trpv1*^{-/-} mice (Figure 1C), and in C57BL/6J mice pretreated with the TRPV1 antagonist, SB366791 (Supplementary Figure 1A), supporting previous evidence that ethanol selectively targets TRPV1 to signal acute pain (16). In contrast, TRPV1 deletion or antagonism did not affect ethanol-evoked mechanical allodynia (Figure 1D and Supplemental Figure 1B). Thus, whereas direct TRPV1 engagement mediates acute ethanol-evoked nociception, ethanol induces sustained mechanical allodynia by a TRPV1-independent mechanism. Ethanol-induced nociception and allodynia were similar in *Trpv4*^{-/-} mice and in WT littermates (Supplementary Figure 1C and D).

Acetaldehyde and TRPA1 mediate sustained allodynia to local and intragastric administration of ethanol

ADH mediates the first step of alcohol metabolism, converting ethanol to the saturated aldehyde acetaldehyde, which can activate TRPA1 (20). We examined the contribution of ADH and TRPA1 to ethanol-evoked allodynia. Intragastric or intraplantar

pretreatment of C57BL/6J mice with 4-methylpyrazole (4-Mp), a selective ADH inhibitor, prevented ethanol-evoked allodynia (Figure 1E and F). The nociceptive response evoked by intraplantar ethanol observed in *Trpa1*^{+/+} mice was also present in *Trpa1*^{-/-} mice (Figure 1G). However, mechanical allodynia produced by intraplantar ethanol in *Trpa1*^{+/+} mice was absent in *Trpa1*^{-/-} mice (Figure 1H). Systemic (i.p.) or intraplantar administration of A967079, a TRPA1 antagonist, 2 h after ethanol reversed sustained allodynia (Supplementary Figure 1E and F). Intraplantar injection of acetaldehyde (1-20 nmol) into the hind paw of C57BL/6J mice replicated the actions of ethanol, causing a dose-dependent immediate and transient nociceptive response (Figure 1I), followed by a delayed and prolonged (1-8 h) allodynia (Figure 1J). Both responses were absent in *Trpa1*^{-/-} mice (Figure 1K and L). Systemic (i.p.) or intraplantar administration of A967079 reversed immediate nociception and sustained allodynia evoked by intraplantar acetaldehyde in C57BL/6J mice (Supplementary Figure 1G-I). Furthermore, the acute nociceptive response and the delayed mechanical allodynia induced by intraplantar acetaldehyde in *Trpv1*^{+/+} mice remained unaffected in *Trpv1*^{-/-} mice (Supplementary Figure 1J and K). The results are consistent with the hypothesis that ethanol induces allodynia by a mechanism that entails metabolism to acetaldehyde, which activates TRPA1.

Examination of the responses evoked by local injection of ethanol or acetaldehyde provides mechanistic insights into alcohol-induced pain. However, the ingestion of alcohol causes peripheral neuropathy in alcoholics. To mimic these circumstances, we administered graded doses of ethanol (1-4 ml/kg of ethanol 15% in 0.9% NaCl) to mice by *intra*gastric administration. Even at the highest dose (15%, 4 ml/kg, *intra*gastric), ethanol did not induce acute nociception or affect motor coordination, evaluated using a rotarod: no falls were observed in mice receiving either vehicle (n=8) or ethanol (15%, 4 ml/kg, n=8). However, *intra*gastric ethanol evoked a dose-related delayed and sustained

(1-6 h) mechanical allodynia in C57BL/6J mice and *Trpa1*^{+/+} mice, but not in *Trpa1*^{-/-} mice (Figure 2A and B). Ethanol-evoked mechanical allodynia was preserved in *Trpv1*^{-/-} or *Trpv4*^{-/-} mice (Supplementary Figure 1L and M). Systemic (i.p.) or intraplantar administration of A967079 to C57BL/6J mice reversed allodynia evoked by intragastric ethanol (Figure 2C and D).

After gavage, ethanol levels in plasma, liver and paw were maximal at 30 min, and declined to baseline at 3 h (Figure 2E), when mechanical allodynia was maximal (e.g., Figure 2A). The temporal dissociation between ethanol levels in plasma and tissues and allodynia suggests that ethanol does not directly activate TRPA1 to cause allodynia. Administration of the ADH inhibitor 4-Mp (intra-gastric) before ethanol prevented allodynia (Figure 2F). These results suggest that acetaldehyde, but not ethanol, activates TRPA1 to initiate allodynia.

Schwann cell ADH converts ethanol to acetaldehyde in peripheral tissues

Ethanol is mainly converted to acetaldehyde by ADH in the liver. However, ADH is expressed in other tissues (23-26). We detected mRNAs encoding ADH1, ADH5 and ADH7 in homogenates of mouse paw (Figure 3A). ADH immunoreactivity was confined to the nerve trunk within the paw, where it was co-expressed with S100, a specific marker of Schwann cells, but not in PGP9.5-positive nerve fibers (Figure 3B and C and Supplementary Figure 2A). Exposure of cultured mouse Schwann cells to ethanol induced the generation of acetaldehyde, a response that was prevented by 4-Mp (Figure 3D). Local (intraplantar) administration of ethanol to the paw also resulted in increased paw tissue levels of acetaldehyde within 15 min (Figure 3E). The local (intraplantar) administration of 4-Mp inhibited acetaldehyde formation (Figure 3F) and allodynia (Figure 1F) induced by intraplantar ethanol. The effects of intra-gastric ethanol on allodynia and acetaldehyde levels were partially reduced by pretreatment with

intraplantar (Figure 3G and H), or completely attenuated by, [intra](#)gastric 4-Mp (Figure 3H and 2F). These results suggest that Schwann cells in the paw express ADH and convert ethanol to acetaldehyde. This local generation to acetaldehyde, together with the hepatic generation of acetaldehyde, can cause TRPA1-dependent sustained allodynia.

Acetaldehyde via TRPA1 generates ROS that sustain ethanol-evoked allodynia

To strengthen the hypothesis that acetaldehyde initiates allodynia by activating TRPA1, we treated mice with systemic (0.1-1 mg/kg, i.p.) acetaldehyde. Acetaldehyde (i.p.) did not affect motor coordination, as no falls was observed with either vehicle (n=8) or acetaldehyde (1 mg/kg, n=8). Acetaldehyde (i.p.) did not cause detectable acute nociceptive behavior, but evoked a dose-dependent, delayed and prolonged (1-8 h) mechanical allodynia in C57BL/6J mice (Figure 4A). Acetaldehyde did not cause allodynia in *Trpa1*^{-/-} mice (Figure 4B). Systemic (i.p.) and intraplantar A967079 prevented acetaldehyde-evoked allodynia in C57BL/6J mice (Figure 4C and D). However, acetaldehyde formation in liver and paw after [intra](#)gastric ethanol did not coincide with allodynia (Figure 4E); the levels of acetaldehyde in the liver and paw had returned to baseline by 3 h after [intra](#)gastric ethanol (Figure 4E), when allodynia was robustly maintained (Figure 2A). Furthermore, administration of the ADH inhibitor 4-Mp ([intra](#)gastric) after ethanol did not affect allodynia (Figure 4F). These results suggest the existence of additional mechanisms of ethanol-induced allodynia.

Both ethanol and acetaldehyde can release ROS (27-29). ROS and their carbonylic byproducts, including 4-HNE, activate TRPA1 (17, 21). To examine the contribution of ROS to ethanol-evoked allodynia, we treated mice with the ROS scavenger, phenyl- α -tert-butyl nitron (PBN). PBN (i.p. or intraplantar) reversed the allodynia evoked by ethanol ([both intra](#)plantar and [intra](#)gastric) (Figure 4G and H; Supplementary Figure 3A and B) or acetaldehyde (Figure 4I and J; Supplementary Figure 3C and D). Ethanol

([intra](#)gastric or [intra](#)plantar) increased H₂O₂ and 4-HNE levels in the paw (Figure 5A and B). However, while H₂O₂ levels were elevated for 3 h, [4-HNE content, measured by either immunofluorescence or by a biochemical assay](#), persisted for 6 h (Figure 5A and B). To test the hypothesis that the late phase of allodynia was mainly due to RCS, N-acetyl cysteine (NAC), which efficiently scavenges α,β -unsaturated aldehydes, including 4-HNE (30), was given (i.p.) to mice 5 h after ethanol ([intra](#)gastric). NAC (i.p.) attenuated mechanical allodynia at 6 h (Figure 5C). These results suggest that carbonylic derivatives, which are more stable and longer acting than ROS (30), sustain the final phase of allodynia. To support this hypothesis, PBN, which selectively scavenges ROS, was ineffective in the final phase of allodynia (Figure 5C).

Administration of the ADH inhibitor 4-Mp (Figure 5D) or the ROS scavenger, PBN (Figure 5E), blunted the ethanol-induced increase in H₂O₂ levels. Acetaldehyde (i.p. or [intra](#)plantar) increased H₂O₂ in paw tissue (Figure 5F), an effect that was inhibited by PBN (Figure 5G). Surprisingly, we observed that pharmacological blockade or genetic deletion of TRPA1 attenuated both ethanol- and acetaldehyde-evoked increases in H₂O₂ in the paw (Figure 5E and 5G-I). We have recently reported the presence of different NOX isoforms in Schwann cells of the mouse sciatic nerve, where they co-localize with TRPA1 to increase oxidative stress (22). Here, we observed that Schwann cells of plantar nerve fibers expressed NOX1 and TRPA1 (Figure 6A and B and [Supplementary Figure 2A](#)). A NOX1 antagonist (ML171, i.p.) reversed allodynia evoked by ethanol ([intra](#)gastric) and acetaldehyde (i.p.) (Figure 6C).

Our results suggest that ADH in the liver or in Schwann cells of the sciatic nerve converts ethanol to acetaldehyde; Schwann cell-derived acetaldehyde might activate TRPA1 in an autocrine manner to generate ROS and RCS, which could amplify and sustain allodynia. To specifically define the role of Schwann cell TRPA1 in ethanol-evoked nociception, we studied mice with Schwann cell-specific deletion of TRPA1.

Mice with conditional ablation of TRPA1 in Schwann cells (*Plp1-Cre^{ERT};Trpa1^{fl/fl}*) (22) exhibited a normal acute nociception after intraplantar ethanol or AITC (TRPA1 agonist) (Supplementary Figure 4A). As these two responses are mediated by neuronal TRPV1 and TRPA1, respectively, the results indicate that the neuronal channel is unaffected by deletion of Schwann cell TRPA1. However, allodynia and generation of H₂O₂ in the paw evoked by intraplantar or **intra**gastric ethanol were attenuated in *Plp1-Cre^{ERT};Trpa1^{fl/fl}* mice (Figure 6D and E).

To further support the involvement of Schwann cell TRPA1 in ethanol-evoked mechanical allodynia, mice were locally treated with the TRPA1 antisense oligonucleotide (TRPA1 AS-ODN) or its mismatched (TRPA1 MM-ODN) analogue (both intraplantar) (Supplementary Figure 4C) or with the activated form of tamoxifen (4-hydroxytamoxifen, 4-OHT) (intraplantar) (Supplementary Figure 4G). Both treatments were given by injection in the vicinity of the plantar nerve trunk, before ethanol (intraplantar or intra

gastric). In mice treated with TRPA1 AS-ODN or 4-OHT, acute nociception responses by intraplantar ethanol or AITC (dependent on neuronal TRPV1 and TRPA1, respectively) were preserved (Supplementary Figure 4E and I), indicating that neuronal TRPV1 and TRPA1 were unaffected. However, colocalization of TRPA1 with the Schwann cell marker, S-100, in the plantar nerve was markedly reduced (Supplementary Figure 4D and H), confirming selective deletion of TRPA1 in Schwann cells. After intra

gastric ethanol, mechanical allodynia was attenuated solely in the paw treated with the TRPA1 AS-ODN, while it was unaffected in the TRPA1 MM-ODN treated paw (Supplementary Figure 4F). Similar results were obtained with local treatment with 4-OHT. Notably, 4-OHT attenuated mechanical allodynia evoked by intra

gastric ethanol only on the paw treated with 4-OHT, but not in the contralateral paw (Supplementary Figure 4J). These data support the hypothesis that ethanol-evoked allodynia is initiated and maintained by Schwann cell TRPA1.

To specifically investigate the contribution of neuronal TRPA1, we studied mice with selective deletion of TRPA1 in primary sensory neurons (*Adv-Cre;Trpa1^{fl/fl}*) (31). AITC-induced nociception was attenuated in *Adv-Cre;Trpa1^{fl/fl}* mice, which confirms deletion of the functional channel (Supplementary Figure 4B). In *Adv-Cre;Trpa1^{fl/fl}* mice, ethanol-induced acute nociception was preserved (Supplementary Figure 4B). However, whereas allodynia evoked by **intra**gastric or **intra**plantar ethanol was attenuated, H₂O₂ formation was unaffected (Figure 6F and G). Thus, in contrast with the Schwann cell channel, TRPA1 expressed by nociceptor signals pain, but does not contribute to oxidative stress generation.

Chronic ethanol ingestion evokes ROS formation and allodynia dependent on Schwann cell TRPA1

In WT mice, daily ingestion of an ethanol (5% for 28 d) containing diet (32) induced a progressively increasing mechanical allodynia that was apparent at 5-8 d, stabilized after two wk and maintained for the entire period of observation (Figure 7A and B). Both *Trpa1^{-/-}* and *Plp1-Cre^{ERT};Trpa1^{fl/fl}* mice were protected from the development of allodynia (Figure 7B). At day 28 after the initiation of the ethanol diet, the allodynia observed in WT mice was reversed by treatment (i.p.) with the TRPA1 antagonist, A967079, or with the ROS scavenger, PBN (Figure 7C). At day 28, WT mice showed increased levels of H₂O₂ and 4-HNE in the plantar nerve that were attenuated in *Trpa1^{-/-}* and *Plp1-Cre^{ERT};Trpa1^{fl/fl}* mice (Figure 7D). However, the loss of PGP9.5 positive IENF observed at day 28 was unaffected in either *Trpa1^{-/-}* or *Plp1-Cre^{ERT};Trpa1^{fl/fl}* mice (Figure 7E). At day 28, the levels of ethanol or ACD in the paw of *Trpa1^{-/-}* and *Plp1-Cre^{ERT};Trpa1^{fl/fl}* mice were not different from those measured in respective WT and control mice (Supplementary Figure 5A-D).

Ethanol evokes ADH- and TRPA1-dependent ROS formation by human Schwann cells

Our findings reveal an unexpected but critical role for Schwann cells in ethanol-evoked mechanical allodynia in mice. To assess whether these findings could translate to humans, we studied primary cultures of human Schwann cells (HSC) and Schwann cells in sections of human skin. HSC in culture expressed immunoreactive S100 and immunoreactive ADH (Figure 8A). In nerve bundles in biopsies of human skin, immunoreactive ADH colocalized with S100 (Figure 8B and [Supplementary Figure 2B](#)). mRNA encoding multiple isoforms of ADH (1A, 1B, 1C and 5) was amplified from HSC in culture (Figure 8C). Exposure of HSC to ethanol caused a concentration-dependent generation of acetaldehyde that was inhibited by 4-Mp, and thus depends on ADH activity (Figure 8D). S100-positive HSC in culture (Figure 8E) and in sections of human skin also expressed immunoreactive TRPA1 (Figure 8F and [Supplementary Figure 2B](#)). Cultured HSC expressed TRPA1 mRNA (Figure 8G). Exposure of HSC to AITC, acetaldehyde or H₂O₂ elicited increases in intracellular calcium that were attenuated by A967079 (Figure 8H). Prolonged exposure of HSC to ethanol induced a delayed and sustained increase in calcium responses, which was attenuated by pretreatment with 4-Mp or A967079 (Figure 8I). S100-positive HSC in culture and in sections of human skin also expressed immunoreactive NOX1 (Figure 8J and K and [Supplementary Figure 2B](#)). In addition, cultured HSC expressed NOX1 mRNA (Figure 8L). AITC, acetaldehyde or H₂O₂ elicited calcium dependent increases in H₂O₂ in HSC that were reduced by A967079 (Figure 8M).

Discussion

Our results show that intraplantar injection of ethanol in the mouse hind paw causes two sensory responses, which are temporally and mechanistically distinct. After an immediate and short-lived (5 min) nociceptive response, mice exhibited a delayed and prolonged (1-6 h) mechanical allodynia. TRPV1 antagonism or deletion prevented the immediate nociceptive response, which is thus mediated by ethanol activation of TRPV1, as previously reported (16). In contrast, TRPV1 disruption did not affect the delayed and sustained mechanical allodynia, which occurs by a different mechanism.

Genetic or pharmacological impairment of ADH that results in increased acetaldehyde levels enhances the susceptibility of affected individuals to [alcohol-evoked symptoms](#) (13, 14). Our observation that pretreatment with the ADH inhibitor, 4-Mp, prevented the allodynia evoked by intraplantar ethanol and that intraplantar injection of acetaldehyde caused allodynia similar to that evoked by ethanol support the hypothesis that acetaldehyde mediates the prolonged allodynic effect of ethanol. The findings that genetic deletion or pharmacological antagonism of TRPA1 prevented ethanol- and acetaldehyde-evoked allodynia are consistent with the hypothesis that the aldehyde and not its precursor gates TRPA1 (20) and plays a major role in the allodynia that mimics the neuropathic pain observed in alcoholics. In contrast, deletion of TRPV4, a proalgesic channel expressed by a subset of nociceptors, did not affect either acute nociception or allodynia. Thus, while acute nociception is due to a direct action of ethanol on TRPV1, delayed and sustained allodynia is mediated by TRPA1, *via* ADH-dependent generation of acetaldehyde.

We investigated the contribution of TRPA1 to pain after oral administration of ethanol, which more closely resembles the situation in alcoholics. In contrast to intraplantar administration, intragastric administration of ethanol did not cause acute pain-related behavior. However, intragastric ethanol did cause delayed and sustained

allodynia in wild-type but not *Trpa1*^{-/-} mice; deletion of either TRPV1 or TRPV4 did not affect allodynia. The ability of intraperitoneal acetaldehyde to mimic the response evoked by intragastric ethanol implicates this metabolite as a mediator of TRPA1-dependent allodynia. Although the major site of alcohol metabolism is the liver, where the bulk of acetaldehyde is generated (25, 26), several extrahepatic cells express ADH (23, 24). The ADH inhibitor, 4-Mp, when given locally (intraplantar administration), prevented acetaldehyde increase and allodynia evoked by local (intraplantar) ethanol, and, although partially, reduced increases in acetaldehyde and allodynia elicited by intragastric ethanol. Complete inhibition of allodynia and increases in acetaldehyde levels evoked by intragastric ethanol were, however, obtained by systemic 4-Mp administration. These results suggest that acetaldehyde, which mediates allodynia, derives in part from the systemic circulation, and in part from local production within the paw tissue. ADH mRNA and protein were confined to Schwann cells that ensheath sensory nerve fibers in the paw. The ability of the paw tissue and cultured mouse Schwann cells to convert ethanol into acetaldehyde in a 4-Mp-sensitive manner supports the proposal that Schwann cells are the local source of acetaldehyde, which engages TRPA1 to mediate allodynia.

Whereas the TRPA1 antagonist, A967079, inhibited ethanol-evoked allodynia when administered before or after ethanol, the ADH inhibitor, 4-Mp, prevented allodynia only when given before ethanol. This finding suggests that, whereas TRPA1 engagement is constantly required, acetaldehyde is necessary to initiate, but is not sufficient to maintain, allodynia. The transient (1-h duration) increase in acetaldehyde levels in the paw, compared to the sustained allodynia (6 h), strengthens the view that the prolonged allodynia is not maintained by acetaldehyde. Acetaldehyde can generate ROS (27, 29), which are among the several endogenous ligands of TRPA1 (17-19). H₂O₂ levels peaked in paw homogenates 1-3 h and returned to baseline 6 h after ethanol. However, in the mouse paw immunostaining for the carbonylic byproduct of oxidative stress, 4-HNE (33),

a known TRPA1 activator (21), increased 3 h, and peaked 6 h after ethanol when allodynia was still robustly present. In agreement with the time courses of H₂O₂ and 4-HNE levels in the mouse paw, treatment with the ROS scavenger, PBN, attenuated allodynia 3 h, but not 6 h, after ethanol, while the aldehyde scavenger, NAC, was effective 6 h after ethanol. These findings suggest that TRPA1 engagement by mediators efficiently scavenged by PBN does not outlast ~4 h after exposure to ethanol, whereas attenuation of allodynia 6 h after ethanol is provided exclusively by compounds able to scavenge aldehydic compounds, such as 4-HNE. The ability of the ROS scavenger, PBN, to attenuate paw allodynia indicates that oxidative stress sustains allodynia and raises the question of how ethanol/acetaldehyde generate ROS. We recently reported in a mouse model of sciatic nerve injury that ROS, which sustain mechanical allodynia, are produced *via* the TRPA1/NOX1 pathway in Schwann cells ensheathing sciatic nerve fibers (22). Therefore, we investigated the possibility that a similar mechanism contributes to ethanol-evoked allodynia. In support of this hypothesis, *Plp1-Cre^{ERT};Trpa1^{fl/fl}* mice, which selectively lack TRPA1 in Schwann cells, showed attenuated allodynia and reduced H₂O₂ levels in paw tissue. NOX1 has been reported as the major enzyme isoform responsible for the TRPA1-dependent oxidative burst in Schwann cells (22). We confirmed this finding since the selective NOX1 inhibitor, ML171 (34), attenuated ethanol-evoked allodynia.

Finally, we asked whether the TRPA1 which mediates ethanol-evoked allodynia is exclusively the channel expressed by Schwann cells, or if the neuronal channel might also contribute. Mice with selective deletion of TRPA1 in primary sensory neurons, *Adv-Cre;Trpa1^{fl/fl}* mice (31), exhibited a markedly attenuated ethanol-evoked paw allodynia. However, the increased levels of H₂O₂ in the paw tissue were unaffected. These observations indicate that the Schwann cell TRPA1/NOX1 pathway is necessary to maintain the prolonged oxidative stress generation required to target the neuronal

TRPA1, which eventually sustains allodynia. *Plp1-Cre^{ERT};Trpa1^{fl/fl}* mice are selectively deficient of TRPA1 in the Schwann cell and oligodendrocyte lineage. Thus, the implication of oligodendrocytes in the brain signaling of allodynia evoked by intragastric ethanol should be considered. However, several observations suggest that initiation and maintenance of paw allodynia is promoted by a series of local events driven by TRPA1 of Schwann cell ensheathing plantar nerve. *Plp1-Cre^{ERT};Trpa1^{fl/fl}* mice not only failed to produce allodynia, but were unable to generate the local oxidative stress response that is required to sustain allodynia. Local treatment with a TRPA1 AS-ODN or with the active tamoxifen metabolite, 4-OHT, which directly binds to the tamoxifen-inducible estrogen receptor, attenuated intragastric ethanol-evoked allodynia only in the treated paw, without affecting the pain response in the contralateral side. These findings imply that the drugs did not diffuse to distant sites, including the brain, but maintained their action confined to the treated paw. Thus, the most parsimonious hypothesis is that Schwann cell TRPA1, by promoting local oxidative stress generation, is necessary and sufficient to sustain ethanol-evoked allodynia. Nonetheless, these observations do not exclude a contribution of oligodendrocyte TRPA1 to the central processing of the pain response. The generation of mice lacking TRPA1 solely in Schwann cells would be required to definitively determine the selective role of TRPA1 in this cell type.

Painful neuropathy is produced by chronic alcohol ingestion and is associated with peculiar pathological features, such as the loss of IENF (5). We reproduced a chronic condition in mice by feeding them an ethanol containing diet. The observation that both *Trpa1^{-/-}* and *Plp1-Cre^{ERT};Trpa1^{fl/fl}* mice did not develop allodynia indicated that TRPA1 and specifically the channel expressed by Schwann cells is necessary and sufficient to generate the painful condition. Reduced levels of either H₂O₂ or 4-HNE in the plantar nerve of *Trpa1^{-/-}* and *Plp1-Cre^{ERT};Trpa1^{fl/fl}* mice and the ability of the TRPA1 antagonist and the ROS scavenger to reverse allodynia, suggest that chronic ethanol ingestion

activates a proalgesic mechanism identical to that induced by acute ethanol exposure. Thus, the oxidative stress that signals pain is generated by a sustained gating of Schwann cell TRPA1 by acetaldehyde generated by the daily ethanol ingestion.

Our results show that in mice receiving chronic ethanol administration deletion of Schwann cell TRPA1 does not ameliorate IENF loss, but does attenuate allodynia. Thus, Schwann cell TRPA1 and the ensuing oxidative stress burst are not crucial for the neuropathy and there is no stringent correspondence between IENF degeneration and neuropathic pain. After the loss of IENF, the remaining extraepithelial nerve fibers with their ensheathing Schwann cells are sufficient to elicit mechanical allodynia. Various interventions, including the immunomodulator, minocycline (35), erythropoietin (36), a poly(ADP-ribose) polymerase inhibitor (37) and a TRPA1 antagonist (38), have been reported to attenuate IENF loss and the ensuing neuropathic pain-responses. A series of differences may explain the discrepancy with our current data, including the causative agent of the neuropathy, alcohol vs. streptozotocin and paclitaxel, or in the case of TRPA1, systemic treatment with an antagonist that non-selectively targets TRPA1, not solely in Schwann cells, but in all cells where it is expressed.

The presence of thiamine deficiency in heavy alcohol drinkers suggested that the beriberi neuropathy was the underlying cause of the neurological symptoms in alcoholics. However, investigation of respective clinicopathological features has clearly differentiated the two conditions (7). Alcoholic neuropathy is sensory-dominant and predominantly shows loss of small fibers, while thiamine deficiency neuropathy is motor-dominant with mainly large fiber loss (7). The small-fiber polyneuropathy documented in heavy alcohol drinkers with normal thiamine status (39) further supported the direct role of alcohol and acetaldehyde, and not of thiamine deficiency, in alcoholic neuropathy (7, 39, 40). Assessment of ethanol-evoked allodynia in mice underscores the implication of TRPA1 either in acute (single administration) or chronic (prolonged exposure) settings.

However, pain (with or without burning quality) is the initial major symptom of alcoholic neuropathy; it develops slowly, extending over a period of months, and is associated with allodynia and hyperalgesia (3). Thus, a limitation of the present murine study is that only one (mechanical allodynia) among the various pain modalities reported by alcoholics has been investigated.

While TRPV1 is key to evoke the acute nociceptive behavior caused by local exposure to ethanol, TRPA1 uniquely mediates the prolonged paw allodynia that models in mice one pain symptom observed in patients. However, multiple ethanol-derived mediators contribute to the TRPA1-mediated paw allodynia. Acetaldehyde generated by liver ADH (Supplementary Figure 6) and locally by Schwann cell ADH commits Schwann cell TRPA1/NOX1 to generate ROS. ROS released from Schwann cells engage TRPA1 in nociceptors initially and up to 3 h after ethanol. The peroxidation-dependent generation of carbonylic byproducts, including 4-HNE, sustains the final TRPA1 targeting. The translational value of the present findings is strengthened by the observation that human Schwann cells are fully equipped to exert all the functions found in mouse Schwann cells. Human Schwann cells express ADH, TRPA1 and NOX1 mRNA and protein, and are capable of converting ethanol into acetaldehyde. Human Schwann cells respond to ethanol (*via* acetaldehyde), acetaldehyde and H₂O₂ with a TRPA1-dependent calcium response and the ensuing generation of oxidative stress. Thus, inhibition of any of the steps reported here in mice may be translated to human Schwann cells and could be beneficial to attenuate pain associated with alcohol consumption in patients.

The presence of ADH in Schwann cells that express TRPA1/NOX1 and their ability of generating oxidative stress identifies an autocrine pathway that we propose as a major contributing mechanism in **alcohol-induced mechanical allodynia**. Moreover, this pathway may be important in other conditions produced by exposure to alcohol. The

reported presence of TRPA1 in oligodendrocytes (41) suggests that similar detrimental mechanisms may operate in the central nervous system to mediate the toxic effect associated with alcohol ingestion. Further studies are required to explore whether Schwann cell TRPA1 mediates pain-like responses evoked by chronic ethanol in humans.

Methods

Animals

The following mouse strains were used: C57BL/6J (male, 20-25 g, 5-6 wk; Envigo); littermate WT (*Trpa1*^{+/+}) and TRPA1-deficient mice (*Trpa1*^{-/-}, B6.129P-Trpa1^{tm1Kykw}/J, 25-30 g, 5-8 wk, Jackson Laboratories) (42); littermate WT (*Trpv4*^{+/+}) and TRPV4-deficient (*Trpv4*^{-/-}) mice (25-30 g, 5-8 wk) (43); and littermate WT (*Trpv1*^{+/+}) and TRPV1-deficient mice (*Trpv1*^{-/-}, B6.129X1-Trpv1^{tm1Jul}/J, 25-30 g, 5-8 wk, Jackson Laboratories). All these strains were generated by C57BL/6 background.

To selectively delete *Trpa1* gene in primary sensory neurons, 129S-Trpa1^{tm2Kykw}/J mice (*floxed Trpa1*, *Trpa1*^{f/f}, Stock No: 008649; Jackson Laboratories), which possess loxP sites on either side of the S5/S6 transmembrane domains of the *Trpa1* gene, were crossed with hemizygous *Advillin-Cre* male mice (44). The progeny (*Adv-Cre*; *Trpa1*^{f/f}) was genotyped by standard PCR for *Trpa1* and *Advillin-Cre*. Mice negative for *Advillin-Cre* (*Adv-Cre*⁻; *Trpa1*^{f/f}) were used as control. Successful *Advillin-Cre* driven deletion of TRPA1 mRNA was confirmed by RT-qPCR (45). To generate mice in which the *Trpa1* gene was conditionally silenced in Schwann cells/oligodendrocytes homozygous 129S-Trpa1^{tm2Kykw}/J (*floxed TRPA1*, *Trpa1*^{f/f}, Stock No: 008649, Jackson Laboratories), were crossed with hemizygous B6.Cg-Tg(*Plp1-Cre*^{ERT})3Pop/J mice (*Plp1-Cre*^{ERT}, Stock No: 005975, Jackson Laboratories), expressing a tamoxifen-inducible Cre in myelinating cells (*Plp1*, proteolipid protein myelin 1) (22). The progeny (*Plp1-Cre*; *Trpa1*^{f/f}) was genotyped by standard PCR for *Trpa1* and *Plp1-Cre*^{ERT} (22). Mice negative for *Plp1-*

Cre^{ERT} ($Plp1-Cre^{-};Trpa1^{fl/fl}$) were used as control. Both positive and negative mice to Cre^{ERT} and homozygous for floxed $Trpa1$ ($Plp1-Cre^{ERT};Trpa1^{fl/fl}$ and $Plp1-Cre^{ERT-};Trpa1^{fl/fl}$, respectively) were treated with intraperitoneal (i.p.) tamoxifen (1 mg/100 μ l in corn oil, once a day, for 5 consecutive d) (22), resulting in Cre-mediated ablation of $Trpa1$ in PLP-expressing Schwann cells/oligodendrocytes. Successful Cre-driven deletion of TRPA1 mRNA was confirmed by RT-qPCR (22). In addition, some $Plp1-Cre^{ERT};Trpa1^{fl/fl}$ and $Plp1-Cre^{ERT-};Trpa1^{fl/fl}$ were treated with the activated form of tamoxifen (4-hydroxytamoxifen, 4-OHT, intraplantar, i.pl., 0.02 mg/10 μ l once a day for 4 consecutive d).

Study design

Group size of n=8 animals for behavioral experiments were determined by sample size estimation using G*Power (v3.1) (46) to detect size effect in a post-hoc test with type 1 and 2 error rates of 5 and 20%, respectively. Allocation concealment of mice to vehicle(s) or treatment(s) group was performed using a randomization procedure (<http://www.randomizer.org/>). The assessors were blinded to the identity (genetic background or allocation to treatment group) of the animals. Identity of the animals was unmasked to assessors only after data collection. Every effort has been made to minimize the discomfort and pain of the animals in each phase of the study. Mice were housed in a temperature- and humidity-controlled *vivarium* (12 h dark/light cycle, free access to food and water, 8 animals per cage). Mice were acclimatized in a quiet, temperature-controlled room (20-22°C) for 1 h before behavioral studies, that were done between 9 a.m. and 5 p.m. Animals were anaesthetized with a mixture of ketamine and xylazine (90 mg/kg and 3 mg/kg, respectively, i.p.) and euthanized with inhaled CO₂ plus 10-50% O₂. If not otherwise indicated, reagents were obtained from Sigma-Aldrich (Milan, Italy).

In functional and biochemical studies ethanol was given by i.pl. (30%) or i.g. (15%, 4 ml/kg) administration and acetaldehyde by i.pl. (20 nmol) or i.p. (0.1 mg/kg) administration. Vehicle of i.pl. or i.g. ethanol and i.pl. or i.p. acetaldehyde was 0.9% NaCl. Vehicle the various drugs was 4% DMSO and 4% Tween80 in 0.9% NaCl for i.pl. or i.p. administration and, 0.5% carboxymethylcellulose for i.g. administration. Twenty μ l/site were injected in all i.pl. administrations. SB366791, N-(3-methoxyphenyl)-4-chlorocinnamide (1 mg/kg, i.p.) or vehicle were administered 30 min before i.pl. ethanol or vehicle. A967079, [(1E,3E)-1-(4-Fluorophenyl)-2-methyl-1-penten-3-one oxime] and phenyl- α -tert-butyl nitron (PBN) (both, 100 mg/kg, i.p. or 100 μ g i.pl.) or their vehicle, were administered 1 h after i.pl. or i.g. ethanol and i.pl. or i.p. acetaldehyde or their vehicle. PBN (100 mg/kg, i.p.) or vehicle were also given 5 h after i.g. ethanol. 4-methylpyrazole (4-Mp, 50 mg/kg, i.g. or 100 μ g, i.pl.) or vehicle were administered 30 min before i.pl. or i.g. ethanol or vehicle and 2 h after i.g. ethanol or vehicle. N-acetyl cysteine (NAC, 250 mg/kg, i.p.) or vehicle were administered 5 h after i.g. ethanol. ML171 [2-acetylphenothiazine] (60 mg/kg, i.p.) (Tocris Bioscience) or vehicle were administered 2 h after i.g. ethanol and i.p. acetaldehyde or their vehicles.

Phosphorothioate-modified TRPA1 AS-ODN (sequence: 5'-TATCGCTCCACATTGCTAC-3') and TRPA1 MM-ODN (sequence: 5'-ATTCGCCTCACATTGTCAC-3') (22) (10 nmol/10 μ l, i.pl.) were administered once a day for 4 consecutive d. Some mice treated with TRPA1 AS/MM-ODN or with 4-OHT were tested for the acute nociceptive response to AITC (20 nmol, i.pl.) or ethanol (30%, i.pl.) or their vehicles (0.5% DMSO or 0.9% NaCl, respectively).

Blood for ethanol assay was obtained from anesthetized mice at 15, 30, 60 and 180 min after i.g. ethanol. Liver and hind paw tissues for ethanol and acetaldehyde assays were obtained from mice euthanized 15, 30, 60 and 180 min after i.pl. or i.g. ethanol. Some mice were treated with 4-Mp (100 μ g, i.pl. or 50 mg/kg, i.g.) 30 min before or 1 hr

after i.pl. or i.g. ethanol or their vehicles and euthanized 2 h after ethanol. For H₂O₂ assay, hind paw tissues were taken from mice euthanized before and 1, 3, 6 and 8 h after i.pl. or i.g. ethanol and acetaldehyde or their vehicles. In additional experiments, paw tissues were taken from mice treated 3 h before with i.pl. or i.g. ethanol or acetaldehyde or their vehicles that 1 h before with A967079 (100 mg/kg, i.p.) or PBN (100 mg/kg, i.p.) or their vehicles. For the 4-HNE-histidine protein adducts assay, paw tissues were taken from mice euthanized before and 1, 3, 6 and 8 h after i.g. ethanol.

For chronic alcohol administration, one or two mice were housed *per* cage and were initially fed the control Lieber-DeCarli diet (F1259, Bio-Serv) *ad libitum* for 5 d to acclimatize them to the liquid food and tube feeding. Afterward, ethanol-fed groups were allowed free access to the ethanol Lieber-DeCarli diet containing 5% (vol/vol) ethanol (F1258, Bio-Serv), daily for 28 d (32). Control mice were pair-fed (*i.e.* calorically matched to the ethanol-fed mice) with the control diet in which equal calories of maltose-dextrin was consumed in place of ethanol (32). The feeding tubes contained 30 or 50 ml of ethanol or control liquid diet for one or two mice, respectively. Mice in both the experimental groups were healthy and, displayed normal reflexes and alertness. A967079 and PBN (both, 100 mg/kg, i.p.), were administered at day 28 after ethanol or control liquid diet. Liver and paw tissues for ethanol and acetaldehyde assays were obtained from mice euthanized at day 28 after ethanol or control liquid diet.

Acute nociceptive behavior, hind paw mechanical allodynia and rotarod test

To assess acute nociceptive responses, mice were placed in a plexiglass chamber immediately after ethanol (15-80% in 0.9% NaCl, i.pl.), acetaldehyde (0.1-10 nmol/site in NaCl, i.pl.), allyl isothiocyanate (AITC, 10 nmol in 0.5% DMSO, i.pl.) or their respective vehicles, and the total time (nociception time, s) spent in licking and lifting the injected right hind limb (21) was recorded for 5 min. Mechanical allodynia was evaluated by

applying the von Frey filaments to the posterior hind paw of mice, before (basal threshold) and after (1-24 h) ethanol (15-80% in 0.9% NaCl, i.pl.; 1-4 ml/kg of 15% in 0.9% NaCl, i.g.), acetaldehyde (1-20 nmol/site in 0.9% NaCl, i.pl.; 0.1-1 mg/kg in 0.9% NaCl, i.p.) or respective vehicles and, in mice fed with the Lieber-DeCarli or control diet over 28 d. Mechanical threshold was determined by using the up-and-down paradigm (47).

Locomotor function, coordination, and sedation of animals were tested by using a rotarod apparatus (UgoBasile). Twenty-four h before the experiments, mice were trained on the rotarod apparatus, programmed at 8 rpm, until they remained without falling for 60 s. The day of the experiment, the latency (s) to the first fall and the number of falls were recorded. Cut-off time was 240 s.

Ethanol, acetaldehyde, H₂O₂ and 4-HNE-histidine protein adducts assays

For ethanol assay, blood taken into heparin containing syringes *via* direct cardiac puncture from anesthetized mice, was centrifuged at 10,000 rpm for 5 min and the plasma was collected. For ethanol and acetaldehyde assay paw and liver tissues from euthanized mice were homogenized in PBS (0.1 M) by using a tissue homogenizer (Qiagen SpA) for 30 s, centrifuged 10,000 rpm for 10 min, and supernatants collected. Ethanol content was determined by a colorimetric assay (ab65343, Abcam) according to the manufacturer's protocol, and expressed as nmol/ml (plasma) and nmol/mg of protein (tissues). Acetaldehyde content (nmol/mg of protein) was determined by a colorimetric assay (Megazyme) according to the manufacturer's protocol.

The H₂O₂ content was determined in the paw tissue by using the Amplex Red[®] assay (Invitrogen). Briefly, tissues were rapidly placed into modified Krebs/HEPES buffer (composition in mmol/l: 99.01 NaCl, 4.69 KCl, 2.50 CaCl₂, 1.20 MgSO₄, 1.03 KH₂PO₄, 25.0 NaHCO₃, 20.0 Na-HEPES, and 5.6 glucose [pH 7.4]), minced and

incubated with Amplex red (100 μ M) and HRP (1 U/ml) (1 hour, 37°C) in modified Krebs/HEPES buffer protected from light (48). Fluorescence excitation and emission were at 540 and 590 nm, respectively. H₂O₂ production was calculated using H₂O₂ standard and expressed as μ mol/l of mg of dry tissue.

4-HNE-histidine (4-HNE-His) protein adduct content was quantified in paw tissues by a colorimetric assay (OxiSelect HNE-His Adduct ELISA Kit, Cell Biolabs, Inc) according to manufacturer's protocol. Paw tissues were homogenized in PBS (0.1 M), added of a protease inhibitor cocktail (1 tablet/100 ml) for 30 s and centrifuged (10,000 rpm, 10 min, 4°C). Supernatants were assayed for the measurement of total protein content by a Bradford assay (Bio-Rad) and 4-HNE-His content (expressed as μ g/mg of protein).

Cell cultures

Human embryonic kidney 293 (HEK293) cells stably transfected with the cDNA for human TRPA1 (hTRPA1-HEK293) were cultured as previously described (49). Human Schwann cells (HSC, #1700, CliniScience) were cultured in Schwann cell medium (#1701, CliniScience) according to the manufacturer's protocol. Human alveolar type II epithelium-like adherent cell line (A549) (CCL-185™, American Type Culture Collection) were cultured in RPMI with 10% FBS, 2 mM glutamine, 100 U penicillin, 100 μ g/ml streptomycin and 1 mM HEPES. All cells were used when received without further authentication.

Schwann cells were isolated from sciatic nerves of C57BL/6J mice. The epineurium was removed, and nerve explants were divided into 1 mm segments and dissociated enzymatically using collagenase (0.05%) and hyaluronidase (0.1%) in HBSS (2 h, 37°C). Cells were collected by centrifugation (800 rpm, 10 min, room temperature) and the pellet was resuspended and cultured in DMEM containing: 10% fetal calf serum, 2 mM

L-glutamine, 100 U/ml penicillin, 100 mg/ml streptomycin. Three days later, cytosine arabinoside (10 mM) was added to remove fibroblasts. All cells were cultured in an atmosphere of 95% air and 5% CO₂ at 37°C.

Assays in cultured cells

Calcium imaging. HSC were plated on glass coated (poly-L-lysine, 8.3 μM) coverslips and [Ca²⁺]_i response was measured as previously reported (22). HSC were exposed to AITC (100 μM), H₂O₂ (10 mM) and acetaldehyde (10 mM) or their vehicles (0.1% DMSO or 0.9% NaCl) in the presence or absence of A967079 (50 μM) or its vehicle (0.3% DMSO). In other experiments, HSC were exposed to ethanol (10 mM) or its vehicle. In this case the delayed [Ca²⁺]_i response was monitored for ~150 min in the presence or absence of A967079 (50 μM) or 4-Mp (100 μM) or their vehicle (0.3% DMSO). Results were expressed as % increase in Ratio_{340/380} over baseline normalized to the maximum effect induced by ionomycin (5 μM) added at the end of each experiment (% change in R_{340/380}).

Acetaldehyde assay. Mouse Schwann cells and HSC were plated in 48-well plates and maintained in 5% CO₂ and 95% O₂ at 37°C until 90% of confluence. The cultured medium was replaced with PBS added with ethanol (1-100 mM), ethanol (10 mM) plus 4-Mp (100 μM) or vehicle (0.9% NaCl) and maintained in 5% CO₂ and 95% O₂ at 37°C for 3 h. Then, supernatants were collected, and acetaldehyde content was assayed by using a colorimetric assay (Megazyme) according to the manufacturer's protocol. Acetaldehyde content was expressed as μmol/l. The cytotoxicity to different stimuli was tested by using the MTT assay viability test.

H₂O₂ assay. H₂O₂ was determined by the Amplex Red[®] assay. HSC were plated in 96-well clear bottom black (5x10⁵ cells/well) and maintained in 5% CO₂/95% O₂ (24 h, 37°C). The cultured medium was replaced with Krebs/HEPES buffer added with

A967079 (30 μ M) or vehicle (0.3% DMSO) for 10 min at room temperature. HSC were then stimulated with AITC (100 μ M), H₂O₂ (200 nM) and acetaldehyde (10 mM) or their vehicle (0.01% DMSO, Krebs/HEPES), added with Amplex red (50 μ M) and HRP (1 U/ml, 30 min, room temperature, protected from light). Some experiments were performed in Ca²⁺-free Krebs/HEPES buffer containing ethylenediaminetetraacetic acid (EDTA, 1 mM). Signal was detected 60 min after exposure to stimuli. H₂O₂ release was calculated using H₂O₂ standards and expressed as nmol/l.

Immunofluorescence

Anesthetized mice were transcardially perfused with PBS and 4% paraformaldehyde. Paw tissues were removed, post-fixed for 24 h, and paraffin embedded. Human and mouse FFPE sections (5 μ m) were incubated with primary antibodies (all from Abcam): TRPA1 (ab58844, rabbit polyclonal, 1:400), S100 (ab14849, mouse monoclonal [4B3], 1:300), protein gene product 9.5 (PGP9.5, ab8189, mouse monoclonal [13C4/I3C4], 1:600), NOX1 (ab131088, rabbit polyclonal, 1:250), 4-HNE (HNEJ-2, ab48506, mouse monoclonal, 1:40) and alcohol dehydrogenase (ab108203, rabbit monoclonal [EPR4439], 1:200) diluted in fresh blocking solution (PBS, pH 7.4, 2.5% NGS). To confirm specificity, TRPA1, NOX1 and ADH primary antibodies were pre-adsorbed (1:1, overnight, 4°C, before adding to tissue sections) with their respective antigen peptides: TRPA1 synthetic peptide (sequence: CEKQHELKLIQKME, Twin Helix srl); ADH recombinant protein, (#NBP1-99053, Novus Biologicals), NOX1 recombinant protein (#PCPKAB7187921P, Promocell). Sections were then incubated with the fluorescent polyclonal secondary antibodies, Alexa Fluor 488 and 594 (1:600, Invitrogen), and coverslipped using mounting medium with DAPI (Abcam). The product of the differences from the mean (PDM) image was used for the qualitative analysis of colocalization. The PDM image is a pseudo-colored, generated

by pixel that is equal to the PDM value at the location (Image J, NIH).

Human Schwann cells were grown on glass coated (poly-L-lysine, 8.3 μ M) coverslips and cultured for 2-3 days before being used for staining. Cells were then fixed in ice-cold methanol/acetone (5 min at -20°C), washed with PBS and blocked with NGS (10%) (1 h, room temperature). The cells were then incubated with the primary antibodies: TRPA1 (ab58844, rabbit polyclonal, 1:400), S100 (ab14849, mouse monoclonal [4B3], 1:300), NOX1 (ab131088, rabbit polyclonal, 1:250) and alcohol dehydrogenase (ab108203, rabbit monoclonal [EPR4439], 1:200) diluted in fresh blocking solution (PBS, pH 7.4, 2.5% NGS). Cells were finally incubated with fluorescent polyclonal secondary antibodies (1:600, Alexa Fluor 488, and 594, Invitrogen) (2 h, room temperature) and mounted using mounting medium with DAPI (Abcam). Fluorescence images were obtained using an Olympus BX51 microscope (Olympus).

Immunohistochemistry and intraepidermal nerve fiber (IENF) analysis

Anesthetized mice were transcardially perfused with PBS, followed by 4% paraformaldehyde. Mice paws were removed and placed overnight at 4°C in 10% formalin, transferred to 30% sucrose overnight and then frozen and cryosectioned at 30 μm transversal to long paw axis. Free floating sections were incubated in blocking solution [PBS containing 0.1% Triton X-100 (TBS) and 2.5% NGS] 1 hour at room temperature, then in the primary antibody panaxonal marker PGP9.5 (ab108986, rabbit monoclonal [EPR4118] 1:600, Abcam) diluted in blocking solution overnight at room temperature. Afterward, sections were rinsed in TBS and placed in secondary biotinylated goat anti-rabbit IgG antibody (Vector Laboratories), 1:300 diluted in blocking buffer 2 ho at room temperature. Then placed in avidin-biotin complex solution (Vectastain Elite ABC HRP, Vector Laboratories) for 30 min at room temperature, followed by rinsing in

TBS. The sections were then transferred into peroxidase substrate (ImmPACT DAB, Vector Laboratories) to 4-6 min for the chromogen development reaction and rinsed in distilled water before mounting. For quantitative analysis, IENF were counted either under the light microscope at 40X magnification. Single PGP9.5-positive fibers crossing the epidermis-dermis boundary (basal membrane) were counted, whereas secondary branching is excluded from quantification, according to the European Federation of Neurological Societies (EFNS) guidelines (50).

Real-Time PCR

RNA was extracted from paw tissue and liver obtained from C57BL/6J mice or from human Schwann cells. Total RNA was extracted using the RNeasy Mini kit (Qiagen SpA), according to the manufacturer's protocol. RNA concentration and purity were assessed spectrophotometrically by measuring the absorbance at 260 nm and 280 nm. Reverse transcription was performed with the Qiagen QuantiTect Reverse Transcription Kit (Qiagen SpA) following the manufacturer's protocol. For mRNA relative quantification, rt-PCR was performed on Rotor Gene® Q (Qiagen SpA). The sets of probes for human cells were as follows: ACTB (β -actin): Primer1 CCT TGC ACA TGC CGG AG Primer2 ACA GAG CCT CGC CTT TG Probe /56-FAM/TCA TCC ATG /ZEN/GTG AGC TGG CGG /3IABkFQ/ (NCBI Ref Seq: NM_001101); TRPA1: Primer1 GAA ACC AAA GTG GCA GCT TC Primer2 GAC ATT GCT GAG GTC CAG AA Probe /56-FAM/TGA AGT TCC /ZEN/ACC TGC ATA GCT ATC CTC T/3IABkFQ/ (NCBI Ref Seq: NM_007332); NOX1 Primer1 AAA CAT TCA GCC CTA ACC AAA C Primer2 GAA TCT TCC CTG TTG CCT AGA Probe /56-FAM/ACC ACC CAG /ZEN/TTT CCC ATT GTC AAG A/3IABkFQ/ (NCBI Ref Seq: NM013955); ADH1A: Primer1 GTT TCT TTA ACT CCC ATA GCA CAG Primer2 CAC AAG GAC TCA CCA GTC TC Probe /56-FAM/AGA CAG AAT /ZEN/CAA CAT GAG CAC AGC

AGG /3IABkFQ/ (NCBI Ref Seq: NM_000667); ADH1B: Primer1 GTG CTC ATG TCG TTT CTG TCT Primer2 TCA AGC AGA GAA GAA ATC CAC AA Probe/56-FAM/TGC CCA CCA /ZEN/GCA GAC TGT GA/3IABkFQ/ (NCBI Ref Seq: NM_000668), ADH1C: Primer1 ATC TTA ATG CGA ACT TCA TGA GC Primer2 CAG AAT CAA TAT GAG CAC AGC AG Probe /56-FAM/CCA TTG AGG /ZEN/AGG TAG AGG TTG CAC C/3IABkFQ/ (NCBI Ref Seq: NM_000669); ADH4: Primer1 AGA AAG ACC CAC ACC TCC TA Primer2 GAG TTT GTC TGC TTG GAT GTG Probe /56-FAM/CCC TGG TTC /ZEN/GAC TTG TGC TGT CT/3IABkFQ/ (NCBI Ref Seq: NM_000670); ADH5: Primer1 TGC CAC CTC TAT CTC CTC TAT G Primer2 CCG ACC AGA ATC CGT GAA C Probe /56-FAM/AGC CTT GCA /ZEN/CTT GAT AAC CTC GTT CG/3IABkFQ/ (NCBI Ref Seq: NM_000671); ADH6: Primer1 TGT GGC AGA AAG AGT GTG AT Primer2 CCT CTT GTA TCC CAC CAT CTT G Probe /56-FAM/TCA CCT GGT /ZEN/TTC ACT GTG CTT ACT CC/3IABkFQ/(NCBI Ref Seq: NM_000672).

The sets of probes for mouse tissue were as follows: ACTB: Primer1 GAC TCA TCG TAC TCC TGC TTG Primer2 GAT TAC TGC TCT GGC TCC TAG Probe /56-FAM/CTG GCC TCA /ZEN/CTG TCC ACC TTC C/3IABkFQ/ (NCBI Ref Seq: NM_001101); ADH1: Primer1 AAGACT ACAGCAAACCCATCC Primer2 GACGACGCTT ACACCACAT Probe /56-FAM/CCTTGACAC/Z EN/CA TGACTTCTGCCCT /3IABkFQ/ (NCBI Ref Seq: NM_007409); ADH5: Primer1 TCATCCCCTCT ACATCCCA Primer2 GGT AAATCTGCT AGTCCCCTCT Probe /56-FAM/CCCTTCCCC/Z EN/TGAGTGACCCTT A TTTTC/3IABkFQ/ (NCBI Ref Seq: NM_007410); ADH7: Primer1 TGAAGTT ATTGGGCGTCTTGA Primer2 GTCATAGGTGAGCATCTTGGC Probe /56-FAM/CAGTGTGGT /ZEN/GGTTGGTGCTCCT /3IABkFQ/ (NCBI Ref Seq: NM_009626).

The chosen reference gene was the ACTB. The QuantiTect Probe PCR Kits (Qiagen SpA) was used for amplification, and the cycling conditions were the following: samples were heated to 95°C for 10 min followed by 40 cycles of 95°C for 15 s, and 65°C for 20 s. PCR reaction was carried out in triplicate. Relative expression of mRNA was calculated using the $2^{-\Delta(\Delta CT)}$ comparative method, with each gene normalized against the internal endogenous reference ACTB gene for the same sample.

Statistical analysis

Statistical analysis was performed by the unpaired two-tailed Student's t-test for comparisons between two groups. Group means were compared with a one-way ANOVA, followed, as needed, by the pair-wise comparison of multiple groups that employed the Bonferroni's correction to maintain the experiment-wise error rate at 5%. For behavioural experiments with repeated measures, a two-way mixed model was used to compare the control and treated groups of mice at each time point tested, using the Bonferroni's correction for multiple time points. Statistical analyses were performed on raw data using Prism 5 GraphPad software (GraphPad Software Inc.). $P < 0.05$ was considered statistically significant.

Study Approval

The use of FFPE sections of human skin samples was approved by the Local Ethics Committee (#11989_bio/2018), according to the Helsinki Declaration, and informed consent was obtained. All applicable international, national, and/or institutional guidelines for the care and use of animals were followed. In vivo experiments were in accordance to European Union (EU) guidelines and Italian legislation (DLgs 26/2014, EU Directive application 2010/63/EU) for animal care procedures, and under the University of Florence research permit #194/2015-PR. Animal studies were reported in

compliance with the ARRIVE guidelines (51).

Author contributions.

FDL, RP, PG and RN designing research studies; FDL, SLP, LL, FP, DSMdA and RN conducting experiments; FDL, SLP, LL, FP, DSMdA and RN acquiring data; FDL, MNJ and RN analyzing data; AI providing human tissue samples; FDL, MNJ, RP, NWB, PG and RN writing the manuscript.

Acknowledgments.

We thank AH Morice (University of Hull, UK) for hTRPA1-HEK293 cells and D. Preti (University of Ferrara, Italy) for providing A967079. We also thank Mary K. Lokken for her expert English revision. This study was funded by Ministry for University and Scientific Research (MiUR) Rome, Italy Grant PRIN 201532AHAE_003 (P.G.), and by grants from the National Institutes of Health (NS102722, DE026806, DK118971) and Department of Defense (W81XWH1810431) (N.W.B.).

References

1. Rehm J, Mathers C, Popova S, Thavorncharoensap M, Teerawattananon Y, and Patra J. Global burden of disease and injury and economic cost attributable to alcohol use and alcohol-use disorders. *Lancet*. 2009;373(9682):2223-33.
2. Organization WH. *Global status report on alcohol and health 2018*. 2018.
3. Chopra K, and Tiwari V. Alcoholic neuropathy: possible mechanisms and future treatment possibilities. *Br J Clin Pharmacol*. 2012;73(3):348-62.
4. Singleton CK, and Martin PR. Molecular mechanisms of thiamine utilization. *Curr Mol Med*. 2001;1(2):197-207.
5. Mellion M, Gilchrist JM, and de la Monte S. Alcohol-related peripheral neuropathy: nutritional, toxic, or both? *Muscle Nerve*. 2011;43(3):309-16.
6. Koike H, Misu K, Hattori N, Ito S, Ichimura M, Ito H, et al. Postgastrectomy polyneuropathy with thiamine deficiency. *J Neurol Neurosurg Psychiatry*. 2001;71(3):357-62.
7. Koike H, Iijima M, Sugiura M, Mori K, Hattori N, Ito H, et al. Alcoholic neuropathy is clinicopathologically distinct from thiamine-deficiency neuropathy. *Ann Neurol*. 2003;54(1):19-29.
8. Cederbaum AI. Alcohol metabolism. *Clin Liver Dis*. 2012;16(4):667-85.
9. Eriksson CJ. The role of acetaldehyde in the actions of alcohol (update 2000). *Alcohol Clin Exp Res*. 2001;25(5 Suppl ISBRA):15S-32S.
10. Andrici J, Hu SX, and Eslick GD. Facial flushing response to alcohol and the risk of esophageal squamous cell carcinoma: A comprehensive systematic review and meta-analysis. *Cancer Epidemiol*. 2016;40:31-8.
11. Bagnardi V, Rota M, Botteri E, Tramacere I, Islami F, Fedirko V, et al. Light alcohol drinking and cancer: a meta-analysis. *Ann Oncol*. 2013;24(2):301-8.
12. Boffetta P, and Hashibe M. Alcohol and cancer. *Lancet Oncol*. 2006;7(2):149-56.

13. Xiao Q, Weiner H, and Crabb DW. The mutation in the mitochondrial aldehyde dehydrogenase (ALDH2) gene responsible for alcohol-induced flushing increases turnover of the enzyme tetramers in a dominant fashion. *J Clin Invest.* 1996;98(9):2027-32.
14. Wall TL, Peterson CM, Peterson KP, Johnson ML, Thomasson HR, Cole M, et al. Alcohol metabolism in Asian-American men with genetic polymorphisms of aldehyde dehydrogenase. *Ann Intern Med.* 1997;127(5):376-9.
15. Chen CH, Ferreira JC, Gross ER, and Mochly-Rosen D. Targeting aldehyde dehydrogenase 2: new therapeutic opportunities. *Physiol Rev.* 2014;94(1):1-34.
16. Trevisani M, Smart D, Gunthorpe MJ, Tognetto M, Barbieri M, Campi B, et al. Ethanol elicits and potentiates nociceptor responses via the vanilloid receptor-1. *Nat Neurosci.* 2002;5(6):546-51.
17. Andersson DA, Gentry C, Moss S, and Bevan S. Transient receptor potential A1 is a sensory receptor for multiple products of oxidative stress. *J Neurosci.* 2008;28(10):2485-94.
18. Takahashi N, Kuwaki T, Kiyonaka S, Numata T, Kozai D, Mizuno Y, et al. TRPA1 underlies a sensing mechanism for O₂. *Nat Chem Biol.* 2011;7(10):701-11.
19. Nassini R, Materazzi S, Benemei S, and Geppetti P. The TRPA1 channel in inflammatory and neuropathic pain and migraine. *Rev Physiol Biochem Pharmacol.* 2014;167:1-43.
20. Bang S, Kim KY, Yoo S, Kim YG, and Hwang SW. Transient receptor potential A1 mediates acetaldehyde-evoked pain sensation. *Eur J Neurosci.* 2007;26(9):2516-23.
21. Trevisani M, Siemens J, Materazzi S, Bautista DM, Nassini R, Campi B, et al. 4-Hydroxynonenal, an endogenous aldehyde, causes pain and neurogenic

- inflammation through activation of the irritant receptor TRPA1. *Proc Natl Acad Sci U S A*. 2007;104(33):13519-24.
22. De Logu F, Nassini R, Materazzi S, Carvalho Goncalves M, Nosi D, Rossi Degl'Innocenti D, et al. Schwann cell TRPA1 mediates neuroinflammation that sustains macrophage-dependent neuropathic pain in mice. *Nat Commun*. 2017;8(1):1887.
 23. Galter D, Carmine A, Buervenich S, Duester G, and Olson L. Distribution of class I, III and IV alcohol dehydrogenase mRNAs in the adult rat, mouse and human brain. *Eur J Biochem*. 2003;270(6):1316-26.
 24. Zgombic-Knight M, Ang HL, Foglio MH, and Duester G. Cloning of the mouse class IV alcohol dehydrogenase (retinol dehydrogenase) cDNA and tissue-specific expression patterns of the murine ADH gene family. *J Biol Chem*. 1995;270(18):10868-77.
 25. Seitz HK, and Meier P. The role of acetaldehyde in upper digestive tract cancer in alcoholics. *Transl Res*. 2007;149(6):293-7.
 26. Zakhari S. Overview: how is alcohol metabolized by the body? *Alcohol Res Health*. 2006;29(4):245-54.
 27. Szuster-Ciesielska A, Plewka K, Daniluk J, and Kandefer-Szerszen M. Zinc supplementation attenuates ethanol- and acetaldehyde-induced liver stellate cell activation by inhibiting reactive oxygen species (ROS) production and by influencing intracellular signaling. *Biochem Pharmacol*. 2009;78(3):301-14.
 28. Hoyt LR, Randall MJ, Ather JL, DePuccio DP, Landry CC, Qian X, et al. Mitochondrial ROS induced by chronic ethanol exposure promote hyper-activation of the NLRP3 inflammasome. *Redox Biol*. 2017;12:883-96.

29. Vrsalovic M, Vrsalovic MM, Presecki AV, and Lukac J. Modulating role of alcohol and acetaldehyde on neutrophil and monocyte functions in vitro. *J Cardiovasc Pharmacol.* 2007;50(4):462-5.
30. Aldini G, Carini M, Yeum KJ, and Vistoli G. Novel molecular approaches for improving enzymatic and nonenzymatic detoxification of 4-hydroxynonenal: toward the discovery of a novel class of bioactive compounds. *Free Radic Biol Med.* 2014;69:145-56.
31. Marone IM, De Logu F, Nassini R, De Carvalho Goncalves M, Benemei S, Ferreira J, et al. TRPA1/NOX in the soma of trigeminal ganglion neurons mediates migraine-related pain of glyceryl trinitrate in mice. *Brain.* 2018;6(5050181).
32. Bertola A, Mathews S, Ki SH, Wang H, and Gao B. Mouse model of chronic and binge ethanol feeding (the NIAAA model). *Nat Protoc.* 2013;8(3):627-37.
33. Dalle-Donne I, Aldini G, Carini M, Colombo R, Rossi R, and Milzani A. Protein carbonylation, cellular dysfunction, and disease progression. *J Cell Mol Med.* 2006;10(2):389-406.
34. Gianni D, Taulet N, Zhang H, DerMardirossian C, Kister J, Martinez L, et al. A novel and specific NADPH oxidase-1 (Nox1) small-molecule inhibitor blocks the formation of functional invadopodia in human colon cancer cells. *ACS Chem Biol.* 2010;5(10):981-93.
35. Boyette-Davis J, and Dougherty PM. Protection against oxaliplatin-induced mechanical hyperalgesia and intraepidermal nerve fiber loss by minocycline. *Exp Neurol.* 2011;229(2):353-7.
36. Bianchi R, Buyukakilli B, Brines M, Savino C, Cavaletti G, Oggioni N, et al. Erythropoietin both protects from and reverses experimental diabetic neuropathy. *Proc Natl Acad Sci U S A.* 2004;101(3):823-8.

37. Obrosova IG, Xu W, Lyzogubov VV, Ilnytska O, Mashtalir N, Vareniuk I, et al. PARP inhibition or gene deficiency counteracts intraepidermal nerve fiber loss and neuropathic pain in advanced diabetic neuropathy. *Free Radic Biol Med*. 2008;44(6):972-81.
38. Koivisto A, Hukkanen M, Saarnilehto M, Chapman H, Kuokkanen K, Wei H, et al. Inhibiting TRPA1 ion channel reduces loss of cutaneous nerve fiber function in diabetic animals: sustained activation of the TRPA1 channel contributes to the pathogenesis of peripheral diabetic neuropathy. *Pharmacol Res*. 2012;65(1):149-58.
39. Mellion ML, Silbermann E, Gilchrist JM, Machan JT, Leggio L, and de la Monte S. Small-fiber degeneration in alcohol-related peripheral neuropathy. *Alcohol Clin Exp Res*. 2014;38(7):1965-72.
40. Zambelis T, Karandreas N, Tzavellas E, Kokotis P, and Liappas J. Large and small fiber neuropathy in chronic alcohol-dependent subjects. *J Peripher Nerv Syst*. 2005;10(4):375-81.
41. Hamilton, K K, E K, and Attwell. Proton-gated Ca(2+)-permeable TRP channels damage myelin in conditions mimicking. *D - 0410462*. 2016;529(7587):523-7.
42. Kwan KY, Allchorne AJ, Vollrath MA, Christensen AP, Zhang DS, Woolf CJ, et al. TRPA1 contributes to cold, mechanical, and chemical nociception but is not essential for hair-cell transduction. *Neuron*. 2006;50(2):277-89.
43. Liedtke W, and Friedman JM. Abnormal osmotic regulation in *trpv4(-/-)* mice. *Proceedings of the National Academy of Sciences of the United States of America*. 2003;100(23):13698-703.
44. Guan Z, Kuhn JA, Wang X, Colquitt B, Solorzano C, Vaman S, et al. Injured sensory neuron-derived CSF1 induces microglial proliferation and DAP12-dependent pain. *Nat Neurosci*. 2016;19(1):94-101.

45. Zappia KJ, O'Hara CL, Moehring F, Kwan KY, and Stucky CL. Sensory Neuron-Specific Deletion of TRPA1 Results in Mechanical Cutaneous Sensory Deficits. *eNeuro*. 2017;4(1):0069-16.
46. Faul F, Erdfelder E, Buchner A, and Lang AG. Statistical power analyses using G*Power 3.1: tests for correlation and regression analyses. *Behav Res Methods*. 2009;41(4):1149-60.
47. Dixon WJ. Efficient analysis of experimental observations. *Annu Rev Pharmacol Toxicol*. 1980;20:441-62.
48. Landmesser U, Dikalov S, Price SR, McCann L, Fukai T, Holland SM, et al. Oxidation of tetrahydrobiopterin leads to uncoupling of endothelial cell nitric oxide synthase in hypertension. *J Clin Invest*. 2003;111(8):1201-9.
49. Sadofsky LR, Sreekrishna KT, Lin Y, Schinaman R, Gorke K, Mantri Y, et al. Unique Responses are Observed in Transient Receptor Potential Ankyrin 1 and Vanilloid 1 (TRPA1 and TRPV1) Co-Expressing Cells. *Cells*. 2014;3(2):616-26.
50. Lauria G, Hsieh ST, Johansson O, Kennedy WR, Leger JM, Mellgren SI, et al. European Federation of Neurological Societies/Peripheral Nerve Society Guideline on the use of skin biopsy in the diagnosis of small fiber neuropathy. Report of a joint task force of the European Federation of Neurological Societies and the Peripheral Nerve Society. *Eur J Neurol*. 2010;17(7):903-12, e44-9.
51. Kilkeny C, Browne WJ, Cuthill IC, Emerson M, and Altman DG. Improving bioscience research reporting: The ARRIVE guidelines for reporting animal research. *J Pharmacol Pharmacother*. 2010;1(2):94-9.

Figures

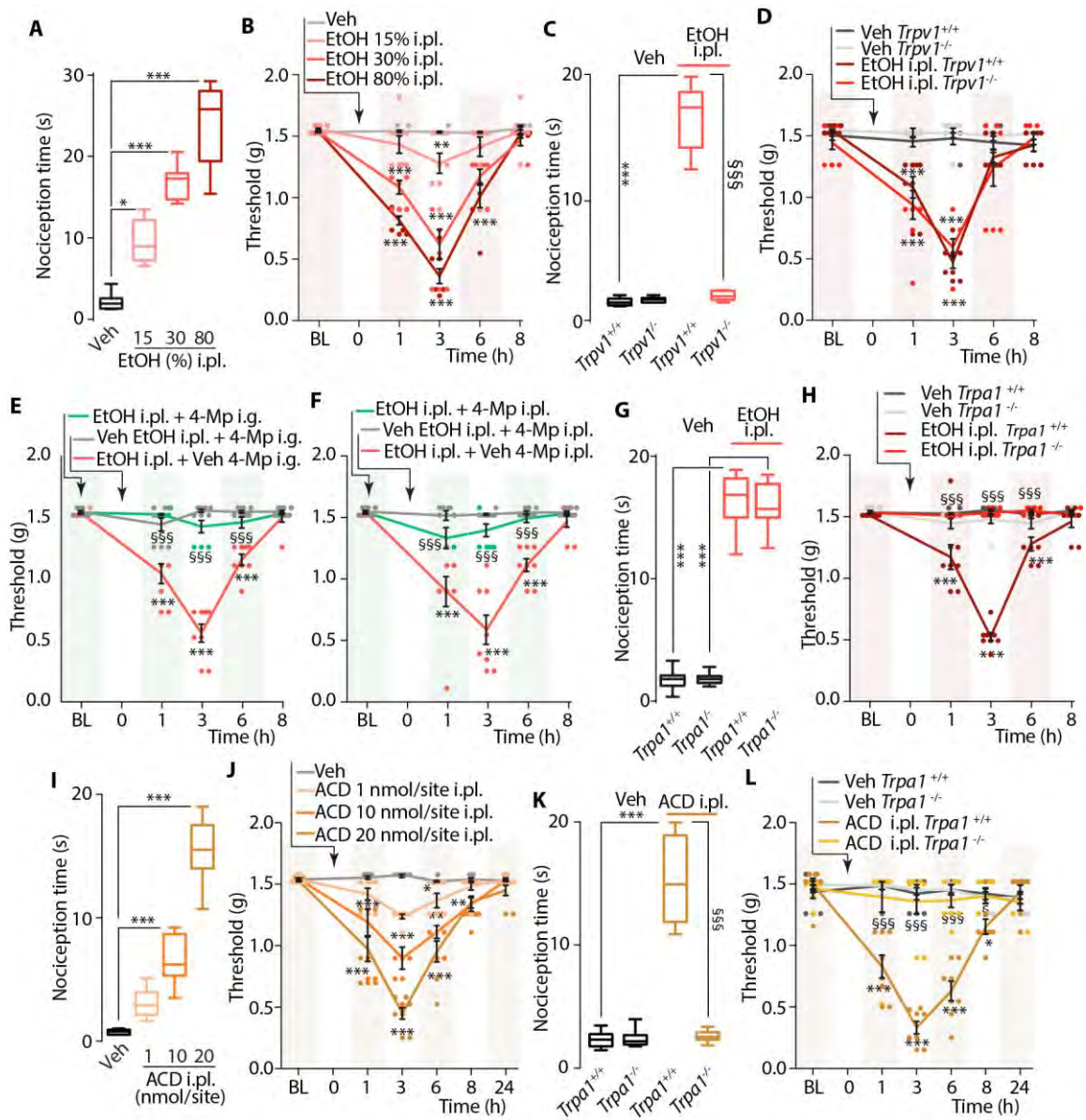


Figure 1. TRPV1 mediates acute nociception and TRPA1 mediates allodynia evoked by local ethanol. (A) Dose-dependent acute nociception and (B) dose- and time-dependent mechanical allodynia evoked by intraplantar (i.pl., 20 μ l) ethanol (EtOH) or vehicle (Veh) in C57BL/6J mice. (C) Acute nociceptive response evoked by EtOH (30%, i.pl.) or Veh in *Trpv1*^{+/+} and *Trpv1*^{-/-} mice. (D) Time-dependent mechanical allodynia evoked by EtOH (30%, i.pl.) or Veh in *Trpv1*^{+/+} and *Trpv1*^{-/-} mice. (E and F) Time-dependent mechanical allodynia evoked by EtOH (30%, i.pl.) or Veh in C57BL/6J mice. (G) Acute nociceptive response evoked by EtOH (30%, i.pl.) or Veh in *Trpa1*^{+/+} and *Trpa1*^{-/-} mice. (H) Time-dependent mechanical allodynia evoked by EtOH (30%, i.pl.) or Veh in *Trpa1*^{+/+} and *Trpa1*^{-/-} mice. (I) Acute nociceptive response evoked by ACD (1, 10, 20 nmol/site i.pl.) or Veh in C57BL/6J mice. (J) Time-dependent mechanical allodynia evoked by ACD (1, 10, 20 nmol/site i.pl.) or Veh in C57BL/6J mice. (K) Acute nociceptive response evoked by ACD (1, 10, 20 nmol/site i.pl.) or Veh in *Trpa1*^{+/+} and *Trpa1*^{-/-} mice. (L) Time-dependent mechanical allodynia evoked by ACD (1, 10, 20 nmol/site i.pl.) or Veh in *Trpa1*^{+/+} and *Trpa1*^{-/-} mice.

pretreated with 4-methylpyrazole (4-Mp, 50 mg/kg, intragastric, i.g., or 100 µg, i.pl.) or Veh 4-Mp. (G) Acute nociceptive response and (H) time-dependent mechanical allodynia evoked by EtOH (30%, i.pl.) or Veh in *Trpa1*^{+/+} and *Trpa1*^{-/-} mice. (I) Dose-dependent acute nociceptive response and (J) dose- and time-dependent mechanical allodynia evoked by acetaldehyde (ACD, 1-20 nmol, i.pl.) or Veh in C57BL/6J mice. (K and L) Acute nociceptive response and time-dependent mechanical allodynia evoked by ACD (20 nmol, i.pl.) or Veh in *Trpa1*^{+/+} and *Trpa1*^{-/-} mice. BL, baseline. Veh is the vehicle of EtOH or ACD. (A, C, G, I and K) box plots with horizontal lines at the 25th percentile, the median, and the 75th percentile and the vertical lines which extend to the minimum and maximum values; (B, D, E, F, H, J and L) mean ± SEM with individual data points overlaid; n=8 mice for each experiment. *P<0.05, **P<0.01, ***P<0.001 vs. Veh, Veh-*Trpv1*^{+/+} and Veh-*Trpa1*^{+/+}; §P<0.05, §§§P<0.001 vs. EtOH, EtOH-*Trpv1*^{+/+}, EtOH-*Trpa1*^{+/+}, ACD and ACD-*Trpa1*^{+/+}; one-way or two-way ANOVA with Bonferroni post-hoc correction.

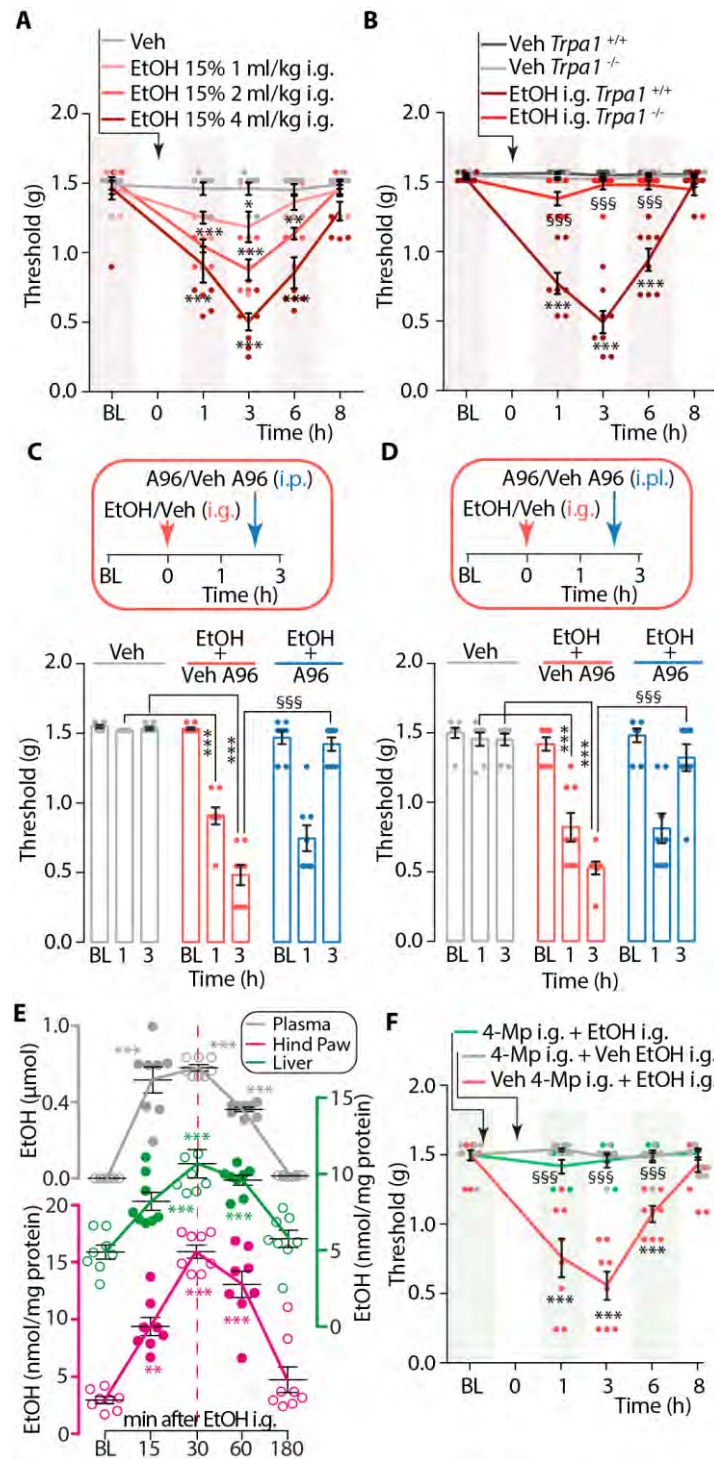


Figure 2. TRPA1 mediates mechanical allodynia evoked by intragastric ethanol in C57BL/6J mice hind paw. (A) Dose-dependent mechanical allodynia evoked by ethanol (EtOH, intragastric, i.g.) or vehicle (Veh). (B) Time-dependent mechanical allodynia evoked by EtOH (15%, 4 ml/kg, i.g.) or Veh in *Trpa1*^{+/+} and *Trpa1*^{-/-} mice. (C and D) Mechanical allodynia evoked by EtOH (15%, 4 ml/kg, i.g.) or Veh after A967079

(A96, 100 mg/kg, intraperitoneal, i.p. or 100 µg/site, intraplantar, i.pl.) or Veh A96 in C57BL/6J mice. (E) Time course of EtOH levels in plasma and liver and hind paw tissue, after EtOH (15%, 4 ml/kg, i.g.) in C57BL/6J mice. (F) Time-dependent mechanical allodynia evoked by EtOH (15%, 4 ml/kg, i.g.) or Veh in C57BL/6J mice pretreated with 4-methylpyrazole (4-Mp, 50 mg/kg, i.g.) or Veh 4-Mp. BL, baseline. Veh is the vehicle of EtOH. Data are mean ± SEM with individual data points overlaid; n=8 mice for each experimental condition. *P<0.05, **P<0.01, ***P<0.001 vs. Veh and EtOH BL; §§§P<0.001 vs. EtOH-*Trpal*^{+/+}, EtOH-A96 and 4-Mp-EtOH; two-way ANOVA with Bonferroni post-hoc correction.

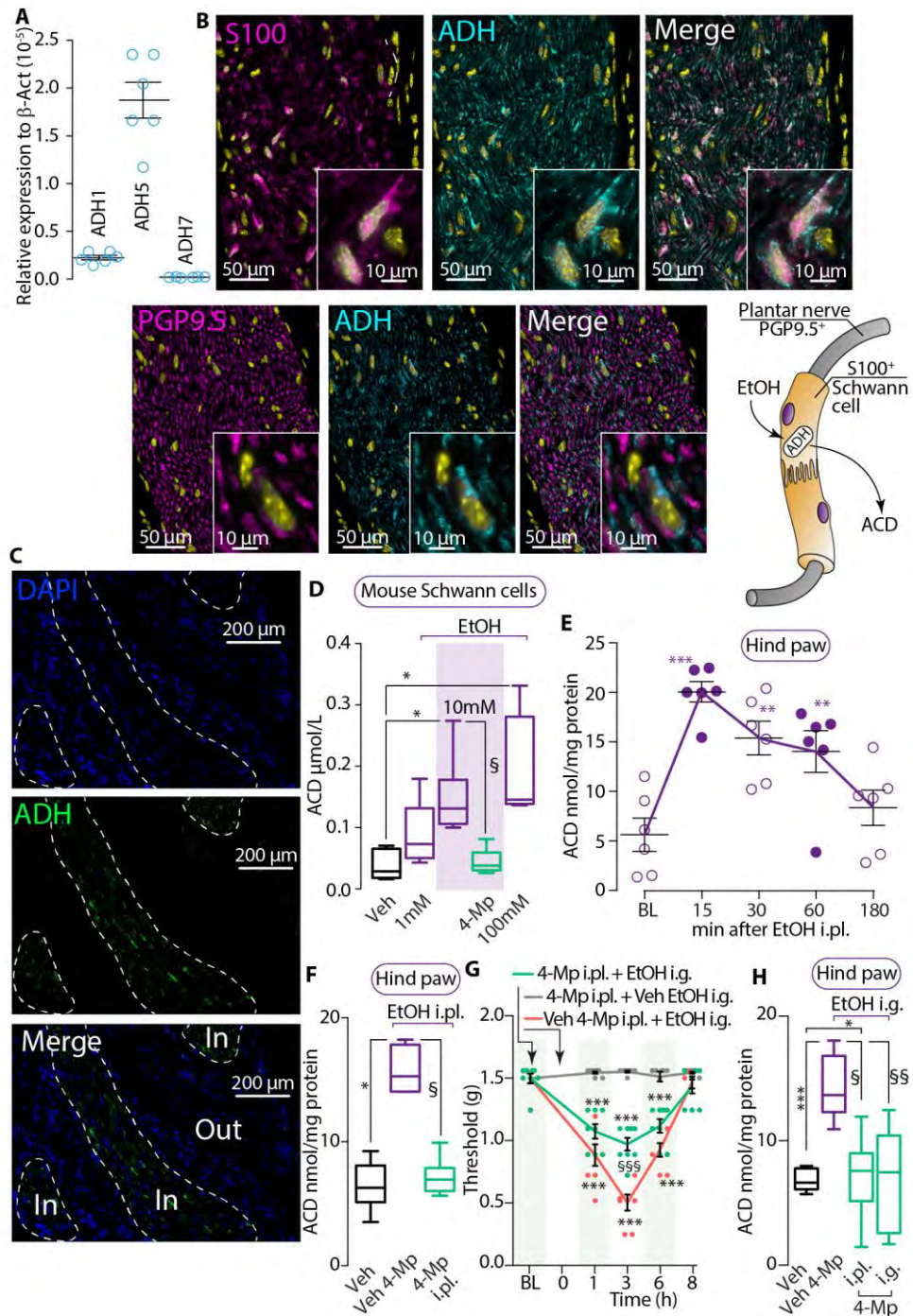


Figure 3. Acetaldehyde is generated by both hepatic and Schwann cell alcohol dehydrogenase. (A) Alcohol dehydrogenase (ADH) 1, 5 and 7 (ADH1, ADH5 and ADH7) mRNA relative expression in hind paw tissue in C57BL/6J mice. (B and C) Representative images of ADH, S100 and PGP9.5 expression in hind paw tissue in C57BL/6J mice. (D) Dose-dependent acetaldehyde (ACD) levels in cultured Schwann cells isolated from C57BL/6J mice and exposed to ethanol (EtOH, 1-100 mM) in the

presence of 4-methylpyrazole (4-Mp, 100 μ M) or vehicle (Veh 4-Mp). (E) Time-dependent ACD levels (hind paw tissue) after intraplantar, (i.pl., 20 μ l) EtOH (30%) in C57BL/6J mice. (F) ACD levels (hind paw tissue) of C57BL/6J mice receiving EtOH (30%, i.pl.) or Veh and pretreated with 4-Mp (100 μ g, i.pl.) or Veh 4-Mp. (G and H) Time-dependent mechanical allodynia and ACD levels (hind paw tissue) in C57BL/6J mice receiving EtOH (15%, 4 ml/kg, intragastric, i.g.) or Veh and pretreated with 4-Mp (100 μ g, i.pl. or 50 mg/kg, i.g.) or Veh 4-Mp. BL, baseline. Veh is the vehicle of EtOH. [In] and [Out] indicate inside and outside, respectively, the *perineurium*, delimited by dashed lines. (D, F and H) box plots with horizontal lines at the 25th percentile, the median, and the 75th percentile and the vertical lines which extend to the minimum and maximum values; (A, E and G) mean \pm SEM with individual data points overlaid; n=6-8 mice for each experimental condition. *P<0.05, ***P<0.001 vs. Veh and ACD BL; §P<0.05, §§§P<0.001 vs. EtOH and EtOH-4-Mp; one-way or two-way ANOVA with Bonferroni post-hoc correction.

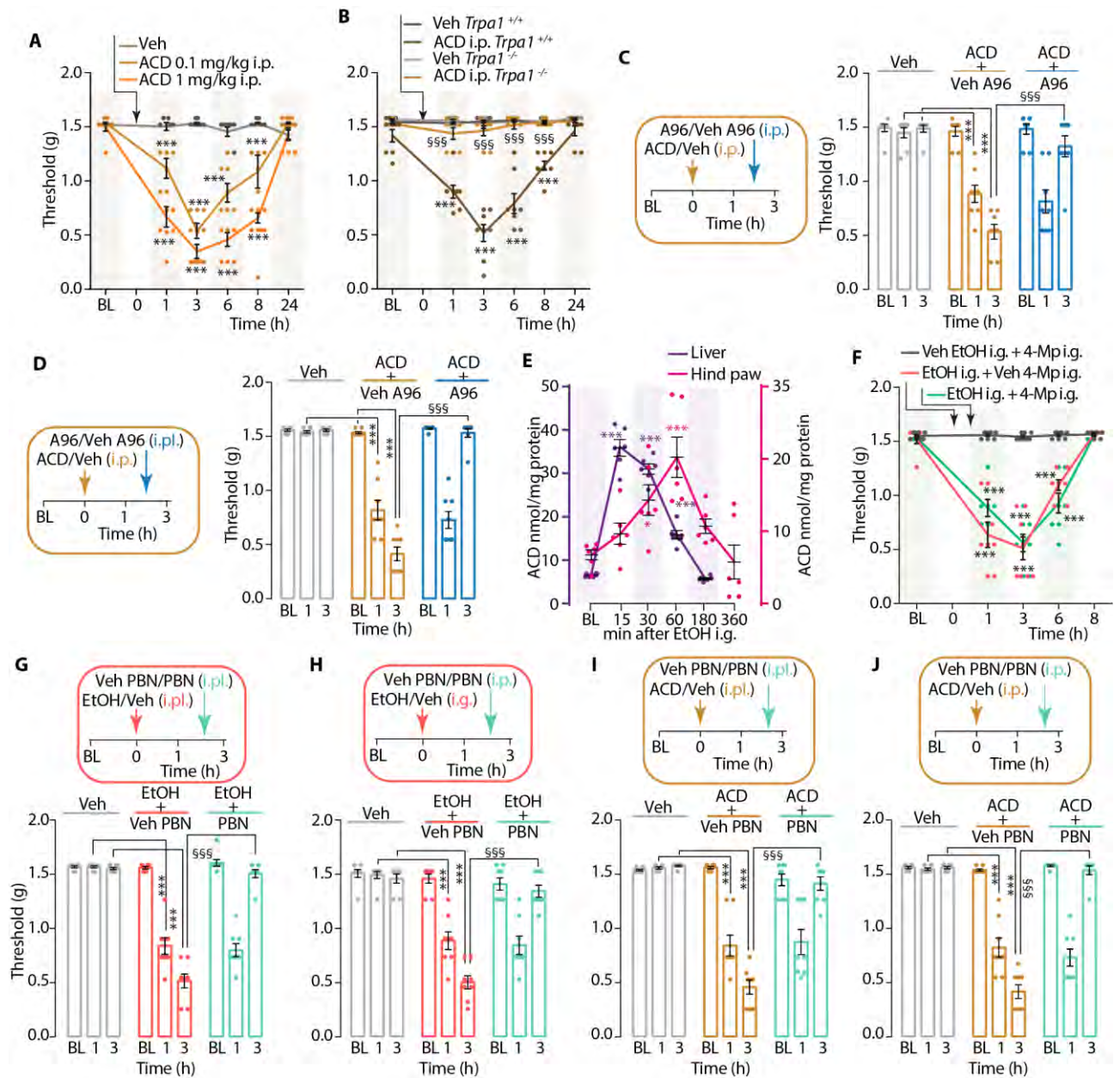


Figure 4. Acetaldehyde via TRPA1 sustains ethanol-evoked allodynia in C57BL/6J mice hind paw. (A) Dose- and time-dependent mechanical allodynia evoked by acetaldehyde (ACD, intraperitoneal, i.p.) or vehicle (Veh). (B) Time-dependent mechanical allodynia evoked by ACD (0.1 mg/kg, i.p.) or Veh in *Trpa1*^{+/+} and *Trpa1*^{-/-} mice. (C and D) Mechanical allodynia evoked by ACD (0.1 mg/kg, i.p.) or Veh after A967079 (A96, 100 mg/kg, i.p. or 100 μ g, intraplantar, i.pl.) or Veh A96 in C57BL/6J mice. (E) Time dependent ACD levels in liver and hind paw tissue after ethanol (EtOH, 15%, 4 ml/kg, intragastric, i.g.) in C57BL/6J mice. (F) Effect of post treatment with 4-

methylpyrazole (4-Mp, 50 mg/kg, i.g.) or Veh 4-Mp on mechanical allodynia evoked by EtOH (15%, 4 ml/kg, i.g.) or Veh, in C57BL/6J mice. (G and H) Mechanical allodynia evoked by EtOH (30%, i.pl. and 15%, 4ml/kg, i.g.) Veh after phenyl- α -tert-butyl nitron (PBN, 100 μ g, i.pl. or 50 mg/kg, i.p.) or Veh PBN in C57BL/6J mice. (I and J) Mechanical allodynia evoked by ACD (10 nmol, i.pl. and 0.1 mg/kg, i.p.) or Veh after PBN (100 μ g, i.pl. or 50 mg/kg, i.p.) or Veh PBN in C57BL/6J mice. BL, baseline. Veh is the vehicle of EtOH and ACD. Data are mean \pm SEM with individual data points overlaid; n=6-8 mice for each experimental condition. *P<0.05, ***P<0.001 vs. Veh and ACD BL; §§§P<0.001 vs. ACD-*Trpa1*^{+/+}, ACD-A96, EtOH-PBN and ACD-PBN; two-way ANOVA with Bonferroni post-hoc correction.

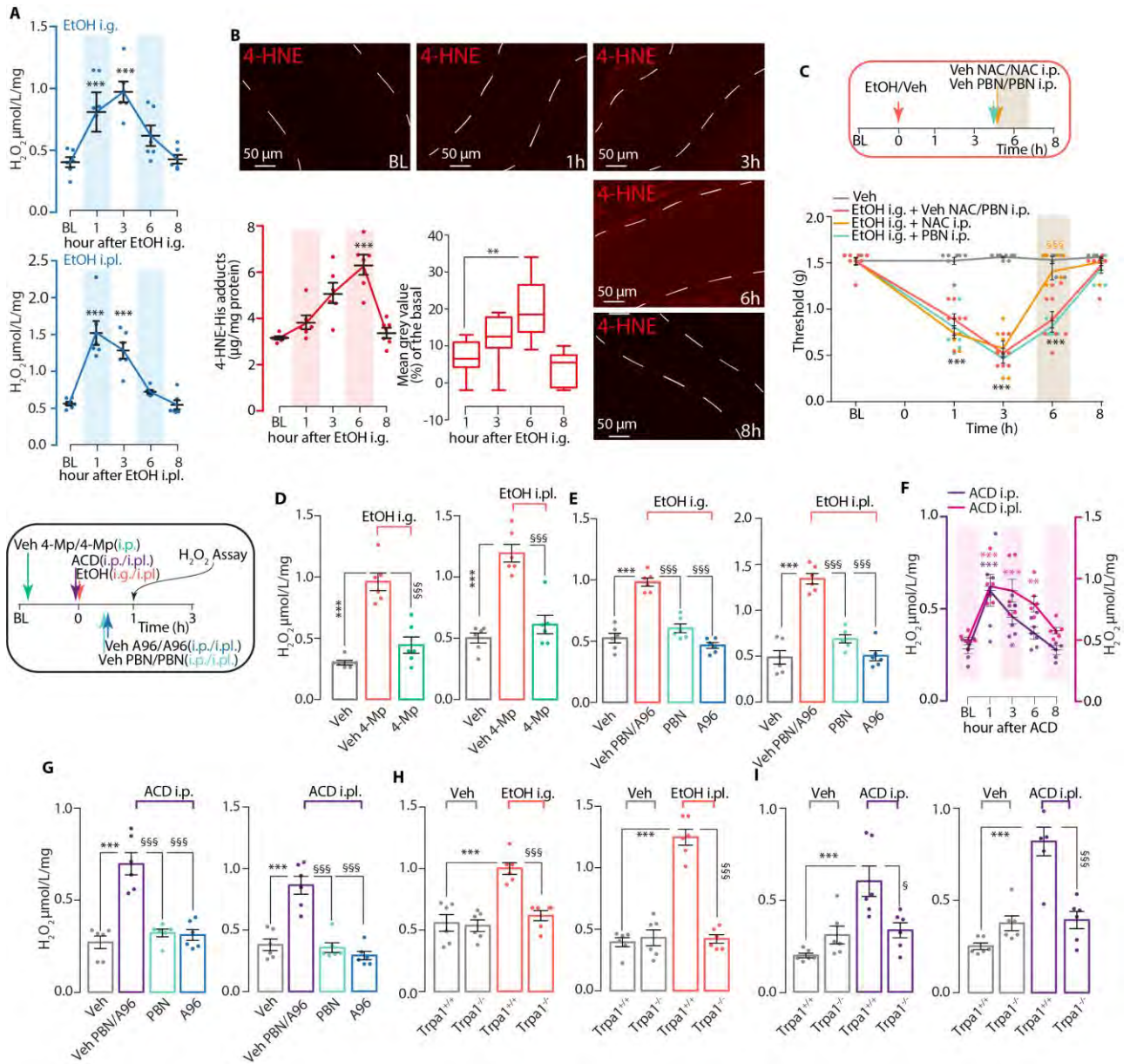


Figure 5. Acetaldehyde via TRPA1 generates ROS that sustain ethanol-evoked allodynia. (A) H₂O₂ levels (hind paw) after ethanol (EtOH, intragastric, i.g. or intraplantar, i.pl.). (B) 4-hydroxynonenal (4-HNE) staining (plantar nerve) and levels (hind paw) after i.g. EtOH (C) Mechanical allodynia evoked by EtOH i.g. or vehicle (Veh) after N-acetyl cysteine (NAC, 250 mg/kg, intraperitoneal, i.p.) and phenyl- α -tert-butyl nitron (PBN, 50 mg/kg, i.p.) or their Veh. H₂O₂ levels (hind paw) after i.g. and i.pl. EtOH or Veh in mice pretreated with (D) 4-methylpyrazole (4-Mp, 50 mg/kg, i.g.), (E) A967079 (A96, 100 mg/kg, i.p.) and PBN (100 mg/kg, i.p.) or their Veh. (F) H₂O₂ levels (hind paw) after acetaldehyde (ACD, 0.1 mg/kg, i.p. or 10 nmol, i.pl.). (G) H₂O₂ levels

(hind paw tissue) after ACD (0.1 mg/kg, i.p. or 10 nmol, i.pl.) or Veh and pretreated with A96 (100 mg/kg, i.p.) or PBN (100 mg/kg, i.p.) or their Veh. **(H)** H₂O₂ levels (hind paw) in *Trpa1*^{+/+} and *Trpa1*^{-/-} mice treated with (H) i.g. and i.pl. EtOH, **(I)** ACD (0.1 mg/kg i.p. and 10 nmol, i.pl.) or their Veh. BL, baseline. Veh is the vehicle of EtOH and ACD. Where not indicated mice are **C57BL/6J** and EtOH doses are: i.g., 15%, 4 ml/kg and i.pl. 30%, 20 µl. **(B)**, 4-HNE mean grey value) box plots with horizontal lines at the 25th percentile, the median, and the 75th percentile and the vertical lines which extend to the minimum and maximum values; all other data are mean ± SEM with individual data points overlaid; n=6-8 mice for each experimental condition. *P<0.05, **P<0.01, ***P<0.001 vs. Veh, ACD-BL and H₂O₂-BL; §P<0.05, §§§P<0.001 vs. EtOH, EtOH-A96, EtOH-PBN, EtOH-*Trpa1*^{+/+}, ACD-A96, ACD-PBN and ACD-*Trpa1*^{+/+}; two-way ANOVA with Bonferroni post-hoc correction.

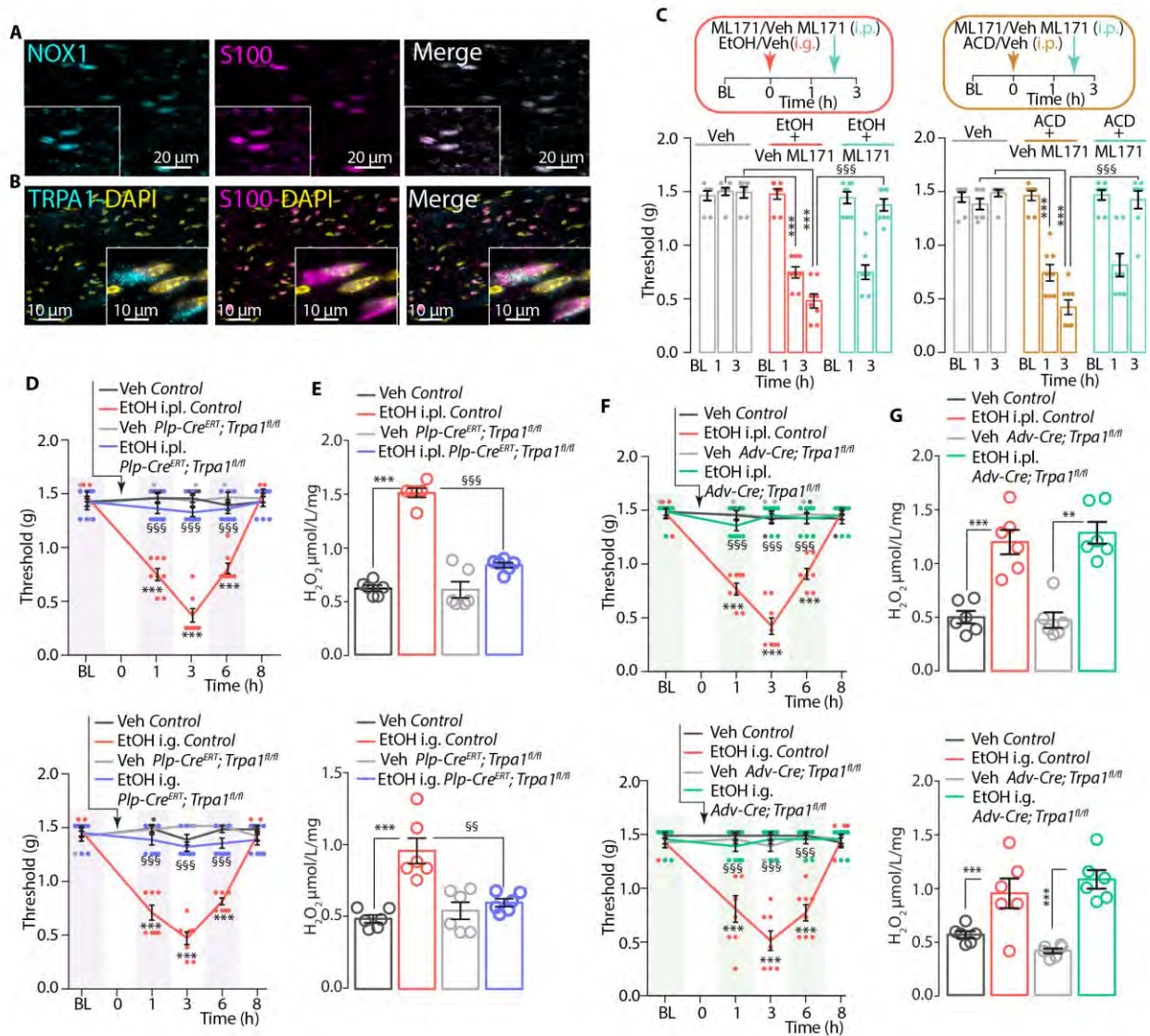


Figure 6. Schwann cell TRPA1 contributes to oxidative stress generation. (A and B) Representative images of NADPH oxidase 1 (NOX1), S100 and TRPA1 expression in plantar nerve of C57BL/6J mice. (C) Mechanical allodynia evoked by ethanol (EtOH, 15%, 4 ml/kg, intragastric, i.g.) and acetaldehyde (ACD, 0.1 mg/kg, intraperitoneal, i.p.) or their vehicle (Veh) after ML171 (100 mg/kg, i.p.) or Veh ML171 in C57BL/6J mice. (D) Time-dependent mechanical allodynia evoked by EtOH (30%, intraplantar, i.pl. and 15%, 4 ml/kg, i.g.) or Veh in *Plp-Cre^{ERT};Trpa1^{fl/fl}* and Control mice. (E) H₂O₂ levels (hind paw) after EtOH (30%, i.pl. and 15%, 4 ml/kg i.g.) or Veh in *Plp-Cre^{ERT};Trpa1^{fl/fl}* and Control mice. (F) Time dependent mechanical allodynia evoked by EtOH (30%, i.pl. and 15%, 4 ml/kg, i.g.) or Veh in *Adv-Cre;Trpa1^{fl/fl}* and Control

mice. (G) H₂O₂ levels (hind paw tissue) after EtOH (30%, i.pl. and 15%, 4 ml/kg, i.g.) or Veh in *Adv-Cre;Trpa1^{fl/fl}* and *Control* mice. BL, baseline. Veh is the vehicle of EtOH and ACD. Dashed lines indicate *perineurium*. Data are mean ± SEM with individual data points overlaid; n=6-8 mice for each experimental condition. **P<0.01, ***P<0.001 vs. Veh; §§P<0.01, §§§P<0.001 vs. EtOH i.g. or EtOH i.pl. control; two-way ANOVA with Bonferroni post-hoc correction.

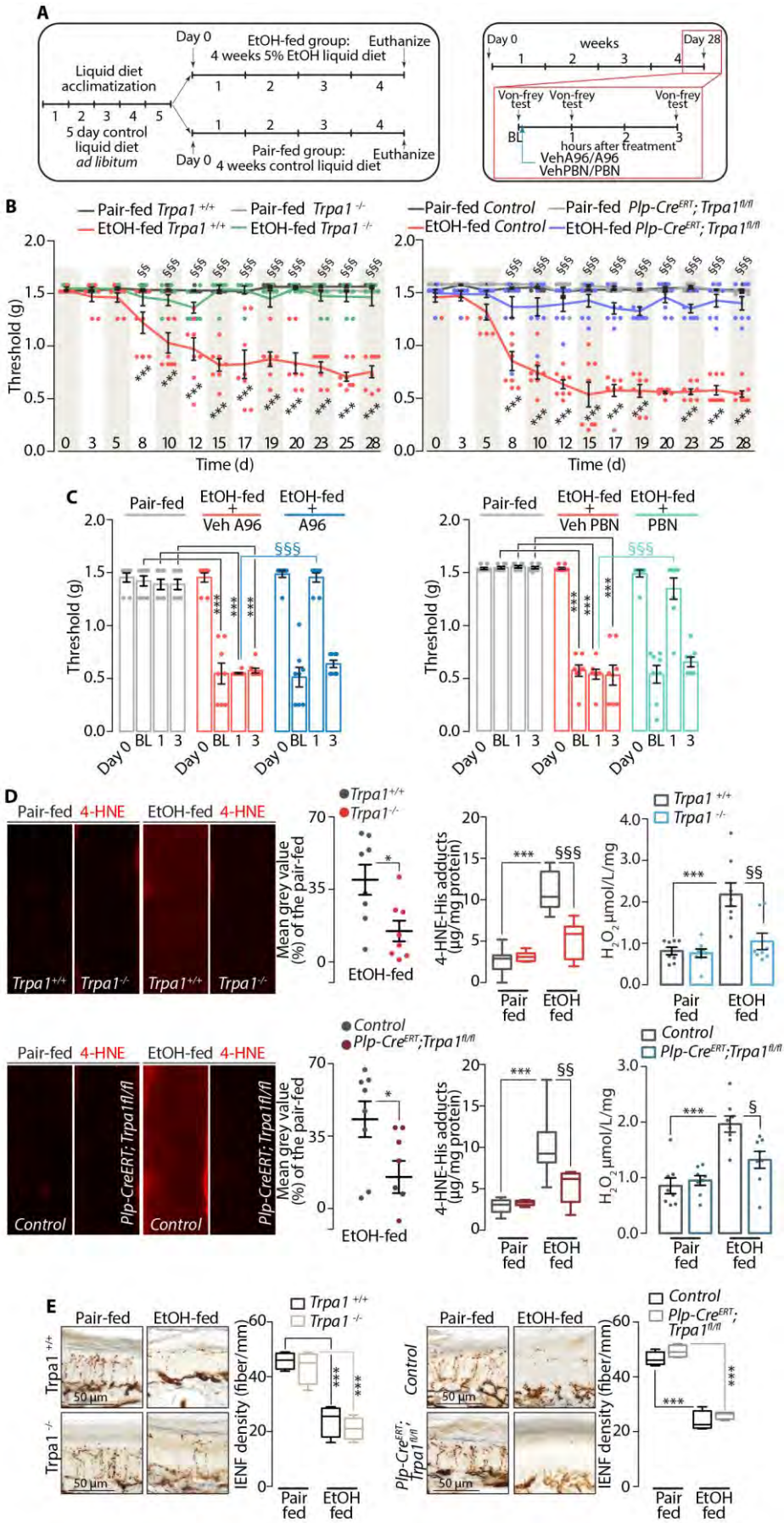


Figure 7. Schwann cell TRPA1 mediates mechanical allodynia evoked by chronic ethanol treatment. (A) Overview of the experimental design of the chronic ethanol (EtOH) feeding model. (B) Time-dependent mechanical allodynia by EtOH- (5% (vol/vol) for 28 days, EtOH-fed) or control (pair-fed)-diet in *Trpa1*^{+/+} and *Trpa1*^{-/-} mice and *Plp-Cre*^{ERT};*Trpa1*^{fl/fl} and *Control* mice. (C) Mechanical allodynia evoked by EtOH- or control-diet at day 28 after A967079 (A96, 100 mg/kg, intraperitoneal, i.p.) and phenyl- α -tert-butyl nitron (PBN, 100 mg/kg, i.p.) or their Veh in C57BL/6J mice. (D) Representative photomicrographs and cumulative data of 4-hydroxynonenal (4-HNE) staining (plantar nerve) and levels (hind paw), and H₂O₂ levels (hind paw) in *Trpa1*^{+/+} and *Trpa1*^{-/-} mice and *Plp-Cre*^{ERT};*Trpa1*^{fl/fl} and *Control* mice at day 28 after EtOH- or control-diet. (E) Representative photomicrograph of PGP9.5 staining and cumulative data of intraepidermal nerve fiber (IENF) density in the paw of *Trpa1*^{+/+} and *Trpa1*^{-/-} mice and *Plp-Cre*^{ERT};*Trpa1*^{fl/fl} and *Control* mice at day 28 after EtOH- or control-diet. BL, baseline. (D, 4-HNE-His and E) box plots with horizontal lines at the 25th percentile, the median, and the 75th percentile and the vertical lines which extend to the minimum and maximum values; all other data are mean \pm SEM with individual data points overlaid; n=8 mice for each experimental condition. *P<0.05, ***P<0.001 vs. pair-fed *Trpa1*^{+/+}, pair-fed control or EtOH-fed Veh A96/A96 day 0; \$P<0.05, \$\$P<0.01, \$\$\$P<0.001 vs. EtOH-fed *Trpa1*^{+/+}, EtOH-fed control or EtOH-fed Veh A96; one-way or two-way ANOVA with Bonferroni post-hoc correction.

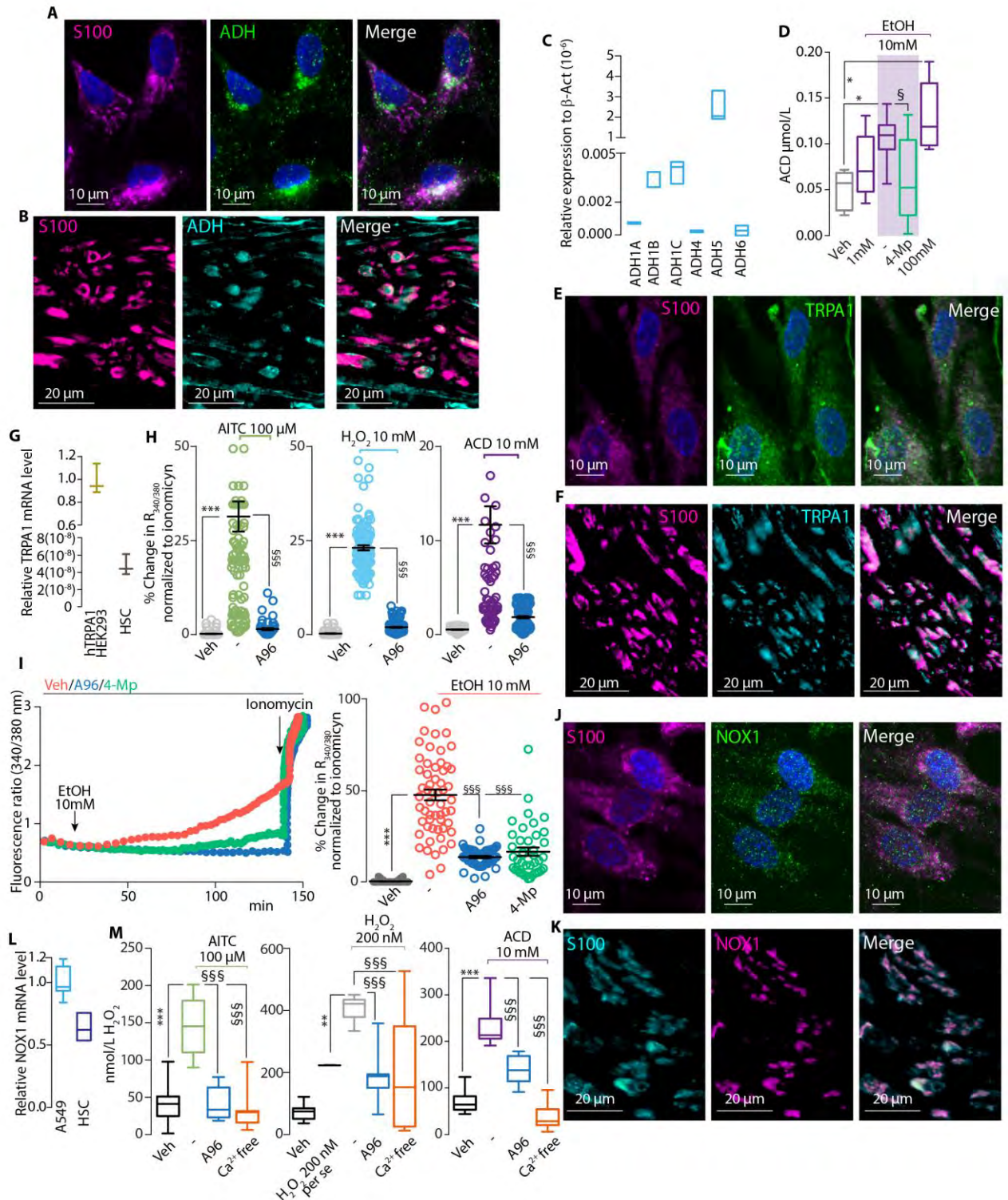


Figure 8. TRPA1 and alcohol dehydrogenase are present in human Schwann cells. Representative images of (A and B) S100 and alcohol dehydrogenase (ADH) expression, (E and F) TRPA1 and (J and K) NOX1 immunofluorescence in cultured human Schwann cells (HSC) and human skin. (C) ADH1A, ADH1B, ADH1C, ADH4, ADH5 and ADH7 mRNA relative expression in HSC. (D) Dose-dependent acetaldehyde

(ACD) levels in HSC exposed to ethanol (EtOH, 1-100 mM) and treated with 4-methylpyrazole (4-Mp, 100 μ M). (G) TRPA1 mRNA expression in HSC relative to human TRPA1-HEK293 cells. (H) Intracellular calcium ($[Ca^{2+}]_i$) response to allyl isothiocyanate (AITC, 100 μ M), H₂O₂ (10 mM) and ACD (10 mM) in HSC in the presence of A967079 (A96, 30 μ M) or its vehicle (Veh). (I) $[Ca^{2+}]_i$ response to EtOH (10 mM) in HSC in the presence of A96 (30 μ M), 4-Mp (100 μ M) or their Veh. (L) NOX1 mRNA expression in HSC relative to A549 cells. (M) H₂O₂ release evoked by AITC (100 μ M), H₂O₂ (200 nM) and ACD (10 mM) in HSC in the presence of A96 (30 μ M), Veh or in Ca²⁺ free medium. Veh is the vehicle of EtOH, AITC, H₂O₂ and ACD. (C, D, G, L and M) box plots with horizontal lines at the 25th percentile, the median, and the 75th percentile and the vertical lines which extend to the minimum and maximum values; n=3 replicates from 2 independent experiments in C, G and L and n=8 replicates from 3 independent experiments in D and M; (H and I) data are mean \pm SEM with individual data points overlaid, 41 to 327 cells n=3 to 5 experiments. *P<0.05, ***P<0.001 vs. Veh; §P<0.05, §§§P<0.001 vs. EtOH (10 mM), AITC (100 μ M), H₂O₂ (200 nM) and ACD (10 mM); one-way ANOVA with Bonferroni post-hoc correction.

Supplemental data

Schwann cells expressing nociceptive channel TRPA1 orchestrate ethanol-evoked neuropathic pain in mice

Francesco De Logu¹, Simone Li Puma¹, Lorenzo Landini¹, Francesca Portelli² Alessandro Innocenti³, Daniel Souza Monteiro de Araujo^{1,4}, Malvin N. Janal⁵, Riccardo Patacchini⁶, Nigel W. Bunnett⁷, Pierangelo Geppetti^{1*}, Romina Nassini¹

¹Department of Health Sciences, Section of Clinical Pharmacology and Oncology, University of Florence, Florence, Italy; ²Department of Health Sciences, Histopathology and Molecular Diagnostics; University of Florence, Florence, Italy; ³Plastic and Reconstructive Microsurgery, Careggi University Hospital, Florence, Italy. ⁴Department of Neurobiology and Program of Neurosciences, Institute of Biology, Fluminense Federal University, Niterói, RJ, Brazil; ⁵Department of Epidemiology and Health Promotion, New York University College of Dentistry, New York, USA; ⁶Department of Corporate Drug Development, Chiesi Farmaceutici SpA, Parma, Italy; ⁷Departments of Surgery and Pharmacology, Columbia University in the City of New York, USA

Corresponding author:

Pierangelo Geppetti, MD

Department of Health Sciences

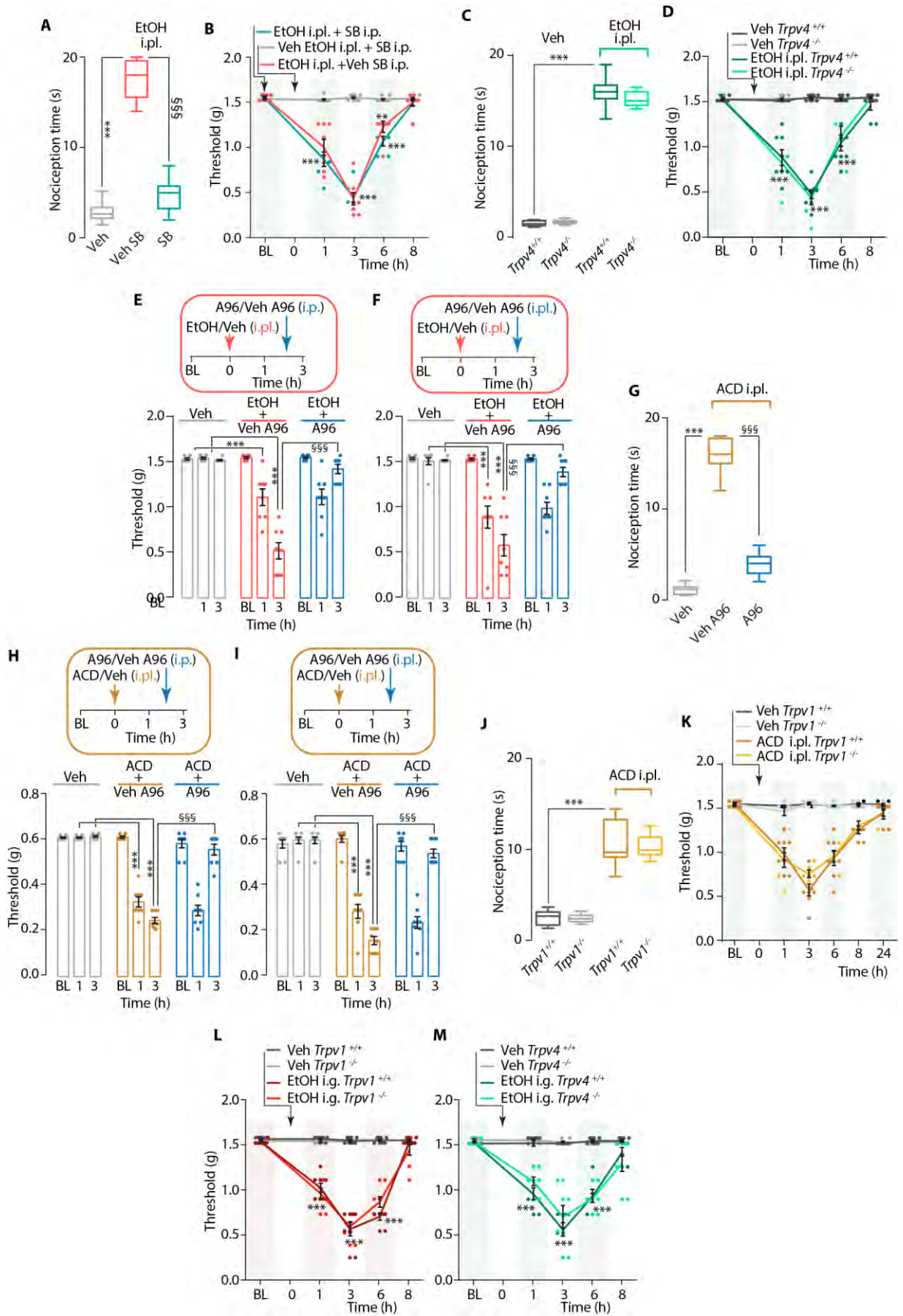
University of Florence

Viale Pieraccini 6, 50139 Florence, Italy

geppetti@unifi.it

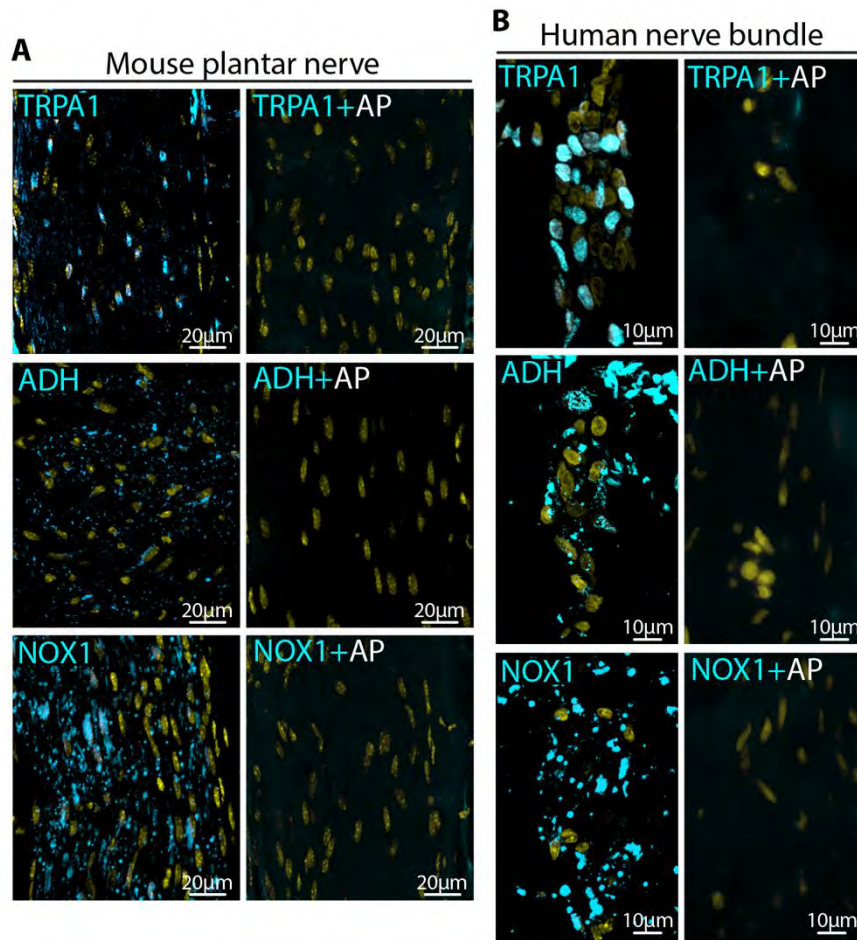
Mobile: +39 349 271 0476

Supplemental figures



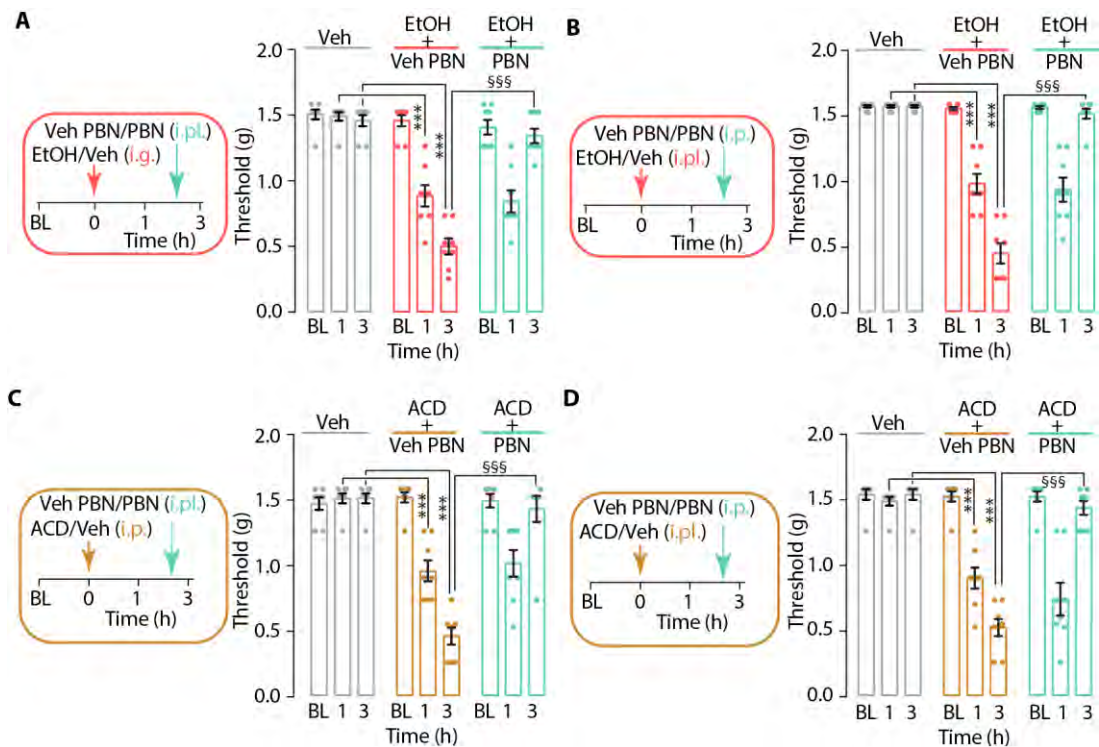
Supplemental Figure 1.

(A) Acute nociceptive response and (B) time-dependent hind paw mechanical allodynia evoked by intraplantar (i.pl., 20 μ l) ethanol (EtOH, 30%) or vehicle (Veh) after pretreatment with intraperitoneal (i.p.) SB366791 (SB, 1 mg/kg) or Veh SB in C57BL/6J mice. Acute nociception response (C) and time-dependent mechanical allodynia (D) after EtOH (30%, i.pl.) or Veh in *Trpv4^{+/+}* and *Trpv4^{-/-}* mice. (E and F) Mechanical allodynia evoked by EtOH (30%, i.pl.) or Veh after A967079 (A96, 100 mg/kg, i.p. or 100 μ g, i.pl.) or Veh A96 in C57BL/6J mice. (G) Acute nociceptive response evoked by acetaldehyde (ACD, 20 nmol, i.pl.) after A96 (100 mg/kg, i.p.) or Veh A96 in C57BL/6J mice. (H and I) Mechanical allodynia evoked by ACD (20 nmol, i.pl.) or Veh, after A96 (100 mg/kg i.p. or 100 μ g, i.pl.) or Veh A96 in C57BL/6J mice. Acute nociception response (J) and time-dependent mechanical allodynia (K) after ACD (20 nmol, i.pl.) or Veh in *Trpv1^{+/+}* and *Trpv1^{-/-}* mice. Time-dependent mechanical allodynia after intragastric (i.g.) EtOH (15%, 4 ml/kg) or Veh in *Trpv1^{+/+}* and *Trpv1^{-/-}* (L) and *Trpv4^{+/+}* and *Trpv4^{-/-}* (M) mice. BL, baseline. Veh is the vehicle of EtOH and ACD. (A, C, G and J) box plots with horizontal lines at the 25th percentile, the median, and the 75th percentile and the vertical lines which extend to the minimum and maximum values; all other data are mean \pm SEM with individual data points overlaid; n=8 mice for each experimental condition. **P<0.01, ***P<0.001 vs. Veh; §§§P<0.001 vs. EtOH-A96, ACD-A96, one-way or two-way ANOVA with Bonferroni post-hoc correction.



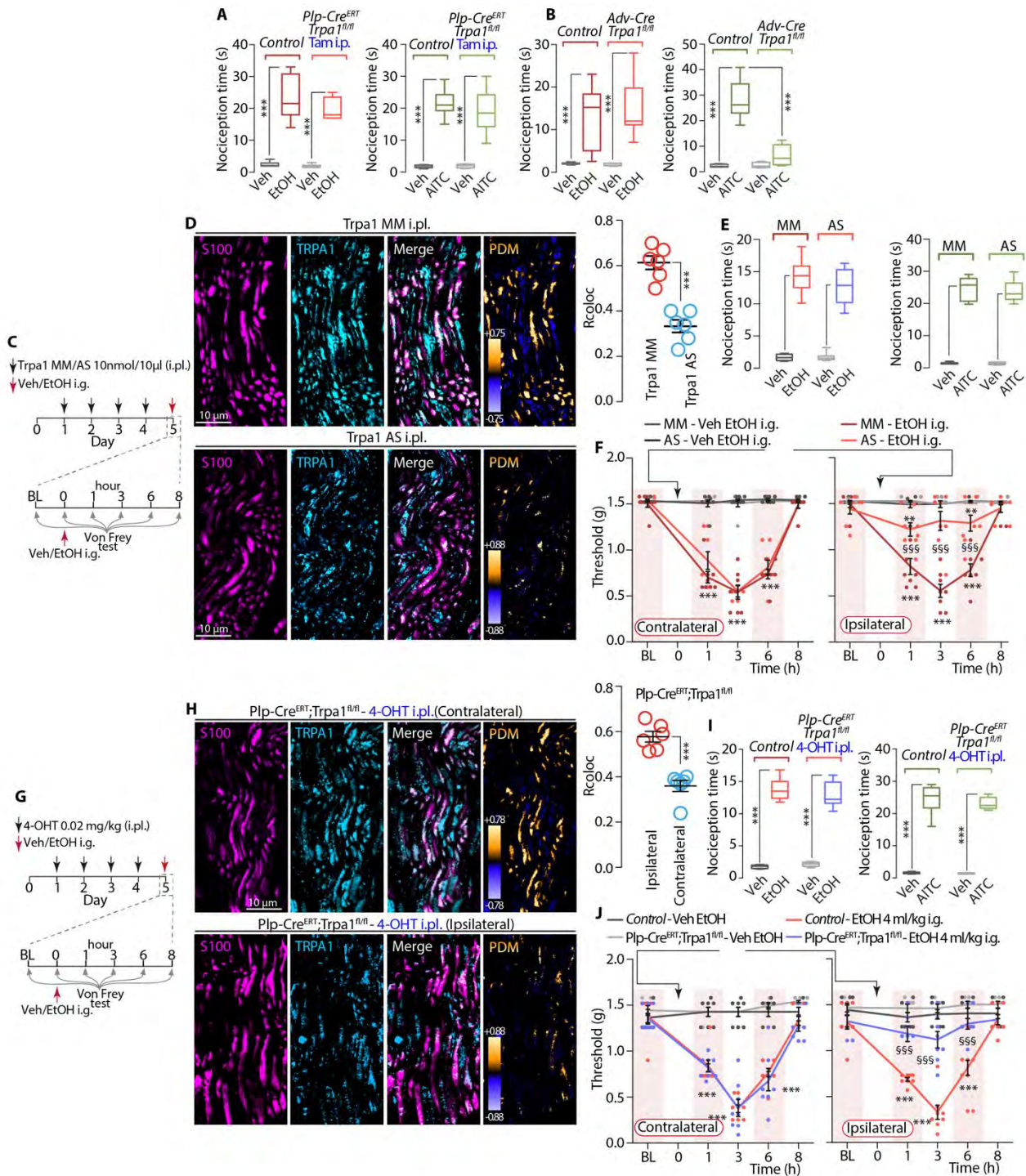
Supplemental Figure 2.

Representative images of TRPA1, NOX1 and ADH staining with primary antibodies pre-incubated with or without their respective antigen peptides (AP) in mouse plantar nerve (A) and nerve bundles in biopsies of human skin (B).



Supplemental Figure 3.

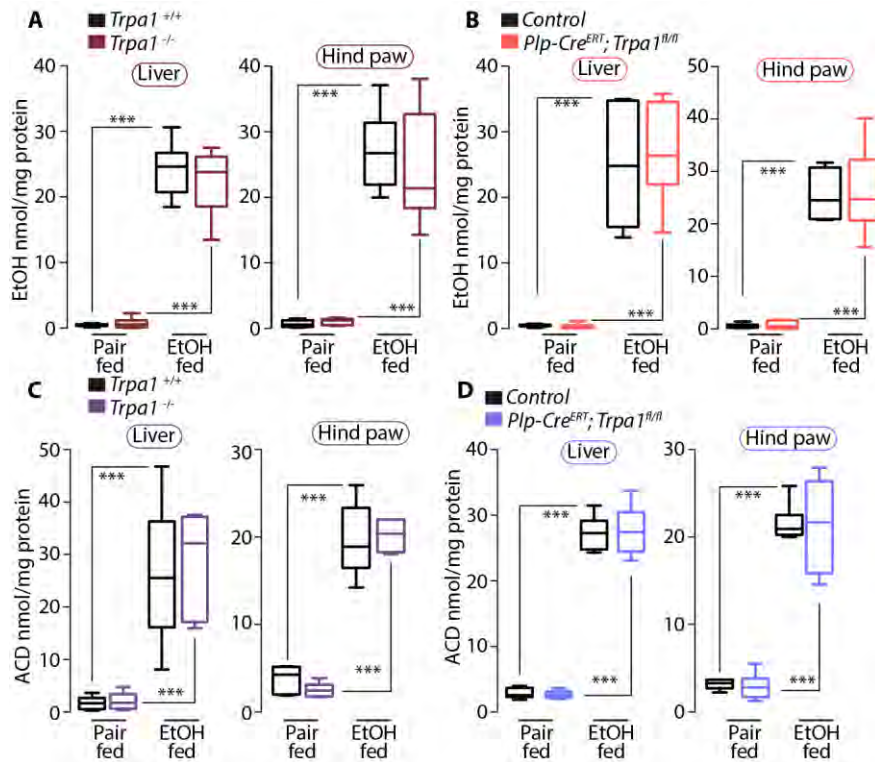
(A) Hind paw mechanical allodynia after intragastric (i.g.) ethanol (EtOH, 15% 4 ml/kg) or vehicle (Veh) and intraplantar (i.pl., 20 μ l) phenyl- α -tert-butyl nitron (PBN, 100 μ g) or Veh PBN, in C5BL/6 mice. (B) Mechanical allodynia after EtOH (30%, i.pl.) or Veh and intraperitoneal (i.p.) PBN (50 mg/kg, i.p.) or Veh PBN in C5BL/6 mice. (C) Mechanical allodynia after acetaldehyde (ACD, 0.1 mg/kg, i.p.) or Veh and PBN (100 μ g, i.pl.) or Veh PBN in C5BL/6 mice. (D) Mechanical allodynia after ACD (20 nmol, i.pl.) or veh and PBN (50 mg/kg, i.p.) or vehicle PBN in C5BL/6 mice. BL, baseline. Veh is the vehicle of EtOH and ACD. Data are mean \pm SEM with individual data points overlaid; n=8 mice for each experimental condition. ***P<0.001 vs. Veh; \$\$\$P<0.001 vs. EtOH and ACD; two-way ANOVA with Bonferroni post-hoc correction.



Supplemental Figure 4.

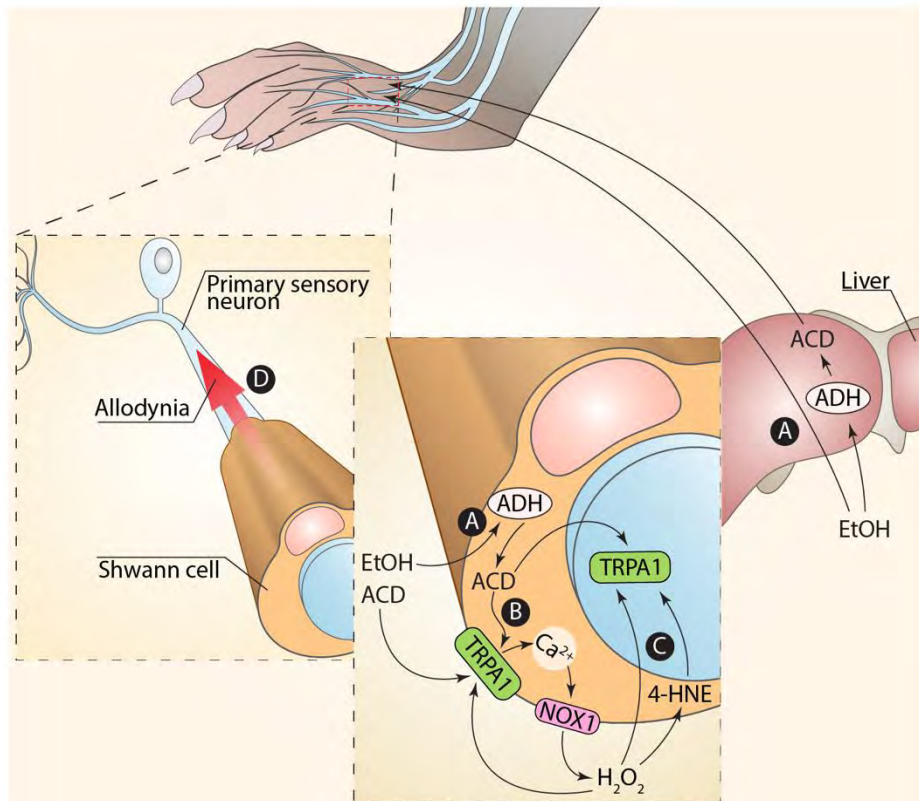
(A) Acute nociceptive response induced by intraplantar (i.pl., 20 μ l) ethanol (EtOH, 30%) or vehicle (Veh) and allyl isothiocyanate (AITC, 10 nmol, i.pl.) or Veh in *Plp1-CreERT;Trpa1^{fl/fl}* and *Control* mice treated with tamoxifen (Tam, 1 mg/100 μ l, intraperitoneal, i.p.). (B) Acute nociception response induced by EtOH (30%, i.pl.) or Veh

and AITC (10 nmol, i.pl.) or Veh in *Adv-Cre;Trpa1^{fl/fl}* and *Control* mice. Veh is the vehicle of EtOH and AITC. Schematic representation of treatment protocols of (C) C57BL/6J mice received TRPA1 AS/MM-ODN (1 nmol/ μ l, i.pl.) and (G) *Plp1-CreERT;Trpa1^{fl/fl}* and *Control* mice received 4-hydroxytamoxifen (4-OHT) (0.02 mg/10 μ l, i.pl.) for 4 consecutive days. Ipsilateral indicates the treated hind paw and the untreated contralateral hind paw was used as control. (D and H) Representative images and qualitative analysis of colocalization by PDM image and colocalization value (Rcoloc) of S100 and TRPA1 expression in plantar nerve. The orange color indicates colocalized pixels and the blue color means segregation. Acute nociceptive response induced by ethanol (EtOH, 30%, i.pl.) or Veh and AITC (10 nmol, i.pl.) or Veh in C57BL/6J mice (E) and in *Plp1-CreERT;Trpa1^{fl/fl}* and *Control* mice (I). Mechanical allodynia after intragastric (i.g.) ethanol (EtOH, 15% 4 ml/kg) or Veh in C57BL/6J mice (F) and in *Plp1-CreERT;Trpa1^{fl/fl}* and *Control* mice (J). (A, B, E, I) Box plots with horizontal lines at the 25th percentile, the median, and the 75th percentile and the vertical lines which extend to the minimum and maximum values, all other data are mean \pm SEM with individual data points overlaid; n=8 mice for each experimental condition. ***P<0.001 vs. Veh; §§§P<0.001 vs. AITC (Control); one-way ANOVA with Bonferroni post-hoc correction.



Supplemental Figure 5.

Ethanol (EtOH) and acetaldehyde (ACD) levels in liver and hind paw tissue after 28 days of an EtOH 5% (vol/vol)- or control-diet in (**A** and **C**) *Trpa1^{+/+}* and *Trpa1^{-/-}* mice and, (**B** and **D**) *Plp1-CreERT;Trpa1^{fl/fl}* and *Control* mice. Box plots with horizontal lines at the 25th percentile, the median, and the 75th percentile and the vertical lines which extend to the minimum and maximum values; n=8 mice for each experimental condition. ***P<0.001 vs. pair-fed mice; one-way ANOVA with Bonferroni post-hoc correction.



Supplemental Figure 6. (A) Intra-gastric ethanol is converted into acetaldehyde (ACD) by alcohol dehydrogenase (ADH) in the liver and in Schwann cells. (B) Hepatic or locally produced ACD targets the Ca²⁺ dependent TRPA1/NOX1 pathway in Schwann cells to release H₂O₂. (C) H₂O₂ and its carbonylic byproduct, 4-hydroxynonenal (4-HNE), gating the neuronal TRPA1 (D) signal allodynia.

Review

Therapeutic Targeting of Endosomal G-Protein-Coupled Receptors

Alex R.B. Thomsen,¹ Dane D. Jensen,¹ Gareth A. Hicks,² and Nigel W. Bunnett^{1,*}

G-protein-coupled receptors (GPCRs) are conventionally considered to function at the plasma membrane, where they detect extracellular ligands and activate heterotrimeric G proteins that transmit intracellular signals. Consequently, drug discovery efforts have focused on identification of agonists and antagonists of cell surface GPCRs. However, β -arrestin (ARR)-dependent desensitization and endocytosis rapidly terminate G protein signaling at the plasma membrane. Emerging evidence indicates that GPCRs can continue to signal from endosomes by G-protein- and β ARR-dependent processes. By regulating the duration and location of intracellular signaling events, GPCRs in endosomes control critically important processes, including gene transcription and ion channel activity. Thus, GPCRs in endosomes, in addition to at the cell surface, have emerged as important therapeutic targets.

Revision of the Plasma-Membrane-Centric View of GPCR Signaling

With almost 1000 members in the human genome, **G-protein-coupled receptors** (GPCRs, see [Glossary](#)) are the largest family of transmembrane signaling proteins [1]. Photons, odorants, tastants, and many hormones and neurotransmitters activate GPCRs, which control most physiological and pathological processes. Over one-third of marketed drugs target GPCRs [2].

GPCRs are conventionally considered to function primarily at the plasma membrane, and drug discovery efforts target cell surface receptors. GPCRs at the plasma membrane interact with extracellular ligands and undergo a conformational change that promotes association with intracellular **heterotrimeric G proteins** ($G\alpha\beta\gamma$), which induces guanine nucleotide exchange, G protein activation, and dissociation of $G\alpha$ and $G\beta\gamma$ subunits [1]. G protein subunits in turn regulate downstream enzymes and effectors that control many cellular processes [1]. GPCR signaling at the plasma membrane is tightly regulated and often transient. **GPCR kinases** (GRKs) phosphorylate activated GPCRs, thereby enhancing their affinity for **β -arrestins** (β ARRs) [3,4]. β ARRs bind phosphorylated GPCRs in two stages: first to phosphorylated residues within the receptor C-terminal tail, and second within the transmembrane core [5]. Since the binding site of β ARRs in the receptor core overlaps with the G-protein-binding site, β ARR recruitment sterically hinders further G protein activation, which desensitizes G protein signaling [5–7]. β ARRs also couple GPCRs to **clathrin** and **adaptor protein-2** (AP2), which mediate endocytosis of GPCRs, removing them from the site of activation [4]. The extent of GRK-mediated phosphorylation of GPCRs is a major determinant of the stability of GPCR/ β ARR complexes, which largely governs the fate of internalized GPCRs. GPCRs with few GRK phosphorylation sites (Class A GPCRs) interact with β ARR in endosomes with low affinity and transiently, and can rapidly recycle back to the plasma membrane. In contrast, GPCRs with many, often clustered, GRK phosphorylation sites (Class B GPCRs) exhibit sustained high-affinity interactions with β ARR in endosomes, and either slowly recycle or traffic to lysosomes for degradation [8,9]. Ligand stability in endosomes

Highlights

G protein signaling by some GPCRs is not only stimulated at the plasma membrane but also from endosomes after β ARR-dependent internalization.

Some GPCRs interact with β ARR in a specific conformation, the 'tail' conformation, where β ARR only is bound to the phosphorylated C-terminal tail and does not block the G-protein-binding site at the intracellular receptor core.

This tail conformation allows GPCRs to interact with G protein and β ARR simultaneously to form GPCR-G protein- β ARR supercomplexes, which provides a mechanistic basis for endosomal G protein signaling by internalized GPCRs.

Endosomal GPCR signaling plays important cell biological and physiological roles. It was recently found that endosomal GPCR signaling plays a central role in regulating nociception.

Agonists and antagonists can be developed to specifically target endosomal GPCRs to achieve more specific modulation of physiological responses.

¹Departments of Surgery and Pharmacology, Columbia University College of Physicians and Surgeons, Columbia University in the City of New York, 21 Audubon Avenue, Room 209, New York City, NY 10032, USA

²Gastroenterology Drug Discovery Unit (GI DDU), Takeda Pharmaceuticals U.S.A. Inc., 35 Landsdowne Street, Cambridge, MA 02139, USA

*Correspondence: nb2733@cumc.columbia.edu (N.W. Bunnett).

also determines the fate of endosomal GPCRs. By degrading neuropeptide ligands in acidified endosomes, endothelin-converting enzyme-1 can destabilize neuropeptide/GPCR/ARR complexes and promote receptor recycling [10,11].

This plasma-membrane-centric view of GPCRs is incomplete since many activated GPCRs traffic, with their ligands, to endosomes, where they can continue to signal by β ARR- and G-protein-dependent mechanisms [12–14]. The concept that GPCRs can signal from endosomes raises important questions. If β ARRs uncouple GPCRs from G proteins at the plasma membrane, how do GPCRs continue to activate G proteins in endosomes? What is the contribution of GPCR signaling at the plasma membrane and in endosomes to complex pathophysiological processes? How is endosomal signaling of GPCRs regulated and can this be exploited for therapy? Are GPCRs in endosomes, rather than at the cell surface, the key therapeutic target? This article reviews the latest developments in endosomal GPCR signaling, and discusses how this information can be used to design more selective and potentially effective drugs.

Paradox of G Protein- and β ARR-Dependent Signaling of GPCRs in Endosomes

By recruiting GPCRs and signaling partners, including components of mitogen-activated protein kinase cascades, to endosomes, β ARRs are key mediators of endosomal signaling of GPCRs [4]. However, G proteins, in addition to β ARRs, also mediate signaling of GPCRs in endosomes. Signaling of G proteins in endosomes was first discovered for the yeast G protein, Gpa1 [15]. A growing number of GPCRs have been shown to activate $G\alpha_s$, $G\alpha_{i/o}$, and $G\alpha_q$ in endosomes of mammalian cells, including the **parathyroid hormone receptor (PTHr)**, **vasopressin type 2 receptor (V_2R)**, **thyroid stimulating hormone receptor (TSHR)**, **luteinizing hormone receptor (LHR)**, **sphingosine-1-phosphate 1 receptor (S1PR1)**, **neurokinin type 1 receptor (NK_1R)**, **calcitonin receptor-like receptor (CLR)**, and **C-C chemokine receptor-1 (CCR1)** [12,14,16–22]. However, the concept of endosomal G protein signaling was met with skepticism because β ARRs compete with G proteins for GPCR binding sites and, once recruited, β ARRs would be expected to terminate G protein signaling [4,7]. High-resolution structural studies have confirmed overlapping binding sites for visual arrestin and **transducin (Gt protein)** at rhodopsin [6,7,23]. Thus, it would seem impossible that GPCR/ β ARR complexes could stimulate G protein signaling from endosomes.

Despite this paradox, class B GPCRs (e.g., PTHr, V_2R , and TSHR), which form stable endosomal complexes with β ARRs through phosphorylation site clusters within the receptor C-terminal tail, stimulate G protein signaling that, unlike Class A GPCRs, is insensitive to agonist wash-out or cell impermeable antagonists [16–19,21,24–26]. In addition, fluorescence microscopy has demonstrated that these internalized and β ARR-associated GPCRs colocalize with G proteins in endosomes [12,17,24,25]. Disrupting the Class B GPCR C-terminal tail- β ARR interaction markedly diminishes the ability of these GPCRs to stimulate endosomal G protein signaling, which suggests a role for β ARRs in directing these signals. For example, deletion of NK_1R C terminus or antagonism of NK_1R / β ARR interactions prevents β ARR recruitment and internalization, as well as endosomal signaling outputs [12]. The correlation between a strong β ARR/GPCR interaction and endosomal G protein signaling was confirmed by exchanging the C-terminal tail of the Class A **β_2 -adrenergic receptor (β_2AR)** with the C-tail of the Class B V_2R , which enhanced interactions of the chimera β_2V_2R with β ARRs and magnified G protein signaling from endosomes [24,27]. Moreover, coexpression of constitutively active β ARR1 enhances sustained endosomal G protein signaling of the PTHr and V_2R , whereas the siRNA knockdown of β ARR1/2 has the opposite effect [18,25,26]. Thus, not only do β ARRs fail to desensitize G protein signaling from endosomal GPCRs, they can also enhance endosomal G

Glossary

Adaptor protein-2 (AP2): binds active β ARR and is directly involved in clathrin-mediated receptor endocytosis.

β -Arrestin (β ARR): interacts with agonist-occupied, phosphorylated GPCRs and mediate GPCR desensitization, endocytosis, and signal transduction.

β_2 -Adrenergic receptor (β_2AR): GPCR for epinephrine that regulates cardiovascular functions.

cAMP: secondary messenger produced by activation of adenylyl cyclase.

C-C chemokine receptor-1 (CCR1): GPCR for chemokines that regulates migration of immune cells.

Clathrin: protein that interacts with β ARRs and adaptins to mediate endocytosis of GPCRs and many other cell surface proteins.

Calcitonin receptor-like receptor (CLR): receptor for CGRP that is expressed in the cardiovascular and nervous systems where it controls vascular tone and nociception. A new target for migraine pain.

cAMP response element binding protein (CREB): cAMP-responsive transcription factor.

Cryoelectron tomography: form of electron microscopy that can be used to provide high-resolution images of macromolecules in intact cells.

Δ FLR: β ARR mutant without the FLR.

Extracellular signal-regulated kinase (ERK): essential component of the mitogen-activated protein kinase signaling pathway.

Fingerloop region (FLR): β ARR region that inserts into the receptor core and blocks GPCR-G protein interactions.

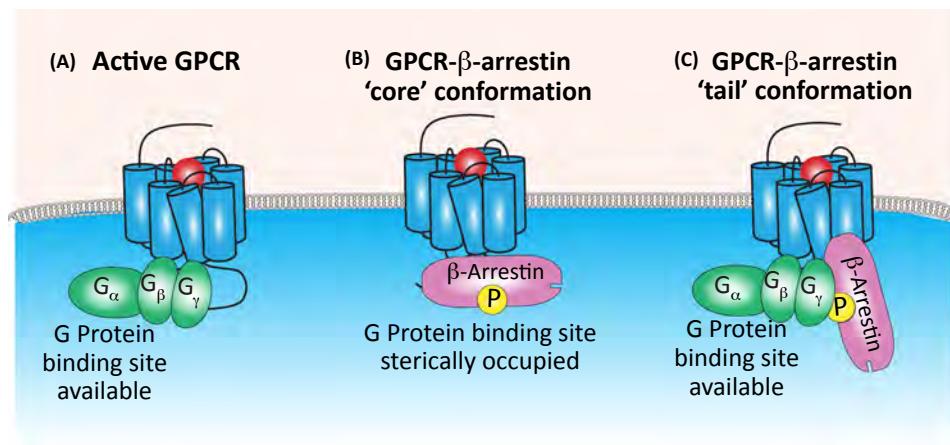
$G\alpha\beta\gamma$ – heterotrimeric G protein: consists of three subunits $G\alpha$, $G\beta$, and $G\gamma$, and is activated by GPCRs to generate signaling outputs throughout the cell.

G-protein-coupled receptor (GPCR): integral membrane protein with seven transmembrane domains. GPCRs are the largest class of receptors, serve to communicate extracellular signals to the inside of the cell, control almost all physiological and pathological processes, and are the target of >30% of clinically used drugs.

protein signaling. How is this possible given the conventional view that β ARRs uncouple GPCRs and G proteins?

Recent biophysical approaches have provided a mechanistic understanding of endosomal G protein signaling (Figure 1). Investigation of the structure of a β_2V_2R/β ARR1 complex using negative stain electron microscopy revealed that the β_2V_2R/β ARR1 complex adopts at least two conformations: (i) a tail conformation, where β ARR1 binds β_2V_2R through the phosphorylated receptor C tail; and (ii) a core conformation, where β ARR1, in addition to binding to the C tail, also binds to the β_2V_2R transmembrane core through a flexible region within β ARR1 (**fingerloop region**, FLR), which sterically blocks the G-protein-binding site [5]. This core conformation is analogous to high-resolution structures of the rhodopsin–visual arrestin complex [6,7]. When complexed in the core conformation, β ARR1 desensitizes G protein signaling in the expected manner, but when complexed in the tail conformation, G protein signaling could proceed normally [27].

The unexpected finding that β ARRs can interact with GPCRs via the phosphorylated C tail only, as well as in the core conformation, has been further investigated using a β ARR1 mutant, **β ARR1(Δ FLR)**, which lacks the FLR that normally interacts with the receptor core. The β_2V_2R/β ARR1(Δ FLR) complex exclusively adopts the tail conformation, and removal of the FLR abolishes its function to desensitize G protein signaling. However, the mutant maintains its ability to promote receptor internalization and β ARR-mediated signaling [27]. Other studies have confirmed the role of the β ARR tail conformation in GPCR internalization and signaling [28–31]. Notably, only Class B GPCRs with phosphorylation site clusters in their C tail form stable tail conformation complexes with β ARR(Δ FLR), suggesting that Class A GPCR are dependent on the core interaction [27].



Trends in Pharmacological Sciences

Figure 1. Conformations of GPCR/ β ARR Complex. (A) GPCRs interact with G proteins through their transmembrane core region to stimulate G protein signaling. (B, C) Upon phosphorylation of the receptor C-terminal tail, GPCRs form complexes with β ARR in two different conformations: one in which the β ARR is bound only to the phosphorylated receptor C-terminal tail and appears to hang from the receptor (tail conformation, B); and a second more fully engaged conformation where, in addition to the tail interaction, a flexible loop in β ARR, termed the fingerloop, inserts into the transmembrane core of the receptor (core conformation, C). Since the insertion of the β ARR fingerloop into the receptor in the core conformation sterically blocks the G-protein-binding site, G protein activation is terminated. However, since β ARR does not occupy the receptor G-protein-binding site in the tail conformation, GPCRs can internalize in complex with β ARR and still stimulate G protein signaling from internalized compartments such as endosomes. Abbreviations: β ARR, β -arrestin; GPCR, G-protein-coupled receptor.

GPCR–APEX (GPCR ascorbate peroxidase): a proximity labeling approach that can be used for the identification of proteins that are closely associated with GPCRs by mass spectrometry.

G-protein-coupled receptor kinases (GRKs): family of kinases that phosphorylate active GPCRs, which triggers β ARR recruitment to phosphorylated receptors.

Gt protein – transducin: heterotrimeric G protein activated by rhodopsin.

Irritable bowel syndrome (IBS): disorder in humans that is characterized by abdominal pain and altered bowel habits (constipation and diarrhea). Although the cause is unknown, IBS often occurs after intestinal inflammation and infection.

Long-acting parathyroid hormone (LA-PTH): modified version of PTH that stimulates PTHR signaling for prolonged periods of time.

Luteinizing hormone receptor (LHR): GPCR for the reproductive LH. LHR is predominantly expressed in testis and ovaries.

Nociceptor: a sensory nerve, with cell bodies in dorsal root and trigeminal ganglia, that is specialized for the detection of painful stimuli in peripheral tissues and for the transmission of painful signals to the central nervous system.

Neurokinin type 1 receptor (NK₁R): GPCR for tachykinin peptides, notably SP. NK₁R is expressed in central and peripheral nervous systems and is involved in nociception, neurogenic inflammation, and smooth muscle cell contraction.

Pituitary adenylate cyclase 1 receptor (PAC1): GPCR for PACAP. PAC1 is expressed in the peripheral and central nervous systems, is involved in neural protection, and is highly expressed in neuroendocrine tumors.

Pituitary adenylate cyclase-activating polypeptide (PACAP): member of the vasoactive intestinal polypeptide family that activates PAC1.

Protease-activated receptor 2 (PAR₂): GPCR for serine (e.g., trypsin, tryptase, and elastase) and cysteine (cathepsin S) proteases. PAR₂ that is activated by proteolytic

These findings can explain the paradoxical role of β ARRs as negative regulators of G protein signaling at the plasma membrane, and positive regulators of G protein signaling in endosomes: when β ARRs binds GPCRs only through the C tail to promote internalization, the entire receptor core region is exposed, and thus β ARRs do not block the G-protein-binding site. Therefore, the receptor maintains its ability to couple to G proteins in endosomes [5,27–29]. In support of this concept, Class B GPCRs including PTHR, V_2R , CCR1, TSHR, and Y_1R promote close proximity between G proteins and β ARR upon activation [18,19,22,25,30]. Furthermore, Class B GPCRs, which form GPCR/ β ARR tail conformation complexes, have been directly shown to interact simultaneously with both G proteins and β ARRs to form GPCR/G protein/ β ARR ‘megaplexes’ [18,24,27,30]. The structural architecture of a megaplex consisting of β_2V_2R /Gs/ β ARR1 has been investigated by electron microscopy, and shows that the GPCR within megaplexes couple with G proteins at the receptor core while interacting with β ARRs through the C tail [24]. The existence of megaplexes can explain how Class B GPCRs can stimulate G protein signaling while being internalized to endosomes by β ARR [24].

Although endosomal signaling has been mostly described for Class B GPCRs, class A GPCRs can also signal from endosomes, albeit by distinct mechanisms. The recruitment of β ARRs to Class A GPCRs, such as the β_2AR , terminates G protein signaling by occluding the G protein-binding site [20,27]. However, following β ARR-mediated receptor internalization, Class A GPCRs can activate a second wave of G protein signaling from endosomes, which appears to proceed after β ARR dissociates from the receptor [20]. In contrast to the large and sustained G protein signals that emanate from Class B GPCRs in endosomes, endosomal G protein signaling of Class A GPCRs is modest and transient.

The assembly of a GPCR/ β ARR complex, which is stabilized by interaction of β ARR with the phosphorylated C tail of the receptor, is generally considered to be necessary for endosomal signaling of GPCRs. This long-held view has been challenged by the discovery of a mechanism of β ARR activation that does not require a stable GPCR/ β ARR complex or the receptor C tail. Atomic level simulations of ARR/GPCR interactions indicate that the transmembrane core and C tail of the receptor, which bind to distinct surfaces of ARR, can independently activate ARR [32]. In the case of the β_1AR and β_2AR , the transient engagement of β ARR with the receptor core can promote the accumulation of β ARR within clathrin-coated endocytic structures after dissociation from the receptor [33]. The sequestration of β ARR in these structures is associated with β ARR-mediated activation of **extracellular signal-regulated kinase** (ERK), without the engagement with an activated receptor.

GPCRs in Endosomes Control Signaling in Time and Space

β ARR-dependent desensitization and endocytosis of GPCRs ensure that signaling at the plasma membrane is fleeting and largely confined to the regulation of plasma-membrane-delimited events (e.g., activation of membrane-associated enzymes, growth factor receptors, and ion channels) (Figure 2, Key Figure). In contrast, GPCR signaling in endosomes can be sustained by β ARR- and G-protein-dependent processes. Given the dynamic nature of the tubulovesicular endosomal network, which ramifies throughout the cytosol, GPCRs in endosomes can generate signals in various subcellular compartments. Compartmentalized signaling may explain how GPCRs, which often activate a common set of G proteins and downstream effectors, can selectively regulate cellular responses.

The use of inhibitors of endocytosis, coupled with biophysical approaches to study GPCR trafficking and signaling with high spatial and temporal resolution, have provided insights into the link between trafficking and signaling of GPCRs. Disruption of clathrin or dynamin inhibits

cleavage within the extracellular C terminus.

Polyethylene glycol (PEG):

synthetic polymer used for formulation and delivery of drugs.

Protein kinase C (PKC): family of kinases that are activated by diacylglycerol and intracellular calcium ions, and which control activity of signaling proteins through phosphorylation.

Parathyroid hormone (PTH): protein hormone secreted by the parathyroid glands that regulates mineral homeostasis.

Parathyroid hormone receptor (PTHr): GPCR for PTH that maintains mineral homeostasis.

Parathyroid hormone-related protein (PTHrP-): protein secreted from cancer cells that activates the PTHR.

Receptor tyrosine kinase (RTK): family of cell surface receptors that are activated by growth factors, cytokines, and hormones.

Sphingosine-1-phosphate 1 receptor (S1P1R): GPCR involved in endothelial cell and lymphocyte regulation.

Substance P (SP): tachykinin family neuropeptide that activates neurokinin receptors.

Trans-Golgi network (TGN): secretory pathway sorting station that directs proteins to different subcellular destinations.

Thyroid stimulating hormone receptor (TSHR): GPCR expressed in the thyroid gland that is activated by TSH to produce thyroxine and triiodothyronine hormones.

Very early endosome (VEE): endosomal compartment physically and biochemically distinct from early endosomes.

Vasopressin type 2 receptor (V2R): GPCR for arginine vasopressin that regulates water homeostasis in the kidney.

Key Figure

Compartmentalized Signaling GPCRs in Endosomes

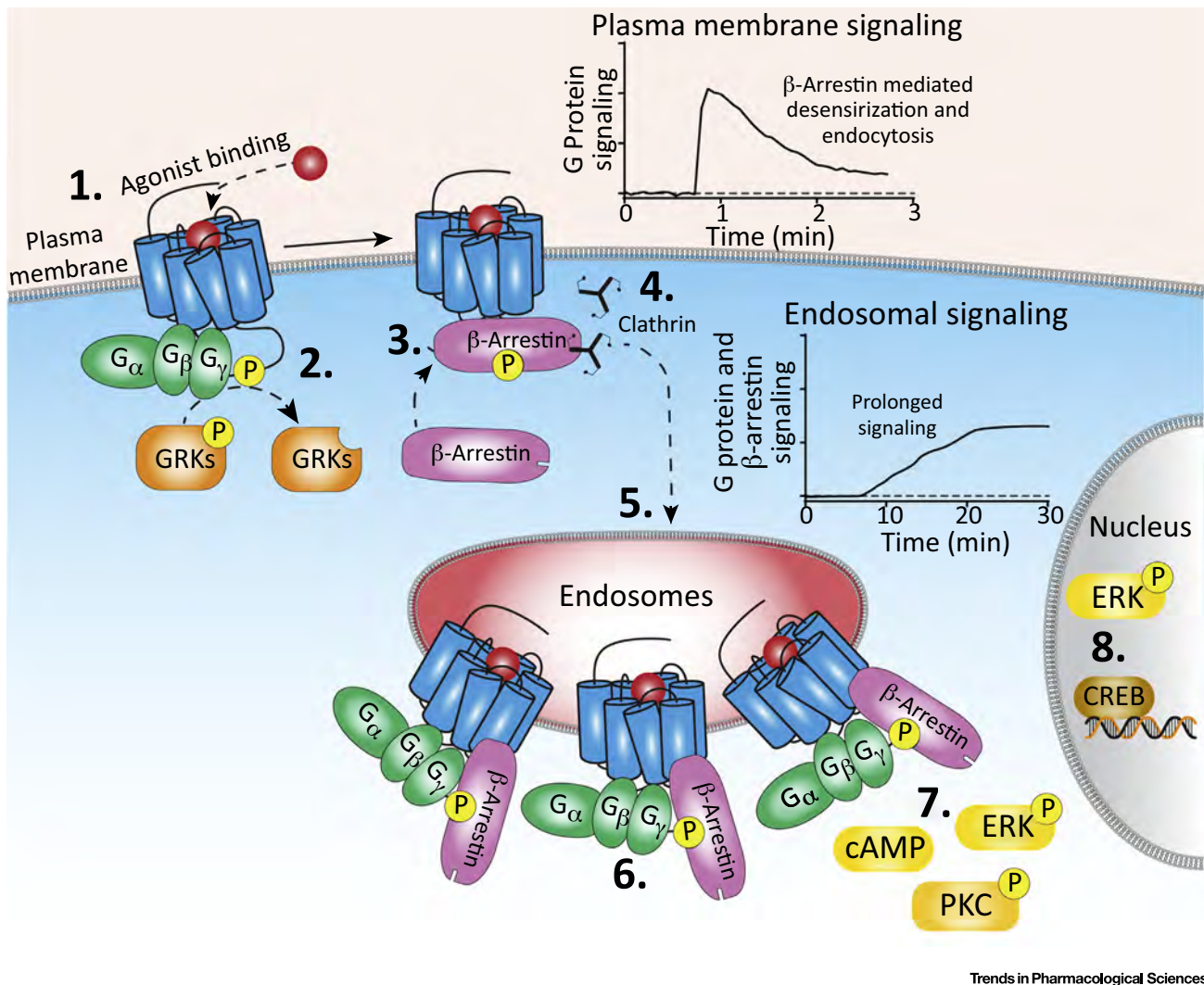


Figure 2. 1. Agonist binding at the plasma membrane stabilizes GPCRs in an active conformation. GPCRs interact with and activate heterotrimeric G proteins, which induce signaling. 2. GPCR kinases phosphorylate C-terminal domains of GPCRs. 3. Recruitment of β ARRs to the phosphorylated GPCR. In addition to the C-terminal tail, β ARRs also bind the GPCR core, which sterically hinders G protein binding and thereby terminates G protein signaling. 4. β ARRs scaffold clathrin and AP2 to mediate GPCR endocytosis. 5. GPCRs continue to signal in endosomes. 6. GPCRs that promote prolonged endosomal G protein signaling can interact with β ARRs in the tail conformation. Since β ARR does not occupy the G-protein-binding site when in complex with a GPCR in the tail conformation, the receptor can form GPCR/G protein/ β ARR complex that continues to stimulate G protein signaling. 7. G-protein- and β ARR-dependent signaling from endosomes leads to generation of second messengers such as cAMP, and phosphorylation of signaling proteins including PKC and ERK1/2, which can regulate nuclear events (8). Abbreviations: AP2, adaptor protein-2; β ARR, β -arrestin; CREB, cAMP response element binding protein; ERK, extracellular signal-regulated kinase; GPCR, G-protein-coupled receptor; GRK, G-protein-coupled receptor kinase; PKC, protein kinase C.

substance P (SP)-evoked endocytosis of the NK₁R, and suppress activation of cytosolic **cAMP** and **protein kinase C** (PKC) and nuclear ERK [12]. In contrast, these treatments do not affect SP stimulation of cAMP at the plasma membrane or ERK in the cytosol, and enhance PKC activation at the plasma membrane. Thus, the NK₁R in early endosomes activates cAMP and PKC in the cytosol and ERK in the nucleus, which proceed by β ARR- and G-protein-dependent mechanisms. The receptor for calcitonin gene-related peptide (CGRP), CLR, signals from endosomes in a similar manner [14]. Barbadin, an inhibitor of β ARR/AP2 interactions, blocks agonist-induced endocytosis of the β_2 AR and V₂R, prevents V₂R-dependent ERK activation, and inhibits β_2 AR- and V₂R-mediated cAMP production [34]. Endosomal signaling of PTHR, TSHR, and β_2 AR also drives cytosolic cAMP production [35]. Signaling of GPCRs in endosomes may underlie long-term effects, since the β_2 AR and NK₁R in endosomes regulate cAMP- and ERK1/2-dependent regulation of transcription [12,35]. Disruption of the endosomal transmembrane peptidase endothelin-converting enzyme-1, which degrades SP in endosomes and destabilizes the NK₁R/ β ARR complex [11], leads to enhanced activation of nuclear ERK [36].

Studies of endosomal signaling of **receptor tyrosine kinases** (RTKs), notably the epidermal growth factor receptor (EGFR), have also provided insights into the mechanisms by which different GPCRs can selectively regulate cellular responses. RTKs, like GPCRs, can internalize by clathrin- and dynamin-mediated mechanisms, and can continue to signal from endosomes. The answer to the quandary of how different growth factors can elicit divergent cellular responses by engaging the same signaling machinery may lie in the mechanisms by which the EGFR signals from endosomes [37]. The use of quantitative high-resolution microscopy has revealed that the phosphorylated EGFR is packaged into discrete amounts or quanta in endosomes; cells respond to increasing amounts of EGF by increasing the number of endosomes, each with a constant amount of phosphorylated EGFR. By altering the number of endosomes containing phosphorylated EGFR, different growth factors can differentially control the cellular response. Thus, the packaging of phosphorylated EGFR in endosomes ensures the fidelity of signaling [37]. This quantal packaging of receptors has not been shown with GPCRs but does provide a possible framework to understand how increased internalization and endosomal signaling of GPCRs can regulate cellular responses.

Given the heterogeneous nature of the endosomal network, it is not surprising that certain subcompartments are particularly important sites of GPCR signaling. For example, **very early endosomes** (VEEs), which lack markers for early endosomes (e.g., Rab5a, phosphatidylinositol-3), are sites of sustained LHR-dependent ERK signaling. The adaptor protein containing pleckstrin homology domain, phosphotyrosine-binding domain, and leucine zipper motif 1 (APPL1) regulates LHR sorting and signaling within VEEs, since APPL1 knockdown causes LHR retention in VEEs and enhanced cAMP responses [38]. Thus, APPL1 mediates rapid LHR recycling from VEEs to the plasma membrane, and APPL1 is a negative regulator of LHR-mediated cAMP production from VEEs.

GPCRs can translocate from endosomes to other organelles, where they can continue to signal. The S1PR1 and TSHR receptor retrogradely traffic from endosomes to the **trans-Golgi network** (TGN). S1PR1 generates sustained G α_i -dependent signals from the TGN [16] and, once trafficked to the TGN and positioned next to the nucleus, TSHR activates G α_s , resulting in cAMP accumulation and the activation of the **cAMP response element binding protein** (CREB) within the nucleus [39]. TSHR in the TGN also generates a delayed yet sustained PKA response. Inhibition of TSHR endocytosis or disruption of the TGN abrogates cAMP and PKA responses. Thus, GPCRs shuttle between the plasma membrane, endosomes and TGN, and

each of these subcellular domains provides a platform to modify and fine-tune cellular responses to extracellular stimuli.

Contribution of Endosomal Signaling of GPCRs to Pathophysiological Control

Recent observations suggest that endosomal signaling of GPCRs regulates important physiological and pathophysiological processes in intact tissues and animals. The NK₁R mediates SP-dependent pain transmission by second-order neurons in the dorsal horn of the spinal cord. Painful stimuli of peripheral tissues, for example, intraplantar injection (injection into the foot) of capsaicin, formalin, or complete Freund's adjuvant, trigger clathrin- and dynamin-dependent endocytosis of the NK₁R in spinal neurons, which is attributable to the release of SP from the central projections of **nociceptors** in the dorsal horn [12]. NK₁R endocytosis correlates with activation of ERK1/2 in spinal neurons [12]. The intrathecal injection of pharmacological inhibitors of dynamin and clathrin, or of dynamin-1 or β ARR siRNA, inhibits NK₁R endocytosis and ERK1/2 activation in spinal neurons, and suppresses mechanical nociception in response to intraplantar injection of capsaicin, formalin or complete Freund's adjuvant. Although disruption of dynamin and clathrin can affect the trafficking of many receptors and channels, selective inhibitors of NK₁R/ β ARR interactions also prevent NK₁R endocytosis and inhibit nociception in mice. Electrophysiological studies in slice preparations of rat spinal cord provide insights into the link between NK₁R endocytosis and pain transmission. Transient stimulation with SP induces a rapid-onset firing of action potentials that persists after washout and is accompanied by NK₁R endocytosis. Inhibitors of dynamin and of signals that derive from the NK₁R in endosomes (PKC and ERK) prevent sustained SP-induced excitation of spinal neurons, which requires persistent signaling of NK₁R from endosomes [12]. The CGRP receptor, CLR, is coexpressed on spinal neurons with the NK₁R, and also undergoes clathrin- and dynamin-dependent endocytosis [14]. Dynamin inhibitors, and inhibitors of ERK and PKC, similarly prevent the sustained actions of CGRP in excitation of spinal neurons. Studies with NK₁R and CLR antagonists that are targeted to endosomes, which is described in 'Therapeutic Targeting of GPCRs in Subcellular Compartments' section, reinforce the concept that endosomes are platforms for sustained SP- and CGRP-mediated pain transmission.

Pituitary adenylate cyclase 1 receptor (PAC1) provides another example of the importance of endosomal signaling in regulating neuronal excitability. PAC1 signaling from endosomes is necessary for MEK/ERK activation in cardiac ganglia neurons [40] and inhibitors of endocytosis block **pituitary adenylate cyclase-activating peptide** (PACAP)-induced increases in neuronal excitability [41]. In the amygdala, endosomal signaling of PAC1 is necessary for neuronal activation and nociceptive responses [42].

Endosomal signaling of GPCRs may contribute to human disease [43]. **Irritable bowel syndrome** (IBS) is characterized by abdominal pain and disrupted bowel habits (constipation and diarrhea). Proteases derived from colonocytes and immune cells that infiltrate the colon wall (e.g., mast cells, macrophages, and neutrophils), and **protease-activated receptor-2** (PAR₂), a GPCR that is expressed by primary sensory neurons or nociceptors, are strongly implicated in IBS pain. Proteases released from biopsies of colon from IBS patients cause a sustained hyperexcitability of nociceptors, a hallmark of chronic pain, and inhibitors of clathrin- and dynamin-dependent endocytosis, and an antagonist of endosomal PAR₂ (described in the section 'Therapeutic Targeting of GPCRs in Subcellular Compartments') prevent excitability of nociceptors, and may represent a novel therapy for IBS pain [43]. However, different proteases can activate PAR₂ and cause pain by distinct signaling mechanisms. Proteases such as trypsin and mast cells tryptase cleave and activate PAR₂ by canonical mechanisms, which include

coupling to G_{α_q} , recruitment of β ARRs, and receptor endocytosis. Inhibitors of dynamin and clathrin-dependent endocytosis and of ERK activation prevent sustained trypsin-induced hyperexcitability of nociceptors and pain, which presumably require PAR_2 endocytosis and endosomal signaling to activate ERK [43]. ERK in turn then regulates ion channels that mediate neuronal hyperexcitability. In contrast, neutrophil elastase and macrophage cathepsin S cleave PAR_2 at different sites and activate the receptor by biased mechanisms, which include coupling to G_{α_s} , but not β ARRs nor endocytosis. Inhibitors of dynamin and clathrin do not affect sustained elastase- and cathepsin-S-evoked nociceptor hyperexcitability or pain, which instead depend on PAR_2 signaling from the plasma membrane, activation of adenylyl cyclase, and cAMP-mediated activation of protein kinase A [43]. These studies provide insights into the relative contributions of signals that emanate from GPCRs at the plasma membrane and in endosomes to pain transmission. They show that the same GPCR can signal by divergent pathways from distinct subcellular domains (plasma membrane or endosomes) to induce a physiological response.

Thus, GPCRs in endosomes signal by mechanisms that are distinct from those that originate from GPCRs at plasma membrane, and can control unique physiological and pathological processes. A better understanding of the signaling events that are regulated by GPCRs at plasma and endosomal membranes, and of the contribution of these signals to the control of physiological and pathophysiological responses, may enable the design of more selective and effective therapies for GPCR-regulated diseases.

Therapeutic Targeting of GPCRs in Subcellular Compartments

The discovery that GPCRs in endosomes can generate sustained signals in subcellular compartments that underlie important pathophysiological processes has implications for therapy with antagonists and agonists. In situations where endosomal signaling mediates disease-relevant processes, for example, chronic pain, antagonists that target GPCRs in endosomes may be a superior therapeutic approach compared with agents that act primarily at the plasma membrane. Conversely, the therapeutic efficacy of agonists of GPCRs could be enhanced by improving their capacity to generate sustained signals from endosomes.

Endosomally Biased GPCR Agonists

Endogenous agonists that stimulate G protein signaling from endosomes tend to bind GPCRs tightly. These agonists include peptides or small proteins that remain associated with GPCRs even in the acidified endosomal lumen. The tight agonist/GPCR association maintains the receptor in an active state within endosomes, and thereby enables continued G protein signaling.

The correlation between tight agonist/GPCR association and sustained endosomal signaling is illustrated by the PTHR, for which there are several peptide agonists. PTH(1–34) displays an exceptional ability to stabilize an active state and remain associated with PTHR for prolonged periods, whereas **PTH-related protein** [PTHrP(1–36)] rapidly dissociates, especially when PTHR is not complexed with G proteins [17,44]. PTH(1–34) remains associated with PTHR in endosomes, leading to sustained endosomal signaling. In contrast, PTHrP(1–36) dissociates from PTHR soon after internalization; in consequence, there is minimal endosomal signaling before the PTHR recycles. The ability of **parathyroid hormone** (PTH), but not PTHrP, to promote sustained endosomal signaling may account for enhanced renal production of 1,25-dihydroxy-vitamin D_3 and resulting increases in serum calcium [45,46].

The V_2R provides another example of the correlation between the stability of agonist/GPCR interaction with the balance between plasma membrane and endosomal signaling. Arginine

vasopressin binds tightly to the V_2R , which results in prolonged internalization and endosomal G protein signaling, whereas oxytocin binds to V_2R with lower affinity and dissociates from the receptor soon after internalization, which results in predominant plasma membrane G protein signaling [18,47]. V_2R -stimulated $G\alpha_s$ /cAMP signaling promotes translocation of aquaporin water channels and epithelial sodium channels (ENaCs) from intracellular vesicles to the apical membrane of collecting duct cells, which increases renal water and sodium reabsorption. The sustained endosomal $G\alpha_s$ /cAMP response to arginine vasopressin explains why it has superior antidiuretic and antinatriuretic effects over oxytocin [18].

Several factors are likely to determine the stability and agonist/GPCR interactions in endosomes and thus the duration of endosomal signals. The charge and conformation of agonists and their receptors, which depend on the local pH and association of the receptor with signaling and regulatory partners, can affect the affinity and duration of agonist/GPCR association in acidic endosomes. The stability of agonists can also determine the half-life of agonist/GPCR complexes in endosomes. By degrading neuropeptides (SP, CGRP, and somatostatin-14) in acidified early endosomes, endothelin-converting enzyme-1 triggers disassembly of agonist/GPCR/ β ARR complexes, promotes receptor recycling, and terminates endosomal ERK signaling [10,11,36]. Analogs that are resistant to this peptidase, including somatostatin-28 and octreotide, induce remarkably sustained sequestration of somatostatin receptors in endosomes, which may explain their therapeutically beneficial actions [48].

An understanding of how the agonist/GPCR residence time affects the subcellular location and endpoints of receptor activation can inform the development of therapeutic agonists with unique and sustained actions. Modified versions of PTH have been made to promote prolonged endosomal PTHR-mediated responses [49,50]. **Long-acting PTH** (LA-PTH), which is a hybrid between modified PTH(1–14) and PTHrP(15–36), binds PTHR much tighter than PTH(1–34) does and promotes remarkably sustained endosomal G protein signaling after agonist washout [50]. A single intravenous injection of LA-PTH promotes hypercalcemia and hypophosphatemia that persists for >48 h, despite clearance from the circulation within 1 h. LA-PTH effectively corrects calcium and phosphorus homeostasis in animals with hypoparathyroidism [50,51].

Thus, the design of GPCR agonists that tightly bind to receptors in endosomes, in a manner that is insensitive to low endosomal pH and to endosomal enzymatic activity, may be an effective strategy to develop drugs with superior and long-lasting efficacy.

Endosomally Biased GPCR Antagonists

The appreciation that GPCR signaling in endosomes can underlie pathology of some chronic diseases suggests that the targeting of endosomal GPCRs with antagonists would offer an improved therapeutic approach. This concept has been explored by conjugating peptidic antagonists of the NK_1R (Spantide) and CLR (CGRP_{8–37}) to **polyethylene glycol** (PEG) and the transmembrane lipid cholesterol [12,14]. Cholesterol-conjugated probes rapidly incorporate into the plasma membrane and then become concentrated and retained in early endosomes containing the NK_1R and CLR. Once accumulated in endosomes, spantide-PEG-cholesterol and CGRP_{8–37}-PEG-cholesterol selectively inhibit signals that emanate from endosomal NK_1R and CLR (e.g., nuclear ERK), without affecting signals from plasma membrane receptors (e.g., cytosolic ERK). Spantide-PEG-cholesterol and CGRP_{8–37}-PEG-cholesterol respectively inhibit sustained SP- and CGRP-induced excitation of spinal neurons in slice preparations, whereas unconjugated antagonists are less effective. When injected intrathecally, spantide-PEG-cholesterol and CGRP_{8–37}-PEG-cholesterol cause a remarkably sustained inhibition of mechanical nociceptive responses to intraplantar injection of capsaicin, formalin, or complete

Freund's adjuvant, compared to unconjugated antagonists [12,14]. In a similar manner, a cholestanol-conjugated antagonist of PAR₂ prevents the capacity of proteases that are released from biopsies of colonic mucosa obtained from patients with IBS to cause sustained hyperexcitability of nociceptors [43]. Such endosomally targeted antagonists of PAR₂ could represent a treatment for the common problem of IBS pain.

These studies reveal that endosomally targeted GPCR antagonists not only inhibit sustained endosomal signaling, but more effectively inhibit pain than conventional antagonists in preclinical models. The modification of existing antagonists to target endosomes or to promote their sustained interactions with GPCRs in endosomes may enhance their therapeutic efficacy. The results raise the possibility that the inability of antagonists to engage GPCRs in endosomes explains the limited efficacy of some of these agents in chronic diseases, where GPCRs could be largely internalized due to the continuous release of endogenous ligands.

Concluding Remarks and Future Perspectives

The traditional views that GPCR signaling emanates principally from the plasma membrane and that cell surface GPCRs are the optimal target for therapeutically beneficial drugs are incomplete. Upon activation at the cell surface, many GPCRs and agonists traffic to endosomes, where they can continue to signal by G protein- and β ARR-dependent mechanisms. In contrast to the signals that arise from GPCRs at the plasma membrane, which are rapidly terminated by β ARR-mediated receptor desensitization and endocytosis, signals from GPCRs in endosomes are often sustained. As GPCRs traffic through the endosomal network, they can generate signals in subcellular microdomains that control important cellular responses, including gene transcription in the nucleus and channel activity at the plasma membrane. Thus, endosomes are not merely a conduit for GPCR trafficking to degradatory or recycling pathways, but are a vital site of intracellular GPCR signaling.

Our knowledge of GPCR signaling from endosomes is incomplete (see Outstanding Questions). Structural studies have provided major insights into the molecular mechanisms by which GPCRs can engage G proteins and β ARRs. However, these studies mostly focus on plasma membrane signaling events, rely on the use of GPCRs that are stabilized by extensive mutations or crosslinking, usually require antibodies or nanobodies to stabilize signaling complexes, and offer a fleeting snapshot of the structural underpinnings of signal transduction. New technologies are required to reveal the molecular details of signaling by unmodified GPCRs and their spectrum of signaling and regulatory partners in subcellular microdomains of functionally relevant cells and in real time. Approaches such as **cryoelectron tomography**, which can provide structural information about protein signaling complexes in intact cells, may be useful in this regard [52]. GPCRs in endosomes can engage G proteins (G_s , $G_{i/o}$, and G_q) and β ARRs, which in turn control formation of second messengers (e.g., cAMP) and activation of kinases (e.g., PKC and ERK). However, the ability of GPCRs in endosomes to control activation of the full spectrum of signaling pathways awaits further investigation. Unbiased proteomic approaches, including **GPCR-APEX**, can be used to identify components of GPCR signaling complexes in living cells, and may provide information about the full spectrum of signaling events that emanate from GPCRs in endosomes [53]. Most information about endosomal signaling derives from observations in model cells; cell lines that are used to express and study particular protein-protein interactions and signaling cascades. Unfortunately, the relative contributions of plasma membrane and endosomal signaling to the control of complex pathophysiological processes in intact tissues and animals is poorly understood. The mechanisms that terminate plasma membrane GPCR signaling have been intensively studied, whereas the control of endosomal signaling remains to be fully defined.

Outstanding Questions

How do β ARRs positively modulate endosomal G protein signaling of GPCRs?

Do β ARRs simply increase the endosomal to plasma membrane GPCR ratio to enhance G protein signaling from endosomes?

Do β ARRs in the GPC/G protein/ β ARR megaplex maintain close proximity between GPCRs and G proteins to enhance the activation rate of G proteins?

How is endosomal GPCR signaling regulated?

What scaffolding proteins maintain the endosomal GPCR signaling complex?

What is the termination signal – peptidases that degrade peptide agonists, proteases that cleave GPCRs, phosphatases that dephosphorylate GPCRs?

Although agonists promote GPCR endocytosis, what are the factors that control GPCR trafficking within the cell, from endosomes and the TGN?

Are there specific molecular determinants located within GPCRs, which controls this mode of trafficking?

What regulatory proteins are involved in this mode of trafficking?

What is the relative contribution of plasma membrane and endosomal signaling of GPCRs to physiological control and mechanisms of disease in intact animals?

Are endosomally biased antagonists the optimal therapy?

Does this happen in all cell types or is it regulated differently from one cell/tissue type to another?

The concept that GPCRs in endosomes control important pathophysiological processes has implications for drug discovery and development. Although GPCRs are the single largest target of therapeutic drugs, drug discovery efforts have focused on the identification of agonists or antagonists of GPCRs at the plasma membrane. Whether drugs that preferentially target GPCRs in endosomes might show superior efficacy and selectivity remains to be determined. Agonists of GPCRs are likely to activate GPCRs at the plasma membrane and in endosomes, but whether their therapeutically beneficial effects derive from GPCRs in a defined subcellular region remains to be determined. It may be possible to engineer endosomally biased agonists that preferentially interact with GPCRs in an acidic environment, which could be therapeutically useful. The μ -opioid receptor is a GPCR present on sensory neurons that, when activated, has an analgesic effect. Unfortunately, μ -opioid receptor agonists also give rise to many adverse side effects like constipation and respiratory depression. An analog of fentanyl that preferentially interacts with the μ -opioid receptor in the slightly acidic conditions of injured and diseased tissue is efficacious for the treatment of inflammatory pain but largely devoid of the detrimental side effects of respiratory depression, sedation, and constipation, by virtue of its inability to interact with the receptor at normal extracellular pH [54]. It remains to be determined whether the therapeutically beneficial effects of this analog are due to activation of the μ -opioid receptor in acidified endosomes. Another approach to deliver GPCR ligands to endosomes could be encapsulation into nanoparticles, which enter cells by clathrin-dependent endocytosis and have been used to deliver chemotherapeutic agents to tumor cells [55]. The ability of agonists to activate GPCRs in subcellular compartments could also relate to their distribution throughout the cell. The use of a genetically encoded biosensor, a fluorescent protein that can sense and report changes in cellular responses, to detect activated conformations of opioid receptors in specific cellular domains revealed that whereas peptide agonists activate receptors first at the plasma membrane and then in endosomes, non-peptide drugs such as morphine can also activate receptors in the Golgi apparatus [56]. Whether abnormal activation of GPCRs in subcellular domains contributes to adverse effects of certain agonists deserves further study. During chronic disease, it is likely that many GPCRs redistribute from the plasma membrane to endosomes due to the continued generation of endogenous agonists. Under these circumstances, GPCRs in endosomes are likely to be a valid therapeutic target. However, whether drugs can penetrate the plasma and endosomal membranes and effectively engage GPCR conformations in an acidified endosomal environment in which receptors are likely complexed with multiple signaling and regulatory partners is uncertain. Compartment-specific GPCR ligands, designed to produce beneficial effects by targeting pathological GPCR signaling but without affecting signaling from microdomains that may provoke unwanted side effects represents a novel approach to improve upon current therapies for chronic diseases.

Acknowledgments

Supported by grants from the National Institutes of Health (NS102722, DE026806, DK118971), and Department of Defense W81XWH1810431 (NWB).

Disclaimer Statement

N.B. and G.H. are founding scientists of Endosome Therapeutics Inc.

References

1. Hanlon, C.D. and Andrew, D.J. (2015) Outside-in signaling – a brief review of GPCR signaling with a focus on the *Drosophila* GPCR family. *J. Cell Sci.* 128, 3533–3542
2. Hauser, A.S. *et al.* (2017) Trends in GPCR drug discovery: new agents, targets and indications. *Nat. Rev. Drug Discov.* 16, 829–842
3. Komolov, K.E. and Benovic, J.L. (2018) G protein-coupled receptor kinases: past, present and future. *Cell Signal.* 41, 17–24
4. Peterson, Y.K. and Luttrell, L.M. (2017) The diverse roles of arrestin scaffolds in G protein-coupled receptor signaling. *Pharmacol. Rev.* 69, 256–297

5. Shukla, A.K. *et al.* (2014) Visualization of arrestin recruitment by a G-protein-coupled receptor. *Nature* 512, 218–222
6. Kang, Y. *et al.* (2015) Crystal structure of rhodopsin bound to arrestin by femtosecond X-ray laser. *Nature* 523, 561–567
7. Szczeppek, M. *et al.* (2014) Crystal structure of a common GPCR-binding interface for G protein and arrestin. *Nat. Commun.* 5, 4801–4809
8. Oakley, R.H. *et al.* (2000) Differential affinities of visual arrestin, beta arrestin1, and beta arrestin2 for G protein-coupled receptors delineate two major classes of receptors. *J. Biol. Chem.* 275, 17201–17210
9. Oakley, R.H. *et al.* (1999) Association of beta-arrestin with G protein-coupled receptors during clathrin-mediated endocytosis dictates the profile of receptor resensitization. *J. Biol. Chem.* 274, 32248–32257
10. Padilla, B.E. *et al.* (2007) Endothelin-converting enzyme-1 regulates endosomal sorting of calcitonin receptor-like receptor and beta-arrestins. *J. Cell Biol.* 179, 981–997
11. Roosterman, D. *et al.* (2007) Endothelin-converting enzyme 1 degrades neuropeptides in endosomes to control receptor recycling. *Proc. Natl. Acad. Sci. U. S. A.* 104, 11838–11843
12. Jensen, D.D. *et al.* (2017) Neurokinin 1 receptor signaling in endosomes mediates sustained nociception and is a viable therapeutic target for prolonged pain relief. *Sci. Transl. Med.* 9, eaal3447
13. Vilardaga, J.P. *et al.* (2014) Endosomal generation of cAMP in GPCR signaling. *Nat. Chem. Biol.* 10, 700–706
14. Yarwood, R.E. *et al.* (2017) Endosomal signaling of the receptor for calcitonin gene-related peptide mediates pain transmission. *Proc. Natl. Acad. Sci. U. S. A.* 114, 12309–12314
15. Slessareva, J.E. *et al.* (2006) Activation of the phosphatidylinositol 3-kinase Vps34 by a G protein alpha subunit at the endosome. *Cell* 126, 191–203
16. Mullershausen, F. *et al.* (2009) Persistent signaling induced by FTY720-phosphate is mediated by internalized S1P1 receptors. *Nat. Chem. Biol.* 5, 428–434
17. Ferrandon, S. *et al.* (2009) Sustained cyclic AMP production by parathyroid hormone receptor endocytosis. *Nat. Chem. Biol.* 5, 734–742
18. Feinstein, T.N. *et al.* (2013) Noncanonical control of vasopressin receptor type 2 signaling by retromer and arrestin. *J. Biol. Chem.* 288, 27849–27860
19. Calebiro, D. *et al.* (2009) Persistent cAMP-signals triggered by internalized G-protein-coupled receptors. *PLoS Biol.* 7, e1000172
20. Irannejad, R. *et al.* (2013) Conformational biosensors reveal GPCR signalling from endosomes. *Nature* 495, 534–538
21. Lyga, S. *et al.* (2016) Persistent cAMP signaling by internalized LH receptors in ovarian follicles. *Endocrinology* 157, 1613–1621
22. Gilliland, C.T. *et al.* (2013) The chemokine receptor CCR1 is constitutively active, which leads to G protein-independent, beta-arrestin-mediated internalization. *J. Biol. Chem.* 288, 32194–32210
23. Zhou, X.E. *et al.* (2017) Identification of phosphorylation codes for arrestin recruitment by G protein-coupled receptors. *Cell* 170, 457–469 e13
24. Thomsen, A.R.B. *et al.* (2016) GPCR-G Protein-beta-arrestin super-complex mediates sustained G protein signaling. *Cell* 166, 907–919
25. Wehbi, V.L. *et al.* (2013) Noncanonical GPCR signaling arising from a PTH receptor-arrestin-Gbetagamma complex. *Proc. Natl. Acad. Sci. U. S. A.* 110, 1530–1535
26. Feinstein, T.N. *et al.* (2011) Retromer terminates the generation of cAMP by internalized PTH receptors. *Nat. Chem. Biol.* 7, 278–284
27. Cahill, T.J., 3rd *et al.* (2017) Distinct conformations of GPCR-beta-arrestin complexes mediate desensitization, signaling, and endocytosis. *Proc. Natl. Acad. Sci. U. S. A.* 114, 2562–2567
28. Kumari, P. *et al.* (2016) Functional competence of a partially engaged GPCR-beta-arrestin complex. *Nat. Commun.* 7, 13416–13432
29. Kumari, P. *et al.* (2017) Core engagement with beta-arrestin is dispensable for agonist-induced vasopressin receptor endocytosis and ERK activation. *Mol. Biol. Cell* 28, 1003–1010
30. Wanka, L. *et al.* (2018) Different mode of arrestin-3 binding at the human Y1 and Y2 receptor. *Cell Signal.* 50, 58–71
31. Toth, A.D. *et al.* (2018) Heterologous phosphorylation-induced formation of a stability lock permits regulation of inactive receptors by beta-arrestins. *J. Biol. Chem.* 293, 876–892
32. Latorraca, N.R. *et al.* (2018) Molecular mechanism of GPCR-mediated arrestin activation. *Nature* 557, 452–456
33. Eichel, K. *et al.* (2018) Catalytic activation of beta-arrestin by GPCRs. *Nature* 557, 381–386
34. Beautrait, A. *et al.* (2017) A new inhibitor of the beta-arrestin/AP2 endocytic complex reveals interplay between GPCR internalization and signalling. *Nat. Commun.* 8, 15054–15070
35. Tsvetanova, N.G. and von Zastrow, M. (2014) Spatial encoding of cyclic AMP signaling specificity by GPCR endocytosis. *Nat. Chem. Biol.* 10, 1061–1065
36. Cottrell, G.S. *et al.* (2009) Endosomal endothelin-converting enzyme-1: a regulator of beta-arrestin-dependent ERK signaling. *J. Biol. Chem.* 284, 22411–22425
37. Villasenor, R. *et al.* (2015) Regulation of EGFR signal transduction by analogue-to-digital conversion in endosomes. *eLife* 4, e06156
38. Sposini, S. *et al.* (2017) Integration of GPCR signaling and sorting from very early endosomes via opposing APPL1 mechanisms. *Cell Rep.* 21, 2855–2867
39. Godbole, A. *et al.* (2017) Internalized TSH receptors en route to the TGN induce local Gs-protein signaling and gene transcription. *Nat. Commun.* 8, 443–458
40. May, V. and Parsons, R.L. (2017) G protein-coupled receptor endosomal signaling and regulation of neuronal excitability and stress responses: signaling options and lessons from the PAC1 receptor. *J. Cell Physiol.* 232, 698–706
41. Merriam, L.A. *et al.* (2013) Pituitary adenylate cyclase 1 receptor internalization and endosomal signaling mediate the pituitary adenylate cyclase activating polypeptide-induced increase in guinea pig cardiac neuron excitability. *J. Neurosci.* 33, 4614–4622
42. Missig, G. *et al.* (2017) Parabrachial pituitary adenylate cyclase-activating polypeptide activation of amygdala endosomal extracellular signal-regulated kinase signaling regulates the emotional component of pain. *Biol. Psychiatry* 81, 671–682
43. Jimenez-Vargas, N.N. *et al.* (2018) Protease-activated receptor-2 in endosomes signals persistent pain of irritable bowel syndrome. *Proc. Natl. Acad. Sci.* 115, e7438–7447
44. Dean, T. *et al.* (2008) Altered selectivity of parathyroid hormone (PTH) and PTH-related protein (PTHrP) for distinct conformations of the PTH/PTHrP receptor. *Mol. Endocrinol.* 22, 156–166
45. Horwitz, M.J. *et al.* (2003) Direct comparison of sustained infusion of human parathyroid hormone-related protein-(1-36) hPTHrP-(1-36)] versus hPTH-(1-34) on serum calcium, plasma 1,25-dihydroxyvitamin D concentrations, and fractional calcium excretion in healthy human volunteers. *J. Clin. Endocrinol. Metab.* 88, 1603–1609
46. Horwitz, M.J. *et al.* (2005) Continuous PTH and PTHrP infusion causes suppression of bone formation and discordant effects on 1,25(OH)₂ vitamin D. *J. Bone Miner. Res.* 20, 1792–1803
47. Zalyapin, E.A. *et al.* (2008) Effects of the renal medullary pH and ionic environment on vasopressin binding and signaling. *Kidney Int.* 74, 1557–1567
48. Zhao, P. *et al.* (2013) Agonist-biased trafficking of somatostatin receptor 2A in enteric neurons. *J. Biol. Chem.* 288, 25689–25700
49. Okazaki, M. *et al.* (2008) Prolonged signaling at the parathyroid hormone receptor by peptide ligands targeted to a specific receptor conformation. *Proc. Natl. Acad. Sci. U. S. A.* 105, 16525–16530

50. Maeda, A. *et al.* (2013) Critical role of parathyroid hormone (PTH) receptor-1 phosphorylation in regulating acute responses to PTH. *Proc. Natl. Acad. Sci. U. S. A.* 110, 5864–5869
51. Shimizu, M. *et al.* (2016) Pharmacodynamic actions of a long-acting PTH analog (LA-PTH) in thyroparathyroidectomized (TPTX) rats and normal monkeys. *J. Bone Miner. Res.* 31, 1405–1412
52. Pfeffer, S. *et al.* (2017) Dissecting the molecular organization of the translocon-associated protein complex. *Nat. Commun.* 8, 14516–14525
53. Paek, J. *et al.* (2017) Multidimensional tracking of GPCR signaling via peroxidase-catalyzed proximity labeling. *Cell* 169, 338–349. e11
54. Spahn, V. *et al.* (2017) A nontoxic pain killer designed by modeling of pathological receptor conformations. *Science* 355, 966–969
55. Sun, J. *et al.* (2017) A distinct endocytic mechanism of functionalized-silica nanoparticles in breast cancer stem cells. *Sci. Rep.* 7, 16236–16249
56. Stoeber, M. *et al.* (2018) A genetically encoded biosensor reveals location bias of opioid drug action. *Neuron* 98, 963–976 e5



Published in final edited form as:

Gastroenterology. 2019 May ; 156(6): 1600–1616. doi:10.1053/j.gastro.2019.01.266.

G-Protein–Coupled Receptors Are Dynamic Regulators of Digestion and Targets for Digestive Diseases

Meritxell Canals¹, Daniel P. Poole^{2,3}, Nicholas A. Veldhuis², Brian L. Schmidt⁴, and Nigel W. Bunnett^{2,5,6}

¹Centre for Membrane Proteins and Receptors (COMPARE), School of Life Sciences, University of Nottingham, Nottingham, United Kingdom

²Monash Institute of Pharmaceutical Sciences and Australian Research Council Centre of Excellence in Convergent Bio-Nano Science and Technology, Monash University, Parkville, Victoria, Australia

³Department of Anatomy and Neuroscience, University of Melbourne, Parkville, Victoria, Australia

⁴Bluestone Center for Clinical Research, New York University College of Dentistry, New York, New York

⁵Department of Pharmacology and Therapeutics, University of Melbourne, Parkville, Victoria, Australia

⁶Columbia University College of Physicians and Surgeons, Columbia University, New York, New York

Abstract

G-protein–coupled receptors (GPCRs) are the largest family of transmembrane signaling proteins. In the gastrointestinal tract, GPCRs expressed by epithelial cells sense contents of the lumen, and GPCRs expressed by epithelial cells, myocytes, neurons, and immune cells participate in communication among cells. GPCRs control digestion, mediate digestive diseases, and coordinate repair and growth. GPCRs are the target of more than one third of therapeutic drugs, including many drugs used to treat digestive diseases. Recent advances in structural, chemical, and cell biology research have shown that GPCRs are not static binary switches that operate from the plasma membrane to control a defined set of intracellular signals. Rather, GPCRs are dynamic signaling proteins that adopt distinct conformations and subcellular distributions when associated with different ligands and intracellular effectors. An understanding of the dynamic nature of GPCRs has provided insights into the mechanism of activation and signaling of GPCRs and has shown opportunities for drug discovery. We review the allosteric modulation, biased agonism, oligomerization, and compartmentalized signaling of GPCRs that control digestion and digestive

Reprint requests Address requests for reprints to: Nigel Bunnett, PhD, Columbia University College of Physicians and Surgeons, 21 Audubon Avenue, Room 209, New York, New York 10032. nb33@cumc.columbia.edu.
Author names in bold designate shared co-first authorship.

Conflicts of interest

Nigel W. Bunnett is a founding scientist of Endosome Therapeutics Inc. Research in the laboratories of Nigel W. Bunnett, Daniel P. Poole, and Nicholas A. Veldhuis is funded in part by Takeda Pharmaceuticals Inc.

diseases. We highlight the implications of these concepts for the development of selective and effective drugs to treat diseases of the gastrointestinal tract.

Keywords

Receptors; Signal Transduction; Trafficking; G Proteins; Drug Discovery

G-protein–coupled receptors (GPCRs) are the largest family of transmembrane signaling proteins, with approximately 800 members in the human genome. GPCRs transmit information about the external environment to the interior of the cell and thereby control most physiologic and pathologic processes. Approximately half the GPCRs have a sensory function and mediate olfaction, taste, perception of light, and pheromone signaling. Other GPCRs detect hormones, neurotransmitters, and paracrine factors and mediate communication among cells. GPCRs are the target of more than one third of therapeutic drugs, which illustrates their importance in disease and therapy.¹

The importance, diversity, and complexity of GPCRs are illustrated by their role in digestion and as targets for digestive disease (Figure 1). GPCRs with sensory functions in the digestive tract include receptors of taste buds for sweet, bitter, and savory tastes,² receptors of enteroendocrine cells for amino acids and proteins,³ and receptors of colonocytes for luminal proteases.⁴ GPCRs also sense the products of the microbiome. For instance, secondary bile acids, which are synthesized by bacteria in the colon, activate Takeda GPCR5 on enterochromaffin cells and enteric neurons to evoke peristalsis.⁵ Takeda GPCR5 expressed by cutaneous sensory nerves has been implicated in cholestatic pruritus.^{6,7} GPCRs of epithelial cells, myocytes, enteric neurons, and immune cells participate in cell-to-cell communication in the digestive system. They include receptors for structurally diverse ligands, including biogenic amines (catecholamines, histamine, serotonin), eicosanoids, amino acid transmitters, purine nucleotides, and neuropeptides, peptide hormones, and proteins. Thus, GPCRs orchestrate digestion (secretion, motility, transport), control disease processes (diseases of motility, secretion, inflammation, pain), and regulate growth and repair. Drugs that activate or inhibit GPCRs are effective therapies for digestive diseases (Figure 1).

Although the endogenous ligands of many GPCRs are known, there remain approximately 100 GPCRs with unidentified natural ligands. Some of these orphan GPCRs have roles in the digestive system. For example, the Mas-related GPCR (MRGPR) family is composed of approximately 40 orphan receptors expressed by primary sensory neurons and mast cells.⁸ MrgprX2 (human) or MrgprB2 (murine homologue) is expressed by mast cells and mediates antibody-independent responses to basic secretagogues, including drugs and peptides associated with pseudoallergic reactions.⁹ Substance P (SP), a gut neuropeptide, can activate MrgprX2. Mast cells are in proximity to sensory nerves containing SP and calcitonin gene-related peptide in the intestine.¹⁰ Therefore, neuropeptides and MrgprX2 might mediate the communication between sensory nerves and mast cells. Communication between sensory neurons and mast cells has been implicated in irritable bowel syndrome (IBS).¹¹

GPCRs share a conserved structure with 7 transmembrane domains, 3 extracellular and 3 intracellular loops, and extracellular (N-terminal) and intracellular (C-terminal) tails of varying sizes. GPCRs are grouped into 5 families based on structural and functional similarities. The rhodopsin family (class A) includes receptors for neurotransmitters, peptides, visual pigments, odorants, tastants, and pheromones. The secretin family (class B) is composed of receptors for polypeptide gut hormones, including glucagon, glucagon-like peptides, glucose-dependent insulinotropic polypeptide, secretin, vasoactive intestinal peptide, pituitary adenylate cyclase-activating polypeptide, and growth hormone-releasing hormone. The glutamate family (class C) includes metabotropic glutamate receptors, a calcium-sensing receptor, and γ -aminobutyric acid (GABA) B receptors. Adhesion family GPCRs possess a large extra-cellular N-terminus that is cleaved during activation. The frizzled family, which includes frizzled and smoothed proteins, is activated by lipoglycoproteins of the Wnt family (frizzled) and hedgehog family (smoothed). All GPCR families are represented in the digestive system.

This review highlights how recent advances in structural, chemical, and cellular biology research have provided an understanding of the mechanism of action of GPCRs. The traditional view that GPCRs are simple on and off switches that operate at the surface of cells to control a defined set of intracellular signals has been superseded by the realization that GPCRs are dynamic signaling proteins that can adopt different conformations and subcellular distributions, depending on the mechanisms of their activation.¹²

One aspect of the dynamic nature of GPCRs was exposed using x-ray crystallography and cryo-electron microscopy to probe GPCR structures. These approaches provided information about the organization of transmembrane, loop, and tail domains and their association with agonists, antagonists, G proteins, β -arrestins (ARRBs), and other signaling effectors.¹³⁻¹⁷ Limitations of structural studies of GPCRs include a requirement to stabilize receptors and signaling complexes by mutation, fusion to stabilizing proteins, or with single-domain antibodies (nano-bodies). Moreover, structural studies only provide snapshots of receptors frozen in time. However, structural analyses have shown that GPCRs adopt distinct conformations when bound to different agonists, antagonists, and intracellular effector and regulators. Two pharmacologic paradigms have emerged from an appreciation of the structural dynamism of GPCRs: allosteric modulation¹⁸ and biased agonism.¹⁹ Structural studies also have provided evidence that certain GPCRs exist as oligomers rather than as monomers.^{20,21}

A second component of the dynamic nature of GPCRs was discovered using biosensors, biophysical approaches, and advanced imaging to study the trafficking and signaling of GPCRs in subcellular micro-domains. These studies showed that GPCRs are motile signaling proteins that, at activation, can traffic from the cell surface to endosomes by dynamin- and clathrin-mediated endocytosis. GPCRs in endosomes can generate sustained signals in subcellular compartments (ie, compartmentalized signaling) that control physiologic and pathologic processes.²²⁻²⁷ Thus, GPCRs in endosomes, rather than at the plasma membrane, might be a target for therapy.²⁸

We discuss allosteric modulation, biased agonism, oligomerization, and compartmentalized signaling of GPCRs that control digestion and digestive diseases and consider the implications of these concepts for the development of drugs to treat gastrointestinal diseases.

Allosteric Modulators of GPCRs: Signaling Rheostats

Concept of Allosteric Modulation of GPCRs

Allosteric modulators are drugs or endogenous molecules that fine-tune the ability of agonists to activate GPCRs. The challenge of developing drugs that are selective for a particular GPCR subtype illustrates the potential of allosteric modulation for drug discovery. A single endogenous ligand can activate several GPCRs (eg, acetylcholine activates 5 muscarinic receptors, M₁₋₅Rs). These GPCR subtypes regulate processes within the digestive system and elsewhere. For example, studies in receptor knockout mice indicate that M₁R and M₃R regulate salivary secretion,²⁹ whereas M₂R and M₃R control intestinal smooth muscle contraction.³⁰ M₁R, M₄R, and M₅R function in the central nervous system.³¹ Because the binding sites for endogenous ligands (orthosteric sites; “right” or “proper” in Greek) are conserved between GPCR subtypes, it is challenging to identify subtype-selective drugs that occupy the same site as the natural ligand. An alternative approach to attain subtype selectivity is to develop drugs that bind to a different site (allosteric site; “other” in Greek).^{32,33} Ligands that interact with allosteric sites can induce changes in GPCR conformation that potentiate (positive allosteric modulators [PAMs]) or inhibit (negative allosteric modulators [NAMs]) endogenous agonists (Figure 2). Intracellular effectors, including G proteins and ARRBs, are physiologic allosteric modulators, because interaction with GPCRs induces changes in conformation that alter agonist affinity.^{34,35}

There are advantages to drugs that interact with allosteric rather than orthosteric sites. First, allosteric modulators might provide subtype selectivity, because the allosteric site is likely to be less conserved than the orthosteric site, which evolved to bind the same endogenous transmitter. Second, allosteric ligands modulate the activity of GPCRs that are bound to endogenous ligands, providing an opportunity to fine-tune physiologic responses. Third, because the magnitude of an allosteric effect is limited by cooperativity between orthosteric and allosteric sites, allosteric ligands have a ceiling level beyond which no further modulation occurs, with decreased propensity for overdose and toxicity. These advantages have led to drug discovery efforts focused on the identification of allosteric modulators of GPCRs,¹⁸ some of which have progressed to clinical trials.¹ However, there are only 2 approved allosteric modulators of GPCRs: maraviroc, a chemokine receptor 5 NAM that inhibits human immunodeficiency virus entry,³⁶ and cinacalcet, a calcium-sensing receptor PAM used to treat hyperparathyroidism.³⁷ These drugs were found to be allosteric modulators after regulatory approval.

Translational and Clinical Impact of Allosteric Modulators for Digestive Diseases

Consideration of the clinical utility of allosteric modulators of GPCRs raises 2 questions: are allosteric modulators a potential treatment for digestive diseases and will gastrointestinal-related adverse events prohibit use of PAMs and NAMs for non-gastrointestinal disorders?

PAMs and NAMs have been developed for several GPCRs found in the gastrointestinal tract; some have progressed to clinical trials (Table 1).

PAMs and NAMs have been identified for M₁₋₅R.³⁸ Allosteric targeting of M₁R, M₄R, and M₅R is an attractive treatment for disorders of the central nervous system, including schizophrenia, in which subtype-specificity would limit off-target effects on peripheral M₂R and M₃R, which are expressed in the digestive tract.³⁹ The M₁R PAM benzyl quinolone carboxylic acid alleviates cognitive deficits but induces diarrhea in mice.^{40,41} Compounds with differential positive cooperativity across subtypes could improve cognition with a lower risk of gastrointestinal side effects.⁴² MK-7622, an M₁R PAM, sensitizes M₁R to acetylcholine in the nanomolar range with no effect on M₂R, M₃R, or M₄R up to 100 μ mol/L.⁴³ MK-7622 improved cognitive testing in preclinical models. Two phase I trials tested MK-7622. MK-7622 produced an increase on the sigma band awake electroencephalogram, which indicated alertness. It also reversed the negative cognitive effects induced by scopolamine, a muscarinic receptor antagonist.⁴³ Based on these results, a phase IIa and IIb, multicenter, randomized, double-blind, placebo-controlled, parallel group trial was undertaken to evaluate the efficacy and safety of MK-7622 as an adjunctive therapy to acetylcholinesterase inhibitors for Alzheimer disease ([ClinicalTrials.gov](https://clinicaltrials.gov/ct2/show/study/NCT01852110), identifier [NCT01852110](https://clinicaltrials.gov/ct2/show/study/NCT01852110)). The trial was stopped because MK-7622 failed to improve cognition. Diarrhea, which is induced by acetylcholine, was the most common adverse event. Given the prominent role of M₂R and M₃R in regulating gastrointestinal smooth muscle, peripherally restricted allosteric modulators that fine-tune the actions of acetylcholine might offer a potential therapy for motility and secretory disturbances and visceral pain of IBS.⁴⁴

Opioids and associated μ -, δ -, and k -opioid receptors (μ -opioid receptor [MOR], δ -opioid receptor [DOR], and k -opioid receptor, respectively) are expressed throughout the gut. In addition to their analgesic properties, which are mediated by opioid receptors (ORs) expressed by primary sensory neurons and second-order spinal neurons, opioids inhibit intestinal motility and electrolyte and fluid secretion by activating ORs on enteric neurons. Orthosteric agonists of MOR are used to treat pain (eg, morphine, fentanyl) and diarrhea (eg, loperamide). However, their usefulness is limited by respiratory depression, constipation, and addiction. Morphine-induced analgesia is limited by tolerance (ie, decreased effectiveness with sustained use). MOR PAMs could provide effective therapy without adverse effects by amplifying the actions of endogenous opioids or by allowing a decrease of the dose of synthetic opioids. BMS-986122 is a MOR PAM that potentiates opioids and morphine.^{45,46} However, because respiratory depression and constipation are mediated by MOR, PAMs would be expected to potentiate these side effects. Although MOR is the prominent target of opioid analgesics, DOR also controls intestinal contractility.⁴⁷ DOR is a target for diarrhea-predominant IBS (IBS-D),⁴⁸ and enhancement of enkephalinergic signaling attenuates secretory diarrhea.⁴⁹ BMS-986187 is a DOR PAM that amplifies the actions of DOR agonists.⁵⁰ By modulating endogenous opioids, DOR PAMs have the potential to inhibit motility without causing constipation. Despite the promise of the MOR PAM (BMS-986122) and the DOR PAM (BMS-986187), the therapeutic potential of these drugs is yet to be assessed and they have not been tested in clinical trials.

Allosteric modulators of gut GPCRs have been described for the treatment of other digestive disorders. Glutamate, a transmitter of visceral and somatic pain, can activate ionotropic receptors (ion channels) and metabotropic GPCRs (MGLUR1–8). MGLUR5, which is expressed by vagal afferent endings of the gastroesophageal sphincter, regulates sphincter tone, providing a basis for the development of allosteric modulators of MGLUR5 for gastroesophageal reflux disease (GERD). ADX10059 is a MGLUR5 NAM. A randomized, patient-blind, placebo-controlled trial demonstrated that ADX10059 decreased GERD-related symptoms.⁵¹ Dizziness developed in 75% of participants. Then, ADX10059 was tested, at a lower dose, in a double-blind, placebo-controlled, multicenter trial in participants with proton pump inhibitor-responsive GERD. At this lower dose, ADX10059 increased symptom- and heartburn-free days and decreased regurgitation and sleep disturbance. Mild to moderate dizziness and vertigo were experienced by only 16% and 12% of patients, respectively⁵² ([ClinicalTrials.gov](https://clinicaltrials.gov/ct2/show/study/NCT00820079), identifier [NCT00820079](https://clinicaltrials.gov/ct2/show/study/NCT00820079)). Testing was stopped because long-term administration of ADX10059 in a trial for the prevention of migraine increased hepatic transaminases ([ClinicalTrials.gov](https://clinicaltrials.gov/ct2/show/study/NCT00820105), identifier [NCT00820105](https://clinicaltrials.gov/ct2/show/study/NCT00820105)). Liver enzyme increase resulted from metabolism of ADX10059 rather than MGLUR5 inhibition; therefore, negative allosteric modulation of MGLUR5 remains a viable approach for GERD.

Biased-Agonism of GPCRs: Shapeshifting Receptors and Pathway-Selective Drugs

Concept of Biased Agonism of GPCRs

Biased agonism describes the phenomenon in which the binding of different ligands, including endogenous ligands or drugs, to the same receptor in an identical cellular background results in differential activation of signaling pathways¹⁹ (Figure 3). Although this is the definition of ligand-biased agonism, other descriptions include differential localization of activated GPCRs (location bias) or differential signaling between various cell types (system bias). Biased agonism provides an avenue for pathway-selective drug discovery (ie, the development of drugs that modulate the beneficial pathways rather than those that give rise to adverse effects). Ligand bias can be attributed to different agonists stabilizing distinct conformations of GPCRs that couple to particular signaling effectors. Studies of serotonin receptors bound to the ARRB-biased agonists ergotamine and lysergic acid diethylamide support this concept.⁵³ However, robust structural evidence for this mechanism of biased agonism is lacking and will require studies of GPCRs in multiple activation states. The realization that GPCRs can be differentially activated within intracellular compartments (see Compartmentalized Signaling) has sparked interest in location bias as a therapeutic avenue.⁵⁴ System bias, which can be attributed to differences in the stoichiometric ratios of signaling effectors between cells, also offers a strategy for the design of effective therapies. However, these endeavors require an understanding of the signaling pathways in functionally relevant cells and of how they can be altered during disease, which, in most cases, is still lacking. Biased agonism of GPCRs has implications for physiologic control and drug discovery.

The mechanisms by which serine and cysteine proteases activate protease-activated receptor-2 (PAR₂) illustrate the relevance of biased agonism of a GPCR that controls gut

functions. PAR₂ is expressed throughout the digestive system, where it regulates inflammation, pain, motility, and secretion, and is a therapeutic target for inflammatory and functional disorders.⁵⁵ During disease, proteases become activated and trigger PAR₂ by distinct mechanisms.⁵⁶ Trypsin, from pancreatic secretions and colonocytes, and mast cell tryptase cleave within the extracellular N-terminus of PAR₂ at the R³⁶↓S³⁷ to expose a new N-terminal tethered ligand domain (S³⁷LIGKV). This domain then binds to extracellular loops of cleaved PAR₂, which couples to Ga_q, Ga_s, and ARRBs. PAR₂ internalizes and can continue to signal from endosomes (see Compartmentalized Signaling).^{25,57} This canonical mechanism, which operates in model cell lines and primary sensory neurons, was once considered the only way proteases could activate PAR₂. However, cathepsin-S from macrophages and neutrophil elastase cleave PAR₂ at different sites from trypsin and tryptase and activate PAR₂ by biased mechanisms.^{58,59} Cathepsin-S cleaves at E⁵⁶↓T⁵⁷ to show a distinct tethered ligand (T⁵⁷VFSVDEFSA), which binds to PAR₂ and induces coupling to Ga_s.⁵⁸ Elastase cleaves PAR₂ at S⁶⁷↓V⁶⁸, close to the first transmembrane domain, and activates the receptor by a mechanism that likely involves a conformational change rather than exposure of a tethered ligand and induces PAR₂ coupling to Ga_s and Ga_{12,13}.⁵⁹ After cleavage by cathepsin-S and elastase, PAR₂ couples to neither Ga_q nor ARRBs and does not internalize. An understanding of these mechanisms provides insights into how these proteases signal PAR₂-dependent pain, including inflammatory pain in the colon.²⁵ Trypsin evokes hyperexcitability of primary sensory neurons by mechanisms that depend on protein kinase C and extracellular signal regulated kinase, which are downstream from Ga_q.²⁵ Cathepsin-S and elastase evoke hyperexcitability of neurons by adenylyl cyclase- and protein kinase A- mediated pathways, downstream from Ga_s.^{25,58,59} The mechanisms by which proteases of different selectivity can activate PAR₂ represents biased signaling, in which the receptor couples to different G proteins depending on the site of cleavage. Other GPCRs that control gut functions also might be activated by biased mechanisms, although this has not been studied. Biased agonism is likely to be pertinent for GPCRs for neuropeptides, which often exist in multiple forms that might interact with receptors in different ways.

In addition to its physiologic relevance, biased agonism of GPCRs has implications for drug discovery. A limitation of most agonist drugs is that the same receptor mediates the beneficial and detrimental effects (ie, on-target side effects). For example, MOR mediates morphine-induced analgesia, but also causes constipation and respiratory depression. If the signaling pathways that are responsible for the beneficial and detrimental actions of agonists are known and are different, then it might be possible to develop drugs that activate only the beneficial signaling events, thereby minimizing on-target side effects. Such drugs would be not only receptor specific but also pathway specific, offering selectivity (Figure 3). Although this concept is attractive, the development of pathway-selective biased agonists is challenging.⁶⁰ The signaling pathways that underlie the beneficial and detrimental actions of agonists in vivo are not always known because of the difficulty of studying signaling in primary cells and intact animals.

Despite these challenges, there has been interest in developing pathway-selective biased agonists of ORs that would treat pain without on-target side effects. Interest in this area was sparked by the observation that mice lacking β -arrestin2 (ARRB2) displayed altered

responses to morphine.^{61,62} ARRB2 deletion enhanced and prolonged morphine-induced analgesia, which is attributable to decreased MOR desensitization. In contrast, ARRB2 deletion attenuated morphine-induced tolerance, respiratory depression, and constipation, which suggests that ARRB2 mediates the signaling that underlies these effects.^{61–63} Observations with loperamide, a peripherally restricted MOR agonist, confirmed that ARRB2 mediates opioid-induced constipation.^{64,65} However, ARRB2 plays a role in the digestive tract, where it mediates the development of tolerance to morphine in the colon but not in the ileum.^{66–68} The observation that ARRB2 plays distinct roles in regulating MOR signaling that underlies analgesia vs respiratory suppression and constipation prompted efforts to identify biased agonists of MOR that activate G proteins but not ARRBs. Potentially, G-protein–biased agonists would induce analgesia without on-target side effects. Several candidates have emerged.

Translational and Clinical Impact of Biased Agonists for Digestive Diseases

TRV130 (Oliceridine, Olinvo) is a weak G-protein–biased agonist of MOR.⁶⁹ Consistent with its lesser ability to recruit ARRB2, TRV130 stimulates minimal MOR phosphorylation or internalization compared with other opioids.⁷⁰ TRV130 retains analgesic activity in rodents, with decreased adverse effects of gastrointestinal function and respiration.⁷⁰ [ClinicalTrials.gov](#) lists 10 trials related to TRV130 (Table 1). A double-blind, patient-controlled analgesia phase IIb study was designed to investigate the efficacy, safety, and tolerability of TRV130 compared with morphine and placebo in patients with moderate to severe pain after abdominoplasty ([ClinicalTrials.gov](#), identifier [NCT02335294](#)). Although the analgesic efficacy of TRV130 was similar to that of morphine, TRV130 produced less nausea and vomiting.⁷¹ In healthy men, TRV130 produced greater analgesia than morphine, with a smaller decrease in respiratory function and less nausea and vomiting ([ClinicalTrials.gov](#), identifier [NCT02083315](#)).⁷² These clinical trials do not report whether the incidence of constipation after administration of TRV130 is lower compared with morphine. Oliceridine was granted novel drug application status by the US Food and Drug Administration in 2017, but this application was rejected for safety issues and dosing concerns.

Structure-based drug design has been used to develop G-protein–biased agonists of ORs. PZM21 is a G-protein–biased MOR agonist derived from structure-based drug design efforts facilitated by the resolution of the crystal structure of all OR subtypes.⁷³ Together with PZM-21, multiple G-protein–biased MOR agonists have been identified that provide analgesia with fewer on-target side effects.⁷⁴ However, recent studies suggest that TRV130 and PZM21 retain their undesirable side effects with repeated use despite being G protein biased.^{75,76} Further studies are required to ascertain the therapeutic utility of G-protein–biased agonists of MOR.

Biased agonists of DOR have been tested for analgesic efficacy.⁷⁷ The attractiveness of DOR agonists for clinical use is their decreased propensity to inhibit gastrointestinal motility and cause constipation compared with MOR agonists.^{78,79} The DOR agonists SNC80 and ARM390 produce comparable analgesia but show biased effects at the cellular and behavioral levels.⁸⁰ SNC80 causes endocytosis of DOR, whereas ARM390 does not.

Repeated injection of SNC80 produces analgesic, locomotor, and anxiolytic tolerance and receptor down-regulation. Repeated administration of ARM390 produces analgesic tolerance, but not locomotor or anxiolytic tolerance. Dorsal root ganglia from the mice treated with these agonists demonstrated intact DOR expression, although DOR coupling to calcium channels was lost. ADL5859 and ADL5747 are DOR agonists that, similar to ARM390, produce biased effects in preclinical studies.^{81,82} ADL5747 and ADL5859 produce antinociception in inflammatory and neuropathic pain models, do not activate locomotion, and do not induce DOR internalization. ADL5859 has been tested in clinical trials for analgesic efficacy after molar removal ([ClinicalTrials.gov](https://clinicaltrials.gov/ct2/show/study/NCT009938363), identifier [NCT009938363](https://clinicaltrials.gov/ct2/show/study/NCT009938363)), rheumatoid arthritis ([ClinicalTrials.gov](https://clinicaltrials.gov/ct2/show/study/NCT00626275), identifier [NCT00626275](https://clinicaltrials.gov/ct2/show/study/NCT00626275)), diabetes-induced peripheral neuropathy ([ClinicalTrials.gov](https://clinicaltrials.gov/ct2/show/study/NCT00603265), identifier [NCT00603265](https://clinicaltrials.gov/ct2/show/study/NCT00603265)), and osteoarthritis ([ClinicalTrials.gov](https://clinicaltrials.gov/ct2/show/study/NCT00979953), identifier [NCT00979953](https://clinicaltrials.gov/ct2/show/study/NCT00979953)). ADL5859 did not demonstrate analgesic efficacy in these trials. Preclinical testing showed ADL5747 to have greater analgesic potency than ADL5859 in a model of inflammatory pain in rats. However, it failed to show analgesic efficacy for osteoarthritic pain ([ClinicalTrials.gov](https://clinicaltrials.gov/ct2/show/study/NCT00979953), identifier [NCT00979953](https://clinicaltrials.gov/ct2/show/study/NCT00979953)) and post-herpetic neuralgia ([ClinicalTrials.gov](https://clinicaltrials.gov/ct2/show/study/NCT01058642), identifier [NCT01058642](https://clinicaltrials.gov/ct2/show/study/NCT01058642)).

GPCR Oligomerization: It Takes 2 to Tango

Concept of Oligomerization of GPCRs

Although receptor tyrosine kinases and ion channels can assemble into multimeric functional units, the oligomerization of GPCRs is controversial. In light of this controversy, the International Union of Basic and Clinical Pharmacology developed criteria for the acceptance of GPCR oligomers.⁸³ Criteria include evidence of physical association of GPCRs in native tissues and cells, rather than in transfected cells; evidence of a new or different pharmacologic property of the oligomer in native systems; and the observation of functional changes when one of the protomers is deleted in animals. Despite this controversy, the development of drugs that target components of a GPCR oligomer offers the possibility of selectivity and efficacy (Figure 4).

Oligomerization of Class C GPCRs

The strongest evidence for the existence of dimers comes from class C GPCRs (glutamate, GABA, calcium). Dimerization of some class C GPCRs is necessary for function, in which the association of 2 identical or distinct subunits forms a functional receptor. In contrast to other families, the ligand binding site of these GPCRs is not located within the heptahelical domain, but rather within a large extracellular Venus flytrap domain. Class C GPCR dimers are stabilized by a disulfide covalent linkage between the 2 subunits. Dimerization of these receptors is essential for allosteric coupling between the Venus flytrap domain and the heptahelical domain and thus between sites for ligand binding and G-protein activation. Heterodimerization of the GABA_{B1} and GABA_{B2} receptors is required to mask an endoplasmic reticulum retention sequence, allowing trans-location of receptors to the plasma membrane.^{84–86} Agonist binding to GABA_{B1} allosterically activates GABA_{B2} to initiate intracellular signal transduction. Although this heteromerization was first described in the brain,⁸⁵ it has been postulated to occur in the digestive tract⁸⁷ and is supported by the colocalization of the 2 subunits in the upper gut.⁸⁸ GABA_A and GABA_B receptors are

expressed throughout the gut and can regulate relaxation of the lower esophageal sphincter, gastric and intestinal motility, and colonic pain.⁸⁹ GABA_B agonists have been proposed as a treatment for GERD but the incidence of centrally mediated side effects has limited therapeutic applicability.⁹⁰

Oligomerization of Class A GPCRs

The dimerization of class A GPCRs, although more controversial than for class C GPCRs, illustrates the dynamism of this receptor family, because the assembly of class A oligomers has been proposed to be ligand dependent and to modulate GPCR biogenesis and endocytosis^{91,92} (Figure 4). Dimerization of ORs has attracted attention. Studies of purified receptors reconstituted into a phospholipid bilayer indicate that monomeric MOR can bind agonists and antagonists and is the minimal functional unit necessary for G-protein activation.⁹³ However, structural and functional observations suggest that ORs can dimerize. Antagonist-bound MOR crystalized as a symmetrical dimer with the interfaces within transmembrane helices 5 and 6,²⁰ although these interfaces were not observed in the agonist-bound structure.⁹⁴ MOR homodimers have been detected in heterologous expression systems and in vivo.⁹⁵

MOR can dimerize with DOR, because in recombinant systems a MOR-DOR heterodimer displays binding and functional properties that can be observed in native membranes of wild-type but not of knockout mice.⁹⁶ However, these data have been debated. In transgenic mice expressing DOR fused to green fluorescent protein (GFP), there is little overlap between DOR-GFP and immunoreactive MOR in primary sensory and spinal neurons,⁹⁷ although DOR-GFP and MOR-mCherry are coexpressed in limited neuronal populations.⁹⁸ Within pain pathways, DOR-MOR coexpression is limited to excitatory interneurons and projection neurons in the dorsal horn of the spinal cord and to neurons in parabrachial, amygdala, and cortical regions of the brain.⁹⁹ In these neurons, DOR and MOR traffic and function independently. Despite this controversy, the MOR-DOR heterodimer has been suggested as a therapeutic target that could provide analgesia with decreased tolerance.^{100,101} Bifunctional ligands, composed of a MOR agonist and a DOR antagonist, have been generated with the rationale that DOR antagonists could enhance MOR responses.

Although functional coexpression of MOR and DOR by the same neuron was first demonstrated using electrophysiologic recordings from enteric neurons,¹⁰² the definitive demonstration of MOR-DOR heteromers in enteric neurons is lacking. DOR-GFP is coexpressed in a subpopulation of myenteric neurons with immunoreactive MOR.¹⁰³ However, whether they form heteromers or functionally interact through other mechanisms has not been determined. Electrophysiologic and molecular studies show that MOR and DOR are coexpressed by afferent neurons innervating the mouse colon, where receptors might suppress neuronal excitability during inflammation.¹⁰⁴

Translational and Clinical Impact of GPCR Oligomers for Digestive Diseases

The utility of bivalent drugs that recognize the 2 components of a GPCR dimer is illustrated by finding that a molecule with MOR agonist and DOR antagonist activity (Eluxadoline) acts through the MOR-DOR heteromer¹⁰⁵ (Table 1 and Figure 4). Eluxadoline relieves

abdominal pain in patients with IBS-D ([ClinicalTrials.gov](https://clinicaltrials.gov/ct2/show/study/NCT01553747), identifier [NCT01553747](https://clinicaltrials.gov/ct2/show/study/NCT01553747); [NCT01553591](https://clinicaltrials.gov/ct2/show/study/NCT01553591)).^{48,106} Despite the MOR activity, the drug showed no evidence of abuse potential in phase II and III clinical studies.¹⁰⁷ A clinical trial is open to test whether Eluxadoline is effective for the management of IBS-D in patients with bile acid malabsorption ([ClinicalTrials.gov](https://clinicaltrials.gov/ct2/show/study/NCT03441581), identifier [NCT03441581](https://clinicaltrials.gov/ct2/show/study/NCT03441581)). Eluxadoline will be tested for the management of diarrhea-associated fecal incontinence ([ClinicalTrials.gov](https://clinicaltrials.gov/ct2/show/study/NCT03489265), identifier [NCT03489265](https://clinicaltrials.gov/ct2/show/study/NCT03489265)).

Compartmentalized Signaling: Adding Texture to GPCR Responses

Concept of Compartmentalized Signaling of GPCRs

Although alterations in the conformation of GPCRs might account for allosteric modulation and biased agonism and could explain the altered functions of GPCR oligomers, GPCRs also undergo positional changes during their activation–deactivation cycle, exemplified by agonist-induced endocytosis. Agonist-induced endocytosis in vivo has been demonstrated for the neurokinin-1 receptor (NK₁R) and DOR, because of the availability of selective NK₁R antibodies and transgenic mice expressing DOR-GFP. Physiologic stimuli evoke NK₁R endocytosis in endothelial cells of post-capillary venules at sites of neurogenic inflammation,¹⁰⁸ in enteric neurons during inflammation,¹⁰⁹ and in second-order spinal neurons after painful stimuli.^{24,110,111} Exogenous and endogenously released opioids induce endocytosis of DOR in myenteric neurons.^{47,103} These studies led to the appreciation that GPCRs can signal from endosomes and the plasma membrane, with implications for physiologic control and drug discovery.^{23,26,28} GPCRs in endosomes can generate sustained signals in subcellular compartments (ie, compartmentalized signaling) that contribute to important pathophysiologic processes, and endosomal GPCRs could be an important target for therapy.

Control of Plasma Membrane Signaling of GPCRs

Plasma membrane signaling is regulated by ligand degradation and reuptake and by receptor desensitization and endocytosis and is often transient (Figure 5). Cell-surface peptidases degrade neuropeptides and terminate their biological effects. Neprilysin degrades and inactivates SP and bradykinin and attenuates their proinflammatory actions.^{112–114} Neprilysin deletion causes NK₁R-dependent plasma extravasation in the digestive tract¹¹⁵ and exacerbates inflammation of the intestine by impaired degradation of SP.¹¹⁴ Enkephalin-degrading enzymes regulate activation of ORs, and inhibitors of these enzymes suppress diarrhea by enhancing the antisecretory actions of endogenous opioids.⁴⁹

GPCR desensitization also regulates signaling at the plasma membrane. ARRBs uncouple GPCRs from G proteins and couple GPCRs to the clathrin-mediated endocytic machinery.¹¹⁶ Desensitization of MOR and analgesic tolerance to opioids are associated with a decrease of MOR at the plasma membrane.¹¹⁷ However, tolerance to morphine develops for pain and for motility of the upper gut but not the colon, leading to constipation with escalating doses of opioids that are required to control pain.⁶⁸ Differential functions of ARRBs could account for these differences in tolerance.

Intracellular Signaling of GPCRs

Although endosomes were considered a conduit for receptor trafficking to recycling or degradation pathways, endosomes currently are considered a major site of continued signaling by GPCRs.^{22–27,118–121} GPCRs in endosomes can assemble signaling complexes (signalosomes) in subcellular compartments. The spatial and temporal characteristics of these signals can provide a mechanism underlying specific cellular responses (Figure 5).

The idea of compartmentalized signaling, although initially proposed for cyclic adenosine monophosphate (cAMP),¹²² was first demonstrated for calcium signaling owing to the availability of fluorescent indicators that allowed observations of calcium sparks, puffs, and blinks within living cells.¹²³ The use of genetically encoded Förster resonance energy transfer biosensors that are targeted to particular subcellular domains has shown that most signals are compartmentalized.¹²⁴ Signal compartmentalization can be achieved by the formation of signaling micro-domains, such as those described for receptors that stimulate the formation of cAMP. Here, local second-messenger concentrations are controlled by the proximity of adenylyl cyclase (generates cAMP), phosphodiesterases (degrade cAMP), and cAMP-activated protein kinase A.¹²⁵ Scaffolding proteins that lack enzymatic activity but participate in the organization of signaling effectors can mediate signal compartmentalization. A-kinase anchoring proteins are recognized for their roles in the formation of multi-protein complexes that modulate spatial and temporal cAMP signaling.¹²⁵ ARRBs serve as molecular scaffolds that recruit GPCRs, including PAR₂ and NK₁R, and components of the mitogenactivated protein kinase cascade to endosomes for the activation of extracellular signal regulated kinase in subcellular compartments.^{57,126} Although most descriptions of compartmentalized GPCR signaling in physiologic settings have been focused on the heart and brain, signal compartmentalization in the gastrointestinal tract has been reported for cAMP.¹²⁷

Control of the Endosomal Signaling of GPCRs

The trafficking of GPCRs through the endosomal system, which depends in part on the stability of agonist-GPCR-ARRB complexes, governs the speed of receptor recycling and re-sensitization and the duration of endosomal signals. Initially, GPCRs that exhibited sustained interactions with ARRBs were designated class B GPCRs (eg, NK₁R, PAR₂)^{128,129} and those that exhibited low affinity and transient interactions with ARRBs were termed class A GPCRs (eg, NK₃R, MOR).¹³⁰ Although this initial classification has been linked to the dynamics of receptor internalization and recycling, it has become apparent that not all GPCRs fall in these 2 categories. Despite this, the differential affinity for ARRBs can affect signaling of receptors that are coexpressed in enteric neurons, where the activated NK₁R sequesters ARRBs and thereby inhibits ARRB-dependent desensitization and endocytosis of the NK₃R.¹³⁰ This process could provide a mechanism for sustained signaling by tachykinins through the NK₃R even after the NK₁R is desensitized and internalized.

For neuropeptide receptors, degradation of ligands by endosomal peptidases also determines the stability of agonist-GPCR-ARRB complexes and controls GPCR trafficking and signaling. Endothelin-converting enzyme 1 (ECE1) is a transmembrane peptidase found in

early endosomes of many cells, including enteric neurons and endothelial cells.^{131–134} By degrading SP and calcitonin gene-related peptide in acidic endosomes, ECE1 destabilizes the agonist-GPCR-ARRB complex, which terminates endosomal signaling and promotes receptor recycling and re-sensitization. This mechanism controls the proinflammatory and neurotoxic actions of SP and NK₁R.¹³⁵ The susceptibility of endogenous peptides and peptide drugs to degradation by endosomal ECE1 has implications for physiologic control and therapy. Somatostatin (SST) isoforms exist with 14 or 28 amino acids. The 2 isoforms of SST evoke endocytosis of the SST receptor 2 (SSTR2), which is expressed throughout the enteric nervous system. After activation by SST14, SSTR2 recycles, whereas after activation by SST28, SSTR2 remains in endosomes, from where it can continue to signal.¹³⁶ This difference is attributable to differential susceptibility of the SST isoforms to degradation by ECE1. ECE1 degrades SST14 in endosomes, which destabilizes the SST14-SSTR2-ARRB complex, allowing the receptor to recycle.^{136,137} Because ECE1 does not degrade SST28, SSTR2 remains in endosomes. Although metabolically stable SST analogues (eg, octreotide) are effective treatments for several disorders,¹³⁸ they have side effects in the gastrointestinal tract (constipation, cramps, nausea). Stable SST analogues that are resistant to ECE1 evoke prolonged sequestration of SSTR2 in enteric neurons, which could generate long-lasting signals that underlie beneficial and detrimental actions.¹³⁶

Mechanisms of Endosomal GPCR Signaling

The concept that endosomes are a major site for sustained GPCR signaling was suggested by observations that ARRBs serve as molecular scaffolds that recruit GPCRs and components of the mitogen-activated protein kinase cascades to endosomes.^{57,126} It is apparent that GPCRs in endosomes can signal by ARRB- and G-protein-mediated mechanisms, and that endosomal signaling activates kinases and generates cAMP in defined subcellular compartments^{22–27,118–121} (Figure 5). How is it possible that GPCRs can signal from endosomes by ARRB- and G-protein-mediated mechanisms, when ARRBs uncouple GPCRs from G proteins at the plasma membrane? Structural studies of the β_2 -adrenergic receptor have identified receptor-G protein-ARRB mega-complexes and shown that conformations of GPCR-ARRB complexes retain the capacity to couple to G α subunits.^{139,140}

Translational and Clinical Impact of GPCR Compartmentalized Signaling for Digestive Diseases

The therapeutic relevance of endosomal GPCR signaling is evident.²⁸ Although GPCR signaling at the plasma membrane is transient, endosomal signaling by the same receptor can be sustained and regulate events in the cell, including gene transcription in the case of the β_2 -adrenergic receptor and NK₁R.^{24,121} Endosomal signaling by GPCRs in the pain pathway, including the SP NK₁R and the calcitonin gene-related peptide calcitonin receptor-like receptor in second-order spinal neurons,^{24,27} and PAR₂ in primary spinal afferent neurons,²⁵ is critical for the sustained activation and hyperexcitability of neurons that is a hallmark of chronic pain. Indeed, receptor endocytosis is required for these receptors to exhibit the full repertoire of signaling responses. Inhibitors of clathrin and dynamin and lipid-conjugated antagonists that target NK₁R, calcitonin receptor-like receptor, and PAR₂ in endosomes block signaling derived from endosomal receptors. Such inhibitors provide relief

from pain in preclinical models of somatic and colonic pain,^{24,25,27} illustrating the pathophysiologic relevance of endosomal GPCR signaling. Endosomal-targeted antagonists of PAR₂ could be effective treatments for IBS pain, in which colonic proteases and PAR₂ are strongly implicated.^{25,141,142} Endosomal-targeted agonists and antagonists of GPCRs could provide options for therapy in which this has proved clinically ineffective.²⁸

Future Directions

GPCRs control digestion and digestive diseases and are a target for therapy. GPCRs sense the contents of the lumen, mediate the actions of gut hormones, neurotransmitters, and paracrine agents, and control inflammation and pain. Drugs that activate or inhibit these receptors have been a mainstay for the treatment of digestive disorders (eg, histamine H₂ receptor antagonists for peptic ulcer disease¹⁴³).

However, we have but a superficial understanding of this large and complex family of receptors in digestion and digestive diseases. The functions and roles in the gut of orphan GPCRs, such as MRGPRs, leucine-rich GPCRs, and frizzled and adhesion receptors, are still unknown. The concepts of allosteric modulation, biased agonism, oligomerization, and compartmentalized signaling offer new opportunities for therapy. The successful exploitation of these concepts for the development of superior therapies requires a complete understanding of receptor expression, signaling, and trafficking in important cell types in health and diseased states, which is lacking.

Progress in structural, chemical, and cell biology and genetics will advance the understanding of the function of GPCRs and the development of GPCR-directed therapies. Conventional drug discovery involves screens of libraries of millions of drug-like molecules. Although this approach has yielded success, some GPCRs have been found to be undruggable. An understanding of the structural basis of GPCR activation and signaling, coupled with advances in molecular modeling, has enabled screening of virtual libraries in silico, allowing rational structure-based drug design, even for orphan GPCRs.¹⁴⁴ Cryo-electron microscopy^{13,14} and proximity ligation techniques coupled to mass spectrometry and proteomics¹⁴⁵ have provided fresh insights into the formation and structure of GPCR-signaling platforms. The realization that GPCRs can signal in defined subcellular compartments to control pathophysiologically important processes, such as pain, has led to the development of compartment-selective agonists and antagonists.²⁸ Analysis of compartmentalized signaling using genetically encoded biosensors has shown that some drugs can activate GPCRs in unexpected intracellular locations. Opioid peptides can activate MOR at the plasma membrane and then in endosomes, secondary to receptor endocytosis, whereas morphine also can activate MOR in the Golgi apparatus because of its ability to penetrate membranes.⁵⁴ In this context, developments such as organoids, which replicate the complex organization of organs in tissue culture, and advanced genome editing using CRISPR Cas 9 hold remarkable potential in basic and translational GPCR research.¹⁴⁶ The development of designer receptors exclusively activated by designer drugs and opto-genetics have provided important insights into GPCR signaling pathways that underlie important physiologic processes in vivo. Designer receptors exclusively activated by designer drugs are engineered to respond to inert drugs, but not to endogenous ligands. By using transgenic and

viral-delivery approaches, it is possible to express designer receptors exclusively activated by designer drugs in particular cell types and then examine the consequences of GPCR activation in defined cell types.^{147,148} Chemo-genetic approaches have been used to control the activity of enteric glial cells to investigate their roles in intestinal motility¹⁴⁹ and secretomotor function.¹⁵⁰

Much of the focus of these new technologies has been to define the function of GPCRs in the central nervous system and to develop more effective GPCR-directed therapies for neurologic diseases. In light of the undoubted importance of GPCRs in the digestive system, the application of similar technologies to analysis of gut function could lead to advances in understanding digestive diseases.

Acknowledgments

Funding

This work is supported by the National Institutes of Health (grants NS102722, DE026806, and DK118971), the Department of Defense (grant W81XWH1810431 to Nigel W. Bunnett and Brian L. Schmidt), and the National Health and Medical Research Council of Australia (grant 1121029 to Meritxell Canals and Daniel P. Poole).

Abbreviations used in this paper:

| | |
|--------------|---|
| ARRB | β -arrestin |
| ARRB2 | β -arrestin2 |
| cAMP | cyclic adenosine monophosphate |
| DOR | δ -opioid receptor |
| ECE1 | endothelin converting enzyme 1 |
| GABA | γ -aminobutyric acid |
| GERD | gastroesophageal reflux disease |
| GFP | green fluorescent protein |
| GPCR | G-protein–coupled receptor |
| GRK | G-protein–coupled receptor kinase |
| IBS | irritable bowel syndrome |
| IBS-D | diarrhea-predominant irritable bowel syndrome |
| MGLUR | metabotropic glutamate receptor |
| MOR | μ -opioid receptor |
| MRGPR | Mas-related GPCR |
| NAM | negative allosteric modulator |

| | |
|------------------------|-------------------------------|
| NK₁R | neurokinin-1 receptor |
| OR | opioid receptor |
| PAM | positive allosteric modulator |
| PAR | protease-activated receptor |
| SP | substance P |
| SST | somatostatin |
| SSTR | somatostatin receptor |

References

1. Hauser AS, Attwood MM, Rask-Andersen M, et al. Trends in GPCR drug discovery: new agents, targets and indications. *Nat Rev Drug Discov* 2017;16:829. [PubMed: 29075003]
2. Chaudhari N, Roper SD. The cell biology of taste. *J Cell Biol* 2010;190:285. [PubMed: 20696704]
3. Reimann F, Tolhurst G, Gribble Fiona M. G-protein-coupled receptors in intestinal chemosensation. *Cell Metab* 2012;15:421–431. [PubMed: 22482725]
4. Kong W, McConalogue K, Khitin LM, et al. Luminal trypsin may regulate enterocytes through proteinase-activated receptor 2. *Proc Natl Acad Sci U S A* 1997; 94:8884–8889. [PubMed: 9238072]
5. Alemi F, Poole DP, Chiu J, et al. The receptor TGR5 mediates the prokinetic actions of intestinal bile acids and is required for normal defecation in mice. *Gastroenterology* 2013;144:145–154. [PubMed: 23041323]
6. Abu-Hayyeh S, Ovadia C, Lieu T, et al. Prognostic and mechanistic potential of progesterone sulfates in intrahepatic cholestasis of pregnancy and pruritus gravidarum. *Hepatology* 2016;63:1287–1298. [PubMed: 26426865]
7. Alemi F, Kwon E, Poole DP, et al. The TGR5 receptor mediates bile acid-induced itch and analgesia. *J Clin Invest* 2013;123:1513–1530. [PubMed: 23524965]
8. Solinski HJ, Gudermann T, Breit A. Pharmacology and signaling of MAS-related G protein-coupled receptors. *Pharmacol Rev* 2014;66:570–597. [PubMed: 24867890]
9. McNeil BD, Pundir P, Meeker S, et al. Identification of a mast-cell-specific receptor crucial for pseudo-allergic drug reactions. *Nature* 2015;519:237–241. [PubMed: 25517090]
10. Stead RH, Tomioka M, Quinonez G, et al. Intestinal mucosal mast cells in normal and nematode-infected rat intestines are in intimate contact with peptidergic nerves. *Proc Natl Acad Sci U S A* 1987;84:2975–2979. [PubMed: 2437589]
11. Barbara G, Stanghellini V, De Giorgio R, et al. Activated mast cells in proximity to colonic nerves correlate with abdominal pain in irritable bowel syndrome. *Gastroenterology* 2004;126:693–702. [PubMed: 14988823]
12. Geppetti P, Veldhuis NA, Lieu T, et al. G protein-coupled receptors: dynamic machines for signaling pain and itch. *Neuron* 2015;88:635–649. [PubMed: 26590341]
13. Liang YL, Khoshouei M, Deganutti G, et al. Cryo-EM structure of the active, Gs-protein complexed, human CGRP receptor. *Nature* 2018;561:492–497. [PubMed: 30209400]
14. Liang YL, Khoshouei M, Glukhova A, et al. Phase-plate cryo-EM structure of a biased agonist-bound human GLP-1 receptor-Gs complex. *Nature* 2018;555:121–125. [PubMed: 29466332]
15. Rasmussen SG, Choi HJ, Fung JJ, et al. Structure of a nanobody-stabilized active state of the beta(2) adrenoceptor. *Nature* 2011;469:175–180. [PubMed: 21228869]
16. Rasmussen SG, DeVree BT, Zou Y, et al. Crystal structure of the beta2 adrenergic receptor-Gs protein complex. *Nature* 2011;477:549–555. [PubMed: 21772288]
17. Shukla AK, Westfield GH, Xiao K, et al. Visualization of arrestin recruitment by a G-protein-coupled receptor. *Nature* 2014;512:218–222. [PubMed: 25043026]

Gastroenterology. Author manuscript; available in PMC 2019 May 09.

18. Christopoulos A Advances in G protein-coupled receptor allostery: from function to structure. *Mol Pharmacol* 2014;86:463–478. [PubMed: 25061106]
19. Kenakin T Functional selectivity and biased receptor signaling. *J Pharmacol Exp Ther* 2011;336:296–302. [PubMed: 21030484]
20. Manglik A, Kruse AC, Kobilka TS, et al. Crystal structure of the micro-opioid receptor bound to a morphinan antagonist. *Nature* 2012;485:321–326. [PubMed: 22437502]
21. Wu H, Wacker D, Mileni M, et al. Structure of the human kappa-opioid receptor in complex with JDTic. *Nature* 2012;485:327–332. [PubMed: 22437504]
22. Irannejad R, Tomshine JC, Tomshine JR, et al. Conformational biosensors reveal GPCR signalling from endosomes. *Nature* 2013;495:534–538. [PubMed: 23515162]
23. Irannejad R, Tsvetanova NG, Lobingier BT, et al. Effects of endocytosis on receptor-mediated signaling. *Curr Opin Cell Biol* 2015;35:137–143. [PubMed: 26057614]
24. Jensen DD, Lieu T, Halls ML, et al. Neurokinin 1 receptor signaling in endosomes mediates sustained nociception and is a viable therapeutic target for prolonged pain relief. *Sci Transl Med* 2017;9(392).
25. Jimenez-Vargas NN, Pattison LA, Zhao P, et al. Protease-activated receptor-2 in endosomes signals persistent pain of irritable bowel syndrome. *Proc Natl Acad Sci U S A* 2018;115:E7438–E7447. [PubMed: 30012612]
26. Murphy JE, Padilla BE, Hasdemir B, et al. Endosomes: a legitimate platform for the signaling train. *Proc Natl Acad Sci U S A* 2009;106:17615–17622. [PubMed: 19822761]
27. Yarwood RE, Imlach WL, Lieu T, et al. Endosomal signaling of the receptor for calcitonin gene-related peptide mediates pain transmission. *Proc Natl Acad Sci U S A* 2017;114:12309–12314. [PubMed: 29087309]
28. Thomsen ARB, Jensen DD, Hicks GA, et al. Therapeutic targeting of endosomal G-protein-coupled receptors. *Trends Pharmacol Sci* 2018;39:879–891. [PubMed: 30180973]
29. Gautam D, Heard TS, Cui Y, et al. Cholinergic stimulation of salivary secretion studied with M1 and M3 muscarinic receptor single- and double-knockout mice. *Mol Pharmacol* 2004;66:260–267. [PubMed: 15266016]
30. Matsui M, Motomura D, Fujikawa T, et al. Mice lacking M2 and M3 muscarinic acetylcholine receptors are devoid of cholinergic smooth muscle contractions but still viable. *J Neurosci* 2002;22:10627–10632. [PubMed: 12486155]
31. Thomsen M, Sorensen G, Dencker D. Physiological roles of CNS muscarinic receptors gained from knockout mice. *Neuropharmacology* 2018;136:411–420. [PubMed: 28911965]
32. Christopoulos A, Kenakin T. G protein-coupled receptor allostery and complexing. *Pharmacol Rev* 2002; 54:323–374. [PubMed: 12037145]
33. Monod J, Changeux JP, Jacob F. Allosteric proteins and cellular control systems. *J Mol Biol* 1963;6:306–329. [PubMed: 13936070]
34. De Lean A, Stadel JM, Lefkowitz RJ. A ternary complex model explains the agonist-specific binding properties of the adenylate cyclase-coupled beta-adrenergic receptor. *J Biol Chem* 1980;255:7108–7117. [PubMed: 6248546]
35. Gurevich VV, Pals-Rylaarsdam R, Benovic JL, et al. Agonist-receptor-arrestin, an alternative ternary complex with high agonist affinity. *J Biol Chem* 1997;272:28849–28852. [PubMed: 9360951]
36. Dorr P, Westby M, Dobbs S, et al. Maraviroc (UK-427, 857), a potent, orally bioavailable, and selective small-molecule inhibitor of chemokine receptor CCR5 with broad-spectrum anti-human immunodeficiency virus type 1 activity. *Antimicrob Agents Chemother* 2005; 49:4721–4732. [PubMed: 16251317]
37. Block GA, Martin KJ, de Francisco AL, et al. Cinacalcet for secondary hyperparathyroidism in patients receiving hemodialysis. *N Engl J Med* 2004;350:1516–1525. [PubMed: 15071126]
38. Gentry PR, Sexton PM, Christopoulos A. Novel allosteric modulators of G protein-coupled receptors. *J Biol Chem* 2015;290:19478–19488. [PubMed: 26100627]
39. Conn PJ, Christopoulos A, Lindsley CW. Allosteric modulators of GPCRs: a novel approach for the treatment of CNS disorders. *Nat Rev Drug Discov* 2009;8:41–54. [PubMed: 19116626]

40. Kurimoto E, Matsuda S, Shimizu Y, et al. An approach to discovering novel muscarinic M1 receptor positive allosteric modulators with potent cognitive improvement and minimized gastrointestinal dysfunction. *J Pharmacol Exp Ther* 2018;364:28–37. [PubMed: 29025977]
41. Thomsen M, Lindsley CW, Conn PJ, et al. Contribution of both M1 and M4 receptors to muscarinic agonist-mediated attenuation of the cocaine discriminative stimulus in mice. *Psychopharmacology (Berl)* 2012; 220:673–685. [PubMed: 21964721]
42. Sako Y, Kurimoto E, Mandai T, et al. TAK-071, a novel M1 positive allosteric modulator with low cooperativity, improves cognitive function in rodents with few cholinergic side effects. *Neuropsychopharmacology* 2019;44:950–960. [PubMed: 30089885]
43. Uslaner JM, Kuduk SD, Wittmann M, et al. Preclinical to human translational pharmacology of the novel M1 positive allosteric modulator MK-7622. *J Pharmacol Exp Ther* 2018;365:556–566. [PubMed: 29563325]
44. Wess J, Eglén RM, Gautam D. Muscarinic acetylcholine receptors: mutant mice provide new insights for drug development. *Nat Rev Drug Discov* 2007;6:721–733. [PubMed: 17762886]
45. Burford NT, Clark MJ, Wehrman TS, et al. Discovery of positive allosteric modulators and silent allosteric modulators of the mu-opioid receptor. *Proc Natl Acad Sci U S A* 2013;110:10830–10835. [PubMed: 23754417]
46. Livingston KE, Traynor JR. Disruption of the Na⁺ ion binding site as a mechanism for positive allosteric modulation of the mu-opioid receptor. *Proc Natl Acad Sci U S A* 2014;111:18369–18374. [PubMed: 25489080]
47. DiCello JJ, Saito A, Rajasekhar P, et al. Inflammation-associated changes in DOR expression and function in the mouse colon. *Am J Physiol Gastrointest Liver Physiol* 2018;315:G544–G559. [PubMed: 29927325]
48. Lembo AJ, Lacy BE, Zuckerman MJ, et al. Eluxadoline for Irritable Bowel Syndrome with Diarrhea. *N Engl J Med* 2016;374:242–253. [PubMed: 26789872]
49. Turck D, Berard H, Fretault N, et al. Comparison of racecadotril and loperamide in children with acute diarrhoea. *Aliment Pharmacol Ther* 1999;13(Suppl 6):27–32.
50. Burford NT, Livingston KE, Canals M, et al. Discovery, synthesis, and molecular pharmacology of selective positive allosteric modulators of the delta-opioid receptor. *J Med Chem* 2015;58:4220–4229. [PubMed: 25901762]
51. Keyword C, Wakefield M, Tack J. A proof-of-concept study evaluating the effect of ADX10059, a metabotropic glutamate receptor-5 negative allosteric modulator, on acid exposure and symptoms in gastro-oesophageal reflux disease. *Gut* 2009;58:1192–1199. [PubMed: 19460767]
52. Zerbib F, Bruley des Varannes S, Roman S, et al. Randomised clinical trial: effects of monotherapy with ADX10059, a mGluR5 inhibitor, on symptoms and reflux events in patients with gastro-oesophageal reflux disease. *Aliment Pharmacol Ther* 2011;33:911–921. [PubMed: 21320138]
53. Wacker D, Wang C, Katritch V, et al. Structural features for functional selectivity at serotonin receptors. *Science* 2013;340:615–619. [PubMed: 23519215]
54. Stoeber M, Jullie D, Lobingier BT, et al. A genetically encoded biosensor reveals location bias of opioid drug action. *Neuron* 2018;98:963–976 e5. [PubMed: 29754753]
55. Ossovskaia VS, Bunnett NW. Protease-activated receptors: contribution to physiology and disease. *Physiol Rev* 2004;84:579–621. [PubMed: 15044683]
56. Edgington-Mitchell LE. Pathophysiological roles of proteases in gastrointestinal disease. *Am J Physiol Gastrointest Liver Physiol* 2016;310:G234–G239. [PubMed: 26702140]
57. DeFea KA, Zalevsky J, Thoma MS, et al. beta-arrestin-dependent endocytosis of proteinase-activated receptor 2 is required for intracellular targeting of activated ERK1/2. *J Cell Biol* 2000;148:1267–1281. [PubMed: 10725339]
58. Zhao P, Lieu T, Barlow N, et al. Cathepsin S causes inflammatory pain via biased agonism of PAR2 and TRPV4. *J Biol Chem* 2014;289:27215–27234. [PubMed: 25118282]
59. Zhao P, Lieu T, Barlow N, et al. Neutrophil elastase activates protease-activated receptor-2 (PAR2) and transient receptor potential vanilloid 4 (TRPV4) to cause inflammation and pain. *J Biol Chem* 2015;290:13875–13887. [PubMed: 25878251]
60. Kenakin T Is the quest for signaling bias worth the effort? *Mol Pharmacol* 2018;93:266–269. [PubMed: 29348268]

61. Bohn LM, Gainetdinov RR, Lin FT, et al. Mu-opioid receptor desensitization by beta-arrestin-2 determines morphine tolerance but not dependence. *Nature* 2000; 408:720–723. [PubMed: 11130073]
62. Bohn LM, Lefkowitz RJ, Gainetdinov RR, et al. Enhanced morphine analgesia in mice lacking beta-arrestin 2. *Science* 1999;286:2495–2498. [PubMed: 10617462]
63. Bohn LM, Raehal KM. Opioid receptor signaling: relevance for gastrointestinal therapy. *Curr Opin Pharmacol* 2006;6:559–563. [PubMed: 16935560]
64. Raehal KM, Schmid CL, Medvedev IO, et al. Morphine-induced physiological and behavioral responses in mice lacking G protein-coupled receptor kinase 6. *Drug Alcohol Depend* 2009;104:187–196. [PubMed: 19497686]
65. Raehal KM, Walker JK, Bohn LM. Morphine side effects in beta-arrestin 2 knockout mice. *J Pharmacol Exp Ther* 2005;314:1195–1201. [PubMed: 15917400]
66. Akbarali HI, Inkisar A, Dewey WL. Site and mechanism of morphine tolerance in the gastrointestinal tract. *Neurogastroenterol Motil* 2014;26:1361–1367. [PubMed: 25257923]
67. Kang M, Maguma HT, Smith TH, et al. The role of beta-arrestin2 in the mechanism of morphine tolerance in the mouse and guinea pig gastrointestinal tract. *J Pharmacol Exp Ther* 2012;340:567–576. [PubMed: 22129596]
68. Ross GR, Gabra BH, Dewey WL, et al. Morphine tolerance in the mouse ileum and colon. *J Pharmacol Exp Ther* 2008;327:561–572. [PubMed: 18682567]
69. Chen X-T, Pitis P, Liu G, et al. Structure–activity relationships and discovery of a G protein biased μ opioid receptor ligand, [(3-methoxythiophen-2-yl)methyl]({2-[(9R)-9-(pyridin-2-yl)-6-oxaspiro[4.5]decan-9-yl]ethyl}) amine (TRV130), for the treatment of acute severe pain. *J Med Chem* 2013;56:8019–8031. [PubMed: 24063433]
70. DeWire SM, Yamashita DS, Rominger DH, et al. A G protein-biased ligand at the mu-opioid receptor is potently analgesic with reduced gastrointestinal and respiratory dysfunction compared with morphine. *J Pharmacol Exp Ther* 2013;344:708–717. [PubMed: 23300227]
71. Singla N, Minkowitz HS, Soergel DG, et al. A randomized, Phase IIb study investigating oliceridine (TRV130), a novel micro-receptor G-protein pathway selective (mu-GPS) modulator, for the management of moderate to severe acute pain following abdominoplasty. *J Pain Res* 2017;10:2413–2424. [PubMed: 29062240]
72. Soergel DG, Subach RA, Burnham N, et al. Biased agonism of the mu-opioid receptor by TRV130 increases analgesia and reduces on-target adverse effects versus morphine: a randomized, double-blind, placebo-controlled, crossover study in healthy volunteers. *Pain* 2014;155:1829–1835. [PubMed: 24954166]
73. Manglik A, Lin H, Aryal DK, et al. Structure-based discovery of opioid analgesics with reduced side effects. *Nature* 2016;537:185–190. [PubMed: 27533032]
74. Schmid CL, Kennedy NM, Ross NC, et al. Bias factor and therapeutic window correlate to predict safer opioid analgesics. *Cell* 2017;171:1165–1175 e13. [PubMed: 29149605]
75. Altarifi AA, David B, Muchhala KH, et al. Effects of acute and repeated treatment with the biased mu opioid receptor agonist TRV130 (oliceridine) on measures of antinociception, gastrointestinal function, and abuse liability in rodents. *J Psychopharmacol* 2017;31:730–739. [PubMed: 28142305]
76. Hill R, Disney A, Conibear A, et al. The novel mu-opioid receptor agonist PZM21 depresses respiration and induces tolerance to antinociception. *Br J Pharmacol* 2018;175:2653–2661. [PubMed: 29582414]
77. Charfi I, Audet N, Bagheri Tudashki H, et al. Identifying ligand-specific signalling within biased responses: focus on delta opioid receptor ligands. *Br J Pharmacol* 2015; 172:435–448. [PubMed: 24665881]
78. Gallantine EL, Meert TF. A comparison of the antinociceptive and adverse effects of the mu-opioid agonist morphine and the delta-opioid agonist SNC80. *Basic Clin Pharmacol Toxicol* 2005;97:39–51. [PubMed: 15943758]
79. Eisenstein TK, Rahim RT, Feng P, et al. Effects of opioid tolerance and withdrawal on the immune system. *J Neuroimmune Pharmacol* 2006;1:237–249. [PubMed: 18040801]

80. Pradhan AA, Walwyn W, Nozaki C, et al. Ligand-directed trafficking of the delta-opioid receptor in vivo: two paths toward analgesic tolerance. *J Neurosci* 2010;30:16459–16468. [PubMed: 21147985]
81. Le Bourdonnec B, Windh RT, Ajello CW, et al. Potent, orally bioavailable delta opioid receptor agonists for the treatment of pain: discovery of N,N-diethyl-4-(5-hydroxyspiro[chromene-2,4'-piperidine]-4-yl)benzamide (ADL5859). *J Med Chem* 2008;51:5893–5896. [PubMed: 18788723]
82. Le Bourdonnec B, Windh RT, Leister LK, et al. Spirocyclic delta opioid receptor agonists for the treatment of pain: discovery of N,N-diethyl-3-hydroxy-4-(spiro [chromene-2,4'-piperidine]-4-yl) benzamide (ADL5747). *J Med Chem* 2009;52:5685–5702. [PubMed: 19694468]
83. Pin JP, Neubig R, Bouvier M, et al. International Union of Basic and Clinical Pharmacology. LXVII. Recommendations for the recognition and nomenclature of G protein-coupled receptor heteromultimers. *Pharmacol Rev* 2007; 59:5–13. [PubMed: 17329545]
84. Jones KA, Borowsky B, Tamm JA, et al. GABA(B) receptors function as a heteromeric assembly of the subunits GABA(B)R1 and GABA(B)R2. *Nature* 1998; 396:674–679. [PubMed: 9872315]
85. Kaupmann K, Malitschek B, Schuler V, et al. GABA(B)-receptor subtypes assemble into functional heteromeric complexes. *Nature* 1998;396:683–687. [PubMed: 9872317]
86. White JH, Wise A, Main MJ, et al. Heterodimerization is required for the formation of a functional GABA(B) receptor. *Nature* 1998;396:679–682. [PubMed: 9872316]
87. Kawakami S, Uezono Y, Makimoto N, et al. Characterization of GABA(B) receptors involved in inhibition of motility associated with acetylcholine release in the dog small intestine: possible existence of a heterodimer of GABA(B1) and GABA(B2) subunits. *J Pharmacol Sci* 2004;94:368–375. [PubMed: 15107576]
88. Torashima Y, Uezono Y, Kanaide M, et al. Presence of GABA(B) receptors forming heterodimers with GABA(B1) and GABA(B2) subunits in human lower esophageal sphincter. *J Pharmacol Sci* 2009;111:253–259. [PubMed: 19893276]
89. Hyland NP, Cryan JF. A gut feeling about GABA: focus on GABA(B) receptors. *Front Pharmacol* 2010;1:124. [PubMed: 21833169]
90. Lehmann A, Jensen JM, Boeckxstaens GE. GABA(B) receptor agonism as a novel therapeutic modality in the treatment of gastroesophageal reflux disease. *Adv Pharmacol* 2010;58:287–313. [PubMed: 20655487]
91. Bulenger S, Marullo S, Bouvier M. Emerging role of homo- and heterodimerization in G-protein-coupled receptor biosynthesis and maturation. *Trends Pharmacol Sci* 2005;26:131–137. [PubMed: 15749158]
92. Terrillon S, Bouvier M. Roles of G-protein-coupled receptor dimerization. *EMBO Rep* 2004;5:30–34. [PubMed: 14710183]
93. Kuzak AJ, Pitchiaya S, Anand JP, et al. Purification and functional reconstitution of monomeric mu-opioid receptors: allosteric modulation of agonist binding by Gi2. *J Biol Chem* 2009;284:26732–26741. [PubMed: 19542234]
94. Huang W, Manglik A, Venkatakrishnan AJ, et al. Structural insights into micro-opioid receptor activation. *Nature* 2015;524:315–321. [PubMed: 26245379]
95. He L, Fong J, von Zastrow M, et al. Regulation of opioid receptor trafficking and morphine tolerance by receptor oligomerization. *Cell* 2002;108:271–282. [PubMed: 11832216]
96. Gomes I, Gupta A, Filipovska J, et al. A role for heterodimerization of mu and delta opiate receptors in enhancing morphine analgesia. *Proc Natl Acad Sci U S A* 2004;101:5135–5139. [PubMed: 15044695]
97. Scherrer G, Imamachi N, Cao YQ, et al. Dissociation of the opioid receptor mechanisms that control mechanical and heat pain. *Cell* 2009;137:1148–1159. [PubMed: 19524516]
98. Erbs E, Faget L, Scherrer G, et al. A mu-delta opioid receptor brain atlas reveals neuronal co-occurrence in subcortical networks. *Brain Struct Funct* 2015;220:677–702. [PubMed: 24623156]
99. Wang D, Tawfik VL, Corder G, et al. Functional divergence of delta and mu opioid receptor organization in CNS pain circuits. *Neuron* 2018;98:90–108 e5. [PubMed: 29576387]
100. Fujita W, Gomes I, Devi LA. Heteromers of mu-delta opioid receptors: new pharmacology and novel therapeutic possibilities. *Br J Pharmacol* 2015;172:375–387. [PubMed: 24571499]

101. Zhu Y, King MA, Schuller AG, et al. Retention of supraspinal delta-like analgesia and loss of morphine tolerance in delta opioid receptor knockout mice. *Neuron* 1999;24:243–252. [PubMed: 10677041]
102. Egan TM, North RA. Both mu and delta opiate receptors exist on the same neuron. *Science* 1981;214:923–924. [PubMed: 6272393]
103. Poole DP, Pelayo JC, Scherrer G, et al. Localization and regulation of fluorescently labeled delta opioid receptor, expressed in enteric neurons of mice. *Gastroenterology* 2011;141:982–991 e18. [PubMed: 21699782]
104. Guerrero-Alba R, Valdez-Morales EE, Jimenez-Vargas NN, et al. Co-expression of mu and delta opioid receptors by mouse colonic nociceptors. *Br J Pharmacol* 2018;175:2622–2634. [PubMed: 29579315]
105. Fujita W, Gomes I, Dove LS, et al. Molecular characterization of eluxadoline as a potential ligand targeting mu/delta opioid receptor heteromers. *Biochem Pharmacol* 2014;92:448–456. [PubMed: 25261794]
106. Dove LS, Lembo A, Randall CW, et al. Eluxadoline benefits patients with irritable bowel syndrome with diarrhea in a phase 2 study. *Gastroenterology* 2013; 145:329–338 e1. [PubMed: 23583433]
107. Fant RV, Henningfield JE, Cash BD, et al. Eluxadoline demonstrates a lack of abuse potential in phase 2 and 3 studies of patients with irritable bowel syndrome with diarrhea. *Clin Gastroenterol Hepatol* 2017;15:1021–1029 e6. [PubMed: 28167156]
108. Bowden JJ, Garland AM, Baluk P, et al. Direct observation of substance P-induced internalization of neurokinin 1 (NK1) receptors at sites of inflammation. *Proc Natl Acad Sci U S A* 1994;91:8964–8968. [PubMed: 7522326]
109. Poole DP, Lieu T, Pelayo JC, et al. Inflammation-induced abnormalities in the subcellular localization and trafficking of the neurokinin 1 receptor in the enteric nervous system. *Am J Physiol Gastrointest Liver Physiol* 2015; 309:G248–G259. [PubMed: 26138465]
110. Mantyh PW, DeMaster E, Malhotra A, et al. Receptor endocytosis and dendrite reshaping in spinal neurons after somatosensory stimulation. *Science* 1995; 268:1629–1632. [PubMed: 7539937]
111. Steinhoff MS, von Mentzer B, Geppetti P, et al. Tachykinins and their receptors: contributions to physiological control and the mechanisms of disease. *Physiol Rev* 2014;94:265–301. [PubMed: 24382888]
112. Deddish PA, Marcic BM, Tan F, et al. Neprilysin inhibitors potentiate effects of bradykinin on b2 receptor. *Hypertension* 2002;39:619–623. [PubMed: 11882619]
113. Okamoto A, Lovett M, Payan DG, et al. Interactions between neutral endopeptidase (EC 3.4.24.11) and the substance P (NK1) receptor expressed in mammalian cells. *Biochem J* 1994;299:683–693. [PubMed: 7514869]
114. Sturiale S, Barbara G, Qiu B, et al. Neutral endopeptidase (EC 3.4.24.11) terminates colitis by degrading substance P. *Proc Natl Acad Sci U S A* 1999;96:11653–11658. [PubMed: 10500232]
115. Lu B, Figini M, Emanuelli C, et al. The control of micro-vascular permeability and blood pressure by neutral endopeptidase. *Nat Med* 1997;3:904–907. [PubMed: 9256283]
116. Peterson YK, Luttrell LM. The diverse roles of arrestin scaffolds in G protein-coupled receptor signaling. *Pharmacol Rev* 2017;69:256–297. [PubMed: 28626043]
117. Williams JT, Ingram SL, Henderson G, et al. Regulation of mu-opioid receptors: desensitization, phosphorylation, internalization, and tolerance. *Pharmacol Rev* 2013; 65:223–254. [PubMed: 23321159]
118. Calebiro D, Nikolaev VO, Gagliani MC, et al. Persistent cAMP-signals triggered by internalized G-protein-coupled receptors. *PLoS Biol* 2009;7:e1000172. [PubMed: 19688034]
119. Ferrandon S, Feinstein TN, Castro M, et al. Sustained cyclic AMP production by parathyroid hormone receptor endocytosis. *Nat Chem Biol* 2009;5:734–742. [PubMed: 19701185]
120. Irannejad R, von Zastrow M. GPCR signaling along the endocytic pathway. *Curr Opin Cell Biol* 2014;27:109–116. [PubMed: 24680436]
121. Tsvetanova NG, von Zastrow M. Spatial encoding of cyclic AMP signaling specificity by GPCR endocytosis. *Nat Chem Biol* 2014;10:1061–1065. [PubMed: 25362359]

122. Buxton IL, Brunton LL. Compartments of cyclic AMP and protein kinase in mammalian cardiomyocytes. *J Biol Chem* 1983;258:10233–10239. [PubMed: 6309796]
123. Berridge MJ. Calcium microdomains: organization and function. *Cell Calcium* 2006;40:405–412. [PubMed: 17030366]
124. Halls ML, Canals M. Genetically encoded FRET bio-sensors to illuminate compartmentalised GPCR signalling. *Trends Pharmacol Sci* 2018;39:148–157. [PubMed: 29054309]
125. Willoughby D, Halls ML, Everett KL, et al. A key phosphorylation site in AC8 mediates regulation of Ca(2+)-dependent cAMP dynamics by an AC8-AKAP79-PKA signalling complex. *J Cell Sci* 2012; 125:5850–5859. [PubMed: 22976297]
126. DeFea KA, Vaughn ZD, O'Bryan EM, et al. The proliferative and antiapoptotic effects of substance P are facilitated by formation of a beta-arrestin-dependent scaffolding complex. *Proc Natl Acad Sci U S A* 2000; 97:11086–11091. [PubMed: 10995467]
127. Moon C, Zhang W, Ren A, et al. Compartmentalized accumulation of cAMP near complexes of multidrug resistance protein 4 (MRP4) and cystic fibrosis transmembrane conductance regulator (CFTR) contributes to drug-induced diarrhea. *J Biol Chem* 2015;290:11246–11257. [PubMed: 25762723]
128. Oakley RH, Laporte SA, Holt JA, et al. Association of beta-arrestin with G protein-coupled receptors during clathrin-mediated endocytosis dictates the profile of receptor resensitization. *J Biol Chem* 1999;274:32248–32257. [PubMed: 10542263]
129. Oakley RH, Laporte SA, Holt JA, et al. Differential affinities of visual arrestin, beta arrestin1, and beta arrestin2 for G protein-coupled receptors delineate two major classes of receptors. *J Biol Chem* 2000;275:17201–17210. [PubMed: 10748214]
130. Schmidlin F, Dery O, Bunnett NW, et al. Heterologous regulation of trafficking and signaling of G protein-coupled receptors: beta-arrestin-dependent interactions between neurokinin receptors. *Proc Natl Acad Sci U S A* 2002;99:3324–3329. [PubMed: 11880656]
131. Cattaruzza F, Cottrell GS, Vaksman N, et al. Endothelin-converting enzyme 1 promotes resensitization of neurokinin 1 receptor-dependent neurogenic inflammation. *Br J Pharmacol* 2009;156:730–739. [PubMed: 19222484]
132. Padilla BE, Cottrell GS, Roosterman D, et al. Endothelin-converting enzyme-1 regulates endosomal sorting of calcitonin receptor-like receptor and beta-arrestins. *J Cell Biol* 2007;179:981–997. [PubMed: 18039931]
133. Pelayo JC, Poole DP, Steinhoff M, et al. Endothelin-converting enzyme-1 regulates trafficking and signalling of the neurokinin 1 receptor in endosomes of myenteric neurones. *J Physiol* 2011;589:5213–5230. [PubMed: 21878523]
134. Roosterman D, Cottrell GS, Padilla BE, et al. Endothelin-converting enzyme 1 degrades neuropeptides in endosomes to control receptor recycling. *Proc Natl Acad Sci U S A* 2007;104:11838–11843. [PubMed: 17592116]
135. Jensen DD, Halls ML, Murphy JE, et al. Endothelin-converting enzyme 1 and beta-arrestins exert spatiotemporal control of substance P-induced inflammatory signals. *J Biol Chem* 2014;289:20283–20294. [PubMed: 24898255]
136. Zhao P, Canals M, Murphy JE, et al. Agonist-biased trafficking of somatostatin receptor 2A in enteric neurons. *J Biol Chem* 2013;288:25689–25700. [PubMed: 23913690]
137. Roosterman D, Kempkes C, Cottrell GS, et al. Endothelin-converting enzyme-1 degrades internalized somatostatin-14. *Endocrinology* 2008;149:2200–2207. [PubMed: 18276747]
138. Oberg KE, Reubi JC, Kwakkeboom DJ, et al. Role of somatostatins in gastroenteropancreatic neuroendocrine tumor development and therapy. *Gastroenterology* 2010;139:742–753 e1. [PubMed: 20637207]
139. Cahill TJ III, Thomsen AR, Tarrasch JT, et al. Distinct conformations of GPCR-beta-arrestin complexes mediate desensitization, signaling, and endocytosis. *Proc Natl Acad Sci U S A* 2017;114:2562–2567. [PubMed: 28223524]
140. Thomsen ARB, Plouffe B, Cahill TJ III, et al. GPCR-G protein-beta-arrestin super-complex mediates sustained g protein signaling. *Cell* 2016;166:907–919. [PubMed: 27499021]
141. Cenac N, Andrews CN, Holzhausen M, et al. Role for protease activity in visceral pain in irritable bowel syndrome. *J Clin Invest* 2007;117:636–647. [PubMed: 17304351]

142. Rolland-Fourcade C, Denadai-Souza A, Cirillo C, et al. Epithelial expression and function of trypsin-3 in irritable bowel syndrome. *Gut* 2017;66:1767–1778. [PubMed: 28096305]
143. Brimblecombe RW, Duncan WA, Durant GJ, et al. The pharmacology of cimetidine, a new histamine H₂-receptor antagonist. *Br J Pharmacol* 1975;53:435P–436P.
144. Wacker D, Stevens RC, Roth BL. How ligands illuminate GPCR molecular pharmacology. *Cell* 2017;170:414–427. [PubMed: 28753422]
145. Paek J, Kalocsay M, Staus DP, et al. Multidimensional tracking of GPCR signaling via peroxidase-catalyzed proximity labeling. *Cell* 2017;169:338–349 e11. [PubMed: 28388415]
146. Driehuis E, Clevers H. CRISPR/Cas 9 genome editing and its applications in organoids. *Am J Physiol Gastrointest Liver Physiol* 2017;312:G257–G265. [PubMed: 28126704]
147. Gulbransen BD. Emerging tools to study enteric neuro-muscular function. *Am J Physiol Gastrointest Liver Physiol* 2017;312:G420–G426. [PubMed: 28280142]
148. Zhu H, Roth BL. DREADD: a chemogenetic GPCR signaling platform. *Int J Neuropsychopharmacol* 2014; 18(1).
149. McClain JL, Fried DE, Gulbransen BD. Agonist-evoked Ca²⁺ signaling in enteric glia drives neural programs that regulate intestinal motility in mice. *Cell Mol Gastroenterol Hepatol* 2015;1:631–645. [PubMed: 26693173]
150. Grubisic V, Gulbransen BD. Enteric glial activity regulates secretomotor function in the mouse colon but does not acutely affect gut permeability. *J Physiol* 2017; 595:3409–3424. [PubMed: 28066889]

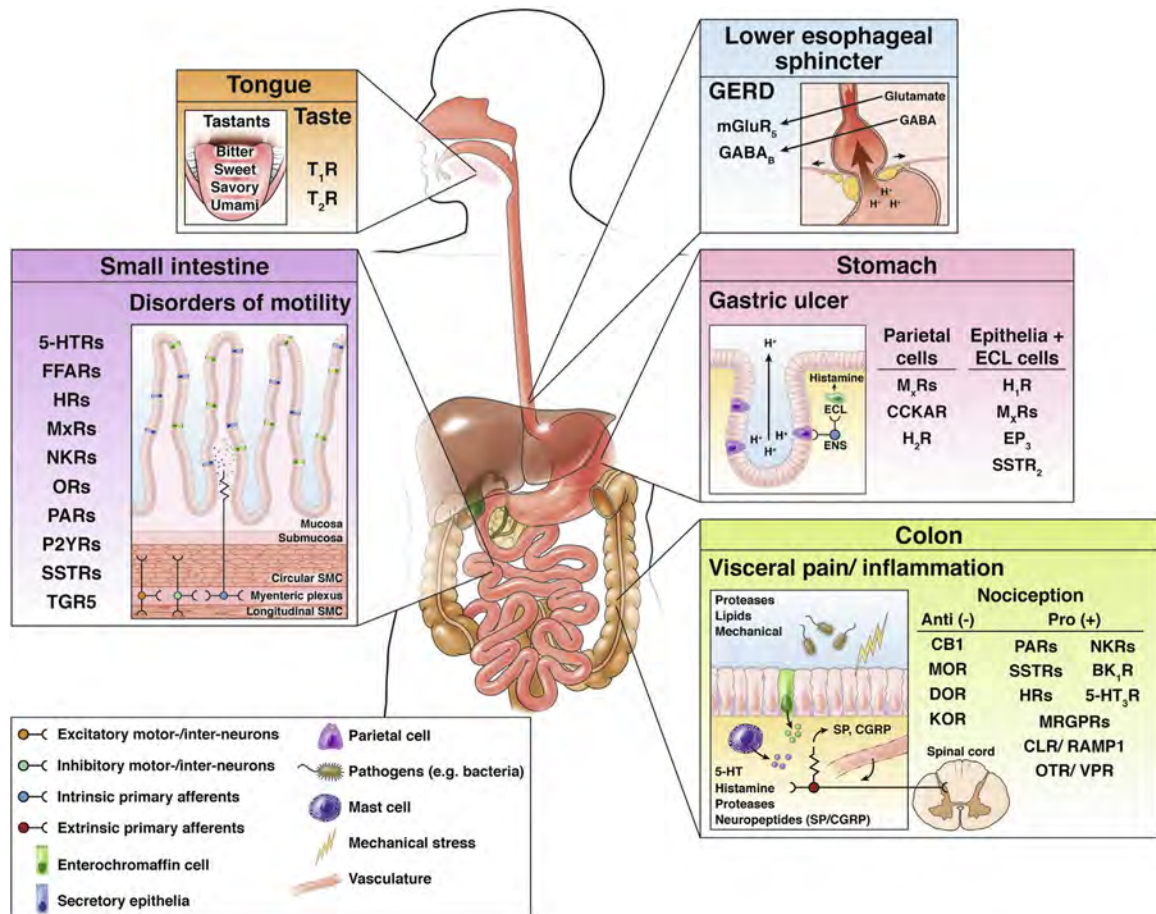


Figure 1.

GPCRs and their ligands in digestion and digestive disease. GPCRs are expressed throughout the digestive tract. Expression of some functionally and clinically important GPCRs in specific cell types in the tongue, lower esophageal sphincter, stomach, small intestine, and colon are depicted. GPCRs control multiple processes in the gut and are targets for common diseases (eg, GERD, gastric ulcer disease, disorders of intestinal motility, colonic pain, and inflammation). 5HT_xR, serotonin receptor; CLR, calcitonin receptor-like receptor; EP₃, prostaglandin receptor 3; FFARs, free fatty acid receptors; GABA_BR, GABA B receptor; H_xR, histamine receptor; M_xR, muscarinic acetylcholine receptor; NKR, neurokinin receptor; OTR, oxytocin receptor; P2YR, purinergic 2Y receptor; RAMP1, receptor activity modifying protein 1; TGR5, Takeda GPCR 5 bile-acid receptor; T_xR, taste receptor; VPR, vasopressin receptor.

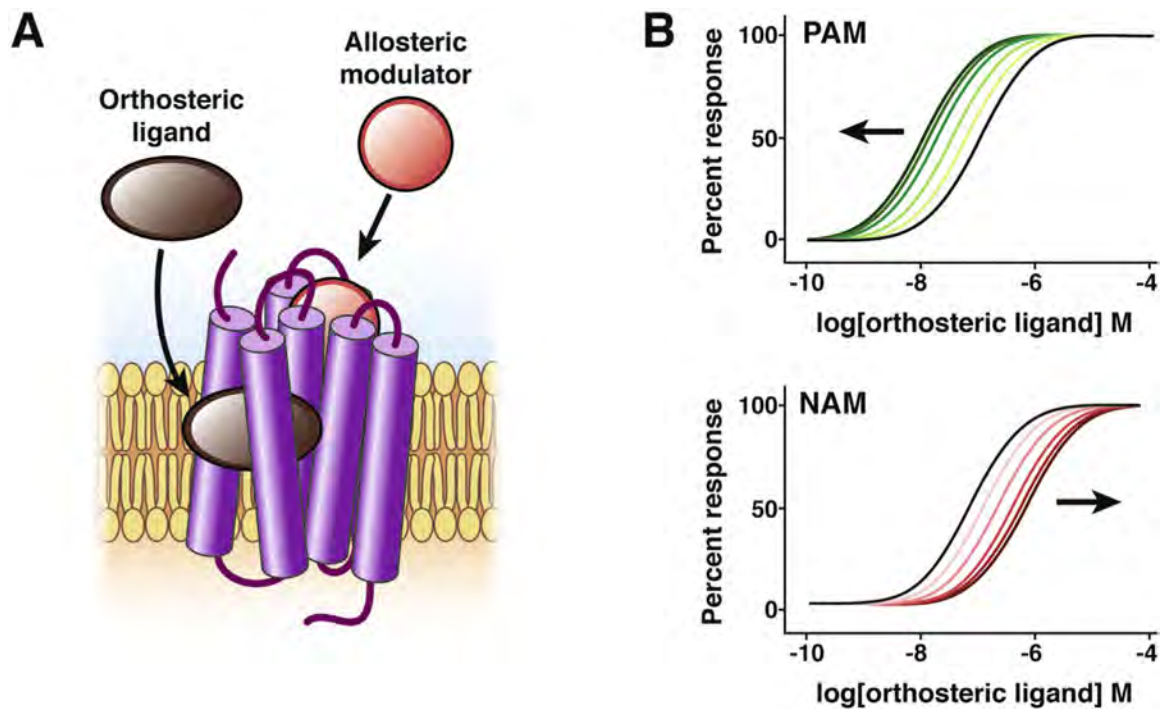


Figure 2.

Allosteric modulation of GPCRs. The orthosteric site of a GPCR is the site where the endogenous ligand (*brown*) binds. Sites that are topographically distinct from the orthosteric site are known as allosteric sites. Ligands that bind to allosteric sites (*red*) can potentiate (PAMs) or depress (NAMs) orthosteric ligand affinity and efficacy. The simulated concentration response curves show the effect of increasing concentrations of PAMs (*green lines*) or NAMs (*red lines*) on the response to a GPCR agonist (*black line*).

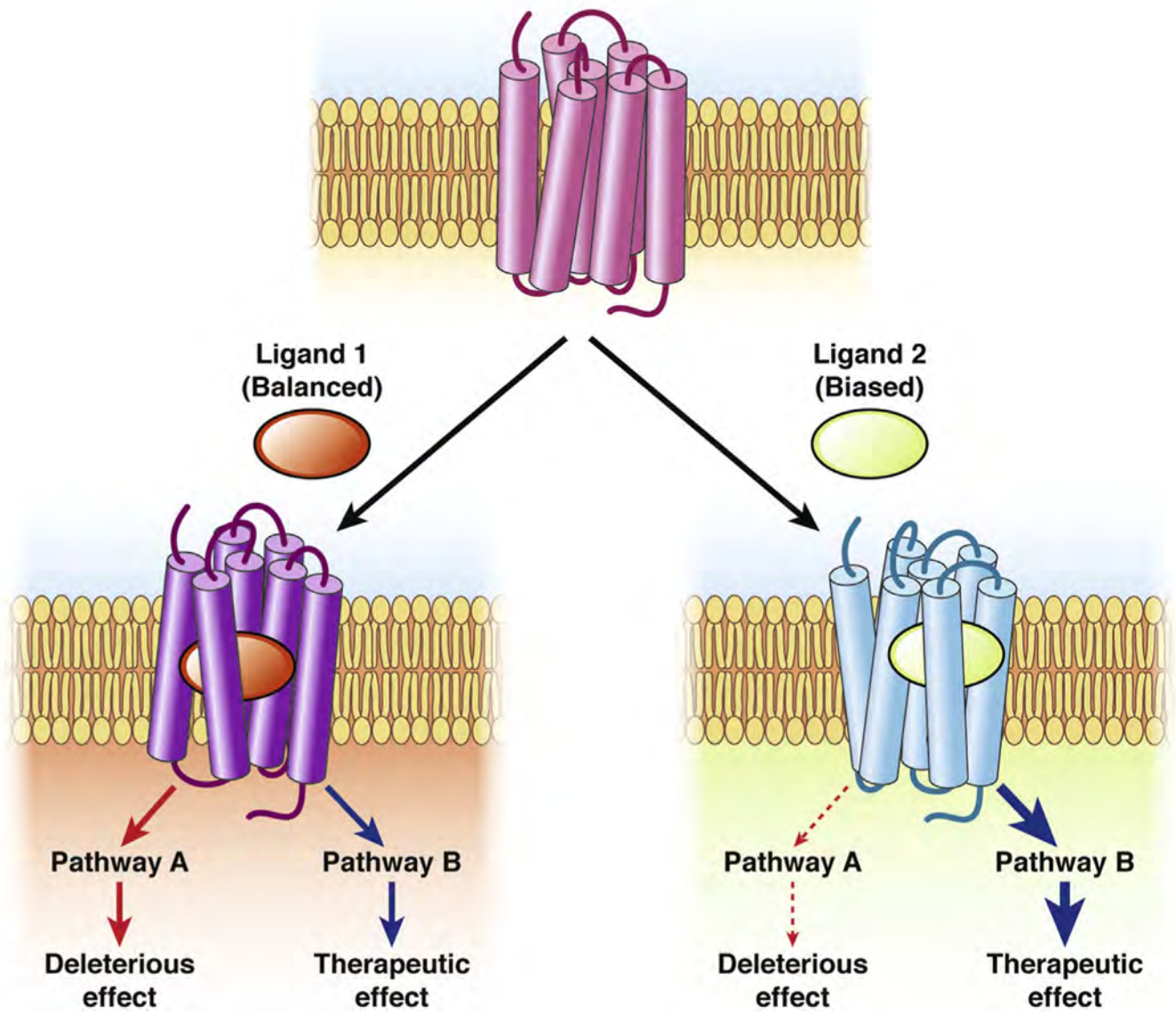


Figure 3.

The therapeutic potential of biased agonists of GPCRs. Biased agonism describes the phenomenon in which different ligands binding to the same GPCR in an identical cellular background elicit distinct signaling outcomes (pathways A and B). Balanced agonists (ligand 1) are those that activate all signaling pathways to the same extent, leading to therapeutic effects but also to deleterious effects. When there is a distinction between the signaling pathways that drive a therapeutic response and those that mediate the adverse effects of a drug, biased agonists provide a novel avenue for pathway-directed therapeutics. In such a case, the drug would only trigger the desired response and spare the unwanted, deleterious effects (ligand 2).

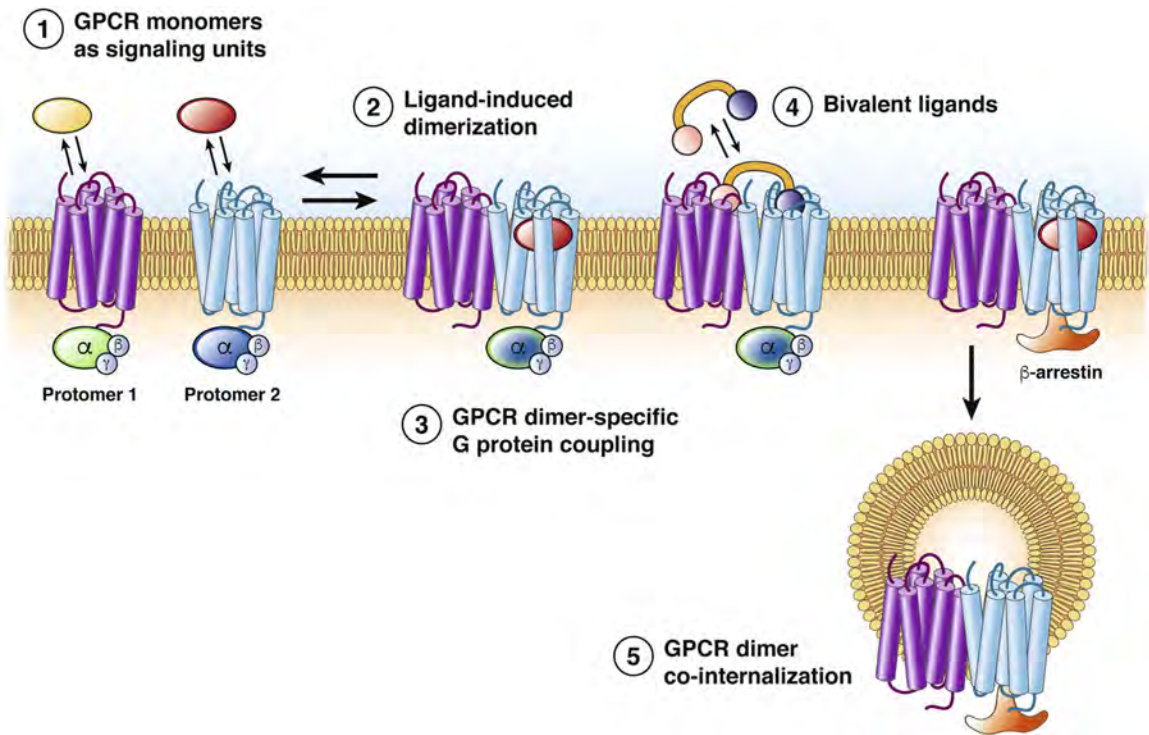


Figure 4.

Potential roles of GPCR dimerization. GPCRs have been shown to function as monomers (1) and dimers (2). (3) The formation of GPCR dimers can be triggered by agonist activation and change the specificity of G-protein coupling. (4) Such differences in effector coupling elicited by dimerization have prompted the development of bivalent drugs, which specifically target the 2 protomers within a dimer. (5) Dimerization also can provide an alternative mechanism of receptor trafficking, in which ligands can promote the co-internalization of the 2 receptors after the stimulation of only 1 protomer. Alternatively, the presence of a protomer that is resistant to agonist-promoted endocytosis, within a heterodimer, can inhibit the internalization of the complex.

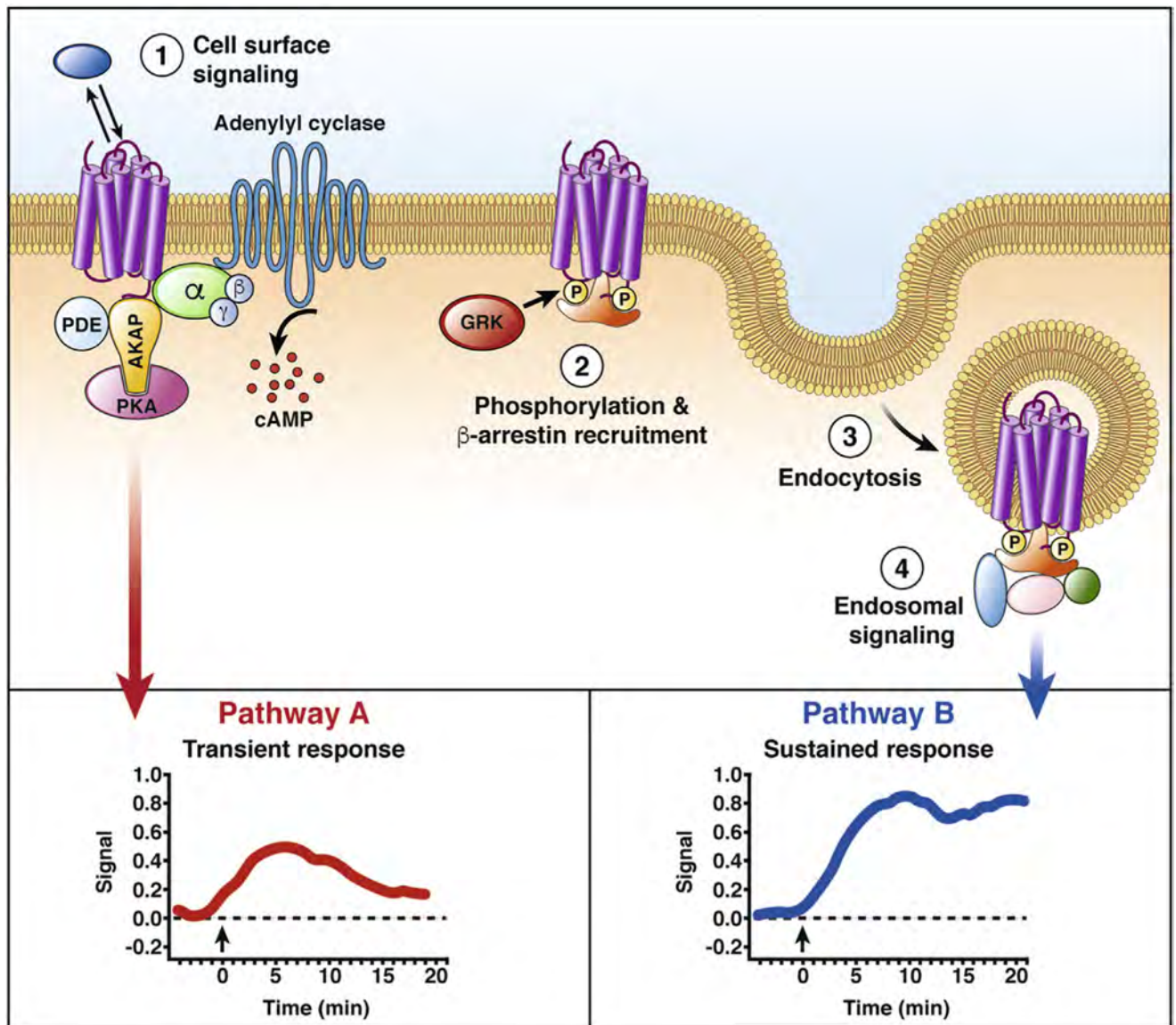


Figure 5. GPCR trafficking and compartmentalized signaling. The formation of GPCR-mediated signaling platforms provides a mechanism to sculpt specific cellular responses. (1) GPCRs at the plasma membrane form multiprotein complexes that participate in the regulation of a specific signaling pathway (pathway A). For example, AKAP interactions with GPCRs can scaffold the formation of complexes that regulate cAMP signaling by bringing in close proximity enzymes that degrade cAMP (PDEs) and kinases that are activated by this second messenger (PKA). (2) With prolonged agonist stimulation, GPCRs are phosphorylated by GRKs. The phosphorylated receptor has higher affinity for the cytosolic protein ARRB. (3) ARRBs are adaptors that promote clathrin- and dynamin-mediated endocytosis of GPCRs. (4) ARRBs scaffold the formation of multi-protein complexes that result in a second wave of intracellular signaling (pathway B). Genetically encoded biosensors have shown differences in the spatial and temporal profile of GPCR signaling from different subcellular locations

(*insets*). AKAP, A-kinase anchor protein; GRK, G-protein receptor kinase; PDE, phosphodiesterase; PKA, protein kinase A.

Author Manuscript

Author Manuscript

Author Manuscript

Author Manuscript

Table 1.

Clinical Trials of Allosteric Modulators, Biased Agonists, and Bivalent Ligands of GPCRs for Treatment of Disorders of the GI Tract or With Side Effects in the GI Tract

| Drug | Mechanism of action | Clinical indication | Potential GI effect | Outcome of trial | ClinicalTrials.gov identifier |
|-----------------------|--------------------------------|---|---|--|--|
| Allosteric modulators | | | | | |
| MK-7622 | M ₁ R PAM | Improved cognition in Alzheimer disease | Diarrhea | Trial stopped for futility; diarrhea was most common side effect | NCT01852110 |
| ADX10059 | MGLUR5 NAM | GERD | Decreased reflux | Further testing stopped due to increased hepatic transaminases | NCT00820079 |
| Biased agonists | | | | | |
| TRY130 | MOR agonist | Pain | Decreased nausea and vomiting; constipation not measured in trials | Analgesia comparable to or better than morphine | NCT02335294, NCT02083315 |
| ADL5859 | DOR agonist | Pain | Possible decreased effect on GI motility vs MOR agonist; however, not measured in trial | No analgesia | NCT00993863, NCT00626275, NCT00603265, NCT00979953 |
| ADL5747 | DOR agonist | Pain | Possible decreased effect on GI motility vs MOR agonist; however, not measured in trial | Not effective for analgesia | NCT00979953, NCT01058642 |
| Oligomer targets | | | | | |
| Eluxadoline | MOR agonist and DOR antagonist | IBS-D abdominal pain | Analgesia for abdominal pain | Approved for clinical use | NCT01553747, NCT01553591 |
| Eluxadoline | MOR agonist and DOR antagonist | IBS-D with bile acid Malabsorption | Improved stool consistency | Recruiting | NCT03441581 |
| Eluxadoline | MOR agonist and DOR antagonist | Diarrhea-associated fecal incontinence | Fewer days with fecal incontinence | Recruitment pending | NCT03489265 |

GI, gastrointestinal.



Sez6 levels are elevated in cerebrospinal fluid of patients with inflammatory pain-associated conditions

Maria Roitman^a, Laura E. Edgington-Mitchell^{b,c,d}, Jon Mangum^e, James Ziogas^e, Alexios A. Adamides^f, Paul Myles^g, Hearan Choo-Bunnett^h, Nigel W. Bunnett^h, Jenny M. Gunnensen^{a,*}

Abstract

Introduction: Seizure-related protein 6 (Sez6) contributes to chronic pain development as *sez6* knockout mice show attenuated pain behaviours after peripheral nerve injury, compared with control mice. The type I transmembrane isoform of Sez6 is cleaved by the β -amyloid precursor protein cleavage enzyme 1 (BACE1), resulting in Sez6 extracellular domain shedding from the neuron surface.

Objectives: To determine whether this BACE1-shed form of Sez6 can be detected in the cerebrospinal fluid (CSF) and whether Sez6 levels in the CSF are altered in neuropathic pain or chronic inflammatory pain (IP).

Methods: We analysed the CSF samples collected during surgery from patients with chronic neuropathic pain ($n = 8$) or IP ($n = 33$), comparing them to the CSF samples from patients with suspected subarachnoid haemorrhage that was subsequently excluded (nonsurgical group, $n = 5$). Western blots were used to determine the relative Sez6 levels in the CSF from the different patient and nonsurgical comparison groups.

Results: The results show that BACE1-shed Sez6 can be readily detected in the CSF by Western blot and that the levels of Sez6 are significantly higher in the IP group than in the nonsurgical comparison group.

Conclusion: The association between elevated Sez6 levels in the CSF and IP is further evidence for persistent alterations in central nervous system activity in chronic IP conditions.

Keywords: Seizure-related protein 6, CSF, Inflammatory pain, Chronic pain, BACE1

Sponsorships or competing interests that may be relevant to content are disclosed at the end of this article.

^a Department of Anatomy and Neuroscience, The University of Melbourne, Parkville, Victoria, Australia, ^b Drug Discovery Biology, Monash Institute of Pharmaceutical Sciences, Monash University, Parkville, Victoria, Australia, ^c Department of Biochemistry and Molecular Biology, Bio21 Molecular Science and Biotechnology Institute, The University of Melbourne, Parkville, Victoria, Australia, ^d Department of Maxillofacial Surgery, College of Dentistry, New York University, New York, NY, USA, ^e Department of Pharmacology and Therapeutics, The University of Melbourne Parkville, Victoria, Australia, ^f Department of Neurosurgery, Royal Melbourne Hospital, Parkville, Victoria, Australia, ^g Department of Anaesthesia and Perioperative Medicine, Alfred Hospital, Melbourne, Victoria, Australia, ^h Department of Surgery, College of Physicians and Surgeons, Columbia University, New York, NY, USA

*Corresponding author. Address: Brain Development and Plasticity, Anatomy and Neuroscience Department, University of Melbourne, Parkville, 3010, Victoria, Australia. Tel.: 161 3 8344 6065. E-mail address: jenny.gunnensen@unimelb.edu.au (J.M. Gunnensen).

Supplemental digital content is available for this article. Direct URL citations appear in the printed text and are provided in the HTML and PDF versions of this article on the journal's Web site (www.painrpts.com).

Copyright © 2019 The Author(s). Published by Wolters Kluwer Health, Inc. on behalf of The International Association for the Study of Pain. This is an open access article distributed under the terms of the Creative Commons Attribution-NonCommercial-ShareAlike License 4.0 (CC BY-NC-SA) which allows others to remix, tweak, and build upon the work non-commercially, as long as the author is credited and the new creations are licensed under the identical terms.

PR9 4 (2019) e719

<http://dx.doi.org/10.1097/PR9.0000000000000719>

1. Introduction

Neuropathic and other forms of chronic pain affect 7% and 13% of the adult population, respectively.^{1,7} Neuropathic pain (NP) arises from a nervous system injury that results in abnormal or spontaneous firing of afferent nociceptive and mechanosensory neurons, a lowered activation threshold of second-order neurons in the spinal cord dorsal horn, and hypersensitisation to stimuli such as heat and touch.^{2,4}

We showed previously that Seizure-related protein 6 (Sez6) is important for the development of neuronal dendrites and synapses.^{5,15} New findings from our laboratory, using a mixed pain model (chronic constriction injury) in mice, have revealed that Sez6 contributes to the development of chronic hyperalgesia and neuroinflammation after nerve injury. In neurons, Sez6 is almost exclusively cleaved by β -amyloid precursor protein cleaving enzyme 1, also known as β -secretase 1 or BACE1.^{12,25} After cleavage of the transmembrane isoform of Sez6 by BACE1, the shed extracellular domain of the protein is released into the cerebrospinal fluid (CSF).²⁰

Because the development of NP and chronic inflammatory pain (IP) involves increased excitatory drive into the spinal cord and into the brain through ascending pathways,^{7,16,26,27} we aimed to test the hypothesis that higher levels of shed Sez6 in the CSF are associated with clinically diagnosed NP or IP. Specifically, this study addressed whether levels of Sez6 in the CSF are significantly changed in surgical patients with (1) chronic NP or (2) chronic IP, compared with a nonsurgical comparison group.

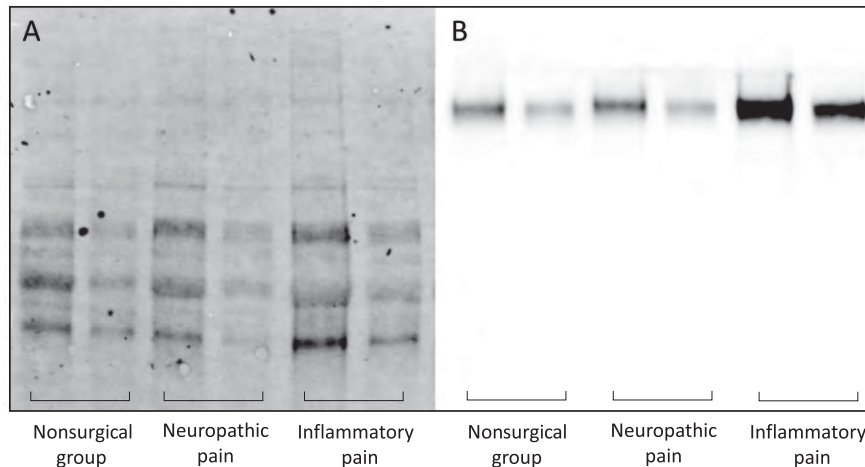


Figure 1. Relative Sez6 levels in the CSF by condition. Example of (A) stain-free and (B) Chemi Hi-Resolution Western blots used for analysis of total protein and Sez6 protein levels, respectively. For each sample, 10 or 5 μL was loaded (left or right lanes of each pair, respectively). CSF, cerebrospinal fluid.

2. Materials and Methods

2.1. Cerebrospinal fluid samples

Cerebrospinal fluid samples from patients undergoing surgery for painful conditions, categorised into NP or IP groups, were obtained from The Alfred Hospital, Melbourne, Victoria, Australia (Alfred Ethics Committee Project No: 247/13), with informed consent. Details of diagnosis and/or surgery are described in Appendix, Table 1 (available at <http://links.lww.com/PR9/A41>). Prescribed medications (see Appendix, Table 1, available at <http://links.lww.com/PR9/A41>) were also taken on the day of CSF collection. Pain severity and intensity scores on the modified Brief Pain Inventory (mBPI) scale were recorded. Cerebrospinal fluid was procured through lumbar puncture before any administration of anaesthetics or analgesics intrathecally, centrifuged to remove any contaminating blood cells, and stored at -80°C . Patient age and sex data are summarised in Appendix, Table 2 (available at <http://links.lww.com/PR9/A41>).

Cerebrospinal fluid samples in the “nonsurgical” comparison group were collected from patients presenting to the emergency department at the Royal Melbourne Hospital, Parkville, Victoria, Australia (RMH Ethics Committee Project ID: HREC 2012-050), with informed consent. Patients in this group presented with a history of sudden-onset headache and, as part of the diagnostic workup, received computed tomography brain scans (that showed no evidence for a subarachnoid haemorrhage) followed by a lumbar puncture, which definitively excluded subarachnoid haemorrhage in all patients in this group. The headaches in these individuals resolved and the cause was not further investigated but presumed to be migraine/tension headache. As indicated in the Appendix, one of these patients had taken Panadol before admission.

2.2. Protein assay and Western blot

Sample protein concentration was measured with the DC Protein Assay (Bio-Rad, Hercules, CA). For Western blots, CSF samples (100 μL) were prepared as follows: 100% trichloroacetic acid was added (10% vol/vol), the samples were then incubated at room temperature for 5 to 10 minutes, and centrifuged (4°C , 20,000g) for 5 minutes. Precipitated protein pellets were dissolved in 100 μL 1x Laemmli buffer, and the pH was adjusted to $>\text{pH}$ 4.6 with ammonia vapour.

For each sample, 2 wells of a Mini-Protean 7.5% TGX precast polyacrylamide gel (Bio-Rad) were loaded (with 5 or 10 μL). Gels were transferred onto nitrocellulose membranes using the Trans-Blot Turbo semidry blotter (Bio-Rad). Membranes were blocked with skim milk powder (5% wt/vol) in 1x tris-buffered saline with 0.05% Tween-20 and incubated with a primary monoclonal antibody (rabbit anti-Sez6, 1/1000 in blocking solution) as described previously,⁵ followed by a goat anti-rabbit HRP-conjugated secondary antibody (Upstate, ID: 12-348), diluted 1/10,000 in blocking solution. Sez6 bands were detected using enhanced chemiluminescence (Clarity ECL, Bio-Rad). The Molecular Image Chemidoc MP System and Image Lab software (Bio-Rad) were used to create a multichannel image. Total protein load was normalised from the Stain-Free blot image, and the specific Sez6 protein signal in each lane was measured from the Chemi Hi-Resolution image (exposure time 90 seconds). An average integrated density value for the Sez6 signal was calculated for each CSF sample. Fold differences were calculated relative to the normalization standard or nonsurgical comparison sample run on the same gel and then the relevant adjustment factor was applied to compare all values with the mean value of all the nonsurgical group

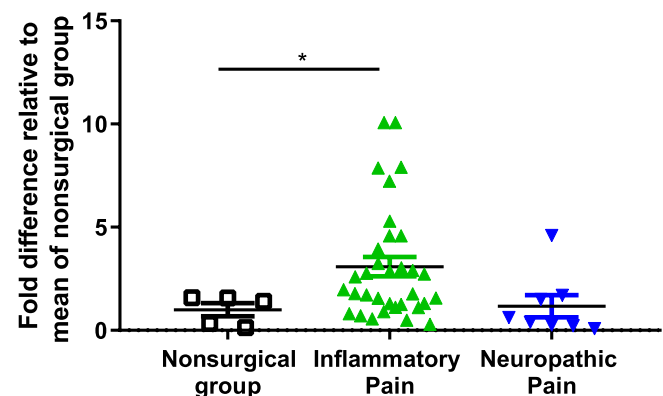


Figure 2. Cerebrospinal fluid Sez6 levels are significantly elevated in inflammatory, but not neuropathic, pain patients compared with samples from the nonsurgical comparison group. A significant increase in shed Sez6 levels in patients with inflammatory pain ($n = 33$, $P < 0.05$) was detected compared to samples from the nonsurgical comparison group ($n = 5$). No significant difference in patients with neuropathic pain ($n = 8$, $p > 0.05$) was observed compared to the control samples. CSF, cerebrospinal fluid.

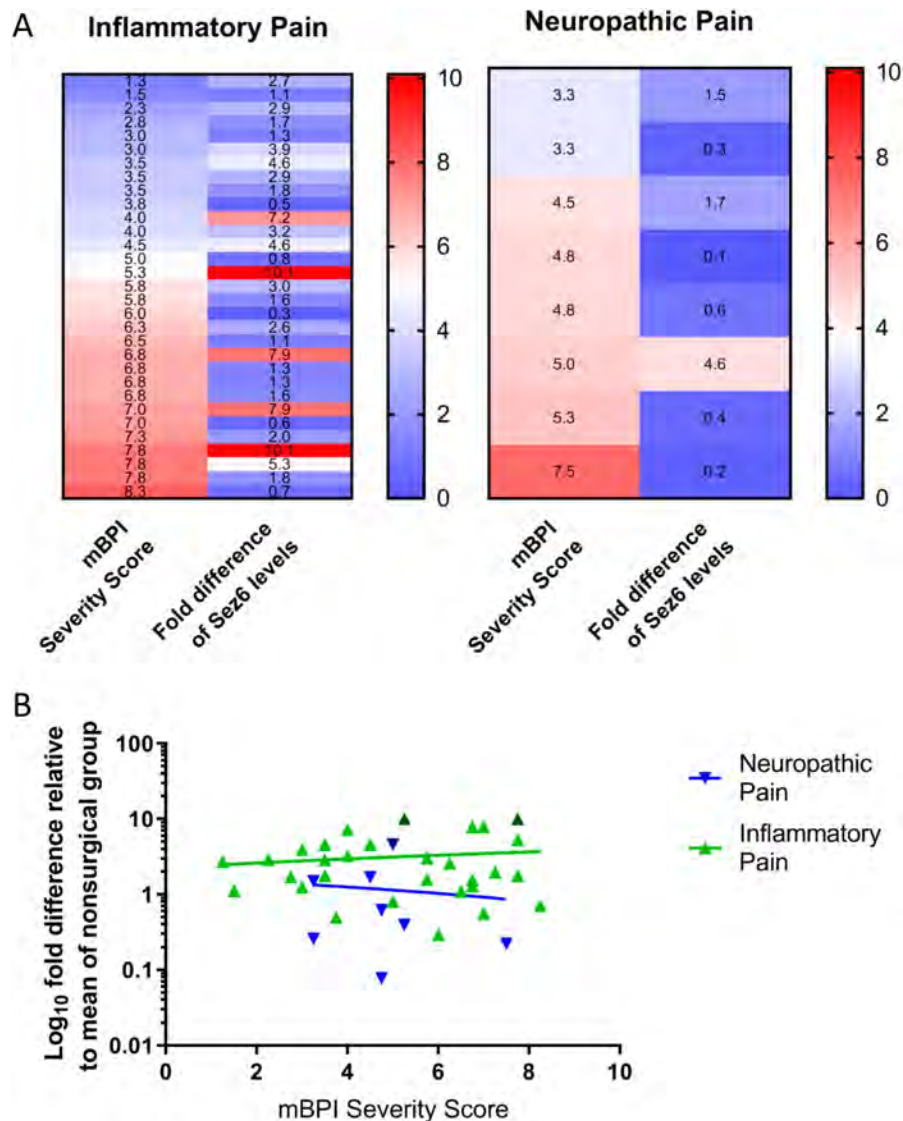


Figure 3. Relative CSF Sez6 levels are not correlated with pain severity scores. (A) Heat maps of modified Brief Pain Inventory (mBPI) pain severity scores and relative Sez6 levels. (B) Linear regression of mBPI pain severity score in patients with neuropathic ($y = -0.1115x + 1.703$) and inflammatory ($y = 0.1118x + 2.484$) pain. Dark triangles represent patient outliers ($1.5 \times$ interquartile range) for relative Sez6 levels. Pain severity scores were not significantly correlated with CSF Sez6 levels ($P > 0.05$). CSF, cerebrospinal fluid.

samples (see Appendix, Tables 3 and 4 for integrated density values and calculations, available at <http://links.lww.com/PR9/A41>). Fold-difference ratios were \log_{10} -transformed to normalize the distribution.

2.3. Statistical analysis

Statistical significance was tested using one-way analysis of variance on \log_{10} -transformed data, followed by the Dunnnett multiple comparisons test. The strength of the correlation between patients' pain severity scores and relative Sez6 levels in the CSF was tested (Pearson correlation).

3. Results

3.1. Sez6 is elevated in the cerebrospinal fluid of patients with inflammatory pain

Sez6 was readily detected in the CSF by Western blot (Fig. 1), and relative Sez6 levels in each CSF sample are plotted in Figure 2.

Levels of shed Sez6 were significantly higher in the CSF of patients with IP relative to the mean of all control samples (mean \pm SEM fold difference = 3.09 ± 0.47 (IP), 1.00 ± 0.32 (controls); $P = 0.038$, $n = 33$ (IP), $n = 5$ (controls); Fig. 2). No significant difference in shed Sez6 levels in the CSF of patients with NP was observed, relative to controls (mean \pm SEM fold difference = 1.17 ± 0.53 (NP), 1.00 ± 0.32 (controls); $P > 0.05$, $n = 8$ (NP), $n = 5$ (controls); Fig. 2).

3.2. No correlation between Sez6 levels and modified Brief Pain Inventory pain severity scores

Tukey boxplots of the Sez6 levels in the CSF from IP and NP groups revealed 2 outliers and 1 outlier, respectively (Appendix, Figure 1, available at <http://links.lww.com/PR9/A41>). All outliers had an mBPI pain severity score of 5.0 or higher (on a scale of 0–10). Heat maps and linear regression plots of mBPI scores against relative CSF Sez6 levels are shown in Figure 3. Severity scores were not correlated with Sez6 CSF levels in patients with

IP (Pearson $r = 0.13$, $R^2 = 0.0169$; $P > 0.05$) or NP ($r = -0.10$, $R^2 = 0.010$; $P > 0.05$).

4. Discussion

Patients with inflammatory, but not neuropathic, pain showed significantly elevated levels of shed Sez6 in the CSF compared with the control patients. In neither group were the CSF levels of Sez6 significantly correlated with reported pain scores. The lack of a strong correlation between various measures of inflammation and subjective measures of pain intensity has been previously reported¹⁹ and is likely attributable to the multifactorial nature of pain.¹

Osteoarthritis (the most common diagnosis of the patients with IP) involves release of inflammatory mediators¹¹ that are capable of sensitising peripheral nociceptors,³ resulting in a lower activation threshold and increased firing of centrally projecting afferent axons in the spinal cord, even with normally innocuous stimuli.¹⁰ Increased excitatory drive and local neuroinflammation, in turn, lead to central nervous system sensitisation,^{9,21} including exaggerated and persistent synaptic long-term potentiation.⁸ The known roles for Sez6 in the development and maintenance of excitatory synapses,¹⁸ and the upregulation of Sez6 mRNA levels during long-term potentiation induction,⁶ suggest that Sez6 may be involved in the activity-dependent chronification of pain and might explain the observed association between elevated Sez6 levels in the CSF and IP conditions.

Sez6 levels in IP samples seem to be segregating into 2 clusters. No obvious commonalities could be identified amongst patients with the highest Sez6 levels, although clearer patterns may emerge if the sample size were increased and/or serial samples were available. If medically indicated, analysing serial samples from individual patients would be preferable to single sample analysis, provided the protocol for repeated CSF collection was standardised. An important consideration, particularly for interpretation of the results presented here, is that levels of A β , itself a product of BACE1 activity, are known to vary diurnally as well as increasing with draw frequency.¹³

Medical biomarkers are important tools for identifying susceptibility to disease, predicting treatment success, and facilitating objective diagnoses.²⁴ A quantitative proteomics study indicated that Sez6 levels in the CSF are elevated in myalgic encephalomyelitis/chronic fatigue syndrome²³ and Sez6 is also implicated in psychiatric disorders, forming part of a CSF biomarker signature for schizophrenia, bipolar disorder, and major depressive disorder.¹⁴ Although all 3 Sez6 family protein members are found in the CSF, only one (Sez6L2) has been identified in blood plasma.²² With the enhanced sensitivity (compared with Western blot) of ELISA-based assays, currently under development for shed Sez6 proteins, detection of Sez6 in serum may soon become feasible.

Because Sez6 is almost exclusively cleaved by BACE1,²⁵ levels of shed Sez6 in the CSF can be used as a direct indicator of BACE1 activity. It will be important to determine whether Sez6 shedding contributes to IP and whether BACE1 inhibitors (currently in clinical trials for the treatment of Alzheimer disease) might be useful for treating conditions associated with elevated CSF Sez6 levels, such as chronic IP.

Disclosures

The authors have no conflict of interest to declare.

This project was supported by NHMRC Project Grant GNT1099930 to J.M. Gunnarsen, NHMRC GNT1091636 to L.E. Edgington-Mitchell, and by grants from the NIH (NS102722,

DE026806, and DK118971) and the Department of Defense (W81XWH1810431) to N.W. Bunnnett.

Acknowledgements

The authors thank Sophie Wallace, Research Manager of the Department of Anaesthesia and Perioperative Medicine at the Alfred Hospital, for provision of deidentified patient data.

Appendix A. Supplemental digital content

Supplemental digital content associated with this article can be found online at <http://links.lww.com/PR9/A41>.

Article history:

Received 22 September 2018

Received in revised form 20 December 2018

Accepted 17 January 2019

References

- [1] Boyden SD, Hossain IN, Wohlfahrt A, Lee YC. Non-inflammatory causes of pain in patients with rheumatoid arthritis. *Curr Rheumatol Rep* 2016; 18:30–8.
- [2] Campbell JN, Meyer RA. Mechanisms of neuropathic pain. *Neuron* 2006; 52:77–92.
- [3] Dray A, Perkins M. Bradykinin and inflammatory pain. *Trends Neurosci* 1993;16:99–104.
- [4] Dworkin RH, Backonja M, Rowbotham MC, Allen RR, Argoff CR, Bennett GJ, Bushnell MC, Farrar JT, Galer BS, Haythornthwaite JA, Hewitt DJ, Loeser JD, Max MB, Saltarelli M, Schmader KE, Stein C, Thompson D, Turk DC, Wallace MS, Watkins LR, Weinstein SM. Advances in neuropathic pain: diagnosis, mechanisms, and treatment recommendations. *Arch Neurol* 2003;60:1524–34.
- [5] Gunnarsen JM, Kim MH, Fuller SJ, De Silva M, Britto JM, Hammond VE, Davies PJ, Petrou S, Faber ES, Sah P, Tan SS. Sez-6 proteins affect dendritic arborization patterns and excitability of cortical pyramidal neurons. *Neuron* 2007;56:621–39.
- [6] Håvik B, Røkke H, Dageyte G, Stavrum AK, Bramham CR, Steen VM. Synaptic activity-induced global gene expression patterns in the dentate gyrus of adult behaving rats: induction of immunity-linked genes. *Neuroscience* 2007;148:925–36.
- [7] Ivanavicius SP, Ball AD, Heapy CG, Westwood FR, Murray F, Read SJ. Structural pathology in a rodent model of osteoarthritis is associated with neuropathic pain: increased expression of ATF-3 and pharmacological characterisation. *PAIN* 2007;128:272–82.
- [8] Ji RR, Kohno T, Moore KA, Woolf CJ. Central sensitization and LTP: do pain and memory share similar mechanisms? *Trends Neurosci* 2003;26:696–705.
- [9] Ji RR, Xu ZZ, Gao YJ. Emerging targets in neuroinflammation-driven chronic pain. *Nat Rev Drug Discov* 2014;13:533–48.
- [10] Kehlet H, Jensen TS, Woolf CJ. Persistent postsurgical pain: risk factors and prevention. *Lancet* 2006;367:1618–25.
- [11] Kidd B. Mechanisms of pain in osteoarthritis. *HSS J* 2012;8:26–8.
- [12] Kuhn PH, Koroniak K, Hogg S, Colombo A, Zeitschel U, Willem M, Volbracht C, Schepers U, Imhof A, Hoffmeister A, Haass C, Roßner S, Bräse S, Lichtenthaler SF. Secretome protein enrichment identifies physiological BACE1 protease substrates in neurons. *EMBO J* 2012;31:3157–68.
- [13] Lucey BP, Gonzales C, Das U, Li J, Siemers ER, Slemmon JR, Bateman RJ, Huang Y, Fox GB, Claassen JA, Slats D, Verbeek MM, Tong G, Soares H, Savage MJ, Kennedy M, Forman M, Sjogren M, Margolin R, Chen X, Farlow MR, Dean RA, Waring JF. An integrated multi-study analysis of intra-subject variability in cerebrospinal fluid amyloid-beta concentrations collected by lumbar puncture and indwelling lumbar catheter. *Alzheimers Res Ther* 2015;7:53.
- [14] Maccarrone G, Ditzel C, Yassouridis A, Rewerts C, Uhr M, Uhlen M, Holsboer F, Turck CW. Psychiatric patient stratification using biosignatures based on cerebrospinal fluid protein expression clusters. *J Psychiatr Res* 2013;47:1572–80.
- [15] Miyazaki T, Hashimoto K, Uda A, Sakagami H, Nakamura Y, Saito SY, Nishi M, Kume H, Tohgo A, Kaneko I, Kondo H, Fukunaga K, Kano M, Watanabe M, Takeshima H. Disturbance of cerebellar synaptic maturation in mutant mice lacking BSRPs, a novel brain-specific receptor-like protein family. *FEBS Lett* 2006;580:4057–64.

- [16] Moalem G, Tracey DJ. Immune and inflammatory mechanisms in neuropathic pain. *Brain Res Rev* 2006;51:240–64.
- [17] Moore RA, Derry S, Taylor RS, Straube S, Phillips CJ. The costs and consequences of adequately managed chronic non-cancer pain and chronic neuropathic pain. *Pain Pract* 2014;14:79–94.
- [18] Nakayama M, Hama C. Modulation of neurotransmitter receptors and synaptic differentiation by proteins containing complement-related domains. *Neurosci Res* 2011;69:87–92.
- [19] Neogi T, Frey-Law L, Scholz J, Niu J, Arendt-Nielsen L, Woolf C, Nevitt M, Bradley L, Felson DT; Multicenter Osteoarthritis (MOST) Study. Sensitivity and sensitisation in relation to pain severity in knee osteoarthritis: trait or state?. *Ann Rheum Dis* 2015;74:682–8.
- [20] Piloni M, Wanngren J, Kuhn PH, Munro KM, Gunnarsen JM, Takeshima H, Feederle R, Voytyuk I, De Strooper B, Levasseur MD, Hrupka BJ, Müller SA, Lichtenthaler SF. Seizure protein 6 and its homolog seizure 6-like protein are physiological substrates of BACE1 in neurons. *Mol Neurodegener* 2016;11:67.
- [21] Raghavendra V, Tanga FY, DeLeo JA. Complete Freund's adjuvant-induced peripheral inflammation evokes glial activation and proinflammatory cytokine expression in the CNS. *Eur J Neurosci* 2004;20:467–73.
- [22] Schutzer SE, Liu T, Natelson BH, Angel TE, Schepmoes AA, Purvine SO, Hixson KK, Lipton MS, Camp DG, Coyle PK, Smith RD, Bergquist J. Establishing the proteome of normal human cerebrospinal fluid. *PLoS One* 2010;5:e10980.
- [23] Schutzer SE, Angel TE, Liu T, Schepmoes AA, Clauss TR, Adkins JN, Camp DG, Holland BK, Bergquist J, Coyle PK, Smith RD, Fallon BA, Natelson BH. Distinct cerebrospinal fluid proteomes differentiate post-treatment Lyme disease from chronic fatigue syndrome. *PLoS One* 2011;6:e17287.
- [24] Schwarz E, Bahn S. The utility of biomarker discovery approaches for the detection of disease mechanisms in psychiatric disorders. *Br J Pharmacol* 2008;153(suppl 1):S133–136.
- [25] Vassar R. BACE1 inhibitor drugs in clinical trials for Alzheimer's disease. *Alzheimers Res Ther* 2014;6:89–14.
- [26] Woolf CJ. Central sensitization: implications for the diagnosis and treatment of pain. *PAIN* 2011;152(3 suppl):S2–15.
- [27] Zhang RX, Ren K, Dubner R. Osteoarthritis pain mechanisms: basic studies in animal models. *Osteoarthritis Cartil* 2013;21:1308–15.

Nanomedicines that Target the Neurokinin 1 Receptor in Endosomes Provide Superior Pain Relief

Paulina D. Ramírez-García^{1,2}, Jeffri S. Retamal^{1,2}, Priyank Shenoy^{1,2}, Wendy Imlach³, Matthew Sykes³, Nghia Truong^{1,2}, Luis Constandil⁴, Teresa Pelissier⁴, Cameron J. Nowell¹, Song Y. Khor^{1,2}, Louis M. Layani^{1,2}, Chris Lumb^{1,2}, Daniel P. Poole^{1,2}, TinaMarie Lieu^{1,2}, Gregory D. Stewart¹, Quynh N. Mai^{1,2}, Dane D. Jensen⁵, Rocco Latorre⁵, Nicole N. Scheff⁶, Brian L. Schmidt⁶, John F. Quinn^{1,2}, Michael R. Whittaker^{1,2}, Nicholas A. Veldhuis^{1,2*}, Thomas P. Davis^{1,2,7*}, Nigel W. Bunnett^{1,2,5,8*}

¹Monash Institute of Pharmaceutical Sciences, Monash University, Parkville, VIC 3052, Australia.

²Australian Research Council Centre of Excellence in Convergent Bio-Nano Science and Technology, Monash University, Parkville, VIC 3052, Australia.

³Monash Biomedicine Discovery Institute, Monash University, Melbourne, VIC 3800, Australia.

⁴Laboratory of Neurobiology, Center for the Development of Nanoscience and Nanotechnology (CEDENNA), University of Santiago de Chile, Santiago 9170022, Chile.

⁵Departments of Surgery and Pharmacology, Columbia University Vagelos College of Physicians and Surgeons, Columbia University in the City of New York, New York City, NY 10032, USA.

⁶Bluestone Center for Clinical Research, New York University College of Dentistry, New York, New York 10010, USA.

⁷Australian Institute for Bioengineering and Nanotechnology, University of Queensland, Brisbane, Queensland 4072, Australia.

⁸Department of Pharmacology and Therapeutics, University of Melbourne, Parkville, VIC 3010, Australia.

* Correspondence:

Nigel W. Bunnett, Ph.D., Columbia University Vagelos College of Physicians and Surgeons, 21 Audubon Avenue, Rm 209, New York City, NY 10032. T: 1212-305-4480; E: nb2733@cumc.columbia.edu.

Thomas P. Davis, Ph.D., Monash Institute of Pharmaceutical Sciences, Monash University, Parkville, VIC 3052, Australia. E: thomas.p.davis@monash.edu.

Nicholas A. Veldhuis, Ph.D., Monash Institute of Pharmaceutical Sciences, Monash University, Parkville, VIC 3052, Australia. E: nicholas.veldhuis@monash.edu.

Abstract

Stimulus-responsive nanoparticles (NPs) are widely used to release drug payloads in specific tissues, such as tumors to induce cytotoxicity, but are seldom used to precisely control disease-relevant intracellular signaling events. During chronic pain, the substance P (SP) neurokinin 1 receptor (NK₁R) redistributes from the plasma membrane to acidified endosomes, where it signals to maintain pain. Hence, the NK₁R in endosomes is a key pain target. Herein, we report that pH-responsive NPs enter cells by clathrin- and dynamin-dependent endocytosis and accumulate in NK₁R-containing endosomes. After intrathecal injection into rodents, pH-responsive NPs containing the FDA-approved NK₁R antagonist Aprepitant (AP) inhibit SP-induced activation of spinal neurons that transmit pain, and provide more complete and persistent relief from nociceptive, inflammatory and neuropathic nociception than free AP, AP in a non-pH responsive NP, or morphine. NPs that deliver antagonists to endosomes offer a much-needed non-opioid treatment for pain, and provide opportunities to redistribute and repurpose established drugs for new indications.

Encapsulation into nanoparticles (NPs) can improve the therapeutic effectiveness of drugs by enhancing stability, tolerability, delivery and retention in diseased tissues ^{1, 2, 3}. There is particular interest in using NPs to deliver anti-cancer drugs, perpetuated by the prospect of engineering NPs to target tumor cells, and by the leaky vasculature and poor lymphatic drainage of solid tumors that promote NP accumulation and uptake ⁴. Stimulus-responsive NPs have been developed to enhance targeted delivery, avoid undesirable exposure and improve efficacy ⁵. Triggers for disassembly and drug release from these NPs include reduced pH, protease activity and altered redox balance within tumors. Despite considerable effort, few NP-based chemotherapeutics have been tested in patients, and the rationale for NP-based drug delivery in cancer has been questioned ⁶.

In addition to development of cancer therapies, there are many potential applications for drug delivery using pH-responsive NPs. For example, inflammation and infection acidify extracellular microenvironments, leading to NP disassembly and drug release ^{7, 8, 9, 10}. Changes in pH within intracellular compartments, including acidification of endosomes and lysosomes, can also be exploited for intracellular drug delivery ¹¹. However, for many applications that require therapeutics to reach cytoplasmic or nuclear targets, the necessity and challenges of endosomal escape limit the usefulness of NP-mediated endosomal delivery ¹². The identification of drug targets within endosomes therefore provides new opportunities for harnessing pH-sensitive materials to chaperone drugs to intracellular targets. Recent advances in understanding the intracellular distribution and activation of G protein-coupled receptors (GPCRs) have created unique opportunities to improve drug efficacy and to repurpose medicines for new applications ^{13, 14, 15, 16, 17, 18, 19, 20, 21, 22}.

GPCRs are an 800-member family of seven transmembrane proteins that control most physiological and pathological processes; GPCRs are the target of >30% of therapeutic drugs ²³. Recent findings demonstrate that GPCR signaling is not confined to the plasma membrane, but also occurs within endosomes ^{20, 24}. Furthermore, "location-biased" compounds can favor interactions with GPCRs in distinct cellular locations leading to unique signaling outcomes of physiological importance ^{16, 21}. In pain pathways, the substance P (SP) neurokinin 1 receptor (NK₁R), the calcitonin gene-related peptide (CGRP) calcitonin receptor-like receptor (CLR), and protease-activated receptor-2 (PAR₂) can generate sustained signals from the endosomes of primary sensory and spinal neurons that promote nociceptive transmission ^{17, 18, 22}. Accordingly, inhibitors of dynamin- and clathrin-dependent endocytosis, and lipid-conjugated antagonists that target these receptors in endosomes provide effective anti-nociception in mice ^{17, 18, 22}. Since these compounds are unlikely to be drug candidates, there remains the need to explore targeted delivery of existing medicines to GPCRs in endosomes. There is considerable scope for investigating whether the treatment of pain could be enhanced by delivering antagonists directly to endosomes that contain activated GPCRs ²⁵.

Herein, we demonstrate the potential for soft polymeric pH-responsive NPs to alter the distribution and efficacy of an FDA-approved NK₁R antagonist (Aprepitant, AP), which is used for treatment of emesis, but has failed in clinical trials for other indications ^{26, 27, 28}. pH-responsive NPs delivered AP to endosomes containing activated NK₁R, and induced a more complete and sustained anti-nociception in preclinical models than conventional therapies, including opioids. NP delivery minimized AP doses required for effective anti-nociception, which potentially avoids activation of off-target pathways. These results demonstrate that NP approaches have potential beyond bulk drug delivery for cancer therapy and in fields where, to date, their applicability has been unrecognized. The use of NPs to direct drugs to subcellular compartments from which GPCRs can generate persistent signals that underlie disease has broad applicability. The discovery that encapsulation within NPs allows delivery of antagonists to GPCRs within

endosomes to enhance and prolong their analgesic properties provides opportunities for the development of much-needed non-opioid therapies for pain.

Results

Synthesis and pH-dependent disassembly of NPs

To obtain pH-responsive and non-responsive NPs, we synthesized diblock copolymers with the same hydrophilic shell of P(PEGMA-co-DMAEMA), but with different hydrophobic cores of P(DIPMA-co-DEGMA) to form pH-responsive NPs, or P(BMA) to form non-pH-responsive NPs (DIPMA or BMA NPs, respectively, Fig. 1A, Supplementary Fig. 1). Gel permeation chromatography (GPC) showed unimodal peaks, where the diblock copolymers shifted toward shorter retention times with increasing molecular weight (Supplementary Fig. 1). ¹H-Nuclear magnetic resonance (¹H-NMR) was used to estimate molecular weight since GPC was calibrated to polystyrene standards. The composition of the polymers was also verified by ¹H-NMR (Supplementary Fig. 1).

DIPMA and BMA NPs were self-assembled in the presence of AP (MK-869²⁶), a hydrophobic NK₁R antagonist, forming DIPMA-AP and BMA-AP NPs, respectively. To generate NPs for delivery of graded concentrations of AP (25, 50 or 100 nM) but a constant concentration of polymer, NPs were self-assembled with graded amounts of AP and a fixed amount of polymer. The AP incorporation (% of initial AP incorporated during self-assembly [mean ± SD]) was: DIPMA-AP 100 nM, 57.8 ± 11.1; 50 nM, 58.4 ± 7.7; 25 nM, 62.6 ± 16.3; BMA-AP, 100 nM, 61.5 ± 12.5; 50 nM, 62.4 ± 11.7; 25 nM, 65.2 ± 16.2 (*n* = 9-27 repeats) (Fig. 1B). DIPMA-AP 100 nM and BMA-AP 100 nM were used for most studies.

Self-assembled NPs are dynamic structures that remain assembled when the concentration of polymer is high enough to favor their assembled state (*i.e.*, above the critical micelle concentration, CMC) (Supplementary Fig. 2). The CMC of DIPMA-empty (DIPMA-Ø) and BMA-Ø NPs were similar (1.9 ± 1.1 and 1.5 ± 1.1 µg/mL, respectively). The CMC of DIPMA-AP (2.4 ± 0.5 µg/mL) was slightly higher than BMA-AP (1.5 ± 0.8 µg/mL) NPs. DIPMA-AP NPs were uniformly spherical, assessed by transmission electron microscopy. Dynamic light scattering indicated 40.4 ± 5.1 nm diameter, with a surface ζ-potential of -0.2 ± 1.6 mV (Fig. 1B, C). DIPMA-Ø NPs were 37 ± 4.2 nm diameter, with a surface ζ-potential of -0.5 ± 2.0 mV. BMA-AP and BMA-Ø NPs were of smaller diameter (28 ± 2.5 and 30 ± 4.4 nm diameter, respectively) but similar ζ-potential (-1.1 ± 2.8 and -0.3 ± 0.3 mV, respectively).

To examine pH-dependent disassembly, NPs were loaded with Nile Red (NR), which fluoresces only in the hydrophobic NP core. DIPMA-NR and BMA-NR NPs were incubated in buffers of graded pH, and NR fluorescence quenching in the aqueous environment was used to evaluate NP disassembly. DIPMA-NR fluorescence declined with increasing acidity, with a 50% decrease in fluorescence at pH 6.08 ± 0.06 (Fig. 1D), consistent with the protonation of the tertiary amine (pK_a 6.1) of DIPMA units and resultant disassembly (Supplementary Fig. 2). BMA-NR fluorescence was unaffected by acidification, which confirms their stability across the pH range (7.4 - 5.0) (Fig. 1D). Kinetic studies of NR quenching at graded pH revealed that DIPMA-NR fluorescence declined to minimum levels within 4 min at pH 6.0 or 5.5 (Fig. 1E) whereas BMA-NR did not decline in acidic buffers (Fig. 1F). There was a small increase in DIPMA-NR fluorescence at pH 6.5 or 7.4 and in BMA-NR fluorescence at pH 7.4, 6.5, 6.0 or 5.5 for unknown reasons. Thus, DIPMA NPs disassemble within minutes of exposure to pH < 6.0.

Clathrin- and dynamin-dependent cellular uptake and pH-dependent disassembly of NPs in NK₁R-positive early endosomes

The uptake and intracellular trafficking of DIPMA NPs labeled with Cyanine 5 (DIPMA-

Cy5) were examined in HEK-293 cells by confocal microscopy. HEK-293 cells were selected because we have previously reported that endosomal trafficking and signaling of the NK₁R is similar in HEK-293 cells and spinal neurons¹⁷. The use of HEK-293 cells facilitated analysis of the colocalization of NPs with GFP-tagged endosomal markers and NK₁R. To examine trafficking to endosomes, DIPMA-Cy5 NPs were incubated with HEK-293 cells expressing Rab5a-GFP, which identifies early endosomes, or Rab7a-GFP, which marks late endosomes. After 30 and 60 min, DIPMA-Cy5 NPs were extensively localized to Rab5a-GFP early endosomes and Rab7a-GFP late endosomes (Fig. 2A, Supplementary Fig. 3A, Supplementary Videos S1, S2). To determine whether NPs traffic to endosomes containing the NK₁R, DIPMA-Cy5 NPs were incubated with HEK-293 cells transfected with rat (r)NK₁R-GFP. After 30 min, cells were challenged with 10 nM SP to promote internalization of rNK₁R-GFP. At 30 and 60 min after SP, rNK₁R-GFP co-localized with DIPMA-Cy5 NPs in endosomes and this distribution was maintained over time in live recordings (Fig. 2B, Supplementary Fig. 3B, Supplementary Video S3). Determination of the Manders overlap coefficient²⁹ confirmed extensive colocalization of DIPMA-Cy5 with the rNK₁R-GFP, Rab5a-GFP and Rab7a-GFP at 30 and 60 min (Fig. 2C). Thus, DIPMA-Cy5 NPs internalize and traffic to endosomes containing rNK₁R-GFP.

We examined the kinetics and mechanism of cellular uptake and disassembly of DIPMA NPs loaded with Coumarin153 (DIPMA-CO), which fluoresces in an aqueous environment but not in the hydrophobic core, by confocal microscopy and high content imaging. When DIPMA-CO NPs were incubated with HEK-293 cells, there was a marked increase in intracellular fluorescence from 1-10 min that continued to increase throughout the 30-min observation period (Fig. 2D, E). The clathrin inhibitor PitStop2 (PS2)³⁰ and the dynamin inhibitor Dyngo4a (Dy4)³¹ attenuated cellular fluorescence (Fig. 2C-E). Bafilomycin A1 (BFA), which inhibits the vacuolar H⁺ATPase that acidifies endosomes, and NH₄Cl, which acts as a lysosomotropic weak base, also suppressed fluorescence (Fig. 2D-F). When non-pH-disassembling BMA-Cy5 NPs were incubated with HEK-293 cells, there was a smaller increase in Coumarin 153 fluorescence from 1-10 min (Fig. 2D, E). Although PS2 and Dy4 suppressed the fluorescence, BFA and NH₄Cl had no effect (Fig. 2D-F). These results are consistent with clathrin- and dynamin-dependent endocytosis, and pH-dependent disassembly of DIPMA NPs in acidified endosomes. BMA NPs also enter cells by clathrin- and dynamin-dependent endocytosis, and release cargo by a mechanism that does not require endosomal acidification.

Biodistribution of DIPMA NPs and delivery of cargo within the spinal cord

To examine NP distribution *in vivo*, we administered DIPMA-Cy5 or BMA-Cy5 NPs to mice by intrathecal (i.t.) injection (L4/L5), a route used to deliver NK₁R antagonists to spinal neurons¹⁷. Cy5 fluorescence, which might be incorporated within NPs or disassembled fluorophore, remained at similar levels within the injection site for up to 24 h, without spreading to distant tissues (Fig. 3A, B). We used confocal microscopy to localize DIPMA-Cy5 and BMA-Cy5 NPs within the dorsal horn of the spinal cord of mice. To mimic the therapeutic situation where NP-encapsulated drugs might be used to treat pain, mice received an intraplantar (i.pl.) injection of capsaicin (CAP) followed by an i.t. injection of NPs. After 1 h, DIPMA-Cy5 and BMA-Cy5 NPs were accumulated in cells throughout laminae I, II and III of the dorsal horn, where they showed a punctate fluorescence concentrated in the perinuclear region (Fig. 3C, Supplementary Videos S4, S5). DIPMA-Cy5 NPs were present in neurons, identified by colocalization with the neuronal marker PGP9.5, although detailed analysis of the cellular distribution was not possible due to loss of NP fluorescence during immunostaining procedures. These results show that NPs remain within the site of administration for prolonged periods. NPs are taken up by cells within superficial laminae of the dorsal horn, including neurons. NPs accumulate in a perinuclear region of spinal neurons.

To evaluate the usefulness of NPs for drug delivery, we made i.t. injections to mice of

either free AP, DIPMA-AP or BMA-AP. At various times after injection, levels of AP were quantified in the spinal cord by LC-MS. At 1 h after injection, the spinal levels of AP were ~2-fold higher for DIPMA-AP than for BMA-AP and ~4-fold higher than for free AP (Fig. 3D). At 4 h, the spinal levels of AP were similar for DIPMA-AP and BMA-AP, and almost undetectable for free AP. Thus, NP encapsulation causes retention of AP within the spinal cord.

Anti-nociceptive effects of NP-encapsulated AP

Whereas AP suppresses acute chemotherapy-induced nausea and vomiting, NK₁R antagonists have shown mixed efficacy for reversing chronic disorders, including depression and pain^{27, 28}. The NK₁R redistributes to endosomes after stimulation with SP, and in pain states it can be maintained in endosomes for extended periods^{17, 32}. Hence, the failure of antagonists may be due to their inability to effectively engage the NK₁R in acidic endosomes²⁵. To examine the hypothesis that incorporation into NPs enhances the anti-nociceptive actions of AP due to delivery to NK₁R-positive endosomes in spinal neurons, AP formulations were administered to mice or rats, including free AP, or AP incorporated into pH-responsive (DIPMA-AP) and non-responsive (BMA-AP) NPs (Fig. 4A). Empty NPs or vehicle were used as controls. Acute and chronic inflammatory and neuropathic nociception were examined.

The assessment of nociception in rodents requires normal motor coordination, which allows paw withdrawal from a painful stimulus. We evaluated motor coordination by a rotarod test. The latency to fall was the same in mice after i.t. injection of vehicle, DIPMA-AP, BMA-AP or DIPMA-Ø NPs (Supplementary Fig. 4). Thus, NPs do not interfere with normal motor coordination.

CAP-evoked mechanical allodynia. AP, NPs or vehicle (5 µL) was administered by i.t. injection to mice 30 min before i.pl. injection to the hindpaw of CAP. CAP activates the transient receptor potential-1 ion channel on primary sensory neurons to evoke SP release within the dorsal horn, NK₁R endocytosis in second order spinal neurons, and consequent acute allodynia^{17, 32}. To assess mechanical nociception, withdrawal responses to stimulation of the plantar surface of the injected hindpaw with calibrated von Frey filaments (VFF) were measured before and after CAP. In mice receiving vehicle or DIPMA-Ø NPs, CAP decreased the VFF threshold from 0.5-4 h, consistent with mechanical allodynia, which returned to baseline after 24 h (Fig. 4B). Free AP (5 µL, 100 nM) and DIPMA-Ø NPs mixed with free AP (100 nM) caused a modest anti-nociception after 1 h (16 ± 4 and 15 ± 3% inhibition respectively), which was not significant after 1.5 h. BMA-AP NPs (100 nM AP) had a similar effect after 0.5-1 h, although the effect was more sustained than free AP, extending for 2 h. DIPMA-AP NPs that delivered the same dose of AP (5 µL, 100 nM) caused marked anti-nociception at 0.5-1 h (1 h, 34 ± 3% inhibition) that was sustained for 4 h (35 ± 2% inhibition), when other treatments were ineffective. Analysis of the integrated response (0-4 h area under curve, AUC) confirmed that DIPMA-AP NPs provided the most effective inhibition of CAP-evoked mechanical allodynia (Fig. 4C).

Complete Freund's adjuvant (CFA)-evoked mechanical hyperalgesia. CFA injection (i.pl.) causes sustained mechanical allodynia and NK₁R endocytosis in spinal neurons^{17, 33}, which allowed examination of the capacity of NP-encapsulated AP administered in a therapeutic manner to reverse inflammatory nociception (Fig. 4A). By 48 h after CFA injection, there was a marked decrease in VFF threshold, consistent with mechanical allodynia (Fig. 4D). Injection of vehicle (i.t.) 48 h after CFA did not affect mechanical hyperalgesia, which persisted for 24 h. AP (5 µL, 100 or 300 nM) dose-dependently reversed hyperalgesia for 2-3 h (1.5 h, % inhibition: 100 nM, 30 ± 6; 300 nM, 47 ± 3%). BMA-AP NPs (100 nM AP) were as effective as free AP (300 nM). DIPMA-AP NPs (100 nM AP) produced a larger inhibition of allodynia than the same dose of free AP (1.5 h, % inhibition: 54 ± 4%), and the inhibition was maintained for 6 h, when other AP treatments were ineffective. Although systemic morphine (3 mg/kg, i.p.) fully reversed the mechanical allodynia after 0.5 h, the effect quickly waned to baseline after 3 h. Analysis of

integrated response (0-8 h AUC, half-width response) indicated that DIPMA-AP NPs produced the most sustained reversal of hyperalgesia (Fig. 4E, F).

Nerve injury-evoked mechanical hyperalgesia. The sural nerve spared (SNS) model produces a stable and robust mechanical hyperalgesia in rats that can last for > 50 days^{34, 35}, which permitted examination of the efficacy of NP-encapsulated AP to relieve chronic neuropathic nociception in another species. To confirm activation of the SP/NK₁R system during chronic neuropathic nociception, we localized the NK₁R in spinal neurons by immunofluorescence. At 10 d after sham surgery, NK₁R immunoreactivity (IR) was largely confined to the plasma membrane of the soma and neurites of laminae I neurons (Supplementary Fig. 5A, Supplementary Video S6). At 10 d after SNS, NK₁R-IR was prominently detected in endosomes of ipsilateral lamina I neurons but was localized to the plasma membrane of contralateral lamina I neurons (Supplementary Fig. 5A, Supplementary Video S7). Quantification of the subcellular localization of NK₁R-IR confirmed receptor endocytosis after SNS. These results suggest activation of the SP/NK₁R system during chronic neuropathic nociception, and are consistent with reports of NK₁R upregulation in the dorsal horn during neuropathic pain³⁶.

At 10 days after surgery, SNS reduced in the pressure that induced withdrawal of the hindpaw (Randal-Selitto test) when compared to sham-operated rats, indicative of mechanical hyperalgesia (Fig. 4A, G). In rats receiving i.t. injection of vehicle, mechanical hyperalgesia was maintained for 7 h (Fig. 4G). Although AP (10 μ L, 100 nM) did not modify withdrawal threshold, AP (300 nM) inhibited withdrawal thresholds after 0.5 h to a maximum of $40 \pm 2\%$ inhibition after 1 h, and return to baseline after 2.5 h. AP (1 μ M) almost fully reversed hyperalgesia after 1 h ($75 \pm 4\%$ inhibition), although hyperalgesia returned to baseline after 3 h (Supplementary Fig. 4). BMA-AP (10 μ L, 100, 300 nM AP) inhibited hyperalgesia to a similar degree as free AP (300 nM). DIPMA-AP (100, 300 nM AP) strongly reversed hyperalgesia, with almost complete inhibition after 1.5 h (300 nM, $80 \pm 4\%$ inhibition) and maintenance for 4.5 h, when none of the other treatments were effective. DIPMA-AP (500 nM) provided complete relief from hyperalgesia for 4.5 h (Supplementary Fig. 6). Although morphine fully reversed hyperalgesia for 2 h, the effect was short-lived compared to DIPMA-AP and was absent after 2.5 h. Analysis of integrated response (0-7 h AUC, half-width response) indicated that DIPMA-AP NPs produced the most sustained reversal of hyperalgesia (Fig. 4H, I).

Thus, encapsulation into pH-responsive DIPMA NPs increases and prolongs the anti-nociceptive actions of AP in models of nociceptive, inflammatory and neuropathic pain in two species. The enhanced effects of DIPMA-AP might be related to the delivery and retention of AP in endosomes of spinal neurons containing the activated NK₁R, and the continued release of AP as DIPMA-AP NPs encounter increasingly acidified endosomal compartments. The anti-nociceptive actions of BMA-AP might be due to non-pH-responsive AP release within neurons by presently unknown mechanisms.

Effects of NP-encapsulated AP on neuronal activity

Nociceptive information transduced by nociceptive sensory neurons (C-fibers) is transmitted to central projecting neurons in the dorsal horn of the spinal cord through the release of glutamate, SP and CGRP³⁷. The amplification of nociceptive information and a decrease in the nociceptive stimulus threshold, known as central sensitization, is a hallmark of chronic pain. To examine sensitization, we measured the threshold current required to activate C-fiber reflexes, and assessed wind-up, a frequency-dependent increase in the excitability of spinal cord neurons induced by electrical stimulation of C-fibers³⁵. The threshold current required for activation of the C-fiber-mediated reflex responses in the ipsilateral biceps femoris muscle was reduced in SNS rats compared to sham controls (SNS, 3.2 ± 2.8 mA; sham, 10.3 ± 1.2 mA, $P < 0.05$), which is consistent with nerve injury-induced sensitization. Application of repeated electrical stimuli (0.1

Hz) lead to a constant and stable C-reflex activity over time, while repeated application of 1.0 Hz electrical stimuli evoked a progressive increase in C-reflex frequency or wind-up (Fig. 5A-F). Administration of AP (10 μ L, 1 μ M i.t.) to SNS rats decreased the C-reflex only at 30 min, but did not affect wind-up. DIPMA-AP NPs (300 nM AP i.t.) decreased C-reflex within 45 min and wind-up activity within 15 min, and inhibited responses for the duration of observations (120 min).

The effectiveness DIPMA-AP to suppress nociception may be due to antagonism of sustained SP-induced excitation of spinal neurons, which requires NK₁R signaling from endosomes¹⁷. To examine this possibility, we made cell-attached patch-clamp recordings from lamina I neurons in slices of rat spinal cord. In vehicle-treated slices, SP (1 μ M, 2 min) caused a rapid onset in action potential firing that was sustained for the 16-min measurement period after washout (Fig. 5G-I). Preincubation with AP (100 nM) or BMA-AP (100 nM AP) had minimal effect on the onset, rate or duration of SP-induced firing. DIPMA-AP (100 nM) did not affect the initial onset of SP-evoked firing, but inhibited the rate of discharge after washout and the duration of excitation. These results support the hypothesis that AP, when delivered in pH-responsive NPs, antagonizes the NK₁R in acidified endosomes and inhibits the signals that drive sustained excitation of spinal neurons and persistent nociception.

Effects of NP-encapsulated AP on NK₁R Signaling in Endosomes

We have previously shown in HEK-293 cells that the NK₁R in endosomes activates extracellular signal-regulated kinase (ERK) in the nucleus and protein kinase C and cAMP in the cytosol¹⁷. ERK mediates SP-induced excitation of spinal neurons and nociception¹⁷. Painful stimuli (CAP, i.pl.) induce phosphorylation of ERK (pERK) in neurons in superficial laminae of the dorsal horn of the mouse spinal cord, which requires NK₁R endocytosis¹⁷. To examine whether NP-encapsulated AP can prevent activation of ERK in spinal neurons *in vivo*, we administered AP, DIPMA-AP, BMA-AP (100 nM, 5 μ L) or vehicle (control) (i.t.) to mice. After 30 min, CAP or vehicle was injected into the paw (i.pl.). The spinal cord was collected 4 h-post CAP. pERK-IR neurons were identified by immunofluorescence. CAP induced a 3.9-fold increase in the number of pERK-IR expressing neurons in laminae I, II and III of the ipsilateral but not contralateral dorsal horn (Fig. 6A, B). Free AP caused a 43% reduction, BMA-AP a 63% reduction and DIPMA-AP an 81% reduction in pERK-IR neurons. Thus, DIPMA-AP inhibited ERK activation in spinal neurons more completely than BMA-AP or free AP, in line with its enhanced efficacy for inhibition of CAP-evoked nociception (Fig. 4B).

We studied primary cultures of mouse striatal neurons to assess SP-induced activation of nuclear ERK *in vitro*. SP induced robust Ca²⁺ signals in striatal neurons that were abolished by pretreatment with AP and thus attributable to NK₁R activation (Supplementary Fig. 7A, B). When striatal neurons were incubated with DIPMA-Cy5 NPs and SP (100 nM) for 30 min, DIPMA-Cy5 NPs were detected in close proximity to endosomes containing NK₁R-IR (Fig. 7C). To examine whether NP-encapsulated AP can inhibit endosomal NK₁R signaling, neurons were preincubated with vehicle, free AP or DIPMA-AP (100 nM, 30 min), washed, and recovered for 30 min. Neurons were then challenged with SP (100 nM) or phorbol 12,13-dibutyrate (PDBU, positive control, 10 μ M) for 30 min. Nuclear pERK-IR and total ERK-IR were detected by immunofluorescence and confocal imaging. SP and PDBU stimulated nuclear pERK (Fig. 7D, Supplementary Fig. 7C). DIPMA-AP reduced responses to basal levels, whereas free AP was ineffective.

Genetically-encoded Förster Resonance Energy Transfer (FRET) biosensors can be used to study GPCR signaling in living cells with high spatiotemporal fidelity³⁸. To examine activation of nuclear ERK, we transfected HEK-293 cells expressing human (h) NK₁R with NucEKAR, an ERK biosensor that is targeted to the nucleus. SP (100 pM - 1 μ M) stimulated a rapid (2 min), sustained and concentration-dependent activation of nuclear ERK (EC₅₀ 5.9 nM) (Supplementary Fig. 8A, B). We examined the capacity of free AP to antagonize the nuclear ERK response to 5

nM SP (~EC₅₀). AP inhibited SP-evoked activation of nuclear ERK, but only at the highest concentrations (0.1, 1, 10 μM; IC₅₀ 45 nM) (Supplementary Fig. 8C, D). To determine whether the NK₁R endocytosis and endosomal signaling is necessary for SP-induced activation of nuclear ERK, we transfected HEK-hNK₁R cells with wild-type (WT) dynamin or dominant negative dynamin K44E, which inhibits NK₁R endocytosis¹⁷. In cells expressing WT dynamin, SP stimulated a rapid and sustained activation of nuclear ERK (EC₅₀ 11.1 nM) (Supplementary Fig. 8E, G). Dynamin K44E attenuated responses to all concentrations of SP, abolished the response to 10 nM SP, and reduced the potency of SP by ~2-fold (EC₅₀ 19.8 nM) and the efficacy by ~30% (Supplementary Fig. 8F, G). Thus, NK₁R endocytosis is necessary for persistent SP-induced activation of nuclear ERK.

To determine whether unloaded NPs affect nuclear ERK activity, we incubated HEK-293 cells for 30 min with DIPMA-Ø or BMA-Ø NPs (10, 20, 30 μg/mL). DIPMA-Ø or BMA-Ø NPs did not activate nuclear ERK at any concentration or time studied (Supplementary Fig. 8H). DIPMA-Ø NPs had no effect on SP- (5 nM) stimulated activation of nuclear ERK in HEK-hNK₁R cells, although 30 μg/mL BMA had a small inhibitory effect (Supplementary Fig. 8I). The effect of NPs on cell viability was examined using alamarBlue, which assess the capability of viable cells to reduce rezasurin to resofurin. Exposure of HEK-293 cells to DIPMA-Ø or BMA-Ø NPs (1-100 μg/mL) for 24 h or 48 h did not affect cell viability (Supplementary Fig. 8J).

To compare the capacity of free AP and NP-encapsulated AP to antagonize the NK₁R in endosomes, we measured SP-induced activation of nuclear ERK in HEK-hNK₁R cells. Cells were preincubated with vehicle, free AP or DIPMA-AP (25, 50, 100 nM AP) for 30 min, and were then challenged with SP (5 nM). In vehicle-treated cells, SP stimulated a rapid and sustained activation of nuclear ERK (Fig. 6E, G). Free AP caused a partial concentration-dependent inhibition of SP-stimulated nuclear ERK activity, whereas DIPMA-AP strongly inhibited the response at all concentrations. To compare the capacity of free AP and NP-encapsulated AP to induce a sustained antagonism of the NK₁R in endosomes, cells were preincubated with vehicle, AP or DIPMA-AP (100 nM) for 30 min, washed, recovered in medium without antagonist for 30 or 120 min, and then challenged with SP. Free AP was now inactive, whereas DIPMA-AP (100 nM) abolished SP-induced activation of nuclear ERK at 30 and 120 min (Fig. 6F-H). Although BMA-AP was less efficacious than DIPMA-AP in assays of nociception (Fig 4) and ERK activity in spinal neurons *in vivo* (Fig. 6A, B), BMA-AP (100 nM) inhibited SP-induced activation of nuclear ERK in HEK-hNK₁R cells to a similar degree as DIPMA-AP (Fig. 6E-H). The intracellular disassembly of BMA-AP NPs by unknown mechanisms might release sufficient quantities of AP to effectively antagonize the NK₁R in endosomes. Non-selective effects of BMA on SP-stimulated nuclear ERK (Supplementary Fig. 8I) might also contribute to inhibition.

Discussion

The realization that GPCRs can signal from subcellular compartments other than the plasma membrane and that these signals control important pathophysiological processes, such as pain^{17, 18, 22}, has implications for drug discovery and delivery²⁵. The rationale for the current study is that the NK₁R redistributes from the plasma membrane to endosomes of spinal neurons after painful stimuli that release SP within the dorsal horn^{17, 28, 32}. The NK₁R in endosomes can generate sustained signals that mediate neuronal excitation and nociceptive transmission¹⁷. Although inhibitors of dynamin and clathrin and lipid-conjugated antagonists that target the NK₁R in endosomes provide effective anti-nociception¹⁷, considerable effort will be required to advance these compounds to the clinic. Dynamin and clathrin inhibitors affect endocytosis and exocytosis of many receptors and channels, which might account for their anti-nociceptive properties. Antagonists can lose potency when covalently conjugated to lipids. Since lipidated antagonists incorporate into plasma and endosomal membranes, and can inhibit signaling in both locations,

they cannot be used to exclusively target endosomal signaling of GPCRs. We used pH-responsive NPs to deliver AP exclusively to endosomes, without loss of potency. AP is an NK₁R antagonist that is an approved treatment for chemotherapy-induced nausea and vomiting^{26, 28}. Encapsulation into NPs resulted in a remarkable increase in the efficacy and duration of action of AP, exceeding the ability of free AP or morphine to provide anti-nociception in preclinical models of nociceptive, inflammatory and neuropathic pain. These findings are consistent with the improved capacity of NP-encapsulated AP to inhibit SP-induced excitation of spinal neurons and to cause a sustained inhibition of endosomal signaling by the NK₁R. Thus, NP uptake and sustained release of AP in acidic endosomes containing the activated NK₁R might account for the enhanced and persistent anti-nociceptive actions of the NP-encapsulated drug. Since endosomes are a dynamic tubulo-vesicular compartment, it is likely that AP, once released from NPs, can antagonize the NK₁R throughout the endosomal system. SP dissociation from the NK₁R in acidic endosomes may allow AP to engage more effectively the NK₁R.

Further studies are necessary before NP-encapsulated drugs can be advanced to clinical trials for the treatment of pain. They include toxicology and pharmacokinetic studies of NP components (monomers and AP), and pharmacodynamic studies that compare the efficacy of AP and NP-encapsulated AP in disease-relevant preclinical models of pain in several species. Therapeutic efficacy could be improved by combining antagonists of different GPCRs into the same NPs, for example antagonists of NK₁R and CLR that co-mediate pain transmission by spinal neurons^{17, 22}. By incorporating targeting groups into the NP shell, it might be possible to selectively deliver NPs to neurons that sense and transmit pain, with further improvement in efficacy and selectivity. Limitations of our study include analysis of evoked nociception in preclinical models rather than the perception of pain, which requires human studies. Analysis of NP uptake, disassembly, efficacy and toxicity focused on model cell lines or primary striatal neurons, rather than spinal neurons that are the likely target of NP-encapsulated AP.

NP-encapsulation might improve the therapeutic efficacy of antagonists and agonists of many GPCRs that continue to signal from endosomes^{15, 20, 25}. Since GPCRs are the target of most clinically-approved drugs, and many drugs fail during development for reasons that are not fully understood, NP encapsulation could advance the development of drugs to treat multiple diseases by altering their intracellular distribution profile to fine-tune signaling processes of pathophysiological importance.

Acknowledgements. Supported by the National Institutes of Health (NS102722, DE026806, DK118971), Department of Defense (PR170507), National Health and Medical Research Council (63303, 1049682, 1031886) (NWB), Australian Research Council Centre of Excellence in Convergent Bio-Nano Science and Technology (NWB, TPD), Center for the Development of Nanoscience and Nanotechnology, and Takeda Pharmaceuticals Inc. (NWB). We thank F. Chiu for mass spectrometry analysis of AP loading and Dr. P. Zhao for her expert advice about signaling assays.

Author contributions. PRG prepared and characterized NPs, examined NP uptake and disassembly, studied SP signaling in model cells, and wrote the manuscript; JSR studied the biodistribution and anti-nociceptive and *in vivo* electrophysiological actions of NPs; PS studied the biodistribution and anti-nociceptive actions of NPs; WI conceived and designed electrophysiological studies on spinal neurons; MS studied excitation of spinal neurons; NT prepared and characterized NPs; LC conceived and designed neuropathic nociception and *in vivo* electrophysiological studies; TP conceived and designed neuropathic nociception; CJN provided expertise in analysis of confocal images; SYK obtained TEM images; LML characterized CMC and pH-disassembly of NPs; CL studied SP signaling in model cells; DPP studied NP uptake;

TML studied anti-nociceptive actions of NPs; GDS prepared striatal neurons; QNM prepared and characterized NPs; DDJ examined NK₁R endocytosis, NP uptake into spinal neurons, and SP signaling in model cells and striatal neurons; RL examined NK₁R endocytosis and NP uptake into spinal neurons; NSN studied NK₁R endocytosis in rats; BLS designed experiments to examine NK₁R endocytosis in rats; JFQ designed NPs and wrote the manuscript; MRW designed NPs; NAV conceived experiments, studied SP signaling in neurons, interpreted results, and wrote the manuscript; TPD conceived experiments and designed NPs; NWB conceived and designed experiments, interpreted results, and wrote the manuscript.

Competing interests. Research in NAV's, DPP's and NWB's laboratories is funded, in part, by Takeda Pharmaceuticals Inc. NWB is a founding scientist of Endosome Therapeutics Inc.

References

1. De Jong WH, Borm P. Drug delivery and nanoparticles: Applications and hazards. *International Journal of Nanomedicine* 2008, **3**(2): 133-149.
2. Farokhzad OC, Langer R. Impact of nanotechnology on drug delivery. *ACS nano* 2009, **3**(1): 16-20.
3. Uhrich KE, Cannizzaro SM, Langer RS, Shakesheff KM. Polymeric Systems for Controlled Drug Release. *Chemical reviews* 1999, **99**(11): 3181-3198.
4. Maeda H, Wu J, Sawa T, Matsumura Y, Hori K. Tumor vascular permeability and the EPR effect in macromolecular therapeutics: a review. *J Control Release* 2000, **65**(1-2): 271-284.
5. Such GK, Yan Y, Johnston AP, Gunawan ST, Caruso F. Interfacing materials science and biology for drug carrier design. *Adv Mater* 2015, **27**(14): 2278-2297.
6. Wilhelm S, Tavares AJ, Dai Q, Ohta S, Audet J, Dvorak HF, *et al.* Analysis of nanoparticle delivery to tumours. *Nature Reviews Materials* 2016, **1**: 16014.
7. Chan JM, Farokhzad OC, Gao W. pH-Responsive Nanoparticles for Drug Delivery. *Molecular Pharmaceutics* 2010, **7**(6): 1913-1920.
8. Lynn DM, Amiji MM, Langer R. pH-Responsive Polymer Microspheres: Rapid Release of Encapsulated Material within the Range of Intracellular pH *Angewandte Chemie International Edition* 2001, **40**(9): 1707-1710.
9. Mura S, Nicolas J, Couvreur P. Stimuli-responsive nanocarriers for drug delivery. *Nature Materials* 2013, **12**(11): 991-1003.
10. Schmaljohann D. Thermo- and pH-responsive polymers in drug delivery. *Advanced drug delivery reviews* 2006, **58**(15): 1655-1670.
11. Zhou K, Wang Y, Luby-Phelps K, Sumer BD, Gao J. Tunable, ultrasensitive pH-responsive nanoparticles targeting specific endocytic organelles in living cells. *Angewandte Chemie International Edition* 2011, **50**(27): 6109-6114.

12. Nelson CE, Kintzing JR, Hanna A, Shannon JM, Gupta MK, Duvall CL. Balancing cationic and hydrophobic content of PEGylated siRNA polyplexes enhances endosome escape, stability, blood circulation time, and bioactivity in vivo. *ACS Nano* 2013, **7**(10): 8870-8880.
13. Calebiro D, Nikolaev VO, Gagliani MC, de Filippis T, Dees C, Tacchetti C, *et al.* Persistent cAMP-signals triggered by internalized G-protein-coupled receptors. *PLoS Biology* 2009, **7**(8): e1000172.
14. Irannejad R, Tomshine JC, Tomshine JR, Chevalier M, Mahoney JP, Steyaert J, *et al.* Conformational biosensors reveal GPCR signalling from endosomes. *Nature* 2013, **495**(7442): 534-538.
15. Irannejad R, von Zastrow M. GPCR signaling along the endocytic pathway. *Current opinion in cell biology* 2014, **27**: 109-116.
16. Irannejad R, Pessino V, Mika D, Huang B, Wedegaertner PB, Conti M, *et al.* Functional selectivity of GPCR-directed drug action through location bias. *Nat Chem Biol* 2017, **13**(7): 799-806.
17. Jensen DD, Lieu T, Halls ML, Veldhuis NA, Imlach WL, Mai QN, *et al.* Neurokinin 1 receptor signaling in endosomes mediates sustained nociception and is a viable therapeutic target for prolonged pain relief. *Science translational medicine* 2017, **9**(392): eaal3447.
18. Jimenez-Vargas NN, Pattison LA, Zhao P, Lieu T, Latorre R, Jensen DD, *et al.* Protease-activated receptor-2 in endosomes signals persistent pain of irritable bowel syndrome. *Proc Natl Acad Sci U S A* 2018, **115**(31): E7438-E7447.
19. Manglik A, Lin H, Aryal DK, McCorvy JD, Dengler D, Corder G, *et al.* Structure-based discovery of opioid analgesics with reduced side effects. *Nature* 2016, **537**(7619): 185-190.
20. Murphy JE, Padilla BE, Hasdemir B, Cottrell GS, Bunnett NW. Endosomes: a legitimate platform for the signaling train. *Proceedings of the National Academy of Sciences of the United States of America* 2009, **106**(42): 17615-17622.
21. Stoeber M, Jullie D, Lobingier BT, Laeremans T, Steyaert J, Schiller PW, *et al.* A Genetically Encoded Biosensor Reveals Location Bias of Opioid Drug Action. *Neuron* 2018, **98**(5): 963-976 e965.
22. Yarwood RE, Imlach WL, Lieu T, Veldhuis NA, Jensen DD, Klein Herenbrink C, *et al.* Endosomal signaling of the receptor for calcitonin gene-related peptide mediates pain transmission. *Proc Natl Acad Sci U S A* 2017, **114**(46): 12309-12314.
23. Hauser AS, Attwood MM, Rask-Andersen M, Schiöth HB, Gloriam DE. Trends in GPCR drug discovery: new agents, targets and indications. *Nature Reviews Drug Discovery* 2017, **16**: 829.
24. Vilardaga JP, Jean-Alphonse FG, Gardella TJ. Endosomal generation of cAMP in GPCR signaling. *Nat Chem Biol* 2014, **10**(9): 700-706.

25. Thomsen ARB, Jensen DD, Hicks GA, Bunnett NW. Therapeutic Targeting of Endosomal G-Protein-Coupled Receptors. *Trends Pharmacol Sci* 2018.
26. Kramer MS, Cutler N, Feighner J, Shrivastava R, Carman J, Sramek JJ, *et al.* Distinct Mechanism for Antidepressant Activity by Blockade of Central Substance P Receptors. *Science* 1998, **281**(5383): 1640.
27. Quartara L, Altamura M, Evangelista S, Maggi CA. Tachykinin receptor antagonists in clinical trials. *Expert Opin Investig Drugs* 2009, **18**(12): 1843-1864.
28. Steinhoff MS, von Mentzer B, Geppetti P, Pothoulakis C, Bunnett NW. Tachykinins and their receptors: contributions to physiological control and the mechanisms of disease. *Physiol Rev* 2014, **94**(1): 265-301.
29. Manders EMM, Verbeek FJ, Aten JA. Measurement of co-localization of objects in dual-colour confocal images. *Journal of Microscopy* 1993, **169**(3): 375-382.
30. Robertson MJ, Deane FM, Stahlschmidt W, von Kleist L, Haucke V, Robinson PJ, *et al.* Synthesis of the Pitstop family of clathrin inhibitors. *Nature protocols* 2014, **9**(7): 1592-1606.
31. Robertson MJ, Deane FM, Robinson PJ, McCluskey A. Synthesis of Dynole 34-2, Dynole 2-24 and Dyngo 4a for investigating dynamin GTPase. *Nature protocols* 2014, **9**(4): 851-870.
32. Mantyh PW, DeMaster E, Malhotra A, Ghilardi JR, Rogers SD, Mantyh CR, *et al.* Receptor endocytosis and dendrite reshaping in spinal neurons after somatosensory stimulation. *Science* 1995, **268**(5217): 1629-1632.
33. Stein C, Millan MJ, Herz A. Unilateral inflammation of the hindpaw in rats as a model of prolonged noxious stimulation: alterations in behavior and nociceptive thresholds. *Pharmacol Biochem Behav* 1988, **31**(2): 445-451.
34. Decosterd I, Woolf CJ. Spared nerve injury: an animal model of persistent peripheral neuropathic pain. *Pain* 2000, **87**(2): 149-158.
35. Bravo D, Ibarra P, Retamal J, Pelissier T, Laurido C, Hernandez A, *et al.* Pannexin 1: A novel participant in neuropathic pain signaling in the rat spinal cord. *Pain* 2014, **155**(10): 2108-2115.
36. Abbadie C, Brown JL, Mantyh PW, Basbaum AI. Spinal cord substance P receptor immunoreactivity increases in both inflammatory and nerve injury models of persistent pain. *Neuroscience* 1996, **70**(1): 201-209.
37. Geppetti P, Veldhuis NA, Lieu T, Bunnett NW. G Protein-Coupled Receptors: Dynamic Machines for Signaling Pain and Itch. *Cell* 2015, **88**(4): 635-649.
38. Halls ML, Canals M. Genetically Encoded FRET Biosensors to Illuminate Compartmentalised GPCR Signalling. *Trends Pharmacol Sci* 2018, **39**(2): 148-157.

39. Chiefari J, Chong YKB, Ercole F, Krstina J, Jeffery J, Le TPT, *et al.* Living Free-Radical Polymerization by Reversible Addition–Fragmentation Chain Transfer: The RAFT Process. *Macromolecules* 1998, **31**(16): 5559-5562.
40. Schindelin J, Arganda-Carreras I, Frise E, Kaynig V, Longair M, Pietzsch T, *et al.* Fiji: an open-source platform for biological-image analysis. *Nat Methods* 2012, **9**(7): 676-682.
41. Zimmermann M. Ethical guidelines for investigations of experimental pain in conscious animals. *Pain* 1983, **16**(2): 109-110.
42. Randall LO, Selitto JJ. A method for measurement of analgesic activity on inflamed tissue. *Arch Int Pharmacodyn Ther* 1957, **111**(4): 409-419.
43. Santos-Nogueira E, Redondo Castro E, Mancuso R, Navarro X. Randall-Selitto test: a new approach for the detection of neuropathic pain after spinal cord injury. *J Neurotrauma* 2012, **29**(5): 898-904.
44. Retamal J, Reyes A, Ramirez P, Bravo D, Hernandez A, Pelissier T, *et al.* Burst-Like Subcutaneous Electrical Stimulation Induces BDNF-Mediated, Cyclotraxin B-Sensitive Central Sensitization in Rat Spinal Cord. *Frontiers in Pharmacology* 2018, **9**: 1143.
45. Imlach WL, Bhola RF, May LT, Christopoulos A, Christie MJ. A Positive Allosteric Modulator of the Adenosine A1 Receptor Selectively Inhibits Primary Afferent Synaptic Transmission in a Neuropathic Pain Model. *Mol Pharmacol* 2015, **88**(3): 460-468.
46. di Porzio U, Daguet MC, Glowinski J, Prochiantz A. Effect of striatal cells on in vitro maturation of mesencephalic dopaminergic neurones grown in serum-free conditions. *Nature* 1980, **288**(5789): 370-373.

Figures and Figure Legends

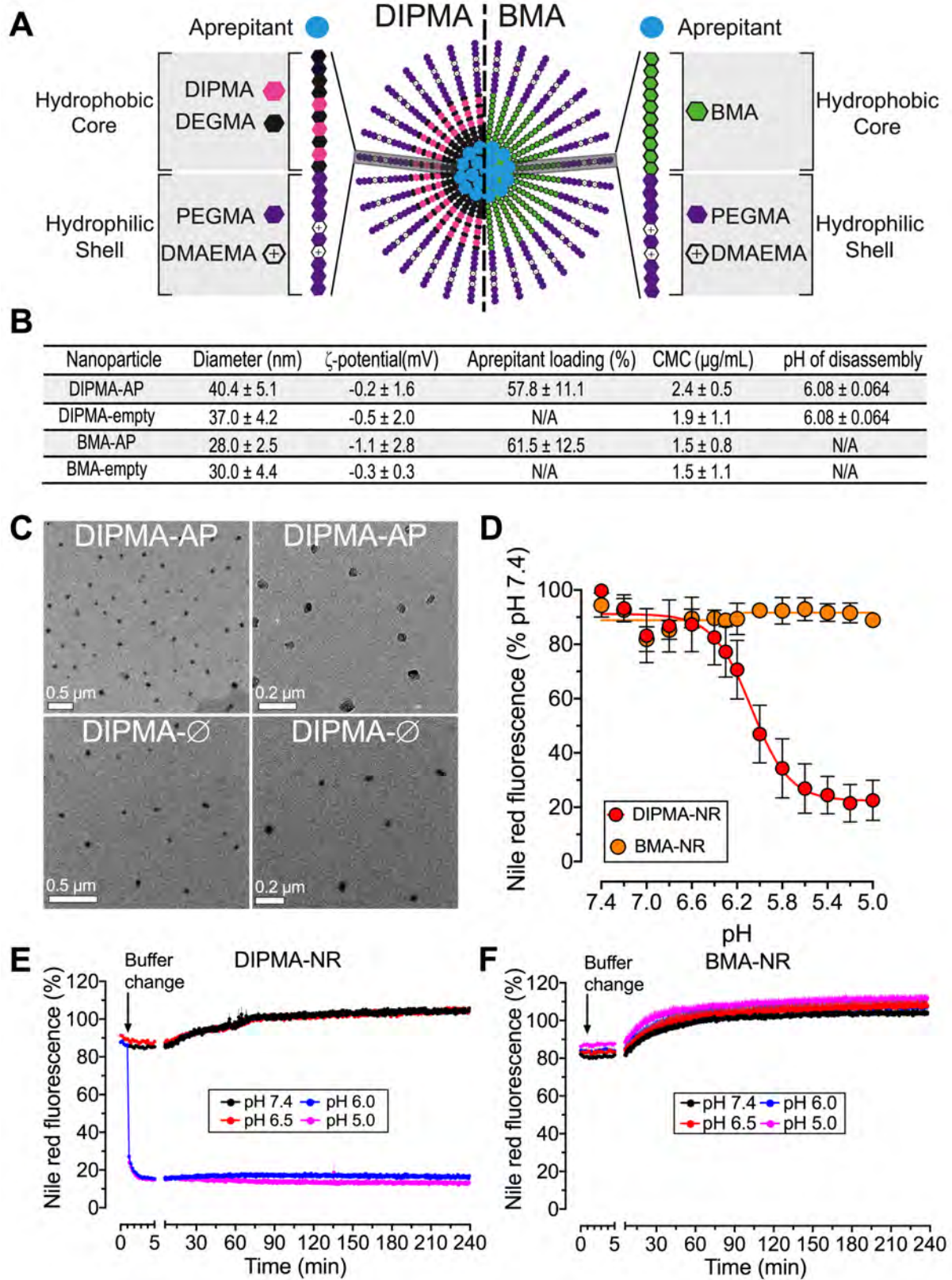


Figure 1. Characterization of DIPMA and BMA NPs. **A.** Structure of pH-responsive (DIPMA) and pH-non-responsive (BMA) NPs. NPs share the same hydrophilic shell of P(PEGMA-co-DMAEMA) but have different hydrophobic cores of P(DIPMA-co-DEGMA) or BMA. **B.** Properties of DIPMA and BMA NPs ($n = 18-25$ experiments, mean \pm SD). **C.** TEM images of DIPMA-AP and DIPMA- \emptyset NPs. **D.** pH-dependent NR quenching of DIPMA-NR and BMA-NR NPs *in vitro*, indicating of NP disassembly ($n = 3$ experiments, triplicate observations). **E, F.** Time course of NR quenching of DIPMA-NR (**E**) and BMA-NR (**F**) NPs *in vitro* and pH 7.4, 6.5, 6.0 and 5.0 ($n = 3$ experiments, triplicate observations).

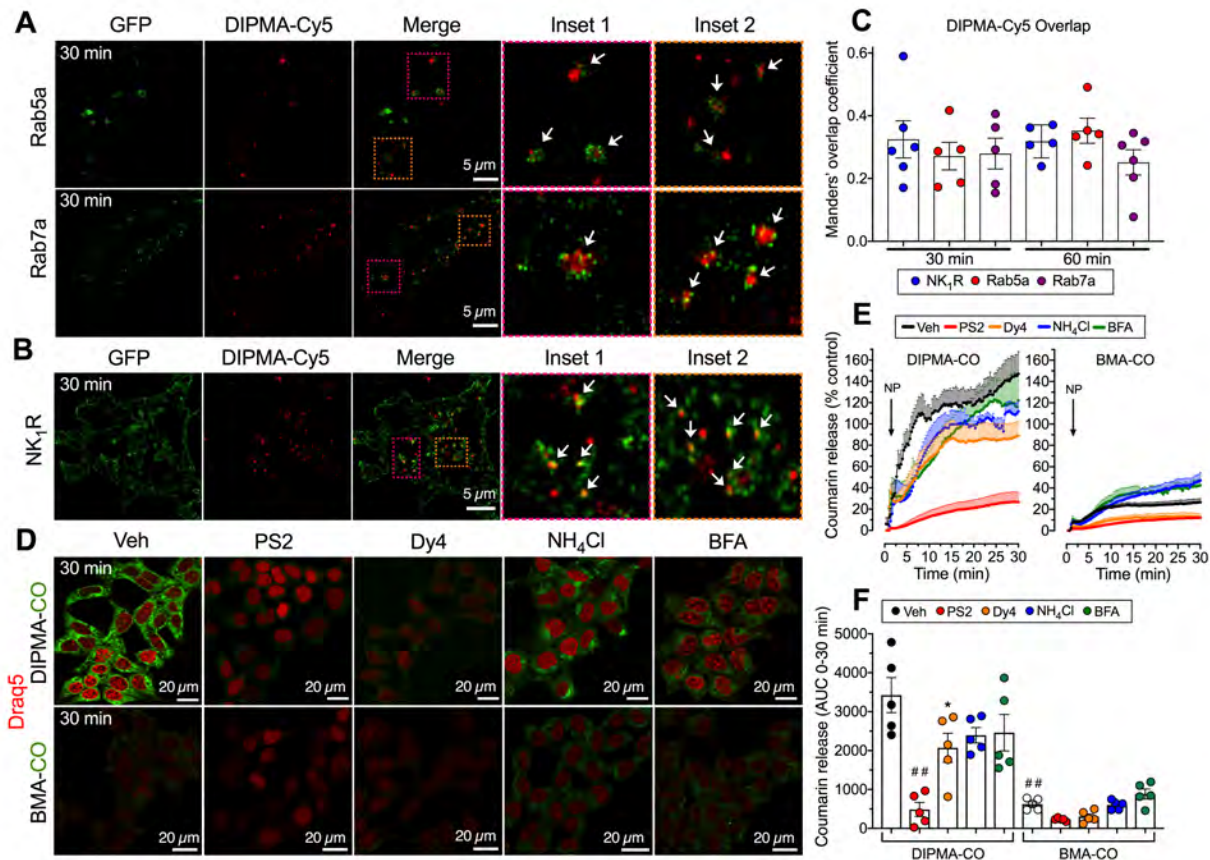


Figure 2. Uptake and disassembly of DIPMA and BMA NPs in HEK-293 cells. **A.** Localization of DIPMA-Cy5 NPs in Rab5a-GFP-positive early endosomes and Rab7a-GFP-positive late endosomes after incubation with HEK-293 cells for 30 min. **B.** Colocalization of DIPMA-Cy5 NPs and NK₁R-GFP in HEK-rNK₁R cells at 30 min after stimulation with SP to induce NK₁R endocytosis. **C.** Manders overlap coefficient to assess the degree of colocalization of DIPMA-Cy5 with NK₁R-GFP, Rab5a-GFP and Rab5a-GFP at 30 min and 60 min. **D-F.** Uptake of DIPMA-CO and BMA-CO NPs into HEK-293 cells. **D.** Representative images at 30 min after addition of DIPMA-CO or BMA-CO NPs; Coumarin 153 is green, Draq5 nuclear stain is red. **E, F.** Quantification of uptake and disassembly of DIPMA-CO and MBA-CO NPs assessed by Coumarin 153 fluorescence. In cells treated with DIPMA-CO, Coumarin 153 rapidly accumulated in the cytosol, indicative of fast NP disassembly. PS2, Dy4, BFA and NH₄Cl inhibited appearance of Coumarin 153 and NP disassembly. In cells treated with BMA-CO, Coumarin 153 slowly accumulated in the cytosol, indicative of minimal NP disassembly. PS2 and Dy4, but not BFA and NH₄Cl, inhibited appearance of Coumarin 153 and NP disassembly. **A, B, D.** Representative images of $n = 5-6$ experiments; **C, E, F.** $n = 5$ experiments. * $P < 0.05$, # $P < 0.001$, ### $P < 0.0001$ compared to DIPMA-CO treated with vehicle.

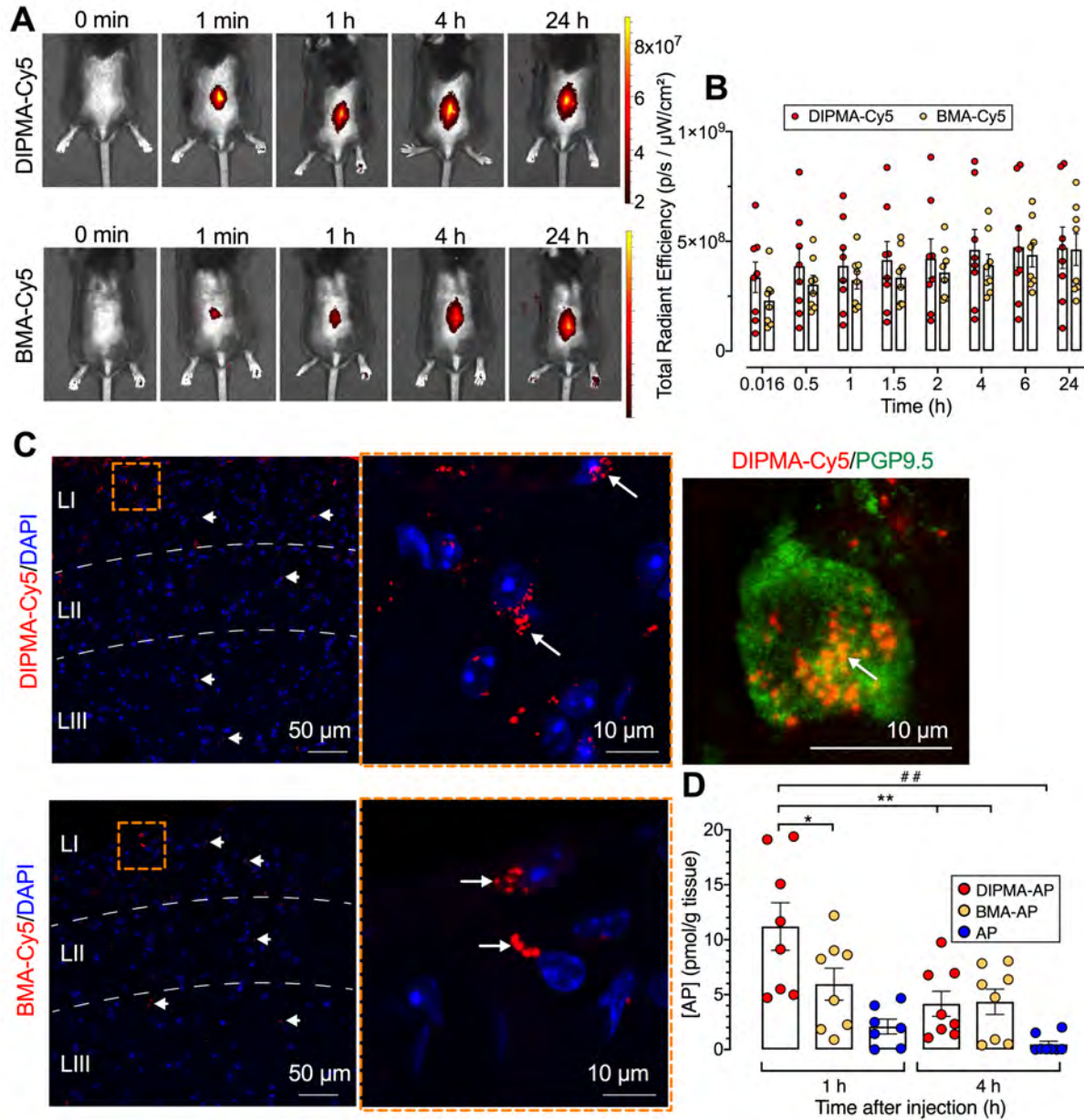


Figure 3. Biodistribution and cellular uptake of NPs and AP delivery. **A.** Distribution of DIPMA-Cy5 and BMA-Cy5 NPs at various times after i.t. injection to mice (representative images of experiments on $n = 7$ mice). **B.** Quantification of the distribution of DIPMA-Cy5 and BMA-Cy5-NPs at various times after i.t. injection to mice assessed as the radiant efficiency of the images ($n = 7$ mice). **C.** Localization of DIPMA-Cy5 and BMA-Cy5 NPs in the dorsal horn (laminae, LI-III) 1 h after i.t. injection. The inset shows accumulation of DIPMA-Cy5 NPs in a perinuclear region of a spinal neuron labeled with anti-PGP9.5. **D.** AP concentrations in the spinal cord measured 1 h and 4 h after i.t. injection of DIPMA-AP, BMA-AP or free AP (100 nM). $n = 7$ or 8 mice. * $P < 0.05$, ** $P < 0.01$, ### $P < 0.0001$.

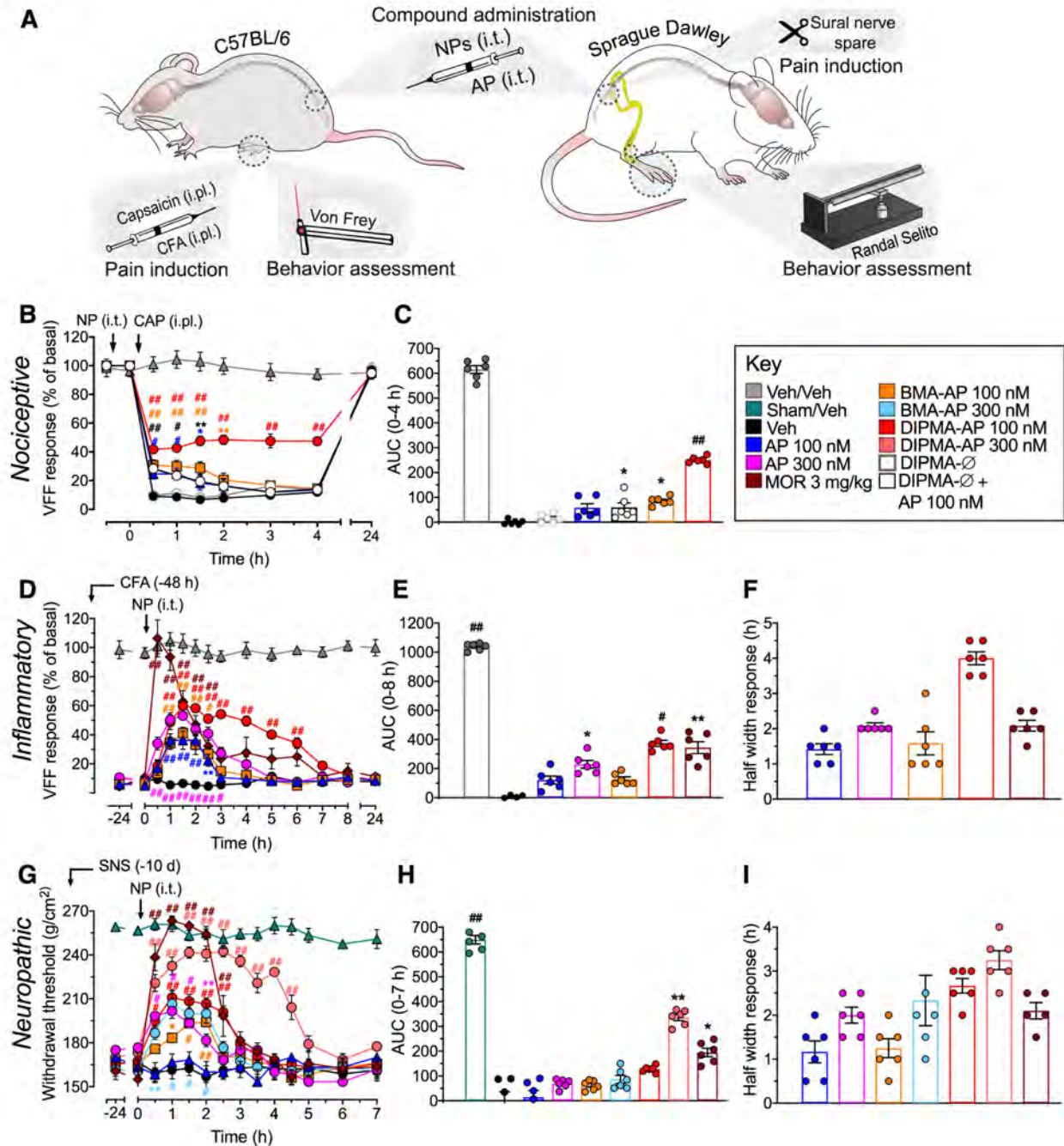


Figure 4. Effects of NPs on nociceptive, inflammatory and neuropathic nociception. A. Experimental models. In the CAP-evoked model of acute nociceptive pain in mice, vehicle (Veh), AP or NP was administered by i.t. injection 30 min before i.p.l. injection of CAP. In the CFA-evoked model of sustained inflammatory nociception in mice, CFA was administered by i.p.l. injection; after 48 h, vehicle, AP or NP was administered by i.t. injection. The SNS model of chronic neuropathic nociception was studied in rats. Vehicle, AP or NP was administered by i.t. injection 10 days after SNS. Paw withdrawal responses were assessed using VFF in mice and the Randall-Selitto test in rats. **B, C.** CAP-induced mechanical allodynia in mice. **D-F.** CFA-evoked mechanical hyperalgesia in mice. **G-I.** SNS-evoked mechanical hyperalgesia in rats. $n = 6$ animals for all experiments. * $P < 0.05$, ** $P < 0.005$, *** or # $P < 0.001$, **** or ## $P < 0.0001$ compared to vehicle.

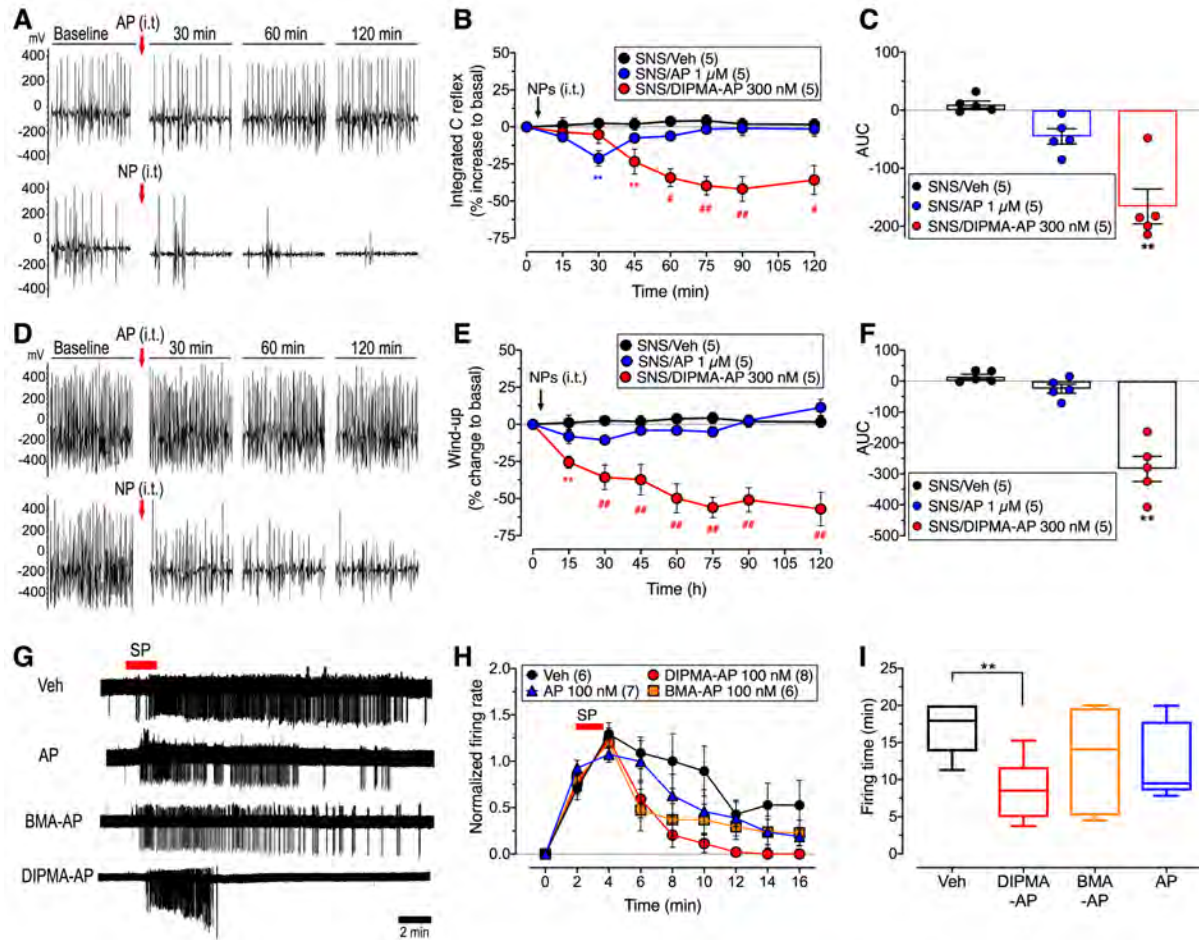


Figure 5. Sensitization and activation of nociceptive transmission. A-F. C-fiber reflex and wind-up in SNS rats. C-fiber reflexes (A-C) and wind-up (D-F) were measured at 10 d after SNS. Vehicle (Veh), AP or DIPMA-AP was administered by i.t. injection. A, D. Representative recordings comparing AP and DIPMA-AP. B, E. Time course of effects. C, F. Integrated responses. $n = 5$ rats studied in each experiment. $**P < 0.005$, $\#P < 0.001$, $###P < 0.0001$ compared to vehicle. G-I. Cell-attached patch-clamp recordings of SP-induced excitation of lamina I neurons in slices of rat spinal cord. G. Representative traces. H. Normalized firing rate. I. Firing time. $n = 6$ for rats for vehicle, $n = 7$ rats for AP, $n = 8$ rats for DIPMA-AP, and $n = 6$ rats for BMA-AP. $**P < 0.01$ compared to vehicle.

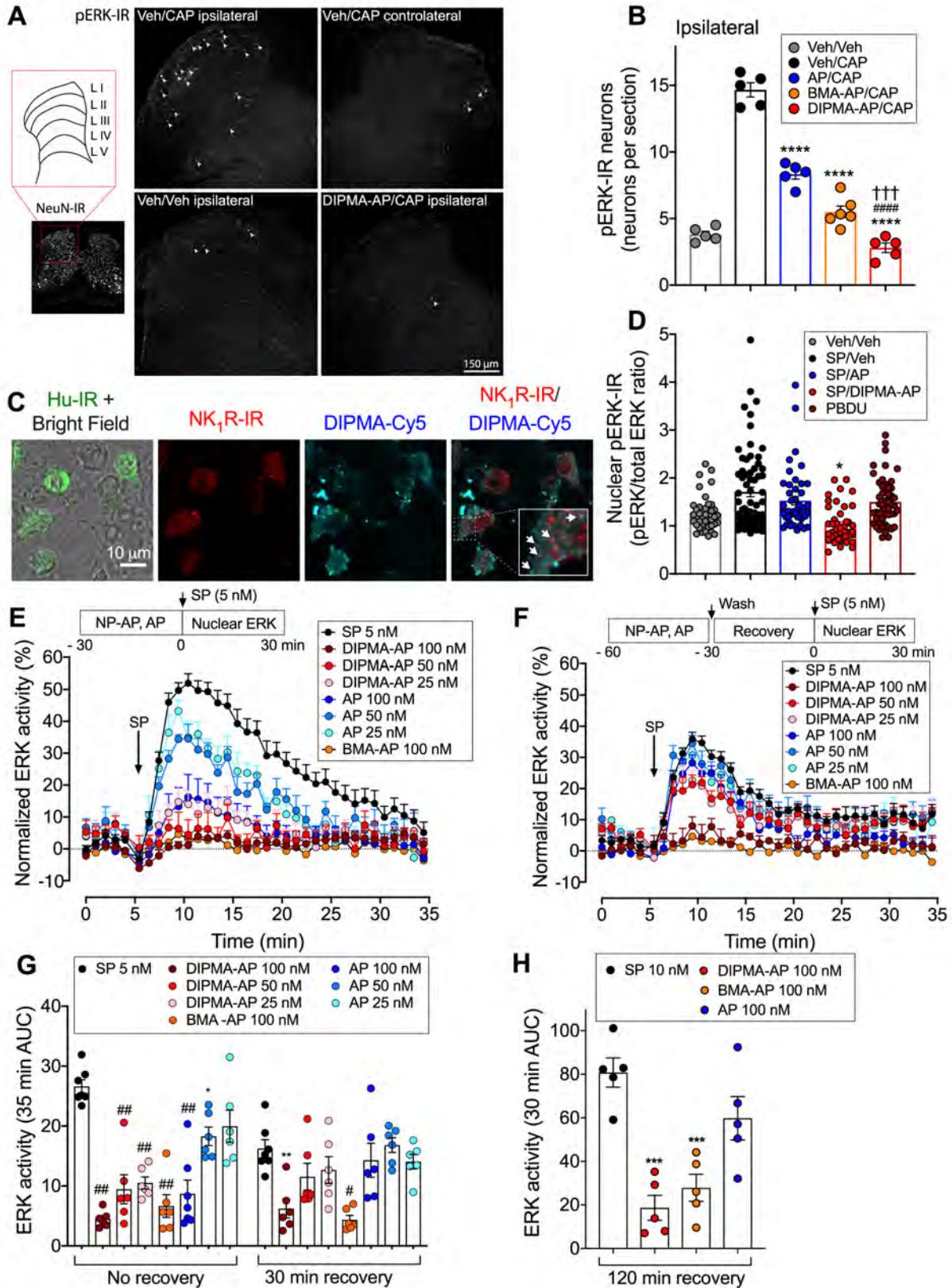


Figure 6. Antagonism of NK₁R signaling in endosomes. A, B. Localization of pERK in the spinal cord. AP, BMA-AP, DIPMA-AP or vehicle (veh) was injected i.t. to mice. After 30 min, CAP or vehicle was injected i.pl. After 4 h, the spinal cord was collected for localization of pERK-IR or NeuN-IR. **A.** Representative images. **B.** The number of pERK-IR neurons per section. $n = 5$ or 6 mice. **** $P < 0.0001$ compared to Veh/CAP; ##### $P < 0.0001$ compared to AP/CAP; ††† $P < 0.001$ compared to BMA-AP/CAP. **C.** Uptake of DIPMA-Cy5 and NK₁R-IR in cultured striatal neurons stimulated with 100 nM SP for 30 min. **D.** SP-induced activation of nuclear ERK (ratio of phospho-ERK1/2 (Thr202/Tyr204) to total ERK) in cultured striatal neurons. $n = 41-69$ neurons from 4 experiments tested with independent NP preparations. * $P < 0.05$ compared to vehicle with SP stimulation. **E-H.** Effects of free AP, DIPMA-AP and BMA-AP on SP-induced activation of nuclear ERK in HEK-hNK₁R cells. Cells were preincubated with vehicle, AP or DIPMA-AP for 30 min; they were either challenged with SP (no recovery, **E**), or were washed, recovered in antagonist-free medium for 30 or 120 min, and then challenged with SP (30 min recovery, **F**). **G, H.** AUC of ERK assays. Results are expressed as normalized values by the maximum nuclear ERK response to 1 μ M PDBu. $n = 5$ or 6 experiments, triplicate observations. * $P < 0.05$, ** $P < 0.005$, # $P < 0.001$, ## $P < 0.0001$ compared to vehicle.

Methods

Materials. Reagents were purchased from Sigma-Aldrich unless otherwise specified.

Synthesis of diblock copolymers. Prior each synthesis, monomers were deinhibited using basic aluminum oxide.

P(PEGMA-co-DMAEMA) hydrophilic block copolymer. The macromolecular chain transfer agent (macro-CTA), P(PEGMA-co-DMAEMA), was synthesized by the reversible addition fragmentation chain (RAFT) polymerization method³⁹ using 2-cyanoprop-2-yl dithiobenzoate (CPBD, 0.0736 g, $3.34 \cdot 10^{-4}$ mol) as a RAFT agent and azobisisobutyronitrile (AIBN, 0.0054 g, $3.34 \cdot 10^{-5}$ mol) as the initiator in a ratio of 1:0.1. The monomers used were poly(ethylene glycol) monomethyl ether methacrylate (PEGMA, 6 g, 0.02 mol) and 2-[*N,N*-(dimethylamino)ethyl] methacrylate (DMAEMA, 0.314 g, 0.001 mol) at a ratio of 10:1. The mixture was dissolved in 30 mL of toluene, deoxygenated by sparging with nitrogen and the reaction performed at 70°C, 400 RPM for 21 h. The final product was purified by dialysis (MWCO 3500, Membrane Filtration Products, USA) against acetone for 96 h to remove remaining monomer. Solvent was evaporated and the product was dried for 24 h in a vacuum oven at 37°C and 1000 mbar.

P(PEGMA-co-DMAEMA)-b-P(DIPMA-co-DEGMA) diblock copolymer. The chain extension reaction was initiated by AIBN (0.0017 g, $1.033 \cdot 10^{-5}$ mol), using the hydrophilic block P(PEGMA-co-DMAEMA, 0.89 g, $6.89 \cdot 10^{-5}$ mol) and the monomers 2-[*N,N*-(diisopropylamino)ethyl] methacrylate (DIPMA, 1.47 g, $6.892 \cdot 10^{-3}$ mol) and di(ethylene glycol) methyl ether methacrylate (DEGMA, 0.1427 g, $7.58 \cdot 10^{-4}$) at a ratio of 0.15:1:100:11. The mixture was dissolved in toluene, deoxygenated as described above, and left to react at 70 °C, 400 RPM for 17.5 h. The final product was purified as described above.

P(PEGMA-co-DMAEMA)-b-P(BMA) diblock copolymer. Butyl methacrylate (BMA, 0.582 g, 0.0041 mol) was polymerized from the hydrophilic P(PEGMA-co-DMAEMA) block by a chain extension reaction in the presence of AIBN (0.0008 g, $5.124 \cdot 10^{-6}$ mol) in toluene. The ratio of [BMA]:[macro-CTA]:[AIBN] used was 120:1:0.2. The solution was deoxygenated and left to react for 15 h at 70 °C and 400 RPM. The final product was purified as previously described.

P(PEGMA-co-DMAEMA)-b-P(DIPMA-co-DEGMA-co-Cy5) diblock copolymer. The chain extension of P(PEGMA-co-DMAEMA, 0.5 g, $3.85 \cdot 10^{-5}$ mol) was done in toluene by adding DIPMA (0.82 g, $4.6 \cdot 10^{-3}$ mol), and 4,4-dimethyl-2-vinyl-2-oxazolin-5-one (VDM, 0.027 g, $1.92 \cdot 10^{-4}$ mol) in the presence of AIBN (0.95 mg, $5.77 \cdot 10^{-6}$ mol) at a ratio of 1:100:11:5:0.15. The mixture was deoxygenated as described above and left to react at 70 °C, 400 RPM for 18 h. Cy5 coupling was performed in a second step by mixing 250 µL of the reaction with Cyanine5 amine (Cy5, 0.008 g, $1.20 \cdot 10^{-5}$ moles). Specifically, the mixture was left to react at room temperature, 400 RPM for 72 h under dark conditions and the final product was purified as described above.

P(PEGMA-co-DMAEMA)-b-P(BMA-co-Cy5) diblock copolymer. The chain extension of P(PEGMA-co-DMAEMA, 0.5 g, $3.87 \cdot 10^{-5}$ mol) was done in toluene by adding BMA (0.66 g, $3.87 \cdot 10^{-3}$ mol), DEGMA (0.073 g, $3.87 \cdot 10^{-4}$) and 4,4-dimethyl-2-vinyl-2-oxazolin-5-one (VDM, 0.027 g, $1.92 \cdot 10^{-4}$ mol) in the presence of AIBN (0.95 mg, $5.77 \cdot 10^{-6}$ mol) at a ratio of 1:120:5:0.15. The mixture was deoxygenated as described above and left to react at 70°C, 400 RPM for 19 h. Cy5 coupling was performed in a second step by mixing 250 µL of the reaction with Cyanine5 amine (Cy5, 0.008 g, $1.20 \cdot 10^{-5}$ moles). Specifically, the mixture was left to react at room temperature, 400 RPM for 72 h under dark conditions and the final product was purified as described above.

Analysis of block copolymers

Gel permeation chromatography (GPC). The molecular weights of polymers were determined by GPC using a Shimadzu (Kyoto, Japan) liquid chromatography system equipped with a (RID-10A)

differential refractive index detector ($\lambda = 633$ nm) and SPD-20A ultraviolet detector. Samples were fractionated using 5.0 μm bead-size guard column (50 \times 7.8 mm) and three Shodex KF-805L columns (300 \times 8 mm, 10 μm n=bead-size, 5000 Å pore size) in series at 40°C. The eluent used was *N,N*-dimethylacetamide (DMAC, HPLC grade, with 0.03% w/v LiBr) with a flow rate of 1 mL/min. A molecular weight calibration curve was produced using polystyrene standards with narrow molecular weights distribution ranging from 500 to 2 \times 10⁶ Da.

Proton-nuclear magnetic resonance (¹H-NMR). The conversion of polymers was assessed by ¹H-NMR analysis using a Bruker Avance III 400 Ultrashield Plus spectrometer (USA) at 400 MHz running Topspin, version 1.3, using deuterated chloroform (chloroform-d) as solvent. Conversions (Conv%) and repeating monomer units (n) were calculated by ¹H-NMR using peak integrals (I) where the subscript number indicates the location of the peak in ppm (I_x). The Conv% and n for P(PEGMA-co-DMAEMA) were calculated using the ¹H-NMR spectra (Supplementary Fig. 1D.i) with $Conv\% = 100 \times \frac{(I_{4-4.6} - I_{5.7})}{I_{4-4.6}}$, $n_{PEGMA} = \frac{I_{4.25} - I_{2.5}}{I_{7.8-7.9}}$ and $n_{DMAEMA} = \frac{I_{2.5}}{I_{7.8-7.9}}$. Conv% and n for P(PEGMA-co-DMAEMA)-b-(DIPMA-co-DEGMA) were calculated using the ¹H-NMR spectra (Supplementary Fig. 1D.ii) with $Conv\% = 100 \times \frac{(PEGMA\ n + DEGMA\ n)}{(PEGMA\ n_{theoretical} + DEGMA\ n_{theoretical})}$, $n_{DIPMA} = \frac{I_3 + I_{2.6}}{2 \times I_{4-4.6}} \times (n_{PEGMA} + n_{DMAEMA})$ and $n_{DEGMA} = \frac{I_{3.396}}{I_{3.378}} \times n_{PEGMA}$. Conv% and n for P(PEGMA-co-DMAEMA)-b-(BMA) were calculated using the ¹H-NMR spectra (Supplementary Fig. 1D.iii) with $Conv\% = 100 \times \frac{BMA\ n}{BMA\ n_{theoretical}}$ and $BMA\ n = \frac{I_{3.93}}{I_{4-4.2}} \times (PEGMA\ n + DEGMA\ n)$. Conv% and n for P(PEGMA-co-DMAEMA)-b-(DIPMA-co-DEGMA-co-VDM) and P(PEGMA-co-DMAEMA)-b-(BMA-co-VDM) were calculated as described for P(PEGMA-co-DMAEMA)-b-(DIPMA-co-DEGMA) and P(PEGMA-co-DMAEMA)-b-(BMA) (¹H-NMR spectra not shown).

Self-assembly of NPs. P(PEGMA-co-DMAEMA)-b-P(DIPMA-co-DEGMA) was used as the diblock copolymer to self-assemble pH-responsive NPs. P(PEGMA-co-DMAEMA)-b-P(BMA) was used to self-assemble control NPs that do not possess pH responsive properties. For the self-assembly of NPs loaded with AP, a mixture of a mixture of 5 mg of diblock copolymer and 53.5, 26.75 or 13.375 μg of AP was dissolved in 0.5 mL of tetrahydrofuran (THF). Empty (\emptyset) NPs were self-assembled without adding AP. The mixture was then added into 4.5 mL of phosphate-buffered saline (PBS) under vigorous stirring at a flow rate of 1.2 mL/h, using a Harvard Apparatus syringe pump (USA) at room temperature. Assemblies of pH-responsive NPs loaded with AP (DIPMA-AP) and non-pH responsive NPs loaded with AP (BMA-AP) were dialyzed against PBS under nitrogen flow for 24 h (MWCO 3500, Membrane Filtration Products, USA). Assemblies of pH-responsive NPs without AP (DIPMA- \emptyset and BMA- \emptyset) were dialyzed using Slide-A-Lyzer mini dialysis devices MWCO 3.5K (Thermo Fisher Scientific, USA) for 24 h. The assembly of NPs for live cell imaging and biodistribution studies was done as described for NPs without AP. The diblock copolymers used were P(PEGMA-co-DMAEMA)-b-P(DIPMA-co-DEGMA-co-Cy5) and P(PEGMA-co-DMAEMA)-b-(BMA), which include Cy5 on the hydrophobic portion, resulting in NPs with Cy5 localized in the core (DIPMA-Cy5 and BMA-Cy5).

Characterization of NPs

Dynamic light scattering (DLS). The size distribution of NPs was determined by DLS using a Zetasizer Nano ZS ZEN3600 particle size analyzer (Malvern, UK). DIPMA-AP, DIPMA- \emptyset and BMA-AP (1 mg/mL) were added to polystyrene cuvettes. Light scattering was measured at 25°C and 173° backscatter angle.

Ultra-performance liquid chromatography mass spectrometry (LC-MS). AP loading into the core of NPs was assessed by LC-MS using a Waters Micromass Quattro Premier triple quadrupole mass spectrometer coupled to a Waters Acquity UPLC (USA). Freeze-dried DIPMA-AP and BMA-AP (1 mg/mL) were dissolved in a 5:2 mixture of DMSO:0.1% formic acid in water. The samples

were prepared for analysis by mixing an aliquot of each preparation with internal standard solution (diazepam, 5 µg/mL) in a 5:2 proportion and made up to 500 µL with the dilution solvent (1:1 mixture of 50% acetonitrile and 0.1% formic acid). Samples were fractionated on a Supelco Ascentis Express RP Amide column (50 mm by 2.1 mm, 2.7 µm particle size) equipped with a Phenomenex SecurityGuard precolumn fitted with a Synergi Polar cartridge and both maintained at a column temperature of 40°C. AP loading was quantified against AP standards (0.016 to 20 µM). The mobile phase consisted of 0.05% formic acid in water and acetonitrile and compounds were eluted under gradient conditions. Mass spectrometry was conducted in positive electrospray ionization conditions and elution of compounds monitored with multiple-reaction monitoring.

pH-dependent disassembly of NPs and kinetics of cargo release. Nile Red (NR) is a solvatochromic dye that fluoresces only in non-polar solvents, allowing determination of the pH of disassembly for the NPs. Specifically, the pH of disassembly is identified by observing the loss of fluorescence of NR due to release of NR from the core of NPs. NPs were self-assembled using 0.1 mg of NR per mg of polymer and dialyzed as previously described. pH-responsive NPs loaded with Nile red (DIPMA-NR) and non-pH responsive NPs loaded with NR (BMA-NR) were prepared at a concentration of 200 µg/mL. For pH-dependent disassembly studies, NPs were suspended in a mixture of 0.1 M citric acid and 0.2 M Na₂HPO₄ buffer solutions with a pH range from 7.6 to 5.0. pH-dependent disassembly was assessed by measuring NR fluorescence (excitation/emission 552/636nm) using a FlexStation 3 (Molecular Devices, CA, USA). The time course of NP disassembly was examined by measuring NR fluorescence at pH 7.4, 6.5, 6.0 and 5.0 over a 12 h period using a CLARIOstar (BMG LABTECH, Germany).

Determination of critical micelle concentration (CMC). CMC was determined by the pyrene I₁/I₃ ratio²³. A pyrene stock solution (50 µM) was prepared in THF and 5 µL of pyrene stock were added to 995 µL of graded concentrations of NPs (400 to 0.5 µg/mL), obtained by diluting NP stock solutions in PBS. The mixture was stirred for 3 h at room temperature and the fluorescence spectrum of pyrene was recorded from 360 to 410 nm using an excitation wavelength of 336 nm in a Shimadzu Spectrofluorophotometer RF5301PC (Kyoto, Japan). The emission intensities measured at 373 nm (I₁) and 384 nm (I₃) were used to calculate the pyrene I₁/I₃ ratio.

Transmission electron microscopy (TEM). The morphology of NPs was determined by TEM imaging using a Tecnai F20 transmission electron microscope at an accelerating voltage of 200 kV at ambient temperature. An aliquot (5 µL) of 0.1 wt% NP solution (diluted with Milli-Q water) was deposited on a Formvar coated copper grid (GSCu100F-50, Proscitech, Australia) and was allowed to dry overnight in air and at room temperature.

Cell lines. The human (h) NK₁R ORF with a CD8 signal sequence and N-terminal FLAG-tag was cloned into pcDNA5 FRT/TO between KpnI and NotI restriction sites using Gibson Assembly (NEB). A stable cell line expressing hNK₁R (HEK-hNK₁R) was produced by cotransfecting FlpN HEK-293 cells with 0.5 µg of the hNK₁R vector and 4 µg of pOG44, using polyethylenimine (PEI, Polysciences, USA) at a 1:6 DNA:PEI ratio. Cells (~0.7x10⁶) were seeded into a T-25 tissue culture flask (Perkin Elmer, USA) in Dulbecco's modified Eagle medium supplemented with penicillin (50 U/mL) and streptomycin (50 U/mL) (DMEM/pen/strep) and incubated for 24 h (37°C, 5% CO₂). The medium was changed to fresh DMEM/pen/strep prior the transfection and the flask was then incubated for 24 h (37°C, 5% CO₂) before the medium was changed to DMEM supplemented with 10% (v/v) fetal bovine serum (FBS) and hygromycin B (200 µg/ml, ThermoFisher Scientific) (DMEM/FBS/Hygro).

NP trafficking in cell lines. HEK-293 cells were plated on poly-D-Lysine coated chambers (ibidi, Germany) in DMEM supplemented with 10% (v/v) FBS (DMEM/FBS). After 24 h, cells were

transfected with 300 ng of rat (r) NK₁R-GFP/chamber using PEI at a 1:6 ratio and cultured for further 48 h. To identify endosomal compartments, HEK-293 cells were infected with Rab5a-GFP (resident in early endosomes) or Rab7a-GFP (late endosomes) (CellLight, Thermo Fisher Scientific, USA) 16 h before imaging. To examine localization of NPs, cells were incubated in Leibovitz's L-15 medium with DIPMA-Cy5 NPs (20 µg/mL, 30 min, 37°C) or vehicle, followed by addition of SP (10 nM). Cells were imaged at 30 and 60 min post-SP addition using a Leica SP8 confocal microscope equipped with HCX PL APO 40x (NA 1.30) and HCX PL APO 63x (NA 1.40) oil objectives. Images were analyzed using Fiji⁴⁰ and deconvolved with Huygens Professional version 18.04 (Scientific Volume Imaging, The Netherlands, <http://svi.nl>), using the CMLE algorithm with signal to noise ratio 10 and 100 iterations. Colocalization was evaluated by determination of the Manders overlap coefficient²⁹.

Uptake and disassembly of NPs in HEK-293 cells. Coumarin 153 is a solvatochromic dye that fluoresces only in polar solvents, allowing detection of the release of Coumarin loaded in the core of NPs observed as the appearance of Coumarin fluorescence in intact cells. NPs were self-assembled using 0.5 mg of Coumarin 153 per mg of DIPMA or BMA polymer (DIPMA-CO and BMA-CO). HEK-293 cells were preincubated for 30 min with vehicle (Hank's Balanced Salt Solution, HBSS), dynamin inhibitor (Dyngo4a, Dy4, 30 µM)³¹, clathrin inhibitor (Pitstop2, PS2, 30 µM)³⁰, vacuolar H⁺ATPase inhibitor (Bafilomycin A1, BFA, 1 µM) or NH₄Cl (20 mM), which acts as a lysosomotropic weak base. Nuclei were stained using Draq5. Images were obtained with a Leica SP8 confocal microscope using HCX PL APO 63x (NA 2.0) oil objective. Images were taken every 10 s for 30 min, where the first 5 readings correspond to baseline images prior the addition of DIPMA-CO NPs (20 µg/mL). All images were analyzed using Fiji⁴⁰. Kinetic data were normalized to fluorescence of free Coumarin (5 µg/mL) at 30 min.

Animals. Adult male C57BL/6 mice (6-10 weeks) and pregnant Asmu:Swiss mice were from the Monash Animal Research Platform. Adult male Sprague-Dawley rats (225–250 g) were purchased from the facilities of the Faculty of Medicine of the University of Chile. Animals were housed in groups of 4, maintained in a temperature (22 ± 4°C) and humidity-controlled environment with a 12 h light/dark cycle. Food and water were available *ad libitum*. For behavioral tests, investigators were blinded to the treatment groups, animals were randomly assigned to treatments, and animals were studied during the light cycle. Animals were euthanized by anesthetic overdose and thoracotomy. Studies on animals were in accordance with the Guide for the Care and Use of Laboratory Animals of the National Institutes of Health and adhered to the ethical guidelines of the International Association for the Study of Pain⁴¹. Studies were approved by the animal ethics committee of Monash Institute of Pharmaceutical Sciences, Monash University and the Bioethics Committee of the University of Santiago of Chile.

Drug administration

Mice. The following drugs were administered by i.t. injection (5 µL) into the intervertebral space (L4/L5) of conscious mice: AP (100, 300 nM), NPs delivering an equivalent dose of AP (DIPMA-AP, BMA-AP, 10 µg/mL - 100 nM AP, 30 µg/mL - 300 nM AP), controls (10 µg/mL of DIPMA-Ø and a mixture of 10 µg/mL of DIPMA-Ø and AP 100 nM), or vehicle (artificial cerebrospinal fluid, aCSF). Treatments were administered 30 min prior to rotarod experiments and the induction of acute nociceptive pain or 48 h after the establishment of inflammatory nociception. For biodistribution studies, DIPMA-Cy5 or BMA-Cy5 NPs (50 µg/mL) were administered i.t. immediately after obtaining control images. For localization of NPs in the spinal cord, DIPMA-Cy5 or BMA-Cy5 NPs (50 µg/mL) were administered i.t. 30 min after the induction of acute nociception with CAP (see below). Morphine (3 mg/kg intraperitoneal injection, i.p.) was administered 48 h after induction of inflammatory nociception.

Rats. Drugs were administered by i.t. injection (10 μ L) into the intervertebral space (L4/L5) of conscious rats: AP (100, 300 nM, 1 μ M), NPs loaded with AP (DIPMA-AP, BMA-AP, 10 μ g/mL - 100 nM AP, 30 μ g/mL - 300 nM AP, 50 μ g/mL - 500 nM AP), DIPMA- \emptyset NPs (10, 30, 50 μ g/mL), or vehicle (aCSF). Treatments were administered 10 days after sural nerve transection. For electrophysiological studies, drugs were administered by i.t. injection under anesthesia (isoflurane 1.2-1.5%): AP (1 μ M) or NPs (DIPMA-AP, BMA-AP, 30 μ g/mL - 300 nM AP). Morphine (3 mg/kg, i.p.) was administered 10 days after sural nerve transection.

Biodistribution of NPs in the spinal cord. Mice were sedated (2% isoflurane) and placed in an *in vivo* imaging system (IVIS spectrum Lumina II, Perkin Elmer, USA). Posterior images were obtained using the Perkin Elmer Living Image software v4.3.1. After collection of a baseline image, DIPMA-Cy5 or BMA-Cy5 NPs (50 μ g/mL) were administered i.t. (5 μ l). Images were collected at 0.5, 1, 1.5, 2, 4, 8 and 24 h post DIPMA-Cy5 or BMA-Cy5 administration.

Uptake of NPs in the spinal cord. DIPMA-Cy5 or BMA-Cy5 NPs were administered to mice (i.t.). After 30 min, CAP (5 μ g) was administered by subcutaneous i.pl. injection (10 μ L) into the left hindpaw under sedation (2% isoflurane). At 1 h after NP administration, mice were transcardially perfused with 50 ml of PBS followed by 50 ml of ice-cold 4% paraformaldehyde (PFA). The spinal cord was removed, immersion fixed in 4% PFA (2 h, 4°C) and cryoprotected in PBS containing 30% sucrose (24 h, 4°C). The spinal cord (L3-L6) was embedded in TFM (General Data, Cincinnati OH), and 30 μ m serial coronal sections were cut and mounted on Colorfrost Plus microscope slides (Fisher Scientific, USA). Sections were washed 2x in PBS, counter-stained with DAPI (5 μ g/ml, 5 min) and cover-slipped with ProLong Glass mounting medium (ThermoFisher Scientific). Some sections were processed to detect neurons. Sections were blocked in PBS containing 0.2% Triton X-100 and 10% normal horse serum (NHS) (30 min, room temperature). Sections were incubated with rabbit anti-PGP9.5 (1:500, Abcam ab27053) in PBS containing 0.2% Triton X-100 and 3% NHS (60 min, room temperature). Sections were washed 4x in PBS and incubated with donkey anti-rabbit Alexa 488 (1:1000, ThermoFisher Scientific) (30 min, room temperature). Sections were imaged on Leica SP8 confocal microscope with HC PLAPO 40X or 63X oil objective.

Determination of AP concentration in the spinal cord. AP (100 nM) or NPs delivering an equivalent dose of AP (DIPMA-AP, BMA-AP, 10 μ g/mL - 100 nM AP) was administered by i.t. injection to conscious mice. Mice were killed 1 h and 4 h post-treatment. The spinal cord (L2-L6) was removed for determination of the tissue concentration of AP by LC-MS as described above.

Rotarod test. A rotarod test was used to assess whether the i.t. injection of NPs would affect normal motor function and thereby impede studies of nociception that require examination of paw withdrawal from a painful stimulus. Prior to experiments, mice were acclimatized and trained on the rotarod apparatus for three consecutive runs on two successive days. On the day of the experiment, three baseline readings were recorded and a cut-off threshold of 120 second was pre-set. NPs (DIPMA-AP, BMA-AP, DIPMA- \emptyset , 10 μ g/mL) or vehicle (aCSF) was injected i.t. as described above. Subsequently, the latency of mice to fall (seconds) were recorded at 30, 60, 90, 120, 180 and 240 min post-injection¹⁷.

Induction and assessment of acute and inflammatory nociception in mice

Nociceptive pain. CAP (5 μ g) or vehicle (0.9% NaCl) was administered by i.pl. injection (10 μ L) into the left hindpaw of sedated mice (2% isoflurane) 30 min after i.t. injection of drugs¹⁷.

Inflammatory pain. CFA (0.5 mg/mL) or vehicle (0.9% NaCl) was administered by i.pl. injection (10 μ L) into the left hindpaw of sedated mice (2% isoflurane)^{17, 33}. Drugs were administered by i.t. injection 48 h after CFA.

Mechanical allodynia. Mechanical nociception was assessed by measuring withdrawal thresholds to stimulation of the plantar surfaces of the ipsilateral and contralateral hindpaws with calibrated von Frey filaments (VFF) ¹⁷. Prior to experiments, mice were acclimatized to the experimental apparatus and environment for 2 h on 2 successive days. VFF withdrawal thresholds were measured in triplicate to establish a baseline for each mouse. For the CAP model, VFF withdrawal thresholds were measured at 30 min intervals for the first 2 h after i.t. drug administration, then at 60 min intervals for the next 2 h, and finally after 24 h. For the CFA model, VFF withdrawal thresholds were measured every 30 min for the first 3 h after i.t. or i.p. drug administration, then at 60 min intervals for the next 5 h, and finally after 24 h. Results were normalized to the baseline withdrawal thresholds of each mouse. Results are expressed as a percentage of baseline, as area under curve (AUC), and as the half width response (the duration of the effect of each treatment calculated as the time to attain 50% of the maximal analgesic response).

pERK localization in mouse spinal cord. Vehicle (control), free AP, BMA-AP or DIPMA-AP (all 100 nM AP) was administered by i.t. injection to mice as described above. After 30 min, mice were sedated (2% isoflurane) and vehicle (0.9% NaCl) or CAP (5 µg) was administered by i.p. injection (10 µl) into the left hind paw. After 4 h, sections of spinal cord (L3-L6) were prepared as described above. Sections were preincubated in 10% normal donkey serum (NDS) in 0.1 M PBS (1 h, room temperature), followed by rabbit anti-phospho-p44/42 MAPK (ERK1/2) (Thr202/Tyr204) (1:200; #4370; Cell Signaling Technology, Danvers, MA) and guinea-pig anti-NeuN (1:1000, Millipore, #abN90) in PBS containing 0.3% Triton X-100 and 5% NDS (overnight, 4°C). Sections were washed 4x in 0.1 M PBS containing 0.3% Triton X-100 and incubated with donkey anti-rabbit Alexa 488 and donkey anti-guinea-pig Alexa 568 (1:1000, ThermoFisher Scientific) (45 min, room temperature). Sections were washed 5x in PBS, counter-stained with DAPI (10 µg/ml, 5 min) and cover-slipped with ProLong Glass mounting medium (ThermoFisher Scientific). Sections were imaged on Leica SP8 confocal microscope with HC PLAPO 40X oil objective for counting pERK-IR neurons or a 20X objective to collect representative images. For each experimental group, 6 sections of ipsilateral and contralateral dorsal horn were imaged. Only pERK-positive neurons co-labelled with NeuN were counted. To avoid re-counting the same neurons, the analyzed sections were 100 µm apart. The total number of neurons was averaged for each group.

Induction and assessment of neuropathic nociception in rats

Neuropathic pain. Neuropathic nociception was induced in rats using a variation of the sural nerve spared (SNS) injury model, which induces rapid onset and sustained mechanical and thermal hyperalgesia ³⁴. Under anesthesia (2% isoflurane), the 3 terminal distal branches of the sciatic nerve (tibial, common peroneal, sural nerves) were identified and the sural nerve was transected ³⁵. For controls (sham), rats underwent a similar surgery but without transection of the sural nerve. After surgery, ketoprofen (3 mg/kg) and enrofloxacin (5 mg/kg) were administered subcutaneously (s.c.) for 2 days.

Mechanical hyperalgesia. Mechanical hyperalgesia was assessed in rats by measuring hindpaw withdrawal pressure thresholds using an algometer (Ugo Basile, Italy) with a cut-off value of 570 g to prevent injury ^{42, 43}. Mechanical hyperalgesia was evaluated before (basal) and 5, 9 and 10 days after the surgery. After the evaluation at day 10, drugs were administered by i.t. or i.p. injection, and withdrawal thresholds were recorded every 30 min for 7 h. Results are expressed as the paw withdrawal pressure threshold (g.cm²), AUC and half-width response.

Electrophysiological assessment of the C-fiber-evoked nociceptive reflex and wind-up activity in rats. Nociceptive synaptic transmission was evaluated by measurement of electromyographic (EMG) activity associated with the hind limb-flexion nociceptive reflex evoked by electrical activation of C fibers of the sural nerve (C-reflex) as described previously ⁴⁴. Rats

were maintained under anesthesia (1.2-1.5% isoflurane in oxygen using a diaphragm rodent facemask) and placed on a regulated thermal pad ($37 \pm 0.5^\circ\text{C}$). EMG activity was measured using a pair of platinum stimulation electrodes inserted subcutaneously into the lateral part of the third and fourth toes, and recording electrodes inserted through the skin into the ipsilateral biceps femoris muscle³⁵. The C-reflex corresponds to the integration of the reflex response into a 150-450 ms time window post-stimulus. Wind-up is a potentiation of the C-reflex response when the stimulating frequency is increased to 1 Hz. The wind-up score corresponds to the slope of the first seven consecutive C-reflex recordings obtained at 1 Hz stimulation. After recording to obtain a stable C-reflex response (~30 min), the threshold for C-reflex was estimated and the rats remained stimulated at 2X the threshold intensity for the duration of the experiment. The C-reflex was evaluated by the mean of 15 consecutive stimuli at 0.1 Hz while the next 7 stimuli at 1 Hz were used to evaluate wind-up. Recordings were made 10 days after surgery before (basal) and 30, 60, 90 and 120 min after i.t. drug administration. The integrated C-reflex responses were expressed as a percentage of basal response.

Cell-attached patch clamp recordings of rat spinal neurons. Parasagittal slices (340 μm) were prepared from rat lumbar spinal cord as described^{17, 45}. Slices were transferred to a recording chamber and superfused with aCSF (2 ml.min⁻¹, 36°C). Dot-contrast optics were used to identify large (capacitance ≥ 20 pF), putative NK₁R-positive neurons in lamina I based on their position, size and fusiform shape with dendrites that were restricted to lamina I. Spontaneous currents were recorded from NK₁R-positive lamina I neurons in cell-attached configuration in voltage-clamp. Slices were preincubated in DIPMA-AP (10 $\mu\text{g}/\text{ml}$ -100 nM AP), BMA-AP (10 $\mu\text{g}/\text{ml}$ -100 nM AP) or AP (100 nM) for 120 min, washed and incubated in antagonist-free aCSF for a further 30-60 min before recording. Slices were challenged with SP (1 μM , 2 min) and firing rate for each cell was normalized to the response between the 2-4 min time points, which was not significantly different between groups. The firing time was determined as the duration of the response to last action potential.

NK₁R localization in rat spinal cord. At 10 days after sham or SNS surgery, rats were anesthetized and transcardially perfused with 250 ml PBS followed by 250 ml 4% PFA. The spinal cord was removed, immersion fixed in 4% PFA (2 h, 4°C), and cryoprotected in 30% sucrose in 0.1 M PBS (24 h, 4°C). The spinal cord (L3-L6) was embedded in TFM (General Data, Cincinnati OH), and 30 μm serial coronal sections were cut into 48 well plates containing PBS. Free floating sections were blocked in PBS containing 0.3% Triton x-100 and 10% NDS (1 h, room temperature). Sections were incubated with rabbit anti-NK₁R (1:1000, #94168) and guinea-pig anti-NeuN (1:1000, Millipore, abn90) in PBS containing 0.3% Triton X-100 and 3% NDS (overnight, 4°C). Sections were washed 4x in PBS and incubated with donkey anti-rabbit Alexa488 and donkey anti-guinea-pig Alexa568 (1:1000, ThermoFisher Scientific) (2 h, room temperature). Sections were washed 5x in PBS, counter stained with DAPI (10 $\mu\text{g}/\text{ml}$, 5 min), and mounted onto ColorFrost Plus slides (VWR) with ProLong Glass mounting medium (ThermoFisher Scientific). Sections were imaged on Leica SP8 confocal microscope with a HC PL APO 63x oil objective (NA 1.4). Z stacks of NK₁R-positive neurons in lamina I of the dorsal horn were collected with a digital zoom of 5. To quantify NK₁R endocytosis in lamina I neurons, the border of the cytoplasm of the soma was delineated by NeuN fluorescence. NK₁R immunoreactivity within 5 pixels (0.5 μm) of the border was defined as plasma membrane receptor. The ratio of plasma membrane to cytosolic NK₁R-IR fluorescence was determined in >6 lamina I neurons per condition.

DIPMA-Cy5 uptake, Ca²⁺ mobilization and ERK signaling in striatal neurons

Neuronal isolation and culture. Primary striatal neurons were dissociated from E15-16 Asmu:Swiss mouse embryos as described⁴⁶. Neurons were plated on poly-D-lysine coated 8-

well chamber slides (ibidi GmbH, Germany) in Neurobasal™ medium supplemented with B-27™, 2 mM L-glutamine- and penicillin/streptomycin at a density of 200,000 cells per well.

NP uptake and NK₁R localization. At 5 days after isolation, neurons were equilibrated in HEPES buffered saline (10 mM HEPES, 0.5% BSA, 10 mM D-glucose, 2.2 mM CaCl₂·H₂O, MgCl₂·6H₂O, 2.6 mM KCl, 150 mM NaCl, pH 7.4) for 30 min and then incubated with 50 µg/ml DIPMA-Cy5 and 100 nM SP for 30 min. Neurons were fixed in 2% PFA and 1% sucrose in PBS (room temperature, 20 min) and blocked in PBS containing 0.3% Triton x-100 and 5% NHS for 24 h, 4°C. Neurons were stained as described above for rat spinal cord slices, using rabbit anti-NK₁R and mouse anti-Hu (HuC/HuD Monoclonal Antibody 16A11, ThermoFisher Scientific; 24 h, 4°C), washed in 4 X PBS, and incubated with donkey anti-rabbit Alexa594 and donkey anti-mouse Alexa488 (1:500, ThermoFisher Scientific; 24 h, 4°C). Neurons were then counter-stained with DAPI. Images were obtained on a Leica SP8 confocal microscope with HCX PL APO 63x (NA 1.40) oil objective.

Ca²⁺ imaging. At 5 days after isolation, neurons were incubated with Fura-2 AM ester (2 µM, 45 min, 37°C, ThermoFisher Scientific) in HEPES-buffered saline containing 4 mM probenecid and 0.05% pluronic F127. Neurons were recovered in fresh HEPES buffered saline for 30 min before imaging on a Leica DMI-6000B microscope with HC PLAN APO 0.4NA X10 objective at 37°C. Images were collected at 1.5 s intervals (excitation: 340 nm/ 380 nm; emission: 530 nm). To assess the functional expression of NK₁R, neurons were preincubated with 300 nM AP or vehicle (DMSO), and challenged with 100 nM SP and followed by 5 mM KCl.

ERK activity. At 8 days after isolation, neurons were equilibrated for 30 min in HEPES buffered saline and then preincubated with DIPMA-AP (10 µg/ml-100 nM AP), AP (100 nM) or vehicle (PBS) for 30 min. Neurons were washed, recovered for 30 min, and challenged with SP (100 nM) or the positive control, phorbol 12,13-dibutyrate (PDBu) (10 µM) for 30 min. Neurons were fixed in 4% PFA (20 min, 4°C) and blocked (0.3% Triton x-100 and 5% NHS; 24 h, 4°C). Neurons were incubated with rabbit anti-phospho-p44/42 MAPK (ERK1/2 phospho-Thr202/Tyr204, 1:100, #4370, Cell Signaling Technology) and mouse anti-p44/42 MAPK (1:100, #4696, Cell Signaling Technology) (24 h, 4°C). Neurons were washed 4x in PBS and incubated with donkey anti-rabbit Alexa488 and donkey anti-mouse Alexa647 (1:500, ThermoFisher Scientific) (2 h, room temperature). The nucleus was counter-stained with DAPI. Neurons were imaged using a Leica SP8 confocal microscope with HCX PL APO 63x (NA 1.40) oil objective. Nuclei of neurons were selected as regions of interest and the ratio of phospho-ERK to total ERK was calculated using mean fluorescence intensity values. The mean ERK ratio for all neurons within a single well was determined and the means of 4 experiments were compared for statistical analyses.

FRET assays of endosomal NK₁R signaling. HEK-hNK₁R cells (~2x10⁶) were seeded into 90 mm Petri dish (Corning™, USA) in DMEM/FBS/Hygro and incubated for 24 h (37°C, 5% CO₂). Prior to the transfection, the medium was changed to fresh DMEM/FBS/Hygro and nuclear ERK (nucEKAR) sensor was transfected (2.5 µg nucEKAR DNA/dish) using PEI at a 1:6 ratio¹⁷. After 24 h, cells were plated in poly-L-lysine coated black 96 well CulturPlate (Perkin Elmer, USA) and incubated for further 24 h (37°C, 5% CO₂). On the day of the assay, cells were serum-starved for 6-8 h, and were then equilibrated in HBSS, supplemented with 12 mM 4-(2-hydroxyethyl)piperazine-1-ethanesulfonic acid (HEPES) at 37°C in CO₂-free incubator. FRET was assessed using a PHERAstar FS (BMG LABTECH, Germany) with an optic module FI 430 530 480 and measurements were made every 1 min. Baseline was measured for 5 min followed by stimulation with SP, vehicle (HBSS) or PDBu (1 µM), and further measurements for 30 min. For the SP concentration response curve, half logarithm dilutions of SP were added (1 µM to 100 pM) and the half-maximal effective concentration (EC₅₀) was determined using the area under the curve (AUC) after SP addition (30 min reading). For the AP concentration response curve, logarithmic dilutions of AP (10 µM to 1 pM) were added 30 min prior baseline measurements, followed by the addition of 5 nM of SP. The half maximal inhibitory concentration (IC₅₀) was determined for AP as described. To assess the effect of NPs on nuclear ERK signaling, DIPMA-

Ø, DIPMA-AP, BMA-Ø or BMA-AP (30, 20, 10 µg/mL) was added 30 min prior to baseline measurements, followed by the addition of SP 5 nM or vehicle. Data were expressed as vehicle corrected values, normalized by the maximum response to the positive control.

Cell viability assays. HEK-hNK₁R cells were incubated with DIPMA-Ø or BMA-Ø NPs (1-100 µg/mL) for 24 and 48 h. Medium was replaced by phenol red-free DMEM, followed by the addition of 10% (v/v) alamarBlue reagent (ThermoFisher Scientific, USA). Cells were incubated with alamarBlue for 2 h (37°C, 5% CO₂) and fluorescence of the reduced active compound, resofurin, was measured (510/610nm exc/em) using a ClarioStar (BMG LABTECH, Germany).

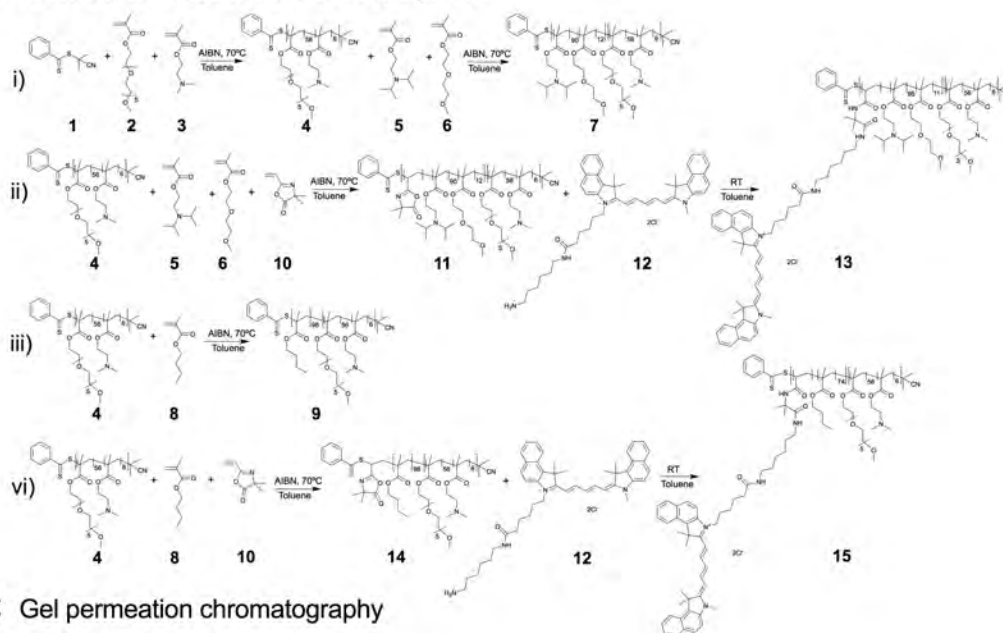
Statistical analyses. Data were analyzed using Graph Prism 8 (GraphPad Software, Inc., La Jolla, CA, USA). Data are presented as mean ± SEM, unless noted otherwise. A 2-tailed Student's t test was used for two comparisons. For multiple comparisons, results were compared using one- or two-way ANOVA followed by Dunnett's multiple comparison test (nociception), Bonferroni multiple comparison (immunostaining), or Tukey's multiple comparison test (FRET). A *P*<0.05 was considered significant.

SUPPLEMENTARY INFORMATION

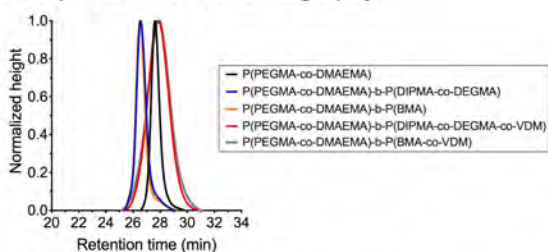
Supplementary Figures

| Polymer | Conversion (%) | GPC | | | ¹ H-NMR | | | | |
|--|----------------|------------|------|------------|--------------------|--------|-------|-------|-----|
| | | Mn (g/mol) | PDI | Mn (g/mol) | Composition | | | | |
| | | | | | PEGMA | DMAEMA | DIPMA | DEGMA | BMA |
| P(PEGMA-co-DMAEMA) | 54 | 12,377 | 1.20 | 17,600 | 56 | 6 | - | - | - |
| P(PEGMA-co-DMAEMA)-b-(DIPMA-co-DEGMA) | 92 | 17,581 | 1.36 | 39,444 | 56 | 6 | 91 | 12 | - |
| P(PEGMA-co-DMAEMA)-b-P-(BMA) | 82 | 18,225 | 1.37 | 31,654 | 56 | 6 | - | - | 98 |
| P(PEGMA-co-DMAEMA)-b-(DIPMA-co-DEGMA-co-VDM) | 95 | 19,380 | 1.22 | 39,881 | 56 | 6 | 95 | 11 | - |
| P(PEGMA-co-DMAEMA)-b-P-(BMA-co-VDM) | 62 | 18,576 | 1.29 | 28,220 | 56 | 6 | - | - | 74 |

B Raft polymerization of diblock copolymers



C Gel permeation chromatography



D Proton nuclear magnetic resonance

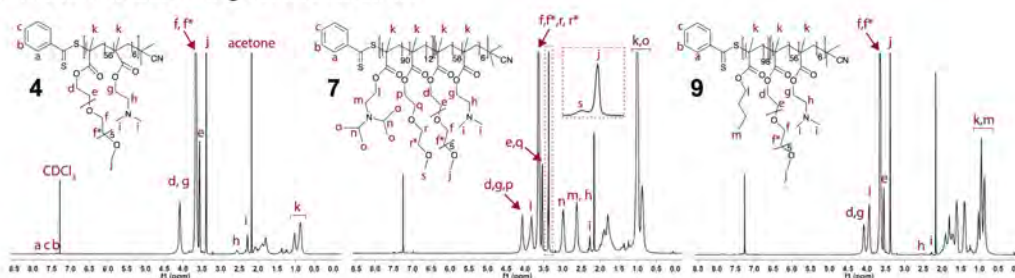


Figure S1. Synthesis and characterization of P(PEGMA-co-DMAEMA)-b-P(DIPMA-co-DEGMA) and P(PEGMA-co-DMAEMA)-b-P(BMA-co-DEGMA) diblock copolymers. A. Characterization of the hydrophilic block copolymers and the diblock copolymers. **B. i)** Sequential RAFT polymerization indicating synthesis of the hydrophilic block using (1) CPDB, (2) PEGMA and (3) DMAEMA to form (4) p(PEGMA-co-DMAEMA); synthesis of P(PEGMA-co-DMAEMA)-b-P(DIPMA-co-DEGMA) by chain extension reaction, where addition of the pH-responsive monomer (5) DIPMA and the charge screening monomer (6) DEGMA to (4) the hydrophilic block forms (7) the diblock P(PEGMA-co-DMAEMA)-b-P(DIPMA-co-DEGMA); **ii)** Addition of (5) DIPMA, (6) DEGMA and (10) VDM to (4) the hydrophilic block to form the intermediate (11), followed by the addition of (12) Cy5 to form the final Cy5 conjugated polymer (13) P(PEGMA-co-DMAEMA)-b-P(DIPMA-co-DEGMA-co-Cy5). **iii)** Addition of (8) BMA to (4) the hydrophilic block forms (9) P(PEGMA-co-DMAEMA)-b-P(BMA). **iv)** Addition of (8) BMA and (10) VDM to (4) the hydrophilic block to form the intermediate (14), followed by the addition of (12) Cy5 to form the final Cy5 conjugated polymer (15) P(PEGMA-co-DMAEMA)-b-P(BMA-co-Cy5). **C.** GPC traces showing a shift from P(PEGMA-co-DMAEMA) to higher molecular weight (*i.e.*, shorter retention time) after chain extension to form P(PEGMA-co-DMAEMA)-b-P(DIPMA-co-DEGMA) and P(PEGMA-co-DMAEMA)-b-P(BMA-co-DEGMA). **D.** ¹H-NMR spectra of the resulting polymers indicating the successful incorporation of the monomers.

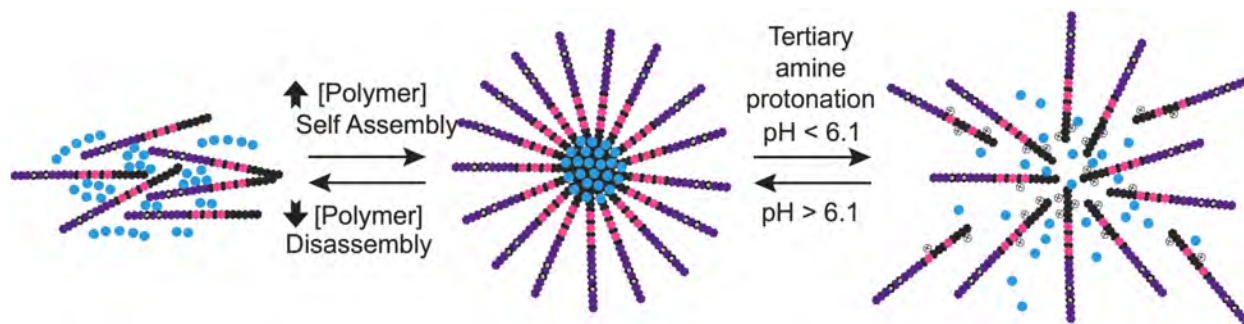


Figure S2. Mechanism of concentration-dependent self-assembly and pH-dependent disassembly of DIPMA NPs. Increasing concentrations of polymer result in NP self-assembly in an aqueous solution. DIPMA NPs possess a tertiary amine on the DIPMA units located in the core. At $\text{pH} < 6.1$, protonation results in a change from neutral to positive charge on DIPMA that induce like-like charge repulsion, which destabilizes the NP core with the subsequent disassembly and release of cargo.

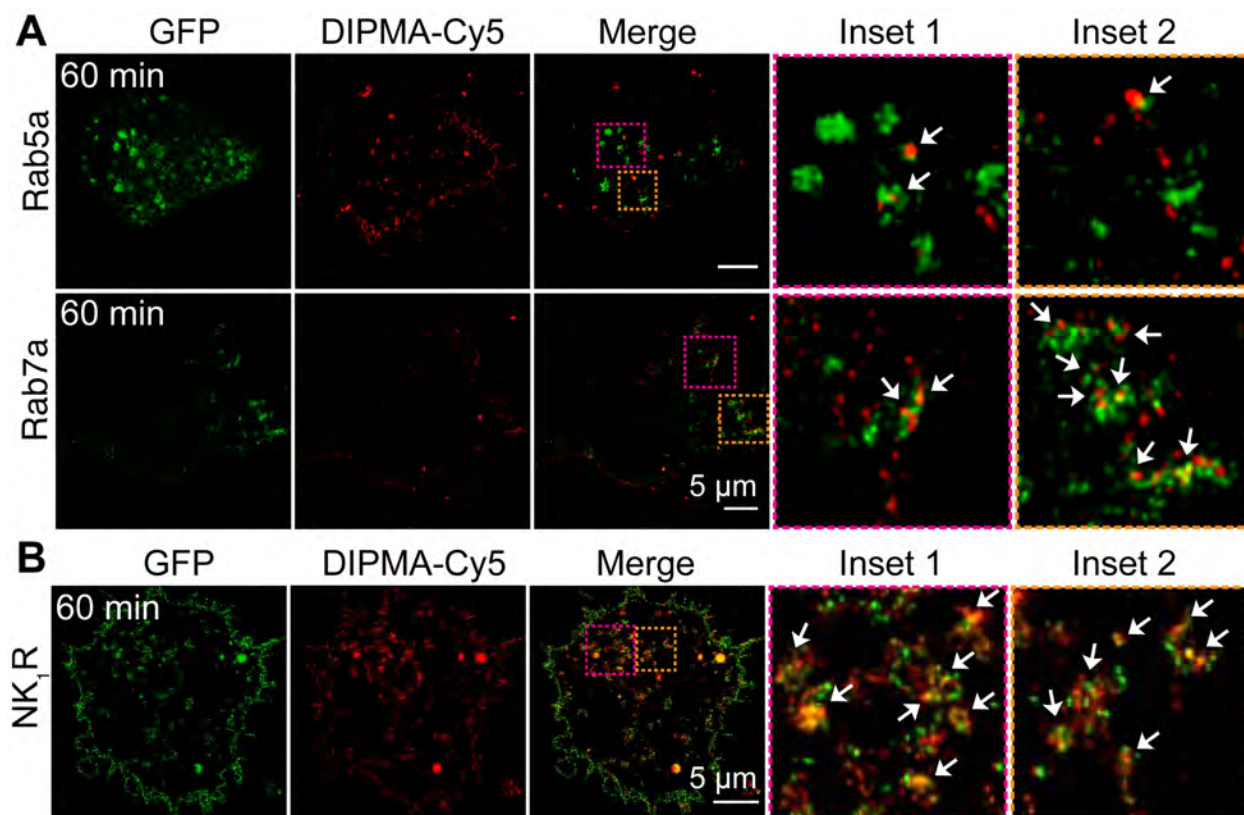


Figure S3. Uptake of DIPMA-Cy5 NPs in HEK-293 cells. **A.** Localization of DIPMA-Cy5 NPs in Rab5a-GFP early endosomes and Rab7a-GFP late endosomes after incubation with HEK-293 cells for 60 min. **B.** Colocalization of DIPMA-Cy5 NPs and NK₁R-GFP in HEK-rNK₁R cells at 60 min after stimulation with SP to induce NK₁R endocytosis. Representative results, $n = 5-6$ experiments.

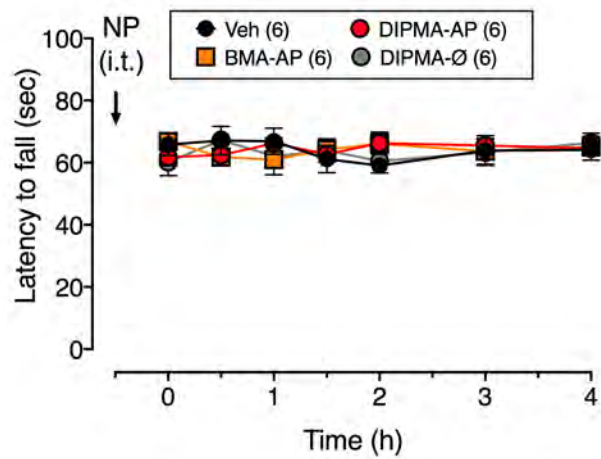


Figure S4. Rotarod latency. Effects of i.t. injection of vehicle (Veh), DIPMA-Ø, BMA-AP or DIPMA-AP NPs on latency to fall in mice, assessed using rotarod. $n = 6$ mice.

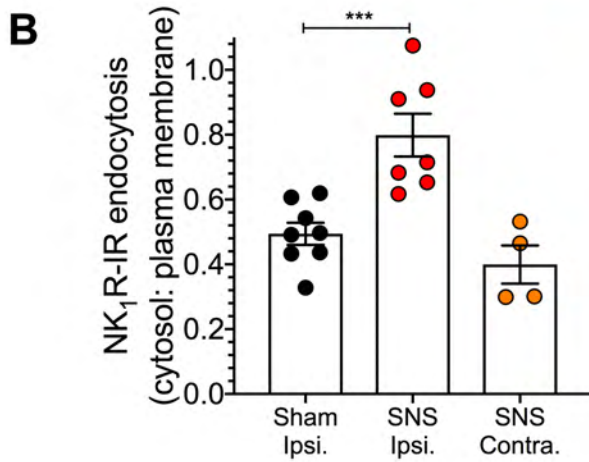
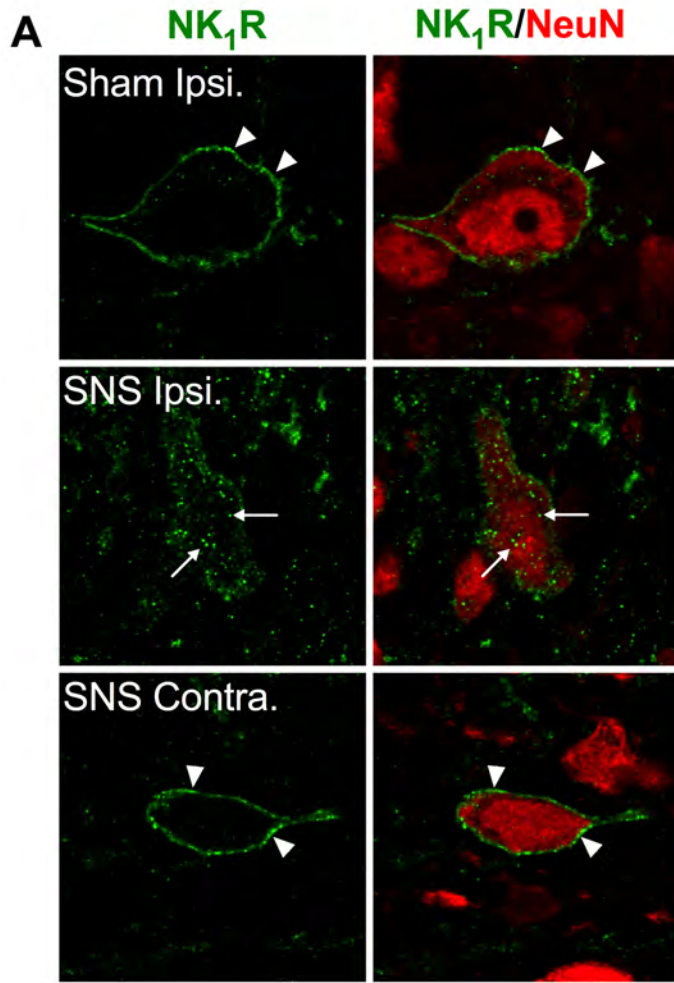


Figure S5. NK₁R endocytosis in chronic neuropathic nociception. The NK₁R was localized in the dorsal horn of rats 10 days after SNS or sham surgery. **A.** Localization of NK₁R-IR and NeuN-IR to the ipsilateral (Ipsi.) or contralateral (Contra.) lamina I dorsal horn of sham or SNS rats. Arrow heads denote plasma membrane. Arrows denote endosomes. **B.** Quantification of NK₁R endocytosis, assessed as the cytosol:plasma membrane pixel intensity for NK₁R-IR neurons. *n* = 4-8 rats, ****P*<0.001.

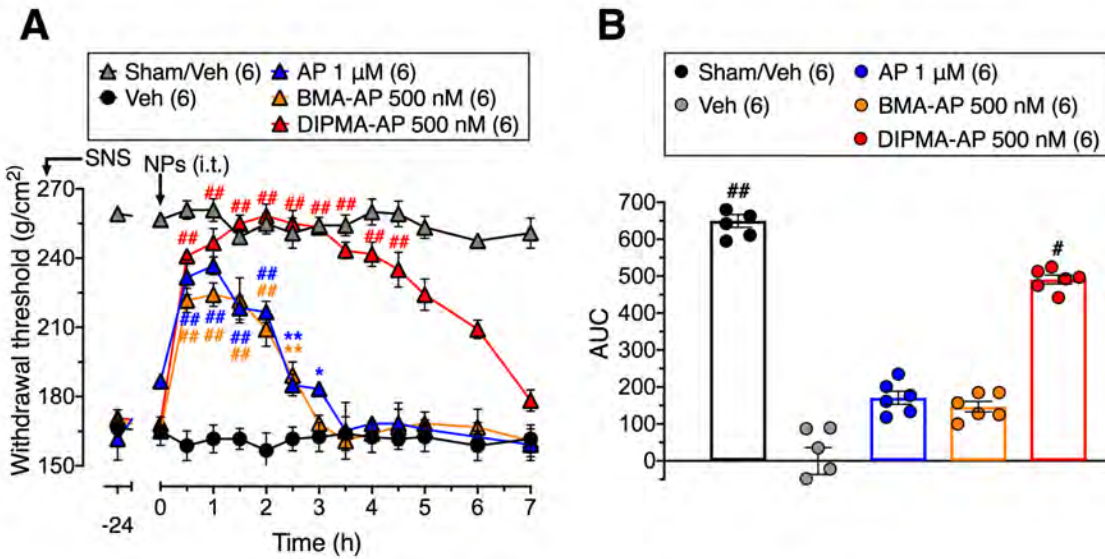


Figure S6. Effects of NPs on neuropathic nociception. The SNS model of chronic neuropathic pain was studied in rats. Vehicle, AP or NP was administered by i.t. injection 10 days after SNS or sham surgery. Paw withdrawal responses were assessed using the Randall-Selitto test. **A.** Time course. **B.** Area under curve (AUC) from 0-7 h. $n = 6$ rats studied in each experiment. * $P < 0.05$, ** $P < 0.005$, # $P < 0.001$, ## $P < 0.0001$ compared to vehicle.

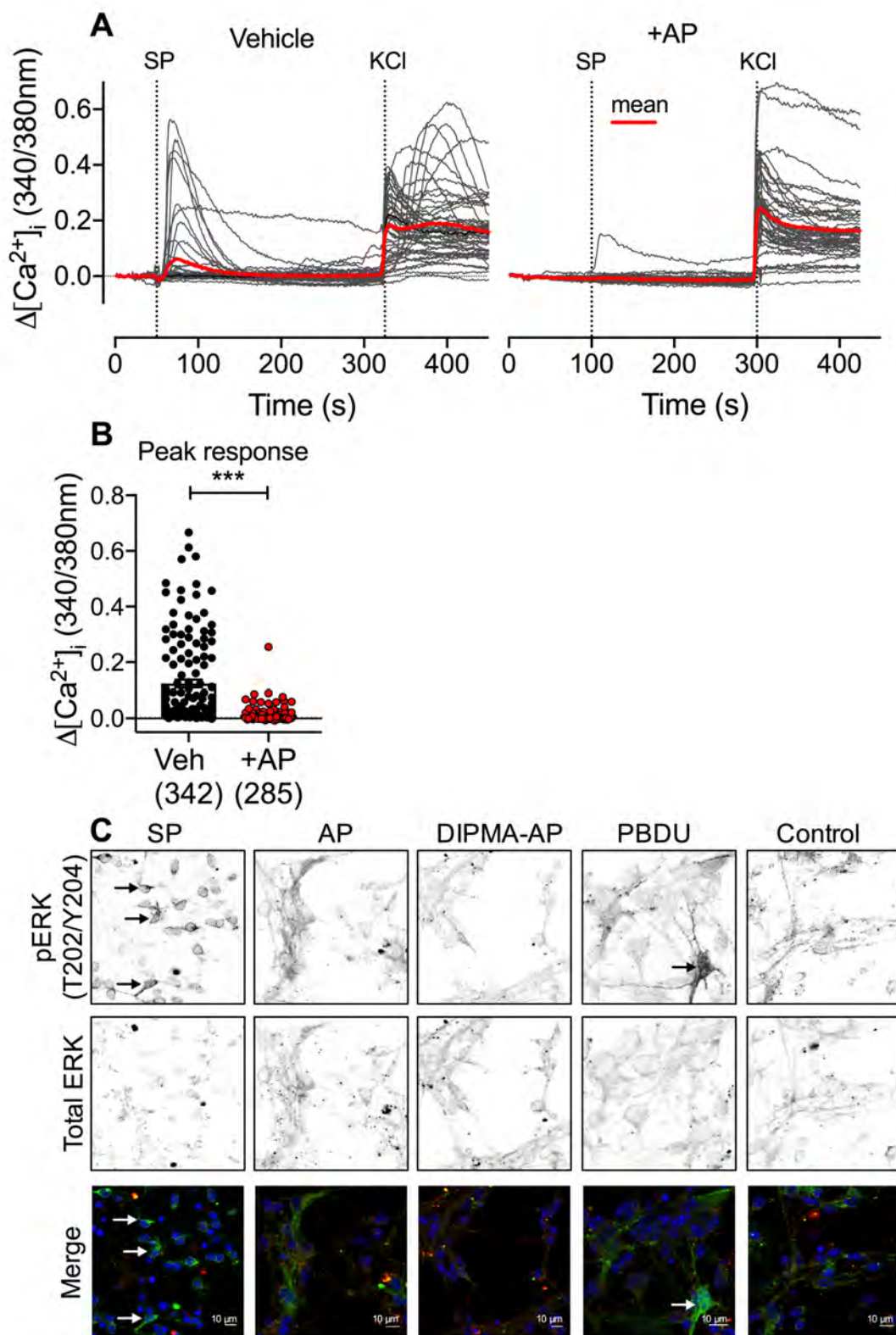


Fig. S7. SP signaling in mouse striatal neurons. SP (100 nM)-induced Ca^{2+} signaling in striatal neurons pretreated with vehicle or AP. **A.** Representative traces. **B.** Peak responses from $n = 342$

or 285 neurons. *** $P < 0.001$, $n = 3$ experiments. **C.** Representative images of phospho-ERK and total ERK immunostaining in cultured striatal neurons.

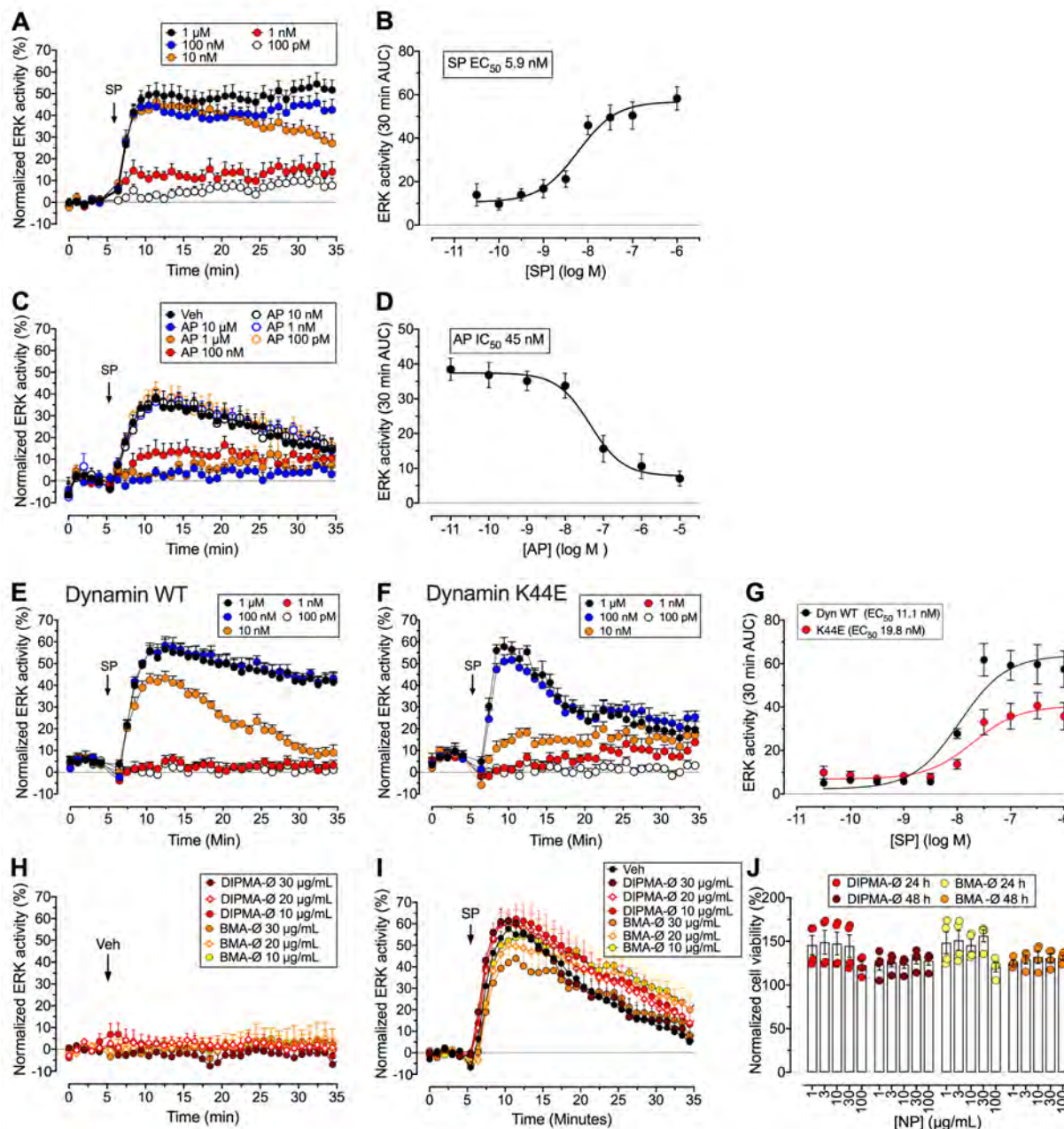


Figure S8. Nuclear ERK activity in HEK-293 cells. A-D. SP activation of nuclear ERK in HEK-hNK₁R cells. **A.** Effects of graded concentrations of SP on nuclear ERK activity. **B.** SP concentration-response curves. **C.** Effects of graded concentrations of AP on nuclear ERK response to SP (5 nM). **D.** AP concentration-response curves. *n* = 7-8 experiments, triplicate observations. **E-G.** SP-induced activation of nuclear ERK in HEK-hNK₁R cells expressing dynamin wildtype (Dyn WT, **E**) or dynamin K44E (Dyn K44E, **F**). **G.** SP concentration-response curves. *n* = 6 experiments, triplicate observations. **H, I.** Effects of DIPMA-Ø and BMA-Ø on basal nuclear ERK activity in HEK-293 cells (**H**) and on SP-stimulated nuclear ERK activity in HEK-hNK₁R cells (**I**) over 30 min. *n* = 4-7 experiments, triplicate observations. **J.** Effects DIPMA-Ø and BMA-Ø on viability of HEK-293 cells over 24 h and 48 h. *n* = 4 experiments, triplicate observations.

Supplementary Videos

Video S1. Localization of DIPMA-Cy5 NPs and Rab5a-GFP in HEK-293 cells. The video shows trafficking of DIPMA-Cy5 NPs (red) to Rab5a-GFP early endosomes (green). Cells were incubated with DIPMA-Cy5 NPs for 30 min.

Video S2. Localization of DIPMA-Cy5 NPs and Rab7a-GFP in HEK-293 cells. The video shows trafficking of DIPMA-Cy5 NPs (red) to Rab7a-GFP late endosomes (green). Cells were incubated with DIPMA-Cy5 NPs for 30 min.

Video S3. Localization of DIPMA-Cy5 NPs and NK₁R-GFP in HEK-293 cells. The video shows trafficking of DIPMA-Cy5 NPs (red) and NK₁R-GFP (green). Cells were incubated with DIPMA-Cy5 NPs for 90 min and with SP for 60 min to induce NK₁R endocytosis.

Video S4. Localization of DIPMA-Cy5 NPs in the mouse dorsal horn. The video is a 3D projection of DIPMA-Cy5 NPs in the perinuclear region of lamina I cells in the dorsal horn of the mouse spinal cord. The image was taken at 1 h after i.t. injection of NPs. Nuclei are stained with DAPI.

Video S5. Localization of DIPMA-Cy5 NPs in the mouse dorsal horn. The video is a 3D projection of BMA-Cy5 NPs in the perinuclear region of lamina I cells in the dorsal horn of the mouse spinal cord. The image was taken at 1 h after i.t. injection of NPs. Nuclei are stained with DAPI.

Video S6. Localization of NK₁R-IR in the rat dorsal horn after sham surgery. The video is a 3D projection showing the subcellular localization of NK₁R-IR (green) of lamina I spinal neuron (NeuN, red). The image was taken at 10 d after sham surgery.

Video S7. Localization of NK₁R-IR in the rat dorsal horn after SNS surgery. The video is a 3D projection showing the subcellular localization of NK₁R-IR (green) of lamina I spinal neuron (NeuN, red). The images was taken at 10 d after SNS surgery.

This document is confidential and is proprietary to the American Chemical Society and its authors. Do not copy or disclose without written permission. If you have received this item in error, notify the sender and delete all copies.

Application of a sulfoxonium ylide electrophile to generate cathepsin X-selective activity-based probes

| | |
|-------------------------------|---|
| Journal: | <i>Journal of Medicinal Chemistry</i> |
| Manuscript ID | Draft |
| Manuscript Type: | Article |
| Date Submitted by the Author: | n/a |
| Complete List of Authors: | <p>Mountford, Simon; Monash Institute of Pharmaceutical Sciences, Medicinal Chemistry Anderson, Bethany; The University of Melbourne, Biochemistry and Molecular Biology; Monash Institute of Pharmaceutical Sciences, Drug Discovery Biology Szabo, Monika; CSIRO, Hoang, My-Linh; Monash Institute of Pharmaceutical Sciences, Medicinal Chemistry Diao, Jiayin; Monash Institute of Pharmaceutical Sciences, Drug Discovery Biology Aurelio, Luigi; Monash Institute of Pharmaceutical Sciences Campden, Rhiannon; University of Calgary Lindstrom, Erik; Medivir AB Sloan, Erica; Monash University, Drug Discovery Biology Yates, Robin; University of Calgary Bunnett, Nigel; Columbia University, Surgery; Monash Institute of Pharmaceutical Sciences, Drug Discovery Biology; The University of Melbourne Thompson, Philip; Monash Institute of Pharmaceutical Sciences, Medicinal Chemistry & Drug Action Edgington-Mitchell, Laura; The University of Melbourne, Biochemistry and Molecular Biology; Monash Institute of Pharmaceutical Sciences, Drug Discovery Biology; New York University College of Dentistry, Oral and Maxillofacial Surgery</p> |
| | |

SCHOLARONE™
Manuscripts

1
2
3 **Application of a sulfoxonium ylide electrophile to generate cathepsin X-selective activity-**
4 **based probes**
5

6
7 Simon J. Mountford^{1*}, Bethany M. Anderson^{2,3*}, Monika Szabo¹, My-Linh Hoang¹, Jiayin Diao³,
8 Luigi Aurelio¹, Rhiannon I. Campden⁴, Erik Lindström⁵, Erica K. Sloan³, Robin M. Yates⁴, Nigel W.
9 Bunnett^{3,6,7}, Philip E. Thompson¹, Laura E. Edgington-Mitchell^{2,3,8#}
10

11
12 ¹Medicinal Chemistry, Monash Institute of Pharmaceutical Sciences, Monash University,
13 Parkville, Victoria, Australia.

14
15 ²Department of Biochemistry and Molecular Biology, Bio21 Molecular Science and
16 Biotechnology Institute, The University of Melbourne, Parkville, Victoria, Australia.

17
18 ³Drug Discovery Biology, Monash Institute of Pharmaceutical Sciences, Monash University,
19 Parkville, Victoria, Australia.

20
21 ⁴Snyder Institute for Chronic Disease and Department of Biochemistry and Molecular Biology,
22 University of Calgary, Calgary, Alberta, Canada.

23
24 ⁵Medivir AB, Huddinge, Sweden.

25
26 ⁶Departments of Surgery and Pharmacology, Columbia University, New York, New York, USA.

27
28 ⁷ Department of Pharmacology and Experimental Therapeutics, The University of Melbourne,
29 Parkville, Victoria, Australia.

30
31 ⁸Department of Oral and Maxillofacial Surgery, New York University College of Dentistry,
32 Bluestone Center for Clinical Research, New York, New York, USA.

33
34
35 *These authors contributed equally to this work

36
37 #Corresponding author: Laura E. Edgington-Mitchell laura.edgingtonmitchell@unimelb.edu.au
38
39

40
41 **Keywords:** protease, cathepsin, activity-based probes, functional imaging, cancer
42
43
44
45
46
47
48
49
50
51
52
53
54
55
56
57
58
59
60

Summary

Cathepsin X/Z/P is cysteine cathepsin with unique carboxypeptidase activity. Its expression has been associated with several cancer types and neurodegenerative diseases, although its roles during normal physiology are still poorly understood. Advances in our understanding of its function have been hindered by a lack of available tools that can specifically measure the proteolytic activity of cathepsin X. Here, we present a series of new activity-based probes that incorporate a novel sulfoxonium ylide warhead. These probes exhibit improved specificity and potency for cathepsin X compared to previously reported probes. We demonstrate the ability of these probes to detect the activity of cathepsin X in cell and tissue lysates, in live cells and *in vivo* and to localize active cathepsin X in mouse tissues by confocal microscopy. Finally, we present an improved method to generate chloromethylketones, necessary intermediates for synthesis of acyloxymethylketones probes, by way of sulfoxonium ylide intermediates. Sulfoxonium ylide probes are more potent and specific than the acylmethylketone analogues, further validating the utility of this new warhead. In conclusion, the probes presented in this study will be valuable for investigating cathepsin X pathophysiology and for validating its proteolytic activity as a clinical biomarker for multiple diseases.

Introduction

Cathepsin X (also referred to as cathepsin Z or P) is a cysteine cathepsin protease that is unique among its family members in that it exhibits strict carboxypeptidase activity. It is one of the most recently discovered cysteine cathepsins, and its functions during health and disease are still incompletely understood. Cathepsin X contributes to adhesion and maturation of macrophages and dendritic cells and suppresses clathrin-dependent phagocytosis through cleavage of profilin.^{1,2} Cathepsin X regulates hormone signaling, where its cleavage of bradykinin, kallidin, or angiotensin leads to alterations in specificity towards their cognate receptors and divergent downstream signaling.³ Cathepsin X is also expressed by neurons, where its cleavage of α -enolase regulates survival and the outgrowth of neurites⁴. Furthermore, cathepsin X expression is enriched in amyloid plaques, where it may have a protective effect against neurodegenerative disorders such as Alzheimer's disease,^{5,6} and in the spinal cord during neuropathic pain.⁷ Upregulation of cathepsin X mRNA has been reported in pathology-free regions of multiple sclerosis-affected brains,⁸ and it has been implicated in the generation of IL-1 β ^{9,10} (and in mediating neuroinflammation.⁹ It is also upregulated in the microenvironment of breast,¹¹ pancreatic,¹² prostate,¹³ and gastric cancers,^{14,15} where it likely promotes tumor invasion. Thus, cathepsin X holds promise as a clinical biomarker and therapeutic target in diverse diseases.

Like most cathepsins, cathepsin X is synthesized as a zymogen that becomes activated in the acidic environment of endolysosomes. Once activated, it may also be negatively regulated by endogenous inhibitors, though likely not cystatin C or stefin A.^{16,17} In addition to its proteolytic functions, cathepsin X can also promote integrin-mediated signaling through an Arg-Gly-Asp (RGD) motif in its pro-domain.¹² As a result of these complex modes of post-translational regulation, traditional biochemical methods that survey total protein levels rarely reflect the pool of proteolytically active enzyme. The ability to specifically measure its activity in its native environment is therefore required to define its precise proteolytic functions during health and disease.

1
2
3 To this end, efforts have been focused on developing fluorescent activity-based probes (ABPs)
4 for cathepsin X. ABPs are small molecules that contain an electrophilic moiety (warhead), a
5 recognition sequence that confers selectivity, and a fluorophore for detection.¹⁸⁻²⁰ When active,
6 the protease initiates a nucleophilic attack on the warhead, resulting in the formation of a
7 covalent, irreversible bond. Assessment of probe labeling can then be used to quantify protease
8 activity by SDS-PAGE (in-gel fluorescence), fluorescent microscopy, flow cytometry or optical
9 imaging of whole tissues or organisms. Importantly, the covalent nature of probe binding allows
10 for target confirmation by immunoprecipitation with specific antibodies or affinity purification
11 followed by proteomic analysis.
12
13
14
15
16
17
18
19
20

21 Probes with absolute specificity for cathepsin X have not been previously reported. BMV109, a
22 fluorescently quenched ABP with a tetrafluorophenoxymethyl ketone warhead, is a pan-
23 cathepsin probe that targets X, B, S, and L.²¹ Because cathepsin X is a similar size as cathepsin B,
24 one of the most abundant and ubiquitously expressed cathepsins, it can be difficult to clearly
25 resolve these two proteases by SDS-PAGE, which precludes accurate quantification by in-gel
26 fluorescence. MGP140 is an epoxide-based probe that exhibits greater specificity for cathepsin X
27 than BMV109, but also potently reacts with cathepsin B.²² If mice are pretreated with GB11-NH₂,
28 an inhibitor of cathepsin B, S, and L, prior to MGP140 injection, specific labeling of cathepsin X
29 can be achieved. However, this manipulation of the system results in hyperactivation of cathepsin
30 X, possibly a compensatory response due to the loss of cathepsin B activity. Thus, it is crucial to
31 develop probes with improved specificity for cathepsin X to allow for a more detailed
32 investigation of its physiological activity.
33
34
35
36
37
38
39
40
41
42
43
44

45 Herein, we describe a series of ABPs containing a novel sulfoxonium ylide warhead that exhibit
46 previously unseen selectivity for cathepsin X. We applied these probes to measure cathepsin X
47 activity in lysates and live cells, and in live mice. We also used the sulfoxonium ylide as a stepping
48 stone to access chloromethylketones, which are intermediates in the synthesis of
49 acyloxymethylketones (AOMK), warheads commonly used in probes for cathepsins and other
50 cysteine proteases. This new method does not require generation of diazomethanes to access
51
52
53
54
55
56
57
58
59
60

1
2
3 chloromethylketones and is thus a safer alternative to the previously used methods. By
4 comparison to the sulfoxonium ylide probes, AOMK probes bearing identical recognition
5 sequences exhibited unique specificity profiles, and no detectable reactivity with cathepsin X.
6
7 Thus, sulfoxonium ylide probes represent a clear advancement in the tools that are available to
8
9 study cathepsin X function.
10
11
12
13

14 Results

15 16 17 18 *Design and characterization of a sulfoxonium ylide probe.*

19
20
21 To explore new potential warheads for cysteine cathepsins, we designed and synthesized an ABP
22 containing a dimethyl sulfoxonium ylide electrophile. This design was initially inspired by a
23 dimethyl sulfonium salt reported to inhibit cathepsin B in 1988 by Shaw.²³ To increase the
24 electrophilicity of this warhead, and thus its reactivity with the catalytic cysteine residue, we
25 modified the dimethyl sulfonium salt to a dimethyl sulfoxonium ylide. We also incorporated a
26 valine residue as the P1 recognition sequence and a sulfo-Cyanine 5 (sCy5) fluorophore to yield
27 our initial probe, sCy5-Val-SY (**17**; **Fig 1**), synthesized according to **Scheme 1**.
28
29
30
31
32
33
34
35

36 To determine its reactivity profile, we first incubated sCy5-Val-SY (**17**) with protein lysates
37 prepared from RAW264.7 cells, an immortalized mouse macrophage line that contains high levels
38 of active cysteine cathepsins.²¹ Cells were lysed in citrate buffer (pH 5.5) to provide optimal
39 conditions for preserving cathepsin activity, and the probe was added at 1 μ M for 20 minutes.
40 We then resolved the lysates by SDS-PAGE and scanned the gel for sCy5 fluorescence using a
41 flatbed laser scanner. We observed exclusive, concentration- and time-dependent labeling of a
42 ~35-kDa protease (**Fig 2A, S1A-B**). This labeling was prevented by pretreatment of the lysates
43 with JPM-OEt, a pan-cysteine cathepsin inhibitor, confirming that this protease was a member of
44 the cysteine cathepsin family (**Fig 2A**). In contrast, MDV-590 – a specific inhibitor for cathepsin
45 S²⁴ – did not compete for sCy5-Val-SY (**17**) binding. We compared the labeling profile to that of
46 BMV109, the pan-cathepsin probe, and found that the sCy5-Val-SY (**17**)-labeled protease was the
47
48
49
50
51
52
53
54
55
56
57
58
59
60

1
2
3 same molecular weight as BMV109-labeled cathepsin X.²¹ We confirmed that this protease was
4 indeed cathepsin X by immunoprecipitating sCy5-Val-SY (**17**)-labeled lysates with a cathepsin X-
5 specific antibody (**Fig 2B**).
6
7
8
9

10 Next, we tested the ability of sCy5-Val-SY (**17**) to label cathepsin X in mouse splenic lysates. As
11 we observed in macrophage lysates, the probe exhibited exclusive reactivity with cathepsin X in
12 splenic lysates from wildtype mice, and this labeling was absent in lysates prepared from spleens
13 of cathepsin X-deficient mice (**Fig 2C**). By comparison, BMV109 strongly labeled cathepsin B and
14 to a lesser extent, cathepsin S and L.
15
16
17
18
19

20
21 Having observed unique specificity of sCy5-Val-SY (**17**) in cell and tissue lysates, we sought to
22 assess the probe's permeability and specificity profile in living RAW264.7 cells. After incubating
23 the probe (at 1 μ M) with live cells for increasing lengths of time or with increasing probe
24 concentrations (for 2 hours), we analyzed lysates by in-gel fluorescence as above. Here, we
25 observed time- and concentration-dependent labeling of two proteases (**Fig 2D, S1C**), which we
26 identified as cathepsin X and S by immunoprecipitation (**Fig 2E**) and competition with MDV-590
27 (**Fig 2F**), respectively. We were surprised to see cathepsin S labeling in live cells, given its lack of
28 binding to sCy5-Val-SY (**17**) in cell lysates, where we had confirmed high levels of cathepsin S
29 activity with BMV109. This suggests that the reactivity of cathepsin S with the sulfoxonium ylide
30 is dependent on the labeling conditions. We attempted to explore this by lysing the cells in
31 various buffers that might mimic the endosomal environment of cathepsin S, but we were not
32 able to improve the labeling of cathepsin S in lysates (not shown).
33
34
35
36
37
38
39
40
41
42
43

44
45 Nonetheless, the sulfoxonium ylide probe exhibited clear labeling of cathepsin X in lysates and
46 live cells with considerably improved selectivity compared to BMV109 (**Fig 2D,F**). To our
47 knowledge, it is the first covalent ABP for cathepsin X that does not also bind to cathepsin B or L.
48 As observed in **Fig 2**, it is difficult to distinguish cathepsin X labeling from cathepsin B with
49 BMV109 due to the similarity in size of the two proteases. However, sCy5-Val-SY (**17**) allows for
50 clear delineation of cathepsin X activity.
51
52
53
54
55
56
57
58
59
60

Sulfoxonium ylide library with variable P1 residues

To improve the specificity and potency of the probe for cathepsin X, we generated a small library of sulfoxonium ylide probes by varying the amino acids in the P1 position (**Scheme 1, Table 1**). In RAW264.7 lysates, probes bearing Ile (**18**), Leu (**19**), Nle (**20**), and Phe (**21**) all showed similar specificity for cathepsin X as sCy5-Val-SY (**17**), with sCy5-Leu-SY (**19**) and sCy5-Nle-SY (**20**) exhibiting a clear improvement in potency (**Fig 3A**). The probe bearing Cbz-Lys (**23**), in which the sCy5 was attached via the lysine side chain, exhibited a loss of specificity, favoring cathepsin S over X and B. sCy5-Phe-Val-SY (**24**), in which a P2 Phe residue was incorporated, also exhibited a loss of specificity (**Fig 3A, S2**). The labeling profile of this probe was similar to BMV109, though it showed improved potencies for cathepsin X and S compared to BMV109. A hydrophobic S2 pocket is a feature of virtually all cysteine cathepsins, which may explain the increased affinity of a dipeptide probe for other members of the family.²⁵

In murine kidney lysates, Leu and Nle conferred the most potency and specificity for cathepsin X, with Cbz-Lys (**23**), Phe (**21**), and Phe-Val (**24**) yielding broader reactivity, and Val and Ile exhibiting weaker labeling (**Fig 3B, S2**).

To examine the potency and permeability of the sulfoxonium ylide probe series in living cells, we applied them to RAW264.7 cells for two hours. Probes bearing Trp (**22**), Val (**17**), Ile (**18**), Leu (**19**), Nle (**20**), and Phe (**21**) labeled cathepsin X and S to similar extents and with similar potency, while Cbz-Lys (**23**) exhibited a preference for cathepsin S and Phe-Val (**24**) labeled B and L in addition to X and S (**Fig 3C, S2A,C-G**). We confirmed the 25-kDa protease labeled by sCy5-Nle-SY (**20**) to be cathepsin S by competition with two cathepsin S-specific inhibitors, MDV-590 and Z-FL-COCHO (**Fig S2B**).

We tested the specificity of these probes for cathepsin X in a human breast cancer line known to express very low levels of cathepsin S, MDA-MB-231^{HM}.²⁶ These cells also allowed us to test

1
2
3 whether the probes could bind to human cathepsin X (in addition to mouse cathepsin X shown
4 previously). When we incubated the probes with MDA-MB-231 cells for shorter time periods, we
5 observed very little labeling of cathepsin X (not shown); however, clear labeling was observed
6 after overnight incubation (**Fig 3D**). This likely reflects differences in the rates of endocytosis
7 between macrophages and tumor cells and suggests that the probes may be taken up directly
8 into the endolysosomal pathway rather than by diffusion through membranes. The sulfoxonium
9 ylide probe series generally shows specific labeling of cathepsin X in these cells, with minimal
10 cross-reactivity occurring only at 5 μ M. Cbz-Lys(sCy5)-SY (**23**) and especially sCy5-Phe-Val-SY (**24**)
11 exhibited the most cross-reactivity with cathepsin B and L.
12
13
14
15
16
17
18
19
20

21 *In vivo characterization of sCy5-Nle-SY*

22
23
24

25 Taking into consideration all of the data from cell and tissue lysates and live mouse and human
26 cells, sCy5-Nle-SY (**20**) emerged as the probe showing the highest potency and selectivity for
27 cathepsin X. Thus, we elected to move forward with this probe for *in vivo* studies. We injected
28 the probe into mice intravenously, and after two hours of circulation, tissues were harvested,
29 lysed, and analyzed for probe labeling by fluorescent SDS-PAGE. We observed labeling of
30 cathepsin X in liver, kidney, colon, stomach, and spleen (**Fig 4A**), and this was confirmed by
31 immunoprecipitation with a cathepsin X antibody (**Fig 4B**). While some labeling of cathepsin S
32 was also observed, the overall specificity profile was clearly improved compared to BMV109,
33 which also strongly labels cathepsin B and L.
34
35
36
37
38
39
40
41
42

43 It is important to note that, in addition to cathepsin X and S, we also observed labeling of
44 additional species *in vivo* at 55 and 15 kDa with sCy5-Nle-SY (**20**). The 55-kDa species was weakly
45 observed when kidney lysates were labeled, but not the 15-kDa species. We synthesized a
46 biotinylated Nle-SY probe in attempt to affinity purify these species; however, labeling with this
47 probe was much weaker than the sCy5 probe suggesting that sCy5 contributes in part to
48 selectivity (not shown). Efforts to develop new affinity probes are ongoing.
49
50
51
52
53
54
55
56
57
58
59
60

1
2
3 We then used confocal microscopy to image sCy5-Nle-SY (**20**) fluorescence in kidney cryosections
4 after *in vivo* probe administration. We observed strong punctate sCy5 fluorescence reminiscent
5 of endolysosomal staining, and this signal largely overlapped with immunoreactive cathepsin X (**Fig**
6 **5**). Thus, we could use sCy5-Nle-SY (**20**) to distinguish active cathepsin X relative to total cathepsin
7 X in tissues after *in vivo* administration.
8
9
10
11
12
13

14 *Sulfoxonium ylides as a new route to acyloxymethylketone probes*

15
16
17

18 Many of the reported activity-based probes for cysteine proteases incorporate AOMK or
19 phenoxyethylketone (PEK) warheads.^{21,27-31} Synthesis of these electrophiles requires
20 generation of chloromethylketone intermediates, a process that has historically been achieved
21 through generation of diazomethane, an extremely explosive yellow gas. We devised a new
22 synthetic route to access the chloromethylketones via a sulfoxonium ylide intermediate (**Scheme**
23 **2, Table 2**), thereby avoiding this potentially dangerous reaction.
24
25
26
27
28
29
30

31 Using this method, we successfully generated three AOMK probes bearing Nle (**31**), Phe (**32**), and
32 Cbz-Lys (**33**), suggesting that this method could be broadly applied to the synthesis of diverse
33 ABPs. We compared the reactivity of the new AOMK probes with the corresponding sulfoxonium
34 ylide probes. The AOMK probes were much less potent than the ylide probes, suggesting reduced
35 reactivity. These probes labeled cathepsin B and S, but not X (**Fig 6A**), which is in line with
36 previous data demonstrating limited reactivity of cathepsin X with the AOMK warhead.²² We also
37 tested sCy5-Nle-AOMK *in vivo* and analyzed its labeling in tissues. Only weak labeling of cathepsin
38 B and S was observed in the colon, but not in other tissues examined (**Fig 6B**).
39
40
41
42
43
44
45
46

47 **Discussion and Conclusion**

48
49
50

51 We have designed a new dimethyl sulfoxonium ylide warhead that exhibits unique selectivity
52 towards cysteine cathepsin proteases in cell lysates, live cells, and in mouse and human tissues.
53 Our best probe, sCy5-Nle-SY (**20**) is the most potent and selective probe for cathepsin X to date,
54
55
56
57
58
59
60

1
2
3 showing specificity in cell lysates and cells that express low levels of cathepsin S. While this probe
4 does cross-react with cathepsin S in live macrophages and *in vivo*, it does not appreciably label
5 cathepsin B or L, which is a clear improvement over the only other covalent probes that target
6 cathepsin X (BMV109, MGP140, DCG04). The use of sCy5-Nle-SY (**20**) allows for clear
7 measurement of the activity of the cathepsin X by SDS-PAGE, whereas this was difficult with
8 previous probes due to confounding levels of cathepsin B labeling.
9
10
11
12
13
14
15

16 Furthermore, we established that the sulfoxonium ylide warhead is stable enough for *in vivo*
17 detection of cathepsin X activity. While the probe is most reliable in gel-based analyses of tissue
18 lysates, sCy5-Nle-SY (**20**) signal was bright enough to detect by confocal microscopy. In
19 conjunction with cathepsin X-specific antibodies, this method can distinguish active from inactive
20 cathepsin X by cellular imaging and in the future could be applied to advance our understanding
21 of the function of cathepsin X in animal models of disease.
22
23
24
25
26
27
28

29 Little is known about the preferred cleavage sequence for cathepsin X and this may be partially
30 due to the difficulties in profiling carboxypeptidases with fluorogenic substrate libraries (*i.e.*, its
31 preference for a free carboxylic acid limits the choice and placement of the fluorophore). A study
32 by Devanathan and colleagues used a fluorogenic substrate library based on the aminobenzoic
33 acid-Phe(4-NO₂) fluorophore-quencher pair to explore the preferred P1 and P2 residues of
34 cathepsin X.³² In the P1 position, weak reactivity was observed with Met, Phe, Tyr, Thr, Gln, Glu,
35 Lys and Arg; however, Val, Ile, Leu, and Trp (among others) were not tolerated at all. By contrast,
36 these residues were among the most potent in the P1 position of our sulfoxonium ylide library.
37 In a similar study by Puzer and colleagues, in which aminobenzoic acid and Lys(dinitrophenol)
38 were used as the fluorophore quencher pair, Leu was well tolerated in the P1 position.³³ In both
39 screens, most residues were well tolerated in the P2 position, with the exception of proline. In
40 direct contrast to this, cathepsin X has been shown to cleave natural substrates such as CXCL-12
41 with proline at the P2 position.³⁴ Collectively, these studies demonstrate the dependence of
42 probe structure on specificity and warrant the development of larger sulfoxonium ylide libraries
43 with greater diversity of P1, P2 and P3 residues. Given the observed crossreactivity of the current
44
45
46
47
48
49
50
51
52
53
54
55
56
57
58
59
60

1
2
3 probes with other as yet unknown proteases (*e.g.*, in the kidney), we anticipate that expanding
4 the sulfoxonium ylide library will open the door to selective ABPs and inhibitors for other
5 proteases in addition to cathepsin X.
6
7
8
9

10 In conclusion, our new sulfoxinium ylide-based probes will be valuable for understanding the
11 contribution of cathepsin X to normal physiology and disease and for establishing cathepsin X
12 and a drug target and diagnostic marker for cancer and other inflammatory and
13 neurodegenerative diseases.
14
15
16
17
18

19 **Materials and Methods**

20 *General Purification and Characterization Methods*

21
22 RP-HPLC was performed on a Phenomenex Luna C-8 column (100 Å, 10 µm, 250 × 21.5 mm)
23 utilising a Waters 600 semi-preparative HPLC incorporating a Waters 486 UV detector. The
24 eluting profile was a linear gradient of 0–60% buffer A to buffer B (buffer A: 0.1% TFA in
25 water; buffer B: 0.1% TFA in acetonitrile) over 60 min at a flow rate of 15 mL min⁻¹. Compound
26 identity was confirmed by ESI-MS, using a Shimadzu LCMS2020 instrument, incorporating a
27 Phenomenex Luna C-8 column (100 Å, 3 µm, 100 × 2.00 mm) and analysed at a wavelength of
28 214nm. The eluting profile was 0.1% TFA in water for 4 min, followed by a linear gradient as
29 specified of buffer A to buffer B, at a flow rate of 0.2 ml min⁻¹.
30
31
32
33
34
35
36
37
38
39

40 *Nuclear magnetic resonance*

41
42 NMR spectra were obtained using a Bruker Avance III Nanobay spectrometer coupled to the BACS
43 60 automatic sample changer. The spectrometer was equipped with a 5 mm PABBO BB-1H/D Z-
44 GRD probe. ¹H NMR spectra were obtained at 400MHz. Each resonance was assigned according
45 to the following convention: chemical shift (δ), measured in parts per million (ppm) relative to
46 the residual non-deuterated solvent peak chloroform (unless otherwise specified) as an internal
47 reference relative to trimethylsilane(δ=0), multiplicity, coupling constants (*J* Hz), number of
48 protons and assignment. Multiplicities are denoted as (s) singlet, (d) doublet, (dd) doublet of
49 doublets, (t) triplet, (q) quartet or (m) multiple.
50
51
52
53
54
55
56
57
58
59
60

Carbon nuclear magnetic resonance

¹³C NMR spectra were obtained at 100MHz. Each resonance was assigned according to the following convention: chemical shift (δ), measured in parts per million (ppm) relative to the residual non-deuterated solvent peak chloroform (unless otherwise specified) as an internal reference relative to trimethylsilane($\delta=0$), number of carbons and assignment.

Liquid Chromatography Mass Spectra

LCMS were conducted on an Agilent UHPLC/MS 1260 instrument (Pump: 1200 Series G1311A Quaternary pump, Autosampler: 1200 Series G1329A Thermostated Autosampler, Detector: 1200 Series G1314B Variable Wavelength Detector). Eluting profile was a linear gradient of 5-100%B over 2.5 min at a flow rate of 0.5 mL/min. Solvent A: water 0.1% formic acid, solvent B: acetonitrile 0.1% formic acid. Liquid chromatography conditions; reverse phase HPLC analysis, Column: Poroshell 120 EC-C18 3.0 X 50mm 2.7-micron, column temperature: 35°C, injection volume: 1uL, Detection: monitored at 254 nm and 214 nm. Mass spectrum conditions ion source: quadrupole, Ion Mode: API-ES, drying gas temp: 350°C. Principle ion peaks (m/z) are reported with intensities of the base peak in brackets.

High resolution mass spectra

HRMS were conducted on an Agilent 6224 TOF LC/MS Mass Spectrometer coupled to an Agilent 1290 Infinity (Agilent, Palo Alto, CA). All data were acquired and reference mass corrected via a dual-spray electrospray ionisation (ESI) source. Mass Spectrometer Conditions: Ionisation mode: Electrospray Ionisation Drying gas flow: 11 L/min, Solvent A = aqueous 0.1% formic acid, Solvent B = acetonitrile/0.1% formic acid. Found and calculated ion peaks (m/z) are reported.

Analytical HPLC analyses

Analytical HPLC analyses were done on an Agilent 1260 Infinity Analytical HPLC coupled with a 1260 Degasser: G1322A, 1260 Binary Pump: G1312B, 1260 HiP ALS autosampler: G1367E, 1260 TCC: G1316A and 1260 DAD detector: G4212B. The column used was a Zorbax Eclipse Plus C18

1
2
3 Rapid Resolution 4.6 X 100mm 3.5-micron. The sample injection volume was 2 μ L which was run
4 in 0.1% TFA in acetonitrile at a gradient of 5 – 100% over 10 min with a flow rate of 1 mL/min.
5
6 Detection methods were with 214 nm and 254 nm.
7
8
9

10 *General Method A: Preparation of nitrophenyl esters.*

11
12 Triethylamine (1.2 equiv.) was added to a solution of the Boc-protected amino acid (1 equiv.) in
13 CH_2Cl_2 (5 mL). The stirred mixture was cooled to 0°C and 4-nitrophenylchloroformate (1.2 equiv.)
14 was added. After 10 min, DMAP (0.1 equiv.) was added and the mixture stirred at 0°C for 6 h. The
15 reaction mixture was further diluted with CH_2Cl_2 (15 mL) and washed with saturated NaHCO_3
16 solution (10 mL), 0.1 M HCl solution (10 mL), brine (10 mL), and then dried (MgSO_4), filtered and
17 solvent reduced in vacuo to give the crude product.
18
19
20
21
22
23
24

25 *General Method B: Preparation of sulfoxonium ylides*

26
27 Trimethylsulfoxonium iodide (4 equiv.) was suspended in dry THF (5 mL) and KO^tBu (4 equiv.)
28 added. The mixture was stirred at reflux for 3 h with the exclusion of light. The reaction was
29 cooled to 0°C and a solution of the nitrophenyl ester (1 equiv.) in THF was added dropwise and
30 stirred for 18 h. The reaction was quenched with H_2O (30 mL) and the solution concentrated in
31 vacuo to remove the THF. The remaining aqueous solution was extracted with EtOAc (3 x 30 mL).
32 The combined organic extract was washed with brine (15 mL), dried (MgSO_4), filtered and the
33 solvent removed in vacuo to give the crude product.
34
35
36
37
38
39
40
41

42 *General Method C: Preparation of chloromethyl ketones.*

43
44 To a solution of the sulfoxonium ylid (1 equiv.) in dry THF (5 mL) was added 4M HCl in dioxane
45 (1.15 equiv.). The solution was stirred at reflux for 4 h. Solvents were removed in vacuo and the
46 residue treated with EtOAc (20 mL) and washed with H_2O (15 mL) and saturated NaHCO_3 solution
47 (15 mL). The organic layer was dried (MgSO_4), filtered and concentrated in vacuo to give the crude
48 product.
49
50
51
52
53

54 *General Method D: Preparation of acyloxymethyl ketones (AOMK).*

Potassium Fluoride (3 equiv.) was suspended in DMF (1 mL) and sonicated for 1 min. 2,6-Dimethylbenzoic acid (1.1 equiv.) was added to the suspension and stirred at ambient temperature for 5 min. The chloromethyl ketone (1 equiv.) was added and the mixture stirred at ambient temperature for 18 h. DMF was removed in vacuo and the resulting residue was treated with EtOAc (20 mL) and washed with a saturated NaHCO₃ solution (15 mL). The organic layer was dried (MgSO₄), filtered, and solvent removed in vacuo to give the crude product.

General Method E: Sulfo-cyanine 5 labelling of the sulfoxonium ylides and acyloxymethyl ketones (AOMK).

The boc-protected sulfoxonium ylide or boc-protected acyloxymethyl ketones (AOMK) (1 equiv.) were treated with a 1:1 mixture of TFA and CH₂Cl₂ (2 mL) and stirred at ambient temperature for 1 h. Volatile components were removed under a stream of nitrogen. To the resulting residue was added DMF (300 μL) and DIPEA (4 equiv.). Separately, Sulfo-Cy5 (1 equiv.) and PyClock (2 equiv.) were dissolved in DMF (300 μL) and DIPEA (4 equiv.) and stirred for 2 min before adding to the above solution. The reaction mixture was stirred at ambient temperature for 18 h excluding light.

4-Nitrophenyl (tert-butoxycarbonyl)-L-valinate (1)

Ice cold dry DMF (20 mL) was slowly added to 4-nitrophenylchloroformate (2.27 g, 11.2 mmol) and stirred for 10 min under a nitrogen atmosphere. The mixture was then gradually warmed to ambient temperature. A solution of boc-L-valine (2.02 g, 9.30 mmol) in DMF (7 mL) was added dropwise followed by triethylamine (1.50 mL, 10.8 mmol). Stirring was continued for 1 h. The reaction mixture was diluted with EtOAc (50 mL) and washed with H₂O (3 x 30 mL) and brine (30 mL). The organic layer was dried (MgSO₄), filtered and concentrated under reduced pressure to give the crude product. Purification by column chromatography (SiO₂, 10-13% EtOAc : Petroleum Spirits) yielded the product as a viscous, colourless oil (2.01 g, 64%). HRMS (ESI⁺): Found: *m/z* 361.1386 (M + Na)⁺, C₁₆H₂₂N₂NaO₆⁺ requires *m/z* 361.1370. ¹H NMR (400 MHz, CDCl₃) δ 8.29 – 8.23 (m, 2H), 7.31 – 7.25 (m, 2H), 5.05 (d, *J* = 8.4 Hz, 1H), 4.44 (dd, *J* = 8.6, 5.1 Hz, 1H), 2.37 – 2.24 (m, 1H), 1.45 (s, 9H), 1.09 (d, *J* = 6.8 Hz, 3H), 1.03 (d, *J* = 6.9 Hz, 3H). ¹³C NMR (101 MHz, CDCl₃) δ

1
2
3 170.6 (C), 155.9 (C), 155.3 (C), 145.7 (C), 125.4 (CH), 122.5 (CH), 80.6 (C), 59.1 (CH), 31.2 (CH),
4 28.4 (CH₃), 19.3 (CH₃), 17.9 (CH₃). LC-MS (ESI⁺) *m/z*: 339.3 (M + H)⁺ (40%), 360.8 (M + Na)⁺ (80%).
5
6
7

8 9 *4-Nitrophenyl (tert-butoxycarbonyl)-L-isoleucinate (2)*

10 The title compound was prepared via Method A from boc-L-isoleucine (200 mg, 0.86 mmol), 4-
11 nitrophenylchloroformate (209 mg, 1.04 mmol), DMAP (11 mg, 0.09 mmol) and Et₃N (145 μL,
12 1.04 mmol) in CH₂Cl₂ to give the crude product as a colourless oil. Purification by column
13 chromatography (SiO₂, Petroleum Spirits : EtOAc 9:1) yielded the product as a white solid (259
14 mg, 85%). ¹H NMR (401 MHz, CDCl₃) δ 8.31 – 8.25 (m, 2H), 7.33 – 7.27 (m, 2H), 5.03 (d, *J* = 7.8 Hz,
15 1H), 4.49 (dd, *J* = 8.3, 5.2 Hz, 1H), 2.11 – 1.97 (m, 1H), 1.65 – 1.52 (m, 1H), 1.47 (s, 9H), 1.38 – 1.23
16 (m, 1H), 1.07 (d, *J* = 6.8 Hz, 3H), 1.00 (t, *J* = 7.4 Hz, 3H). LC-MS (ESI⁺) *m/z*: 252.9 (M – Boc + H)⁺
17 (100%), 374.9 (M + Na)⁺ (60%).
18
19
20
21
22
23
24
25

26 27 *4-Nitrophenyl (tert-butoxycarbonyl)-L-leucinate (3)*

28 The title compound was prepared via Method A from boc-L-leucine (200 mg, 0.86 mmol), 4-
29 nitrophenylchloroformate (209 mg, 1.04 mmol), DMAP (11 mg, 0.09 mmol) and Et₃N (145 μL,
30 1.04 mmol) in CH₂Cl₂ to give the crude product as a yellow oil. Purification by column
31 chromatography (SiO₂, Petroleum Spirits : EtOAc 9:1) yielded the product as a white solid (192
32 mg, 63%). ¹H NMR (401 MHz, CDCl₃) δ 8.32 – 8.24 (m, 2H), 7.35 – 7.28 (m, 2H), 4.91 (d, *J* = 7.8 Hz,
33 1H), 4.59 – 4.44 (m, 1H), 1.89 – 1.73 (m, 2H), 1.73 – 1.62 (m, 1H), 1.46 (s, 9H), 1.03 (d, *J* = 2.1 Hz,
34 3H), 1.02 (d, *J* = 1.9 Hz, 3H). LC-MS (ESI⁺) *m/z*: 252.9 (M – Boc + H)⁺ (100%), 374.9 (M + Na)⁺ (55%).
35
36
37
38
39
40
41
42

43 44 *4-Nitrophenyl (S)-2-((tert-butoxycarbonyl)amino)hexanoate (4)*

45 The title compound was prepared via Method A from boc-L-norleucine (200 mg, 0.86 mmol), 4-
46 nitrophenylchloroformate (209 mg, 1.04 mmol), DMAP (11 mg, 0.09 mmol) and Et₃N (145 μL,
47 1.04 mmol) in CH₂Cl₂ to give the crude product as a light yellow solid. Purification by column
48 chromatography (SiO₂, Petroleum Spirits : EtOAc 9:1) yielded the product as a white solid (198
49 mg, 65%). HRMS (ESI⁺): Found: *m/z* 375.1534 (M + Na)⁺, C₁₇H₂₄N₂NaO₆⁺ requires *m/z* 375.1527.
50
51
52
53
54
55
56
57
58
59
60 ¹H NMR (401 MHz, CDCl₃) δ 8.32 – 8.25 (m, 2H), 7.33 – 7.27 (m, 2H), 4.99 (d, *J* = 7.3 Hz, 1H), 4.50

(dd, $J = 13.0, 7.4$ Hz, 1H), 2.02 – 1.91 (m, 1H), 1.86 – 1.74 (m, 1H), 1.51 – 1.35 (m, 13H), 0.95 (t, $J = 7.2$ Hz, 3H). LC-MS (ESI⁺) m/z : 252.9 (M – Boc + H)⁺ (100%), 374.9 (M + Na)⁺ (95%).

4-Nitrophenyl (tert-butoxycarbonyl)-L-phenylalaninate (5)

The title compound was prepared via Method A from boc-L-phenylalanine (200 mg, 0.75 mmol), 4-nitrophenylchloroformate (182 mg, 0.90 mmol), DMAP (9 mg, 0.08 mmol) and Et₃N (126 μ L, 0.90 mmol) in CH₂Cl₂ to give the crude product as a white solid. Purification by column chromatography (SiO₂, CH₂Cl₂) yielded the product as a white solid (251 mg, 86%). ¹H NMR (401 MHz, CDCl₃) δ 8.29 – 8.22 (m, 2H), 7.40 – 7.29 (m, 3H), 7.25 – 7.21 (m, 2H), 7.17 – 7.11 (m, 2H), 5.03 (d, $J = 7.0$ Hz, 1H), 4.80 (dd, $J = 13.6, 6.4$ Hz, 1H), 3.31 – 3.15 (m, 2H), 1.45 (s, 9H). LC-MS (ESI⁺) m/z : 286.9 (M – Boc + H)⁺ (60%), 408.8 (M + Na)⁺ (40%).

4-Nitrophenyl (tert-butoxycarbonyl)-L-tryptophanate (6)

The title compound was prepared via Method A from boc-L-tryptophan (200 mg, 0.66 mmol), 4-nitrophenylchloroformate (159 mg, 0.79 mmol), DMAP (8 mg, 0.07 mmol) and Et₃N (110 μ L, 0.79 mmol) in CH₂Cl₂ to give the crude product as a yellow solid. Purification by column chromatography (SiO₂, Petroleum Spirits : EtOAc 2:1) yielded the product as a white solid (200 mg, 72%). ¹H NMR (401 MHz, CDCl₃) δ 8.22 – 8.13 (m, 3H), 7.60 (d, $J = 7.9$ Hz, 1H), 7.41 (d, $J = 8.1$ Hz, 1H), 7.25 – 7.22 (m, 1H), 7.16 – 7.11 (m, 2H), 7.03 – 6.98 (m, 2H), 5.15 (d, $J = 7.6$ Hz, 1H), 4.91 – 4.80 (m, 1H), 3.50 – 3.35 (m, 2H), 1.45 (s, 9H). LC-MS (ESI⁺) m/z : 325.9 (M – Boc + H)⁺ (100%).

4-Nitrophenyl N^α-((benzyloxy)carbonyl)-N^ε-(tert-butoxycarbonyl)-L-lysinate (7)

Ice cold dry DMF (20 mL) was slowly added to 4-nitrophenylchloroformate (1.27 g, 6.31 mmol) and stirred for 10 min under a nitrogen atmosphere. The mixture was then gradually warmed to ambient temperature. A solution of N^α-benzyloxycarbonyl-N^ε-(tert-butoxycarbonyl)-L-lysine (2.00 g, 5.26 mmol) in DMF (5 mL) was added dropwise followed by triethylamine (879 μ L, 6.31 mmol). Stirring was continued for 20 h. The reaction mixture was diluted with EtOAc (50 mL) and washed with H₂O (4 x 20 mL) and brine (20 mL). The organic layer was dried (MgSO₄), filtered and

1
2
3 concentrated under reduced pressure to give the crude product as a yellow oil. Purification by
4 column chromatography (SiO₂, CH₂Cl₂ : EtOAc 95:5) yielded the product as a white solid (672 mg,
5 25%). ¹H NMR (401 MHz, CDCl₃) δ 8.27 (d, *J* = 8.9 Hz, 2H), 7.40 – 7.27 (m, 7H), 5.63 – 5.49 (m, 1H),
6 5.14 (s, 2H), 4.64 – 4.49 (m, 2H), 3.15 (s, 2H), 2.10 – 1.82 (m, 2H), 1.56 – 1.47 (m, 4H), 1.42 (s, 9H).
7 LC-MS (ESI⁺) *m/z*: 401.9 (M – Boc + H)⁺ (100%), 524.8 (M + Na)⁺ (20%).
8
9
10
11
12
13

14 *4-Nitrophenyl (tert-butoxycarbonyl)-L-phenylalanyl-L-valinate (8)*

15 Fmoc-Val-OH (679 mg, 2.0 mmol) was dissolved in a solution of DCM and triethylamine (842 μL,
16 6.0 mmol) and added to 2-chlorotrityl resin (1.0 g, 1 mmol) (1 meq/g). The mixture was shaken
17 at ambient temperature for 1h. The resin was washed with DCM (3 x 5 mL). A solution of MeOH
18 (1 mL) in DCM (5 mL) and triethylamine (0.5 mL) was added to the resin and shaken for 30 min
19 at ambient temperature. Fmoc deprotection was carried out by treatment with 20% piperidine
20 in DMF for 10 minutes and then washed with DMF (3 x 5 mL). Boc-Phe-OH (531 mg, 2.0 mmol)
21 and PyBOP (1.04g, 2.0 mmol) were dissolved in a solution of DCM and triethylamine (842 μL, 6.0
22 mmol) and added to the resin. The mixture was shaken at ambient temperature for 1h and then
23 drained, washed with DCM (3 x 5 mL) and dried under vacuum. The dipeptide was cleaved from
24 the resin by treatment with 20% HFIP in DCM containing 1% TIPS for 2h. The resin was filtered
25 and the filtrate reduced in vacuo to give the crude product (180 mg). To a solution of 4-
26 nitrophenylchloroformate (116 mg, 0.58 mmol) in dry THF (1 mL) was added dry DMF (150 μL) at
27 0°C. The reaction was stirred for 10 min under a nitrogen atmosphere before gradually being
28 warmed to ambient temperature. A solution of (tert-Butoxycarbonyl)-L-phenylalanyl-L-valine
29 (175 mg, 0.48 mmol) in THF (1 mL) and triethylamine (80 μL) was added dropwise to the above
30 suspension. Stirring was continued for 20 min. The reaction mixture was diluted with EtOAc and
31 washed with H₂O. The organic layer was dried (MgSO₄), filtered and concentrated under reduced
32 pressure to give the crude product (220 mg) as a pale yellow solid.
33
34
35
36
37
38
39
40
41
42
43
44
45
46
47
48
49

50 *tert-butyl (S)-(1-(dimethyl(oxo)-λ⁶-sulfanylidene)-4-methyl-2-oxopentan-3-yl)carbamate (9)*

51 The title compound was prepared via Method B from 4-nitrophenyl (tert-butoxycarbonyl)-L-
52 valinate (SJM-724-20) (100 mg, 0.30 mmol). The resulting crude product was purified by column
53
54
55
56
57
58
59
60

1
2
3 chromatography (SiO₂, EtOAc) and recrystallised from diethyl ether to yield the product as a
4 white solid (58 mg, 67%). HRMS (ESI⁺): Found: m/z 292.1573 (M + H)⁺, C₁₃H₂₆NO₄S⁺ requires m/z
5 292.1577. ¹H NMR (401 MHz, CDCl₃) δ 5.23 (d, J = 8.4 Hz, 1H), 4.50 (s, 1H), 3.94 (dd, J = 8.6, 5.4
6 Hz, 1H), 3.42 (s, 3H), 3.39 (s, 3H), 2.10 – 1.99 (m, 1H), 1.43 (s, 9H), 0.94 (d, J = 6.7 Hz, 3H), 0.87 (d,
7 J = 6.8 Hz, 3H). ¹³C NMR (101 MHz, CDCl₃) δ 187.89 (C), 155.94 (C), 79.11 (C), 70.07 (CH), 61.89
8 (CH), 42.25 (CH₃), 42.00 (CH₃), 31.90 (CH), 28.43 (CH₃), 19.60 (CH₃), 17.66 (CH₃). LC-MS (ESI⁺) m/z :
9 291.9 (M + H)⁺ (85%).
10
11
12
13
14
15
16
17

18 *tert-butyl ((3S,4S)-1-(dimethyl(oxo)-λ⁶-sulfanylidene)-4-methyl-2-oxohexan-3-yl)carbamate (10)*

19 The title compound was prepared via Method B from 4-nitrophenyl (tert-butoxycarbonyl)-L-
20 isoleucinate (SJM-724-64) (200 mg, 0.57 mmol). The resulting crude product was purified by
21 column chromatography (SiO₂, EtOAc : MeOH, 95:5) to yield the product as a cream solid (126
22 mg, 73%). HRMS (ESI⁺): Found: m/z 306.1735 (M + H)⁺, C₁₄H₂₈NO₄S⁺ requires m/z 306.1734. ¹H
23 NMR (401 MHz, CDCl₃) δ 5.21 (d, J = 8.9 Hz, 1H), 4.49 (s, 1H), 3.97 (dd, J = 8.7, 5.7 Hz, 1H), 3.41
24 (s, 3H), 3.38 (s, 3H), 1.83 – 1.73 (m, 1H), 1.53 – 1.46 (m, 1H), 1.43 (s, 9H), 1.18 – 1.04 (m, 1H), 0.91
25 (d, J = 6.7 Hz, 3H), 0.90 (t, J = 7.5 Hz, 3H). ¹³C NMR (101 MHz, CDCl₃) δ 187.8 (C), 155.8 (C), 79.1
26 (C), 70.0 (CH), 61.3 (CH), 42.4 (CH₃), 42.1 (CH₃), 38.5 (CH), 28.5 (CH₃), 24.9 (CH₂), 15.9 (CH₃), 11.9
27 (CH₃). LC-MS (ESI⁺) m/z : 305.9 (M + H)⁺ (100%).
28
29
30
31
32
33
34
35
36
37

38 *tert-butyl (S)-1-(1-(dimethyl(oxo)-λ⁶-sulfanylidene)-5-methyl-2-oxohexan-3-yl)carbamate (11)*

39 The title compound was prepared via Method B from 4-nitrophenyl (tert-butoxycarbonyl)-L-
40 leucinate (SJM-724-76) (170 mg, 0.48 mmol). The resulting crude product was purified by column
41 chromatography (SiO₂, EtOAc : MeOH, 95:5) to yield the product as a white solid (118 mg, 80%).
42 HRMS (ESI⁺): Found: m/z 306.1735 (M + H)⁺, C₁₄H₂₈NO₄S⁺ requires m/z 306.1734. ¹H NMR (401
43 MHz, CDCl₃) δ 5.04 (d, J = 8.3 Hz, 1H), 4.51 (s, 1H), 4.16 – 4.06 (m, 1H), 3.41 (s, 3H), 3.38 (s, 3H),
44 1.75 – 1.62 (m, 2H), 1.62 – 1.50 (m, 1H), 1.43 (s, 9H), 0.94 (d, J = 4.9 Hz, 3H), 0.93 (d, J = 4.9 Hz,
45 3H). ¹³C NMR (101 MHz, CDCl₃) δ 189.2 (C), 155.6 (C), 79.2 (C), 68.7 (CH), 55.6 (CH), 43.4 (CH₂),
46 42.4 (CH₃), 42.1 (CH₃), 28.5 (CH₃), 25.0 (CH), 23.2 (CH₃), 22.3 (CH₃). LC-MS (ESI⁺) m/z : 305.9 (M +
47 H)⁺ (80%).
48
49
50
51
52
53
54
55
56
57
58
59
60

tert-butyl (S)-(1-(dimethyl(oxo)- λ^6 -sulfanylidene)-2-oxoheptan-3-yl)carbamate (12)

The title compound was prepared via Method B from 4-nitrophenyl (S)-2-((tert-butoxycarbonyl)amino)hexanoate (SJM-724-116) (170 mg, 0.48 mmol). The resulting crude product was purified by column chromatography (SiO₂, EtOAc : MeOH, 95:5) to yield the product as a white solid (128 mg, 87%). HRMS (ESI⁺): Found: *m/z* 306.1738 (M + H)⁺, C₁₄H₂₈NO₄S⁺ requires *m/z* 306.1734. ¹H NMR (401 MHz, CDCl₃) δ 5.19 (d, *J* = 8.1 Hz, 1H), 4.49 (s, 1H), 4.00 (dd, *J* = 13.4, 7.5 Hz, 1H), 3.37 (s, 3H), 3.35 (s, 3H), 1.78 – 1.62 (m, 1H), 1.53 – 1.43 (m, 1H), 1.39 (s, 9H), 1.33 – 1.18 (m, 4H), 0.84 (t, *J* = 7.0 Hz, 3H). ¹³C NMR (101 MHz, CDCl₃) δ 188.6 (C), 155.6 (C), 79.1 (C), 68.9 (CH), 57.0 (CH), 42.3 (CH₃), 42.0 (CH₃), 33.8 (CH₂), 28.4 (CH₃), 27.7 (CH₂), 22.6 (CH₂), 14.0 (CH₃). LC-MS (ESI⁺) *m/z*: 306.0 (M + H)⁺ (100%).

tert-butyl (S)-(4-(dimethyl(oxo)- λ^6 -sulfanylidene)-3-oxo-1-phenylbutan-2-yl)carbamate (13)

The title compound was prepared via Method B from 4-nitrophenyl (tert-butoxycarbonyl)-L-phenylalaninate (SJM-724-68) (200 mg, 0.75 mmol). The resulting crude product was purified by column chromatography (SiO₂, CH₂Cl₂) to yield the product as a beige solid (141 mg, 80%). HRMS (ESI⁺): Found: *m/z* 340.1579 (M + H)⁺, C₁₇H₂₆NO₄S⁺ requires *m/z* 340.1577. ¹H NMR (401 MHz, CDCl₃) δ 7.29 – 7.17 (m, 5H), 5.22 (d, *J* = 8.1 Hz, 1H), 4.32 (dd, *J* = 14.5, 7.4 Hz, 1H), 4.26 (s, 1H), 3.35 (s, 3H), 3.25 (s, 1H), 3.05 – 2.93 (m, 2H), 1.41 (s, 9H). LC-MS (ESI⁺) *m/z*: 339.9 (M + H)⁺ (100%).

tert-butyl (S)-(4-(dimethyl(oxo)- λ^6 -sulfanylidene)-1-(1H-indol-3-yl)-3-oxobutan-2-yl)carbamate (14)

The title compound was prepared via Method B from 4-nitrophenyl (tert-butoxycarbonyl)-L-tryptophanate (SJM-724-112) (170 mg, 0.40 mmol). The resulting crude product was purified by column chromatography (SiO₂, EtOAc : MeOH, 95:5) to yield the product as a white solid (118 mg, 78%). HRMS (ESI⁺): Found: *m/z* 379.1697 (M + H)⁺, C₁₉H₂₇N₂O₄S⁺ requires *m/z* 379.1686. ¹H NMR (401 MHz, CDCl₃) δ 8.44 (s, 1H), 7.63 (d, *J* = 7.9 Hz, 1H), 7.32 (d, *J* = 8.1 Hz, 1H), 7.13 (t, *J* = 7.3 Hz, 1H), 7.08 – 6.98 (m, 2H), 5.40 (d, *J* = 7.8 Hz, 1H), 4.37 (dd, *J* = 13.3, 7.1 Hz, 1H), 4.25 (s, 1H), 3.19 (s, 3H), 3.26 – 3.09 (m, 2H), 2.99 (s, 3H), 1.43 (s, 9H). ¹³C NMR (101 MHz, CDCl₃) δ 187.5

(C), 155.5 (C), 136.1 (C), 128.2 (C), 123.0 (CH), 121.9 (CH), 119.3 (CH), 119.2 (CH), 111.7 (C), 111.3 (CH), 79.4 (C), 70.0 (CH), 57.8 (CH), 41.8 (CH₃), 41.6 (CH₃), 29.3 (CH₂), 28.54 (CH₃). LC-MS (ESI⁺) *m/z*: 378.9 (M + H)⁺ (100%).

benzyl tert-butyl (7-(dimethyl(oxo)-λ⁶-sulfanylidene)-6-oxoheptane-1,5-diyl)(S)-dicarbamate (15)

The title compound was prepared via Method B from 4-Nitrophenyl *N*^α-((benzyloxy)carbonyl)-*N*^ε-(*tert*-butoxycarbonyl)-L-lysinate (SJM-724-40) (200 mg, 0.40 mmol). The resulting crude product was purified by column chromatography (SiO₂, EtOAc : MeOH, 9:1) to yield the product as a white solid (138 mg, 76%). HRMS (ESI⁺): Found: *m/z* 455.2216 (M + H)⁺, C₂₂H₃₅N₂O₆S⁺ requires *m/z* 455.2210. ¹H NMR (401 MHz, CDCl₃) δ 7.33 – 7.23 (m, 5H), 5.79 (d, *J* = 7.9 Hz, 1H), 5.04 (s, 2H), 4.72 (bs, 1H), 4.52 (s, 1H), 4.07 (dd, *J* = 13.1, 7.6 Hz, 1H), 3.32 (s, 3H), 3.30 (s, 3H), 3.09 – 2.97 (m, 2H), 1.79 – 1.67 (m, 1H), 1.59 – 1.50 (m, 1H), 1.50 – 1.26 (m, 4H), 1.38 (s, 9H). ¹³C NMR (101 MHz, CDCl₃) δ 187.6 (C), 156.1 (C), 136.7 (C), 128.5 (CH), 128.1 (CH), 128.0 (CH), 78.9 (C), 69.5 (CH), 66.6 (CH₂), 57.1 (CH), 42.0 (CH₃), 41.8 (CH₃), 40.3 (CH₂), 33.4 (CH₂), 29.7 (CH₂), 28.4 (CH₃), 22.5 (CH₂). LC-MS (ESI⁺) *m/z*: 454.9 (M + H)⁺ (100%).

tert-butyl ((S)-1-(((S)-1-(dimethyl(oxo)-λ⁶-sulfaneylidene)-4-methyl-2-oxopentan-3-yl)amino)-1-oxo-3-phenylpropan-2-yl)carbamate (16)

The title compound was prepared via Method B from 4-Nitrophenyl (*tert*-butoxycarbonyl)-L-phenylalanyl-L-valinate (MS-4-182) (200 mg, 0.41 mmol). The resulting crude product was purified by column chromatography (SiO₂, CHCl₂: MeOH 98:2) to yield the title product (68 mg, 38%).

sCy5-Val-SY (17)

The title compound was prepared via Method E from *tert*-butyl (*S*)-(1-(dimethyl(oxo)-λ⁶-sulfanylidene)-4-methyl-2-oxopentan-3-yl)carbamate (SJM-724-24) (5 mg, 0.017 mmol). The resulting crude product was purified by RP-HPLC and lyophilized to yield the product as a blue solid (7.9 mg, 56%). HRMS (ESI⁺): Found: *m/z* 830.3159 (M + H)⁺, C₄₁H₅₆N₃O₉S₃⁺ requires *m/z* 830.3173. HPLC Gradient 0 → 60% B over 10 min, *t*_R = 13.35 min, >95% purity.

sCy5-Ile-SY (18)

The title compound was prepared via Method E from tert-butyl ((3*S*,4*S*)-1-(dimethyl(oxo)- λ^6 -sulfanylidene)-4-methyl-2-oxohexan-3-yl)carbamate (SJM-724-92) (10 mg, 0.033 mmol). The resulting crude product was purified by RP-HPLC and lyophilized to yield the product as a blue solid (3 mg, 11%). HRMS (ESI⁺): Found: m/z 844.3340 (M + H)⁺, C₄₂H₅₈N₃O₉S₃⁺ requires m/z 844.3330. HPLC Gradient 0 → 60% B over 10 min, t_R = 13.61 min, >95% purity.

sCy5-Leu-SY (19)

The title compound was prepared via Method E from tert-butyl (*S*)-(1-(dimethyl(oxo)- λ^6 -sulfanylidene)-5-methyl-2-oxohexan-3-yl)carbamate (SJM-724-96) (10 mg, 0.033 mmol). The resulting crude product was purified by RP-HPLC and lyophilized to yield the product as a blue solid (14.7 mg, 53%). HRMS (ESI⁺): Found: m/z 844.3328 (M + H)⁺, C₄₂H₅₈N₃O₉S₃⁺ requires m/z 844.3330. HPLC Gradient 0 → 80% B over 15 min, t_R = 14.29 min, >95% purity.

sCy5-Nle-SY (20)

The title compound was prepared via Method E from tert-butyl (*S*)-(1-(dimethyl(oxo)- λ^6 -sulfanylidene)-2-oxoheptan-3-yl)carbamate (SJM-724-124) (10 mg, 0.033 mmol). The resulting crude product was purified by RP-HPLC and lyophilized to yield the product as a blue solid (17.4 mg, 63%). HRMS (ESI⁺): Found: m/z 844.3335 (M + H)⁺, C₄₂H₅₈N₃O₉S₃⁺ requires m/z 844.3330. HPLC Gradient 0 → 80% B over 15 min, t_R = 14.35 min, >95% purity.

sCy5-Phe-SY (21)

The title compound was prepared via Method E from tert-butyl (*S*)-(4-(dimethyl(oxo)- λ^6 -sulfanylidene)-3-oxo-1-phenylbutan-2-yl)carbamate (SJM-724-72) (10 mg, 0.029 mmol). The resulting crude product was purified by RP-HPLC and lyophilized to yield the product as a blue solid (13.1 mg, 51%). HRMS (ESI⁺): Found: m/z 878.3157 (M + H)⁺, C₄₅H₅₆N₃O₉S₃⁺ requires m/z 878.3173. HPLC Gradient 0 → 100% B over 15 min, t_R = 13.57 min, >95% purity.

sCy5-Trp-SY (22)

The title compound was prepared via Method E from tert-butyl (S)-(4-(dimethyl(oxo)-λ⁶-sulfanylidene)-1-(1H-indol-3-yl)-3-oxobutan-2-yl)carbamate (SJM-724-120) (10 mg, 0.026 mmol). The resulting crude product was purified by RP-HPLC and lyophilized to yield the product as a blue solid (6 mg, 25%). HRMS (ESI⁺): Found: *m/z* 917.3277 (M + H)⁺, C₄₇H₅₇N₄O₉S₃⁺ requires *m/z* 917.3282. HPLC Gradient 0 → 80% B over 15 min, *t*_R = 14.49 min, >95% purity.

Cbz-Lys(sCy5)-SY (23)

The title compound was prepared via Method E from benzyl tert-butyl (7-(dimethyl(oxo)-λ⁶-sulfanylidene)-6-oxoheptane-1,5-diyl)(S)-dicarbamate (SJM-724-48) (10 mg, 0.022 mmol). The resulting crude product was purified by RP-HPLC and lyophilized to yield the product as a blue solid (10 mg, 46%). HRMS (ESI⁺): Found: *m/z* 993.3785 (M + H)⁺, C₅₀H₆₅N₄O₁₁S₃⁺ requires *m/z* 993.3806. HPLC Gradient 0 → 100% B over 15 min, *t*_R = 13.93 min, >95% purity.

sCy5-Phe-Val-SY (24)

The title compound was prepared via Method E from tert-butyl ((S)-1-(((S)-1-(dimethyl(oxo)-λ⁶-sulfaneylidene)-4-methyl-2-oxopentan-3-yl)amino)-1-oxo-3-phenylpropan-2-yl)carbamate (MS-4-186) (10 mg, 0.022 mmol). The resulting crude product was purified by RP-HPLC and lyophilized to yield the product as a blue solid (4.6 mg, 21%). HRMS (ESI⁺): Found: *m/z* 977.3855 (M + H)⁺, C₅₀H₆₄N₄O₁₀S₃ requires *m/z* 977.3857. HPLC Gradient 0 → 60% B over 10 min, *t*_R = 5.22 min, >95% purity.

tert-butyl (S)-(1-chloro-2-oxoheptan-3-yl)carbamate (25)

The title compound was prepared via Method C from tert-butyl (S)-(1-(dimethyl(oxo)-λ⁶-sulfanylidene)-2-oxoheptan-3-yl)carbamate (SJM-724-124) (40 mg, 0.13 mmol). The resulting crude product was purified by column chromatography (SiO₂, Petroleum Spirits : EtOAc, 9:1) to yield the product as a white solid (20 mg, 58%). ¹H NMR (401 MHz, CDCl₃) δ 5.02 (d, *J* = 6.4 Hz, 1H), 4.47 (dd, *J* = 12.6, 7.7 Hz, 1H), 4.26 (d, *J* = 4.8 Hz, 2H), 1.92 – 1.75 (m, 1H), 1.60 – 1.47 (m, 1H), 1.43 (s, 9H), 1.39 – 1.25 (m, 4H), 0.90 (t, *J* = 7.1 Hz, 3H). ¹³C NMR (101 MHz, CDCl₃) δ 202.0

(C), 155.6 (C), 80.4 (C), 57.5 (CH), 46.8 (CH₂), 31.3 (CH₂), 28.4 (CH₃), 27.6 (CH₂), 22.5 (CH₂), 13.9 (CH₃). LC-MS (ESI⁺) *m/z*: 164.1.0 (M – Boc + H)⁺ (100%).

tert-butyl (S)-(4-chloro-3-oxo-1-phenylbutan-2-yl)carbamate (26)

The title compound was prepared via Method C from *tert-butyl (S)-(4-(dimethyl(oxo)-λ⁶-sulfanylidene)-3-oxo-1-phenylbutan-2-yl)carbamate* (SJM-724-72) (50 mg, 0.15 mmol). The resulting crude product was purified by column chromatography (SiO₂, Petroleum Spirits : EtOAc, 9:1) to yield the product as a white solid (30 mg, 68%). HRMS (ESI⁺): Found: *m/z* 320.1018 (M + Na)⁺, C₁₅H₂₀ClNNaO₃⁺ requires *m/z* 320.1024. ¹H NMR (401 MHz, CDCl₃) δ 7.35 – 7.23 (m, 3H), 7.19 – 7.13 (m, 2H), 5.06 (d, *J* = 5.7 Hz, 1H), 4.66 (dd, *J* = 13.0, 6.0 Hz, 1H), 4.17 (d, *J* = 16.2 Hz, 1H), 3.98 (d, *J* = 16.2 Hz, 1H), 3.08 (dd, *J* = 13.8, 6.7 Hz, 1H), 2.99 (dd, *J* = 13.4, 7.1 Hz, 1H), 1.40 (s, 9H). ¹³C NMR (101 MHz, CDCl₃) δ 201.5 (C), 155.3 (C), 135.7 (C), 129.3 (CH), 129.1 (CH), 127.5 (CH), 80.6 (C), 58.6 (CH), 47.6 (CH₂), 37.8 (CH₂), 28.4 (CH₃). LC-MS (ESI⁺) *m/z*: 198.0 (M – Boc + H)⁺ (100%).

benzyl tert-butyl (7-chloro-6-oxoheptane-1,5-diyl)(S)-dicarbamate (27)

The title compound was prepared via Method C from *benzyl tert-butyl (7-(dimethyl(oxo)-λ⁶-sulfanylidene)-6-oxoheptane-1,5-diyl)(S)-dicarbamate* (SJM-724-48) (130 mg, 0.29 mmol). The resulting crude product was purified by column chromatography (SiO₂, Petroleum Spirits : EtOAc, 3:1) to yield the product as a white solid (60 mg, 51%). HRMS (ESI⁺): Found: *m/z* 435.1664 (M + Na)⁺, C₂₀H₂₉ClN₂NaO₅⁺ requires *m/z* 435.1657. ¹H NMR (401 MHz, CDCl₃) δ 7.38 – 7.27 (m, 5H), 5.68 (d, *J* = 5.7 Hz, 1H), 5.09 (s, 2H), 4.62 (s, 1H), 4.59 – 4.47 (m, 1H), 4.26 (d, *J* = 2.1 Hz, 2H), 3.16 – 3.00 (m, 2H), 1.92 – 1.81 (m, 1H), 1.70 – 1.57 (m, 1H), 1.54 – 1.27 (m, 4H), 1.40 (s, 9H). ¹³C NMR (101 MHz, CDCl₃) δ 201.6 (C), 156.4 (C), 136.1 (C), 128.7 (CH), 128.4 (CH), 128.3 (CH), 79.4 (C), 67.3 (CH₂), 57.9 (CH), 46.6 (CH₂), 39.6 (CH₂), 30.8 (CH₂), 29.8 (CH₂), 28.5 (CH₃), 22.2 (CH₂). LC-MS (ESI⁺) *m/z*: 434.9.0 (M + Na)⁺ (100%).

(S)-3-((tert-butoxycarbonyl)amino)-2-oxoheptyl 2,6-dimethylbenzoate (28)

The title compound was prepared via Method D from *tert-butyl (S)-(1-chloro-2-oxoheptan-3-yl)carbamate* (SJM-724-148) (20 mg, 76 μmol). The resulting crude product was purified by

column chromatography (SiO₂, Petroleum Spirits : EtOAc, 95:5) to yield the product as a white solid (18 mg, 63%). HRMS (ESI⁺): Found: m/z 400.2097 (M + Na)⁺, C₂₁H₃₁NNaO₅⁺ requires m/z 400.2094. ¹H NMR (401 MHz, CDCl₃) δ 7.23 – 7.17 (m, 1H), 7.04 (d, J = 7.8 Hz, 2H), 5.15 – 4.96 (m, 3H), 4.40 (dd, J = 12.5, 7.7 Hz, 1H), 2.39 (s, 6H), 1.97 – 1.86 (m, 1H), 1.67 – 1.54 (m, 1H), 1.45 (s, 9H), 1.41 – 1.30 (m, 4H), 0.94 – 0.88 (m, 3H). ¹³C NMR (101 MHz, CDCl₃) δ 202.8 (C), 169.1 (C), 155.7 (C), 135.8 (C), 132.7 (C), 129.8 (CH), 127.8 (CH), 80.4 (C), 66.9 (CH₂), 57.0 (CH), 31.4 (CH₂), 28.4 (CH₃), 27.4 (CH₂), 22.5 (CH₂), 20.0 (CH₃), 14.0 (CH₃). LC-MS (ESI⁺) m/z : 399.9 (M + Na)⁺ (100%). HPLC Gradient 0 → 60% B over 10 min, t_R = 13.35 min, >95% purity.

(S)-3-((*tert*-butoxycarbonyl)amino)-2-oxo-4-phenylbutyl 2,6-dimethylbenzoate (**29**)

The title compound was prepared via Method D from *tert*-butyl (*S*)-(4-chloro-3-oxo-1-phenylbutan-2-yl)carbamate (SJM-724-152) (25 mg, 84 μmol). The resulting crude product was purified by column chromatography (SiO₂, Petroleum Spirits : EtOAc, 95:5) to yield the product as a white solid (27 mg, 78%). HRMS (ESI⁺): Found: m/z 434.1944 (M + Na)⁺, C₂₄H₂₉NNaO₅⁺ requires m/z 434.1938. ¹H NMR (401 MHz, CDCl₃) δ 7.35 – 7.18 (m, 6H), 7.05 (d, J = 7.6 Hz, 2H), 5.06 (d, J = 7.3 Hz, 1H), 4.94 (dd, J = 43.1, 17.0 Hz, 2H), 4.62 (dd, J = 14.0, 7.0 Hz, 1H), 3.18 (dd, J = 14.0, 6.4 Hz, 1H), 3.04 (dd, J = 14.0, 7.2 Hz, 1H), 2.39 (s, 6H), 1.42 (s, 9H). ¹³C NMR (101 MHz, CDCl₃) δ 202.2 (C), 169.1 (C), 155.4 (C), 135.9 (C), 135.8 (C), 132.7 (C), 129.8 (CH), 129.5 (CH), 128.9 (CH), 127.8 (CH), 127.3 (CH), 80.5 (C), 67.3 (CH₂), 58.1 (CH), 37.5 (CH₂), 28.4 (CH₃), 20.0 (CH₃). LC-MS (ESI⁺) m/z : 433.8 (M + Na)⁺ (100%).

(S)-3-(((benzyloxy)carbonyl)amino)-7-((*tert*-butoxycarbonyl)amino)-2-oxoheptyl 2,6-dimethylbenzoate (**30**)

The title compound was prepared via Method D from benzyl *tert*-butyl (7-chloro-6-oxoheptane-1,5-diyl)(*S*)-dicarbamate (SJM-724-52) (50 mg, 121 μmol). The resulting crude product was purified by column chromatography (SiO₂, Petroleum Spirits : EtOAc, 3:1) to yield the product as a white solid (57 mg, 89%). HRMS (ESI⁺): Found: m/z 549.2571 (M + Na)⁺, C₂₉H₃₈N₂NaO₇⁺ requires m/z 549.2571. ¹H NMR (401 MHz, CDCl₃) δ 7.38 – 7.29 (m, 5H), 7.23 – 7.17 (m, 1H), 7.04 (d, J = 7.5 Hz, 2H), 5.66 (d, J = 5.9 Hz, 1H), 5.11 (s, 2H), 5.12 – 4.95 (m, 2H), 4.65 (s, 1H), 4.52 – 4.41 (m,

1
2
3 1H), 3.18 – 3.00 (m, 2H), 2.39 (s, 6H), 2.04 – 1.89 (m, 1H), 1.78 – 1.64 (m, 1H), 1.58 – 1.35 (m, 4H),
4
5 1.41 (s, 9H). ¹³C NMR (101 MHz, CDCl₃) δ 202.3 (C), 169.1 (C), 156.4 (C), 136.2 (C), 135.8 (C), 132.5
6
7 (C), 129.9 (CH), 128.7 (CH), 128.4 (CH), 128.3 (CH), 127.8 (CH), 79.3 (C), 67.3 (CH₂), 66.8 (CH₂),
8
9 57.5 (CH), 39.7 (CH₂), 30.9 (CH₂), 29.8 (CH₂), 28.5 (CH₃), 22.0 (CH₂), 20.0 (CH₃). LC-MS (ESI⁺) *m/z*:
10
11 426.9 (M –Boc + H)⁺ (100%).
12
13

14 *sCy5-Nle-AOMK (31)*

15
16 The title compound was prepared via Method E from (*S*)-3-((tert-butoxycarbonyl)amino)-2-
17
18 oxoheptyl 2,6-dimethylbenzoate (SJM-724-156) (8 mg, 21 μmol). The resulting crude product was
19
20 purified by RP-HPLC and lyophilized to yield the product as a blue solid (13.9 mg, 72%). HRMS
21
22 (ESI⁺): Found: *m/z* 916.3869 (M + H)⁺, C₄₉H₆₂N₃O₁₀S₂⁺ requires *m/z* 916.3871. HPLC Gradient 0 →
23
24 80% B over 15 min, *t_R* = 17.37 min, >95% purity.
25
26

27 *sCy5-Phe-AOMK (32)*

28
29 The title compound was prepared via Method E from (*S*)-3-((tert-butoxycarbonyl)amino)-2-oxo-
30
31 4-phenylbutyl 2,6-dimethylbenzoate (SJM-724-172) (5 mg, 12 μmol). The resulting crude product
32
33 was purified by RP-HPLC and lyophilized to yield the product as a blue solid (6.5 mg, 56%). HRMS
34
35 (ESI⁺): Found: *m/z* 950.3718 (M + H)⁺, C₅₂H₆₀N₃O₁₀S₂⁺ requires *m/z* 950.3715. HPLC Gradient 0 →
36
37 80% B over 15 min, *t_R* = 17.36 min, >95% purity.
38
39

40 *Cbz-Lys(sCy5)-AOMK (33)*

41
42 The title compound was prepared via Method E from (*S*)-3-(((benzyloxy)carbonyl)amino)-7-((tert-
43
44 butoxycarbonyl)amino)-2-oxoheptyl 2,6-dimethylbenzoate (SJM-724-176) (5 mg, 9 μmol). The
45
46 resulting crude product was purified by RP-HPLC and lyophilized to yield the product as a blue
47
48 solid (6.5 mg, 64%). HRMS (ESI⁺): Found: *m/z* 1065.4351 (M + H)⁺, C₅₇H₆₉N₄O₁₂S₂⁺ requires *m/z*
49
50 1065.4348. HPLC Gradient 0 → 80% B over 15 min, *t_R* = 17.48 min, >95% purity.
51
52

53 *Key Resources*

1
2
3 A table summarizing the source of all key reagents (antibodies, chemicals, biochemical assays,
4 cell lines and mouse strains) can be found within the supplemental information.
5
6
7
8
9

10 *Cell Culture*

11 RAW264.7 or MDA-MB-231^{HM} cells were cultured in DMEM containing 10% fetal bovine serum
12 and 1% antibiotic/antimycotic. RAW264.7 cells were passaged by scraping with a rubber
13 policeman, while MDA-MB-231^{HM} cells were lifted with 0.02% EDTA in phosphate-buffered saline
14 (PBS).
15
16
17
18
19

20 *Animals*

21 All experiments involving animals were approved by the Monash University Animal Ethics
22 Committee. Male C57BL/6J mice were obtained from the Monash Animal Research Platform
23 and used in accordance with the guidelines at 8-10 weeks of age. Snap-frozen spleens from
24 wildtype and cathepsin X knockout mice, as described in,³⁵ were obtained from the University
25 of Calgary and used in accordance with the University of Calgary Animal Care and Use
26 Committee.
27
28
29
30
31
32
33
34
35

36 *Cell lysate labeling and SDS-PAGE analysis.*

37 Cells were harvested by scraping, washed once with PBS, and resuspended in lysis buffer
38 containing 50 mM citrate [pH 5.5], 0.5% CHAPS, 0.1% Triton X-100, and 4 mM DTT. Cells were
39 incubated on ice for at least 10 minutes with intermittent vortexing followed by centrifugation
40 (21g at 4°C for 5 minutes). Cleared supernatants were then transferred to a fresh tube and
41 protein concentration was determined by BCA. Total protein (50 µg) was aliquoted into tubes in
42 a final volume of 20 µl lysis buffer. Where indicated, JPM-OEt or MD-590 were added from a 100x
43 DMSO stock and incubated at 37°C for 20 minutes prior to probe addition. The indicated
44 concentration of probe was added from a 100x DMSO stock. Labeling was carried out at 37°C for
45 20 minutes, and the reactions were quenched by the addition of 5x sample buffer (200 mM Tris-Cl
46 [pH 6.8], 8% SDS, 0.04% bromophenol blue, 5% β-mercaptoethanol, and 40% glycerol). Samples
47
48
49
50
51
52
53
54
55
56
57
58
59
60

1
2
3 were then boiled for five minutes and proteins were resolved on a 15% SDS-PAGE gel. The gels
4 were scanned on a Typhoon 5 flatbed laser scanner at 633/670 nm excitation/emission to detect
5 sCy5 fluorescence.
6
7
8
9

10 *Live cell labeling*

11 RAW cells or MDA-MB-231^{HM} cells were plated in 12-well plates. Where indicated, MDV-590 a
12 closely related analogue to the cathepsin S-specific inhibitor MIV-247 (Hewitt et al., 2016), Z-FL-
13 COCHO³⁶ or DMSO (vehicle) was added at 10 μ M or 20 μ M, respectively, from a 1000x DMSO
14 stock for overnight incubation. When the cell density reached 80%, the indicated probes were
15 added at the indicated concentrations from a 1000x DMSO stock and allowed to incubate for the
16 indicated time. Media was then removed and replaced with PBS. The cells were then scraped and
17 transferred to tubes, and lysis and SDS-PAGE analysis were carried out as above, except skipping
18 the probe addition step.
19
20
21
22
23
24
25
26
27
28

29 *Tissue analysis*

30 Tissues or biopsies were harvested from healthy mice or patients, respectively, and snap frozen.
31 At the time of analysis, lysis buffer was added at 10x volume:weight, and tissues were sonicated
32 on ice. Cleared lysates were labeled with the indicated probe and analyzed as above. For *in vivo*
33 labeled tissues, mice were first injected intravenously via the tail vein with sCy5-Nle-SY, BMV109
34 or sCy5-Nle-AOMK (50 nmol in 100 μ l 10% DMSO/PBS or vehicle control). Tissues were harvested
35 after two hours and analyzed as above except without further probe addition.
36
37
38
39
40
41
42
43

44 *Immunoblotting*

45 After detection of in-gel fluorescence, human cancer samples were transferred to a nitrocellulose
46 membrane using the TransBlot system (Biorad). Loading and transfer efficiency were assessed by
47 Ponceau Stain (Sigma). The membrane was then incubated overnight at 4°C with a goat anti-
48 cathepsin X antibody (1:1000) in Odyssey Blocking Buffer (LiCor) diluted by 50% in PBS containing
49 0.05% Tween-20 (PBS-T). After washing the membrane three times with PBS-T, it was incubated
50
51
52
53
54
55
56
57
58
59
60

1
2
3 with donkey anti-goat-IRDYE800 (1:10,000) at RT for one hour. After washing, binding was
4 detected by scanning the membrane on a Typhoon 5 (IR-long filter).
5
6
7

8 9 *Immunoprecipitation assay*

10 Probe-labeled lysate from above (in sample buffer) was divided into input or pulldown (~50 µg
11 total protein each). The input sample was stored at -20°C. The pulldown sample was diluted in
12 500 µl IP buffer (PBS [pH 7.4], 0.5% NP-40, 1 mM EDTA). Goat anti-cathepsin X antibody (10 µl)
13 was added along with 40 µl slurry of pre-washed Protein A/G agarose beads. Samples were
14 rotated overnight at 4°C. Beads were then washed four times with IP buffer followed by a final
15 wash in 0.9% NaCl. Beads were then resuspended in 2x sample buffer and boiled. The pulldown
16 supernatants, alongside the input samples, were analyzed by fluorescent SDS-PAGE as above.
17
18
19
20
21
22
23

24 25 *Confocal microscopy*

26 Kidney tissues from mice that received sCy5-Nle-SY (or vehicle control) above were fixed
27 overnight in 4% paraformaldehyde in PBS followed by overnight cryoprotection in 30% sucrose.
28 Tissues were embedded in OCT, frozen on dry ice, and sectioned at 10µm. Immunostaining for
29 cathepsin X was carried out according to standard protocols. In brief, sections were air dried,
30 fixed in cold acetone for 10 minutes, air dried again, and then rehydrated in PBS. Sections were
31 blocked in PBS containing 3% normal horse serum with 0.1% Triton X-100. Goat anti-cathepsin X
32 was added at 1:100 in blocking buffer overnight at 4°C. Sections were then washed, and
33 secondary antibody, donkey anti-goat-AlexaFluor594 was added at 1:500 for 1 hour at room
34 temperature. Sections were stained with DAPI for 5 minutes, washed, and mounted with ProLong
35 Diamond. Staining was analyzed using a Leica SP8 inverted confocal microscope.
36
37
38
39
40
41
42
43
44
45
46

47 48 *Statistical Analysis*

49 All experiments were performed with at least three biological replicates. Data are reported as
50 means ± SEM. Statistical significance was determined by comparing two groups using a Student's
51 t test, and p values of less than 0.05 were considered significant.
52
53
54
55
56
57
58
59
60

Acknowledgements

We thank Cameron Nowell for maintaining the imaging facilities at the Monash Institute of Pharmaceutical Sciences. MDA-MB-231^{HM} cells were a kind gift from Dr. Zhou Ou, Fudan University, Shanghai Cancer Center. LEM was supported by an Early Career Fellowship from the National Health and Medical Research Council of Australia (NHMRC, GNT1091636), a Grimwade Fellowship funded by the Russell and Mab Grimwade Miegunyah Fund at the University of Melbourne, a DECRA Fellowship from the Australian Research Council (ARC, DE180100418) and by seed grants from Monash University. NWB was supported by grants from the National Institutes of Health (NS102722, DE026806, DK118971) and the United States Department of Defense (W81XWH1810431).

Declarations of Interest

NWB is a founding scientist of Endosome Therapeutics Inc. Research in NWB's laboratory is supported in part by Takeda Pharmaceuticals, Inc.

Author Contributions

LEM conceived study, planned all experiments, analyzed data, wrote manuscript, and contributed funding. SJM, MLH, MS, and LA synthesized the compounds included in the study. SJM completed the compound characterization and contributed to the writing of the manuscript. BMA, MLH, and JD executed the experiments and collected data. RIC and RMY contributed cathepsin X knockout tissues for the study. EKS provided MDA-MB-231^{HM} cells. EL provided cathepsin S inhibitor. PT contributed intellectually and supervised the compound synthesis. NB contributed funds for the work.

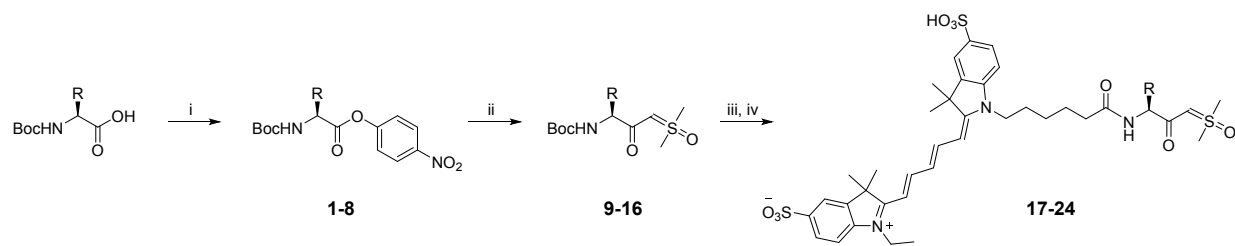
References

- (1) Obermajer, N.; Švajger, U.; Bogyo, M.; Jeras, M.; Kos, J. Maturation of Dendritic Cells Depends on Proteolytic Cleavage by Cathepsin X. *J Leukocyte Biol* **2008**, *84* (5), 1306–1315.
- (2) Pečar Fonović, U.; Kos, J. Cathepsin X Cleaves Profilin 1 C-Terminal Tyr139 and Influences Clathrin-Mediated Endocytosis. *PLoS ONE* **2015**, *10* (9), e0137217–13.

- 1
2
3 (3) Nögler, D. K.; Kraus, S.; Feierler, J.; Mentele, R.; Lottspeich, F.; Jochum, M.; Faussner, A.
4 A Cysteine-Type Carboxypeptidase, Cathepsin X, Generates Peptide Receptor Agonists.
5 *Int Immunopharmacol* **2010**, *10* (1), 134–139.
6
7 (4) Obermajer, N.; Doljak, B.; Jamnik, P.; Fonović, U. P.; Kos, J. Cathepsin X Cleaves the C-
8 Terminal Dipeptide of Alpha- and Gamma-Enolase and Impairs Survival and
9 Neuritogenesis of Neuronal Cells. *Int J Biochem Cell Biol* **2009**, *41* (8-9), 1685–1696.
10
11 (5) Wendt, W.; Zhu, X.-R.; Lübbert, H.; Stichel, C. C. Differential Expression of Cathepsin X
12 in Aging and Pathological Central Nervous System of Mice. *Exp Neurol* **2007**, *204* (2),
13 525–540.
14
15 (6) Hafner, A.; Glavan, G.; Obermajer, N.; Živin, M.; Schliebs, R.; Kos, J. Neuroprotective
16 Role of Γ -Enolase in Microglia in a Mouse Model of Alzheimer's Disease Is Regulated by
17 Cathepsin X. *Aging Cell* **2013**, *12* (4), 604–614.
18
19 (7) Leichsenring, A.; Bäcker, I.; Wendt, W.; Andriske, M.; Schmitz, B.; Stichel, C. C.; Lübbert,
20 H. Differential Expression of Cathepsin S and X in the Spinal Cord of a Rat Neuropathic
21 Pain Model. *BMC Neurosci* **2008**, *9* (1), 80–13.
22
23 (8) Huynh, J. L.; Garg, P.; Thin, T. H.; Yoo, S.; Dutta, R.; Trapp, B. D.; Haroutunian, V.; Zhu, J.;
24 Donovan, M. J.; Sharp, A. J.; Casaccia, P. Epigenome-Wide Differences in Pathology-Free
25 Regions of Multiple Sclerosis–Affected Brains. *Nat Neurosci* **2013**, *17* (1), 121–130.
26
27 (9) Allan, E. R. O.; Campden, R. I.; Ewanchuk, B. W.; Tailor, P.; Balce, D. R.; McKenna, N. T.;
28 Greene, C. J.; Warren, A. L.; Reinheckel, T.; Yates, R. M. A Role for Cathepsin Z in
29 Neuroinflammation Provides Mechanistic Support for an Epigenetic Risk Factor in
30 Multiple Sclerosis. *J Neuroinflammation* **2017**, *14* (103), 1–11.
31
32 (10) Orłowski, G. M.; Colbert, J. D.; Sharma, S.; Bogyo, M.; Robertson, S. A.; Rock, K. L.
33 Multiple Cathepsins Promote Pro-IL-1 β Synthesis and NLRP3-Mediated IL-1 β
34 Activation. *Journal Immunol* **2015**, *195* (4), 1685–1697.
35
36 (11) Edgington-Mitchell, L. E.; Rautela, J.; Duivenvoorden, H. M.; Jayatilleke, K. M.; van der
37 Linden, W. A.; Verdoes, M.; Bogyo, M.; Parker, B. S. Cysteine Cathepsin Activity
38 Suppresses Osteoclastogenesis of Myeloid-Derived Suppressor Cells in Breast Cancer.
39 *Oncotarget* **2015**, *6* (29), 27008–27022.
40
41 (12) Akkari, L.; Gocheva, V.; Kester, J. C.; Hunter, K. E.; Quick, M. L.; Sevenich, L.; Wang, H.-
42 W.; Peters, C.; Tang, L. H.; Klimstra, D. S.; Reinheckel, T.; Joyce, J. A. Distinct Functions
43 of Macrophage-Derived and Cancer Cell-Derived Cathepsin Z Combine to Promote
44 Tumor Malignancy via Interactions with the Extracellular Matrix. *Genes Dev* **2014**, *28*
45 (19), 2134–2150.
46
47 (13) Nögler, D. K.; Krüger, S.; Kellner, A.; Ziomek, E.; Ménard, R.; Buhtz, P.; Krams, M.;
48 Roessner, A.; Kellner, U. Up-Regulation of Cathepsin X in Prostate Cancer and Prostatic
49 Intraepithelial Neoplasia. *Prostate* **2004**, *60* (2), 109–119.
50
51 (14) Bernhardt, A.; Kuester, D.; Roessner, A.; Reinheckel, T.; Krueger, S. Cathepsin X-
52 Deficient Gastric Epithelial Cells in Co-Culture with Macrophages: Characterization of
53 cytokine response and migration capability after *Helicobacter pylori* infection. *J Biol*
54 *Chem* **2010**, *285* (44), 33691–33700.
55
56 (15) Krueger, S.; Kalinski, T.; Hundertmark, T.; Wex, T.; Küster, D.; Peitz, U.; Ebert, M.;
57 Nögler, D. K.; Kellner, U.; Malfertheiner, P.; Naumann, M.; Röcken, C.; Roessner, A. Up-

- 1
2
3 Regulation of Cathepsin X in Helicobacter Pylori Gastritis and Gastric Cancer. *J Pathol*
4 **2005**, *207* (1), 32–42.
- 5
6 (16) Nägler, D. K.; Zhang, R.; Tam, W.; Sulea, T.; Purisima, E. O.; Ménard, R. Human
7 Cathepsin X: a Cysteine Protease with Unique Carboxypeptidase Activity. *Biochem*
8 **1999**, *38* (39), 12648–12654.
- 9
10 (17) Duivenvoorden, H. M.; Rautela, J.; Edgington-Mitchell, L. E.; Spurling, A.; Greening, D.
11 W.; Nowell, C. J.; Molloy, T. J.; Robbins, E.; Brockwell, N. K.; Lee, C. S.; Chen, M.;
12 Holliday, A.; Selinger, C. I.; Hu, M.; Britt, K. L.; Stroud, D. A.; Bogyo, M.; Möller, A.;
13 Polyak, K.; Sloane, B. F.; O'Toole, S. A.; Parker, B. S. Myoepithelial Cell-Specific
14 Expression of Stefin a as a Suppressor of Early Breast Cancer Invasion. *J Pathol* **2017**,
15 *243* (4), 496–509.
- 16
17 (18) Edgington, L. E.; Verdoes, M.; Bogyo, M. Functional Imaging of Proteases: Recent
18 Advances in the Design and Application of Substrate-Based and Activity-Based Probes.
19 *Curr Op Chem Biol* **2011**, *15* (6), 798–805.
- 20
21 (19) Edgington, L. E.; Bogyo, M. In Vivo Imaging and Biochemical Characterization of
22 Protease Function Using Fluorescent Activity-Based Probes. *Curr Protoc Chem Biol*
23 **2013**, *5* (1), 25–44.
- 24
25 (20) Sanman, L. E.; Bogyo, M. Activity-Based Profiling of Proteases. *Annu Rev Biochem* **2014**,
26 *83* (1), 249–273.
- 27
28 (21) Verdoes, M.; Oresic Bender, K.; Segal, E.; van der Linden, W. A.; Syed, S.; Withana, N. P.;
29 Sanman, L. E.; Bogyo, M. Improved Quenched Fluorescent Probe for Imaging of
30 Cysteine Cathepsin Activity. *J Am Chem Soc* **2013**, *135* (39), 14726–14730.
- 31
32 (22) Paulick, M. G.; Bogyo, M. Development of Activity-Based Probes for Cathepsin X. *ACS*
33 *Chem Biol* **2011**, *6* (6), 563–572.
- 34
35 (23) Shaw, E. Peptidyl Sulfonium Salts. a New Class of Protease Inhibitors. *J Biol Chem* **1988**,
36 *263* (6), 2768–2772.
- 37
38 (24) Hewitt, E.; Pitcher, T.; Rizoška, B.; Tunblad, K.; Henderson, I.; Sahlberg, B. L.;
39 Grabowska, U.; Classon, B.; Edenius, C.; Malcangio, M.; Lindstrom, E. Selective
40 Cathepsin S Inhibition with MIV-247 Attenuates Mechanical Allodynia and Enhances the
41 Antiallodynic Effects of Gabapentin and Pregabalin in a Mouse Model of Neuropathic
42 Pain. *J Pharmacol Exp Ther* **2016**, *358* (3), 387–396.
- 43
44 (25) Turk, V.; Stoka, V.; Vasiljeva, O.; Renko, M.; Sun, T.; Turk, B.; Turk, D. Cysteine
45 Cathepsins: From Structure, Function and Regulation to New Frontiers. *BBA - Proteins*
46 *and Proteomics* **2012**, *1824* (1), 68–88.
- 47
48 (26) Chang, X.-Z.; Li, D.-Q.; Hou, Y.-F.; Wu, J.; Lu, J.-S.; Di, G.-H.; Jin, W.; Ou, Z.-L.; Shen, Z.-Z.;
49 Shao, Z.-M. Identification of the Functional Role of AF1Q in the Progression of Breast
50 Cancer. *Breast Cancer Res Treat* **2007**, *111* (1), 65–78.
- 51
52 (27) Edgington, L. E.; van Raam, B. J.; Verdoes, M.; Wierschem, C.; Salvesen, G. S.; Bogyo, M.
53 An Optimized Activity-Based Probe for the Study of Caspase-6 Activation. *Chem Biol*
54 **2012**, *19* (3), 340–352.
- 55
56 (28) Edgington, L. E.; Verdoes, M.; Ortega, A.; Withana, N. P.; Lee, J.; Syed, S.; Bachmann, M.
57 H.; Blum, G.; Bogyo, M. Functional Imaging of Legumain in Cancer Using a New
58 Quenched Activity-Based Probe. *J Am Chem Soc* **2013**, *135* (1), 174–182.
- 59
60

- 1
2
3 (29) Edgington, L. E.; Berger, A. B.; Blum, G.; Albrow, V. E.; Paulick, M. G.; Lineberry, N.;
4 Bogyo, M. Noninvasive Optical Imaging of Apoptosis by Caspase-Targeted Activity-
5 Based Probes. *Nat Med* **2009**, *15* (8), 967–973.
6
7 (30) Verdoes, M.; Edgington, L. E.; Scheeren, F. A.; Leyva, M.; Blum, G.; Weiskopf, K.;
8 Bachmann, M. H.; Ellman, J. A.; Bogyo, M. A Nonpeptidic Cathepsin S Activity-Based
9 Probe for Noninvasive Optical Imaging of Tumor-Associated Macrophages. *Chem Biol*
10 **2012**, *19* (5), 619–628.
11
12 (31) Oresic Bender, K.; Ofori, L.; van der Linden, W. A.; Mock, E. D.; Datta, G. K.; Chowdhury,
13 S.; Li, H.; Segal, E.; Sanchez Lopez, M.; Ellman, J. A.; Figdor, C. G.; Bogyo, M.; Verdoes,
14 M. Design of a Highly Selective Quenched Activity-Based Probe and Its Application in
15 Dual Color Imaging Studies of Cathepsin S Activity Localization. *J Am Chem Soc* **2015**,
16 *137* (14), 4771–4777.
17
18 (32) Devanathan, G.; Turnbull, J. L.; Ziomek, E.; Purisima, E. O.; Ménard, R.; Sulea, T.
19 Carboxy-Monopeptidase Substrate Specificity of Human Cathepsin X. *Biochem Biophys*
20 *Res Comm* **2005**, *329* (2), 445–452.
21
22 (33) Puzer, L.; Cotrin, S. S.; Cezari, M. H. S.; Hirata, I. Y.; Juliano, M. A.; Stefe, I.; Turk, D.;
23 Turk, B.; Juliano, L.; Carmona, A. K. Recombinant Human Cathepsin X Is a
24 Carboxymonopeptidase Only: a Comparison with Cathepsins B and L. *Biol Chem* **2005**,
25 *386* (11), 2321–2325.
26
27 (34) Staudt, N. D.; Aicher, W. K.; Kalbacher, H.; Stevanovic, S.; Carmona, A. K.; Bogyo, M.;
28 Klein, G. Cathepsin X Is Secreted by Human Osteoblasts, Digests CXCL-12 and Impairs
29 Adhesion of Hematopoietic Stem and Progenitor Cells to Osteoblasts. *Haematologica*
30 **2010**, *95* (9), 1452–1460.
31
32 (35) Sevenich, L.; Schurigt, U.; Sachse, K.; Gajda, M.; Werner, F.; Muller, S.; Vasiljeva, O.;
33 Schwinde, A.; Klemm, N.; Deussing, J.; Peters, C.; Reinheckel, T. Synergistic Antitumor
34 Effects of Combined Cathepsin B and Cathepsin Z Deficiencies on Breast Cancer
35 Progression and Metastasis in Mice. *Proc Nat Acad Sci* **2010**, *107* (6), 2497–2502.
36
37 (36) Walker, B.; Lynas, J. F.; Meighan, M. A.; Brömme, D. Evaluation of Dipeptide A-Keto-B-
38 Aldehydes as New Inhibitors of Cathepsin S. *Biochem Biophys Res Comm* **2000**, *275* (2),
39 401–405.
40
41
42
43
44
45
46
47
48
49
50
51
52
53
54
55
56
57
58
59
60



Scheme 1. Synthesis of sCy5-AA-SY probes. i) 4-Nitrophenylchloroformate, Et₃N, DMAP, CH₂Cl₂, 0°C, 6h. ii) SOME₃⁺I⁻, KOTBu, THF, reflux, then cool to 0°C and add nitrophenyl ester. iii) TFA/CH₂Cl₂ (1:1), iv) sulfo-Cy5, PyClock, DIPEA, DMF, r.t., 18h.

| Compound | Amino Acid |
|----------|------------------------------|
| 1 | Boc-Val |
| 2 | Boc-Ile |
| 3 | Boc-Leu |
| 4 | Boc-Nle |
| 5 | Boc-Phe |
| 6 | Boc-Trp |
| 7 | Cbz-Lys(boc) |
| 8 | Boc-Phe-Val |
| 9 | Boc-Val |
| 10 | Boc-Ile |
| 11 | Boc-Leu |
| 12 | Boc-Nle |
| 13 | Boc-Phe |
| 14 | Boc-Trp |
| 15 | Cbz-Lys(Boc) |
| 16 | Boc-Phe-Val |
| 17 | Val |
| 18 | Ile |
| 19 | Leu |
| 20 | Nle |
| 21 | Phe |
| 22 | Trp |
| 23 | Cbz-Lys (sCy5 on side chain) |
| 24 | Phe-Val |

Table 1 Amino Acids used in compounds 1-24 (Scheme 1)



Scheme 2. Synthesis of sCy5-AA-AOMK probes via a sulfoxonium ylide intermediate. i) 1.15 eq HCl in dioxane, THF, reflux, 4 h. ii) 2,6-dimethylbenzoic acid, KF, DMF, r.t, 18 h. iii) TFA/CH₂Cl₂ (1:1), iv) sulfo-Cy5, PyClock, DIPEA, DMF, r.t, 18h.

| Compound | Amino Acid |
|-----------|------------------------------|
| 25 | Boc-Nle |
| 26 | Boc-Phe |
| 27 | Cbz-Lys(Boc) |
| 28 | Boc-Nle |
| 29 | Boc-Phe |
| 30 | Cbz-Lys(Boc) |
| 31 | Nle |
| 32 | Phe |
| 33 | Cbz-Lys (sCy5 on side chain) |

Table 2 Amino Acids used in compounds 25-33 (Scheme 2)

FIGURE 1

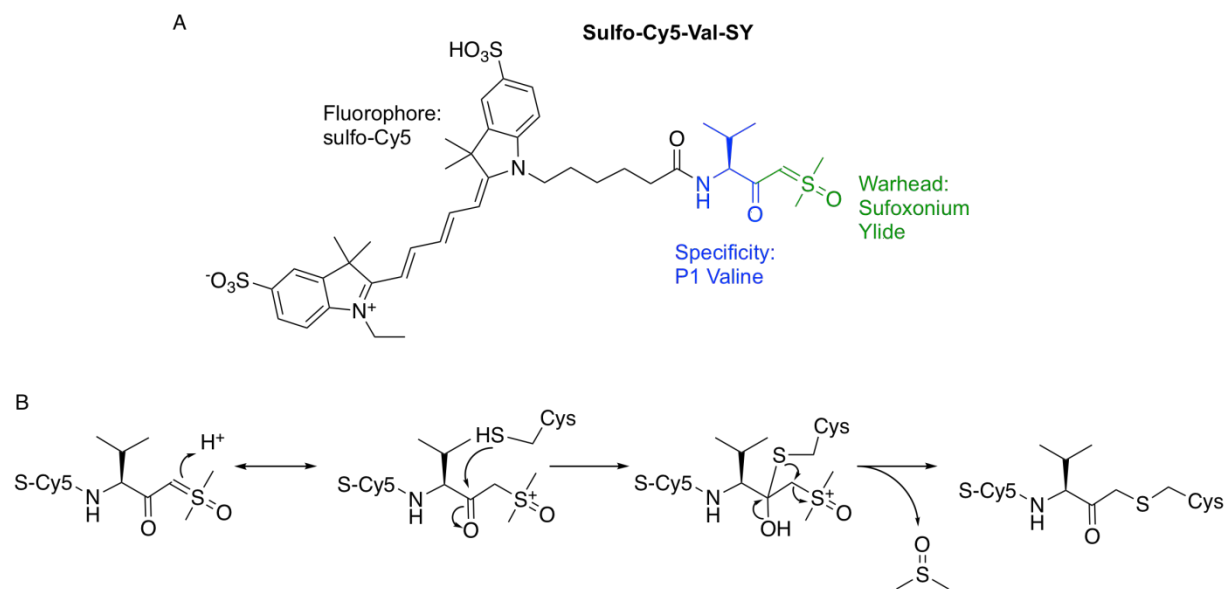


Figure 1. Design of a sulfoxonium ylide-based activity-based probe. (A) Structure of sCy5-Val-SY (**17**) probe. (B) The proposed mechanism through which sCy5-Val-SY binds to an activated cysteine protease.

FIGURE 2

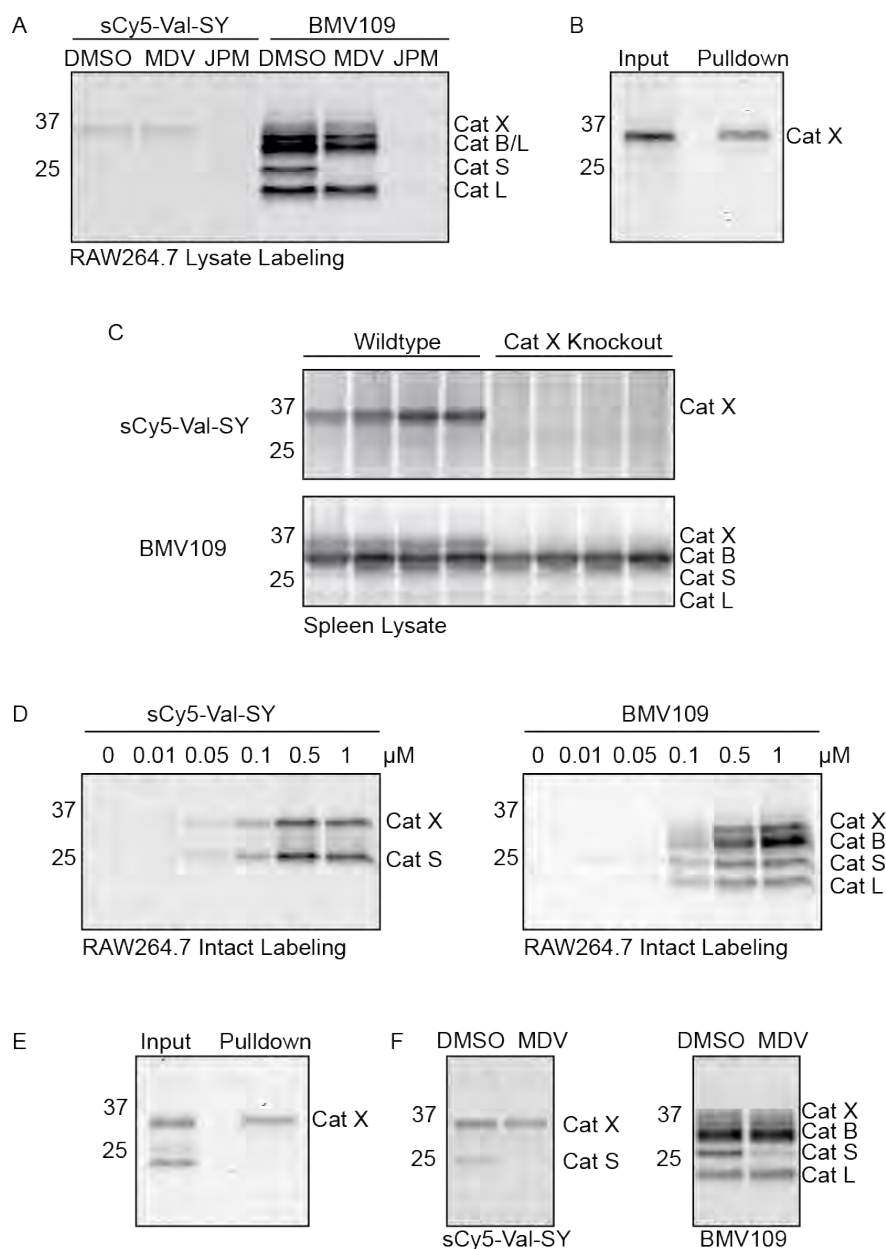


Figure 2. *In vitro* characterization of sCy5-Val-SY (17). (A) Labeling of RAW264.7 lysates with sCy5-Val-SY or BMV109 alone or after pretreatment with 10 μ M MDV-590 (cathepsin S inhibitor) or JPM-OEt (pan cysteine cathepsin inhibitor). (B) Immunoprecipitation of sCy5-Val-SY-labeled samples in A with a cathepsin X-specific antibody. (C) Labeling of splenic lysates from wildtype or cathepsin X-deficient mice with sCy5-Val-SY or BMV109. (D) Labeling of living RAW264.7 cells with increasing doses of sCy5-Val-SY or BMV109 for two hours. (E) Immunoprecipitation of sCy5-Val-SY-labeled samples in D with a cathepsin X-specific antibody. (F) Labeling of living RAW264.7 cells, with and without overnight pretreatment with 10 μ M MDV-590, with sCy5-Val-SY or BMV109 (1 μ M, two hours). Also refer to **Fig S1**.

FIGURE 3

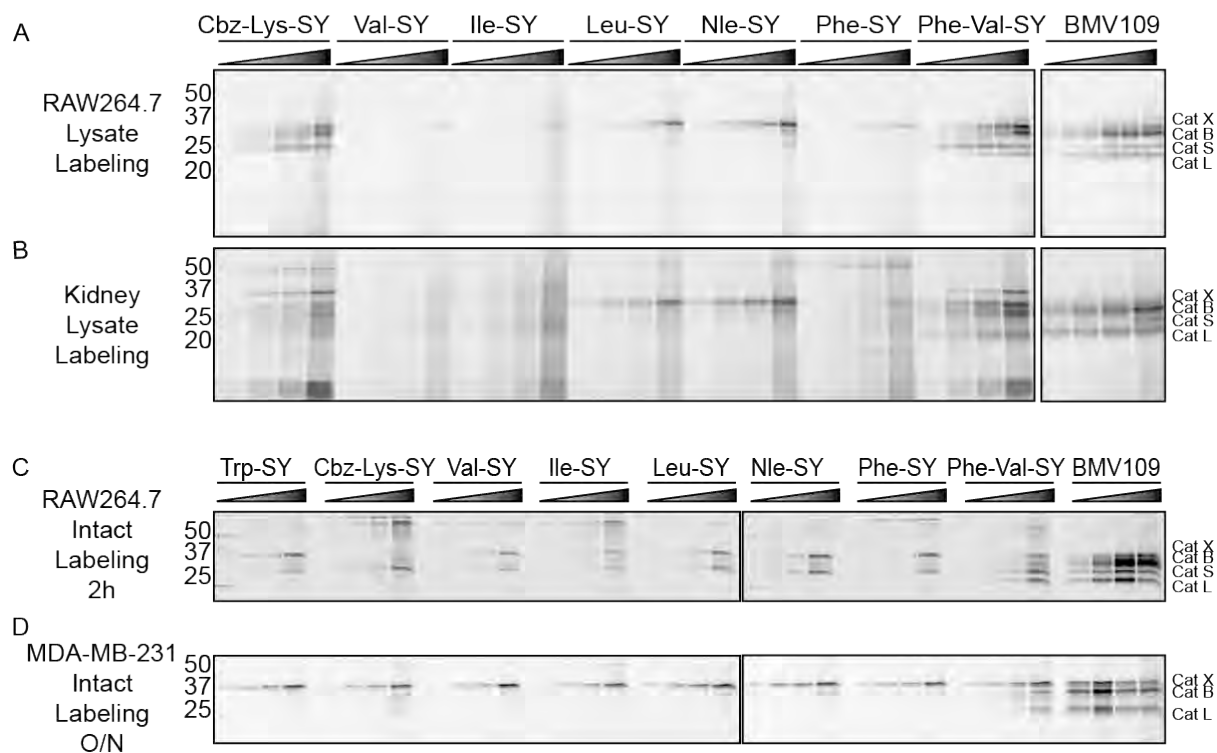


Figure 3. *In vitro* characterization of a sulfoxonium ylide library in lysates and live cells. Labeling of (A) RAW264.7 lysates (0.01, 0.05, 0.1, 0.5, 1, 5 μ M), (B) kidney lysates (0.1, 0.5, 1, 5 μ M), (C) live RAW264.7 cells (0.1, 0.5, 1, 5 μ M) or (D) live MDA-MB-231^{HM} cells (0.1, 0.5, 1, 5 μ M) with the indicated SY probe or BMV109, as analyzed by in-gel fluorescence. Also refer to **Fig S2**.

FIGURE 4

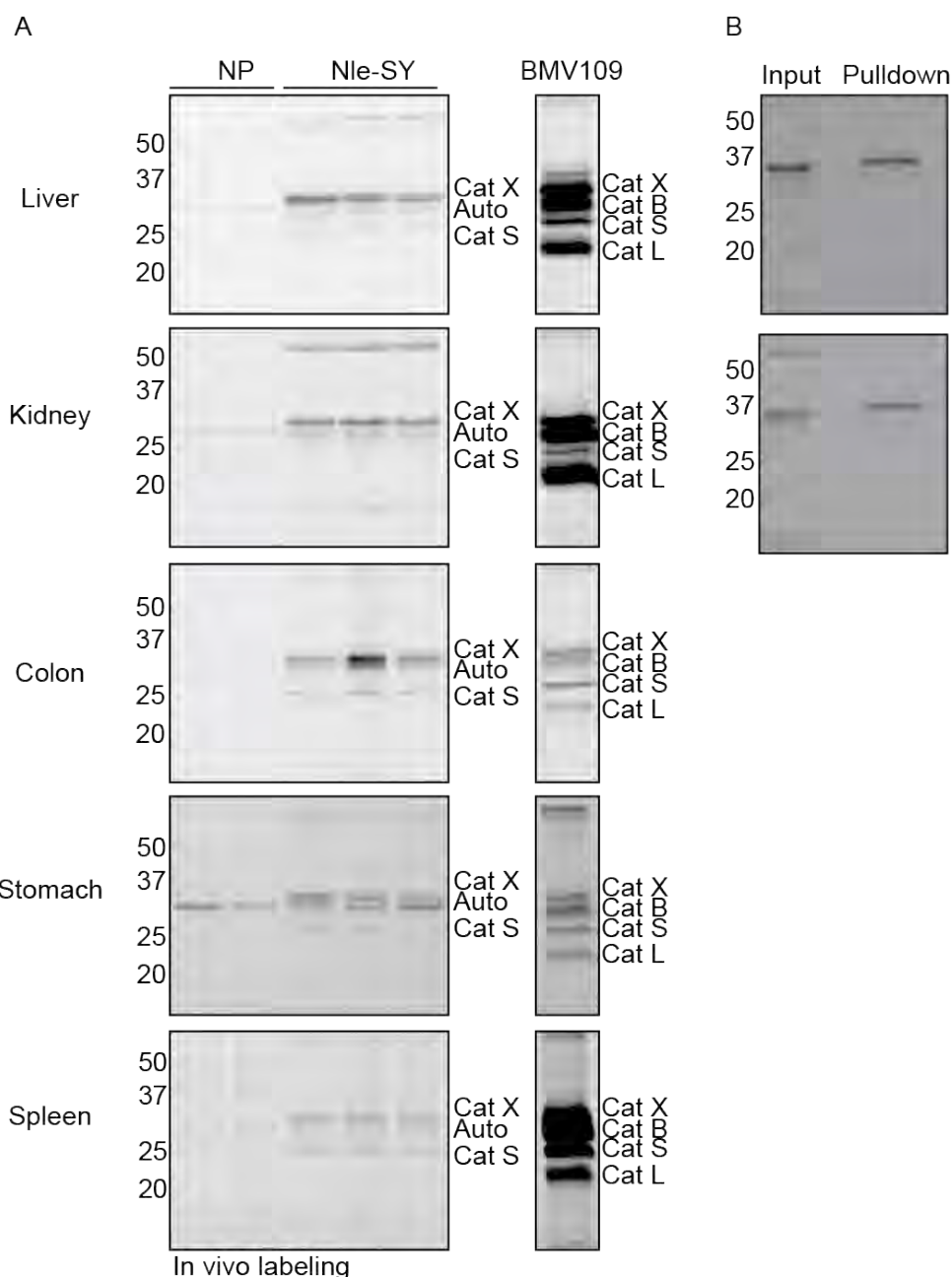


Figure 4. *In vivo* characterization of sCy5-Nle-SY (20). (A) SDS-PAGE and in-gel fluorescence of tissue lysates prepared from mice that received no probe (NP), sCy5-Nle-SY, or BMV109. BMV109-labeled samples are cut from the same gel and are presented at the same gain setting as the other samples in the corresponding tissue. Gains for each tissue were set individually to display optimal contrast for cathepsin X labeling. An autofluorescent band was observed in the no-probe control (labeled as Auto). (B) Immunoprecipitation of liver and kidney samples from A with a cathepsin X-specific antibody. Also refer to **Fig S2**.

FIGURE 5

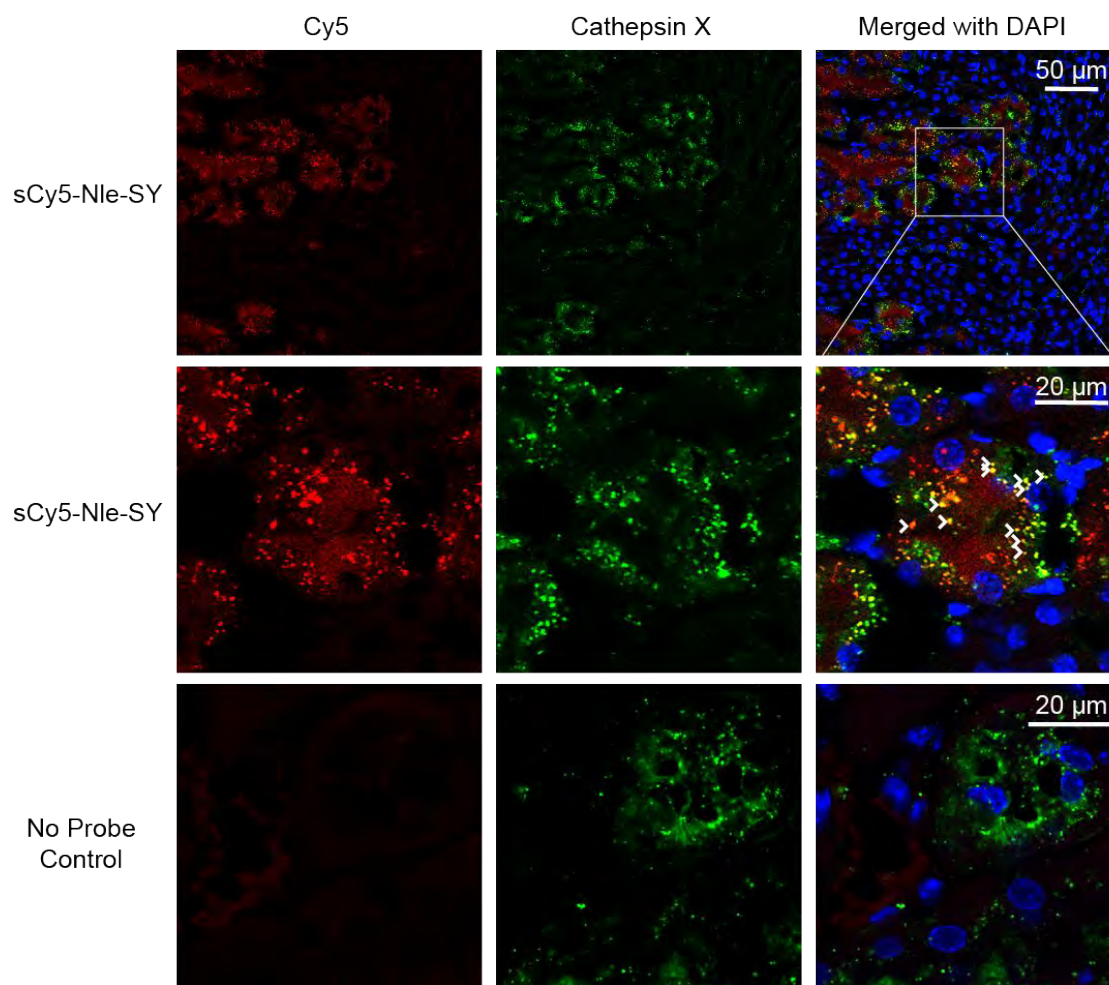
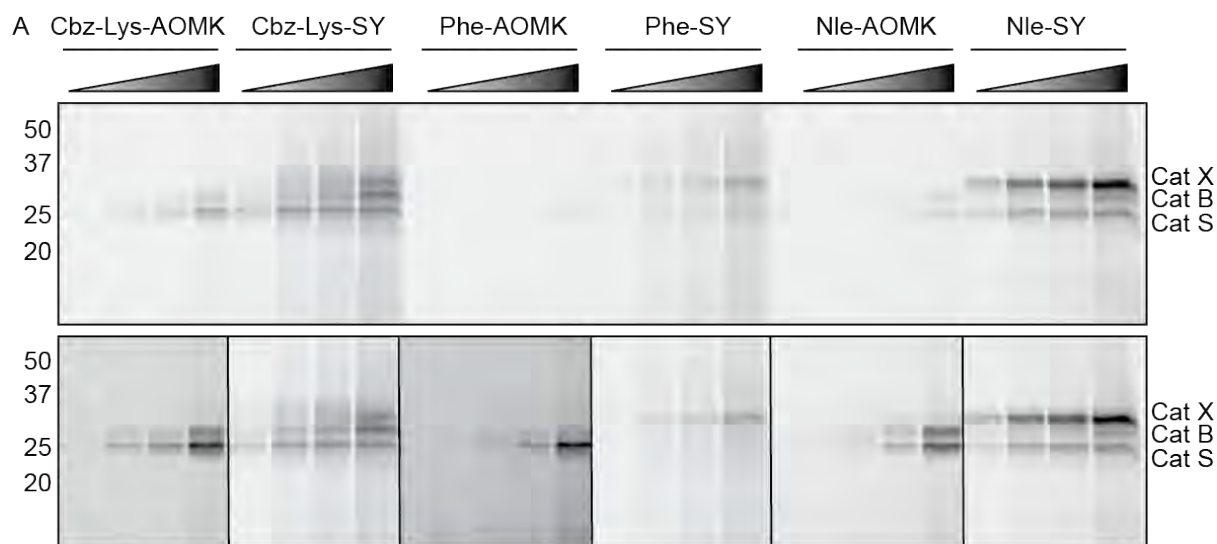


Figure 5. Confocal microscopy of cathepsin X labeling in kidney with sCy5-Nle-SY. Kidney sections from sCy5-Nle-SY-injected mice or no-probe control were analyzed for sCy5 fluorescence (red) or cathepsin X immunoreactivity (green) along with DAPI (blue) to visualize nuclei. The middle row is a zoomed in image of the top row, as denoted by the white box. White arrowheads point to areas where the probe and immunoreactive cathepsin X are overlaid.

FIGURE 6



Bottom: Optimized Gain for AOMK

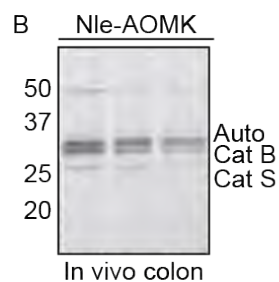
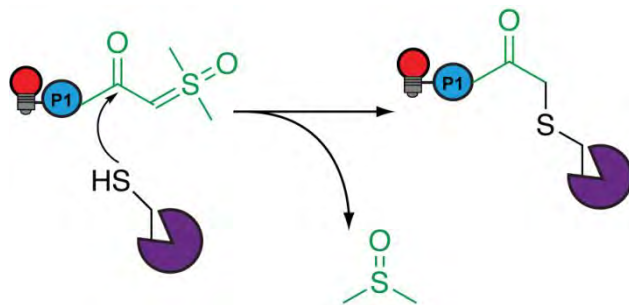
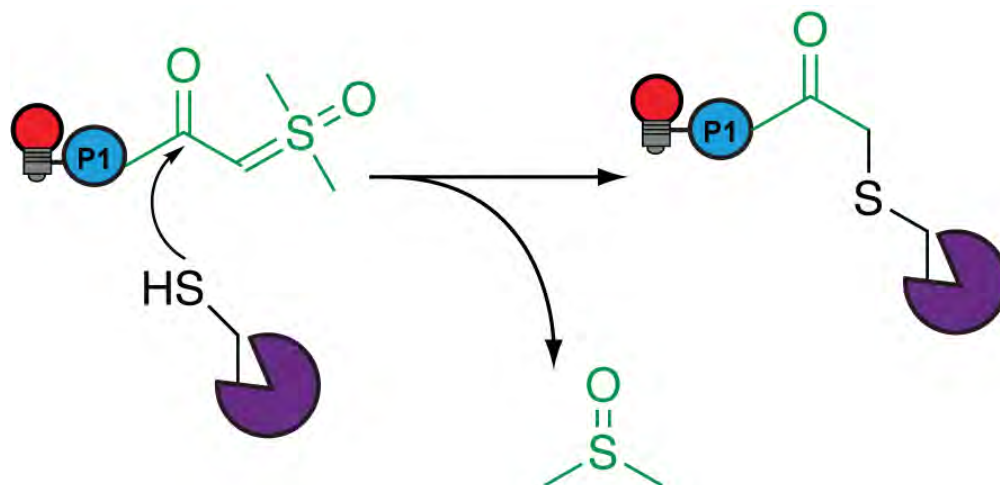


Figure 6. *In vitro* and *in vivo* characterization of AOMK and sulfoxonium ylide probes. (A) Labeling of living RAW264.7 cells with the indicated AOMK and SY probes (0.1, 0.5, 1, 5 μ M), as analyzed by in-gel fluorescence. In the top panel, gain settings are equal for all samples. In the bottom panel, gain settings were individually set to show optimal contrast for the AOMK probes. (B) *In vivo* labeling of colons with sCy5-Nle-AOMK probe. The top band is an autofluorescent protein that appears in no-probe controls (labeled as Auto).

1
2
3
4
5
6
7
8
9
10
11
12
13
14
15
16
17
18
19
20
21
22
23
24
25
26
27
28
29
30
31
32
33
34
35
36
37
38
39
40
41
42
43
44
45
46
47
48
49
50
51
52
53
54
55
56
57
58
59
60

For Table of Contents Only





Application of a chemical probe to detect neutrophil elastase activation during inflammatory bowel disease

Bethany M. Anderson^{1,2}, Daniel P. Poole², Luigi Aurelio³, Garrett Z. Ng¹, Markus Fleischmann^{1,4}, Paulina Kasperkiewicz⁵, Celine Morissette⁶, Marcin Drag⁵, Ian R. van Driel¹, Brian L. Schmidt⁷, Stephen J. Vanner⁶, Nigel W. Bunnett^{2,8,9} & Laura E. Edgington-Mitchell^{1,2,7*}

¹Department of Biochemistry and Molecular Biology, Bio21 Molecular Science and Biotechnology Institute, The University of Melbourne, Parkville, VIC, Australia

²Drug Discovery Biology, Monash Institute of Pharmaceutical Sciences, Monash University, Parkville, VIC, Australia

³Medicinal Chemistry, Monash Institute of Pharmaceutical Sciences, Monash University, Parkville, VIC, Australia

⁴Department of Cellular Immunology, Institute of Experimental Immunology, University Hospital Bonn, Germany

⁵Department of Bioorganic Chemistry, Wroclaw University of Technology, Wroclaw, Poland

⁶Gastrointestinal Diseases Research Unit, Kingston General Hospital, Queen's University, Kingston, ON, Canada

⁷Department of Oral and Maxillofacial Surgery, New York University College of Dentistry, Bluestone Center for Clinical Research, New York, New York, USA

⁸Departments of Surgery and Pharmacology, Columbia University, New York, New York, USA

⁹Department of Pharmacology and Experimental Therapeutics, The University of Melbourne, Parkville, VIC, Australia.

* To whom correspondence should be addressed:

Laura E. Edgington-Mitchell
Department of Biochemistry & Molecular Biology
Bio21 Institute for Molecular Sciences and Biotechnology
The University of Melbourne
Melbourne, VIC 3150, Australia
laura.edgingtonmitchell@unimelb.edu.au
Tel. +61390354630

Keywords: activity-based probe; elastase; protease activity; inflammation; inflammatory bowel disease

ABSTRACT

Neutrophil elastase is a serine protease that has been implicated in the pathogenesis of inflammatory bowel disease. Due to post-translational control of its activation and high expression of its inhibitors in the gut, measurements of total expression poorly reflect the pool of active, functional neutrophil elastase. Fluorogenic substrate probes have been used to measure neutrophil elastase activity, though these tools lack specificity and traceability. PK105 is a recently described fluorescent activity-based probe, which binds to neutrophil elastase in an activity-dependent manner. The irreversible nature of this probe allows for accurate identification of its targets in complex protein mixtures. We describe the reactivity profile of PK105b, a new analogue of PK105, against recombinant serine proteases and in tissue extracts from healthy mice and from models of inflammation induced by oral cancer and *Legionella pneumophila* infection. We apply PK105b to measure neutrophil elastase activation in an acute model of experimental colitis. Neutrophil elastase activity is detected in inflamed, but not healthy, colons. We corroborate this finding in mucosal biopsies from patients with ulcerative colitis. Thus, PK105b facilitates detection of neutrophil elastase activity in tissue lysates, and we have applied it to demonstrate that this protease is unequivocally activated during colitis.

INTRODUCTION

Neutrophil elastase (NE) is a serine protease found within azurophilic granules of neutrophils.¹ During infection, active NE contributes to killing of pathogens, and mice lacking NE are more susceptible to bacterial and fungal infections.¹ NE also mediates inflammation by processing cytokines, chemokines and growth factors.¹ Furthermore, NE cleaves the extracellular N termini of protease-activated receptors (PARs), a family of G protein-coupled receptors (GPCRs), to initiate cellular signaling events that lead to inflammation and pain.²⁻⁴

NE has recently been implicated in the pathogenesis of inflammatory bowel diseases (IBD), which are characterized by chronic and relapsing inflammation in the gastrointestinal tract.⁵ IBD comprises ulcerative colitis (UC) and Crohn's disease (CD), both of which are associated with diarrhea, rectal bleeding, increased urgency and pain. Mice lacking one copy of NE and a closely related neutrophil serine protease, proteinase 3 (PR3), exhibit improved symptoms in mouse models of colitis.⁶ Enforced expression of elafin, an endogenous serine protease inhibitor, either by intracolonic administration of adenoviral vectors or introduction of elafin-expressing lactic acid bacteria, resulted in attenuation of symptoms in mouse models of colitis.⁶ Treatment with a NE-selective inhibitor also reduced colitis symptoms.⁷

Colonic mucosal biopsies from patients with IBD exhibit elevated NE expression compared to healthy controls at both mRNA and protein levels.^{8,9} Because NE is expressed as an inactive zymogen and can be tightly controlled by endogenous inhibitors once activated, measures of mRNA or total protein expression rarely reflect the pool of active functional enzyme.¹⁰ Thus, tools to measure the specific activity of NE are required.

Commercially available chromogenic and fluorogenic substrate probes, including AAPV-p-nitroanilide and BODIPY-FL-elastin, respectively, have indicated an increase in elastase-like activity in biopsies from UC and CD patients and in mouse models of IBD.^{6,7,11,12} However, these probes lack specificity and can be cleaved by multiple proteases.^{5,10} Because the probes do not bind directly to the proteases upon cleavage, it is difficult to estimate the proportion of cleavage that is dependent on NE. Thus, improved tools are required to specifically measure NE activation and to improve our understanding of its functions during IBD pathogenesis.

We previously applied a fluorescent activity-based probe (ABP) for NE, Cy5-V-DPP, to track NE activation during colitis.¹³ This probe contained a sulfonated cyanine 5 (Cy5) fluorophore and a P1 valine residue coupled to a diphenylphosphonate electrophile (DPP; 'warhead') that reacts with the active site serine of active NE in a covalent, irreversible manner (**Fig 1**). While Cy5-V-DPP efficiently labeled recombinant NE and NE in cells with high expression (e.g., bone marrow), we had little success in detecting NE activity in colitis tissues, presumably due to a lack of sensitivity. Use of hybrid combinatorial substrate libraries allowed for optimization of the NE substrate recognition sequence, which was coupled to Cy5 and the DPP warhead to generate the ABP, PK105.¹⁴⁻¹⁷ While PK105 has been extensively characterized in purified neutrophils, its efficacy and specificity for NE in more complex tissue lysates has not been explored until now.

Herein, we characterized the reactivity profile of PK105b, an analogue of PK105, and explored its efficacy in complex tissue lysates. We applied PK105b in a mouse model of acute colitis and in human mucosal biopsies from patients with IBD to clearly measure activation of NE in inflamed tissue.

RESULTS

Selectivity and potency of PK105b against purified serine proteases

We synthesized an analogue of our previously published PK105 probe,¹⁶ in which the polyethylene glycol (PEG) linker was omitted and sulfoCy5 was used in place of the unsulfonated version (**Fig 1**). This change allowed for a more direct comparison to our Cy5-V-DPP probe,¹³ which included sulfoCy5 and no PEG. We tested the reactivity of the PK105 analogue, referred to as PK105b hereafter, against recombinant serine proteases, and compared its potency with Cy5-V-DPP. After incubation of proteases with increasing concentrations of probes for 30 minutes, the proteins were resolved by SDS-PAGE and binding was detected by in-gel fluorescence. Both probes clearly labeled NE and PR-3 in a concentration-dependent manner (**Fig 2A**), though PK105b was more potent than Cy5-V-DPP. PK105b also clearly labeled trypsin, another serine protease, while trypsin binding by Cy5-V-DPP was negligible (**Fig 2A**). Using a commercially available fluorogenic substrate probe, AAPV-AMC, we compared the ability of the two probes to inhibit recombinant NE. Like Sivelestat, a commonly used NE inhibitor, PK105b immediately inhibited rNE activity at 0.1 μM while Cy5-V-DPP only partially inhibited rNE activity at 1 and 10 μM (**Fig 2B**). These results indicate that PK105b binds to rNE more rapidly and more potently than Cy5-V-DPP.

Selectivity and potency of PK105b in normal tissue lysates

We compared the ability of PK105b and Cy5-V-DPP to detect protease activity in lysates prepared from mouse bone marrow. Two proteases were labeled by PK105b (**Fig 2C**), and the 25-kDa protein was confirmed to be NE by immunoprecipitation with an NE-specific antibody (**Fig 2D**). NE was specifically labeled by Cy5-V-DPP, but with a much lower potency than PK105b. We also examined the reactivity of the probes in lysates prepared from mouse pancreas, a tissue rich in serine proteases. With PK105b, we observed strong labeling of 25-kDa proteins that was much more apparent than labeling by Cy5-V-DPP (**Fig 2E**). Immunoprecipitation of PK105b-labeled lysates revealed that the target proteases consisted of a combination of NE, pancreatic elastase (PE), and trypsin 3 (Try3, also known as PRSS3 or mesotrypsin; **Fig 2F**).

Validation of PK105b in inflamed tissues

To determine the effectiveness of PK105b to measure NE activation in inflamed tissues, we used a mouse model of *Legionella pneumophila* infection. *L. pneumophila* infection may result in Legionnaire's disease, a common cause of community or hospital-acquired

pneumonia, and is associated with high neutrophil infiltration in the lung.^{18,19} PK105b labeling was significantly increased in lysates prepared from infected lung tissues compared to uninfected lungs (**Fig 3A,C**). The identity of the major 25-kDa species was confirmed to be NE by immunoblotting (**Fig 3B,D-E**) and immunoprecipitation (**Fig 3F**) with an NE-specific antibody. We also confirmed that PK105b binding was mediated by the DPP warhead and the specificity region, as the labelling could be competed by pre-treatment with PK101¹⁴⁻¹⁵, a biotinylated (non-fluorescent) analogue of PK105 (**Fig 3G**). As neutrophils are the predominant source of NE during *L. pneumophila* infection, we also examined PK105b labelling in neutrophils from infected-lungs, which were sorted by flow cytometry at >97% purity (**Fig S1**). Within this population of cells, we observed specific labeling of NE by PK105b (**Fig 3H**).

We next determined the utility of PK105b to detect NE activation in a cancer setting, which is also rich in neutrophils.²⁰⁻²² Specifically, we utilized a mouse orthotopic xenograft model of oral squamous cell carcinoma in which human cancer cells (HSC-3) were injected into the tongue.²³ In this context, we observed clear labeling of a 25-kDa species in tumor tissues, but not normal tongue tissues (**Fig 4A,C**). This species coincided with the size of mature NE as determined by immunoblot (**Fig 4B,D-E**) and immunoprecipitation (**Fig 4F**) with an NE-specific antibody. Several other high-molecular weight species were abundantly labeled by PK105b in these lysates (**Fig 4A**), but they have not yet been identified. Nonetheless, they are likely to be binding to PK105b through the DPP and specificity region, and not Cy5, as binding could largely be competed with PK101, the non-fluorescent PK105 analogue (**Fig 4G**).

Application of PK105b to measure NE activation in experimental colitis

Having validated PK105b in inflamed mouse tissues, we next applied this probe to investigate NE activation during acute experimental colitis induced by trinitrobenzenesulfonate (TNBS). As expected, mice exhibited loose stools, delayed defecation, weight loss (**Fig S2A**), and colon shortening (**Fig S2B**). We also observed damage to the mucosa by histological evaluation, as well as edema and inflammatory infiltrate (**Fig S2C**). We analyzed colon lysates for NE activation by PK105b labeling and measurement of in-gel fluorescence. In proximal colons from healthy and inflamed mice, we observed little PK105b labeling. By contrast, in the distal region of inflamed colons, which is most affected in the TNBS model, we observed clear labeling of a 25-kDa protein (**Fig 5A**). This band was virtually absent in distal colons of healthy mice that received vehicle instead of TNBS (**Fig 5A**). We confirmed the identity of the protease to be NE by immunoprecipitation with an NE-specific antibody (**Fig 5D**). All of the PK105b bands could be competed by PK101, the non-fluorescent PK105 analogue (**Fig 5E**).

We also transferred the fluorescent gels to nitrocellulose membranes in order to immunoblot the samples for total NE expression. In all proximal colons and in healthy distal colons, we observed bands at 37 and 25 kDa (**Fig 5B**). In the TNBS-treated distal colons, a new band appeared just below the 25-kDa protein. Only the lower species was labeled by PK105b, as revealed by overlay of the Cy5 fluorescence (**Fig 5C**) and immunoprecipitation (**Fig 5D**). As above, PK105b labeling could be competed by pre-treatment with PK101 (**Fig 5E**). To verify that the appearance of this smaller NE species was not an artefact of probe labeling, we immunoblotted inflamed distal colon samples in the presence and absence of PK105b. The smaller species was detected regardless of the presence of PK105b (**Fig 5F**). Taken together, these data suggest that NE is subject to trimming in inflamed regions of the colon that permits its activation and thus its reaction with the PK105b probe.

For comparison, we also tested our previous NE probe, Cy5-V-DPP, in distal colon lysates and labeling of the 25-kDa species was barely distinguishable from the background (**Fig 5G**). Thus, PK105b is clearly superior to Cy5-V-DPP for its ability to detect NE activity in

tissue lysates. Both probes exhibit binding to several species in the 50-75-kDa range (**Fig 5A**), and future proteomics assays will be required to determine their identity. Furthermore, we investigated secreted proteases found in the lumen of the colon (either luminal flush or in fecal pellets) with PK105b (**Fig 6A**). In both samples, we observed two labeled proteases at 25 kDa. Immunoprecipitation confirmed low levels of NE in these samples, with pancreatic elastase and trypsin 3 being the predominant species (**Fig 6C**). Nonetheless, NE activity could be clearly delineated by PK105b in lysates from colon tissues.

Application of PK105b to measure NE activation in mucosal biopsies from IBD patients

To translate our findings in mouse colitis to human disease, we examined PK105b labeling in mucosal biopsies from patients (**Table 1**). As in mice, we observed a significant increase in labeling in samples from patients with active UC compared to healthy individuals brought in for routine colonoscopy screening (**Fig 7A,D**). In contrast to mice, where we observed a single 25-kDa species at labeled by PK105b, three species were labeled in human mucosal lysates, with the smallest form having the most activity. The banding pattern resembled that which was observed with recombinant human NE (**Fig 2A** and in References 24 and 25). We confirmed these bands to be NE by immunoprecipitation with an NE-specific antibody (**Fig 7G**), and could be competed with PK101 (**Fig 7H**).

Furthermore, when the same samples were immunoblotted for total NE expression, we observed NE bands in the healthy tissue at 37 and 25 kDa (**Fig 7B**). UC tissues, however, displayed an additional doublet that was smaller than the 25-kDa species. The most active species, as indicated by PK105b labeling, corresponded to these smaller species (**Fig 7C,G**). Thus, as we observed in mouse colitis, NE undergoes trimming during human UC that permits its activation and binding to PK105b.

Patient #13 was originally diagnosed with UC and we initially considered this biopsy to be an outlier given the low levels of NE activation. Upon follow-up studies, however, this diagnosis was re-evaluated and the patient was found to have an ileal stricture. The biopsies analyzed in this study were taken from normal tissue regions. These data therefore highlight the potential utility of using NE activity as a potential diagnostic marker for ulcerative colitis.

DISCUSSION

While PK105 was selective for NE in purified neutrophils, its ability to label NE in tissue lysates, which contain many cell types and proteases, had not been established. We tested PK105b, a close analogue of PK105 in bone marrow, pancreas, inflamed lungs, oral cancer, and human and mouse colitis tissues and fecal samples. Due to the covalent nature of PK105b, we could verify that NE was clearly targeted by this probe. We also observed that PK105b exhibited cross-reactivity with other serine proteases such as pancreatic elastase, proteinase-3, trypsin 3 and other unknown proteases. This cross-reactivity was dependent on the tissues examined, with greater selectivity observed in purified lung neutrophils, lung tissue, and human colon biopsies and more cross-reactivity in pancreas, fecal samples, and cancer tissue. We confirmed that all PK105b binding was mediated by the DPP warhead in combination with the specificity region, and not due to non-specific binding via the Cy5 fluorophore, as all labeling could be blocked by pre-treatment with PK101, a non-fluorescent analogue of PK105.

While PK105b clearly has limitations, it is advantageous over traditional substrate probes such as AAPV-p-nitroanilide and BODIPY-FL-elastin, as these tools do not bind their targets covalently and the extent of their cross-reactivity in various contexts cannot readily be determined. Additionally, PK105b was advantageous over our previous diphenylphosphonate probe, Cy5-V-DPP.¹³ In competition assays with the fluorogenic substrate, AAPV-AMC, PK105b reacted with rNE much more rapidly and potently than Cy5-

V-DPP, most likely mediated by the improved specificity region in PK105b. This likely explains the enhanced sensitivity of PK105b in tissue lysates compared to Cy5-V-DPP. Thus, PK105b is one of the most effective tools available to study NE.

We applied PK105b to investigate NE activation during mouse colitis. In inflamed colons, we observed labeling of active NE, which was significantly increased compared to control tissue. Probe-labeled NE corresponded to the most mature species of NE detected by immunoblotting, which was not present in healthy tissue. We corroborated these findings in human colitis using mucosal biopsies from patients with UC, unequivocally demonstrating for the first time that NE is activated in IBD. Thus, PK105b is well suited for detection of both mouse and human NE during IBD and will be a valuable resource for future investigation of NE function. Furthermore, it may have utility as a diagnostic agent for IBD and for validating target engagement and efficacy of neutrophil elastase inhibitors in preclinical development as therapeutic agents.

EXPERIMENTAL PROCEDURES

Probe synthesis and characterization

Refer to supplemental materials for information on the synthesis of PK105b. Cy5-V-DPP¹³ and PK101¹⁴ were synthesized in house as described previously.

Recombinant protease labeling

Recombinant proteases (500 ng) were diluted in 20 μ l of phosphate-buffered saline (PBS): human neutrophil elastase (Elastin Products Company), porcine pancreatic trypsin type II-S (beta trypsin; Sigma), and human proteinase-3 (Sigma). PK105b or Cy5-V-DPP (0, 0.1, 0.5 or 1 μ M) was added from a 100x DMSO stock, and reaction was carried out at 37°C for 30 minutes. Proteins were solubilized in 4x sample buffer (40% glycerol, 200 mM Tris-Cl [pH 6.8], 8% SDS, 0.04% bromophenol blue, 5% beta-mercaptoethanol), boiled and resolved on a 15% SDS-PAGE gel under reducing conditions. Probe labeling was detected by scanning the gel for Cy5 fluorescence on a Typhoon 5 flatbed laser scanner (GE Healthcare). Detailed protocols for ABP application are available in Reference 26.

Fluorogenic substrate assay

Recombinant neutrophil elastase (20 nM) was diluted in PBS, and MeOSuc-Ala-Ala-Pro-Val-AMC (AAPV-AMC; 20 μ M; Bachem) was diluted in PBS containing PK105b (0.2 μ M), Cy5-V-DPP (2 or 20 μ M), sivelestat (2 μ M; Sigma) or 2% DMSO (vehicle control). The two solutions were mixed 1:1 in an opaque 96-well plate (100 μ l final volume), and probe-dependent fluorescence (355 nm excitation/ 460 nm emission) was immediately measured at 30s intervals over the course of 1h on a FLUOstar Omega plate reader (BMG Labtech).

Animal ethics

All animal experiments were conducted in accordance with the guidelines for the use of laboratory animals in research and approved protocols. Experiments involving healthy mice and colitis experiments were approved by the Monash University Animal Ethics Committee. Oral cancer experiments were approved by the Committee on Animal Research at New York University. Legionella experiments were approved by the University of Melbourne Animal Ethics Committee.

Ex vivo tissue labeling

Bone marrow was obtained by flushing tibias and femurs from healthy C57BL/6J mice with PBS. Cells were washed and resuspended in PBS prior to sonication on ice. Tissues were

lysed by sonication on ice in PBS (10µl/mg tissue), and supernatants were cleared by centrifugation at 21g for 10 min at 4°C. Total protein (60 µg, as measured by BCA assay, Pierce) was aliquoted in a total volume of 20 µl PBS, and probe labeling and SDS-PAGE was carried out as above. Where indicated, PK101 (10 µM) was added for 10 minutes prior to the addition of PK105b.

Western blotting

Fluorescent gels were transferred to nitrocellulose membranes and blotted using the Turbo Blot system (BioRad). Membranes were blocked using Li-Cor Odyssey blocking buffer diluted by 50% with PBS containing 0.05% Tween 20. Sheep anti-mouse neutrophil elastase/ELA2 (1:1000; R&D AF4517) was incubated overnight at 4°C. Secondary antibody (goat-IR800, 1:5000; LiCor) was incubated for one hour at room temperature. Binding was detected by scanning with the IRLong filter on the Typhoon 5.

Immunoprecipitation

PK105b-labeled lysates (boiled in sample buffer) were divided into input and immunoprecipitation (IP) samples (100 µg each). The IP samples were diluted in 500 µl IP buffer (PBS [pH 7.4], 1 mM EDTA, 0.5% NP-40) along with 10 µl antibody: Sheep anti-neutrophil elastase/ELA2 (R&D AF4517); rabbit anti-PRSS3 (Abcam ab105123); rabbit anti-pancreatic elastase (Abcam ab21593). Protein A/G beads (40 µl slurry; Santa Cruz) were washed with IP buffer and then added to the sample. Tubes were rocked overnight at 4°C. Beads were washed four times with IP buffer and once with 0.9% sodium chloride. After the last wash, all buffer was removed and beads were boiled in 2x sample buffer (20 µl). Supernatants were then analyzed, alongside the input sample, by fluorescent SDS-PAGE as above.

Legionella pneumophila infection model

C57BL/6 mice were infected by intranasal inoculation with 2.5×10^6 *L. pneumophila* 130b ΔflaA in 50 µL of PBS. Three days after infection, lungs were collected, minced and digested in 4 mL RPMI-1640 (Gibco) containing 3% FCS, 1 mg/mL DNaseI (Sigma-Aldrich) and 1 mg/mL Collagenase III (Worthington). Cells were collected by filtration through a 70-µm filter, centrifuged and red blood cells lysed by resuspension in buffer containing 150 mM ammonium chloride and 50 mM Tris-HCl (pH 7.5) for 5 min. After washing with PBS containing 0.1% BSA and 2 mM EDTA, cells were stained with anti-Ly6G-FITC (1A8, BD Pharmingen), anti-CD11c-PE (N418, eBioscience), anti-Siglec-F-BV421 (E50-2440, BD Horizon), anti-CD64-Alexa 647 (X54-5/7.1, BD Pharmingen) and anti-FcγII/III (2.4G2, WEHI monoclonal facility) for 30 min at 4°C. Cells were washed and resuspended in FACS buffer with 0.25 µg/mL 7-AAD. Neutrophils were isolated using a Beckman Coulter MoFlo Astrios cell sorter into FCS and pellets of 10^6 cells snap frozen at -80°C. Purities were assessed post-sorting using the same gating strategy. Purified neutrophils were lysed on ice in PBS with 0.1% Triton X-100, and supernatants were cleared by centrifugation. Alternatively, lung tissues from the same mice were snap frozen at the time of harvest and processed as above.

Oral cancer model

Female BALB/c nude mice (6–8 weeks old, Charles River Laboratories) were injected in the left lateral tongue under anesthesia (3×10^5 HSC-3 human oral squamous cell carcinoma cells suspended in 50 µl vehicle [1:2 mixture of DMEM and Matrigel; Becton Dickinson], or vehicle alone). After two weeks, the resulting xenografted tumors and vehicle-injected tongues were excised, snap frozen, and analyzed as above.

Colitis model

Mice were purchased from the Monash University in-house colony. Colitis was induced in 10-week old male C57BL/6J mice by intracolonic infusion of picrylsulfonic acid solution (2,4,6-Trinitrobenzenesulfonic acid solution, TNBS; Sigma; 2.5 mg dissolved in 50% ethanol). Body weight and symptoms were recorded daily, and mice were humanely killed after three days. Upon colon extraction, luminal fluids were collected by flushing colons with PBS. Solids were removed by centrifugation and supernatant was concentrated using a 3-kDa cut-off centrifugal filter (Amgen). Pieces of proximal and distal colon were frozen for protease analysis or fixed in 4% paraformaldehyde overnight, paraffin embedded, sectioned, and stained with haematoxylin and eosin.

Human mucosal biopsies

Human mucosal biopsies were obtained from individuals during colonoscopy procedures at Hotel Dieu Hospital in Kingston, Ontario, Canada. Informed written and verbal consent was obtained prior to enrolment and all protocols were approved by and carried out in accordance with the guidelines and regulations of the Queen's University Human Ethics Committee. Patients were well-characterized individuals with active UC or healthy individuals undergoing routine colonoscopy for cancer screening (**Table 1**). For UC patients, biopsies were obtained from sites of active inflammation. Fresh biopsies were washed in PBS and then snap frozen for protease analysis as above.

Statistical analysis

All experiments were performed with at least three biological replicates. Data are reported as means \pm SEM. Statistical significance was determined by comparing two groups using a Student's t test, and p values of less than 0.05 were considered significant.

Data

availability

All data generated or analyzed during this study are included in this published article (and its Supplementary Information files).

ACKNOWLEDGEMENTS

We thank Cameron Nowell for maintaining the imaging facilities at the Monash Institute of Pharmaceutical Sciences and The Peter Doherty Institute Immunology flow cytometry facility, where neutrophil isolation was performed. LEM was supported by an Early Career Fellowship from the National Health and Medical Research Council of Australia (NHMRC, GNT1091636), a Grimwade Fellowship from the Russell and Mab Grimwade Miegunyah Fund at The University of Melbourne, a DECRA Fellowship from the Australian Research Council (ARC, DE180100418) and seed grants from Monash University. NWB was supported by grants from the National Institutes of Health (NS102722, DE026806, DK118971) and the United States Department of Defense (W81XWH1810431). IRvD, GZN, and MF were supported by NHMRC grants (GNT1145244). MF was also supported by a fellowship by the German Research Council (DFG GRK 2168) and a Graduate Research Scholarship from The University of Melbourne. The content is solely the responsibility of the authors and does not necessarily represent the official views of the National Institutes of Health.

CONFLICTS OF INTEREST

NWB is a founding scientist of Endosome Therapeutics Inc. Research in NWB and DP's laboratories is supported in part by Takeda Pharmaceuticals, Inc.

AUTHOR CONTRIBUTIONS

LEM conceived study, planned all experiments, analyzed data, contributed funding, coordinated all collaborators, and wrote the manuscript. PK and MD produced the PK105 probe and contributed intermediates towards the synthesis of PK105b, which was made by LA. BMA obtained the biological data. GZN, MF, and IRvD provided samples for the *L. pneumophila* experiments. BLS provided the oral cancer tissues. DPP and NB contributed funding and intellectual input. SV and CM provided the human mucosal biopsies.

REFERENCES

1. Korkmaz, B., Horwitz, M. S., Jenne, D. E. & Gauthier, F. Neutrophil elastase, proteinase 3, and cathepsin G as therapeutic targets in human diseases. *Pharmacol. Rev.* **62**, 726–759 (2010).
2. Zhao, P. *et al.* Neutrophil Elastase Activates Protease-activated Receptor-2 (PAR2) and Transient Receptor Potential Vanilloid 4 (TRPV4) to Cause Inflammation and Pain. *J. Biol. Chem.* **290**, 13875–13887 (2015).
3. Lieu, T. *et al.* Antagonism of the proinflammatory and pronociceptive actions of canonical and biased agonists of protease-activated receptor-2. *Brit. J. Pharmacol.* **173**, 2752–2765 (2016).
4. Jimenez-Vargas, N. N. *et al.* Protease-activated receptor-2 in endosomes signals persistent pain of irritable bowel syndrome. *Proc. Nat. Acad. Sci.* **115**, E7438–E7447 (2018).
5. Edgington-Mitchell, L. E. Pathophysiological roles of proteases in gastrointestinal disease. *Am. J. Physiol. Gastrointest. Liver Physiol.* **310**, G234–239 (2015).
6. Motta, J. P. *et al.* Modifying the Protease, Antiprotease Pattern by Elafin Overexpression Protects Mice From Colitis. *Gastroenterol.* **140**, 1272–1282 (2011).
7. Morohoshi, Y. *et al.* Inhibition of neutrophil elastase prevents the development of murine dextran sulfate sodium-induced colitis. *J. Gastroenterol.* **41**, 318–324 (2006).
8. Uchiyama, K. *et al.* Serpin B1 protects colonic epithelial cell via blockage of neutrophil elastase activity and its expression is enhanced in patients with ulcerative colitis. *Am. J. Physiol. Gastrointest. Liver Physiol.* **302**, G1163–G1170 (2012).
9. Kuno, Y. *et al.* Possible involvement of neutrophil elastase in impaired mucosal repair in patients with ulcerative colitis. *J. Gastroenterol.* **37**, 22–32 (2002).
10. Edgington, L. E., Verdoes, M. & Bogyo, M. Functional imaging of proteases: recent advances in the design and application of substrate-based and activity-based probes. *Cur. Op. Chem. Biol.* **15**, 798–805 (2011).
11. Gecse, K. *et al.* Increased faecal serine protease activity in diarrhoeic IBS patients: a colonic luminal factor impairing colonic permeability and sensitivity. *Gut* **57**, 591–599 (2008).
12. Motta, J. P. *et al.* Food-Grade Bacteria Expressing Elafin Protect Against Inflammation and Restore Colon Homeostasis. *Sci. Translat. Med.* **4**, 158ra144 (2012).
13. Edgington-Mitchell, L. E. *et al.* Fluorescent diphenylphosphonate-based probes for detection of serine protease activity during inflammation. *Bioorg. Med. Chem. Lett.* **27**, 254–260 (2017).
14. Kasperkiewicz, P. *et al.* Design of ultrasensitive probes for human neutrophil elastase through hybrid combinatorial substrate library profiling. *Proc. Nat. Acad. Sci.* **111**, 2518–2523 (2014).
15. Lechtenberg, B. C., Kasperkiewicz, P., Robinson, H., Drag, M. & Riedl, S. J. The Elastase-PK101 Structure: Mechanism of an Ultrasensitive Activity-based Probe Revealed. *ACS Chem. Biol.* **10**, 945–951 (2015).

16. Kasperkiewicz, P., Altman, Y., D'Angelo, M., Salvesen, G. S. & Drag, M. Toolbox of Fluorescent Probes for Parallel Imaging Reveals Uneven Location of Serine Proteases in Neutrophils. *J. Am. Chem. Soc.* **139**, 10115–10125 (2017).
17. Kasperkiewicz, P., Poreba, M., Groborz, K. & Drag, M. Emerging challenges in the design of selective protease substrates, inhibitors and activity-based probes for indistinguishable proteases. *FEBS J.* **284**, 1518–1539 (2017).
18. Brown, A. S. *et al.* Cooperation between Monocyte-Derived Cells and Lymphoid Cells in the Acute Response to a Bacterial Lung Pathogen. *PLoS Pathog.* **12**, e1005691–20 (2016).
19. Brown, A. S., Yang, C., Hartland, E. L. & van Driel, I. R. The regulation of acute immune responses to the bacterial lung pathogen *Legionella pneumophila*. *J. Leukocyte Biol.* **101**, 875–886 (2017).
20. Lerman, I. & Hammes, S. R. Neutrophil elastase in the tumor microenvironment. *Steroids* **133**, 96–101 (2018).
21. Kistowski, M. *et al.* A Strong Neutrophil Elastase Proteolytic Fingerprint Marks the Carcinoma Tumor Proteome. *Mol. Cell Proteomics* **16**, 213–227 (2017).
22. Scheff, N. N. *et al.* Tumor necrosis factor alpha secreted from oral squamous cell carcinoma contributes to cancer pain and associated inflammation. *Pain* **158**, 2396–2409 (2017).
23. Lam, D. K., Dang, D., Zhang, J., Dolan, J. C. & Schmidt, B. L. Novel Animal Models of Acute and Chronic Cancer Pain: A Pivotal Role for PAR2. *J. Neurosci.* **32**, 14178–14183 (2012).
24. Dau, T., Sarker, R. S. J., Yildirim, A. O., Eickelberg, O. & Jenne, D. E. Autoprocessing of neutrophil elastase near its active site reduces the efficiency of natural and synthetic elastase inhibitors. *Nat. Comm.* **6**, 1–8 (2015).
25. Schulz-Fincke, A.-C., Blaut, M., Braune, A. & Gütschow, M. A BODIPY-Tagged Phosphono Peptide as Activity-Based Probe for Human Leukocyte Elastase. *ACS Med. Chem. Lett.* **9**, 345–350 (2018).
26. Edgington, L. E. & Bogyo, M. In vivo imaging and biochemical characterization of protease function using fluorescent activity-based probes. *Curr. Protoc. Chem. Biol.* **5**, 25–44 (2013).

| Pt # | Symptoms | Medication | Pathology | Endoscopy |
|------|--------------------------|----------------------|--|---------------------------------------|
| 1 | none | none | normal tissue | none |
| 2 | none | none | normal tissue | none |
| 3 | none | none | normal tissue | none |
| 4 | none | none | normal tissue | none |
| 5 | flare-up, 15-20 bm/d | Steroids, biologic | chronic inflammation, severe activity | pancolitis, Mayo 3 distal, 2 proximal |
| 6 | flare-up, 10 bm/d | none | chronic inflammation, moderate to severe activity | pancolitis, Mayo 2 |
| 7 | chronic active, 4 bm/d | none | chronic inflammation, mild activity | proctitis, Mayo 1 |
| 8 | chronic active, 2-3 bm/d | 5-ASA | chronic inflammation, marked activity | pancolitis, Mayo 3 distal, 2 proximal |
| 9 | new onset, 6-8 bm/d | none | chronic inflammation, moderate activity | pancolitis, Mayo 2 |
| 10 | chronic active, 12bm/d* | Steroid enema, 5-ASA | chronic inflammation, mild activity | proctitis, Mayo 2 |
| 11 | flare-up, 6-8 bm/d | Imuran | acute, chronic inflammation, deep ulcers | ileocolitis, deep ulcers |
| 12 | flare-up, 4-5bm/d | 5-ASA | chronic inflammation, severe activity | colitis |
| 13 | flare-up, pain, +2bm/d | 5-ASA | normal tissue; chronic stricture with no active inflammation | ileal stricture, blind biopsies |
| 14 | flare-up, 2-5bm/day | none | chronic inflammation, moderate activity | pancolitis, Mayo 1-2 |

5-ASA = 5 aminosalicylic acid; *= mucous, but infrequent stool; ** suspected flare up initially but with further imaging dx. with chronic stricture with no active inflammation; bm = bowel movement, most were bloody

Table 1. Profiles of patients from which mucosal biopsies were collected.

FIGURE LEGENDS

Figure 1. Structures of PK105¹⁶, PK105b, and Cy5-V-DPP¹³.

Figure 2. Comparison of selectivity profile for PK105b and Cy5-V-DPP. (A) Recombinant serine proteases (neutrophil elastase, proteinase 3, or trypsin) were incubated with increasing concentrations of Cy5-V-DPP or PK105b and binding was assessed by in-gel fluorescence. (B) Kinetic measurements of recombinant neutrophil elastase activity using the fluorogenic substrate probe, AAPV-AMC in the presence of DMSO (vehicle control) or the indicated concentration of PK105b, Cy5-V-DPP or Sivelestat. Error bars are shown as mean \pm SEM. (C,E) Lysates from mouse bone marrow or pancreas were incubated with increasing concentrations of Cy5-V-DPP or PK105b and binding was assessed by in-gel fluorescence. (D,F) PK105b-labeled lysates were immunoprecipitated with antibodies for neutrophil elastase, pancreatic elastase (PE) or trypsin 3 (Try3), as indicated. In (F), gain settings for pulldowns were enhanced in order to observe faint bands (right panel). Note: Cy5-V-DPP and PK105b labeling are depicted at equal gain settings, set independently for each sample type.

Figure 3. Detection of NE activity in *L. pneumophila*-infected lung tissue. (A) Lysates prepared from uninfected or *L. pneumophila*-infected lungs were labeled with 1 μ M PK105b and analyzed by in-gel fluorescence (n=3-5). *Indicates high-molecular weight species of unknown identity. (B) Total NE expression in the samples in (A) was measured by immunoblotting with an NE-specific antibody. (C,D) Densitometry analysis of active NE in (A) and total mature NE in (B), respectively. (E) Ratios of active to total mature NE in the samples. (F) Labeling of NE by PK105b in infected lung tissue was confirmed by immunoprecipitation with an NE-specific antibody. (G) Competition of PK105b labeling in an infected lung lysate with PK101. (H) PK105b labeling in neutrophils isolated from infected lung tissue, as analyzed by in-gel fluorescence (refer to Fig S1 for sorting strategy). Error bars are shown as mean \pm SEM.

Figure 4. Detection of NE activity in oral cancer tissues. (A) Lysates prepared from normal mouse tongues or HSC-3 oral cancer tissues were labeled with 1 μ M PK105b and analyzed by in-gel fluorescence (n=3-5). *Indicates high-molecular weight species of unknown identity. (B) Total NE expression in the samples in (A) was measured by immunoblotting with an NE-specific antibody. (C,D) Densitometry analysis of active NE in (A) and total mature NE in (B), respectively. (E) Ratio of active to total mature NE in the samples. Error bars are shown as mean \pm SEM. (F) NE labelling in cancer tissue was confirmed by immunoprecipitation with an NE-specific antibody. (G) Competition of PK105b labeling in oral cancer tissue lysate with PK101.

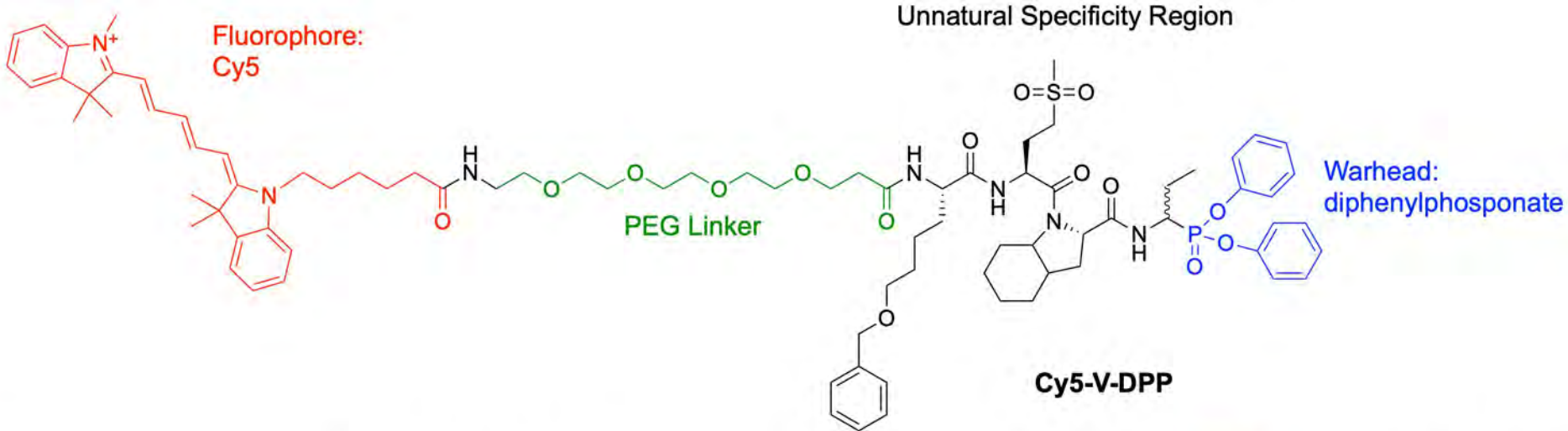
Figure 5. Application of PK105b to measure NE activation in acute experimental colitis. (A) Distal or proximal colons were excised from mice with acute colitis induced by TNBS and labeled *ex vivo* with 1 μ M PK105b. Probe binding was detected by in-gel fluorescence (n=3-5). *Indicates high-molecular weight species of unknown identity. (B) Immunoblotting of samples in (A) with an NE-specific antibody to reveal total NE expression. (C) Merged image of PK105b labeling (active NE; magenta) and immunoblot (total NE expression; green). (D) Immunoprecipitation of PK105b-labeled inflamed distal colon lysate with a NE-specific antibody. (E) Competition of PK105b labeling in inflamed distal colon lysates with PK101. (F) In-gel fluorescence and NE immunoblot of distal colon lysates with or without PK105b labeling. (G) Distal colon lysates from A labeled with Cy5-V-DPP.

Figure 6. Luminal protease activity in acute experimental colitis. (A-B) Labeling of luminal fluids or fecal pellets from control or TNBS-treated mice with PK105b. (C) Immunoprecipitation of PK105b-labeled fecal samples with NE, PE, or trypsin 3-specific

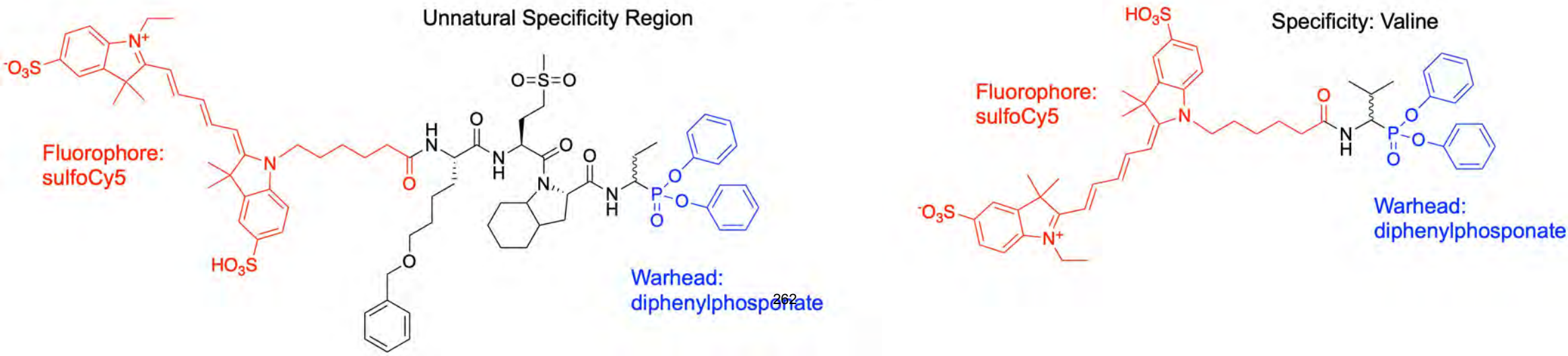
antibodies. Gain settings for the pulldowns were enhanced in order to observe faint bands (right panel).

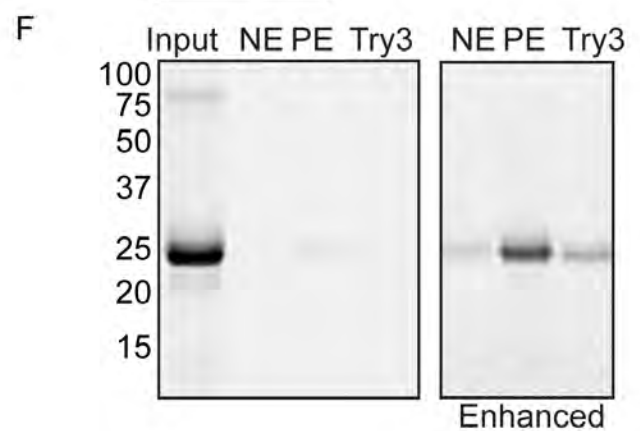
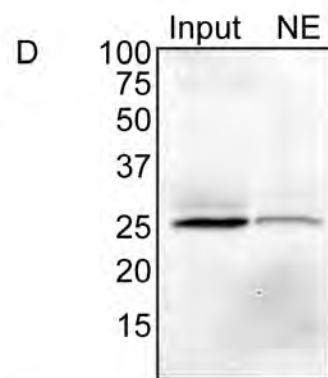
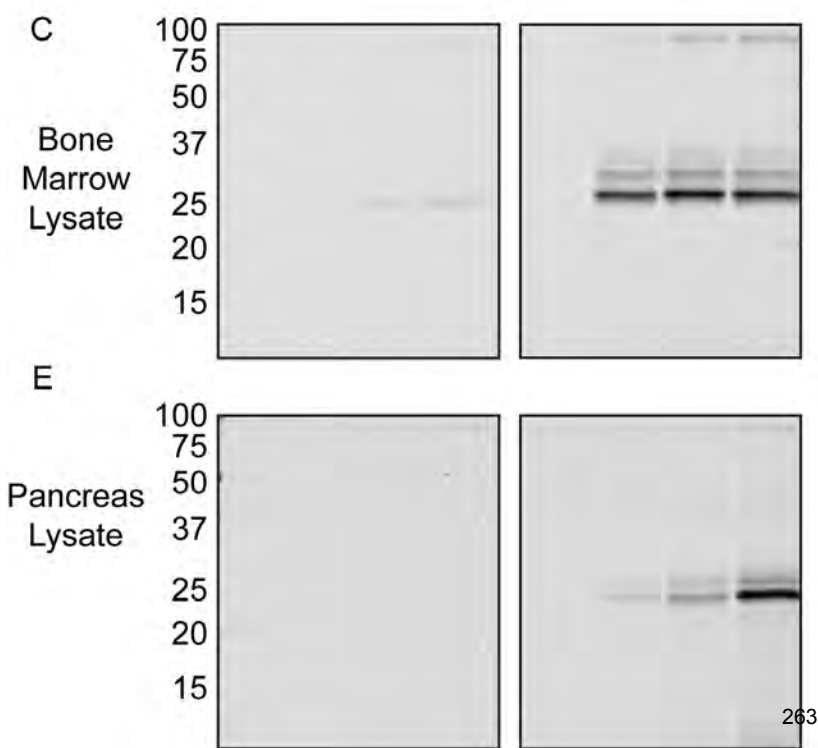
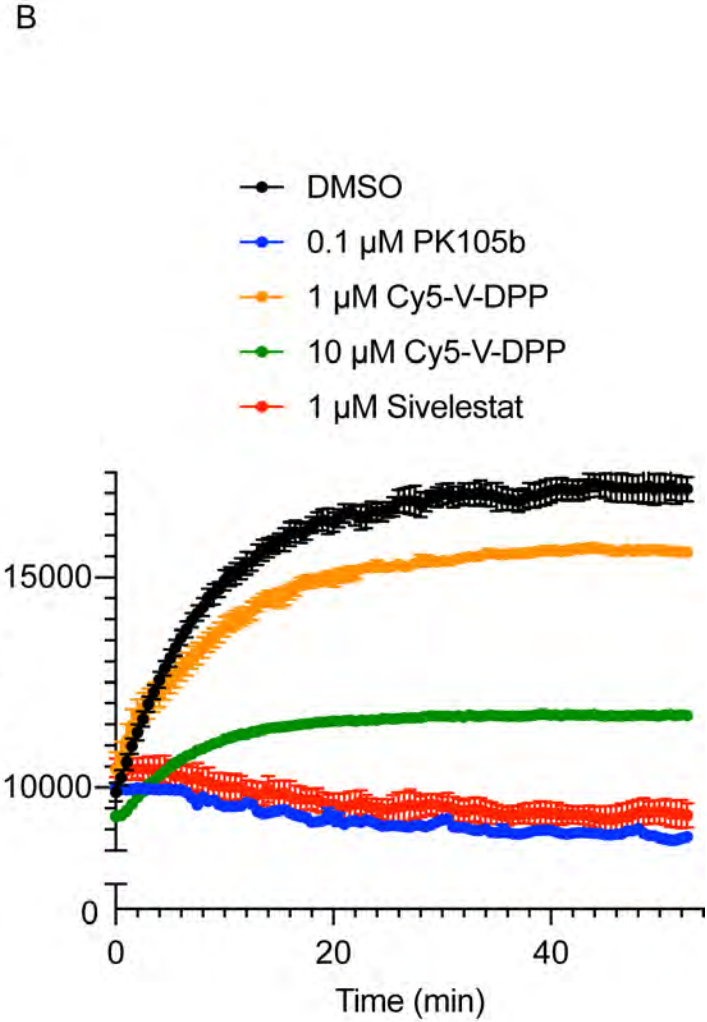
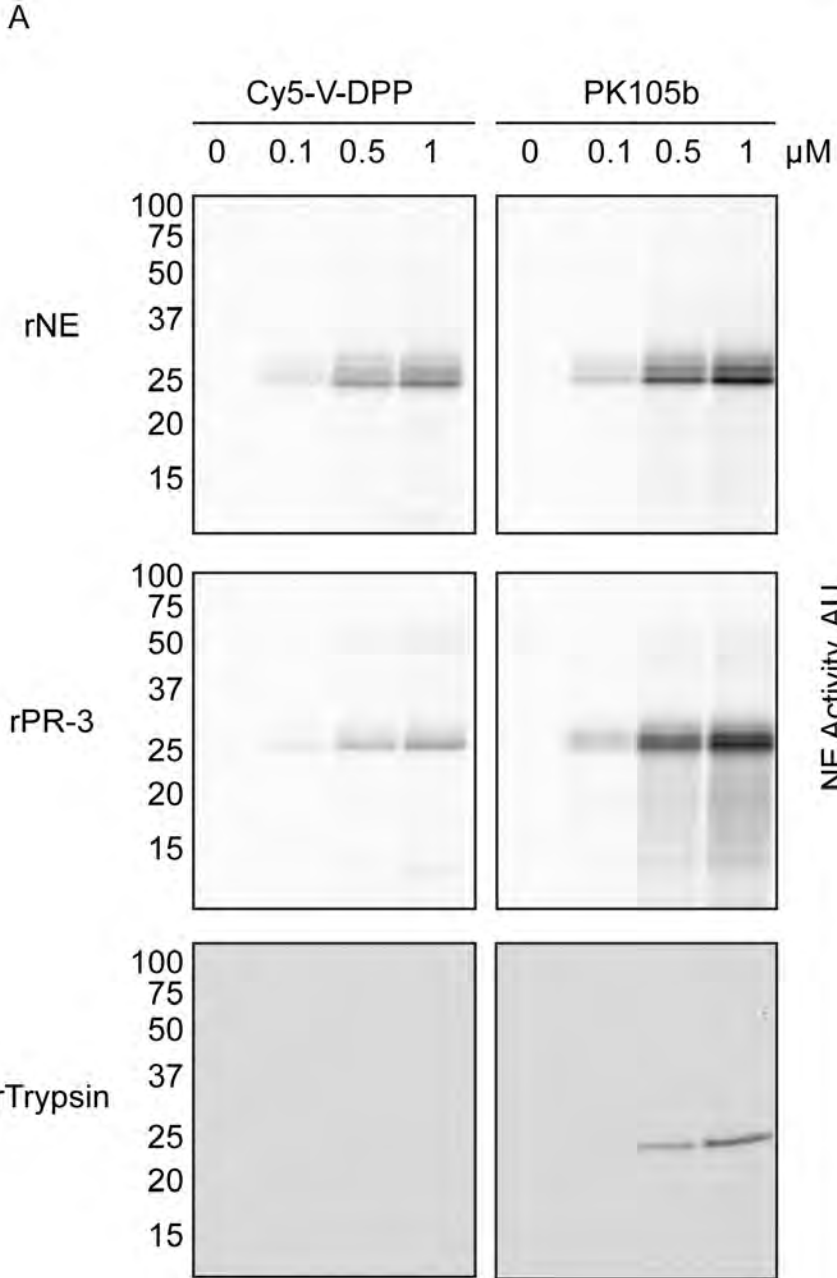
Figure 7. Application of PK105b to measure NE activation in mucosal biopsies from patients with IBD. (A) Mucosal biopsies from healthy controls (n=5) or patients with active UC (n=9) were labeled *ex vivo* with 1 μ M PK105b. Probe binding was assessed by in-gel fluorescence. (B) Samples in (A) were immunoblotted for total NE expression. (C) Merged image of PK105b labeling (active NE; magenta) and immunoblot (total NE expression; green). (D,E) Densitometry of active NE in (A) and total mature NE in (B), respectively. (F) Ratio of active to total mature NE in the biopsy lysates. Error bars are shown as mean \pm SEM. (G) Immunoprecipitation of PK105b-labeled UC biopsy lysates with an NE-specific antibody. Gain settings for pulldown were enhanced in order to view faint bands (right panel). (H) Competition of PK105b labeling in inflamed colon lysates with PK101.

PK105

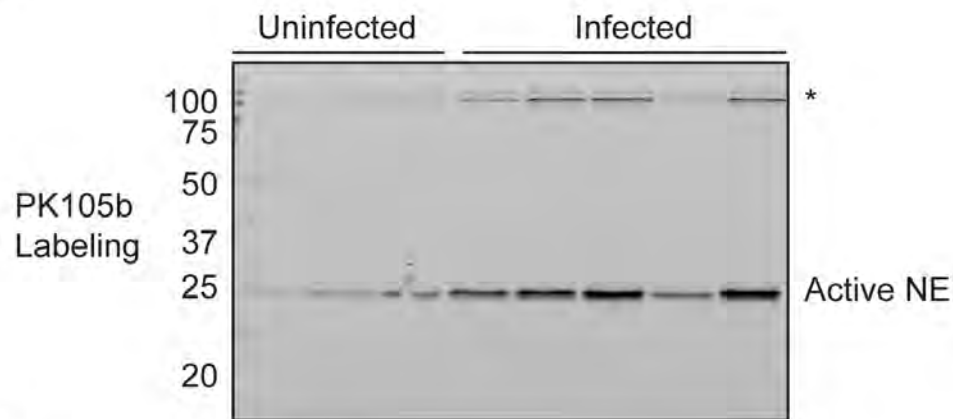


PK105b

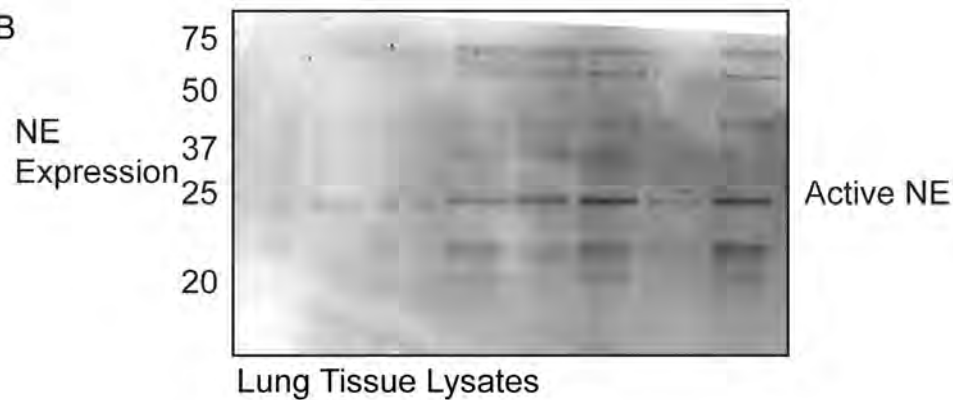




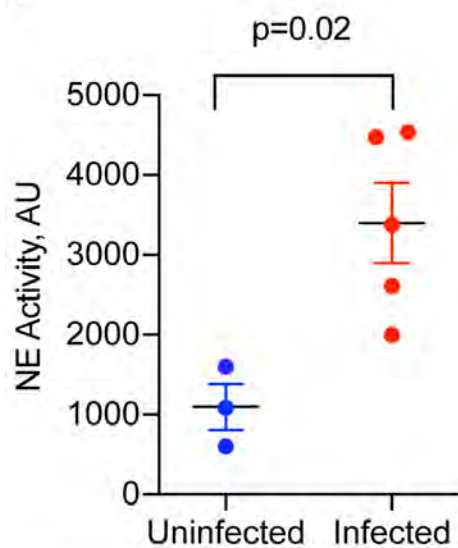
A



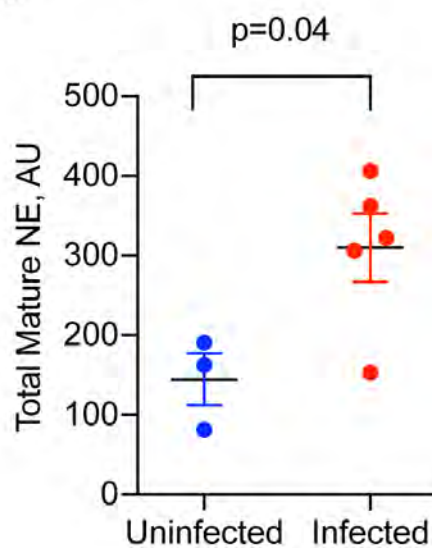
B



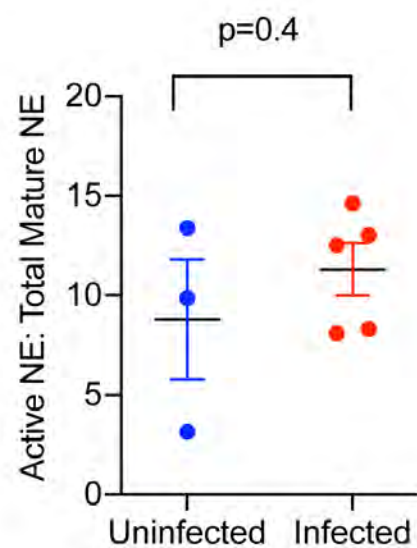
C



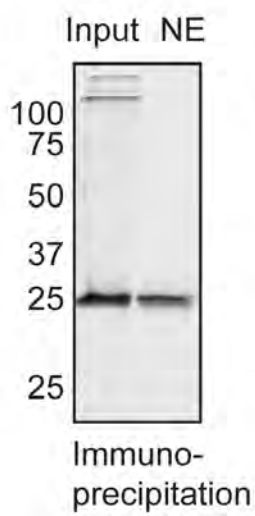
D



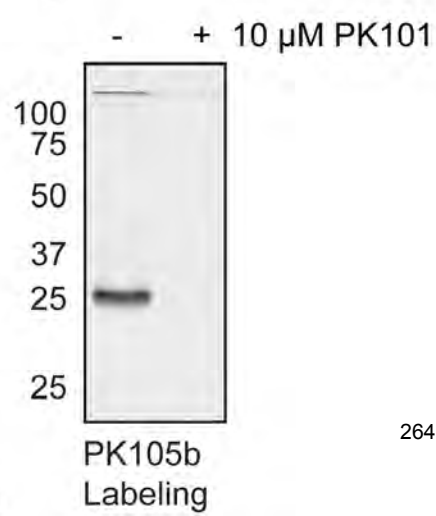
E



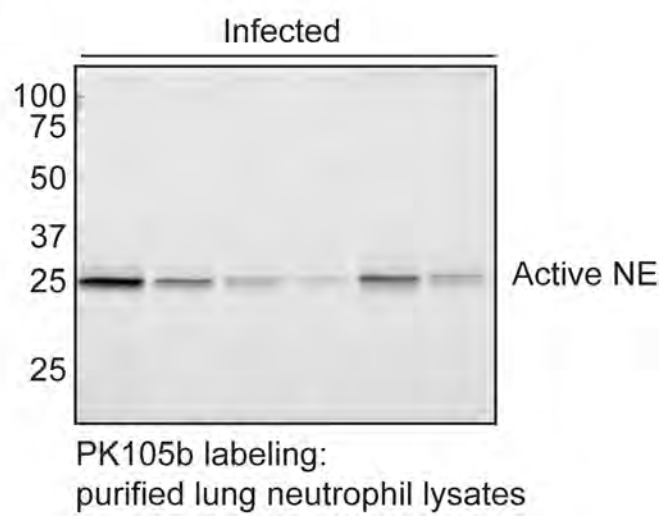
F

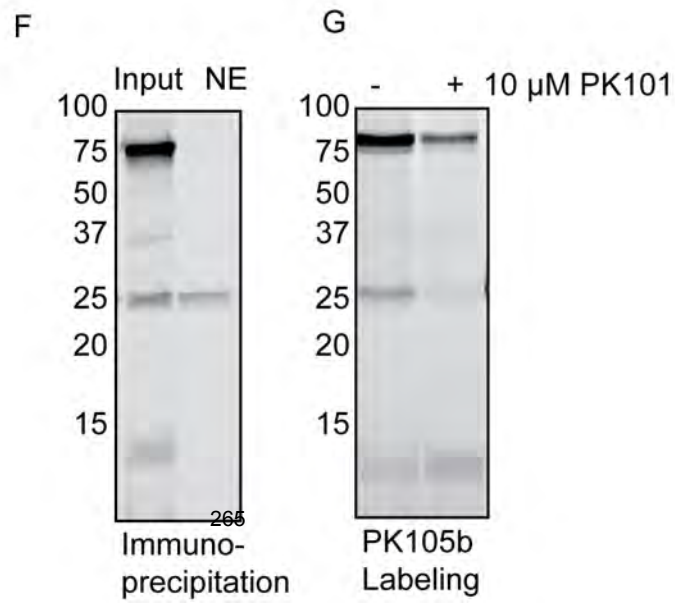
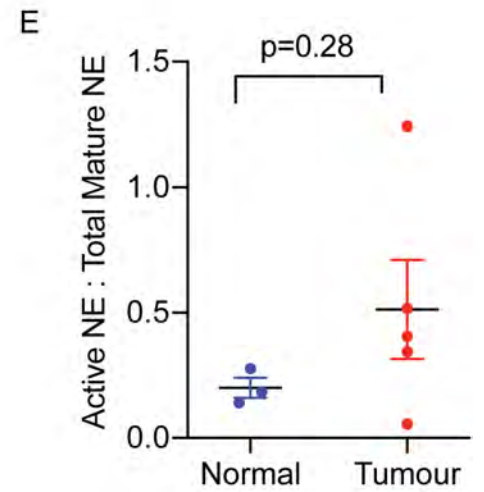
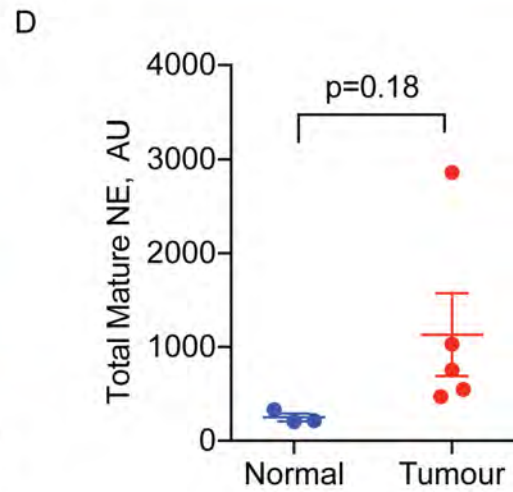
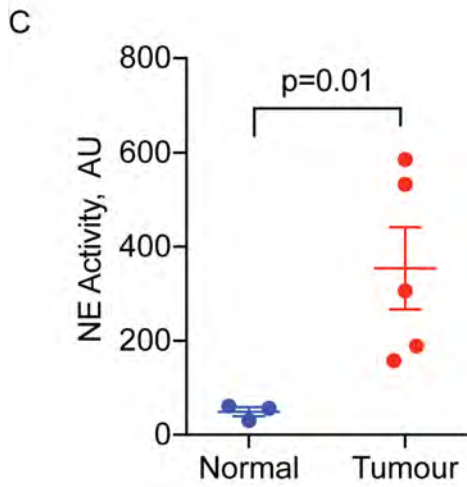
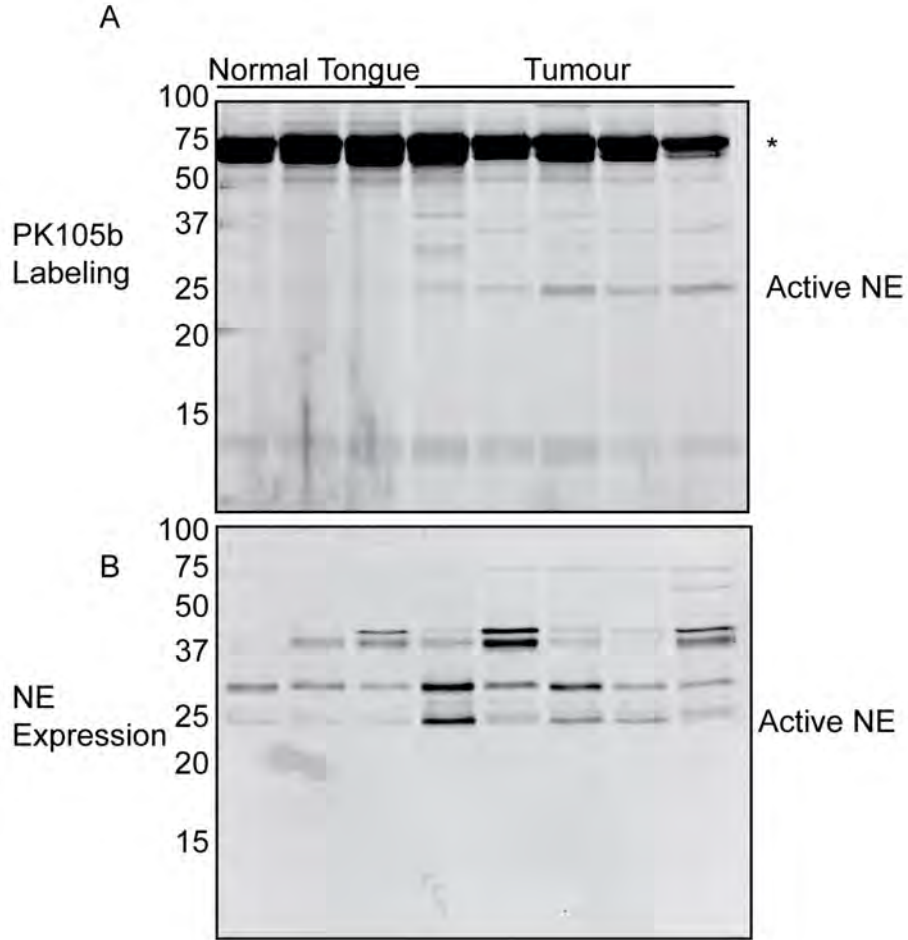


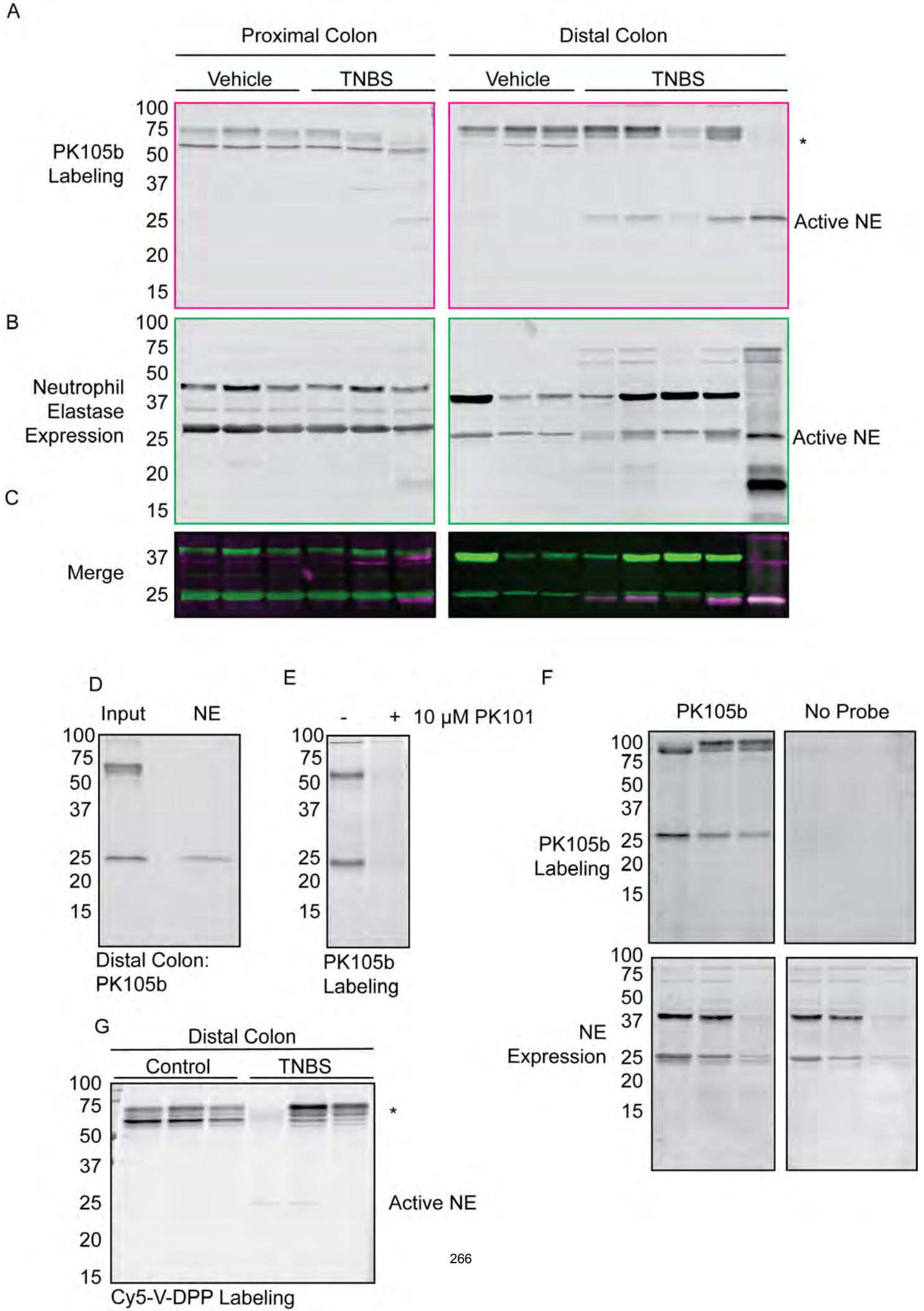
G

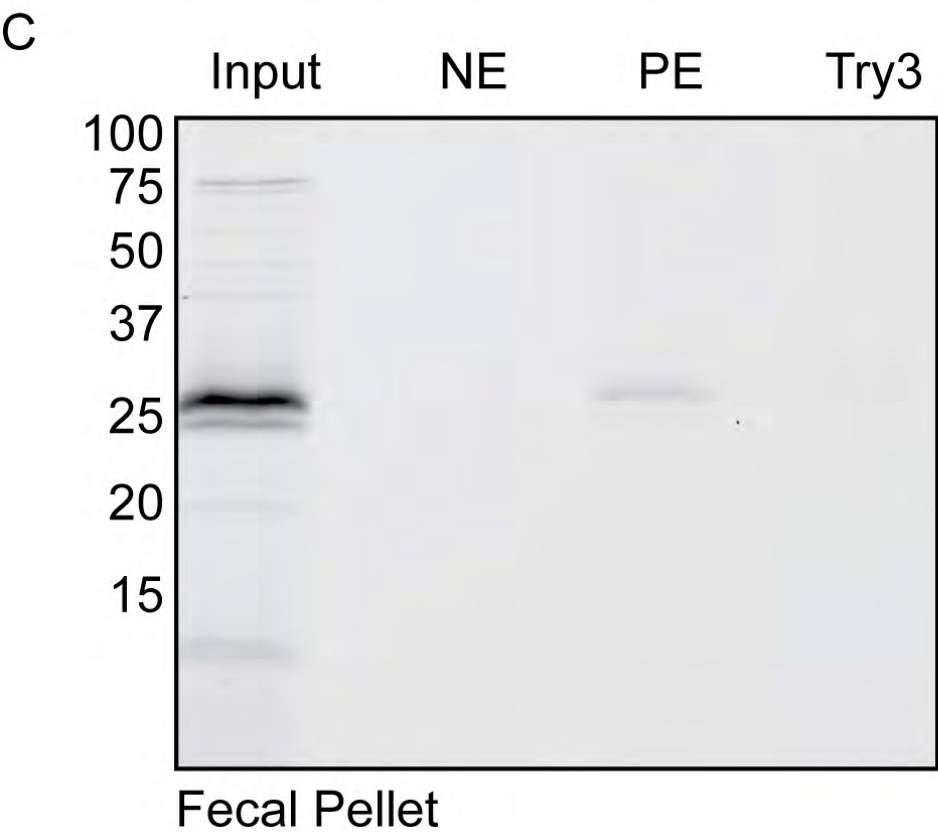
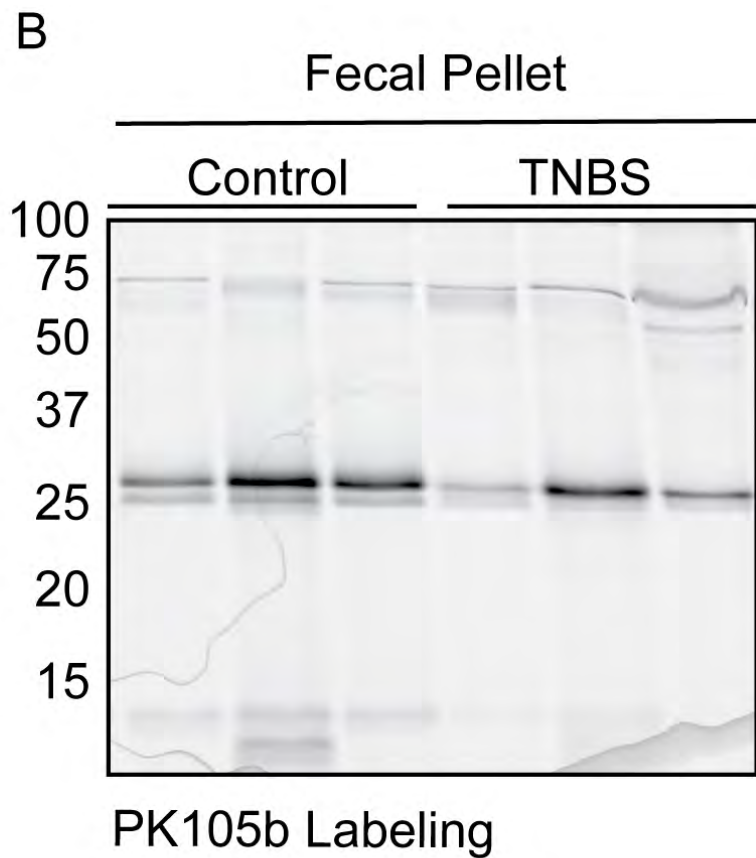
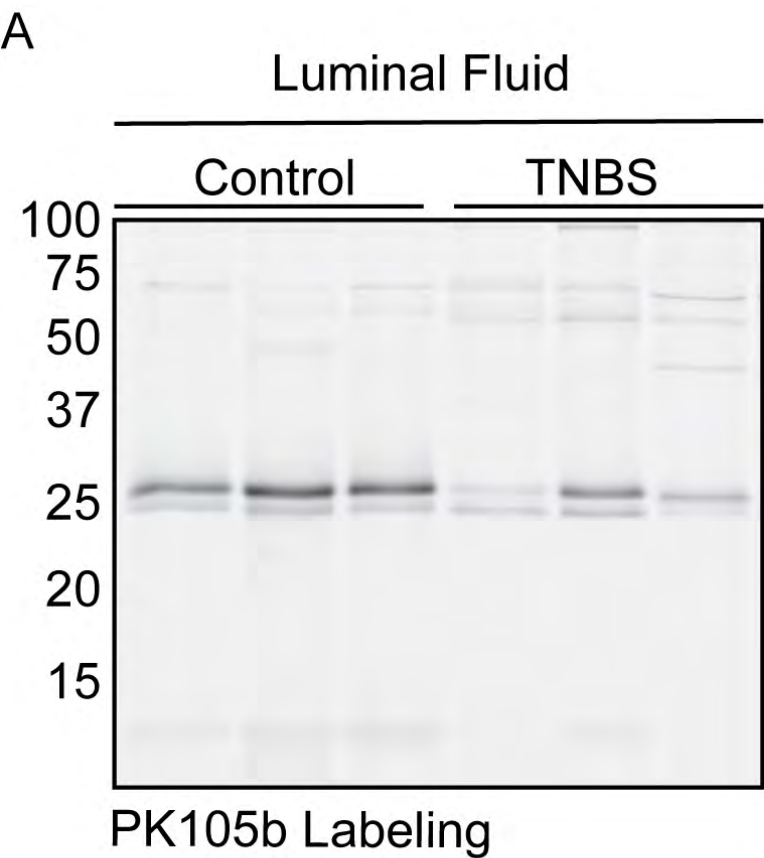


H









Human Mucosal Biopsies

